europhysics
conference
abstracts

13 th European Conference on

Controlled Fusion and Plasma Heating

Schliersee/14–18 April 1986

Contributed Papers, Part II
Editors: G. Briffod, M. Kaufmann

Published by: European Physical Society

Series Editor: Prof. S. Methfessel, Bochum

Managing Editor: G. Thomas, Geneva

Volume
10 C
Part II

13 th European Conference on

Controlled Fusion and Plasma Heating

Schliersee/14–18 April 1986

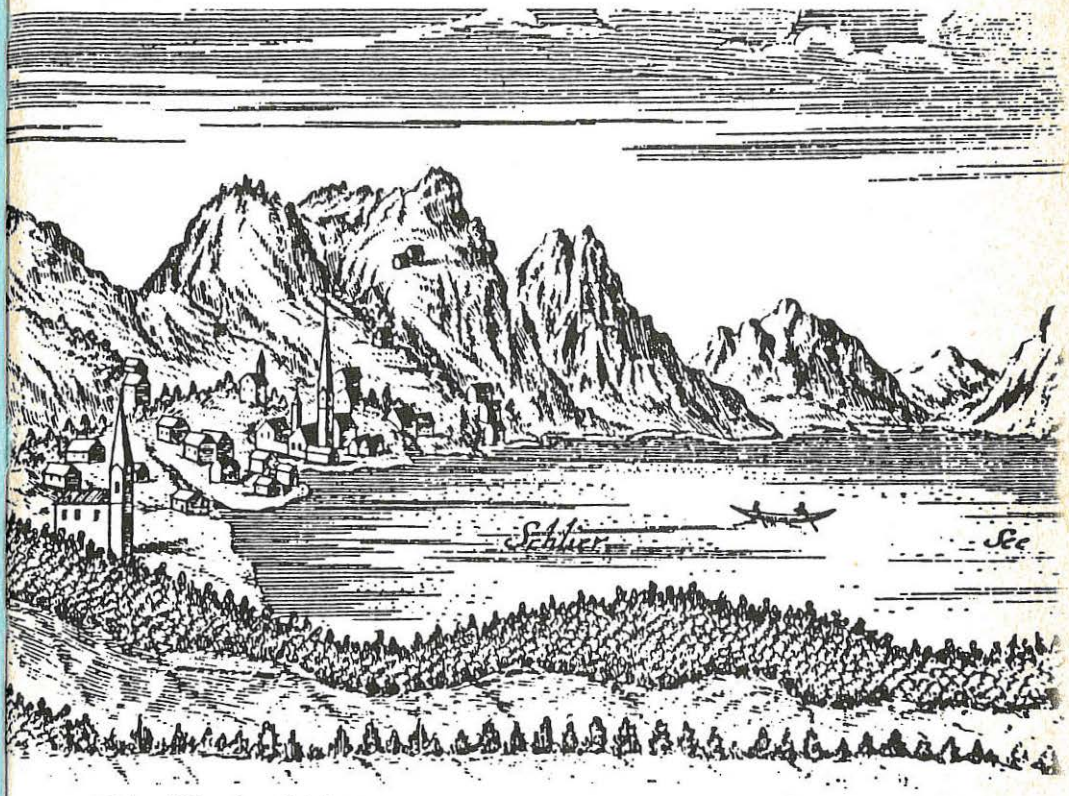

Michael Weening: Schliersee

Contributed Papers, Part II
Editors: G. Briffod, M. Kaufmann

ECA 10 C

EUROPHYSICS CONFERENCE ABSTRACTS is published by the
European Physical Society, 1986

The 13th European Conference on Controlled Fusion and Plasma Heating was held at Schliersee, Fed. Rep. of Germany from 14 to 18 April 1986. It was organized by Max-Planck-Institut für Plasmaphysik, Garching, Fed. Rep. of Germany on behalf of the Plasma Physics Division of the European Physical Society (EPS).

According to the new EPS arrangement the conference was held in spring and, because this is an even-numbered year, it concentrated on controlled fusion and plasma heating. The main topics therefore were

Plasma Confinement
Plasma Heating

with the following subtopics:

A Tokamaks
B Stellarators
C Alternative Confinement Schemes
D Plasma Edge Physics
E Alfvén and Ion Cyclotron Heating
F Electron Cyclotron Heating
G Neutral Injection Heating
H Lower Hybrid Heating and Current Drive

The Conference Programme included 18 invited lectures, 27 orally contributed papers and more than 200 papers presented in poster sessions.

The contributed papers of this 2-volume publication are photographically reduced in size from the originals provided by the authors.

Programme Committee/Paper Selection Committee

G. Briffod (Chairman), CEN, Grenoble, France
M. Kaufmann (Vice-Chairman), IPP, Garching, Fed. Rep. of Germany
T. Consoli, CEC, Brussels, Belgium
A. Gibson, JET, Abingdon, United Kingdom
C. Gormezano, CEN, Grenoble, France
G. Grieger, IPP, Garching, Fed. Rep.of Germany
H. DeKluiver, FOM, Nieuwegein, The Netherlands
F. Santini, ENEA, Frascati, Italy
V. Shafranov, Kurchatov Institute, Moscow, USSR
E. Sindoni, University of Milan, Milan, Italy

The invited papers and two post deadline orally contributed papers will be published by Pergamon Press in the journal "Plasma Physics and Controlled Fusion" Vol. 28 No. 9a and sent free of charge to each registered participant.

CONTENT OF VOLUME II

VOLUME I

A. TOKAMAKS

Oral Presentations

Poster Presentations

Poster Presentations

Poster Presentations

Poster Presentations

B. STELLARATORS

Oral Presentations

Poster Presentations

Poster Presentations

C. ALTERNATIVE CONFINEMENT SCHEMES

Oral Presentations

Poster Presentations

Poster Presentations

D. PLASMA EDGE PHYSICS

Poster Presentations

E. ALFVEN AND ION CYCLOTRON HEATING

Oral Presentations

Poster Presentations

Poster Presentations

VOLUME II

Poster Presentations

F. ELECTRON CYCLOTRON HEATING

Oral Presentations

Poster Presentations

Poster Presentations

G. NEUTRAL INJECTION HEATING

Oral Presentations

Poster Presentation

(see next page)

VOLUME II

Poster Presentations

H. LOWER HYBRID HEATING AND CURRENT DRIVE

Oral Presentations

Poster Presentations

VOLUME II

Poster Presentations

Poster Presentations

Alfvén and Ion Cyclotron Resonance Heating

ICRF H-MODE AND $2\Omega_{CH}$/D(H)-MINORITY HEATING ON ASDEX

K.Steinmetz, F.Wagner, F.Wesner, A.Izvozchikov[1], J.-M.Noterdaeme, F.Ryter[2], J.Bäumler, G.Becker, H.S.Bosch, M.Brambilla, F.Braun, H.Brocken, A.Eberhagen, R.Fritsch, G.Fussmann, O.Gehre, J.Gernhardt, G.v.Gierke, E.Glock, O.Gruber, G.Haas, J.Hofmann, F.Hofmeister, G.Janeschitz, F.Karger, M.Keilhacker[3], O.Klüber, M.Kornherr, K.Lackner, M.Lenoci[4], G.Lisitano, E.van Mark, F.Mast, H.M.Mayer, K.McCormick, D.Meisel, V.Mertens, E.R.Müller[3], H.Murmann, H.Niedermeyer, A.Pietrzyk[5], W.Poschenrieder, S.Puri, H.Rapp, H.Röhr, J.Roth, K.-H.Schmitter, F.Schneider, C.Setzensack, G.Siller, P.Smeulders[3], F.Söldner, E.Speth, K.-H.Steuer, O.Vollmer, H.Wedler, D.Zasche

Max-Planck-Institut für Plasmaphysik, Euratom Association,
D-8046 Garching, FRG

INTRODUCTION

ICRH experiments in the ASDEX divertor tokamak have now been operated in the $2\Omega_{CH}$ regime and D(H)-minority mode. This paper presents the status of these investigations and compares some of the most interesting features of the RF scenarios with neutral beam heating (NI) in the same machine under optimized and reproducible plasma parameters. The achievement of the H-mode with ICRH alone is reported. Considerations on possible synergetic effects of the combination of ICRH with NI /1/ and impurity studies during ICRH /2/ are presented separately.

$2\Omega_{CH}$ (67 MHz) and D(H)-heating (33.5 MHz) experiments are being routinely conducted in excess of 2 MW launched power for pulse lengths of up to 1 s. In addition to the combined scenarios of NI + ICRH, pure $2\Omega_{CH}$ and D(H) heating up to maximal power have now been applied in extensive studies of diverted discharges and in the case of carbonised walls /3/.

EXPERIMENTAL RESULTS

Electron and ion heating properties of both RF scenarios are compared in Figs. 1 and 2. Direct central electron heating (Fig. 1) measured via the initial slope of the sawteeth is clearly higher in the minority mode than at $2\Omega_{CH}$. The electron heating efficiency, $\bar{n}_e \Delta T_e(0)/P^{IC}_{dep}$ of about 4.0 and $1.8 \cdot 10^{13}$ eV/kW cm^3, for D(H) and $2\Omega_{CH}$ (H-plasma), respectively, is also higher in the minority case ($n_H/n_e \sim 0.05$), which, however, was partly due to the better confinement properties of deuterium plasmas. Figure 2 presents the ion heating at RF power below 1 MW: The minority regime exhibits an efficiency as high as the NI H-mode ($4.2 \cdot 10^{13}$ eV/kW cm^3, $H^o \rightarrow D^+$) /4/, which is consistent with the good confinement observed at that RF power level (see Figs. 4 and 5).

Now to the global heating efficiencies of the various scenarios: Recent investigations on $2\Omega_{CH}$-heating and its combination with NI gave rather promising results /5/. When combining ICRH with NI, an important question is whether the RF heating efficiency becomes improved with increasing T_i (target) or by coupling of the IC wave to the fast beam particles. In the case of carbonised walls where heating is not degraded by deleterious impurity radiation, the increase of T_i due to NI preheating (Fig. 3)

---

[1]Academy of Sciences, Leningrad, USSR; [2]CEN Grenoble, France; [3]Assigned to JET Joint Undertaking, England; [4]ENEA Frascati, Italy; [5]University of Washington, Seattle, USA

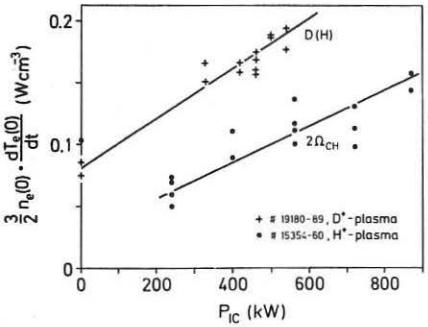

Fig. 1: Direct e-heating of $2\Omega_{CH}$ and D(H) scenarios.

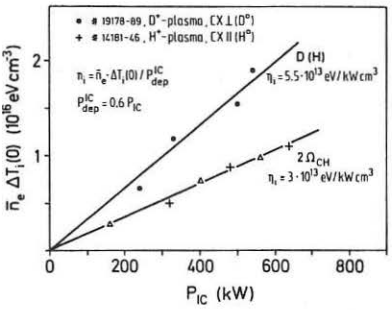

Fig. 2: Ion heating for both ICRF regimes.

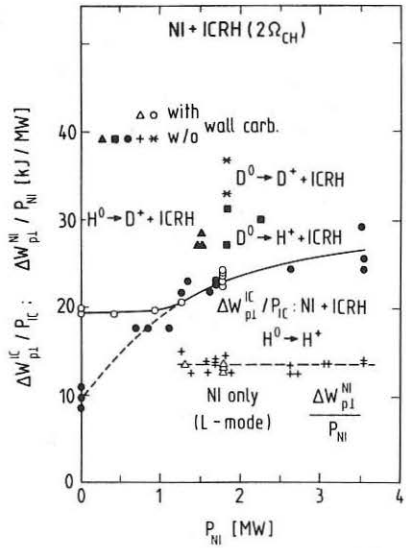

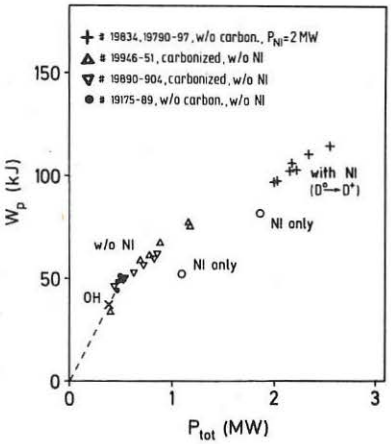

Fig. 4: Plasma energy versus total heating power for D(H), NI and NI+D(H) heating

Fig. 3: Heating efficiencies of $2\Omega_{CH}$, NI and NI+$2\Omega_{CH}$

improves the IC efficiency only by about 25 % from about 20 kJ/MW (w/o NI, $T_i \sim 0.5$ keV) to 25 kJ/MW at $P_{NI} = 3.5$ MW ($T_i \sim 2.2$ keV). Coupling of the IC wave to the beam is in fact observed in CX-spectra, but obviously to an extent which is not sufficient enough to improve the heating: On comparison of ICRH discharges with additional $H^0 \rightarrow D^+$ or $D^0 \rightarrow H^+$ (Fig. 3) the RF efficiency turns out to be independent of the beam species. Owing to the isotope effect on confinement $2\Omega_{CH}$-heated discharges in deuterium and helium with a small amount of hydrogen ($n_H/n_e > 10$ %) show even better efficiencies ($D^0 \rightarrow D^+ +$ ICRH in Fig. 3). No heating at the fourth IC harmonics of D^+ and $^4He^{2+}$ could be noted.

As a general feature, energy and particle confinement of ICRH-heated plasmas are systematically better than those of the NI L-mode but appear still within the combined error bars. The plasma energy for minority heating at low power scales as well as the ohmic phase (Fig. 4). With increasing RF power W_p bends towards an L-mode behaviour, staying, however, at a slightly higher level than NI. In combination with NI, W_p and thus τ_E^I are improved, too, a feature also observed at $2\Omega_{CH}$ /5/. The energy confinement times of $2\Omega_{CH}$, D(H) and NI(L) modes normalized to the ohmic values are presented in Fig. 5. Careful experimental investigations on the RF power absorption lead to $\alpha = 0.6$ and 0.7, without and with beam preheating respectively. For pure NI heating $\alpha = 0.8$ to 0.9 was found, in good agreement with the beam deposition calculations. As shown for various $2\Omega_{CH}$ regimes, carbonisation strongly reduces the central radiation /2, 3/, thus improving the confinement. At high power ($P_{IC} \sim 5\ P_{OH}$) both RF scenarios reach about equal τ_E^I ($\sim 0.6\ \tau_E^\Omega$) while below 700 kW the D(H)-confinement still remains as good as the ohmic one. Assuming equal global heating efficiencies (~ 20 kJ/MW) for the D(H) and 2Ω modes, but with W_p^{OH} (D(H), D^+-plasma) > W_p^{OH} ($2\Omega_{CH}$, H^+-plasma) the superior confinement of D(H) at low power in comparison to $2\Omega_{CH}$ can be explained.

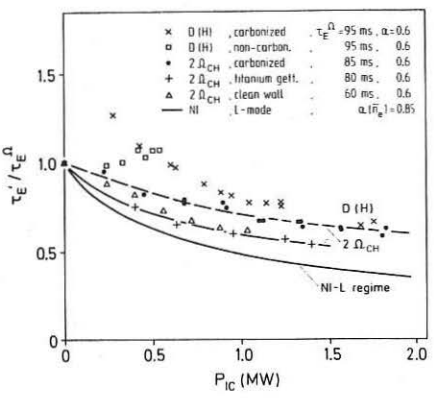

Fig. 5: Normalized confinement times versus launched RF power for various heating scenarios.

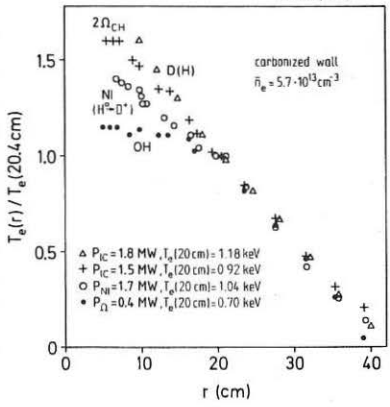

Fig. 6: Normalized T_e profiles of OH, NI, $2\Omega_{CH}$ and D(H)

Rather narrow power deposition profiles are expected theoretically for ICRF heating. In fact, ICRH is accompanied by T_e profiles strongly peaked on axis (Fig. 6) confirming a rather local power deposition. Well outside the q = 1 zone, however, the profiles of OH, ICRH (2Ω, D(H)) and NI appear to be almost invariant if normalized to T_e at $r \sim a/2$ indicating a 'profile consistency' within the so-called confinement zone /6/. When the IC resonance layer is shifted from the plasma centre to half radius, the T_e profile does not vary much while the global heating is maintained with slightly reduced sawteeth amplitude.

ICRF H-mode studies have been performed with and without NI. In combination with NI under optimized conditions the additional ICRF power can switch the plasma into the H-mode. For the first time, the H-mode has

been achieved with ICRH alone in the D(H)-minority regime at an absorbed RF power of about 1.1 MW. The H-mode is marginally reached showing all characteristic signatures of rising n_e and W_p, and frequent ELMs (Fig. 7). The typical development of an edge electron temperature pedestal is also

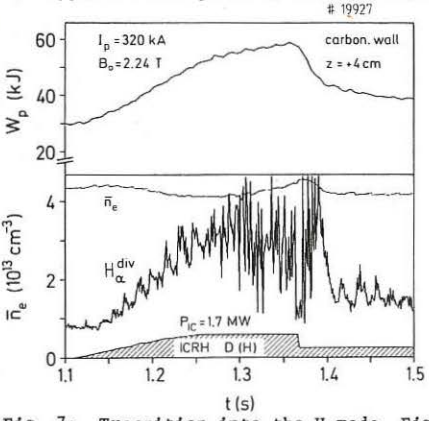

Fig. 7: Transition into the H-mode of an ICRF-heated plasma.

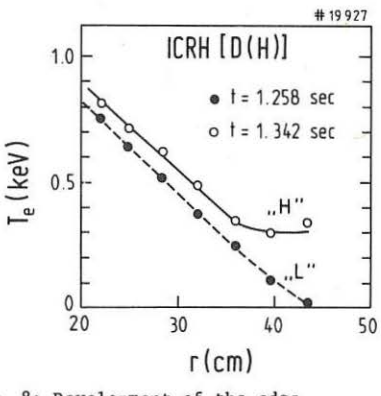

Fig. 8: Development of the edge T_e profile in the ICRH L and H-phase.

observed (Fig. 8) which is rather similar to the behaviour found with NI heating /7/. The occurrence of a short ELM-free H-phase (see Fig. 7 at t = 1.365 s) gives rise to a shrinking of the scrape-off-layer and changes the antennae coupling to such an extent, however, that in all cases one of the RF generators terminates operation by voltage breakdown in the vacuum line when operating at the RF power limit. To keep the H-mode with ICRH somewhat higher RF power than available at present appears to be necessary.

CONCLUSIONS

Global heating and confinement of $2\Omega_{CH}$ and D(H)-regimes are found to be almost equal at high RF power and appear to be well comparable to or even somewhat better than the NI L-mode. For the first time ICRH has now shown the potential to access the H-mode.

ACKNOWLEDGEMENTS

The kind help of J. Winter and P. Wienhold (KFA Jülich) in providing the CD_4-gas for carbonisation, and the excellent support of the ASDEX, ICRH and NI operation teams are gratefully acknowledged.

REFERENCES

/1/ F. Wagner et al., this conference.
/2/ G. Janeschitz et al., this conference.
/3/ W. Poschenrieder et al., this conference.
/4/ A. Stäbler et al., Proc. 4th Int. Symp. on Heating in Toroidal Plasmas, Rome, Vol. I (1984) 3.
/5/ K.Steinmetz et al., Plasma Physics and Controlled Fusion 28 (1986) 235.
/6/ H. Murmann et al., this conference.
/7/ M.Keilhacker et al., Plasma Physics and Controlled Fusion 26 (1984) 49.

Energy Confinement Scaling of ICRF-Heated Plasmas in JIPP T-IIU Tokamak

Y. Ogawa, R. Akiyama, R. Ando, Y. Hamada, S. Hirokura, J. Fujita, E. Kako, K. Kawahata, Y. Kawasumi, S. Kitagawa, K. Masai, K. Matsuoka, A. Mohri, S. Morita, M. Mugishima, N. Noda, K. Ohkubo, I. Ogawa, M. Sasao, K.N. Sato, S. Tanahashi, Y. Taniguchi, K. Toi, T. Watari, K. Yamazaki,

Institute of Plasma Physics, Nagoya University,
Nagoya 464, Japan

ABSTRACT

For an ICRF-heated plasma with a heating power density of 1.6 MW/m^3, the radiation is successfully suppressed at the level of 20~30% for the total input power. The deterioration of the energy confinement time is observed as the rf power is increased ($\tau_E \propto P_{tot}^{-\alpha}$, α=0.2~0.4), but it is not so remarkable compared with an NBI L-mode scaling (α=0.58). Significant improvement is also observed, as the plasma current is increased. also observed. From the temporal evolutions of the electron temperature, the deposition profile of the rf power is estimated fitting to the form of $P_{rf,e}(r)=P_{rf,e}(0)(1-(r/a)^2)^k$ with $P_{rf,e}(0)$=1.57MW/m^3 and k=1.7. It is also estimated that the electron thermal diffusivity χ_e is ~ 0.65 m^2/s at $n_e = 9\times 10^{19}$ m^{-3}.

1. Introduction: In the JIPP T-IIU tokamak (R/a = 0.91m/0.23m, B_T = 3T) a high power ICRF heating up to 1.6 MW has been conducted, where two-ion-hybrid heating scheme is applied with 10 % hydrogen minority, and the rf with the frequency of 40 MHz is launched from the high-field-side. We have paid much attension to reduce the radiation for ICRF-heated plasmas. We have carried out *in situ* carbon coating (called as carbonization in TEXTOR[1]), and achieved a remarkable reduction of the radiation loss. From spectroscopic and bolometric measurements, it is confirmed that iron, which is a dominant source in the case of no carbonization, is remarkably suppressed, and the radiation power at the plasma center is reduced with a factor of ~ 1/20. The detail of the carbonization is presented elsewhere[2] . Furthermore, we have done antenna phasing experiments with five antennas installed side by side, by changing the phase relations between them continuously from $\Delta\varphi$=0 to $\Delta\varphi=\pi$. However, the radiation was not reduced so much by the antenna phasing[3] . By using this radiation-loss-reduced plasma, the global property of the energy confinement time τ_E and one-dimensional transport characteristics are examined for ICRF-heated plasmas with various diagnostics.

2. Global Characteristics of ICRF-Heated Plasmas: The total stored energy is independently derived with two methods, i.e., W_{mag} from $(\beta_P+l_i/2)$ and W_{kin} from the integration of plasma parameters. The electron temperature $T_e(r,t)$ is measured with a 10-channel ECE grating polychromator, the ion temperatures $T_{H,D}$ (r=0,t) are with a mass-separated charge exchange analyzer and a neutron detector, and the line-averaged density is with 2mm wave and HCN laser interferometers. The internal inductance l_i is evaluated with the electron temperature profile measured. As the input power is increased, the current profile becomes slightly flat; i.e., l_i = 1.4 for P_{rf} = 0 and l_i = 1.27 for P_{rf} = 1.25 MW. Figure 1 shows the total stored energy as a function of the total input power ($P_{WI}+P_{rf}$). A good agreement is shown between the values of

W_{mag} and W_{kin} , and the slight difference at the high power level may be attributed to the high energy component of hydrogen ions, which is not taken into the estimation of the kinetic energy W_{kin} .

The global energy confinement time τ_E ($=W_{mag}/(P_{OH}+P_{rf})$) is plotted in Fig. 2 for two cases of I_P=320 kA and 280 kA. The deterioration of the energy confinement time can be seen as the input power is increased. The empirical L-mode scaling derived by Kaye-Goldston [4] is also shown for I_P=320 kA and $\bar{n}_e$ =9× 10^{19} m^{-3} . The dependence on the input power ($\tau_E \propto (P_{OH}+P_{rf})^{-\alpha}$, α=0.2 ~ 0.4), however, is weaker than that of K-G scaling (α = 0.58). The rf power absorbed inside the confinement region is derived from the decay rate of the total stored energy, yielding $W_{mag} \sim 0.8 \cdot P_{rf}$. Plotting the effective confinement time τ_E^* defined by $W_{mag}/(P_{OH}+0.8 \cdot P_{rf})$ as a function of the effective input power (i.e., $P_{OH}+0.8 \cdot P_{rf}$), it could be stressed that the degradation of the confinement time becomes much weaker than that of K-G scaling. In addition, Fig. 2 shows that the confinement time strongly depends on the plasma current, which is similar to the L-mode characteristics. From these results, we expect for the ICRF-heated plasma that the energy confinement time is less deteriorated as the rf power is increased, compared with the L-mode scaling of NBI-heated plasmas, and is improved with higher plasma current.

3. One-Dimensional Transport Analysis for ICRF-Heated Plasmas: We have analyzed the electron transport for an I_P = 280 kA discharge with P_{rf} = 0.9 MW. The temporal evolutions of the electron temperature obtained with ECE measurement are shown in Fig. 3. The plasma density is raised during the rf pulse from $\bar{n}_e$ = 3.5× 10^{19} m^{-3} to $\bar{n}_e$ = 8× 10^{19} m^{-3} . The electron temperature increases up to $T_e(0)$ = 2.0 keV, and begins to decrease during the rf pulse due to the density increase, but the electron stored energy does not decrease, as shown in Fig. 1. From the analysis of the decay rate just after the rf power is turned off, the deposition profile of the rf power to electrons is derived, as shown in Fig. 4. It is fitted to the form of

$$P_{rf,e}(r) = P_{rf,e}(0)(1 - (r/a)^2)^k \quad , \qquad (1)$$

with $P_{rf,e}(0)$ = 1.57 MW/m^3 and k = 1.7. The total absorbed power evaluated by integrating eq.(1) gives 0.53 MW, although the total rf power is P_{rf} = 0.9 MW. This discrepancy is reasonably accounted for, because the coupling of the rf power to the core plasma is 80%, among which the fraction for the electron heating is calculated to be 80% with Fukuyama's code [5] .

Here we should remark that the amplitude of sawtooth is not so large ($\Delta T_{p-p}/\bar{T}$~ 20%) compared with those in JET and PLT ($\Delta T_{p-p}/\bar{T}$~ 40-50%) [6,7] . This difference of the sawtooth amplitude would be attributed to the heating mode; that is, in JIPP T-IIU the power deposition is relatively broad, as shown in Fig. 4, since the plasma is heated by the mode-converted Ion Bernstein wave, while in JET and PLT the power deposition is very localized around the ion cyclotron layer. Therefore, the deposition power inside q=1 surface (r/a = 0.3) is about 20-30% in JIPP T-IIU, which is relatively small compared with that in JET (50-80%).

The electron heat conduction can be evaluated with a high accuracy for the radiation loss reduced plasma. The electron thermal diffusivity χ_e is given by

$$\chi_e(r) = \frac{1}{4\pi^2 R_0 r n_e(r) \left| \frac{\partial T_e}{\partial r} \right|} \int_0^r (P_{OH} + P_{rf,e} - P_{ei} - P_{rad} - \dot{W}_e - P_{conv.}) dV_P \quad . \qquad (2)$$

In Fig. 5, each term in the right-hand-side of eq.(2) is plotted as a function of the minor radius, and the value of χ_e is also presented. Inside $q < 1$ ($r/a \sim 0.3$) and outside $r/a \sim 0.7$, the values of χ_e have less meaning, because of the sawtooth relaxation and the convection effect, respectively. At the region $0.3 < r/a < 0.7$, the conduction loss is dominant, the other loss channels (P_{ei} , P_{rad} *etc.*) being insignificant. The value of χ_e is around 0.65 m^2/s at $n_e = 9 \times 10^{19}\ m^{-3}$, and shows a broad profile because the density profile is very flat at $r/a < 0.7$ in this experiment. The energy confinement time determined by the electron heat conduction, $\langle \tau_E \rangle$ ($= a^2/(4\chi_e)$), is calculated to be $\sim$ 20 ms. Since the value of $\langle \tau_E \rangle$ is consistent with the global energy confinement time τ_E, given in Fig. 2, we could say that the electron heat conduction govern the plasma confinement for almost whole plasma volume.

References

[1] J. Winter *et al.*, J. Nucl. Mater., 128&129 (1984) 841.
[2] N. Noda *et al.*, to be published in Jpn. J. Appl. Phys..
[3] R. Ando, to be published.
[4] S.M. Kaye and R.J. Goldston, Nucl. Fusion 25 (1985) 65.
[5] A. Fukuyama, *et al.*, Nucl. Fusion, 23 (1983) 1005.
[6] J. Jacquinot *et al.*, Plasma Physics and Controlled Fusion, 28 (1986) 1.
[7] J.C. Hosea *et al.*, 12th Europ. Conf. on Plasma Physics and Controlled Fusion, 2 (1985) 120.
[8] M. Kasai *et al.*, Nucl. Fusion, 25 (1985) 1437.

Figure Captions

Fig. 1 Total stored energies, derived from the magnetics W_{mag} and the kinetics W_{kin} , as a function of the total input power $P_{OH}+P_{rf}$. The time behaviours of the electron and ion stored energies are also shown.

Fig. 2 Global energy confinement time τ_E defined by $W_{mag}/(P_{OH}+P_{rf})$ as a function of the total input power $P_{OH}+P_{rf}$ for I_P=320 kA (circles) and 280 kA (triangles). The energy confinement time derived by Kaye-Goldston is also plotted (solid line) for I_P=320 kA and $\bar{n}_e = 9 \times 10^{19}\ m^{-3}$.

Fig. 3 Temporal evolutions of the electron temperature for different major radius, measured with a 10-channel ECE grating polychromator.

Fig. 4 Deposition profile of the rf power to electrons derived from the decay rate of the electron temperature just after the turn off of the rf power. These data are fitted to the form of $P_{rf,e}(r) = P_{rf,e}(0)(1-(r/a)^2)^k$ with $P_{rf,e}(0) = 1.57\ MW\ m^{-3}$ and $k = 1.7$.

Fig. 5 Local power balance derived from the experimental data and the electron thermal diffusivity χ_e as a function of the minor radius (r/a).

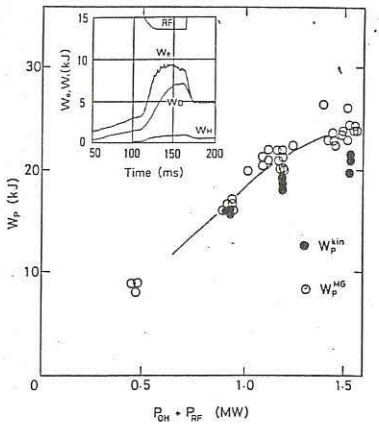

Fig. 1

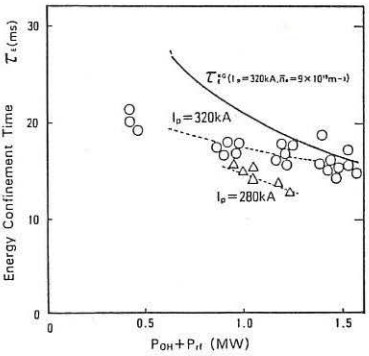

Fig. 2

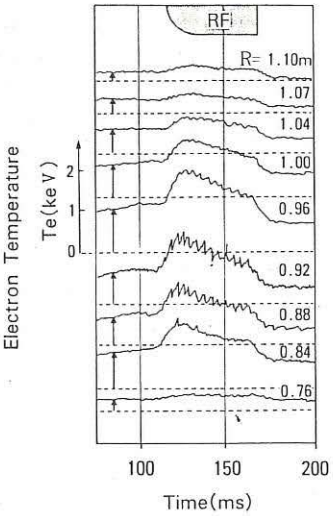

Fig. 3

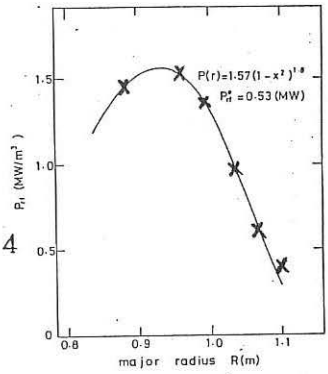

Fig. 4

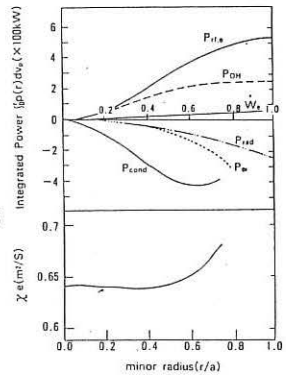

Fig. 5

ICRF HEATING OF PASSING IONS IN TMX-U*

A. W. Molvik, G. Dimonte,† J. Barter,† R. Campbell,† W. F. Cummins, S. Falabella, S. W. Ferguson, J. H. Foote, P. Poulsen

Lawrence Livermore National Laboratory, University of California, Livermore, CA 94550

ABSTRACT

By placing ion-cyclotron resonant frequency (ICRF) antennas on both sides of a midplane gas-feed system in the central cell of the Tandem Mirror Experiment-Upgrade (TMX-U), our results have improved in the following areas: (a) The end losses out both ends show a factor of 3 to 4 increase in passing-ion temperatures and a factor of 2 to 3 decrease in passing-ion densities. (b) The passing-ion heating is consistent with Monte Carlo predictions. (c) The plasma density can be sustained by ICRF plus gas fueling as observed on other experiments.

I. SYMMETRIC PASSING-ION HEATING

We introduced ICRF heating into the TMX-U experiment to reduce the collisionality of passing ions and, thereby, keep the thermal-barrier collisional filling rate below the pumping rate [1]. This is one of the necessary conditions for successful operation of a thermal-barrier tandem mirror. A thermal barrier is a depression of the plasma potential in each end cell that isolates central-cell electrons from the warmer electrons at the positive potential peak, which provides axial plugging [2]. ICRF heating can reduce filling both by heating the passing ions and by reducing their density through trapping in the central cell.

The locations of ICRF antennas and resonances, electron-cyclotron resonant heating (ECRH) resonances, and gas fueling are shown in Fig. 1. The ICRF system is discussed in greater detail elsewhere [3,4].

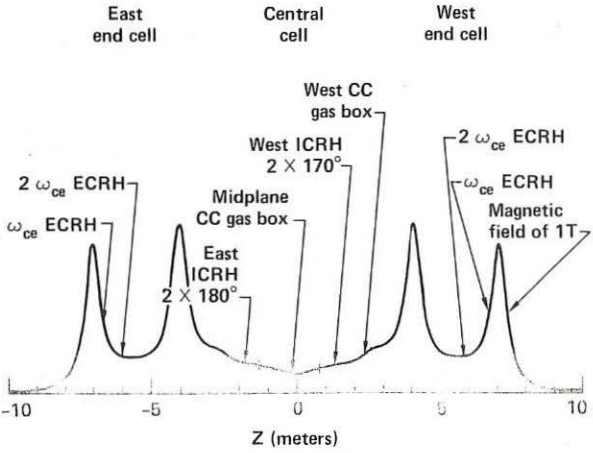

Fig. 1. TMX-U fueling and rf heating locations with a magnetic-field strength that reaches a maximum of 2.3 T. Lines between the antennas and the midplane CC (central-cell) gas box indicate the ion-cyclotron resonance locations.

Previous experiments in TMX-U used gas fueling 2.25 m west of the central-cell midplane, and a double half-turn loop 1.26 m west of the midplane [3]. These experiments demonstrated efficient perpendicular heating of trapped ions, and good agreement between plasma loading and the predictions of the code [5] ANTENA. Figure 2 shows measurements with a new diagnostic: the end-loss ion spectrometers (ELIS) [6]. The ELIS measures: the plasma potential from the low energy cutoff of the ion distribution, the parallel ion temperature (which we equate with the passing-ion temperature) from the slope below the high energy cutoff, and the end-loss current density from the integral of all the channels. For the east-end losses that passed through ICRF resonances, the bulk of the ion-energy distribution was heated; whereas, for the west-end losses that did not have to pass through a resonance, the bulk of the ion distribution was much colder although a tail was heated to similar energies as the bulk in the east end. The west-end loss current (Fig. 2) was larger by a factor of 2 to 3.

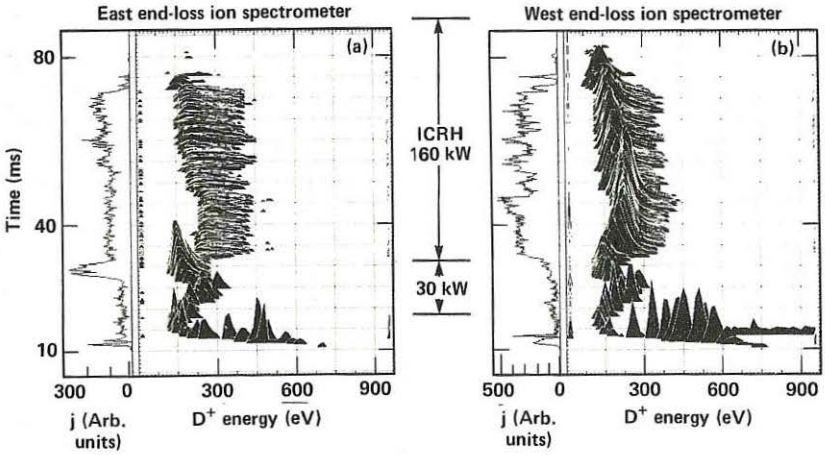

Fig. 2. Fueling from the West CC gas box results in heating toward the east end, but less toward the west because ions can flow to the west end without passing through an ICRF resonance where they would be heated or trapped. The currents and ion-energy distributions are from the ELIS. (3/12/86 Shot 29.) (Note that the current scales are different on each graph.) The CC density is 3 to 4 × 10^{12} cm^{-3}.

Present experiments use a more symmetrical arrangement, with gas fueling near the central-cell midplane (0.25 m east) and double half-turn antennas toward both ends of the central cell. The frequencies, 2.88 MHz east and 2.55 MHz west, are selected to provide an ion-cyclotron resonance that will damp slow waves between each antenna and the gas box. Newly ionized particles must make a minimum of one pass through a resonance before reaching an end cell. The disadvantage of midplane gas fueling is that the energy

confinement time is reduced because, on each bounce, the central-cell ions pass through the gas box, where they have a finite probability of being lost by charge exchange.

The results from the new arrangement are similar at both ends as predicted [7]: the end-loss bulk-ion temperature is increased by a factor of 3 to 4, and the end-loss current is reduced by a factor of 2 to 3 (Fig. 3). The collisional filling of the thermal barriers is proportional to $n_p T_p^{-1.5}$ [see Ref. 1], the passing-ion density and temperature. This filling rate is reduced by a factor of more than 10 for the data shown here. However, despite the reduction in passing-ion collisionality, the maximum density at which thermal-barrier operation is obtained has not increased significantly, indicating that other effects are limiting operation.

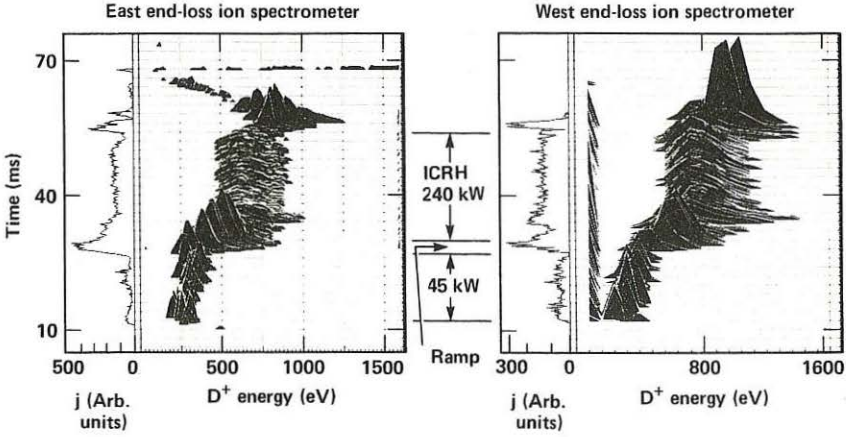

Fig. 3. Fueling from the midplane CC gas box results in similar increases in temperature and decreases in current for both ends.

II. COMPARISON WITH MONTE CARLO PREDICTIONS

We believe that the passing-ion heating occurs in a single pass through the resonance because only the temperature at the nearest end is affected substantially when one ICRF system turns off earlier. Based on this observation, we plot the passing-ion temperature (measured by the east ELIS) vs the ICRF power radiated from the east antenna (Fig. 4) and find a nearly linear relationship. Similar results are obtained at the west end.

Figure 4 shows the predictions of a Monte Carlo code [8] by a line through three computed points. The code used the following parameters: central-cell density $n_c = 3 \times 10^{12}$ cm^{-3}, the data varied from 0.7 to 3.5 $\times 10^{12}$ cm^{-3}; electron temperature T_e = 42 eV compared with the data from 20 to 80 eV; a radial confinement time of 26 ms; and 0.5 of the radiated power absorbed by ions, compared with typical experimental efficiencies of 0.2 to 0.5. This agreement between code and experiment is quite good considering

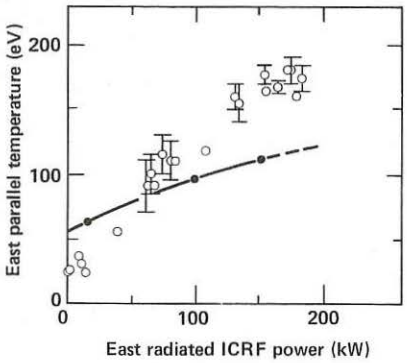

Fig. 4. The parallel ion temperature to each end, with midplane gas fueling, increases with the radiated power from the ICRF antenna nearest that end. The line is the Monte Carlo prediction described in the text. The CC density is 0.7 to 3.5 × 10^{12} cm^{-3}.

that the code has not been iterated with the data. For example, better agreement would be obtained by increasing T_e proportionally to the ICRF power in the Monte Carlo code as observed in the experiment.

III. ICRF-SUSTAINED OPERATION

Operation with the midplane central-cell gas-box fueling and ICRF power can sustain the plasma density and temperature in TMX-U as previously predicted [9] and demonstrated in other tandem mirrors [10], but which did not occur with the west gas-box fueling of TMX-U. We now typically sustain plasma densities of 1 to 3 × 10^{12} cm^{-3} for the duration of the ICRF and midplane gas.

*This work was performed under the auspices of the U.S. Department of Energy by the Lawrence Livermore National Laboratory under contract number W-7405-ENG-48.
†TRW, Redondo Beach, CA. 90278

REFERENCES

1. A. W. Molvik and S. Falabella, Lawrence Livermore National Laboratory Report UCID-19342 (1982).
2. D. E. Baldwin and B. G. Logan, Phys. Rev. Lett. 43, 1318 (1979).
3. A. W. Molvik et al., Proc. of the 4th Internat'l Symp. on Heating in Toroidal Plasmas, Rome, Italy, March 21-28, 1984, ISPP, p. 433.
4. S. W. Ferguson et al., Proc. of 11th Symp. on Fusion Engineering, IEEE, Austin, TX, Nov. 18-22, 1985.
5. B. McVey, MIT Report PFC/RR-84-12 (1984).
6. J. H. Foote et al., Rev. Sci. Instrum. 56, 1117 (1985).
7. A. W. Molvik et al., Proc. Sixth Topical Conference on Radiofrequency Plasma Heating, Callaway Gardens, GA, AIP, New York (1985), p. 79.
8. R. Campbell, T. Rognlien, and G. Dimonte, Lawrence Livermore National Laboratory Report UCID-20274 (1984), pp. 5-62.
9. J. Kesner et al., Nuc. Fusion 22, 549 (1982).
10. J. R. Ferron et al., Phys. Rev. Lett. 51, 1955 (1983).

POWER DEPOSITION PROFILES IN TEXTOR UNDER ICRH MODE CONVERSION CONDITIONS

R.R. Weynants,* D. Van Eester, V.P. Bhatnagar, R. Koch

Laboratoire de Physique des Plasmas - Laboratorium voor Plasmafysica
Association "Euratom-Etat belge" - Associatie "Euratom-Belgische Staat"
Ecole Royale Militaire - B 1040 Brussels - Koninklijke Militaire School

INTRODUCTION.

Ion-cyclotron resonance heating is applied to TEXTOR using two $\lambda/4$ antennae having the geometry shown in Fig. 1 [1]. In the present paper we derive the power deposition profiles obtained when launching 1 MW into a typical TEXTOR (H)-D plasma with $0.05 < \eta = n_H/n_D < 0.25$, $n_e = 4 \times 10^{13}(1 - r^2/a^2)\,cm^{-3}$, $T_e = 840(1 - r^2/a^2)^2\,eV$, $T_H = T_D = 650(1 - r^2/a^2)^2\,eV$, $f = 27$ MHz, $B_T = 2$ T, $R_o = 1.75$ m, $a = 0.46$ m, $I_p = 400$ kA, $j(r) = j_o(1 - r^2/a^2)^3$.

Coupling calculations yield antenna spectra which have a gaussian shape with a FWHM of $k_{//} = 6\ m^{-1}$ and a maximum $k_{//}$ of 13 m^{-1}. Given these values of $k_{//}$ and of η, theory [2] foresees that no tunneling can happen through the mode confluence zone existing in this two-component plasma. As the power is predominantly launched from the high field side (HFS), mode conversion heating will play the dominant role under these conditions.

The power deposition profiles are obtained using ray-tracing which allows for self-consistent evolutions of the $k_{//}$ spectrum. The final spectrum is found to bear little resemblance with that imposed by the antenna. In order to account for 100 % absorption of the mode converted ion Bernstein waves (IBW) we are forced to invoke harmonic damping of impurity ions, which even under the low impurity conditions reached on TEXTOR presents itself as a strong absorption mechanism.

Reasonable agreement is obtained between theory and experiment concerning the shape of the deposition profiles and the relative power sharing among the plasma species.

RAY-TRACING AND WAVE DISPERSION CHARACTERISTICS.

When using ray-tracing to study ICRH on a machine of the size of TEXTOR we are operating at the borderline of the applicability range of the applied

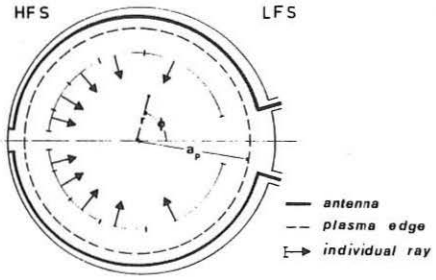

Fig. 1. Poloidal cross-section of the plasma with position of the two antennae and of the initial rays used in the ray-tracing.

technique [3, 4]. Ray-tracing is, however, up to now the only method suited to the study of local investigations of the various damping mechanisms on the IBW owing to a direct definition and self-consistent evolution of $k_{\parallel}$, the wavenumber parallel to the total magnetic field. The generated power deposition profiles can, a posteriori, be rendered plausible by noting that most of the absorption takes place on the short-wavelength IBW which satisfies the usual WKB requirements.

We start rays at r = 35 cm as shown in Fig. 1 with a typical initial k_θ value of 6 m^{-1}, k_ϕ = o and with a poloidal spacing chosen so as to give equal power to each ray. In Fig. 2, we plot the projections of some of these rays (aa', bb', cc') in the poloidal (r,ϕ) plane for the case η = 0.25. The rays shown leave the HFS boundary as magnetoacoustic waves (MAW). At a certain surface in the plasma the rays fold over and the wave nature changes to an IBW character. The envelope (caustic) of all rays constitutes a clear boundary separating a region where no ray can come, from one where through each point two rays can pass of MAW - or IBW-nature. To each point correspond then two $|k_\perp|$ values, the contour lines of which are also represented in Fig. 2. The family of equi-$|k_\perp|$ lines has the same envelope C_1 as the rays which is the line along which the surface $|k_\perp|$ (r, ϕ) is folded over.

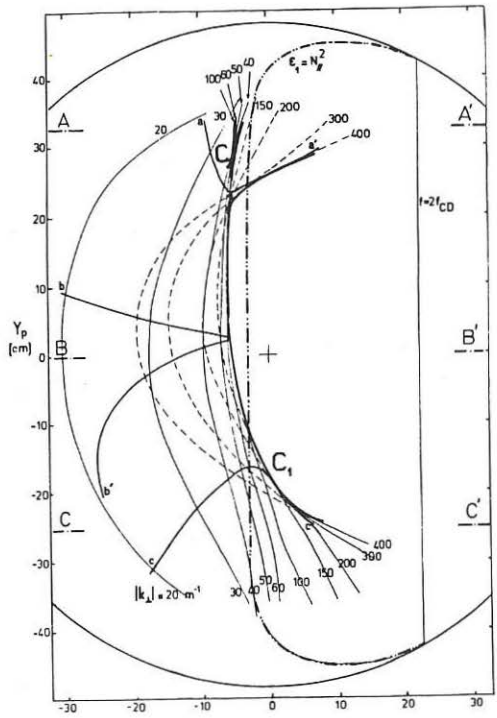

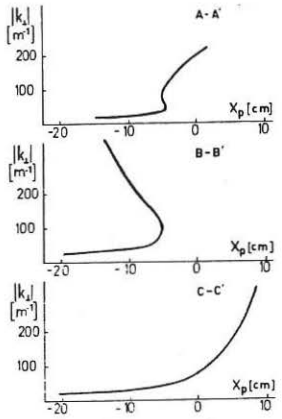

Fig. 3. Cuts through $|k_\perp|$-surface along AA', BB' and CC' of Fig. 2.

Fig. 2. Poloidal projection of typical ray-trajectories and equi-$|k_\perp|$ contours. Full lines belong to waves with MAW-character, broken ones to IBW.

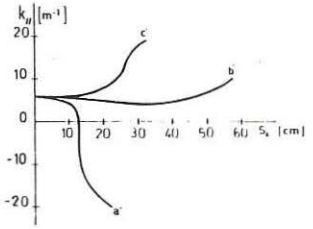

Fig.4. Evolution of $k_{\parallel}$ along poloidal projection of ray-trajectory for 3 rays of Fig.2.

The topology of this surface can be better appreciated with the aid of the cuts AA', BB' and CC' represented in Fig. 3. Of particular interest is cut AA' which reveals the existence of a subset of envelopes C_2, already discovered in [5]. The so-obtained mode conversion surface is, for large distances away from the y-axis [5, 6] and because the evolution of $k_{\parallel}$ is followed self-consistently, quite different from the traditional $\varepsilon_1 - c^2k_{\parallel}^2/\omega^2 = o$ line [7] which is shown for comparison.

This behavior of $k_{\parallel}$ is also of particular relevance for wave absorption. In Fig. 4, we plot $k_{\parallel}$ as a function of the distance along the poloidal projection of the trajectory $s_{\perp}$ for the three rays shown in Fig. 2. It can be recognized that, after conversion into an IBW and because of the presence of the poloidal magnetic field, the wave experiences huge variations of $k_{\parallel}$ [5], thus making the resulting power spectrum quite insensitive to the initial $k_{\parallel}$ conditions. Optimization of $k_{\parallel}$-shaping [8] under these conditions is not a trivial matter.

POWER DEPOSITION PROFILES.

Figure 5a shows for $\eta = 0.05$ the energy deposition profile p(r) obtained when launching 1 MW distributed evenly over the ten rays of Fig. 1 and when the usual damping mechanisms ($\omega = k_{\parallel}V_e$, $\omega = 2\omega_{CD}$, $\omega = \omega_{CH}$) are taken into account.

Compared to a typical OH deposition profile (inset of Fig. 5a) the rf profile is broad and the majority of power is taken by the electrons. The minority species are mainly heated by the rays coming from the LFS after many transits over the proton cyclotron layer (± 20 at $\eta = 0.05$ and ± 50 at $\eta = 0.25$) and will equilibrate mainly on the deuterons [9]. HFS rays such as cc' in Fig. 2 can also partly damp on the protons due to a strong broadening of the cyclotron layer width coming from a large $k_{\parallel}$ increase.

It should be stressed that the rays radiated from a certain sector of the antenna ($-165° < \phi < -120°$ for $\eta = 0.05$ and $135° < \phi < 160°$ for $\eta = 0.25$) end up in the plasma edge as essentially unattenuated IBW, due to too moderate $k_{\parallel}$ increases (ray b' of Fig. 4). As a result about 30 % of the launched power might be lost in the edge at $\eta = 0.05$ and 15 % at $\eta = 0.05$.

It was suggested recently [10] that an admixture of heavy ions might constitute an alternative damping mechanism, the IBW being subject to quite efficient damping at the first harmonic cyclotron layer of the impurity species. A satisfactory ray-tracing description can be obtained [11] by considering the impurity effects as a first order correction affecting the power transport but not the ray path.

Our calculations confirm that the intrinsic impurities in TEXTOR (e.g. O^{6+} at $n_{O^{6+}}/n_e = 0.005$) are capable of profoundly influencing the power balance. The different ionisation states are considered in accordance with coronal equilibrium and radially distributed according to published line brilliance distributions. The energy deposition profiles including the

impurity damping are shown in Fig. 5b. Note that some energy was depleted by the impurities at the expense of the electrons. The integrated power taken up by the different species shows that the absorption gap is now practically bridged :

η	e	H	O^{6+}
0.05	0.43	0.2	0.32
0.25	0.57	0.25	0.10

It should be stressed that the impurity ions develop a high energetic tail [9] of typically 40 keV such that 80 % or more of the energy they pick up is finally given to the electrons. We conclude that in both cases about 3/4 of the power is given to the electrons and 1/4 to the deuterons.

COMPARISON WITH THE EXPERIMENT.

The detailed experimental power balance [1] indicates that the average power density amounts to 0.14 W cm^{-3} with a maximum central power deposition of 0.23 W cm^{-3}, pointing to very broad deposition profiles such as implied by our calculations. The heat rate of electrons and ions is found to be 1.1 respectively 0.7 eV.$10^{13}cm^{-3}.kW^{-1}$. Given the expected difference in species confinement, the change in loop voltage and in equipartition power, these figures are not inconsistent with the above power sharing.

REFERENCES.

1. A.M. Messiaen et al.,Plasma Physics and Controlled Fusion 28(1985) 71.
2. M. Brambilla et al., Plasma Physics and Controlled Fusion 27(1985) 1.
3. M. Brambilla et al., Plasma Physics 24 (1982) 1188.
4. V.P. Bhatnagar et al., Nucl. Fusion 24 (1984) 955.
5. F.W. Perkins, Nucl. Fusion 17 (1977) 1197.
6. TFR Group et al., Nucl. Fusion 22 (1982) 1577.
7. R. Klima et al., Nucl. Fusion 15 (1975) 1157.
8. R.R. Weynants, Heating in Toroid. Plasmas, Vol.I (Roma,1984) 211.
9. T.H. Stix, Nucl. Fusion 15 (1975) 737.
10. A.V. Longinov et al.,Heating in Toroid.Plasmas,Vol.I(Roma,1984) 489.
11. R.R. Weynants et al., to be published.

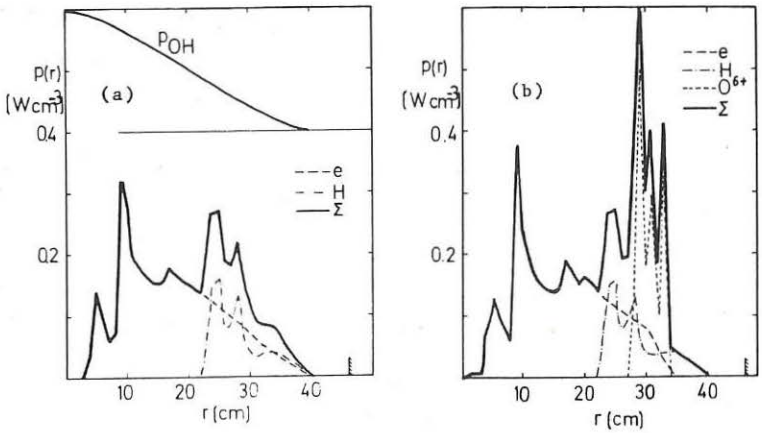

Fig. 5. Power deposition profiles for η = 0.05 without (a) and with (b) O^{6+} impurity. The inset of (a) shows a typical OH deposition profile.

* Senior Research Associate at the NFSR, Belgium.

IDENTIFICATION OF ION CYCLOTRON EMISSION FROM CHARGED FUSION PRODUCTS

G.A. Cottrell, P.P. Lallia, G. Sadler, P. van Belle

JET Joint Undertaking, Abingdon, Oxon, OX14 3EA

Abstract We have made measurements of the Ion Cyclotron Emission (ICE) Spectrum from JET D^+ ohmic plasmas using an ICRF antenna in reception mode. The spectra (10-100 MHz) show a number of bright emission peaks with (a) frequencies proportional to the magnetic field and (b) intensities correlated with the total DD neutron yield (Y_{DD}) of the discharge. We have compared the observed intensities of the spectra with the thermal black body emission and find the peaks to be of superthermal origin. We examine the hypothesis that the peaks are generated by the confined charged fusion products from the DD reaction which emit ICE at harmonics of the cyclotron frequency and have used a particle orbit tracing code to generate model spectra to assist interpretation of the data.

1. Introduction

The possibility of observing optically thick ($\tau >> 1$) ICE in large and dense thermonuclear tokamak plasmas has stimulated experiments on TFR (CLARK 1984) and JET (COTTRELL 1985) to attempt to measure emission from the thermal ions. However, in large and hot D^+ plasmas, the superthermal population of fusion products radiate significantly in the ion cyclotron frequency range. For deuterium, the following primary reactions take place with equal probability:

$$ {}^2_1D + {}^2_1D \begin{cases} \xrightarrow{50\%} {}^3_2He\ (0.8MeV) + {}^1_0n\ (2.5MeV) \\ \xrightarrow{50\%} {}^3_1T\ \ (1.0MeV) + {}^1_1P\ (3.0MeV) \end{cases} \qquad (1) $$

In addition, secondary reactions can take place between the fast products of (1) and the thermal deuterium:

$$ {}^3_2He + {}^2_1D \rightarrow {}^1_1P\ (14.6MeV) + {}^4_2He\ (3.7MeV) \qquad (2) $$

$$ {}^3_1T + {}^2_1D \rightarrow {}^4_2He\ (3.6MeV) + {}^1_0n\ (14.7MeV) \qquad (3) $$

In experiments reported here we have attempted to identify the mechanism for producing the ICE as emission from charged fusion products. We have done this by deliberately replacing the D^+ plasma ions by H^+ ions in the plasma thereby changing its fusion reactivity and observing changes to the ICE intensity.

2. Experimental

In a sequence of discharges with almost constant overall conditions (I_p = 2.0MA, B_T = 2.6T, $\bar{n}_e = 1.5 \times 10^{19} m^{-3}$), the deuterium ionic fraction was varied by changing the torus filling gas from D_2 to H_2.

Complete replacement of D^+ with H^+ could not be achieved owing to the desorption of residual deuterium from the vessel walls. However, within the range of concentration studied the total DD reaction rate, Y_{DD} (derived from 2.5 MeV neutron flux measurements (JARVIS et. al 1984)) varied by a factor of ~ 6. ICE measurements were made with the system described earlier (COTTRELL 1985); frequency and amplitude calibration of the detection system being made by mixing two standard frequency calibrators (20 and 50 MHz) with the incoming signal. Figure 1 shows two

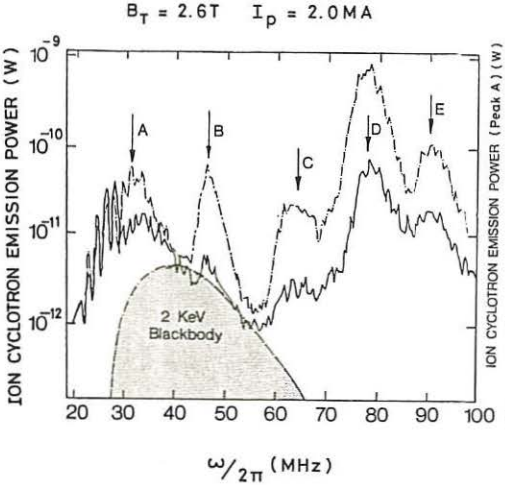

Figure 1: Ion Cyclotron Emission (ICE) spectra from two JET D^+ ohmic discharges with different DD fusion reactivities. Upper (dashed) curve obtained from a discharge with a total fusion neutron yield ~ 6 time the value corresponding to the lower (solid) curve. Other plasma parameters were almost constant. Also shown is the expected thermal black body spectrum ($\omega = 2\omega_{cD}$) from the majority ions.

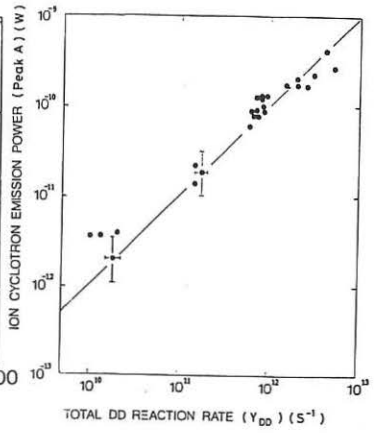

Figure 2: Variation of measured intensity of ICE peak A (see Fig 1) with the total DD reaction rate (Y_{DD}) determined from 2.5 MeV fusion neutron measurements.

superposed spectra from two discharges, each having different values of Y_{DD}. Prominent peaks can clearly be seen in both spectra; qualitatively these spectra are similar to ones published earlier (COTTRELL 1985) in which the frequencies of the peaks were found to be proportional to the applied magnetic field of the discharge indicating a cyclotronic origin. However, in the present experiments we have found the amplitude of the ICE to increase with total DD fusion yield Y_{DD} (Figure 2). The linear correlation of ICE power (of the 31MHz (peak A) in Fig 1) with Y_{DD} is consistent with emission from a primary DD fusion product (Eq.1).

It is of interest to compare the measured ICE level with the expected thermal black body level from the bulk ions (temperature T_i). In the (H)D minority regime we would expect the plasma to be close to optically thick.

The blackbody power which can be coupled to the antenna is then given by: $P_{BB} = kT_i \left[1 - \rho_c^2\right] \Delta f \, \Delta\Omega \, \Delta A$ where ρ_c is the voltage reflexion coefficient at the antenna-plasma interface and Δf, $\Delta\Omega$, ΔA are the receiver bandwidth, antenna solid angle and antenna area respectively. The antenna-plasma coupling resistance has been estimated for frequencies in the range (25-47) MHz by separate transmission and reflexion experiments. Assuming a parabolic form for the radial variation of $T_i(R)$, P_{BB} can be related to emission frequency in a manner analogous to that used in tokamak ECE measurements. The expected thermal spectrum is shown plotted in Fig 1 and suggests that the measured broad underlying component could be thermal radiation. However the bright, narrow emission peaks A, B and C etc are of non-thermal origin.

3. Model

We have attempted to model the basic features of the non-thermal spectrum on the basis that it represents cyclotron emission from the charged fusion products. Even though the birth distribution of the fusion products is strongly localised to the central region of the tokamak discharge, the high energies of these particles leads to significant orbital excursions. For this reason, we have used a code to model the distribution of ICE from the charged products. The code traces the full individual particle orbits (MARTIN 1985). We have modelled the D-shaped JET magnetic topology and have included the Shafranov shift, and divergence-free magnetic fields. At each point along the orbit the contribution to the harmonic cyclotron emission power is calculated. For cyclotron emission perpendicular to the magnetic field, the power radiated in the n^{th} harmonic of the cyclotron frequency, ω_{ci}, of a particle of charge + Ze and perpendicular velocity $v_\perp$ is

$$P_n = \frac{(Ze)^2 \, \omega_{ci}^2 N}{8\pi^2 \, \varepsilon_o c} \left[\frac{n \, v_\perp \, N}{c}\right]^2 J_n'^2 \left[\frac{n \, v_\perp \, N}{c}\right] \qquad (4)$$

where $N(\sim \omega_{pi}/\omega_{ci})$ is the refractive index of the medium, and J_n' is the derivative of the n^{th} order Bessel function (eg BEKEFI 1966). This expression shows the strong weighting for the emission to particles with high perpendicular velocities. The number of fast fusion products in the plasma is $N^* \sim Y_{DD} \, \tau_S$, where τ_S is the classical slowing down time. In our experiments $\tau_S \sim 0.3$s giving $N^* \lesssim 3 \times 10^{13}$, constituting a fraction $\sim 2 \times 10^{-8}$ of the plasma ions. The optical depth at $2\omega_{ci}$ is $\tau = \frac{\pi}{2} \beta_i R_o \frac{\omega_{pi}}{c}$ where β_i is the ratio of the pressure of the fusion products to the magnetic field pressure. We find $\tau \sim 10^{-5}$ and have therefore neglected the self-absorption of the ICE. In our model, test particles were lauched sequentially, scanning with increments in both velocity and real space in the discharge. By integration over the isotropic birth distribution function thus generated, ICE spectra were synthesized, using Eq. 4. We do not calculate the slowing down spectrum in this model.

For the plasma conditions relevant to the discharges in Fig. 1 we show in Fig.3 the calculated ICE source emission functions for the 3 primary products as well as the α-particle. The amplitude of the α-particle emission has been weighted by 0.02, corresponding to the expected burn-up (of T^+) fraction in the present conditions. The spectra show a number of harmonic emission peaks having the property $\omega \propto B_T$ (as seen experimentally), and a significant peak at ~ 28 MHz (close to peak A)

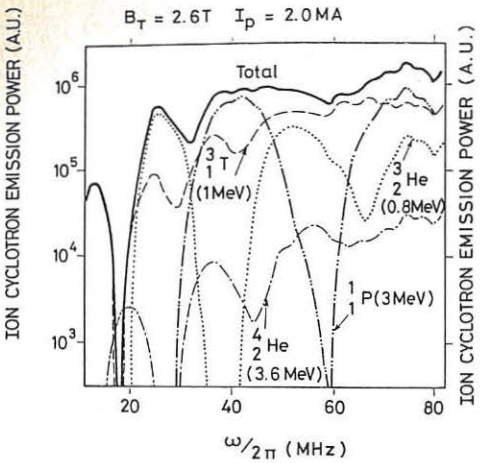

Figure 3: Calculated source emission spectrum from fusion products for conditions of Fig.1. No correction has been made for (i) slowing down of the fusion products, (ii) absorption.

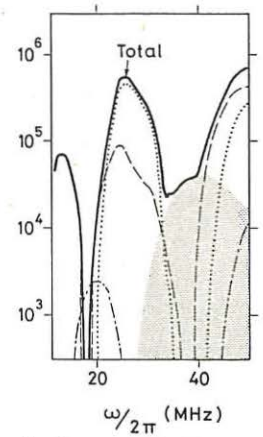

Figure 4: Same as Fig.3 except that absorption at $\omega = 2\omega_{cD}$ has been taken into account coupled with re-emission by the indicated blackbody spectrum (shaded).

coming predominantly from $\frac{3}{2}$ He fundamental radiation. Above 35 MHz the spectra become harmonically overlapped giving a quasi-continuum. Fig. 4 shows the effect of including a bulk plasma absorption model at $\omega = 2\omega_{cD}$. Here it is assumed that the fusion particle radiation from ω_{cH}, $2\ \omega_{c^4He}$ and $3\ \omega_{c^3T}$ is absorbed by the optically thick plasma and replaced by blackbody radiation at the bulk ion temperature (2 KeV). This model shows reasonable qualitative agreement with the experimental spectrum in the range 25-50 MHz. Above this frequency, uncertainties in the antenna response make detailed comparison more difficult. However we may expect to see bands of absorption at higher harmonic frequencies of the bulk plasma ions; these bands can be thought of as being analogous to the Fraunhofer absorption lines seen in solar spectra.

Acknowledgements:
It is a pleasure to thank Drs J Jacquinot, T Hellsten, C Lashmore-Davies and W Core for useful discussions and M Brandon for help in performing the experiments.

References

CLARK, W H M 1984 Proc. 4th Int Symposium on Heating in Toroidal Plasmas. Rome Vol 1, 385-391. (EUR 9341 EN)

COTTRELL, G A 1985 Proc Workshop on Application of RF Waves to tokamak Plasmas. Varenna Vol II, 710-716. (EUR 10333 EN)

JARVIS O N, GORINI G, HONE M, KALLNE J, MERLO V, SADLER G, VAN BELLE P 1985. Paper 185 in Proc of 12th European Conference on Controlled Fusion and Plasma Physicss, Budapest, Hungary.

BEKEFI, G 1966 Radiation Process in Plasmas. Wiley, Page 180

MARTIN, G 1985 Doctoral Thesis, Universite de Paris-Sud. Orsay N°694 France.

MAGNETIC FLUCTUATIONS IN THE SCRAPE OFF LAYER OF TFR DURING ADDITIONAL HEATING EXPERIMENTS

TFR GROUP and A.TRUC*
Presented by J. OLIVAIN

ASSOCIATION EURATOM-CEA SUR LA FUSION
Département de Recherches sur la Fusion Contrôlée
Centre d'Etudes Nucléaires
Boîte Postale n°6. 92265 FONTENAY-AUX-ROSES (FRANCE)

Introduction

Anomalous electron energy transport in Tokamak plasmas, either in ohmic or auxiliary heating regimes, is a very puzzling problem. Turbulence observed through density fluctuations or (and) magnetic fluctuations is usually considered responsible for the supplementary losses. Density fluctuations are inferred from coherent scattering experiments. Magnetic fluctuations are difficult to measure in the plasma body. Only in two small tokamaks : Caltech [1] and Macrotor [2] magnetic fluctuations were obtained in part of the plasma core ($r/a > 2/3$, a being the plasma radius). Conversely several groups have reported magnetic fluctuations measurements in the scrape off layer of large Tokamaks. Especially ISX [3] and TCA [4] groups have reported experimental results and made comparisons between gross confinement time and magnetic fluctuations level. The object of this paper is to pursue their work. We wish to compare density fluctuations and magnetic turbulence in ohmic and auxiliary heating phase, in analogy to previous work [5].The task is long, especially in determining the confinement times for many shots. Only preliminary comparisons will be given here, focusing attention on the magnetic results.

Experiment

a) Experimental set up

CO_2 scattering experiment has been described elsewhere [6]. Three magnetic coils have been installed into the TFR plasma chamber ($a < r < 28$ cm). They let simultaneously analyzing the time derivative ($\delta \dot{B}$) of the local radial, toroidal and poloidal magnetic field components. Each coil is screen by a fine metallic cylinder and finally protected in an alumina box. Metallic screen leads to a cut off frequency $f_o \sim 470$ kHz e.g. pick up magnetic signal below 470 kHz is proportional to $\delta \dot{B}$ whereas higher frequencies are integrated. However, electrostatic signal can also be collected through a parasitic capacitor (through the alumina box). This parasitic signal, proportional to ω^2, could be dominant at high frequency. Local potential fluctuations $\delta\varphi$ are estimated via the ion saturation current I_s of a Langmuir probe.

* Laboratoire PMI, Ecole Polytechnique, Palaiseau, Cedex, France
* This research is carried out in the frame of a general agreement between EURATOM-CEA and the PMI Laboratory of Ecole Polytechnique.

$$\frac{e\delta\varphi}{T_e} \sim \frac{\delta I_s}{I_s} \sim 30\ \%$$

As a consequence, signals collected below 350 kHz are essentially magnetic signals proportional to $\delta \dot{B}$, the higher frequencies being subject to more subtle interpretation.

b) Global magnetic fluctuations

A typical output signal, after Fourier analysis, is shown in Fig.1 The two large peaks are identified as n = 1 and n = 2 tearing modes (n: toroidal number). Largest mode corresponds to an amplitude $\delta B \sim 7$ gauss while the second has only a 0.9 gauss amplitude. However the fact that anomalous electron transport is present whatever or not macroscopic modes exists, suggests that these macroscopic modes are likely not directly responsible for the enhancement of electron transport by turbulence. As a consequence, in the following, these large coherent modes will be eliminated by proper filters and only magnetic turbulence comprised between 30 to 350 kHz will be analyzed.

c) Broadband magnetic turbulence (B.M.T) in ohmic regime

The amplitude decreases monotically as a function of frequency, following a law well approximated by a power law

$$\delta B \sim \omega^{-2.6 \pm 0.4}$$

for the δB_r and δB_θ components. δB_r is usually larger than δB_θ (a run of many similar shots gives for instance $\delta B_r^2 = 16 \pm 4$ and $\delta B_\theta^2 = 7.5 \pm 3$ in the same arbitrary units). Henceforth δB^2 or $\delta \dot{B}^2$ will be considered, in regard of theoretical considerations.

The aim of this work is to make a systematical study of the amplitude of the BMT as a function of the electron energy confinement time in experimental conditions where τ is changed. Several τ can be envisaged and tested (central or radially integrated transport electron energy confinement time, global confinement time). Here, after having checked that Alcator law ($\tau_E \sim n\sqrt{q(a)}$) is reasonably satisfied in previous ohmic experiments, BMT will be compared to the parameter $n\sqrt{q}$ as a relative estimator of the confinement time, this estimator being essentially justified by its time saving advantage.

Time evolution of BMT and frequency integrated density fluctuations are analyzed during the final part of the current rise and during the current plateau (Fig.2). Compared to the parameter $n\sqrt{q}$, both quantities show a different evolution. Whereas density fluctuations follow a monotonic linear relationship, showing a continuous decay of fluctuations when confinement is increased, BMT presents an evolution with two opposite phases. Using a regressive code, we are able to estimate the influence of the plasma current and the density in the two phases for the two signals

$$\frac{\langle \delta n^2 \rangle}{n^2} \sim q^{-0.5 \pm 0.3}\, n^{-1.1 \pm 0.3} \quad \text{for density fluctuations}$$

and

$$(\delta B_{r,\theta})^2 \sim \begin{cases} q^{-2 \pm 1}\, n^{1.3 \pm 0,4} & \text{current rise} \\ n^{-0.7 \pm 0.2} & \text{current plateau} \end{cases} \quad \text{for BMT}$$

By analyzing several shots, we can draw Fig.3. Whereas $\frac{<\delta n^2>}{n^2}$ varies proportionally to $n^{-1} q^{-1/2} \sim \tau^{-1}$, δB_r^2 and δB_θ^2 are very scattered and show no well defined relationship.

d) BMT in auxiliary heating phases

An increase of BMT is observed during auxiliary heating experiments. Fig.4 shows the result of a set of measurements during neutral injection experiments, whereas Fig.5 shows the same measurements during electron cyclotron heating experiments. A large spreading in experimental results make inopperent a comparison between BMT level and confinement time and does not let us to conclude. Extra parameters, as recycling and plasma displacements, are likely to play a role. However, a large increase of BMT (factor 2 to 6 in δB^2) is always noted during auxiliary phase, value large compared to the reduction in confinement time (20 to 50 %).

Conclusion

From this study and the preceeding one[5], we confirm that density fluctuations $\frac{<\delta n^2>}{n^2}$ vary as the inverse of the confinement time whereas magnetic fluctuations $\delta B_{r,\theta}$ have a more erratic evolution. Exept in the current plateau phase of the ohmic regime where a relationship of the type $B^2_{r,\theta} \propto \tau^{-1}$ is not excluded, no close connection between plasma body confinement and outer magnetic turbulence is revealed.

Figure captions

Fig.1 Frequency spectra of the magnetic component δB_r
(a) 0-100 kHz spectra (ΔF = 1 kHz)
(b) 30-500 kHz spectra (ΔF = 10 kHz)

Fig.2 a) q(a) and nl plasma parameters as a function of time
b) magnetic components δB_r^2, δB_θ^2 and relative density fluctuations $\frac{<\delta n^2>}{n^2}$ as a function of time for the same shot.

Fig.3 Inverse confinement time, estimated by the $n_{eo}^{-1} q(a)^{-1/2}$ parameter compared to relative density fluctuations and magnetic turbulence

Fig.4 Relative magnetic turbulence increase as a function of the power of neutral beam injection.

Fig.5 Relative magnetic turbulence increase as a function of the electron cyclotron power injection

References

1 Hedemann M.A., Gould, R.W., Bull. Am. Phys. Soc. 25 (1980) 975
2 Zweben, S.J., Liewer, P.C., Gould, R.W. J. Nucl. Matter 111 and 112 (1982) 39
3 MURAKAMI, M. et al. TENTH Int. Conf. on Plasma Physics and Conf. Nucl. Fusion Res. London 1984 IAEA-CN-44/A-II-2
4 Duperrex, P.A et al. Phys. lett. 106A, 3 (1984) 133
5 TFR Group and A. Truc -EUR-CEA-FC 1284 Report (1986) -submitted for publication in Nuclear Fusion

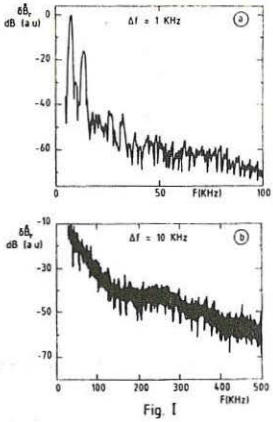

Fig. I

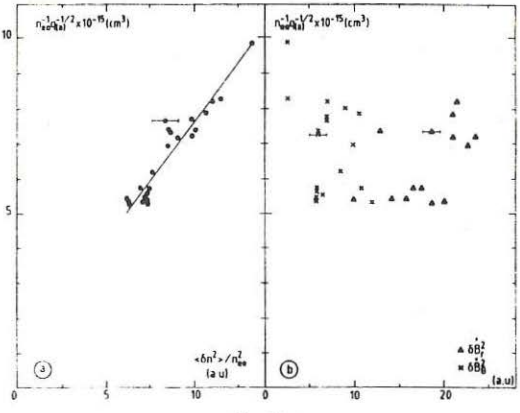

Fig. III

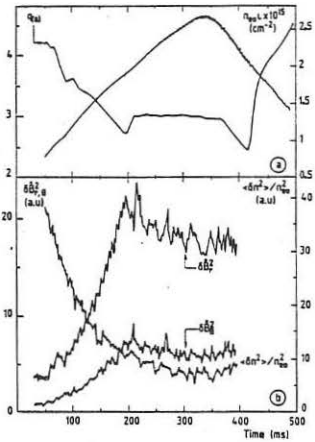

Fig. II

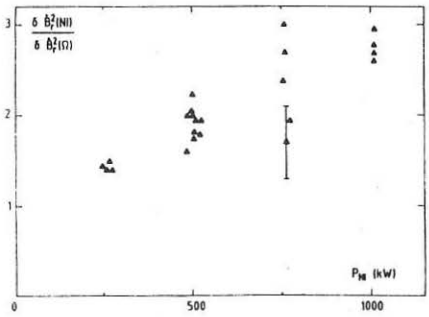

Fig. IV

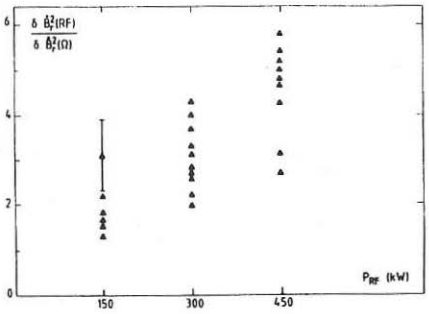

Fig. V

OBSERVATION OF DENSITY FLUCTUATIONS LOCALIZED AT THE RESONANCE LAYER DURING ALFVEN WAVE HEATING

R. Behn, G.A. Collins, J.B. Lister and H. Weisen

Centre de Recherches en Physique des Plasmas
Association Euratom - Confédération Suisse
Ecole Polytechnique Fédérale de Lausanne
21, Av. des Bains, CH-1007 Lausanne / Switzerland

Abstract

We report on the first observations of density fluctuations at the resonant layer during Alfvén Wave heating in a tokamak. Whereas loading and external magnetic probe measurements[1] show excellent agreement with the cold plasma model of the Shear Alfvén Wave if finite ω/ω_{ci} effects and toroidal coupling are taken into account, these new observations demonstrate the importance of kinetic effects.

Introduction

New insight on the processes underlying Alfvén Wave heating has been gained following the installation on the TCA tokamak of a novel laser diagnostic based on the phase constrast method[2,3,4]. This instrument uses an 8 Watt CO_2 laser beam expanded to fill the 23 x 4 cm wide NaCl windows giving access to the outer two thirds of a poloidal section. The transmitted light is optically processed to produce an image of the plasma, where the small ($\sim 10^{-3}$) phase shifts caused by refractive perturbations are revealed as intensity variations, which are recorded by HgCdTe detectors (Fig. 1). Even though it needs no external reference beam, this method provides an interferometer equivalent response for fluctuations with wavelengths below an adjustable cutoff $\Lambda_c(\Lambda_c < 20cm)$. This is adequate for wavelengths in the centimetric range, as predicted for the kinetic Alfvén Wave in the conditions of TCA. (B_T =1.5 T, Te(0) ≈ 800 eV, $\bar{n}_e$ typically $2\text{-}6.10^{19} m^{-3}$, R = 0.61m, a = 0.18m, q(a) ≈ 3.2, working gas D_2 or H_2). Each of the eight groups of antennae is fed separately by the 2.5 MHz generator, so that the dominant toroidal (n) and poloidal (m) mode numbers can be determined by their relative phasings. The antennae excite a fast magnetosonic wave, which is heavily damped when the Shear Alfvén Wave resonance condition [1] is met at some radius in the plasma, defining the resonance layer.

At the high temperatures characteristic of the bulk, kinetic theory [5] predicts a strongly damped, radially inwards propagating wave, with a large electrostatic component, that has its wavefield maximum near the resonance layer. Owing to the essentially cylindrical symmetry of the waves, the pattern of line integrated fluctuations is closely related to the original radial wave pattern. The signals from the

detector(s) are mixed with reference signals from the generator to yield the in phase and in quadrature components. From these the relative phase and amplitude of the density fluctuations are calculated.

Results

Figure 2 shows the amplitude and phase in a deuterium plasma obtained with various combinations of antenna phasings refered to by (N,M), when the detector viewed a chord at r/a = 0.33. The spectrum was scanned by increasing the density during the 60 ms RF pulse.

A strong signal is seen shortly after (and sometimes during) the loading peaks of the discrete AW spectrum, signalling the passing of a new resonant layer, sweeping outwards accross the viewing chord as the density rises. The decreasing phase indicates that the interior of the wave is retarded with respect to the outside. Evidence of toroidal coupling from loading measurements [6] is confirmed, eg. (N,M) = (2,1) also excites (n,m) = (2,0) waves. Modes with a poor loading show low level fluctuations. (The same scale was used for the five cases in the figure.) The appearance and disappearance of the resonance surfaces for different excitation structures demonstrates the toroidal mode purity in the continua, as seen in the discrete spectrum by antenna loading measurements [1].

The (n,m) = (4,-1) wave is of particular interest because no (4,-1) discrete Alfvén wave is observed on TCA, showing that these fluctuations appear independently of the discrete spectrum.

Sawteeth activity is often seen to modulate the amplitude and, to a lesser extend, the phase of the signals, indicating the sensitivity of the waves to changes in the plasma profiles. The short scale spikes on Fig. 2 were caused by sawteeth.

The localised radial wave structure and its inward direction of propagation are demonstrated on Fig. 3 obtained from a series of 20 reproducible discharges in hydrogen, where the detector position was scanned from shot to shot (antenna current 630 A peak, 100 kW coupled to the plasma, $n_e = 3.5 \times 10^{19}$). On the contour plot of Fig. 4, we see the detected amplitude as a function of position and density for the same discharges, shown together with the wavefronts (dashed, half-wavelength spacing). The amplitude is seen to be peaked near the estimated (2,0) and (2,-1) resonant layer positions (solid lines). Initial measurements for the (4,-1) continuum show a similar evolution of the profile as a function of density. Unlike the (2,0), the fluctuation level at the threshold is almost zero for the central chord. We attribute this to the difference in poloidal mode number parity.

Conclusions

Using a novel laser diagnostic specifically built for this purpose, we have revealed the existence of driven density fluctuations that have

the features of the Kinetic Alfvén Wave. Further progress is expected from the planned installation of a multi-element detector, which will set us free from the necessity of time consuming repetitive shots to obtain fluctuation profiles.

References

[1] G.A. Collins et al., Phys. Fluids, in press (1986).
[2] H. Weisen, Infrared Phys., 25 (1985) 543.
[3] H. Weisen, Proc. 2nd Int. Symposium on Laser-Aided Plasma Diagnostics, Culham, 10-12 sept. 1985.
[4] H. Weisen, Plasma Phys. Contr. Fusion, in press (1986).
[5] A. Hasegawa, L. Chen, Phys. Rev. Lett., 35 (1975) 370.
[6] K. Appert et al., Phys. Rev. Lett., 54, (1985) 1671.

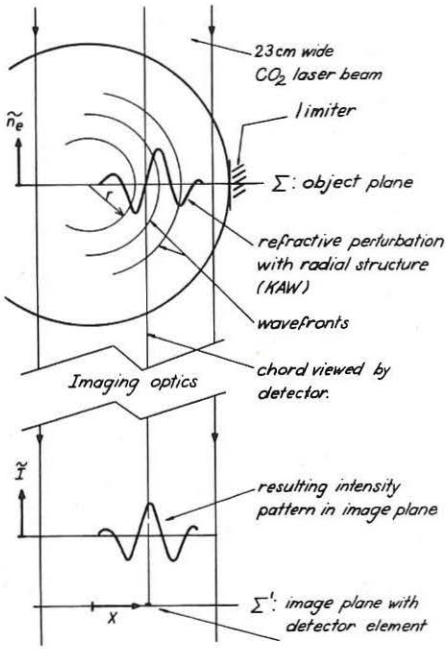

fig.1 Setup

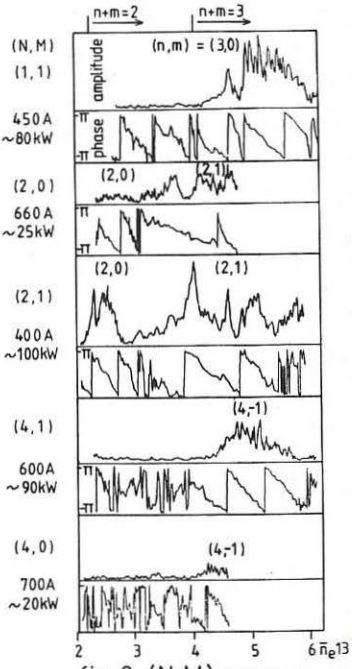

fig.2 (N,M) scan

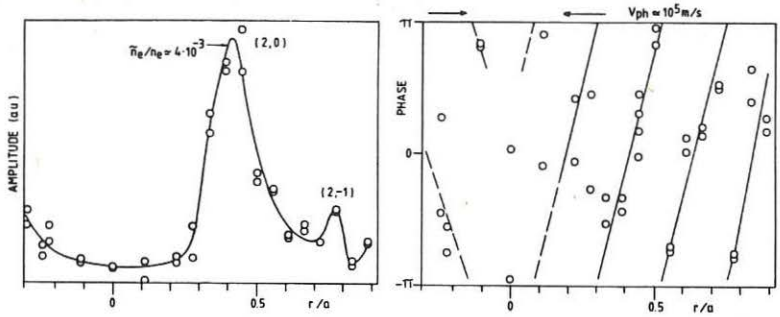

fig. 3 Amplitude and phase profile (2,0) continuum

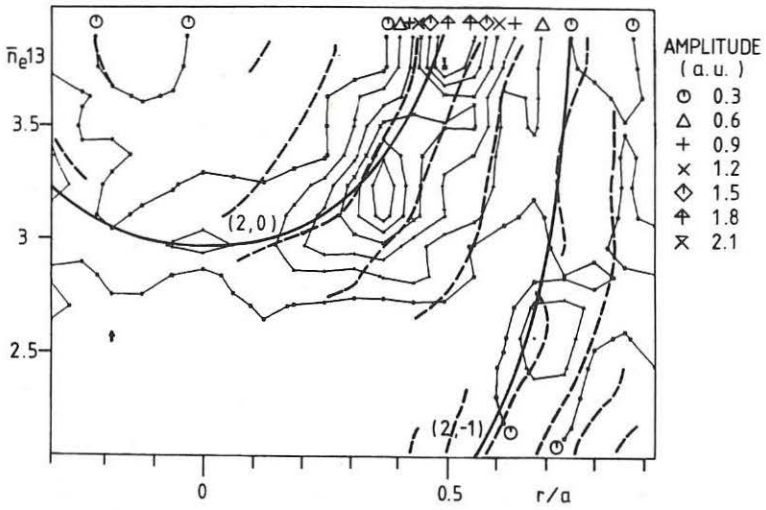

fig. 4 Contour plot

ALFVEN WAVE DAMPING IN INHOMOGENEOUS PLASMAS

G. Bertin, G. Einaudi and F. Pegoraro

Scuola Normale Superiore, Pisa - Italy

The damping of shear-Alfvén waves in inhomogeneous plasmas is independent of dissipation and is determined by the global profiles of the plasma density and of the magnetic field. This damping arises from the singularity of the ideal equations at the spatial location where the mode frequency is equal to the Alfvén frequency. Such singularity leads to a jump of the mode amplitude which can be determined by invoking either causality or dissipation. While both causality and dissipation correctly determine the mode damping rate, dissipation is needed in order to obtain a regular mode amplitude. When dissipation is introduced, the logarithmic singularity of the mode amplitude is regularized on a lengthscale proportional to the square root of the relevant inverse Reynolds number. In this paper the above results are derived in a wave number space representation which simplifies the comparison with the low frequency resistive instabilities (resistive internal kink and tearing modes).

Within the framework of ideal MHD the dispersion equation of shear Alfvén modes in an inhomogeneous plasma slab is given by

$$\frac{d}{dx}\,\rho\,[\,\omega^2 - \omega_A^2(x)\,]\,\frac{d}{dx}\,\xi \;=\; k^2\rho\,[\,\omega^2 - \omega_A^2(x)\,]\,\xi \qquad , \qquad (i)$$

with k the wave vector on the magnetic surfaces labeled by x and $\omega_A(x) = k_\parallel c_A$. In the neighbourhood of a (simple) zero of $\omega^2 - \omega_A^2(x)$ at $x = x_0$, the solutions for the x-component ξ of the displacement vector behave as $\xi \sim A_\pm + B \ln|(x - x_0)/x_0|$ where $A_\pm$ and B are integration constants. Since $A_\pm$ can take different values for $x \gtrless x_0$, the solutions of (1) have an additional integration constant for each zero of $\omega^2 - \omega_A^2(x)$ (ideal Alfvén continuum) [1-4].

The ideal equations are not valid around x_0 where dissipative processes add an important contribution which depends on higher x-derivatives. Dissipation regularizes the mode amplitude and causes damping. However the mode damping rate can be computed directly from the ideal equations by invoking causality [2]. By assuming a complex frequency and continuing the

mode amplitude analytically from positive to negative values of $\gamma = \mathrm{Im}\,\omega$, the solution of (1) around $x = x_0$ reads [5]

$$\xi = A + B \ln (i\hat{x} + \hat{\gamma}) \tag{2}$$

$$= A + B \left[\ln(\hat{x}^2 + \hat{\gamma}^2)^{\frac{1}{2}} + i \arctan (\hat{x}/\hat{\gamma}) + i\pi \, \mathrm{sgn}(x) H(-\hat{\gamma}) \right]$$

where $\hat{x} = (x - x_0)/x_0$, $\hat{\gamma} = \gamma [\partial\omega_A/\partial\hat{x}]^{-1}_{\hat{x}=0}$, $\mathrm{sgn}\,(\hat{x}) = \pm 1$ for $\hat{x} \gtrless 0$, H is the step function and $\partial\omega_A/\partial\hat{x}$ is chosen to be positive. For negative values of $\hat{\gamma}$, i.e. for damped modes, the branch cut of the logarithm in (2) crosses the real axis and the mode amplitude is discontinuous with a jump $2\pi i B$ [1]. By imposing this jump condition to the solutions of Eq. (1), γ can be computed selfconsistently. In particular γ can be proved to be negative by constructing a quadratic form from Eq. (1). This form has an imaginary contribution which arises from the discontinuity at $x = x_0$ and gives

$$\gamma/\omega = -2\pi H(-\gamma) \left[|B|^2 / \int_a^b \rho \left(\left|\frac{d\xi}{dx}\right|^2 + k^2 |\xi|^2 \right) dx \right] \rho \left. \frac{\partial \ln \omega_A}{\partial x} \right|_{x=x_0} \tag{3}$$

where a and b label the boundaries of the plasma slab.

Causality gives a definite prescription for computing $\hat{\gamma}$ but leaves the mode amplitude discontinuous. In order to study the effect of dissipation on this discontinuity it is convenient to refer to the solutions of Eq. (1) for $x \to x_0$ and $d/dx >> kx_0$ in α-space, where α is the Fourier variable conjugated to $\hat{x}$, i.e. to the solutions of

$$\alpha \left(\frac{d}{d\alpha} + \hat{\gamma} \right) \alpha\hat{\xi} = 0 \quad . \tag{4}$$

Here $\hat{\xi}$ is the Fourier transform of ξ extended over the singular layer around $x = x_0$. Solutions that are regular in x-space must vanish for $|\alpha| \to \infty$. On the other hand, (4) is a local approximation of the full dispersion equation and is only valid for $|\alpha|$ large compared to kx_0. For $\delta\alpha \to 0$, where δ is the characteristic width of the singular layer, $\hat{\xi}$ can be discontinuous, i.e. the integration constant in (4) can be different for positive and negative values of α. As shown in general in [6], such a discontinuity does not lead to a singularity in x-space but is related to the

asymptotic behaviour of the solution in the singular layer for $\hat{x}/\delta \to \infty$. The choice of the integration constant in (4) that satisfies the causality prescription leads to $\hat{\xi}(\alpha) = (2\pi i/\alpha)H(\alpha)\exp(-\hat{\gamma}\alpha)$ which vanishes for $\alpha < 0$ and diverges for $\alpha \to +\infty$ if $\hat{\gamma} < 0$. A different interpretation of the choice of the integration constant in (4) follows by requiring the wave energy to be convected towards larger values of $|\alpha|$, i.e. deeper insider the singularity with no energy being reflected from it (radiation boundary condition). Since in α-space, energy is carried at the group velocity $\partial\omega_A/\partial\hat{x}$, which we have chosen to be positive, the radiation condition requires the mode amplitude to vanish for negative values of α .

If electron resistivity and/or ion viscosity are taken into account, Eq. (4) becomes

$$\alpha\left(\frac{d}{d\alpha} + \hat{\gamma}\right)\alpha\hat{\xi} = -(\varepsilon/2)\alpha^4\hat{\xi} \quad , \tag{5}$$

where $\varepsilon = [\, c^2\eta/4\pi + \mu/\rho\,]\,/(x_0^2\,\partial\omega_A/\partial\hat{x})_{\hat{x}=0}$ and the effects of the resistivity η and of the viscosity μ simply add up [4]. The corresponding solutions are $\hat{\xi} = (C_{\pm}/\alpha)\exp(-\hat{\gamma}\alpha - \varepsilon\alpha^3/6)$. For the solution to be regular for $|\alpha| \to \infty$ the integration constant C_- must vanish. Therefore dissipation leads to the same choice of the integration constant as required for the ideal equations by causality. Furthermore the discontinuity of the solution for "small" α is unchanged. Thus the jump condition to be imposed on the solutions of the ideal equations is unchanged and the damping rate is unaffected by dissipation [3]. The cubic term in α in the exponent of $\hat{\xi}$ overcomes the growing linear term for

$$\alpha \sim (6\hat{\gamma}/\varepsilon)^{\frac{1}{2}} \quad . \tag{6}$$

Since $\hat{\gamma}$ is independent of resistivity, the discontinuity due to the branch cut of the ideal solution on the real x-axis is regularized within a layer that has a width of order $\varepsilon^{\frac{1}{2}}$.

The α-space representation of the mode amplitude [6] makes it possible to compare the above results to those obtained for low frequency resistive instabilities for which the growth rate depends on the magnitude of the dissipation coefficient. In fact a common dispersion equation in the singular layer can be given which generalizes Eq. (5) and describes both shear-Alfvén modes and low frequency resistive instabilities. The different dependence of γ on dissipation can be traced back to the changing location of the

turning points [6] of the dispersion equation as the frequency is increased. For low frequency modes the turning points are not far from the real axis and within the range of values of α for which the local approximation is valid. For shear-Alfvén waves they split into two pairs: one pair moves far in the complex plane and only leads to an exponentially small reflection coefficient as consistent with the radiation boundary condition in Eq. (4). The second pair moves towards small values of α where the local approximation is not valid in agreement with the fact that the damping of shear-Alfvén modes is obtained within the ideal equations alone.

Finally we note that the above conclusions on Alfvén modes are supported by explicit analytical solutions of the global problem found either by considering special equilibrium magnetic configurations or by carrying out an asymptotic analysis for special regimes of the considered perturbations. In Ref. [3] the complex eigenvalue ω is derived for a magnetic equilibrium configuration in which B_0^2 is piecewise either a constant or a linear function of x, so that the ideal solution is expressed in terms of exponential and modified Bessel functions. Asymptotic techniques are applied in Ref. [4] to a wide class of current sheets of astrophysical interest. In these configurations the magnetic field direction is inverted across the current sheet and modes of the bending type obey a shear-Alfvén mode equation. Two Alfvén singularities occur, symmetrically located with respect to the neutral layer where the magnetic field vanishes. The explicit solution is obtained for long bending waves, i.e. for waves that are larger than the thickness of the current sheet.

References

[1] J.P. Boris, Ph.D. dissertation, Princeton University, 1968

[2] J.H. Tataronis and W. Grossmann, Z. Phys., 261,203,1973

[3] Y. Mok and G. Einaudi, J. Plasma Physics, 33, 199, 1985

[4] G. Bertin and B. Coppi, Astrophys. J., 298, 387, 1985

[5] G. Bertin, G. Einaudi and F. Pegoraro, Scuola Normale Superiore, Report 1/1986. To be published on Comments on Plasma Physics and Controlled Fusion.

[6] F. Pegoraro and T.J. Schep, Rijnhuizen Report P.P. 85/03 to be published on Plasma Phys. and Controlled Fusion

EXCITATION OF ALFVEN WAVES IN TOKAMAK PLASMAS

G.G. Borg, M.H. Brennan, R.C. Cross, J.A. Lehane and A.B. Murphy

School of Physics, University of Sydney
N.S.W. 2006, Australia

Introduction

In the Alfven wave heating scheme, an external antenna excites the fast wave which carries wave energy across magnetic field lines into the interior of the plasma. Mode conversion (and absorption) occur at (and close to) the Alfven resonance layer where the imposed parallel phase velocity equals the local Alfven speed. High heating efficiency and low impurity generation require that only a small fraction of the RF power is coupled into unwanted wave modes near the plasma surface.

In the experiments reported here, it is shown that incorrect choice of antenna design and frequency will result in direct excitation of unwanted Alfven waves near the plasma surface. Radial profiles of the wave fields excited by a correctly designed antenna show penetration of significant wave energy to the interior of the plasma.

The Experiment

The experiments were carried out in a hydrogen plasma in the TORTUS tokamak [1]. In all cases the toroidal field, B_ϕ, was 0.8 T and the plasma minor radius was 10.0 cm. Except when probes were inserted into the plasma to determine radial profiles of the wave fields, the plasma current had a peak value of 16 kA and a duration of 20 ms. This resulted in a plasma with central and edge parameters of $n_e \sim 10^{19} m^{-3}$, $T_e \sim 100$ eV and $n_e \sim 10^{18} m^{-3}$, $T_e \sim 10$ eV respectively. For the experiments in which probes were inserted into the plasma, a short current pulse of 2.5 ms duration and peak current 8-14 kA was used. This plasma had similar density to the longer duration plasma and central and edge temperatures of 30 eV and 10 eV.

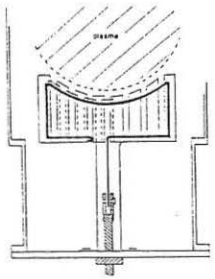

Fig. 1 80° Poloidal sector antenna.

Two antennas were used. Both were located just outside the plasma in the shadow of the limiter. The first, a small loop antenna, consisted of an insulated rectangular wire loop of dimensions 9 cm x 2.5 cm. The second was a shielded, all-metal antenna extending 80° in the poloidal direction and 4 cm in the toroidal direction (Fig. 1). The antennas were fed by a 300 W RF amplifier.

The poloidal components, b_θ, of the wave fields at the plasma edge were detected by an array of six differential coils inserted in a quartz tube which encircled the plasma poloidally at r = 11.2 cm. By moving the array between shots, a complete poloidal profile was obtained in 5 or 6 shots. Radial profiles of b_θ, b_ϕ and b_r were obtained using two probes each containing six small coils spaced at intervals of 2 cm and inserted into one of two fixed quartz tubes (6 mm O.D.) inserted to the centre of the plasma from the top and bottom of the discharge vessel.

Results - Small Loop Antenna

A typical poloidal profile of the wave b_θ component at r = 11.2 cm is shown in Fig. 2 for an excitation frequency of 4 MHz ($\omega/\omega_{ci} = 0.33$). The antenna was located at $\phi = 0$, $\theta = 0$ (top) with its plane vertical and parallel to B_ϕ. The probe array was located at $\phi = 135°$. There is clear evidence of direct excitation of the Alfven wave which is guided along magnetic field lines which pass through and close to the antenna. The four peaks are identified as follows:

$\theta = 30°$	Ray propagating along field line on the high field side
$\theta = -50°$	Ray propagating around low field side
$\theta = 100°$	Additional toroidal transit on high field side
$\theta = -130°$	Additional toroidal transit on low field side

Further ray transits around the torus are intercepted by the limiter or do not intercept the probe array. When I_p or B_ϕ is varied, the poloidal locations of the peaks vary in the expected manner as q(a) is varied. The poloidal width of the peaks is not strongly frequency-dependent up to $\omega \sim 0.7\ \omega_{ci}$.

The wave amplitude inside the plasma was observed to decrease almost monotonically with distance from the plasma surface. It is clear that the small loop antenna couples only weakly to the fast wave. The coupling to the fast wave was increased somewhat when the antenna was rotated so that its plane, and hence all current elements, was perpendicular to B_ϕ. The observed radial profile was highly asymmetric suggesting the presence of several modes; that is not surprising, given the small dimensions of the antenna.

A comparison was made between the amplitude of the direct high field side ray (see Fig. 2) for the antenna plane aligned parallel to B_ϕ as for Fig. 2 and perpendicular to B_ϕ. The results are shown in Fig. 3. It is seen that the efficiency of direct excitation of the Alfven wave near the plasma surface is increased as ω approaches ω_{ci} and when antenna current elements are parallel to the magnetic field. This result is in agreement with theoretical predictions [2] of wave excitation by a dipole antenna.

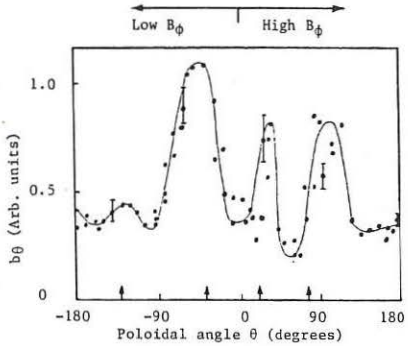

Fig. 2 b_θ vs θ at plasma edge with antenna parallel to B_ϕ. Arrows indicate calculated positions of field lines passing through the antenna.

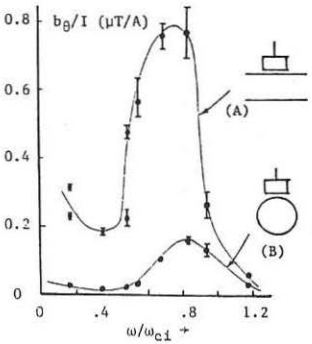

Fig. 3 b_θ (normalised to antenna current I) for the high field side direct ray with antenna (A) parallel, (B) perpendicular to B_ϕ.

The 80° Sector Antenna

The poloidal distribution of b_θ at the plasma edge when the 80° sector antenna was used was somewhat different from that for the small loop antenna. In particular, for the 80° sector antenna, most of the wave energy at the plasma edge was confined to the poloidal sector defined by the antenna. The general features of the poloidal distribution can be attributed to direct excitation of the Alfven wave primarily by the currents in the two side arms of the antenna. Such excitation is not predicted by MHD theory [2]; finite frequency effects may be sufficient to account for this excitation.

The observed frequency dependence of the efficiency of direct excitation of the Alfven wave was similar to that observed for the small loop antenna (Fig. 3).

Radial profiles of b_θ, b_r and b_ϕ were obtained at several frequencies. Generally, b_θ and b_r were comparable in magnitude while b_ϕ was an order of magnitude smaller. At some frequencies broad peaks in b_θ and b_r were observed. Examples of b_θ and b_r profiles for two frequencies, 3.4 MHz and 4.2 MHz, are shown in Fig. 4. There is very little internal structure at 3.4 MHz. The profiles are similar to those observed with the small loop antenna: there appears to be only a weak Alfven resonance layer inside the plasma; the wave fields are due primarily to direct excitation of the Alfven wave.

At 4.2 MHz there is clear evidence of structure in the wave fields inside the plasma. The positions of the peaks in b_θ and b_r move to smaller radii as the plasma density falls. Although there is insufficient experimental data to unambiguously determine the nature of the observed peaks, they are consistent with the excitation of the Alfven resonance via the fast wave, as is required for Alfven wave heating. Experiments are in progress, using three antennas, to better define the toroidal and poloidal mode numbers and hence to provide a more direct comparison with theory.

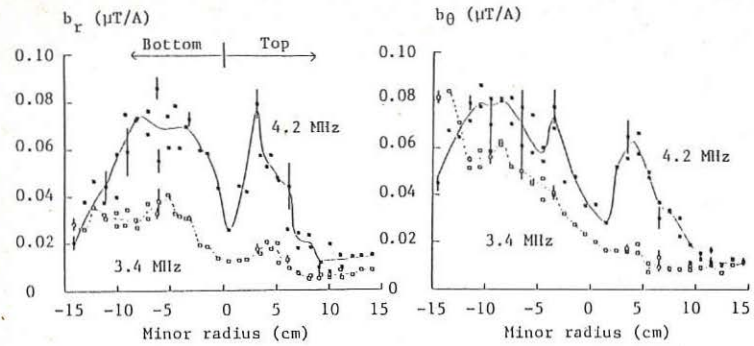

Fig. 4 Radial profiles of b_r and b_θ (normalized to antenna current) at ϕ = 180° for the 80° sector antenna at ϕ= 0°, r = -10 cm.

As was the case with the small loop antenna, the radial profiles are asymmetric with a clearly increasing amplitude for radial positions close to the antenna.

Measurements were also made of the antenna impedance as a function of frequency. The impedance was observed to rise smoothly from zero at $\omega \sim 0.1\ \omega_{ci}$ to $\sim 0.35\ \Omega$ at $\omega \sim 1.6\ \omega_{ci}$. The origin of this loading is not clear.

Conclusion

The experimental results presented here clearly indicated that, in Alfven wave heating experiments, unwanted direct excitation of the Alfven wave near the surface of the plasma can be minimised if all antenna current elements are oriented perpendicular to the steady magnetic field. The experimental results also show that a single all metal, shielded poloidal antenna can effectively couple energy into the interior of the plasma. Experiments currently in progress are aimed at establishing whether an antenna system with two or three antennas is significantly more effective than a single antenna.

References

[1] R.C. Cross et al., Atomic Energy in Australia 24, 2 (1981).

[2] G.G. Borg et al., Plasma Phys. and Contr. Fusion 27, 1125 (1985).

CURRENT-DRIVEN LOW FREQUENCY INSTABILITIES IN A MAGNETIZED TWO-ION PLASMA

R. Bharuthram*, M.A. Hellberg+ & D. Johnstone+

*U. of Durban-Westville & U. of Natal, Durban, South Africa
+U. of Natal, Durban, South Africa

1. Introduction: An obliquely propagating electrostatic wave in a cold, collisional, magnetized two-ion plasma with ω_R near the ion-ion hybrid (Buchsbaum) frequency, ω_B, may be driven unstable by an electron drift V_d along $\vec{B}_o = B_o\hat{z}$ for $k_z V_d > \omega_B$ [1,2]. This resistive ion-ion hybrid drift instability (RIHDI) satisfies the dispersion relation

$$1 = \left\{\frac{\omega_{pL}^2}{\omega^2 - \Omega_L^2} + \frac{\omega_{pH}^2}{\omega^2 - \Omega_H^2}\right\}\frac{k_x^2}{k^2} + \left\{\frac{\omega_{pL}^2 + \omega_{pH}^2}{\omega^2}\right\}\frac{k_z^2}{k^2}$$

$$+ \left\{\frac{\omega' \omega_{pe}^2}{(\omega - k_z V_d)(\omega'^2 - \Omega_e^2)}\right\}\frac{k_x^2}{k^2} + \left\{\frac{\omega_{pe}^2}{\omega'(\omega - k_z V_d)}\right\}\frac{k_z^2}{k^2}, \qquad (1)$$

where $\omega' = \omega - k_z V_d + i\nu_{ei}$, with $\omega = \omega_R + i\gamma$, ν_{ei} the electron-ion collision frequency and L(H) refer to light (heavy) ions.

For low collision frequency $\nu_{ei} << \omega_B$, the two-stream ion-ion hybrid instability (TSIHI) was reported [3]. The RIHDI for $\omega_B < k_z V_d < \Omega_L$ then arises when collisions extend the unstable region beyond the two-stream unstable range.

We now identify analytically the origin of the TSIHI. Numerical results over a wider range of ν_{ei} and V_d are presented, relating the observations of [2], [3] and [4]. Parameter values used are appropriate for an argon-helium mixture in a laboratory discharge device used for basic plasma studies, with $N_L = N_H$, $\omega_B = 3.2\Omega_H$, and $k_z/k \sim (m_e/M)^{1/2}$, where M is the average ion mass.

2. Origin of the TSIHI: With appropriate assumptions [5] equ. (1) reduces to

$$\frac{\omega_{pL}^2}{\omega^2 - \Omega_L^2} + \frac{\omega_{pH}^2}{\omega^2 - \Omega_H^2} + \frac{k_z^2 \omega_{pe}^2}{k^2(\omega - k_z V_d)^2} = 0. \qquad (2)$$

Following the approach of [6], we consider the interaction between an electron beam mode ($\omega_R \approx k_z V_d$) and waves having $\Omega_H \lesssim \omega_R \lesssim \Omega_L$.

If $\xi = (k_z/k)^2 \omega_{pe}^2/(\omega_{pL}^2 + \omega_{pH}^2) \ll 1$, equ. (2) may be cast in the form

$$(\omega^2 - \omega_B^2)[(\omega - k_z V_d)^2 - \xi^2 \omega_\alpha^2] = \xi^2 \omega_B^2 \omega_\beta^2, \qquad (3)$$

where

$$\omega_\alpha^2 = (\omega_{pL}^2 \Omega_L^2 + \omega_{pH}^2 \Omega_H^2)/(\omega_{pL}^2 + \omega_{pH}^2)$$

and

$$\omega_\beta^2 = \frac{\omega_{pL}^2 \omega_{pH}^2 (\Omega_L^2 - \Omega_H^2)^2}{(\omega_{pL}^2 \Omega_H^2 + \omega_{pH}^2 \Omega_L^2)(\omega_{pL}^2 + \omega_{pH}^2)} .$$

Equ. (3) illustrates the fact that the instability results from the reactive coupling between a positive energy Buchsbaum mode ($\omega \cong \omega_B$) and a negative energy electron beam mode ($\omega \cong k_z V_d - \xi\omega_\alpha$). For $N_L = N_H$ and $M_L \ll M_H$, these two solutions may be used to obtain the reduced dispersion relation for the TSIHI,

$$(\omega - \omega_B)\left\{\omega - k_z V_d + \frac{(k_z/k)\,\omega_{pe}\,\omega_\alpha}{(\omega_{pL}^2 + \omega_{pH}^2)^{\frac{1}{2}}}\right\} = -\frac{1}{4}\frac{k_z (2M_L/m_e)^{\frac{1}{2}}}{k(1 + M_L/M_H)^{\frac{1}{2}}}\frac{(M_H/M_L)^2\,\omega_B^2}{(1 + M_H/M_L)^{3/2}} .$$

3. Numerical studies ($\nu_{ei} \ll \omega_B$; $k_z V_d \lesssim 2\Omega_L$):
Using $\nu_{ei} = 0$ or $0.03\,\omega_B$, four regimes are identified:

(a) $\Omega_H < k_z V_d < \omega_B$. For $\nu_{ei} = 0$, complex conjugate roots (two-stream-like) occur with $\omega_R \cong k_z V_d$ for $k_z/k \to 0$ (k varying). As k_z/k is increased, ω_R drops to and falls below Ω_H. The growing mode is a two-stream heavy ion instability. For $\nu_{ei} \neq 0$, the two-stream behaviour is similar. The RIHDI does not occur as $k_z V_d < \omega_B$.

(b) $\omega_B < k_z V_d < \Omega_L$. As discussed in [3], the TSIHI occurs for both $\nu_{ei} = 0$ and $\nu_{ei} \neq 0$, extending in the latter case into the RIHDI for k_z/k beyond the two-stream unstable region.

(c) $k_z V_d \gtrsim \Omega_L$. For $\nu_{ei} = 0$, results are shown in Fig. 1. For nearly perpendicular propagation, coupling between the beam modes 1 and 2 yields a growing mode with $\omega_R \cong \Omega_L$: the two-stream light ion instability (TSLII). For larger k_z/k, mode 2 couples with the Buchsbaum mode 3 to yield the TSIHI reported above. In the interval $0.5 \lesssim (k_z/k)/(m_e/M)^{1/2} \lesssim 0.9$ all three modes are stable. Collisions broaden the unstable ranges of both instabilities (Fig. 2), i.e. a resistive drift instability also occurs at the light ion cyclotron frequency (RLIDI).

(d) $k_z V_d > \Omega_L$. As V_d is increased, the width of the stable interval in

Fig. 1 decreases, and for $k_z V_d > 4.5\ \omega_B$ it vanishes even for $\nu_{ei} = 0$. However, close study of the growth rate behaviour enables one to draw up an extended stability diagram, Fig. 3 (cf. [4]), for the two-stream and resistive drift instabilities near ω_B and Ω_L. Insensitivity to ν_{ei} and M_H/M_L makes the diagram nearly universal for low ν_{ei}, $N_L = N_H$ plasmas.

4. Collisional effects:

(a) Dependence of γ on ν_{ei} for the RIHDI has been studied, using the parameter values of Lee [2]. These have $(k_z/k)/(m_e/M)^{1/2} > 1$ and $k_z V_d > 40\ \omega_B$ (Fig. 4). The predicted linear dependence [1] holds over a wide range of ν_{ei}, as found for smaller k_z/k and $k_z V_d < \Omega_L$ [3]. Analytically it can be shown that the first peak in the curve occurs at $\nu_{ei} \cong |\omega_R - k_z V_d|$ (not $\nu_{ei} \cong \Omega_H$ as suggested in [3]), the trough at $\nu_{ei} \cong \Omega_e k_z/k$ and the second peak at $\nu_{ei} \cong \Omega_e$. As seen from Fig. 4, Lee's [2] value $\nu_{ei} > k_z V_d$ is beyond the range of validity of the equation solved by him.

(b) Whereas for $\nu_{ei} \ll k_z V_d$, collisions cause separation of the coupled beam modes ($\omega_R \cong k_z V_d$) and introduce the resistive drift modes (Fig. 5), higher collision frequencies destroy any relationship between the beam modes (Fig. 6) and thus Lee [2] could not observe the TSIHI. The stability diagram is then no longer applicable.

(c) If $T_i = T_e$, then for $\nu_{ei} \gg \omega_B$, collisions between heavy ions and light ions cannot be neglected. For Lee's [2] parameter values, these are found to stabilize the RIHDI.

Acknowledgements: This research is supported in part by the CSIR and AEC. MAH is grateful for the hospitality of the IPP, Garching.

References:

1. Lee, K.F. and Chu, L.W.M. 1979 Phys. Fluids 22, 382.

2. Lee, K.F. 1979 J. Plasma Phys. 22, 59.

3. Grayson, D.J. and Hellberg, M.A.1984 J. Plasma Phys. 32, 387.

4. Bharuthram, R. and Hellberg, M.A. 1985 S. Afr. J. Phys. 8, 35.

5. Bharuthram, R. and Hellberg, M.A. 1986 J. Plasma Phys. 34 (To be published)

6. Lashmore-Davies, C.N. and Martin, T.J. 1973 Nucl. Fusion 13, 193.

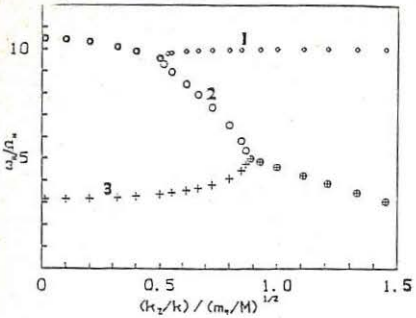

Fig.1: Dispersion plot for $k_z V_d = 1.04\Omega_L = 3.2\,\omega_B$; $\nu_{ei} = 0$; k varying.

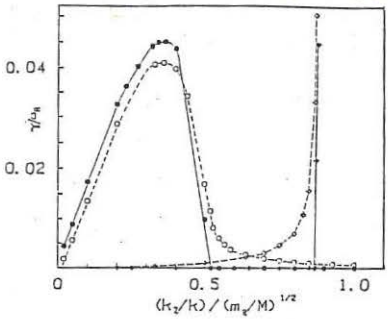

Fig.2: Growth rate plot for case of Fig.1, with collisional broadening (open versus closed symbols) of $\omega_B(0)$ and $\Omega_L(\diamond)$ instabilities; $\nu_{ei}=0.03\omega_B$.

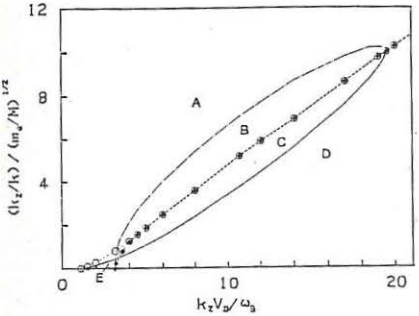

Fig.3: Stability diagram for $\nu_{ei} << \omega_B$. Unstable modes are in A (TSIHI), B(TSIHI, RLIDI), C(RIHDI,TSLII), D(TSLII), E(none).

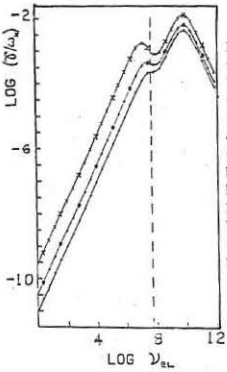

Fig.4: Growth rate versus collision frequency for RIHDI ($\omega_R \cong \omega_B$). Upper curve has Lee parameters: $k_z/k = 2(m_e/M)^{1/2}$, $k_z V_d = 40\omega_B$. Lower curves have V_d doubled and trebled. $\nu_{eL}=\nu_{eH} = 0.5\nu_{ei}$.

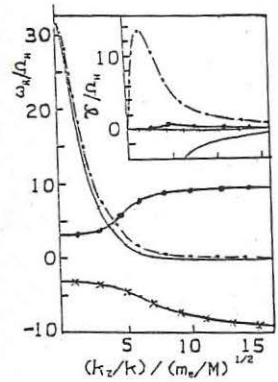

Fig.5: Dispersion and growth rate (inset) plots for $k_z V_d = 10\omega_B$; $\nu_{ei} = \omega_B$.

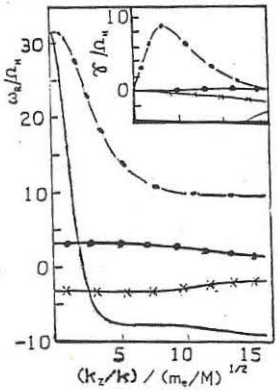

Fig.6: As for Fig.5, but for $\nu_{ei} = 30\omega_B$.

ICRF WAVE PROPAGATION AND ABSORPTION IN STELLARATOR MAGNETIC FIELDS*

E. F. Jaeger, D. B. Batchelor, and H. Weitzner+

Oak Ridge National Laboratory, P.O. Box Y,
Oak Ridge, Tennessee 37831 USA
+New York University, 251 Mercer Street,
New York, New York 10012, USA

Ion cyclotron heating is being used on the Heliotron-E device and is planned for the ATF torsatron for high power, steady-state experiments. The complicated magnetic field structure of these stellarator devices and the relatively large value of λ/L make the approximations of plane stratification, which is useful for many tokamak applications, of questionable validity. We have therefore developed a finite difference code to study ion cycloton wave coupling, propagation and absorption in 2-dimensional, helically symmetric equilibria.

Also recent measurements in the Soviet Union on the L-2 stellarator have demonstrated efficient heating of a pure hydrogen plasma ($n_0 \sim 1\text{-}2 \times 10^{13}$ cm^{-3}) with ICRH power in the range of the first harmonic of the ion cyclotron frequency.[1] Since conventional theory for tokamak plasmas shows that heating at the fundamental ion cyclotron resonance is ineffective, there has been some interest in understanding the theoretical basis for the observed fundamental heating on L-2. Kovrizhnykh and Moroz[2] studied mode structure for the fast magnetosonic wave in a cylindrical metal waveguide filled with plasma. The assumed magnetic field is uniform in the axial direction and the applied frequency equals the ion cyclotron frequency everywhere. They find that for $10^{13} < n_{av} < 3.8 \times 10^{13}$ cm^{-3} (as in L-2), only the m = 1 mode exists, E_+ is a surface wave, and significant heating is possible only near the plasma edge. For $n > 3.8 \times 10^{13}$ cm^{-3}, m = 0,2 modes can also be excited with secondary maxima for E_+ inside the plasma. This implies heating inside the plasma too.

In this paper, we address the questions of 2-ion hybrid and fundamental heating in stellarators by extending the full wave calculations for tokamaks and mirrors in Ref. 3 to the case of a straight, helically symmetric stellarator. Global solutions of the ICRF wave fields are found numerically in the cold plasma limit for parameters typical of the L-2 and ATF stellarators. The component of the wave electric field parallel to $\vec{B}$ is assumed zero and helical symmetry is used to Fourier decompose the

+Research sponsored by the Office of Fusion Energy, U.S. Department of Energy, under Contract No. DE-AC05-840R21400 with Martin Marietta Energy Systems, Inc.

solution in the longitudinal (z) direction. The remaining set of two-coupled, 2-dimensional partial differential equations in r and $\phi \equiv \theta - kz$ (k is the helical pitch) is solved by finite differencing. Energy absorption and antenna impedance are calculated from an ad hoc collisional model. Similar calculations for parameters typical of Heliotron-E and ATF have been carried out in Japan by A. Fukeyama et al.[4] using finite element analysis and including parallel electric fields. Fukayama et al., however only consider the case of minority heating at the two ion hybrid resonance. We also consider direct heating of the majority ions at the fundamental ion cyclotron frequency, and compare to similar cases of minority heating at the two ion hybrid.

1. Equilibrium Model - In the helically symmetric system, it is useful to transform from cylindrical coordinates (r,θ,z) to helical coordinates (r,ϕ,z') where $\phi = \theta - kz$, $z' = z$, and $k = 2\pi/L_p$ where L_p is the helical field periodic length in z. Note that ϕ = constant is the equation of a helix. Helical symmetry requires that the unperturbed magnetic field $\vec{B}_o$ be only a function of r and ϕ but not z'; i.e., the field at one point in space depends only on which helix that point is on and not on the position in z. Since $\nabla \cdot \vec{B}_o = 0$ and $\nabla \cdot \vec{J} = 0$ in helical coordinates (r,ϕ,z') and $\vec{B}_o$ and $\vec{J}$ are independent of z' (helical symmetry) we can introduce flux functions $\psi(r,\phi)$, $\chi(r,\phi)$ such that the equilibrium field is given by

$$\vec{B}_o = \frac{1}{r}\frac{\partial \psi}{\partial \phi}\hat{r} - \frac{\hat{\theta} - kr\hat{z}}{1 + k^2r^2}\frac{\partial \psi}{\partial r} + \frac{\chi(\hat{z} + kr\hat{\theta})}{1 + k^2r^2}$$

for the present calculations we have used the Bessel function model where

$$\psi(r,\phi) = B_o \frac{kr^2}{2} - r \sum_l \varepsilon_l I_l'(lkr) \cos(l\phi)$$

$$\chi(r,\phi) = B_o = \text{const.}$$

2. Field Equations - Introducing a right-handed orthogonal coordinate system with unit vectors: $\hat{\nabla\psi}$, $\hat{b} \times \hat{\nabla\psi}$, $\hat{b}$ the plasma current can now be expressed

$$\vec{J}_p = \underline{K} \cdot \vec{E} = (K_\perp \hat{\nabla\psi} \cdot \vec{E} - iK_x \hat{b} \times \hat{\nabla\psi} \cdot \vec{E})\hat{\nabla\psi}$$

$$+ (K_\perp \hat{b} \times \hat{\nabla\psi} \cdot \vec{E} + iK_x \hat{\nabla\psi} \cdot \vec{E})\, \hat{b} \times \hat{\nabla\psi} + (K_\parallel \hat{b} \cdot \vec{E})\, \hat{b}$$

$K_\perp$, K_x and $K_\parallel$ are the standard cold plasma conductivity tensor elements with a Langevin collision term included to broaden the fundamental cyclotron resonance $\omega \to \omega + i\nu$ where typically $\nu/\omega \sim 10^{-2}$. We neglect the parallel component of $\vec{E}$ and consider $\nabla\psi$ and $\hat{b} \times \hat{\nabla\psi}$ components of the wave equation. Fourier analyzing $\vec{E}$ and the antenna current $\vec{J}_{ext}$ in the ignorable coordinate.

$$\vec{E}(r,\phi,z') = \sum_{k_z} E_{k_z}(r,\phi)e^{ik_z z'}, \quad J_{ext}(r,\phi,z') = \sum_{k_z} J_{k_z}(r,\phi)e^{ik_z z'}$$

we obtain two coupled partial differential equations in r and ϕ for rE_r and rE_θ. Boundary conditions are that the tangential component of $\vec{E}$ vanish at r = a. This gives $rE_\theta = 0$, and $E_z = 0$ at r = a. Also we use periodicity in ϕ to give $\vec{E}(\phi = 0) = \vec{E}(\phi = 2\pi)$.

3. Results - Figure 1 shows flux surfaces ψ = const. and the heating geometry where the parameters are chosen to model ATF: l = 2, m = 12, R_T = 2.1 m, B_o = 2T, a = radius of conducting wall = 50 cm. Also shown are the two-ion hybrid resonance contour and the minority hydrogen cyclotron resonance contour where $\eta = n_H/n_D = 0.05$ and f_{RF} = 29 mhz. Figure 2 shows contours of power deposition obtained from the field solutions for this case. The antenna is uniform in the ϕ direction with current flow in the θ direction. The heating is seen to lie between the minority cyclotron resonance layer and the hybrid resonance. There is a slight tendency for contours of constant power deposition to lie along flux surfaces as discussed by Hellsten and Appert et al. for tokamaks. We have also done calculations using the cold conductivity model employed by Appert et al. in which no collision term is used to resolve the minority cyclotron resonance ($\omega \to \omega + i\nu$) but the hybrid resonance is resolved by adding an imaginary part to the conductivity itself ($K_\perp \to K_\perp + 2i\delta c^2/c_A^2$). For these calculations the tendency for heating to lie along flux surfaces is much more pronounced but the antenna loading is nearly the same as obtained with the broadened cyclotron resonance.

Calculations in pure H^+ show good antenna loading but the heat deposition is near the plasma surface where the density is low. Calculations for L2 stellarator having lower density and smaller minor radius, show somewhat better penetration of the heating but not sufficient to explain the on-axis heating reported in the experiment.

References

1. Batyuk, V. A., Blobb, M. A. , Grebenshelukov, S. E. , et al., Proceedings of 11th European Conference on Controlled Fusion and Plasma Physics, Aachen 1983, V7D, Part 1, p. 373.

2. Kovrizhnykh, L. M., and Moroz, P. E., Sov. Phys. Tech. Phys. 29, (1984) 384.

3. Jaeger, E. F., Batchelor, D. B., Weitzner, H., and Whealton, J. H., Proceedings of the Workshop on Numerical Modelling of Plasmas, Varenna, Italy (1985) to be published in Comp. Phys. Commun.

4. Fukayama, A., Okazaki, N., Goto, A., Itoh, S-I, and Itoh, K., Nucl. Fusion 26, (1986) 151.

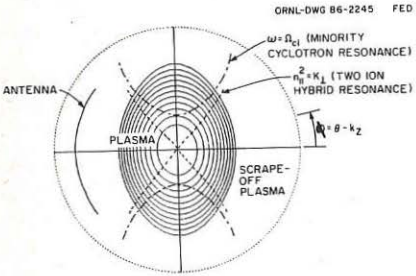

Figure 1. Heating geometry of a straight, helically symmetric stellarator.

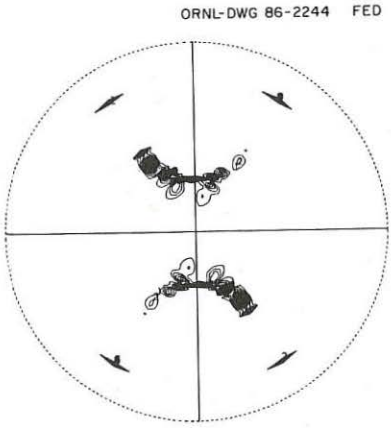

Figure 2. Contours of equal power deposition.

LOCAL DESCRIPTION OF THERMAL PLASMA WITH MAGNETIC INHOMOGENEITY ALONG $\bar{B}_o$

D.W. Faulconer

Laboratoire de Physique des Plasmas - Laboratorium voor Plasmafysica
Association "Euratom-Etat belge" - Associatie "Euratom-Belgische Staat"
Ecole Royale Militaire - B 1040 Brussels - Koninklijke Militaire School

I. INTRODUCTION.

Though the work reported here pertains to general inhomogeneous field configurations, it is presented in the tokamak context where it appears to have greatest relevance. To date, the kinetic description of linear wave interaction in a tokamak in regions neighboring surfaces $\omega = n\Omega$ (species implicit) has been dealt with in two ways. On the one hand, the variation of the equilibrium magnetic field $\bar{B}_o$ parallel to itself resulting from a poloidal field component ($\bar{B}_p.\nabla|\bar{B}_o| \neq 0$) has been neglected ; this allows the derivation of a self-consistent wave equation in perpendicular directions with Fourier analysis providing a nonlocal description in the parallel direction. On the other hand, there are nonlocal solutions which account for parallel $\bar{B}_o$ variation, but with restriction to situations where the field behavior in the resonant region is known to lowest order. Of the work which has been done in these areas, that closest in spirit to the present approach appears in Refs. 1 and 2 to which the reader is referred for further references.

The present contribution examines to what extent one can write a local kinetic description free of the two above assumptions. The local description of nonmagnetized homogeneous plasma [3,4] was early identified with the condition $\omega/k_{\parallel}v_{th} >> 1[(\omega - n\Omega)/k_{\parallel}v_{th} >> 1$ when $\bar{B}_o \neq 0]$. In regions of an inhomogeneous plasma where the second inequality fails ($n \neq 0$) it will be shown that a local description can be retained when the limited extent of the resonance region through which particles pass is accounted for.

II. MODEL AND ANALYSIS.

Considering particles to have constant $v_{\parallel}$ throughout resonance with phase randomization between resonant interactions, Brambilla and Ottaviani [1] have derived the finite Larmor radius equations, calculating current in a form embedding nonlocality in a trajectory-type integral

$$\int_{-\infty}^{\infty} dv_{\parallel}\, v_{\parallel}^{p} \exp(-v_{\parallel}^2/v_{th}^2) \int_{o}^{\infty} d\tau \exp\{i[\omega - n\Omega(\bar{r})]\tau\}\, E(\bar{r} - v_{\parallel}\tau\hat{z}) \qquad (1)$$

where E is a linear combination of field components or their derivatives. We relax the implicit constancy of Ω in the $\hat{z}(\bar{B}_o)$ direction in the integrand of Eqn. (1), accounting for the poloidal passage of particles through the resonance zone, $\Omega(\bar{r})\tau \rightarrow \Omega(\bar{r})\tau - (d\Omega/dz)v_{\parallel}\tau^2/2$ ($d\Omega/dz$ independent of $\bar{r}$). Transforming the variable of integration to $q \equiv k_{\parallel}|v_{\parallel}|\tau \pm b/a$, with $v_{\parallel} = v_{th}V_{\parallel}$, one has to within a dimensional constant factor

$$I_n = \int_{o}^{\infty} dV_{\parallel} V_{\parallel}^{p-1} \exp(-V_{\parallel}^2)\{(-1)^p \int_{-b/a}^{\infty} dq \exp[-(i/V_{\parallel})(aq^2 - b^2/a)]E(k_{\parallel}z + q + b/a)$$

$$+ \int_{b/a}^{\infty} dq \exp[(i/V_{\parallel})(aq^2 - b^2/a)]\, E(k_{\parallel}z - q + b/a)\} \quad (n\neq 0) \qquad (2)$$

where $a = (nd\Omega/dz)/(2k_{\parallel}^2 v_{th})$, $b = [\omega - n\Omega(\bar{r})]/(2k_{\parallel}v_{th})$, $E(k_{\parallel}z + q + b/a) \equiv E\{\bar{r} + (q + b/a)/k_{\parallel}\hat{z}\}$ and nondimensionalization with respect to $k_{\parallel} \equiv |E^{-1}\partial E/\partial z|$

in no way implies an assumed z dependence $\sim \exp(ik_{\parallel}z)$. Remark that unit length in q corresponds to one spatial variation length of E.

In order to appreciate the role played by various parameters in the subsequent development, it is of interest to consider the conditions under which I_n can be evaluated in terms of $E(k_{\parallel}z)$ (strong local representation). These are essentially the conditions under which rapid oscillatory behavior of the second and third exponentials in the integrands gives phase cancellation in q, $V_{\parallel}$ at all points except the endpoints $q = \pm b/a$. Turning first to the q integral, one sees strong phase cancellation when $|\partial(aq^2)/\partial q| = |2aq| >> 1$, this eliminating contributions to the integral from all q except a nonlocal one coming from values around the resonant or stationary phase value $q = 0$, and, if $|2aq|_{q=\pm b/a} = |2b| >> 1$, a local one from the immediate vicinity of the endpoint $q = \pm b/a$. From the first inequality, parameter a can be roughly identified with the inverse of the resonance zone width along $\hat{z}$ seen by a given particle. Inverting the order of integration, one finds $V_{\parallel}$ rapid-phase cancellation when $|aq^2 - b^2/a| >> 1$; this notably eliminates the above nonlocal resonant contribution from $q = 0$ when $|b^2/a| >> 1$, allowing I_n to be expressed purely locally in terms of $E(k_{\parallel}z)$. The physical origin of the rapid-phase effects leading to this local expression are the progressive dephasing of the n^{th} harmonic of a single particle's Larmor motion from the field phase in the case of oscillations in q, and the smearing out of the contribution from a given q due to thermal spread in particle velocities in the case of oscillations in $V_{\parallel}$.

In the absence of the above conditions for local representation of I_n, we render I_n local by expansion of E in q about the local endpoint values $\pm b/a$. This expansion is assumed valid in the region in q giving the major contribution to the q integral, this region being delimited by the effects discussed in the preceding paragraph. For the case $n = 0$, addition of an infinitesimal imaginary causality term to ω allows derivation from Eqn. (1) of the asymptotic representation [same nondimensionalization as for Eqn.(2)]

$$I_o = -\sum_{j=o}^{N-1} E^{(\ )}(k_{\parallel}z)(-i/2b)^{(\ )+1}\,\Gamma\{[p + (\ ) + 1]/2\} \quad (|2b| = |\omega/k_{\parallel}v_{th}| \to \infty) \quad (3)$$

where ( ) is to be filled in with 2j, 2j + 1 when p is respectively even, odd ; henceforth $E^{(j)} = \partial^j E/\partial(k_{\parallel}z)^j$. The impossibility of obtaining a corresponding convergent local representation and the associated existence of Landau damping are established facts.

For $n \neq 0$, one can evaluate the first integral with respect to q in I_n of Eqn. (2) by transformation to the variable $t = (ia)^{1/2} q$, with use of an infinitesimal convergence factor to rotate the infinite portion of the resulting integration path into the sector $|\arg t| < \pi/4$ before expanding E inside the integrand about $t = -(ia)^{1/2}b/a$; the second q integral is performed using $t = (-ia)^{1/2}q$ with the principle branch used for all roots. One finds

$$I_n = \sqrt{\pi}/2 \sum_{j=o}^{\infty} E^{(j)}(k_{\parallel}z)[(-1)^p\{\int_o^{\infty} dV_{\parallel}\, V_{\parallel}^{p-1}\exp(-V_{\parallel}^2 + ib^2/aV_{\parallel}) \times$$

$$\iota^j \operatorname{erfc}\left[-\left(\frac{ia}{V_{\parallel}}\right)^{1/2}\frac{b}{a}\right](V_{\parallel}/ia)^{(j+1)/2}\}+(-1)^j\{a\to -a\}] \quad (n\neq 0) \quad (4)$$

where ι^j erfc is the j-fold repeated integral of the complex complementary error function. Expanding ι^j erfc with formula 7.2.4 of Ref. 5, there results the convergent development

$$I_n = \sqrt{\pi} \sum_{j=o}^{\infty} E^{(j)}(k_{\shortparallel},z)\,[(-1)^p\{(4ia)^{-(j+1)/2} \sum_{k=o}^{\infty} [2(ia)^{1/2}b/a]^k/[k!\Gamma(1+\tfrac{j-k}{2})] \times$$

$$f_m(-ib^2/a)\big|_{m=p+(j-k-1)/2}\} + (-1)^j\{a \to -a\}] \quad (n \neq 0) \qquad (5)$$

where the terms k = j + 2, j + 4, ... are taken to be zero with convergent and asymptotic expansions for f_m given in Sect. 27.5 of the reference (use of the principal branch for roots is understood throughout). The convergent expansion only holds for integral m ; the development for nonintegral m is found to be

$$f_m(x) = 1/2 \sum_{k=o}^{\infty} \Gamma(\tfrac{m+1-k}{2})(-x)^k/k! + \pi/\sin(m\pi) \sum_{k=o}^{\infty} (-1)^k\, x^{2k+m+1}/[\Gamma(2k+m+2)k!] \qquad (6)$$

The asymptotic expansion of I_n follows from substituting the asymptotic expansion of ι^j erfc (7.2.14 of Ref. 5) into Eqn.(4)

$$I_n = 1/2 \sum_{j=o}^{\infty} E^{(j)}(k_{\shortparallel},z)/[j!(-2ib)^{j+1}] \sum_{k=o}^{K-1} [(2k+j)!\Gamma(\tfrac{p+k+j}{2})/\,k!][(-1)^p \times$$

$$(-4ib^2/a)^{-k} + (-1)^j(4ib^2/a)^{-k}] \quad (|4b^2/a| \to \infty,\ n \neq 0) \qquad (7)$$

III. DISCUSSION.

Equations (3),(5) and (7) give the local representation of the integral I_n ; it remains to project onto the coordinates of interest. Taking as example a slab geometry with derivatives of equilibrium density neglected, y, Y coordinate axes normal to both $\bar{B}_o(\shortparallel \hat{z})$ and $\nabla|\bar{B}_o|$, and X-axis parallel to $\nabla|\bar{B}_o|$, the spatial dependence of the coefficients of $E^{(j)}$ in the local representation enters only through the dependence of b on $\Omega(X)$. One redevelops partial differentials in x,y,z in terms of differentials in X,Y,Z($\partial/\partial z = \sin\theta\partial/\partial X + \cos\theta\partial/\partial Z$ etc., θ = angle between $\hat{z},\hat{Z}$), this both in I_n and in the finite Larmor radius equations which incorporate it [1], these having been derived relative to guiding-center coordinates x,y,z. Of course, one could employ flux coordinates at the cost of losing invariance in one of the coordinate directions.

After Fourier analysis in the invariant directions Y, Z, one integrates the resulting system in X, the convergent or asymptotic representations being used for $I_n(X)$ in accord with the respective smallness or largeness of b(X). In principle, describing resonant regions where $b \to 0$ is simply a question of employing enough derivatives $E^{(j)}(\bar{r})$ in the convergent representation. In practice, one is confronted with one of two situations where these derivatives affect wave behavior either strongly or weakly. In the former case one will typically not wish to employ X derivatives of an order which increases the order of the differential system to be solved, so as to avoid introducing new modes. This effectively limits the resonance zone width in z one can treat to several field variation lengths. In the latter case an iterative approach is possible where again, a limited number of derivatives is added in the initial solution so that the order of the system is not raised. This solution is then used to evaluate as many derivatives as necessary, these serving as known inhomogeneous terms in the next iteration.

IV. CONCLUSION.

A local approach allowing description in the vicinity of "strongly dispersive" surfaces ($(\omega - n\Omega)/k_{\shortparallel}v_{th} \not\gg 1$) has been developed by accounting for the particles' poloidal transit through these surfaces. This eliminates the exaggerated phase coherence between particle gyromotion and wave seen

when particle trajectories are taken parallel to the surfaces. Such description can be carried through without presupposing the lowest-order form of the field.

ACKNOWLEDGEMENTS.

The author is grateful for valuable discussions with Professor H. Janssen, Dr. R. Koch, Philippe Lamalle, and Dirk Van Eester.

REFERENCES.

1. M. Brambilla and M. Ottaviani, Plasma Physics 27, 999 (1985).
2. S.-I. Itoh, A. Fukuyama, K. Itoh, and K. Nishikawa, J. Phys. Soc. Jap. 54, 1800 (1985).
3. P.E. Vandenplas and R. Gould, "Study of electromagnetic interactions in plasmas", Contract U.S. Army Signal Res. Develop. Lab. Quart. Progr. Report No. 3, California Institute of Technology, 1960. This and later contributions are summarized in: P.E. Vandenplas, Electron Waves in Bounded Plasmas, Interscience Pub., London-New York-Sydney, 1968.
4. C.R. Obermann, MATT-57, Proj. Matterhorn, Princeton University, 1960.
5. M. Abramowitz and I. Stegun, Handbook of Mathematical Functions, Dover Pub., New York, 1965.

METHOD FOR RAPID EVALUATION OF ANTENNA NEAR-FIELDS

D.W. Faulconer, D.I.C. Pearson, F. Durodié

Laboratoire de Physique des Plasmas - Laboratorium voor Plasmafysica
Association "Euratom-Etat belge" - Associatie "Euratom-Belgische Staat"
Ecole Royale Militaire - B 1040 Brussels - Koninklijke Militaire School

1. INTRODUCTION.

Knowledge of the quasi-static $\bar{E}$ and $\bar{B}$ fields in the immediate vicinity of antennas and electrostatic shield elements is essential to the intelligent design of these components. To the end of calculating such fields, a numerical method has been developed for solving the 2-D Laplace equation which generates the Green's function for a flux or vortex line source inside an arbitrary rectilinear, perfectly conducting external boundary. Line sources can be superposed to simulate eventual internal conductors as well as supplementary conditions to be imposed on the field flux. Such conditions can mock up $\bar{B}(\bar{E})$ flux crossing (running parallel to) the external conducting boundary, allowing this single boundary to model internal conductors as well (see Fig. 1). In the single-boundary case the method is truly computer intensive, freeing the user of the time-consuming adaptations to specific boundaries which characterize finite-difference and finite-element techniques. In essence, he reads in boundary geometry and places line sources. The conformity of the computed representation of the external boundary to the actual one provides a direct visual check on the accuracy of the calculation. The present method is particularly suited to situations where interest is focused on surface quantities and their integrals on boundaries (Sect.2.3).

2. METHOD.

2.1. Overview.

A Schwarz-Christoffel (SC) transformation mapping $\eta > 0$ of the ζ-plane ($\zeta = \xi + i\eta$) onto the internal space enclosed by the external conducting boundary in the z-plane ($z = x + iy$) is generated numerically. Line sources enclosed by the boundary in the z-plane are inversely mapped to the ζ-plane where the problem is solved by the method of images and integrals of various surface densities are performed. If required, fields or surface density distributions in the z-plane are obtained via the SC transformation (end Sect. 2.3). The user works interactively in z-space, disposing line sources by eye.

2.2. Generation and Inversion of Schwarz-Christoffel Transformation.

Let the N segments of the rectilinear external boundary, enumerated in counter-clockwise fashion, be $L_i (i = 1, \ldots, N)$, with i^{th} vertex, having inner angle α_i, at z_i lying between L_{i-1} and $L_i (L_o \equiv L_N)$. We shall generally take z_N at infinity. For an appropriate choice of the ξ_i ($\xi_i > \xi_{i-1}$) and A, the SC transformation (in differential form)

$$dz/d\zeta = A \prod_{i=1}^{N} (\zeta - \xi_i)^{(\alpha_i/\pi)-1} \equiv f'(\zeta) \qquad (1)$$

maps the ξ-axis of the ζ-plane onto the external boundary in the z-plane, with each point ξ_i mapping onto z_i .

Integration of Eqn.(1) between vertices for a trial set, $\tilde{\xi}_i$, gives

$$\tilde{L}_i \equiv \tilde{z}_{i+1} - \tilde{z}_i = \int_{\tilde{\xi}_i}^{\tilde{\xi}_{i+1}} f'(\zeta)d\zeta \qquad (i = 1, \ldots, N\ ;\ \tilde{z}_{N+1} \equiv \tilde{z}_1) \qquad (2)$$

where a numerical integration is generally required. The following function of the $\tilde{L}_i$, and hence of the $\tilde{\xi}_i$, attains the value zero as a sharp absolute minimum when $\tilde{L}_i = L_i (i = 1, \ldots, N)$ (i.e. when the ξ-axis is correctly mapped onto the external conducting boundary)

$$g = \sum_{i=1}^{N} \{|L_i/\tilde{L}_i| + \exp[|\tilde{L}_i/L_i| - 1] - 2\} \qquad (3)$$

When z_N is taken at infinity, we drop the two infinite L_i from the sum using N - 2 as upper limit ; ξ_N is also suppressed (see Sect. 3). Minimizing g to zero with successive trial choices of the $\tilde{\xi}_i (\tilde{\xi}_1 \equiv 0, A \equiv 1)$ gives $\tilde{\xi}_i \to \xi_i$ in the limit. A conjugate gradient method (the MINUIT routine of CERN) has been used for this.

Once the ξ_i are known, the inverse SC transformation is generated from Eqn. (1)

$$\zeta(z) = \int_0^{\zeta(z)} d\zeta = \int_0^z (d\zeta/dz)dz = \int_0^z [f'(\zeta)]^{-1}\, dz \qquad (4)$$

where simultaneous numerical integration in z and ζ-planes is implied. Eqn. (4) serves for mapping source positions and integration interval endpoints (Sect. 2.3) to the ζ-plane.

2.3. Fields and Surface Quantities.

Line sources of identical or opposite strength, each with complex potential of the form $(S/2\pi)\ \ln(\zeta - \zeta_s)$, are imaged at ζ_s and ζ_s^* to give an analytic expression for the potential, $\Omega_s(\zeta - \zeta_s)$, of a source at ζ_s above the ξ-axis [a conducting surface ; arg $(\zeta - \zeta_s)$ in $\ln(\zeta - \zeta_s)$ taken continuous]. One has for B(E) line current (charge) sources : $S = -i\mu_0 I_z$ (q/ε_0), $(\hat{z} = \hat{x} \times \hat{y})$, and for unphysical B(E) flux (vortex) sources useful for imposing supplementary flux conditions (Fig. 1) : S = total $\bar{B}$ flux from source $(-i$(circulation of $\bar{E}$ about source)). For the total complex potential one has $\Omega(\zeta) = \sum_{\text{sources}} \Omega_s(\zeta - \zeta_s)$ and $\Omega(z) = \Omega[\zeta(z)]$. In the magnetostatic case $\underline{B}^*(\zeta) = d\Omega/d\zeta$, $B^*(z) = d\Omega/dz = [f'(\zeta)]^{-1} B^*(\zeta)$. With $\Omega \equiv \Phi + i\Psi$ one has $\bar{B} = \nabla\Phi$ and

$$\int_1^2 \bar{B}.d\bar{l} = \Phi(2) - \Phi(1)$$
$$\int_1^2 \bar{B}.\hat{n}|d\bar{l}| = \Psi(2) - \Psi(1) \quad (\hat{n} \parallel d\bar{l} \times \hat{z}) \qquad (5)$$

relations (5) holding in either plane, where it is understood that the path 1,2 in one plane maps into that in the other. Equality of a given right member in either plane shows equality of the corresponding integral. Identical formulae hold for the electrostatic case. Using Eqn. (1) and the relations directly above Eqn.(5) one has

$$\int_1^2 |B^2(z)||dz| = \int_1^2 |B^2(\zeta)/f'(\zeta)|\,|d\zeta| \qquad (6)$$

where paths in left and right members map into each other.

For an integration path 1,2 circuiting with the conductor on its left, $\hat{z}$-directed surface current density is $\mu_0^{-1} \bar{B}.d\bar{l}/|d\bar{l}|$, charge density, $\varepsilon_0 \bar{E}.\hat{n}$ and ohmic dissipation density $(2\mu_0)^{-3/2}(\omega/\sigma)^{1/2}|B|^2$ (ω = wave angular frequency, σ = conductivity). Once the locations of 1 and 2 in the ζ-plane are known (by Eqn. (4) or, for a vertex, $z_i \to \xi_i$), the integration of the current and charge densities is best considered in the ζ-plane as Eqns. (5)

with $B \leftrightarrow E$ then give the integrals as known functions. Eqn. (6) allows integration of the ohmic density as a known function on the ξ-axis instead of the detailed external boundary in the z-plane.

Field lines in the complex planes follow from integrating $d\zeta/ds = B(\zeta)/|B|$, $dz/ds = f'(\zeta)B(\zeta)/|B|$ where s is arclength in the ζ-plane and Eqn. (1) has been used ; $B \rightarrow E$ gives results for E. Taking real and imaginary parts gives a 4 × 4 system for the vector (ξ, η, x, y) which is efficiently integrated by a variable-step method. Similar remarks apply to inversion(4).

The same integration, following the magnetic line coinciding with a conductor surface, can be used to map surface density distributions from the ζ to the z-plane, it also serving for the integral of ohmic dissipation density on a source-simulated internal conductor. By Eqn. (6), this integral can be performed in the ζ-plane without integrating the equation for dz/ds.

3. SPECIAL TECHNIQUES.

Double-precision minimization of g [Eqn.(3)] over successive $\tilde{\xi}_i$ sequences generally encounters difficulties associated with tight bunching of the $\tilde{\xi}_i$, a case notably met when the external boundary is of re-entrant type with two z_i close together. One such difficulty relates to reordering of the $\tilde{\xi}_i$ out of increasing sequence by the minimization routine. Transformation to N new variables χ_i, where $\xi_i = \xi_{i-1}(1 + \exp \chi_i)$, remedies this problem and smooths the behavior of g when minimization is carried out over $\tilde{\chi}_i$ sequences. Another such difficulty has to do with loss of numerical accuracy due to the singular behavior at the limits of integration of $f'(\zeta)$ in Eqn. (2). This can be dealt with by subtracting from the integrand analytically integrable functions which cancel its endpoint singularity and adding back the integrals of the same functions which are known. However, a further source of error arises when the integration interval length $\tilde{\xi}_{i+1} - \tilde{\xi}_i$ in Eqn. (2) greatly exceeds that of the adjacent interval(s), this allowing the singular behavior of f' at the far edge of the small interval(s) to affect seriously the precision of integration over $[\tilde{\xi}_i, \tilde{\xi}_{i+1}]$. Accuracy was restored with a variable-step method which reduces the integration step at the end(s) of the interval. Similar remarks apply to the integral in the right member of Eqn. (6).

Given these problems of precision which are generally compounded as N increases, it becomes advantageous in the case of large N to place ξ_N at infinity (z_N finite or infinite) with the substitutions $N \rightarrow N - 1$, $\tilde{\xi}_N = \infty$ in Eqns. (1), (2) respectively. The effective elimination of $\tilde{\xi}_N$ reduces by one the dimension of the space in which g is minimized. One can additionally take $\tilde{\xi}_2 = 1$ ($\tilde{\xi}_1 = 0$, $A = 1$), substituting $L_i \rightarrow L_i/L_1$, $\tilde{L}_i \rightarrow \tilde{L}_i/\tilde{L}_1$ in g. This further reduces dimension by one at the cost of only generating the $\tilde{L}_i$ to within a scale factor, the correct scale being incorporated in the SC after minimization by altering the value of A to $L_1/\tilde{L}_1$. In the case of a symmetric configuration, choice of origin at a point of symmetry leads to an important reduction in dimensionality due to symmetry of the $\tilde{\xi}_i$ about the origin.

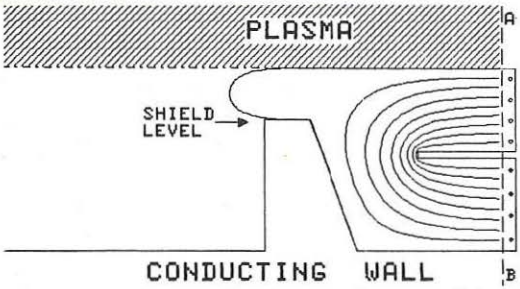

Fig. 1. Equiflux-spaced magnetic contours for a candidate TEXTOR ICRF antenna-limiter configuration in the presence of a plasma simulated by a perfectly conducting surface. The various elements - limiter, wall, central conductor, plasma surface - are all simulated by a single external SC boundary. The eight flux sources(o strength +1,• strength -1)ensure that a constant field crosses normally the line of symmetry AB.

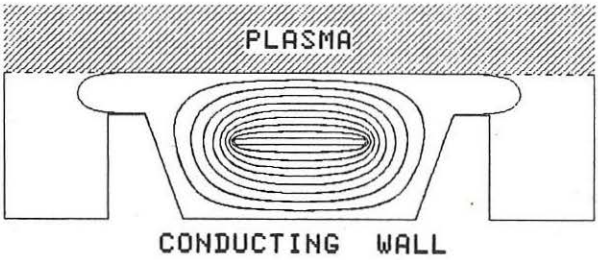

Fig. 2. Same case as Fig. 1 but where a symmetrical transformation is used to simulate wall, limiter and plasma. The internal central conductor surface is mocked up by placing 40 line current sources with intensities adjusted interactively in order that the real conductor surface be matched as closely as possible by a magnetic surface contour.

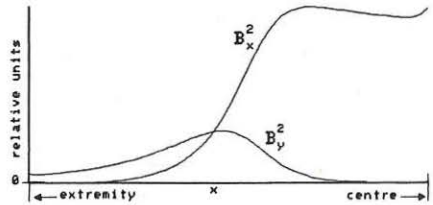

Fig. 3. B_x^2, B_y^2 plotted as functions of x at the electrostatic shield y-position in Fig. 1 (same relative units for both). Relatively large B_x^2 values caused by plasma-induced field compression show greater role in Ohmic loss played by circumferential shield element current than in the case without plasma.

THE EFFECT OF NEUTRAL BEAM INJECTION ON WAVE PROPAGATION IN THE ION CYCLOTRON RANGE OF FREQUENCIES

W.G.F. Core

JET Joint Undertaking, Abingdon, Oxon., OX14 3EA, UK

1. Introduction - The possibility of using neutral injection combined with the fast magnetosonic wave as additional heating of tokamak plasmas is currently of considerable interest and has received some attention in the literature [1]. As is well known, the injection of fast neutral particles leads to the formation of hot energetic ion tails on the bulk plasma ion species. These velocity space distortions modify the dielectric properties of the plasma, and in particular, for heating at the second harmonic frequency, can significantly enhance the absorption of wave energy [2].

In this paper, the effect of NBI on the propagation of waves in the IC range of frequencies is examined. The fast ion component is modelled by superimposing on the bulk plasma ions displaced Maxwellians of the form,

$$f(v_{\parallel},v_{\perp}) = N \exp\left[-(v_{\parallel}-v_{\parallel_0})^2/\alpha - (v_{\perp}-v_{\perp_0})^2/\beta\right]. \qquad (1)$$

Using this form of representation for the ion distribution functions the components of the dielectric are obtained in a form which is amenable to efficient computation. The resulting dispersion equation is then solved numerically for fast wave propagation into the beam/ICRF-plasma systems.

(i) Hydrogen beam injection during fundamental ($\omega=\omega_{cH}$) heating of a minority H/D plasma;

(ii) The seeding of a D-plasma with fast deuterons during bulk ICRF heating at ($\omega=2\omega_{cD}$).

2. The Dispersion Equation - Starting from the Maxwell field equations for electromagnetic wave propagation in a hot multi-component magnetoactive plasma the dispersion equation is readily obtained and can be written as

$$\left|k^2\delta_{ij}-k_ik_j-\frac{\omega^2}{c^2}\varepsilon_{ij}\right| = 0, \qquad (2)$$

where the components of the dielectric tensor in the cylindrical coordinate system $\underline{v}=(v_{\parallel},v_{\perp})$ in velocity space takes the form [3]

$$\varepsilon_{ij} = \delta_{ij} - \sum_S \left(\frac{\omega_{ps}}{\omega}\right)^2 \left\{\delta_{ij} + \sum_{n=-\infty}^{n=\infty} \int d\underline{v} \left(\frac{n\omega_s}{v_{\perp}}\frac{\partial f}{\partial v_{\perp}} + k_{\parallel}\frac{\partial f}{\partial v_{\parallel}}\right) \frac{\pi^s_{ij}}{k_{\parallel}v_{\parallel}+n\omega_{cs}-\omega}\right\}, \qquad (3)$$

where $\omega_{ps}^2 = \frac{4\pi Z_s^2 n_s}{m_s}$, $\omega_{cs} = \frac{Z_s B}{m_s c}$, $k_{\parallel}=\underline{k}\cdot\underline{B}$, $\pi_{11}^s = \lambda_n^2 J_n^2$, $\pi_{12}^s=-\pi_{21}^s = iv_{\perp}\lambda_n J_n J_n'$,

$\pi_{13}^s = \pi_{31}^s = v_{\parallel}\lambda_n J_n^2$, $\pi_{22} = v_{\perp}^2 J_n'^2$, $\pi_{23}^s=-\pi_{32}^s=-iv_{\parallel}v_{\perp}J_n J_n'$, $\pi_{33}^s = v_{\parallel}J_n^2$, $\lambda_n = \frac{n\omega_{cs}}{k_{\perp}}$,

$J_n = J_n(v_{\perp}/\lambda_n)$, $J_n' = dJ_n(x)/dx$, and the summation is over all the plasma species (s).

In the local frame of the toroidal magnetic field, where $k_x=k_{\perp}$, $k_y=0$, $k_z=k_{\parallel}$, Eq.(2) takes the form,

$$A_0 k_{\perp}^4 - 2A_1 k_{\perp}^3 + 4A_2 k_{\perp}^2 - 2A_3 k_{\perp} + A_4 = 0, \qquad (4)$$

where $A_0=\varepsilon_{\parallel}$, $A_1=\varepsilon_{13}k_{\parallel}$, $4A_2=k_{\parallel}^2(\varepsilon_{\parallel}+\varepsilon_{33}) - \varepsilon_{\parallel}(\varepsilon_{22}+\varepsilon_{33}) +\varepsilon_{13}^2-\varepsilon_{12}^2$,

$A_3 = k_{\parallel}^3\varepsilon_{13} + k_{\parallel}(\varepsilon_{12}\varepsilon_{23}-\varepsilon_{13}\varepsilon_{22})$,

$A_4 = k_{\parallel}^4\varepsilon_{33} - k_{\parallel}^2(\varepsilon_{11}\varepsilon_{33}+\varepsilon_{22}\varepsilon_{33}-\varepsilon_{23}^2-\varepsilon_{13}^2)$

$- \varepsilon_{11}\varepsilon_{22}\varepsilon_{33}-\varepsilon_{11}\varepsilon_{23}^2+\varepsilon_{33}\varepsilon_{12}^2-\varepsilon_{22}\varepsilon_{13}^2+2\varepsilon_{12}\varepsilon_{23}\varepsilon_{31}$.

3. Calculation of Permitivity Tensor Components ε_{ij} - Introducing plasma species distributions of the form, Eq.(1) into Eq.(3) the components of the tensor ε_{ij} after some reduction take the form:

$$\varepsilon_{11} = 1 - \sum_{i,e}\left(\frac{\omega_{pj}}{\omega}\right)^2 \{1 - 4\pi^{3/2}\sum_{n=-\infty}^{n=\infty}\{\left(\frac{n\omega_{cj}}{\alpha k_{\parallel}} Z - \frac{1}{2\sqrt{\beta}} Z'\right) I_{n,n}^1 - \frac{n\omega_{cj} v_{\perp_o}}{\alpha k_{\parallel}} Z\, I_{n,n}^o\}\},$$

with similar expressions for the remaining ε_{ij}, and where in the above expressions, $Z(x)$ is the plasma dispersion function, $Z' = dZ/dx$, $x = (\omega - n\omega_{cs} - k_{\parallel}v_{\parallel_o})/k_{\parallel}\sqrt{\beta}$, and

$$I_{p,q}^m = \int_o^{\infty} dv_{\perp} v_{\perp}^m J_p\left(\frac{k_{\perp}v_{\perp}}{\omega_{cs}}\right) J_q\left(\frac{k_{\perp}v_{\perp}}{\omega_{cs}}\right) \exp\left\{-\frac{(v_{\perp}-v_{\perp_o})^2}{\alpha}\right\},$$

$$= \frac{\left(\frac{k_{\perp}}{2\omega_{cs}}\right)^{p+q}}{\left\{\frac{2}{\beta} + \frac{k_{\perp}^2}{2\omega_{cs}^2}\left(\frac{1}{p+1}+\frac{1}{q+1}\right)\right\}^{\frac{p+q+m+1}{2}}} \exp\left\{-\frac{v_{\perp_o}^2}{2\beta}\,\frac{2 + \frac{k_{\perp}^2\beta}{2\omega_{cs}^2}\left(\frac{1}{p+1}+\frac{1}{q+1}\right)}{1 + \frac{k_{\perp}^2\beta}{2\omega_{cs}^2}\left(\frac{1}{p+1}+\frac{1}{q+1}\right)}\right\}$$

$$\cdot \frac{\Gamma(p+q+m+1)}{\Gamma(p+1)\Gamma(q+1)} D_{-(p+q+m+1)}(\mu),$$

where $\mu = \frac{2v_{\perp o}}{\beta}\left\{\frac{2}{\beta} + \frac{k_\perp^2}{2\omega_{cs}^2}\left(\frac{1}{p+1} + \frac{1}{q+1}\right)\right\}^{-\frac{1}{2}}$, and $D_{-a}(\mu)$ is the Parabolic cylindrical function [4].

4. Computational Considerations - To determine the fast wave propagation from the plasma edge to the centre of the discharge Eq.(4) is solved recursively with the full plasma and hot ion dielectric tensor according to the prescription

$$A_o(k_{\perp r-1})k_{\perp r}^4 \cdots A_4(k_{\perp r-1}) = 0.$$

The bulk plasma species profiles take the form

$$T_e(r)=T_i(r)=T(0)\{1-C_1(r/a)^p\}^q,\ n_e(r)=n_i(r)=n(0)\{1-C_2(r/a)^p\}^q,$$

and in order to model the beam, and in particular, the effects of slowing down, energy diffusion, and pitch angle scattering, we take 3-terms of the form given by Eq.(1), with N_i, α_i, β_i, $v_{\parallel oi}$, $v_{\perp oi}$, i=1,2,3, where for component energy E_i, energy spread ΔE_i, and beam angle θ, $\alpha_i = 2\Delta E_i/m\cos^2\theta$, $v_{\parallel oi}^2 = 2E_i/m\sin^2\theta$, with similar expressions for β_i, and v_{oi}^2.

5. Numerical Results - For the aforementioned beam plasma systems we take the standard JET parameters, plasma species temperature $T_e(0)=T_i(0)=2.5$keV, electron density $n_e(0)=3\times10^{13}$cm^{-3}, p=2, q=1, $C_1=0.9$, $C_2=1.0$, beam injection angle at the toroidal axis 45°, minor radius a=125cm, and major radius R_o=296cm. For the beam deposition profile p=2, q=4.

Hydrogen beam injection during fundamental ($\omega=\omega_{cH}$) heating of a minority H/D plasma.

For this configuration, we take E_i=80,60,30keV; ΔE_i=1,5,15keV, N_i=1, magnetic field at the toroidal axis B(0)=2.0T, wave frequency f=33.3MHz, and $k_\parallel = 4\times10^{-2}$cm^{-1}.

In Fig.1 the fast magnetosonic wave propagation characteristics from the edge of the plasma to the centre of the discharge in a minority H/D plasma seeded with energetic protons is shown. For a 15% concentration of plasma minority hydrogen and no beam ions no significant single pass absorption occurs. The effect of increasing the fast ion concentration and maintaining the total minority concentration at 15% leads to enhanced selective wave damping by the injected ions. For 15% concentration of fast ions strong single pass absorption is indicated.

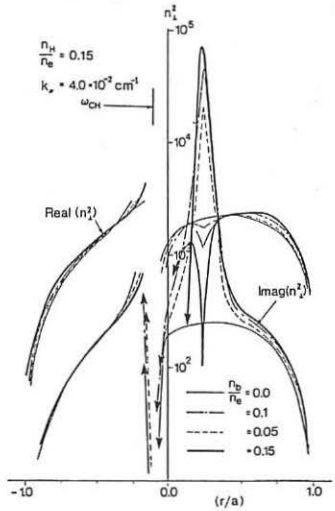

Fig.1

Fast Deuteron injection during ICRF heating of a bulk D-plasma at ($\omega=2\omega_{cD}$).

For this configuration, we take E_i=160,120,60keV, ΔE_i=2,10,30keV, N_i^2=1, magnetic field at the toroidal axis B(0)=2.03T, wave frequency f=29.8MHz, and $k_{\parallel}=4\times10^{-2}cm^{-1}$.

In Fig.2 the effect of introducing energetic deuterons into a D-plasma on the fast wave propagation characteristics during bulk second harmonic heating is shown. For no concentration of fast ions the absorption occurs on or near the resonant surface $\omega=2\omega_{cD}$. The presence of the fast ion components leads to additional damping at the Doppler shifted resonance surface at R, where $\omega=2\omega_{cD}(R)+k_{\parallel}v_{\parallel}$. The build-up of the fast ion concentration gives rise to strong increasing single pass absorption. However, here finite Larmor radius effects play a crucial role in the damping process.

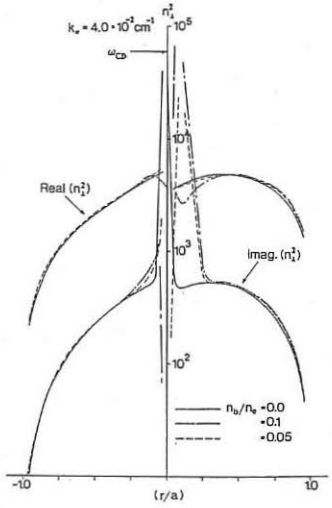

Fig.2

6. Summary - For the model configurations considered here, the preliminary results indicate that the seeding of ICRF heated tokamak plasma systems with fast resonant ions leads to

(i) Strong selective absorption of wave energy by the injected fast ions;
(ii) Damping of the fast wave during fundamental heating of minority ion admixtures is significant even at relatively large concentrations of fast ions.
(iii) For a given injection energy, and for fundamental ICRF operations, near tangential beam injection $\theta\approx0$, provides optimum damping. While for heating at the second harmonic frequency, where finite Larmor radius effects are important, injection in the region of $\theta\approx\pi/2$ is to be preferred.

Finally, for JET operations with a deuterium bulk, and either hydrogen or deuterium injection, strong damping by the fast particles is predicted.

References

[1] S-I. Itoh, A. Fukuyama and K. Itoh, Nucl. Fusion 24 (1984) 224.
[2] T. Hellsten, K. Appert, W. Core, H. Hamnén and S. Succi, 12th Eur. Conf. on C.F.P.P. (1985) 124.
[3] A. Sitenko, Electromagnetic Fluctuations in Plasmas, A.P. (1967).
[4] M. Abramowitz and I. Stegun, Handbook of Mathematical Functions.

THEORY OF EXCITATION OF ASYMMETRIC $k_{//}$-SPECTRUM BY PHASING THE JET ICRF ANTENNAE

V.P. Bhatnagar*, M.P. Evrard*, J. Jacquinot

JET Joint Undertaking, Abingdon, Oxon, OX14 3EA, UK
*From LPP-ERM/KMS; EUR-EB Association, 1040 Brussels, Belgium

1. Introduction

A potentially important application of a radio-frequency heating scheme is the generation of RF driven currents to assist in the plasma equilibrium of a tokamak [1]. In large tokamaks such as JET, the ion-cyclotron resonance heating (ICRH) power-deposition profile is narrow and the power can be deposited locally [2,3]. This feature opens up the possibility of modification and control of current profile in tokamaks by driving current with waves in the ion-cyclotron range of frequencies (ICRF) with a view to stabilizing internal instabilities of a tokamak plasma. ICRF current-drive efficiencies are expected to be low [4] and therefore, no significant experiment of current drive by ICRF in a tokamak has yet been attempted, though, several advantages of ICRF over other RF schemes are evident such as good wave penetration property at high densities. Moreover, in this scheme, one could adjust several parameters like plasma composition, concentration and k//-spectrum for optimised experimental conditions [5].

To drive current in JET by waves in the ICRF either through cyclotron damping on a minority species or by absorption of the mode converted wave power by the plasma electrons via Landau damping, excitation of an asymmetric k//-spectrum is required. For the 1987 heating and current drive experiments in JET, four pairs of ICRF antenna systems will be regularly positioned around the torus. Such a system of antenna structures around the torus can be appropriately phased to produce the desired assymmetric k//-spectrum.

In this paper, we carry out a theoretical study, of the excitation of travelling ICRF waves in JET, based on a 3-D planar antenna-plasma coupling model. The antennae are progressively phased to excite a desired integral number of parallel wavelengths around the torus (n_o = 1, 2, 3 ... etc) where n_o = 3 or 4 is appropriate for mode conversion current drive and a somewhat higher number for the minority current drive.

Several sets of antenna combinations including that of a single pair alone have been analyzed and the results have been examined by looking at the directivity $D(n_o)$ defined as the asymmetry in k//-spectrum of the radiated power normalized to the total power radiated.

2. Theoretical Model

The analysis of excitation of fast magnetosonic waves by an ICRH antenna in a tokamak plasma is generally treated by a full-wave solution in the context of a semi-infinite, planar cold plasma model under single-pass absorption conditions [6,7]. The details of the model and the underlying assumptions have been published previously [6,7]. Applying the

induced emf method, analysis of the boundary value problem associated with this model is well known and is not repeated here, the details of which can be found in Ref. 6 and 7. The complex power radiated by the antenna and delivered to the medium can be written as $P = P_{TE} + P_{TM}$ where P_{TE} and P_{TM} are given in terms of a Fourier Series [6]. An array of antennae in the toroidal direction can be included by providing the appropriate spectrum of currents flowing in the phased antenna array. Travelling waves in a given direction can be excited by progressively phasing the antenna array. In order to gauge the asymmetry of the excited $k_{//}$-spectrum of $R_e(P_{TE})$, we define a directivity D for a given toroidal mode number n_o as [8],

$$D\left(\frac{n_o}{r}\right) = \frac{\sum_{-m}^{m} Re\ \psi\left(\frac{n_o}{R}, \frac{m}{r}\right) - \sum_{-m}^{m} Re\ \psi\left(-\frac{n_o}{R}, \frac{m}{r}\right)}{\sum_{-n}^{n}\sum_{-m}^{m} Re\ \psi\left(\frac{n}{R}, \frac{m}{r}\right)} \qquad (1)$$

Where $2\pi r$ and $2\pi R$ are the poloidal and toroidal periodicities respectively, ψ is the TE radiated power spectrum and m and n represent the poloidal and toroidal mode numbers respectively. The above definition of directivity facilitates the examination of asymmetry for all toroidal mode numbers for a given case of progressive phasing. Note that this definition is related to the asymmetry of the spectrum and does not provide any direct information of the final current drive efficiency.

3. Results of Radiated Power Spectrum and Directivity

Several sets of antenna combinations including that of a single pair alone (as presently installed in JET) have been analyzed. The antennae are progressively phased to excite a desired integral number of parellel wavelengths around the torus (n_o = 1,2,3 ... etc). The results of the 3-D model described in Section 2, incorporate the effects of the finite-length of the antenna including the effect of the feeder currents and current propagation Constant β [7]. In this model, the radiation resistance per unit length (R_3) can be defined (see Ref. 7) by normalizing the quantity $2 \cdot R_e[\Psi]$ by the integral of the square of the current flowing, $I_c = I_o \cos^2 \beta_y\, dy$. These results can then be compared with R_2 obtained from a 2-D model in which the antenna (in the y-direction) is assumed to be infinetely long and the feeders are assumed to be located at infinity. However, in the comparison that is presented here, the product of 2-D $[R_e(\Psi(\frac{n}{R}))]$ and I_c is compared with 3-D $\sum_{-m}^{m} R_e\ (\Psi\ (\frac{n}{R}, \frac{m}{r}))$. In this way, the effect of finite antenna length and β is incorporated in a rough way in the 2-D results, though the effects of the feeders are absent in this model. The radiated power spectrum for a pair of antenna described above is shown in Fig. 1(a) as a function of n for the 2-D and 3-D models. The principal difference exists for small $k_{//} \leq k_o$ ($k_o \equiv$ vacuum propagation constant) related to the effects of feeder currents. (Fig. 1(b) shows the current spectra for the progressively phased antenna elements and the asymmetry is evident. The directivity defined in Section 2 is also plotted for each n nunmber and is shown in Fig 1(c). These curves are antisymmetric and therefore plotted only for positive n numbers.

Figure 2 shows similar plots when 4 pairs of antennae positioned symmetrically around the torus are energized with a progressive phase [8].

The imposed n_o number together with other mode numbers are found in the plasma and the directivity for $n_o = 3$ is about 29% with 3-D model and 22.5% with the 2-D model. The further narrowing and discretization of the excited spectrum is evident as the number of energized antennae is increased.

The results of directivity as a function of the imposed toroidal number by progressively phasing 8 antennae in several groupings obtained from the 2-D and 3-D models are shown in Fig. 3 and 4 respectively. In the 2-D results, the directivety is generally about 22.5%. The directivity values are lower for $n_o = 2$ and 6 in the case of 4G2H and for $n_o = 1$ and 7 in the case of 2G4H (2 groups of 4 housings each) as the phase difference between the corresponding antennae elements of different groups turns out to be an odd multiple of π (due to the fixed regular positioning of these groups of antennae). For $n_o = 0$ and 8, the phase difference is an even multiple of π, and the directivity values drop to zero. Similar behaviour is observed in the results of the 3-D model except that the value for small n numbers are higher (as compared to 2-D) since the 3-D model has higher values of radiated power near $k// \approx k_o$ due to the radial feeder current effects.

4. Summary and Conclusions

Eight travelling wave antennae are successful in imposing a desired toroidal mode number whereas a single pair of antenna system does not impose the desired n_o in the plasma. The asymmetry of the excited spectrum gauged by the directivity defined in Eq. 1 is found to be about 20%. Due to a finite number of antennae energized, it is found that the excited spectrum contributes significantly to other modes too. In current drive calculations and estimation of efficiency, this spectrum should be appropriately taken into account. These other modes may still be beneficial as they may heat the plasma instead. Moreover, the modes adjacent to the imposed one will also produce suprathermal electrons beneficial to current drive. In JET, for $n_o = 4$ at 33 MHz, the energy of the resonant electrons will be about 70 keV [2].

Acknowledgments: The computer codes used in the above calculations were initially developed in collaboration with Drs R. Koch and A.M. Messiaen. It is a pleasure to thank Mr J.J. Ellis for developing the plotting routines.

References

[1] Fisch, N.J., 2nd Joint Grenoble-Varenna Int" Symposium on "Heating in Toroidal Plasmas", Vol. II (1980) 1157
[2] Jacquinot, J., Paper presented at the ERICE Course on Toakamk Startup, Erice, Sicily, Italy 1985
[3] Jacquinot, J., et al, Invited paper, 12th European Conference on Controlled Fusion and Plasma Physics Budapest, hungary (1985)
[4] Cordey, J.G., Plasma Physics and Controlled Fusion, 26 (1984) 123
[5] Chiu, S.C., et al, Nuclear Fusion, 23 (1983) 499
[6] Bhatnagar, V.P., et al, Nuclear Fusion 22 (1982) 279
[7] Messiaen, A.M., et al, 3rd Joint Varenna Grenoble Int. Symp., Grenoble (1982) Vol. 1, 243
[8] Bhatnagar, V.P., et al, JET Report, Under preparation.

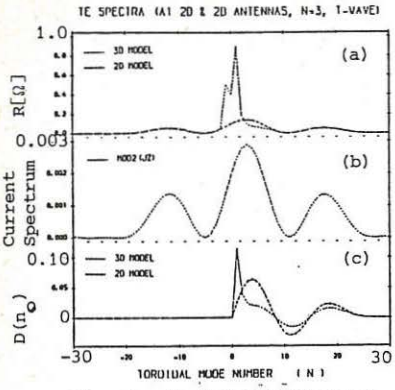

Fig. 1 R, Current Spectrum and D vs n for a pair of antennae

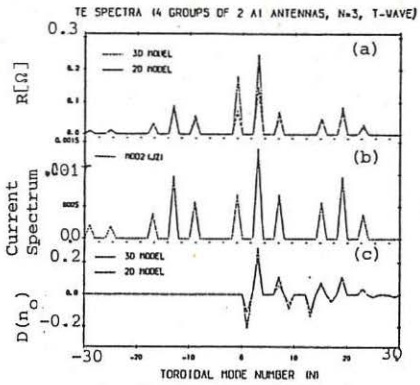

Fig. 2 R, Current Spectrum and D vs n for 8 antennae (4 groups of 2)

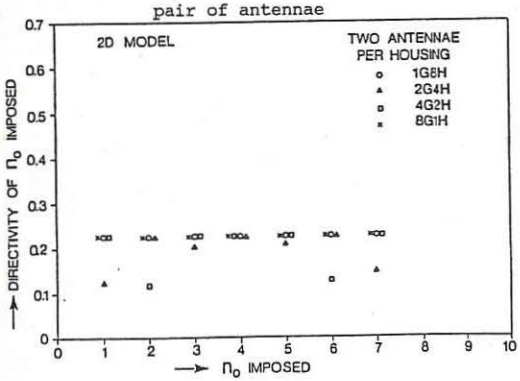

Fig. 3 Directivity vs n obtained from 2-D model for four different groupings of 8 JET antennae [8].

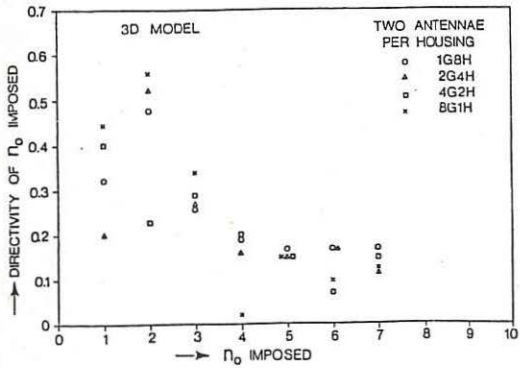

Fig. 4 Directivity vs n obtained from 3-D model for different grouping of 8 JET antennae [8].

PROPERTIES OF DRIVEN BERNSTEIN WAVES IN NONUNIFORM AND IN NONNEUTRAL PLASMAS

R.D. Ferraro, B.D. Fried, G.J. Morales, and S.A. Prasad

Physics Department, University of California at Los Angeles, Los Angeles, CA 90024, USA

Abstract. An analysis is made of the role of plasma density nonuniformity on wave phenomena near cyclotron resonance. Part I of the study examines the properties of ion Bernstein waves driven by an electrostatic antenna in a neutral nonuniform plasma. Part II investigates the effect of self-consistent static electric fields by considering the extreme case of cyclotron resonance in a fully nonneutral plasma.

Introduction. A rigorous analysis of cyclotron resonance heating must include a kinetic description of nonlocal effects caused by nonuniformities in the equilibrium parameters, e.g., density, magnetic field, temperature and self-consistent (ambipolar) static electric fields. A convenient and often used approximation consists of extrapolating the uniform medium (local) dispersion relation by replacing the perpendicular wave vector $\underline{k}_\perp$ by the differential operator $-i\nabla_\perp$. Such a procedure does not properly contain the effect of drifts induced by the nonuniformities, and sometimes violates the self-adjoint structure of the underlying mathematical problem. In the present study we avoid such difficulties by limiting our attention to effects associated with density nonuniformities. This is a relatively simple problem in which the role of the nonuniformity can be systematically investigated. The complementary effect of strong magnetic field nonuniformity on single particle cyclotron resonance has been previously studied by our group.[1] In the two different cases discussed here we start with a kinetic equilibrium (Vlasov) and proceed to generate an exact integro-differential equation describing electrostatic waves near cyclotron resonance. The integral part is expanded in the small parameter $\rho_j(d/dx)$, where ρ_j is the Larmor radius of species j and d/dx is the effective wavenumber along the nonuniformity, to generate an infinite order differential equation in terms of the independent variable x. Truncation of the differential equation to the order required by the choice of driving frequency yields a mathematically consistent description. In both cases analyzed we consider a magnetized plasma slab with a uniform magnetic field $B_0\hat{z}$, and in which electrostatic waves are represented by the potential $\phi_1(x)\exp[i(k_z z + k_y y - \omega t)]$, where k_z, k_y, are the wavenumbers (fixed by the antenna) along the spatially uniform directions, and the complex $\phi_1(x)$ is to be determined for a given real frequency ω.

I. Neutral Plasma. The equilibrium distribution function for the j species is taken as $f_{0j} = n_0 \exp[-v^2/\bar{v}_j^2]\exp[-(x+v_y/\Omega_j)^2/(L^2-\rho_j^2)]\,(\pi\bar{v}_j^2)^{-3/2}$ where $v^2 = v_x^2 + v_y^2 + v_z^2$, v_j is the thermal velocity, and Ω_j is the cyclotron frequency. This choice corresponds to an equilibrium plasma in which the ion and electron species have identical density profiles given by $n(x)=n_0 \exp(-x^2/L^2)$, where n_0 is the peak plasma density. Since in this case the self-consistent electric field $\underline{E}_0$ vanishes exactly, the effects of $\underline{E}_0 \times \underline{B}_0$

drifts (discussed in II) are absent. However, a diamagnetic drift exists and since it increases linearly with position away from the center of the slab ($x = 0$) it can play a role in the coupling properties of antennas located at the plasma edge. The perturbed distribution function f_{1j} is obtained by integrating along unperturbed orbits, which in this case are simple helical trajectories. The oscillating charge density is obtained by integrating f_{1j} over velocities and results in a convolution over positions (too lengthy to write here) because of the x dependence of f_{oj}. Expanding the convolution integral yields the infinite differential form of Poisson's equation

$$\phi_1''(x) - k^2\phi_1(x) = -\sum_j \sum_{\ell=0}^{\infty} k_{Dj}^2(x) \left(\frac{1}{\ell!}\right) \rho_j^{\ell} \alpha_{j\ell}(x)\phi_1^{(\ell)}(x) + \delta(x - x_o), \quad (1)$$

where $\phi_1^{(\ell)}(x)$ represents the ℓ derivative of $\phi_1(x)$, $k^2 = k_x^2 + k_z^2$, and $k_{Dj}(x)$ is the Debye wavenumber of species j. The coefficients $\alpha_{j\ell}(x)$ contain the familiar dependences on the plasma dispersion function $Z(s_{jm})$, $s_{jm} = (\omega + m\Omega_j)/k_z\bar{v}_j$. To first order in ρ_j/L they also depend explicitly on $\Lambda_m(b_j^2) = \exp(-b_j^2)I_m(b_j^2)$, $b_j^2 = k_y^2\rho_j^2/2$ and contain terms proportional to the diamagnetic drift frequency $\omega_{*j}(x)$. The electrostatic antenna appears as a delta function centered at $x = x_o$, having unit normalization for convenience.

In describing ion Bernstein waves having finite $k_y\rho_i$ in the frequency band $\Omega_i < \omega < 2\Omega_i$, only $\ell = 0, 1, 2$ in Eq. (1) need be retained (for higher harmonic bands a higher ℓ truncation must be implemented) and results (to first order in ρ_j/L) in a second order differential equation

$$\frac{d}{dx}\left[D_2 \frac{d}{dx} \phi_1(x)\right] + D_o(x)\phi_1(x) = \delta(x - x_o) , \quad (2)$$

where $D_2 = 1 + \partial D_o/\partial(b_i^2)$, and

$$D_o = -k^2 + 2\sum_j \sum_{m=-\infty}^{\infty} k_{Dj}^2(x) \left[1 + \left(\frac{\omega + \omega_{*j}}{k_z\bar{v}_j}\right) Z(s_{jm})\right] \Lambda_m(b_j^2) \quad (3)$$

The characteristic waveforms obtained from a numerical solution of Eq.(2) are shown in Fig. 1 for $\omega/\Omega_i = 1.7$, $k_y\rho_i = 1$, $L/\rho_i = 10$, $\omega/k_z\bar{v}_e = 3.6$ (weak electron Landau damping). The antenna location is shown by the dashed line on the right and the crosses indicate the zeroes of D_o (i.e., the cut-off points for x propagation). The density profile is shown for reference. The imaginary part is smaller than the real part by more than a factor of 64 because of the small damping, which permits the formation of a partially standing wave pattern upon reflection at the cut-off on the left side. The role played by the self-consistent inclusion of diamagnetic drifts of both ions and electrons is illustrated in Fig. 2 where the quantity $\mathrm{Re}(D_o/D_2)$ (the WKB k_x^2) is plotted (scaled to ρ_i^2) with and without drift effects. In the absence of drifts k_x^2 is symmetric, but for a fixed sign of k_y (>0) the drifts cause two different modifications: 1) an asymmetry develops leading to longer wavelengths for $x < 0$ and shorter wavelengths for $x > 0$; 2) the location of the cut-offs is shifted, resulting in poorer coupling for an antenna on the right and better coupling for one on the left. Reversing the direction of k_y, of course, interchanges the role of right and left. For

weak damping the asymmetry in Re k_x is also exhibited by the imaginary part, as is illustrated in Fig. 3, where the spatial dependence of $\ell n|\phi_1|$ is shown for an antenna on the right (top) and an antenna on the left (bottom). The dashed lines indicating the local slope help visualize the expected enhancement of the damping on the right side. Closer examination of the standing wave patterns on the left and right sides corroborate the elongation and the contraction of the wavelength expected from Fig. 2.

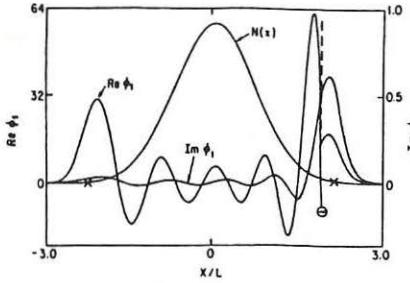

Fig. 1 Spatial pattern of ion Bernstein wave launched by an antenna at the plasma edge for $\omega/\Omega_i = 1.7$, $k_y\rho_i = 1.0$, $\rho_i/L = 0.1$, $\omega/(k_z\bar{v}_e) = 3.6$.

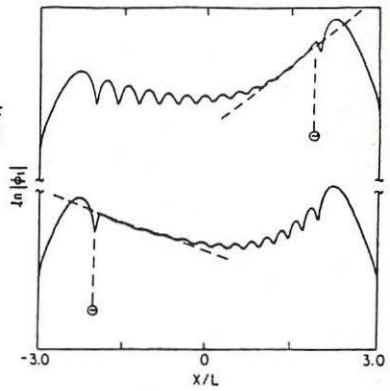

Fig. 3 Asymmetry in damping coefficient and wavelength caused by diamagnetic drift for $\omega/\Omega_i = 1.7$, $k_y\rho_i = 1.0$, $\rho_i/L = 0.1$, $\omega/(k_z\bar{v}_e) = 2.5$.

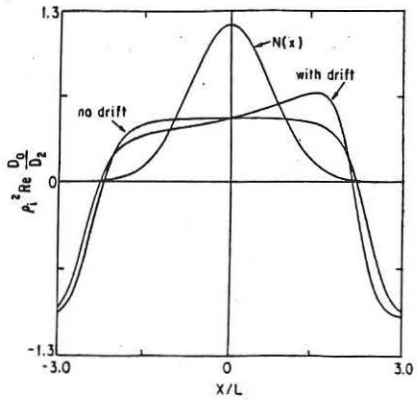

Fig. 2 Role of diamagnetic drift on effective WKB wavenumber $k_x^2 = Re\ D_0/D_2$.

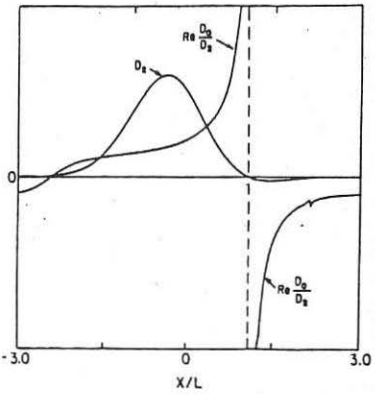

Fig. 4 Zero crossing of D_2 and resonance in $k_x^2 = ReD_0/D_2$ found for $\omega/\Omega_i = 1.57$, $k_y\rho_i = 1.0$, $\rho_i/L = 0.1$.

The inclusion of drifts can cause a significant qualitative modification in $D_2(x)$, i.e., for some parameters it can vanish, resulting in a wave resonance (not a particle resonance), as indicated by the behavior of $Re(D_0/D_2)$ in Fig. 4. The approach to this resonance by a wave launched from an antenna on the left side is shown in Fig. 5.

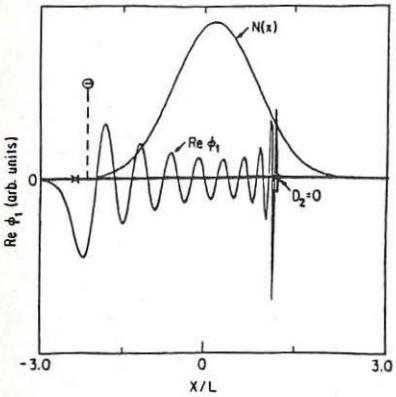

Fig. 5 Approach to resonance of an externally launched wave corresponding to conditions in Fig. 4.

II. Nonneutral Plasma. In a single component magnetized plasma slab, it is found[2] that the self-consistent static electric field creates a drift $v_D(x)$ and causes individual particles to gyrate not at the vacuum cyclotron frequency Ω, but at $\Omega_1(x) = [\Omega^2 - \omega_p^2(x)]^{1/2}$. This implies that for $k_z = 0$, but $k_y \neq 0$, the familiar cyclotron resonance terms take the form $\omega - k_y v_D(x) + m\Omega_1(x)$, i.e., the resonance becomes spatially dependent although B_0 is uniform. In addition to diamagnetic drifts, the equation for $k_y \neq 0$ modes contains derivative corrections due to the anharmonic cyclotron orbits (an effect not present in I). The simplest form of Bernstein modes are obtained for $k_y = k_z = 0$ and exhibit the WKB dispersion relation $(k_x \rho_j)^2 = (\omega^2-\Omega^2)(\omega^2-4\Omega_1^2)/(3\Omega^2\omega_p^2)$.

This work is sponsored by USDOE and ONR.

1. K. Nozaki, B.D. Fried, G.J. Morales, and A. Fukuyama, Phys. Fluids 26, 487 (1983).

2. S.A. Prasad, G.J. Morales, and B.D. Fried, Phys. Rev. Lett. 54, 2336 (1985).

LOCAL ICRF FOKKER-PLANCK HEATING AND INHOMOGENEOUS PLASMA FIELD AND ABSORPTION STUDIES FOR JET

J.E. Scharer and H. Romero

Electrical and Computer Engineering Department
University of Wisconsin - Madison
1415 Johnson Drive
Madison, WI 53706-1689 U.S.A.

I. Introduction We examine the case of fundamental minority ICRF plasma heating in 1-D inhomogeneous tokamaks. Full wave solutions are presented showing the simultaneous occurrence of strong fast wave damping and mode conversion processes. Utilizing this formalism, we examine the case of low and high field incidence for the JET (H)-D regime [1] and present numerical solutions for the wave fields, species power deposition, kinetic flux and reflection and mode conversion coefficients for representative parts of the antenna $k_{\parallel}$ spectrum corresponding to current experiments. The 1-D wave solutions for power deposition are compared with a WKB treatment which shows substantial differences for both minority and second harmonic absorption for the two cases. We next consider a 2-D velocity space, flux averaged Fokker-Planck code to examine regimes where substantial direct electron heating has been observed in (He^3)-D plasmas. A simulation of a single period of the substantial sawtooth pulse is examined with the required direct electron heating, minority heating, absorbed power densities, collisional power transfers and reduced energy confinement times from the ohmic equilibrium case. These solutions show that a substantial component of direct electron heating is required to reproduce the experimental results and that collisional power transfer between the species during the pulse is an important consideration in evaluating the power balance.

II. ICRF Wave Field Solutions Vlasov's equation is solved for the perturbed distribution function assuming the smallness of the local wavelength compared with the largest thermal gyroradius. The effects of an inhomogeneous plasma are incorporated self-consistently by including in our analysis the effects of first-order drift terms of the equilibrium distribution function. To second order in $k_{\perp}\rho$ we obtain the following differential equation for the ICRF field:

$$\frac{d}{dx}\left[\underline{\underline{A}}(x) \cdot \frac{d\vec{E}_{\perp}(x)}{dx}\right] + \underline{\underline{B}}(x) \cdot \frac{d\vec{E}_{\perp}(x)}{dx} + \underline{\underline{C}}(x) \cdot \vec{E}_{\perp}(x) = 0 \qquad (1)$$

$$\vec{E}_{\perp}(x) = \left[E_x(x), E_y(x)\right] \ .$$

The expressions for the coefficient matrices have been given [2]. Equation (1) has the following conservation relation:

$$\frac{d}{dx}\left[S_{em} + S_k\right] + P_{abs} = 0 \qquad (2)$$

where $S_{em}(x) = -\mathrm{Im}\ \{E_y \frac{dE_y}{dx}\}$,

$$S_k(x) \quad m\ \{\vec{E}_\perp^* \cdot \underline{\underline{A}}(x) \cdot \frac{d\vec{E}_\perp}{dx} + \vec{E}_\perp^* \cdot \underline{\underline{B}}(x) \cdot \vec{E}_\perp\}$$

$$P_{abs}(x) = \mathrm{Im}\ \{\frac{d\vec{E}_\perp^*}{dx} \cdot \underline{\underline{A}}(x) \cdot \frac{d\vec{E}_\perp}{dx} - \vec{E}_\perp^* \cdot \underline{\underline{C}}(x) \cdot \vec{E}_\perp + \frac{d}{dx}[\vec{E}_\perp^* \cdot \underline{\underline{B}}(x)] \cdot \vec{E}_\perp\} \ .$$

Figure 1 shows field solutions for fast wave field incidence and equilibrium parameters corresponding to JET. The density ($n_{eo} = 5 \times 10^{13}/cm^3$) and temperature profiles have been assumed parabolic. The hydrogen density is 5% of the electron density, $k_\parallel$ is 6 m-1, and the peak temperature is 5 keV. Note the mode converted field appearing on the x-component of the electromagnetic field. The amount of RF power deposited in the various species is also shown in Fig. (2) and is substantially larger than that predicted by a WKB analysis. For these parameters, 10% of the total power was directly absorbed by the majority species and over 6% by the electrons. Other results show that second harmonic absorption at higher density operation can be comparable to that for hydrogen and that substantial electron heating via mode conversion for high field incidence can take place. We have carried out a parametric study of the reflection, transmission and mode conversion coefficients as a function of $k_\parallel$. Our results for the JET parameters indicated above show that for $k_\parallel < 6\ m^{-1}$, substantial reflections for fast wave incidence from the resonance region occur and range between 10% and 90%.

III. Fokker-Planck ICRF Solutions We consider a solution of a Fokker-Planck equation of the form [3]

$$\frac{\partial f_\beta}{\partial t} = n_o \Gamma_\beta \Big[\frac{1}{v^2}\frac{\partial}{\partial v}\Big[\bar{A} f_\beta + \bar{B}\,\tilde{v}\,\frac{\partial f_\beta}{\partial v} + \bar{C}\,\frac{\partial f_\beta}{\partial \theta}\Big]$$

$$+ \frac{1}{\tilde{v}\, v^2 \sin^2\theta}\frac{\partial}{\partial \theta}\Big[\bar{D} f_\beta + \bar{E}\,\tilde{v}\,\frac{\partial f_\beta}{\partial v} + \bar{F}\,\frac{\partial f_\beta}{\partial \theta}\Big] + \frac{\partial f_\beta}{\partial t}\Big]_{\mathrm{Losses}} \qquad (3)$$

where β denotes the species and two-dimensional velocity space, collisional interactions, a phenomenological energy loss term and flux-averaged quasi-linear ICRF hot plasma heating terms have been included.

We consider an ohmic equilibrium characteristic of JET (He^{3++})-D operation and substantial ohmic heating currents in the 4 MA range with $T_{eO} = 3.5$ keV and $T_{iO} = 2.7$ keV and densities of $n_e = 3 \times 10^{13}/cm^3$ with a 10% concentration of He^3 in deuterium, a residual 5% hydrogen concentration and an energy confinement time of 0.5 s with R = 3.0 m and a = 1.15 m. The magnetic field on axis is taken as 3.3 T with a launched ICRF wave at 33.4 MHz with a representative $k_\parallel = 5\ m^{-1}$ and total absorbed power densities on the axis of 0.25 watt/cm^3. For the ICRF heating sequence the energy confinement time for ions is reduced to 0.3 s and for the electrons to

0.15 s which yields electron temperature dynamics comparable to the experiment.

Figure 3 illustrates the dynamics typical of the runs which were examined. Note that the average energy $\langle E \rangle = (3/2)\, T_{eff}$ for each species is plotted as a function of time for a 150 ms sawtooth. The use of average energy units allows one to describe the resonant nonmaxwellian He^{3++} tails and compare with the other species that make up the plasma. The power balance diagnostics show that in this regime the initial wave energy absorbed by the electrons is about 30% with the remaining 70% going to the minority He^{3++} species. However, initial collisional power transfer from the helium to the electrons is substantial and helps account for the relatively fast rise in the electron temperature. At later stages the absorbed helium power is closely coupled collisionally to the deuterium and power transfer is through this mechanism. Note that the helium average energy does not increase too drastically from the rest of the particle distributions at this concentration and ICRF power density. The majority deuterium is closely coupled to the helium minority and rises more substantially than is observed experimentally.

IV. Discussion Our wave propagation studies indicate that a substantial portion of the ICRF power (> 6%) is directly absorbed by the electrons. The Fokker-Planck runs, however, indicate that about 30% of the power should be directly absorbed by the electrons (in the case of (He^{3++})-D plasmas) before substantial electron sawteeth can be developed. Several factors including rotational transform could contribute to increased electron heating. The recirculation of fast wave energy so that high field incidence does occur would lead to nearly complete mode conversion to an ion Bernstein mode and increased direct electron heating. This can come about provided that a substantial portion of the spectrum of incident power is centered about values of $k_{\parallel}$ smaller than 8 m^{-1}. In this case, reflections of the fast wave energy can be expected and if this power is able to circulate around the tokamak in such a way that high-field incidence is possible, a higher proportion of the net incident power can be expected to be absorbed by the electrons.

References

1. J. Jacquinot et al., "ICRH Heating on JET", Invited Paper, European Physical Society Conference on Controlled Fusion and Plasma Physics, Budapest 2-6 September, (1985).

2. H. Romero and J. Scharer, Proceedings of the Plasma Physics Conference of the American Physical Society, San Diego, (1985). Manuscript is in progress.

3. J. Scharer, J. Jacquinot, P. Lallia and F. Sand, Nuclear Fusion, 25, 435-444 (1985).

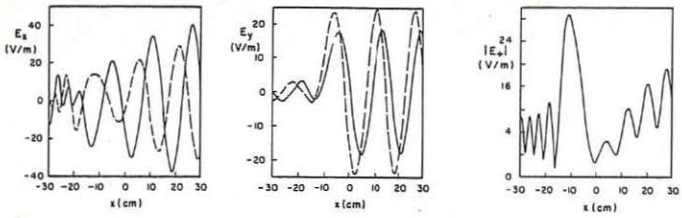

Fig. 1. Field solutions for low field incidence ($k_{||} = cm^{-1}$).

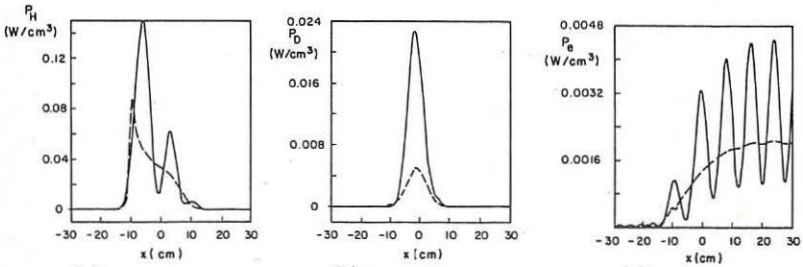

Fig. 2 (a-d). Species power absorption, P_j (WKB dashed), and flux, S.

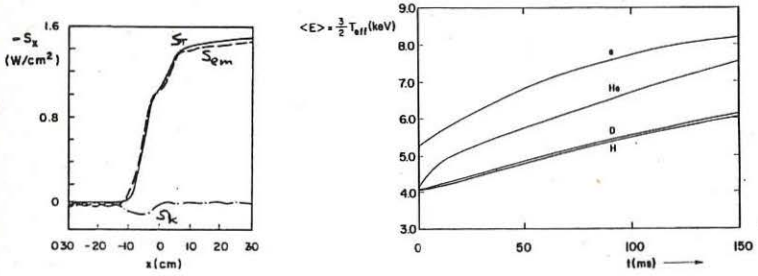

Fig. 3. ICRF Fokker-Planck solution for (He^3)-D.

1-d MODEL FOR PROPAGATION AND ABSORPTION OF H.F. WAVES NEAR ION CYCLOTRON RESONANCES IN TOKAMAK PLASMAS

M.Brambilla, T. Krücken

Max-Planck-Institut für Plasmaphysik, Euratom Association
D-8046 Garching, FRG

Ray tracing has proven an attractive tool for modeling of ICRF heating of large plasmas /1/, not lastly because of the simplicity of its numerical implemention. To be really useful, however, it has to be supplemented by the full-wave analysis of ion cyclotron and ion-ion hybrid resonance. The equations to be solved for this purpose must include the poloidal magnetic field, full parallel dispersion, and perpendicular dispersion to 2d order in the Larmor radius; they have been derived in /2/-/4/. In their general form, they are a set of integro-differential equations in two space variables. In a layer around resonance, however, they can be made one-dimensional: the vertical component of the wavevector, k_z, and the elements of the metric can namely be regarded as constants, compared to the horizontal variation induced in the HF response of the plasma by the vicinity of the resonance itself. This approximation has been discussed in /5/, where expressions were obtained for the mode conversion efficiency and absorption, in a form apt to be used in a ray-tracing code /6/.

The equations solved in /5/ were, however, further idealised by artificially separating mode conversion from cyclotron absorption; in the important scenario of H^+ minority in D^+ plasma, moreover, only the limiting cases of very low and high concentration could be solved analytically, and only a plausible interpolation suggested in between. To overcome these limitations, we have written a numerical code (ONEDIM), which solves the one-dimensional equations in their full generality. They are of the form:

$$\left\{\left(u^*\frac{d}{dx}+i\upsilon^*\right)\left[\underline{\underline{\perp}}\left(1+2\lambda_e+2\lambda_i+\frac{k_\zeta^2}{P}\right)\left(u\frac{d}{dx}+i\upsilon\right)\right]-2\left(k_\zeta^2-\hat{\nu}-\underline{\underline{\perp}}\right)\right\}E_+ +$$

$$-\left\{\left(u\frac{d}{dx}+i\upsilon\right)\left[\underline{\underline{\perp}}\left(1+2\lambda_e-\frac{k_\zeta^2}{P}\right)\left(u\frac{d}{dx}+i\upsilon\right)\right]\right\}E_- = 0$$

$$-\left\{\left(u^*\frac{d}{dx}+i\upsilon\right)\left[\underline{\underline{\perp}}\left(1+2\lambda_e-\frac{k_\zeta^2}{P}\right)\left(u^*\frac{d}{dx}+i\upsilon^*\right)\right]\right\}E_+ +$$

$$+\left\{\left(u\frac{d}{dx}+i\upsilon\right)\left[\underline{\underline{\perp}}\left(1+2\lambda_e+\frac{k_\zeta^2}{P}\right)\left(u^*\frac{d}{dx}+i\upsilon^*\right)\right]-2\left(k_\zeta^2-\hat{\nu}-\underline{\underline{\perp}}\right)\right\}E_- = 0$$

$$\hat{\nu} = \alpha^2 \frac{d^2}{dX^2} - 2i\beta \frac{d}{dX} + \gamma$$

where u, v, α, β, γ, are constants depending on the orientation of the incident wavefronts relative to magnetic surfaces and to the resonance layer; R, L(x), P are the elements of the dielectric tensor in the limit of zero Larmor radius, but with kinetic damping: $\lambda_i(x)$ and $\lambda_e(x)$ are the FLR corrections due to ions (1st harmonic IC damping) and electrons (electron magnetic pumping, (EMP)) respectively; electron Landau damping (ELD) is alo included to lowest order in m_e/m_i. Equations (1) are supplemented by the assumption that a fast wave is incident from one side, and by outward radiation conditions for the transmitted and reflected waves, both fast and slow.

The code ONEDIM is based on a finite element discretisation of (1), with cubic Hermite interpolating functions. The advantages of FEL for problems of this kind, and the outstanding convergence properties of cubic Hermite interpolation in particular, have been emphasied in /7/, and were confirmed by our results. Efficiency was improved by chosing the mesh step to be a fraction of the shortest wavelength existing at each point according to the dispersion relation: typically 200 elements suffice in a JET size plasma with a resonance layer of 30 to 50 cm to achieve an accuracy of at least 10^{-5} both in the field itself and in the energy balance. The integration is fast enough to make possible the incorporation of ONEDIM into the ray tracing code; in the following examples however it has been run as an independent package.

An example of the electric field distribution predicted by the code is shown in Fig. 1 (3 % H^+ in D^+, $n_e = 5 \cdot 10^{13}$ cm^{-3}, $T_e = T_i = 2$ keV, $B_{Tor} = 3.5$ T, $B_{pol} = 0.35$ T, f = 50 MHz, R = 3.2 m at $\omega = \Omega_H = 2\Omega_D$; incoming fast wave from the low magnetic field side along the equatorial plane, with $k_z = 0$ and $n_\varphi = 10$). The ion Bernstein wave to the left of the ion-ion resonance ($R = 3.12$ m) is clearly visible. In spite of its large amplitude it transports only 5.5 % of the incident power, against 6.3 % transmitted to the fast wave: this is due to its partially electrostatic polarisation, which is however not enough for efficient ELD (in the tokamak, absorption by ELD will be enhanced by refraction as this wave propagates towards regions of shorter and shorter wavelengths; the lack of absorption in the 1-dim. model shows that power deposition in the electrons could be appreciably broader than usually admitted). The ions absorb 39.0 % of the power; the rest, i.e. 49.2 %, is reflected. These figures are in excellent agreement with the estimates made in /5/; for example, they confirm the relatively large optical thickness of the evanescence layer in large devices, which reduces the efficiency of mode conversion of low n_φ partial waves with LMFS excitation.

A more systematic comparison of the predictions of the ONEDIM code with the estimates used in ray tracing is made in Fig. 2, which shows the energy balance under the same conditions as above, varying the H^+ concentration. For the low n_φ value considered here, the transition from the minority to the mode conversion regime occurs at about 5 % H^+ concentration.

Figure 3 shows a run with 3 % He_3^{++} minority in a H^+ plasma (n_e = $8 \cdot 10^{13}$, f = 35.6 MHz, n_ϕ = 10, other parameters as in Fig. 1). In this case FLR terms are negligible near the ion-ion resonance, and the cold plasma shear Alfven wave ($n^2 = (R+L)/2$) is excited. This wave propagates away from the IC resonance of He_3^{++}, and is accurately irrotational, hence unaffected by IC and EMP damping. The strong absorption which is nevertheless visible in Fig. 3 is entirely due to ELD. This points to the importance of keeping this damping in two-dimensional simulations as well, not only for a correct evaluation of electron heating, but also to attenuate somewhat the difficulty of having to resolve very short wavelength features.

REFERENCES

/1/ M. Brambilla, Ray Tracing of IH and IC waves, to be published in Comp.Phys.Rep., May 1986, and references therein.

/2/ D.G. Swanson, Proc. 3d Int.Symp. on Heating in Toroidal Plasmas, EUR-7979-EN, 1982, Vol. 1, p. 285.

/3/ P.L. Colestock, R.J. Kashuba, Nucl.Fusion 23 (1983) 763.

/4/ M. Brambilla, M. Ottaviani, Plasma Phys. Contr. Fus. 27 (1985) 919.

/5/ M. Brambilla, M. Ottaviani, Plasma Phs. Contr. Fus. 27 (1985) 1.

/6/ M. Brambilla, Report IPP 4/216, Febr. 1984.

/7/ K. Appert. T. Hellsten, J.Vaclavich, L. Villard, Report IRP 268/85, Sept. 1985 (to be published).

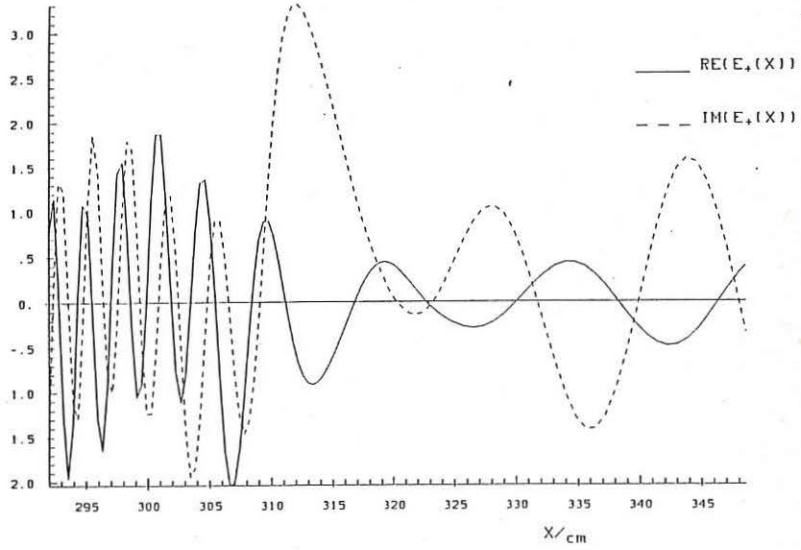

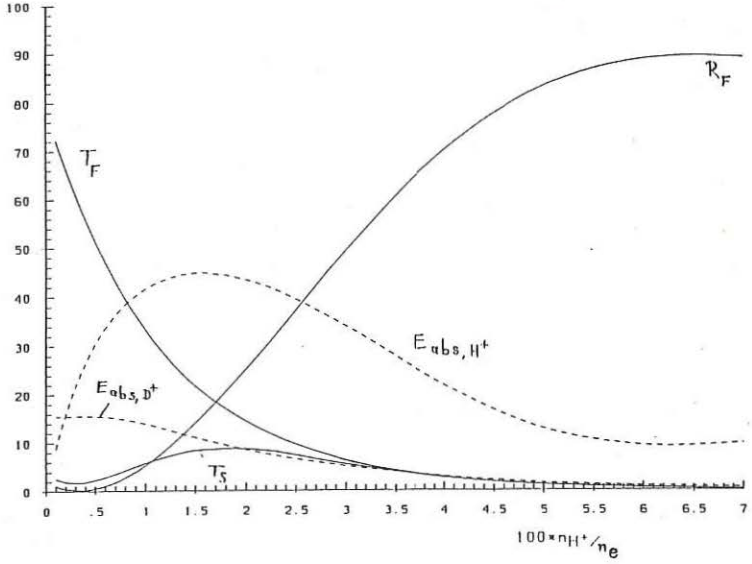
100
90
80
70
60
50
40
30
20
10
0
T_F
R_F
E_{abs,H^+}
E_{abs,D^+}
T_S
0 .5 1 1.5 2 2.5 3 3.5 4 4.5 5 5.5 6 6.5 7
$100 \times n_{H^+}/n_e$

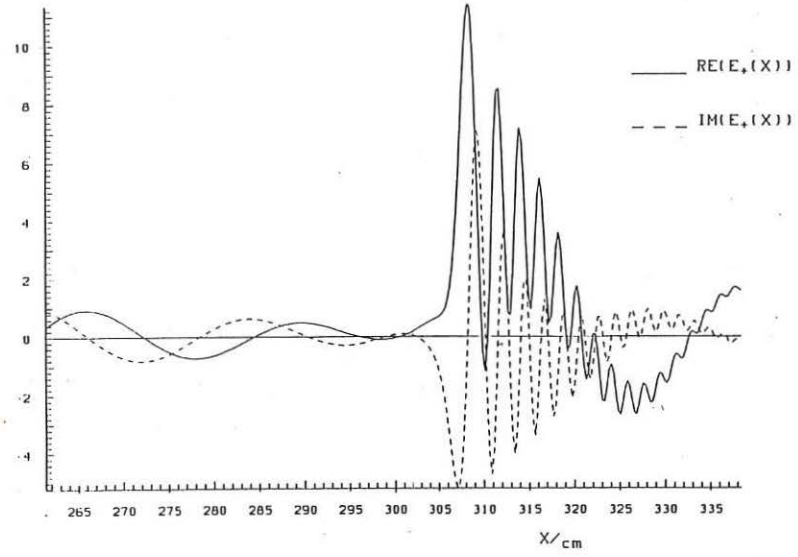
10
8
6
4
2
0
-2
-4
RE(E+(X))
IM(E+(X))
265 270 275 280 285 290 295 300 305 310 315 320 325 330 335
X/cm

A SIMPLIFIED METHOD FOR CALCULATION OF WAVE ABSORPTION IN THE ION-CYCLOTRON RANGE OF FREQUENCIES

A Kay[a], R A Cairns[a] and C N Lashmore-Davies[b]

(a) Dept of Applied Mathematics, University of St Andrews, St Andrews, Fife, KY16 9SS, UK

(b) UKAEA Culham Laboratory, Abingdon, Oxfordshire, OX14 3DB, UK (Eurotam/UKAEA Fusion Association)

Radio frequency heating in the ion cyclotron range of frequencies involves mode conversion of an incoming fast mode to a slow mode which is usually strongly damped and which only propagates in a localised region where the wave frequency is close to a harmonmic of the ion cyclotron frequency. Previous analysis has involved solution of fourth or higher order equations, much work in this area being carried out by Swanson[1-3]. The procedure used is rather complicated, both analytically and computationally, and our object has been to see to what extent the results can be reproduced by a simple analysis involving only a second order equation.

The essential feature of our approach is to treat the localised slow mode as a driven response to the fast mode, so that the detailed structure of the slow mode is neglected. The resulting second order equation is easily solved and has none of the difficulties with growing solutions described by Swanson[1]. In many ways our theory is analogous to the theory of parametric decay involving a highly damped quasi-mode[4].

For example, Swanson[3] shows that near the second harmonic the plasma is described by the equation

$$E_y^{iv} + hE_y''' + \lambda^2 z E_y'' - \gamma h E_y' + (\lambda^2 z + \gamma)E_y = -\left(\frac{\lambda^2\kappa^2}{2}\right) h(E_y'' + E_y) \qquad (1$$

where $h = -Z'(\zeta)/\kappa Z(\zeta)$ with $\zeta = (\omega - 2\Omega_i)/k_\parallel v_i$ and Z the plasma dispersion function. The derivatives in (1) are with respect to z, the distance perpendicular to the field scaled to the perpendicular wave number of the fast mode. The remaining parameters are real quantities depending on the plasma parameters, the gradient scale length and the parallel wavenumber of the incident wave.

With the above normalization the fast wave is simply described by

$$(E_y'' + E_y = 0,$$

so we write (1) in the form

$$(E_y'' + E_y) = \frac{(-E_y^{iv} - hE_y''' + \gamma h E_y' - \gamma E_y)}{\lambda^2 z + \frac{\lambda^2\kappa^2}{2} h} \qquad (2)$$

Clearly for large z the r.h.s. goes to zero. The term in the denominator involving h is complex, so the denominator looks like that corresponding to a damped resonant response. We consider a fast wave, varying as $\exp(\pm iz)$ depending on the direction of incidence, and regard the r.h.s. as a resonant response to this with E_y' going to $\pm iE_y$ and similarly for the higher derivatives.

In this way (2) is reduced to

$$E_y'' + E_y = \frac{(1+\gamma)(-1\mp ih)}{\lambda^2 z + \frac{\lambda^2 \kappa^2}{2} h} E_y. \qquad (3)$$

This is a straightforward differential equation whose solution using standard integration routines presents no problem. In the case of the third harmonic Swanson[2] gives a sixth order equation which we treat in the same way.

We consider first the overall energy balance. Swanson's results indicate that the transmission coefficient is unaffected by damping of the slow wave, but that the reflection coefficient for low field side incidence, which is given by

$$|R|^2 = (1 - |T|^2)^2$$

in an undamped system[5], is reduced by the damping. In Fig 1 we show the reflection coefficient as a function of $k_\parallel$ for parameters where this has already been given by Swanson[1]. Our curve is essentially indistinguishable from his. In the case of the third harmonic Swanson[2] gives an empirical formula for the reflection coefficient in the case where

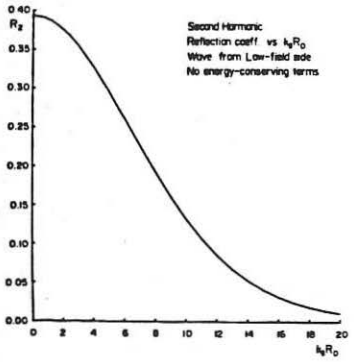

Fig. 1

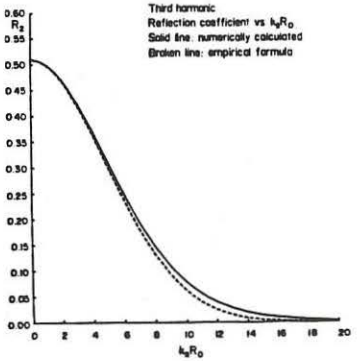

Fig. 2

all resonant species have the same thermal velocities. A comparison between the results of this formula and of integration of our equation is shown in Fig 2. For another set of parameters, to which the formula does not apply, Swanson finds a reflection coefficient of 42.6% while we obtain 44.2%. It appears then, that so far as calculation of the transmission, absorption and reflection of the fast wave is concerned our second order approximation gives good results. We might anticipate that it would be equally useful in the investigation of similar mode conversion processes in different ranges, for example conversion to a Bernstein mode at the second harmonic of the electron cyclotron frequency.

We have also used our second order equation to calculate field and absorption profiles. Fig 3 refers to incidence from the low-field side and shows $E_+ = E_x + iE_y$, a quantity of interest since ion cyclotron absorption depends on it. The modulation of $|E_+|$ on the right occurs because in this region there is a superposition of incident and reflected waves. To the left there is only an outgoing fast wave and the modulus is constant. For incidence from the higher field side there is no reflected wave and this is indicated by the behaviour of $|E_+|$ shown in Fig 4. Similar behaviour occurs at the third harmonic.

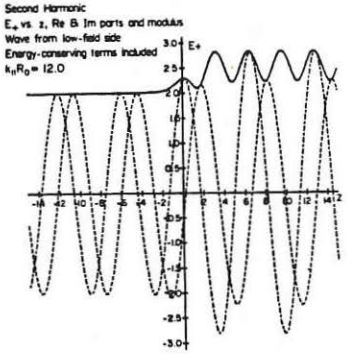

Fig. 3

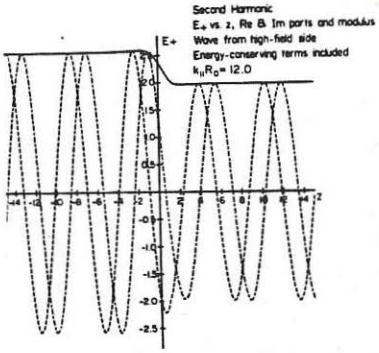

Fig. 4

The absorption profile is also of interest and we have calculated this simply from $\langle \underline{E} \cdot \underline{J} \rangle$. Some profiles for the third harmonic have been calculated for D-T plasma with a small additional concentration of α particles, using parameters for which Swanson[3] has given results. Results for small and large values of k are shown in Figs. 5 and 6 respectively. For large $k_\parallel$ the width and profile of the absorption region is in reasonable agreement with the more elaborate theory, but at small $k_\parallel$ we find less structure and a narrower resonance. Presumably this is a consequence of the fact that the damping of the slow wave is smaller at small $k_\parallel$ and its structure would be expected to be more important.

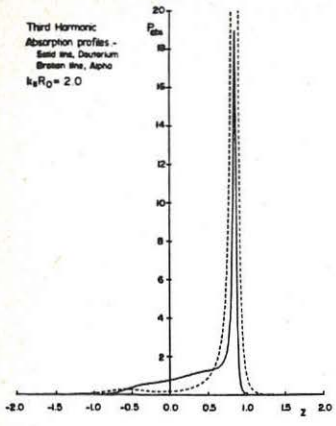

Fig. 5

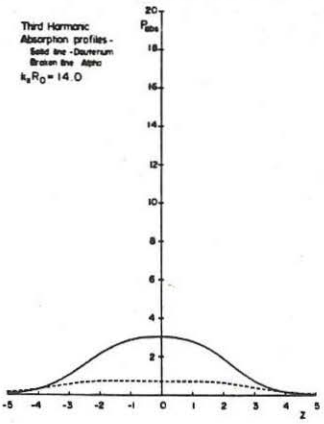

Fig. 6

In conclusion it appears that reducing the problem to a second order equation, by treating terms other than those describing the fast waves as a localised damped response, gives a simple approximation which yields good results for the overall power balance, the wave fields and the absorption profiles.

References

1. D G Swanson, Nuclear Fusion 20 (1980), 949.

2. D G Swanson, Phys. Fluids 28 (1985), 1800.

3. D G Swanson, Phys. Fluids 28 (1985), 2645.

4. K Nishikawa, in Advances in Plasma Physics, Vol 6 (ed A Simon and W B Thompson).

5. R A Cairns and C N Lashmore-Davies, Phys. Fluids 26 (1983), 1268.

DISTORTION OF ION VELOCITY DISTRIBUTIONS IN THE PRESENCE OF ICRH; A SEMI-ANALYTICAL ANALYSIS

D. Anderson*, W. Core+, L.-G. Eriksson*, H. Hamnén+, T. Hellsten+, M. Lisak*

*Chalmers University of Technology, Göteborg, Sweden

+JET Joint Undertaking, Abingdon, England

1. Introduction

Assuming the distribution function of ions heated by ion cyclotron resonance absorption to be essentially isotropic, analytical and semi-analytical approximations are derived for the distribution function. Several different heating scenarios are considered: heating at the fundamental and second harmonic ion cyclotron resonance frequency as well as the case of combined neutral beam and RF-heating with the RF wave frequency tuned to the resonance frequency of the injected ions. The resulting distributions are used to evaluate the weighted velocity space averages of the distributions which determine the fusion reactivity and the collisional power transfer to plasma background particles and to study their scaling with RF-parameters like absorbed power and perpendicular wave number. Furthermore, the importance of higher order finite Larmor radius effects in suppressing the formation of RF-induced high energy tails is analyzed as well as the influence of neutral beam injection angle in the case of the energy clamping scheme. Comparisons based on full 2-D numerical calculations show good agreement with the semi-analytical results.

2. Theory

The evolution of the velocity distribution, f, of ions subject to ion cyclotron resonance absorption is determined by the Fokker-Planck equation

$$\frac{\partial f}{\partial t} = C(f)+Q(f)+S-L \qquad (1)$$

where C and Q are the collision and RF-diffusion operators respectively, S represents the source of the neutral beam injected particles and L is a particle loss term.

The distribution function, which is assumed to be almost isotropic, can be expanded in Legendre polynomials. Using this expansion in eq. (1) and

keeping only the lowest order term (A(v)) corresponding to the isotropic part of f, the following equation is obtained for A(v) in steady state:

$$\frac{1}{v^2}\frac{d}{dv}\left\{\left[-\alpha v^2+\frac{1}{2}\frac{d}{dv}(\beta v^2)\right]A+\left(\frac{1}{2}\beta+K_nG_n\right)v^2\frac{dA}{dv}\right\}+$$

$$+\frac{S_o}{v_o^2}\delta(v-v_o)+\frac{1}{2}\int_{-1}^{+1}L\,d\mu=0 \qquad (2)$$

In eq. (2), α and β denote the collision coefficients corresponding to slowing down and energy diffusion, S_o and v_o are the current and velocity of the injected particles, K_n is a constant proportional to the amplitude square of the left hand component of the RF Wave, μ is the cosine of the particle pitch angle, and $G_n(v)$ is given by

$$G_n(v)=\frac{1}{2}\int_{-1}^{+1}(1-\mu^2)J_{n-1}^2\left(k_\perp v\sqrt{1-\mu^2}/\omega_{ci}\right)d\mu \qquad (3)$$

where the index of the Bessel functions is determined by the heating mode (n=1 and n=2 for heating at the fundamental and second harmonic ion cyclotron resonance frequency respectively). In the absence of neutral beam injected resonant particles (S_o=L=0), eq. (2) can be solved to yield the semi-analytical solution

$$A(v)=A(0)\exp\left(-\int_o^v\frac{-2\alpha v^2+\frac{d}{dv}(\beta v^2)}{\beta v^2+2K_nv^2G_n(v)}\,dv\right) \qquad (4)$$

Eqs. (2)-(4) provide a convenient and accurate approximation for the RF-distorted ion distribution and can be used to investigate the parameter scaling of important physical quantities like collisional power transfer to background plasma particles, fusion reactivity and absorbed RF power.

3. Results

Convenient analytical approximations for A(v) can be obtained from eq. (4), to lowest order in $k_\perp$, for the case of ICRH alone. The degree of distortion of the RF-heated distribution is characterized by the Stix-parameter, ξ, defined by $\xi=t_sP_M/(3n_iT_b)$, where P_M denotes the RF-power absorbed by an equivalent Maxwellian with density, n_i, and a temperature, T_b, equal to the background temperature.

For fundamental heating, assuming a single ion species background plasma and equal electron and ion temperatures, we find, cf. [1,2]

$$A(v)\simeq A(0)\left[\exp(-v^2/v_b^2)+\alpha\exp(-v^2/v_t^2)\right] \qquad (5)$$

where $v_t^2=v_b^2(1+\xi)$. In deriving eq. (5) we have assumed $\xi \gg 1$ and α is given by

$$\alpha\simeq\exp\left[-\frac{35.8}{(\xi A_b)^{2/3}}A\right] \qquad (6)$$

where A and A_b denote the mass numbers of the heated ions and the background ions, respectively. For second harmonic heating we find, [2]

$$A(v) \simeq \frac{A(0)}{\left(1+\frac{2\xi}{5}\frac{v^2}{v_b^2}\right)^{5/(2\xi)}} \qquad (7)$$

The approximations (6) and (7) can be used to assess the distortion of the distributions as expressed, e.g. by the number of tail particles and the tail contribution to the total β-value as well as the importance of higher order finite Larmor radius effects.

Examples of numerical results obtained from eqs. (2)-(4) are given in figs. 1-4. The important tail suppressing effect of increasing $k_\perp$ is demonstrated in figs. 1-2. Fig. 1 shows the suppressed local tail temperature $\left[-\frac{d}{dE}\ln A(v)\right]^{-1}$ for fundamental heating as a function of energy, E, and fig. 2 shows the enhancement of the RF power absorption, P_a, over that of a Maxwellian, P_M, versus the parameter $P_M(0.25/k_\perp)^2$ which is proportional to the electric field squared. Collisional power transfer to the background electrons, P_e, is given in fig. 3 as a function of absorbed power. Finally, fig. 4 shows the scaling of fusion reactivity, $\langle\sigma v\rangle$, with absorbed RF power, P_{RF}, for the energy clamping scheme using fundamental heating. Note the good ageement between the semi-analytical (isotropic) results and the full 2-D numerical calculations for intermediate injection angles, [3].

4. Conclusion

The present results demonstrate that the computationally simple isotropic distributions provide a convenient and accurate means for determining macroscopic physical quantities of special significance for RF heated plasmas. Based on these solutions, the scaling with different parameters can be investigated. In particular we emphasize the importance of higher order Larmor radius effects for the usually employed RF-induced velocity space diffusion constants. Finally we note that the present result should be particularly useful in connection with large numerical codes for describing transport characteristics of RF-heated plasmas, where full 2-D calculations of the ion distributions are too time consuming to be practical.

References

[1] T.H. Stix, Nucl. Fus. 15 (1975), 737.

[2] D. Anderson, W. Core, L.-G. Eriksson, H. Hamnén, T. Hellsten, M. Lisak, internal report CTH-IEFT/PP-1986-02.

[3] T. Hellsten, K. Appert, W. Core, H. Hamnén, S. Succi, 12th European Conf. Contr. Fus. and Plasma Phys., Budapest (1985), FP Tu 038, Conference Abstracts, p. 124.

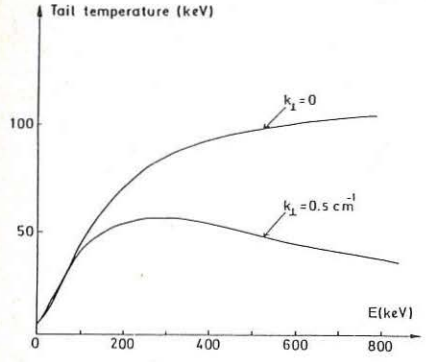

Fig. 1

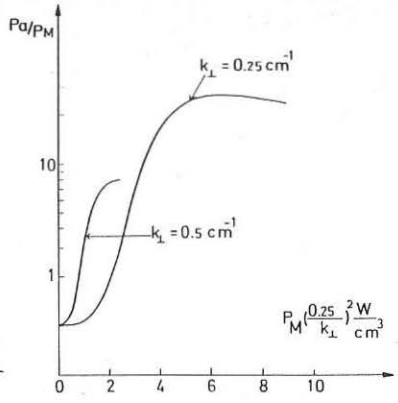

Fig. 2

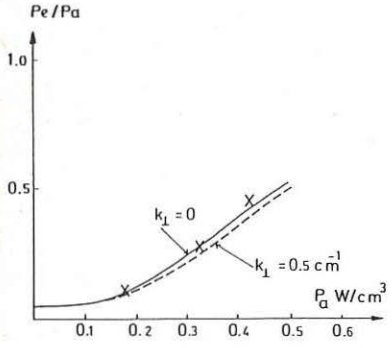

Fig. 3

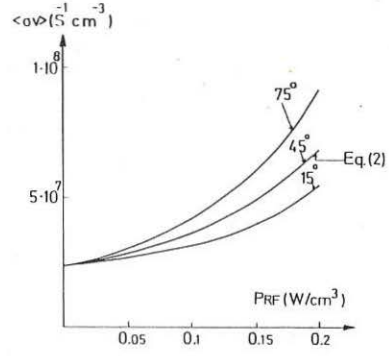

Fig. 4

A 3-D ANALYSIS OF ARBITRARILY SHAPED ICRF ANTENNAS AND FARADAY SHIELDS*

G. L. Chen, J. H. Whealton, T. L. Owens, D. J. Hoffman, and F. W. Baity
Oak Ridge National Laboratory, Oak Ridge, Tennessee 37831, U.S.A.

I. Introduction

Cavity antennas with Faraday shields[1] are proposed to couple ion cyclotron radio frequency (ICRF) power for heating fusion plasmas. This application requires small, high-power, low-frequency antennas. We present the results of a theoretical study of the ICRF antennas[2,3] being developed for this purpose at the Radio-Frequency Test Facility (RFTF). The objectives of this work are to optimize experimental designs and to confirm test results.

Complete analyses of the antennas and Faraday shields are performed using a three-dimensional (3-D) analysis[4] that computes the full wave field and resonance frequency of an antenna by solving the boundary problem of Maxwell's equations or Helmholtz's equations, using the finite difference method with a successive overrelaxation (SOR) convergence scheme. This analysis allows us to model an antenna and Faraday shield of arbitrary shape in Cartesian coordinates. (This does not imply that only right-angle edges and corners are allowed as the cavity boundaries.) The analysis is easily converted to cylindrical coordinates if this is necessary or desirable. We have applied the analysis to three areas: the folded waveguide antenna,[2] the cavity antenna,[3] and the Faraday shield.[3] We describe the model in Section II and discuss the applications in Sections III and IV.

II. Theory Model

For simplicity, we assume that our antenna system is source free and is a perfect conductor. By combining Maxwell's four equations, we find that the wave equation is

$$(\nabla^2 + \mu_0\epsilon_0\omega^2) \begin{Bmatrix} \vec{E} \\ \vec{H} \end{Bmatrix} = 0 , \qquad (1)$$

and the boundary conditions on a perfectly conducting wall are

$$\hat{n} \cdot \vec{E} = 0 , \qquad (2a)$$

$$\hat{n} \times \vec{H} = 0 \ , \qquad (2b)$$

where n is a unit vector outward normal to the surface of the boundary. We solve the scale components of Eqs. (1) and (2) to obtain the full wave field and the resonance frequency ω.

III. The Folded Waveguide

We calculate the lowest few modes of the folded waveguide described in detail by Owens.[2] The fundamental resonance frequency of a 12-cm-wide, 14.5-cm-high, 21.75-cm-deep folded waveguide is 762 MHz, much lower than the resonance frequency (1243 MHz) of a rectangular waveguide of the same size. Figures 1 and 2 show H_x and H_z, respectively, for the folded waveguide. The resonance frequency and the fields, except for H_x, are in excellent agreement with the experimental measurements; H_x is qualitatively consistent with the experiments, but the relative amplitudes between vanes disagree. The measured result[2] shows that H_x has a higher field at the center of the mouth of the waveguide. This discrepancy may arise because the effect of the coaxial input is not properly considered or because the H_x field is mixed with the second harmonic mode, which has a high field at the center of the waveguide mouth and a resonance frequency very close to the fundamental. In Fig. 3, the fundamental resonance frequency is shown as a function of the distance between the end of the vane and the wall. We find that the minimum resonance frequency occurs when this gap is equal to the distance between adjacent vanes.

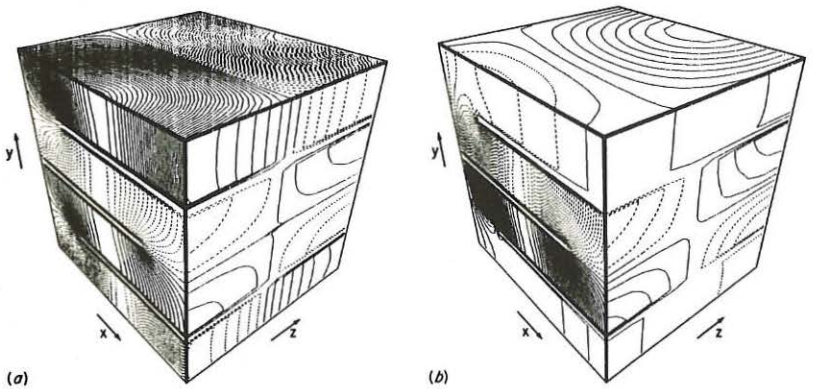

Fig. 1. Contour plots of H_x. (a) Fundamental mode. (b) Second harmonic mode.

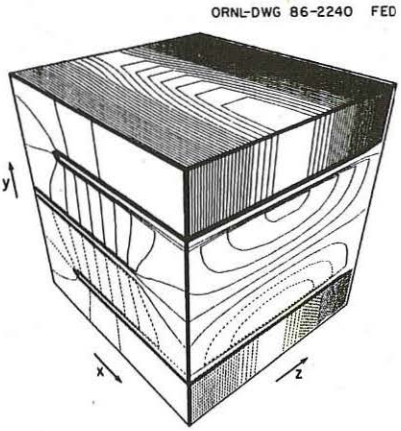

Fig. 2. Contour plot of H_z.

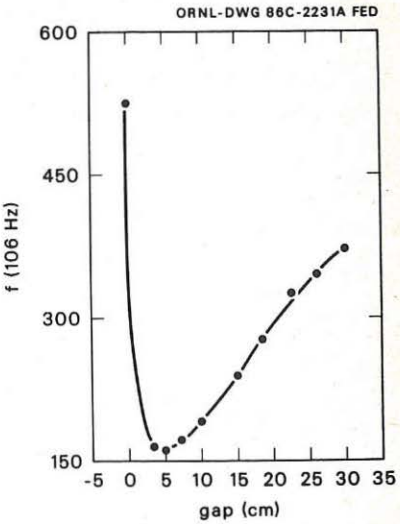

Fig. 3. The fundamental resonance frequency as a function of the gap for a 30 x 48.75 x 97.5 cm folded waveguide with 6 vanes.

IV. Cavity Antenna and Faraday Shield

We have applied our theory to the antenna and Faraday shield being tested for Doublet III-D, as described in Ref. 3. The fundamental driven mode is determined. The current strap is considered as a free parameter. The resonance frequency f is used to determine the inductance L, while the magnetic field (at the plasma edge) per unit current is correlated to the plasma load. A Faraday shield has been added to this antenna configuration to study its effects on the power limits. Table I and Fig. 4 summarize the comparison of theory and experiment. The Faraday shield reduces the inductance of the antenna and the magnetic field passing through the shield. Merely calculating the drop across the shield is not enough to determine how coupling is altered. The current distribution on the strap substantially increases the field near the shield, thereby softening the shield's impact. However, in this calculation, we have assumed that the current and the magnetic field on the strap are constant. A more detailed and realistic current profile is required for further studies.

Table I. Comparison of theory and experiment

	Theory	Measurement
f_{NF}/f_{FS}	55.07/57.20	55.843/58.846
L_{NF}/L_{FS}	1.08	1.11

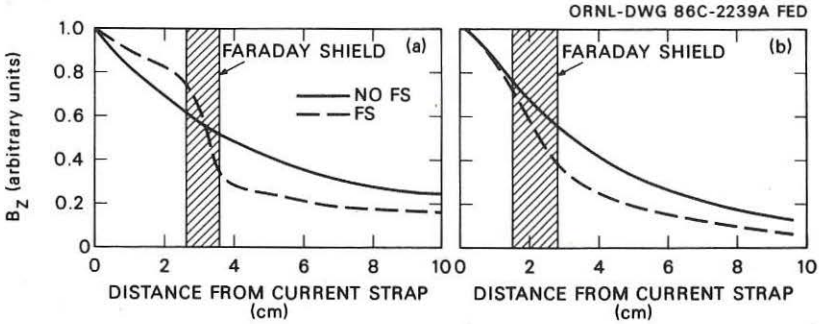

Fig. 4. Toroidal magnetic field B_z vs distance from the current strap. (a) Theory. (b) Measurement.

References

1. For example, S. C. Chiu, Bull. Am. Phys. Soc. 30(9), 1587 (1985); C. M. Fortgang et al., Bull. Am. Phys. Soc. 30(9), 1570 (1985).

2. T. L. Owens, "A Folded Waveguide Cavity Coupler for ICRF Heating," presented at this conference.

3. D. J. Hoffman et al., "ICRH Coupling in DIII-D," presented at this conference.

4. J. H. Whealton et al., A 3-D Analysis of Maxwell's Equations for Cavities of Arbitrary Shape, ORNL/TM-9792, March 1986.

*Research sponsored by the Office of Fusion Energy, U.S. Department of Energy, under Contract No. DE-AC05-84OR21400 with Martin Marietta Energy Systems, Inc.

THE EFFECTS OF EXTERNAL ELECTRIC FIELD ON THE DYNAMICS OF ION-ION INSTABILITY AND TURBULENT HEATING

V.A.Brazhnik, V.V.Demchenko, V.G.Dem'yanov, V.E.D'yakov, V.V.Ol'shansky, S.S.Pavlov, V.I.Panchenko, K.N.Stepanov
Institute of Physics & Technology, the Ukrainian Academy of Sciences, Kharkov 310108, USSR

Introduction. The paper [1] gives the results of numeric simulations of the current-induced instability build-up and saturation, the said instability appearing during relative inertial motion of ion species in a magnetized plasma containing two ion species [2].

This study is focused upon the effects of external electric field on the dynamics of ion-ion instability. The model of macro-particles as described in [3] is employed to facilitate the quantitative analysis. The parametric values of the model agree well with those given in [1].

Ion-Ion Instability in a Constant Electric Field. Let us assume that the constant electric field is turned on somewhere in the beginning which causes a linear increase of the directional $U_{1,2}$ and relative $U = /U_1 - U_2/$ (Fig.1) velocities. The turbulent pulsation energy density W_E (Fig.2) and ion temperature $T_\perp$ rise, too. The oscillation spectrum in the initial phase has a spike only for one harmonic, the one whose wave number corresponds to the dispersion equation of the linear theory[2]. At the time $T = 14.4\ \omega_{T1}^{-1}$ the value W_E reaches a local maximum associated with the trapping of both species by the unstable wave field and the formation of "vortices" can be observed in the ion-phase space. The ions interact with plasma-borne formations of the soliton kind which results in a temperature rise and an insignificant decrease of the ratio $|\vec{U}|/v_{T1}$ (Fig1). In the case of a free ion flux move [1] the slowing-down of relative motion to sub-critical values ($|\vec{U}|/v_{T1} < 2.3$) leads to the saturation of instability and the onset of a quasi-eqilibrium turbilent state. The presence of the constant electric field promoted a continuous ion acceleration and build-up of the "repetitious" single-mode ion-ion instabilities (Fig.2) which is the typical picture of the performance of the amplitude of single-mode unstable oscillations set in motion by the beam of particles with a small spread of velocities. When the current velocity reaches the value $/\vec{U}/ \simeq 4.5\, v_{cr}$ ($U_{cr} = 2.3 v_{T1}$), one can observe a steep drop (more than three-fold) in relative velocity (Fig.1) which is accompanied by a steep leap upwards of the value W_E and a spectral compositional tuning-up of the oscillations. The instability remaining single-moded, its frequency and wave-vector decrease roughly fourfold as compared with ion-ion instability dynamics when current velocity is smaller. The oscillation spectrum gets rich with many

harmonics the amplitudes of which are more or less equal. A sharp rise in plasma temperature is observable along with a dramatic slackening of ion fluxes and instability saturation.

The Influence of the Alternating Electric Field upon the Dynamics of Ion-Ion Instability. Let us assume that a current-carrying plasma is under the action of the pumping field where $\omega_0 \simeq 0.42\ \omega_{pi}$ .The dynamics of ion-ion instability in this case has several peculiarities. First of all, the ion velocities and ion relative velocity oscillate with the pumping speed frequency. The energy density of the fluctuational electric field (Fig.4) at the interval $0 < \omega_{pi} t < 28$ shows four local maxima associated with the build-up and saturation of a single-moded ion-ion instability. Note that ion temperature at this interval keeps on rising. Further on, $(28 < \omega_{pi} t < 31)$ the value W_E takes a jump upwards, and a considerable amount of spectral re-structuring takes place a growing longwave maximum-increment component and satellite-mode ampitude. The electric field of the unstablest mode begins to trap ions which causes a decrease in the intensity of turbulent pulsations, while a greater portion of the particles change states from trapped to free; current velocity rises and a secondary instability occurs. The whole process repeats itself quasi-periodically. At the interval $31 < \omega_{pi} t < 45$ the ion temperature begins to grow and the relative ion flux velocity falls dramatically. At $\omega_{pi} t > 45$ the ratio $|\tilde{U}|/V_{T1}$ oscillates with pumping field frequency and amplitude $|\tilde{U}_{max}|/V_{T1} \approx 0.8$. The ion temperatures $T_{1,2}$ attain a steady-state level which is much higher than $T_{1,2}$ initial temperatures of ions. Yet, the highest temperature in this case is by far much lower than the one achieved when ion-ion instability was forming in a constant electric field.

REFERENCES

1. Brazhnik V.A., Demchenko V.V. et al. Proc.Int.Conf. on Plasma Phys., Lausanne, Switzerland, 1984, v.1, p.89
2. Stepanov K.N., Sizonenko V.L.JETP Letters(in Russian), 1968, v.8, 10, p.592
3. Brazhnik V.A., Demchenko V.V. et al.- M.:ZNII atominform (in Russian), Preprint KFTI 84-10, 1984.

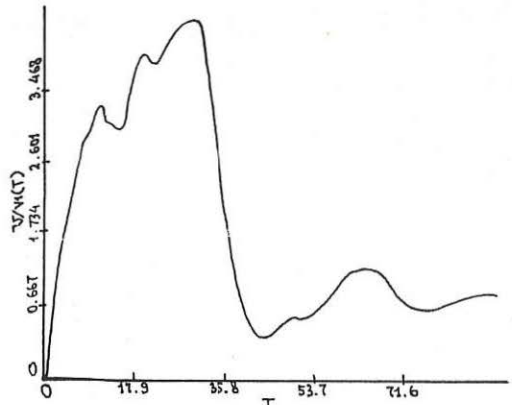

Fig.1. Relative ion velocity vs. time (constant electric field régime)

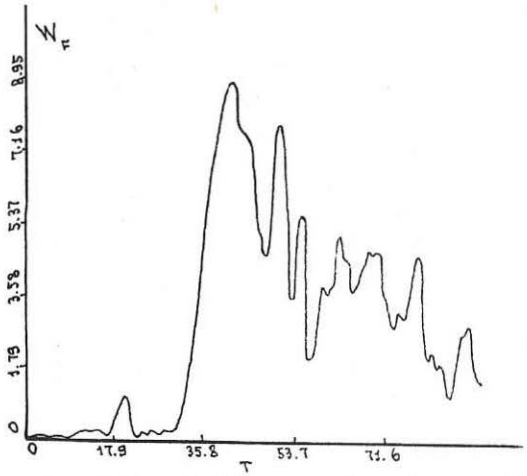

Fig.2. The electrostatic field energy density vs. time (constant electric field régime)

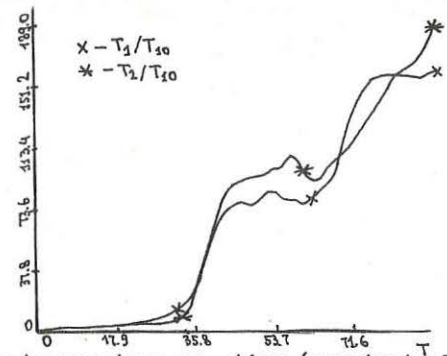

Fig.3. Ion temperature vs. time (constant electric field régime)

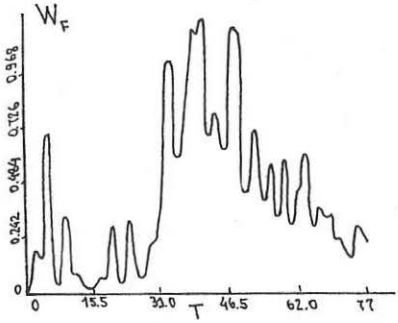

Fig.4. The electrostatic field energy density vs.time (alternate external electric field régime)

THREEDIMENSIONAL TE MODES IN AN INHOMOGENEOUS MAGNETIZED COLD TOROIDAL PLASMA OF ARBITRARY CROSS SECTION

Ferdinand F. Cap

Plasma Physics Group, Institute for Theoretical Physics, University of Innsbruck, Innsbruck, Austria

RF-low frequency heating of fusion plasmas is of practical importance. For low frequencies and long wave-length global wave solutions for toroidal plasmas are necessary. Since Maxwell's equations are not separable into ordinary differential equations in toroidal coordinates a new analytical method is needed /1/. The general solution of a linear partial differential equation contains one arbitrary function (or more, if the differential equation is of higher order than 1). If this arbitrary function is expanded into a series of eigenfunctions of a coordinate system in which the Maxwell equations are separable, an infinite set of expansion coefficients A_n is obtained. Now the new method consists in the following: determine these coefficients A_n in such a way that the electromagnetic boundary conditions on the metallic surface of the toroidal vessel containing the plasma are satisfied for an arbitrary meridional cross section of the torus. The electromagnetic boundary conditions $E_t = 0$ and $B_n = 0$ on the curve $z = z^*(r)$ describing in cylindrical coordinates r,ϕ,z the meridional cross section curve of the torus are given by /1/, /2/ for ϕ = const

$$E_r + E_z \frac{dz^*}{dr} = 0, \quad \frac{dr}{B_r} = \frac{dz^*}{B_z} . \tag{1}$$

In order to solve Maxwell's equations for a cold plasma magnetized by $\vec{B}_o = B_o(r)\vec{e}_\phi$ we need the dielectric tensor /1/

$$\vec{\vec{\varepsilon}} = \begin{pmatrix} \varepsilon_r & 0 & \varepsilon_z \\ 0 & \varepsilon_\phi & 0 \\ -\varepsilon_z & 0 & \varepsilon_r \end{pmatrix} \tag{2}$$

where

$$\varepsilon_r = 1 + \sum_s \omega_{Ps}^2/(\Omega_s^2 - \omega^2), \quad \varepsilon_\phi = 1 - \sum_s \omega_{Ps}^2/\omega^2,$$

$$\varepsilon_z = i\bar{\varepsilon}_z = \sum_s i\Omega_s \omega_{Ps}^2/\omega(\Omega_s^2 - \omega^2).$$

Furthermore one has $\Omega_s = e_s\bar{B}_o R/m_s r$, where R is the major radius of the tours and $\bar{B}_o$ a constant. For axisymmetric problems ($\partial/\partial\phi = 0$) the plasma frequency ω_{Ps} may be calculated using a parabolic density distribution function of the distance $\sqrt{z^2 + (r - R)^2}$ from the magnetic axis as /1/

$$n(r,z) = n_1 - n_o z^2 - n_o(r - R)^2 \tag{3}$$

but for threedimensional modes a solution can be obtained only for "radial density inhomogeneity"

$$n(r) = n_1 - n_o(r - R)^2 \tag{4}$$

In order to solve Maxwell's equations with (2), (4) for the TE-mode E_r, E_z, B_ϕ it is necessary to assume $E_\phi = 0$. This is possible due to the high electric conductivity of a thermonuclear plasma and corresponds to $m_e \to 0$ /3/. Then the threedimensional TE-mode solution of Maxwell's equations can be written

$$\begin{aligned} E_r(r,\phi,z) &= E_r^{(1)}(r,z) + E_r^{(3)}(r)\cos(m\phi) \\ E_z(r,\phi,z) &= f(r)\sin(kz) + E_z^{(3)}(r)\cos(m\phi) \end{aligned} \tag{5}$$

where m and k are separation constants (m integer, k not integer). Furthermore

$$E_r^{(1)} = (-f'k - \gamma\bar{\varepsilon}_z f)/(k^2 - \gamma\varepsilon_r) \tag{6}$$

$$E_r^{(3)} = (E_z^{(3)''} + E_z^{(3)'}/r + HE_z^{(3)})/\gamma\bar{\varepsilon}_z \tag{7}$$

$$\gamma^2 = \omega^2\varepsilon_o\mu_o, \qquad H = \gamma\varepsilon_r - m^2/r^2 \tag{8}$$

$$E_z^{(3)''} + E_z^{(3)'}/r + HE_z^{(3)} - \bar{\varepsilon}_z^2\gamma^2 E_z^{(3)}/H = 0 \tag{9}$$

$$\begin{aligned} f'' + \frac{1}{r}f' + f(-k^2 + \gamma\varepsilon_r - \gamma\bar{\varepsilon}_z^2/\varepsilon_r + \bar{\varepsilon}_z k/r\varepsilon_r) + \\ + fk\bar{\varepsilon}_z'/\varepsilon_r + \varepsilon_r'(f'k^2 + \gamma\bar{\varepsilon}_z kf)/(k^2 - \gamma\varepsilon_r)\varepsilon_r = 0 \end{aligned} \tag{10}$$

All functions in (5) - (10) belong to one and the same eigenvalue γ. The differential equations of second order possess two independent solutions and two integration constants. Since ε_r, $\bar{\varepsilon}_z$ are functions of r due to (4) etc the ordinary differential equations (9), (10) have to be integrated numerically. To do this we need arbitrarily chosen initial conditions, for instance $f_o(r = R - a)$, $f_o'(r = R - a)$ and a first approximative value for γ, the k_n and the m_n taken from the isotropic inhomogeneous axisymmetric mode /4/. The choice of the initial conditions does not influence the eigenvalue γ. We thus obtain solutions in the form of N modes

$$\begin{aligned} E_z(r,\phi,z) = \sum_{n,1}^{N}\Big[& A_n^{(1)} f_n^{(1)}(r;k_n,\gamma)\sin(k_n z) + \\ & + E_z^{(3)}(r;m_n,\gamma)B_n^{(1)}\cos(m_n\phi)\Big] \end{aligned} \tag{11}$$

and E_r from E_z using (6) and (7). Here the superscript (1) = 1, 2 refers to the two initial conditions for the differential equations of second order, n is the subscript for the n-th mode determined by k_n and m_n. All functions belong to the same eigenvalue γ. Defining the meridional cross sectional curve of the toroidal vessel by a set of P points $z_i = z_i^*(r_i)$, i = 1...P and by the local derivatives $(dz^*/dr)_i$ we are able to obtain an analytic smooth curve from the electric boundary condition (1) /1/, /2/, /4/. Due to

Courant's nodal lines theorem /5/ this is proven for the lowest eigenvalue γ. Inserting E_r, E_z from (5) - (11) and $(dz^*/dr)_i$ into the electric condition (1) we obtain a system of linear homogeneous equations for the 4N unknown integration constants (expansion coefficients) $A_n^{(1)}$ and $B_n^{(1)}$. In order to be able to solve these equations we have to choose P = 4N points on $z^*(r)$ and the determinant $D(\gamma,k_n,m_n,r_i,z_i,\phi)$ of the coefficients (containing elements like $f_n^{(1)}(r_i;k_n,\gamma)\sin(k_n z_i)$) has to vanish. For the numerical integration we had chosen first approximative values for γ, k_n, m_n (or $\phi = 0$). Therefore the determinant does not vanish for the given γ. We may now either solve $E_r + E_z \cdot dz^*/dr = 0$, that means a system of P transcendental equations for the 6N unknowns $A_n^{(1)}$, $B_n^{(1)}$, k_n, γ (resp. m_n) with $A_1^{(1)} = 1$ with P = 6N using a computer code or we assume that k_n, m_n are fixed values (which gives better results) and assume that $D(\gamma)$ is a function of γ only. Then the approximate value of γ used for the numerical integration is improved by a regula falsi method. With the new value of γ the numerical integration of (9) and (10) is repeated etc. Experience has shown that N = 2 or 3 and 5 - 11 such iterations are necessary to obtain a value for γ. For a torus with circular cross section ($dz^*/dr = (R - r)/z$) and R = 0.95 m, a = 0.35 m, $n_1 = 10^{20}$ m^{-3}, P = 6, $\phi = 0$, $m_n = 0$, $B_o = 0.1$ Tesla, N = 2, $k_1 = 0$, $k_2 = 6$ we obtained $\omega = 1.2575 \cdot 10^5$. The corresponding electric field lines in the meridional cross section $\phi = 0$ were obtained by integration of $dr/dz = E_r/E_z$ and are shown in Fig. 1.

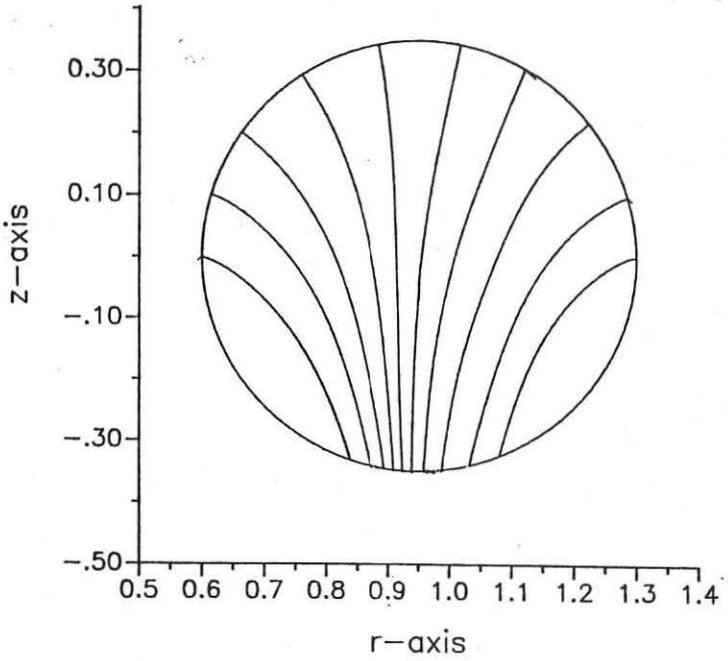

Fig. 1. Electric field lines in inhomogeneous magnetized plasma

Acknowledgement

The financial support of the Austrian Ministry of Research and of the Austrian Academy of Sciences is gratefully acknowledged. Mr. Stössel is thanked for his help in writing computer codes.

References

/1/ F. Cap, Phys.Fl. 28 (6), 1766 (1985)
/2/ F. Cap, 12th Europ.Conf.on Controlled Fusion Plasma Phys., Budapest, 2 - 6 Sept. 1985, 2, p 276
/3/ D. Swanson, Phys.Fl. 17, 2241 (1974)
/4/ F. Cap, IEEE Trans.Vol MTT-32, 1336 (1984)
/5/ R. Courant in R. Courant, D. Hilbert, Methoden der Mathematischen Physik, Band 1, Springer, Berlin

THE USE OF HEAVY-ION MINORITY FOR STEADY-STATE CURRENT DRIVE IN PLASMA

A.V.Longinov, S.S.Pavlov, K.N.Stepanov

Institute of Physics and Technology, the Ukrainian Academy of Sciences, Kharkov 310108, USSR

A scheme of generating a steady-state current in tokamaks by using the cyclotron absorption of the fast wave (FW) at the fundamental harmonic of the ion cyclotron frequency (ICF) for minority ions ($n' \ll n_e$) has been suggested in ref. [1]. This method may be efficient enough if the RF power is absorbed by particles with a sufficiently high $V_{\parallel}'$ value ($V_{\parallel}' \sim$ 4-6 V_{Td}) while their $V_{\perp}'$ is not very large ($V_{\perp}' \lesssim V_{\parallel}'$). However, these conditions are not readily feasible, especially in moderate-size tokamaks. This is probably one of the main reasons why there is no ion cyclotron current drive experiment yet. Here a method is suggested to generate a steady-state current, which is based on sustaining the asymmetry of the resonant heavy minority (HM) ion distribution with using the absorption of a slow wave (SW) at a second harmonic resonance $\omega = 2\omega_c'$. This method is a modification of the HIMH [2].

A scheme of current generation. The essence of the method suggested is seen from the scheme given in Fig. 1. When the FW is excited in the D+H plasma from the HFS, an efficient conversion of FW into SW takes place in the $\omega \approx \omega_{cH}$ region. Even with a relatively low proton concentration ($\gtrsim 5\%$) the effects of FW penetration through the opacity region and FW absorption at $\omega = \omega_{cH}$ and $\omega = 2\omega_{cd}$ resonances may be rather weak [2], therefore, the SW can carry away nearly all the energy injected into the plasma. If there are HM ions with $Z'/A < 1/2$ in the plasma, then in the region of SW propagation there is a zone, where $\omega \approx 2\omega_c'$ (ω_c' being the ICF for the HM). If the HM concentration is high enough so that $\tau = \int \mathrm{Im}\, k_{\perp}\, dR \gg 1$ [3], then the SW is absorbed in the zone $\omega \approx 2\omega_c'$, by the fast ($V_{\parallel}' \gg V_{Td}$) heavy ions having $V_{\parallel}' = (\omega - 2\omega_c'(R))/K_{\parallel} > 0$ (we put $K_{\parallel} > 0$). Note that there may be some other schemes of the SW excitation, for example, the FW excitation from the LFS with the conditions provided for the effective FW→SW conver-

sion [2], or the direct SW excitation from the LFS [4].

Advantages of the proposed current drive scheme. 1) An essentially enhanced efficiency of current generation in the scheme proposed is due to the cutoff of the high energy tails of the heavy-ion distribution function [2]. The role of the cutoff effect is illustrated by Fig. 2. It is seen that the quasilinear diffusion of HM ions takes place only in the region bounded by the cutoff line given by the equation $J_2(K_\perp \rho') = 0$ (J_2 is the Bessel function, $\rho' = V_\perp / \omega'_c$ is the Larmor radius of HM ions). As $K_\perp \rho_d$ can be fairly large for the SW, the cutoff line can correspond to rather low $V_\perp$ values ($V_\perp \lesssim V_{||}$) (from this viewpoint the use of FWs is not efficient). Another important consequence of the tail cutoff effect is the reduced role of trapped HM ions, whose absorption of the SW decreases the current generation efficiency. The HM influence on the SW dispersion [3] increases the $K_\perp \rho_d$ value and therefore enhances the cutoff effect. The dashed line in Fig. 2 shows the cutoff line with allowance for this influence.

2) When the SW propagates from the mode conversion zone to the $\omega \approx 2\omega'_c$ zone, there may occur an essential SW absorption by electrons, the effect being especially important at plasma periphery. The SW absorption by electrons under the conditions considered will be accompanied by steady-state current generation, the process which may be efficient here. Therefore, the direction of this current is important. As it follows from the analysis, the direction of this current coincides with that of the current generated by the ion-cyclotron absorption. This is illustrated by Fig. 3, where the wave vector components are shown in the plane parallel to the equatorial plane of the tokamak. Figure 3 also shows the position of the absorption zone for generating the current consistent with the primary current. The possibility of using antennas with the K_φ symmetric spectrum for current generation in the region not very close to the plasma centre is also seen from this figure.

3) The employment of HM allows one to raise the efficiency of current generation due to the reduction of the ion current fraction (by a factor of 2 at $Z' \gg 1$ as contrasted with the He^3

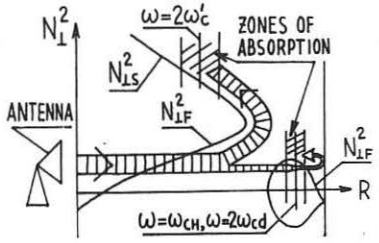

Fig.1

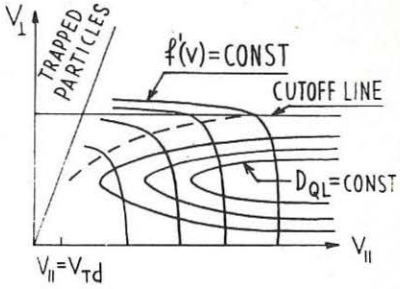

Fig.2

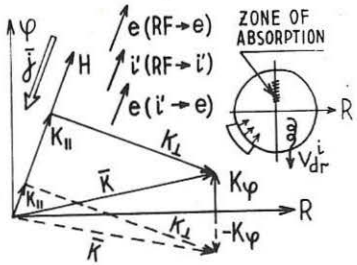

Fig.3

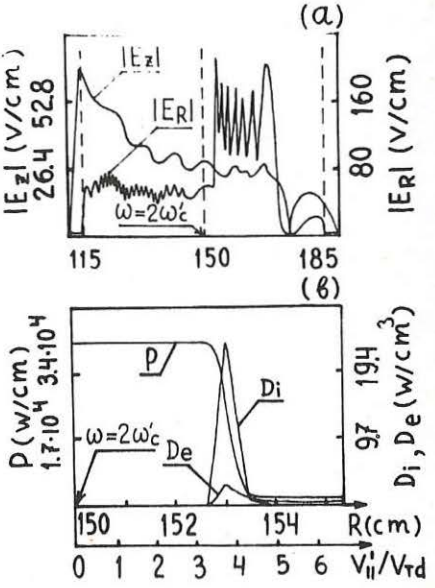

Fig.4 $n_H/n_d=4\%$, $n_{Li^7}/n_d=3\%$, $n_o=7.1\cdot10^{13}$, $T_d=T_H=1$kev, $T_{Li^7}=5$kev, $m=7$

minority case [1], because $j \sim (1 - 1/Z')$. However, in real conditions it is unreasonable to use minority species with $Z' >> 1$, as the production of the necessary current density would require the HM concentrations with high ΔZ_{eff}. Hence, only such species as Li^7, Be^9 etc. can be considered as real candidates for current drive.

The feasibility of the method. Figure 4 presents the results of calculations for FW excitation from the HFS with the model used in [2]. The plasma parameters are typical of T-10. Li^7 ions with a concentration of $n'/n_d = 0.03$ and $T'=5$ keV were used as an HM. The choice of T' allowed us to simulate the situation with an increased particle density in the $V_{||} > V_{Td}$ region, and also, the increased absorption due to the $T'_{\perp}$ growth [2]. The field components E_R, E_z are shown in Fig. 4a, and Fig. 4b shows the energy flux P, the power density absorbed by ions (D_i) and electrons (D_e), and the $V'_{||}$ value for resonant ions. It is seen from Fig. 4 that on approaching the $\omega \approx 2\omega'_c$ zone the injected RF power is absorbed by ions with a high $V'_{||}$ value ($V'_{||} \approx 1.1 \cdot 10^8$ cm/s). Hence, since under these conditions $V_{Td} = 3 \cdot 10^7$ cm/s, the requirement of achieving the highest efficiency in current generation is fulfilled.

Thus, the method considered provides necessary conditions for realizing a highly efficient current generation. The proposed ICRF current drive method can be applied in relatively small up-to-date tokamaks and stellarators (possibly, in combination with other methods).

References

1. N.J. Fisch, Nucl. Fusion 21 (1981) 15.
2. A.V. Longinov, S.S. Pavlov, K.N. Stepanov, Proc. 12th European Conf., (Budapest, 1985) Part 2, p.132.
3. A.V. Longinov, K.N. Stepanov, "Vysokochastotnyj nagrev plazmy (RF heating of plasma), Gorky, Institute of Applied Physics, the USSR Academy of Sciences (1983) 105-210.
4. M. Ono et al., In: 2nd Varenna-Grenoble Symposium, Vol. 1 (1980) 593.

SWEPT FREQUENCY MEASUREMENTS IN A WIDE FREQUENCY AND PLASMA PARAMETER RANGE OF THE COUPLING PROPERTIES OF THE TEXTOR ICRH ANTENNA

P. Descamps, R. Koch, A.M. Messiaen*, P.E. Vandenplas

Laboratoire de Physique des Plasmas - Laboratorium voor Plasmafysica
Association "Euratom-Etat belge" - Associatie "Euratom-Belgische Staat
Ecole Royale Militaire - B 1040 Brussels - Koninklijke Militaire School

INTRODUCTION.

The input impedance Z_A of the TEXTOR antenna [1] is measured over a wide frequency range (20-110 or 60-200 MHz) for a low incident power (≃ 40W) in a deuterium plasma ($n_H/n_D \simeq 5$ %). The complete frequency range is swept many times ($t_{sweep} \simeq 150$ ms) during one tokamak discharge. This leads to the determination of the specific resistance R and inductance L of the antenna.

The dependence of R and L on various plasma parameters is analysed in the entire frequency range [2]. These experimental findings are compared with the predictions of a 3-D model and with similar results obtained at fixed frequency (27 MHz) in the high power experiment [3]. The conclusions of the present study are as follows : R and L dependence on frequency shows no indication of global resonance in the frequency range (30-180 MHz). Experimental data indicates that the edge density has a critical influcence on R, but change of the toroidal field i.e. change of the ion cyclotron layer location does not affect significantly the coupling. Comparison between theory and experiment only shows order of magnitude agreement ; the theoretical predictions also indicate significant sensitivity to edge plasma parameters. Comparison with the high power results indicates the influence of the perturbation of the edge density resulting from the high power RF [3].

EXPERIMENTAL METHOD.

The experimental set-up is connected to the antenna via the vacuum interface used for high power experiments [4]. D.C. breaks at different locations in the system protect it against the high potential differences appearing between the TEXTOR liner and the vessel when the plasma disrupts[figure 1].

Incident and reflected wave amplitudes ($|V^+|$ and $|V^-|$) resulting from antenna mismatch are measured with directional couplers at one point in the line ; a capacitive probe gives the vectorial sum ($|V^+ + V^-|$) of the incident and reflected wave, so that, at this point, the phase is easily computed : $\phi = \pm \arccos\{ \frac{(|V^+ + V^-|/|V^+|)^2 - (1 + (|V^-|/|V^+|)^2)}{2|V^-/V^+|} \}$. The sign is determined through an additional voltage probe measurement made in another point of the line. The antenna impedance can be deduced from the impedance measured at the probe position using transfer matrices of the different line elements.

The main limitation in the measurements comes from the presence of a fixed-length stub used to decrease the VSWR in the line at the high power working frequency (27 MHz). Indeed, the associated deconvolution process leads to amplify errors, thus making the precision requirement on the phase and on the frequency much more stringent.

The frequency reference is a D.C.voltage ramp, proportional to the frequency of the RF output signal. Frequency markers are used to make an absolute calibration of the ramp during the sweep and increase the precision on

* Senior Research Associate at the NFSR, Belgium.

the frequency measurement. Nevertheless, at frequencies such that the stub length is a multiple of a half wavelength, the stub admittance which reaches infinity completely masks the antenna.

EXPERIMENTAL RESULTS.

The evolution of R and L has been studied during discharges at different limiter positions, plasma currents, toroidal fields and plasma densities.

a) Inductance behaviour.

The values of L resulting from measurements in vacuum and during plasma discharges are close. L decreases linearly from a value of $2.5\ 10^{-7}$H/m at 30 MHz to 2.10^{-7} H/m at 180 MHz.

b) Resistance behaviour.

Figures 2 and 3 show the evolution of R as a function of frequency in the ranges [20-110] and [60-180] MHz. The parametric dependence of R is shown on Figs. 2 and 4.One major parameter characterizing the bulk density profile is α_n : $N_e = N_{eo}(1 - (r/a)^{\alpha_n})$.We summarize the results as follow :

(i) Influence of α_n . The frequency dependence of the loading resistance is nearly the same at different times during the plasma discharge but its absolute value changes (Fig. 2). The coupling is high at the beginning of the shot, when the profile is wide and decreases slowly with time to reach a constant value during the density plateau. The study of shots with the same flat top current value I_p, but different α_n values,shows that R increases with α_n (Fig. 4a).

(ii) Influence of N_{eo} . An increase of N_{eo} at constant α_n and a, leads to a small increase of R.

(iii) Influence of a . For a constant value of α_n and central average chord density $\overline{n_{eo}}$ with a larger plasma radius a, the density in the antenna vicinity is higher and R is increased (Fig. 4b).

(iv) Influence of I_p . The raw analysis of the parametric dependence of I_p when $\overline{n_{eo}}$ is kept constant shows that R decreases as I_p increases (Fig.4c). The density profile broadens when I_p is increased, as indicated by α_n. This is in apparent contradiction with the observed dependence on edge density and might be explained by α_n not being representative of the edge density profile at low current.

(v) Influence of B_T. An increase in toroidal field leads to a small increase of R for a constant value of α_n and central density N_{eo}.

(vi) Comparison between the present results at 27 MHz and coupling measurements made during high power operation [3] shows good agreement. Similar parametric dependences are found ; Fig. 5 shows the density dependence of R in both cases. The lower value of R obtained at high power might be related to the perturbation of the plasma edge observed in this case.

COMPARISON BETWEEN THEORY AND EXPERIMENTS.

Experimental results obtained in the range (20-110 MHz) are compared with theoretical values obtained from a 2-D and 3-D model [2], taking into account toroidal and poloidal periodicities, both for a step density profile and for a more realistic profile (Fig. 6). The geometrical characteristics of the antenna studied are [1] : antenna length $2w_y$ = 1.3m,antenna width $2w_z$ = 0.1 m. The effect of bump limiters has been neglected in the model, and the magnetic field is supposed constant and equal to its values at the center of the torus. In the frequency range [20-90 MHz], the 3-D model, using a parabolic density profile with a small density ramp at the edge, gives a good order of magnitude agreement. Curves computed with the step profile and with different edge density values show the great influence of the edge on the theoretical results (Figs.7-8). Further study is necessary to extend the comparison in the frequency range[100-200 MHz].

REFERENCES.

[1] A.M. Messiaen et al.,LPP-ERM ; H.L. Bay et al., IPP-KFA, Plasma Physics and Controlled Fusion, Vol. 28, n° 1A, pp. 71-83, 1986.

[2] A.M. Messiaen et al., "Theoretical aspects of the coupling properties of ICRH antennae". Invited paper Third Varenna-Grenoble Inter. Symp., Grenoble, Vol.I., pp. 243-257, 1982. Edit. Comm. Europ. Communities.

[3] R. Koch et al., "High power coupling properties of the TEXTOR ICRH antennas", this conference.

[4] V.P. Bhatnagar et al., "The high power long pulse cyclotron resonance heating system for TEXTOR". Fusion Technology 1982. Pergamon Press, Vol. 2, pp. 1275-1282. Soft Conference, Jülich, September 1982.

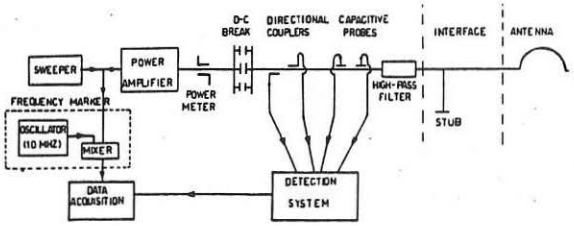

Fig. 1. Experimental set-up.

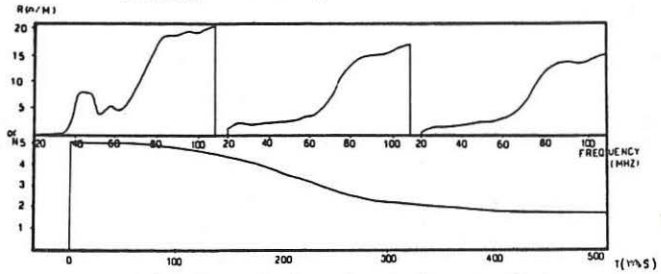

Fig. 2. Evolution of R during the discharge.

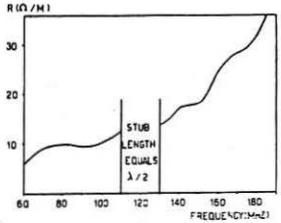

Fig. 3. Evolution of R with frequency in the range [60-190 MHz] during the density plateau.

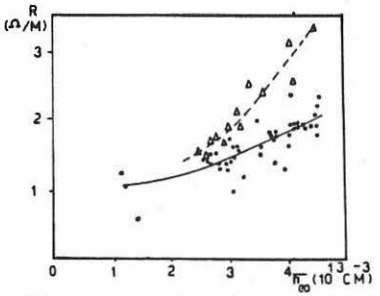

Fig. 5. Comparison between low power and high power experiment; Δ : low power; • : high power.

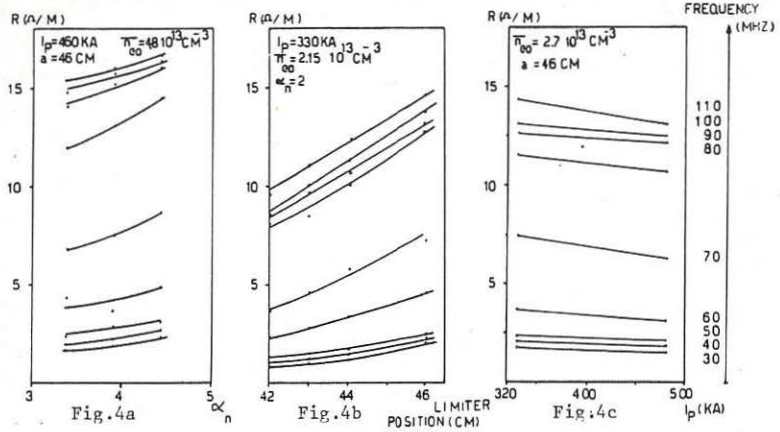

Fig. 4. Influence of plasma parameters on R.

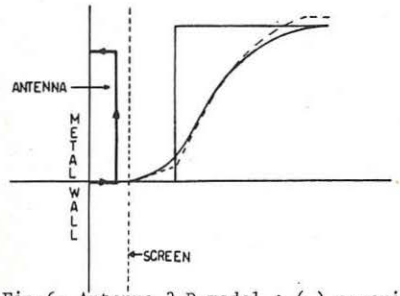

Fig.6. Antenna 3-D model ; (—) experimental density profile,(---) approximation of experimental density curve used for theoretical computation;the step profile is also represented.

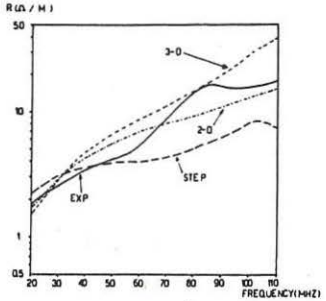

Fig.7. Comparison between experimental results (—) and the values obtained from a 2-D(-·-) and a 3-D model (---) with an edge density* equals $1.5\ 10^{12} cm^{-3}$. The results for the step case are also represented (— —).

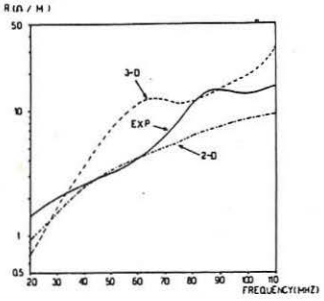

Fig.8. Comparison between experimental results (—) and the values obtained from a 2-D(-·-) and a 3-D model (---) with an edge density* equals $0.5\ 10^{12} cm^{-3}$.

(*) The edge density is the value of the density at the top of the linear ramp.

HIGH POWER COUPLING PROPERTIES OF THE TEXTOR ICRH ANTENNAS

R. KOCH, A.M. MESSIAEN*, R. VAN NIEUWENHOVE

Laboratoire de Physique des Plasmas - Laboratorium voor Plasmafysica
Association "Euratom-Etat belge" - Associatie "Euratom-Belgische Staat"
Ecole Royale Militaire - B 1040 Brussels - Koninklijke Militaire School

1. INTRODUCTION.

The TEXTOR Ion-Cyclotron Resonance Heating (ICRH) system had been designed to couple 2 × 1.5 MW of RF via two λ/4 half turn all-metal antennas [1]. The system was operated at high power for some two years, and we call phase I the operation period ending in summer 85 and phase II the later one. In phase I, the top antenna (A_{IT}) was narrow (average with $2w_z$ = 7 cm), the bottom one (A_{IB}) was wide ($2w_z$ = 20 cm) and the operation regime was mainly (H)-D mode conversion [2]. Phase II antennas were identical (A_{IIT} and A_{IIB} with $2w_z$ = 17 cm) and operated mainly in the low minority concentration regime (n_H/n_D < 1%) [3]. The present paper gives a brief account of the experimental properties of the coupling of these antennas.

2. DETERMINATION OF R AND ωL.

The antenna input impedance is determined using directional couplers and voltage probes in an experimental arrangement described in [1]. The amplitude E_+ of the incoming wave, the phase ϕ and the reflection coefficient $|\Xi|$ characterizing the voltage waveform in the line are computed by regression over the available experimental data. Using the transfer matrices of the different line elements, the antenna input impedance Z_A is computed, yielding, via standard formulae [4], its specific resistance R and inductance L assuming the specific capacitance C to be known from vacuum impedance measurements. For an almost quarter-wavelength antenna, the following approximate relations between the power coupled to the antenna P_A, the antenna short-circuit current I_{cc} and the antenna input voltage V_A hold :

$$4P_A = Rl|I_{cc}|^2 \ , \quad |V_A| = Z_c|I_{cc}| \ , \quad Z_c = \sqrt{L/C}$$

where l = 1.37 m is the antenna length. Typical characteristics of the antennas used in TEXTOR are, for standard conditions (f = 27 MHz, average central chord density $n_{eo} = 3.5 10^{13} cm^{-3}$, plasma radius a_p = 46cm), given in the following table :

Line	Antenna	R_V Ω/m	R Ω/m	ωL Ω/m	C pF	Z_c Ω	f_{res} MHz	V_A/V_L
1	A_{IT}	0.35	1.5	36	145	38.2	32.9	1.4
2	A_{IB}	0.13	0.9	22.1	279	21.6	30.2	1.42
1	A_{IIT}	0.15	1.25	24.4	249	24	30.5	1.3
2	A_{IIB}	0.15	1.15	23.2	249	23.4	31.3	1.2

R_V is the vacuum resistance of the antenna (ohmic losses), V_L is the maximum voltage in the coaxial line, f_{res} is the resonance frequency, and $\omega = 2\pi f$. The capacitance C has been assumed identical for A_{IIT} and A_{IIB} and was estimated from phase I antenna measurements and theoretical w_z-scaling. As seen in the above table, this leads to different L's for A_{IIT} and A_{IIB}.

3. TIME-DEPENDENT BEHAVIOUR.

The temporal evolution of antenna characteristics are determined with a time resolution of 1 ms. Fig. 1 shows an example of such evolutions, for both line ($|\Xi|,\phi,E_+$) and antenna (R,ωL) data. In Fig. 1f, the incident and reflected voltages E_{g+}, E_{g-} at the generator and the voltages measured on probes($V_1,\ldots,V_5$) are also shown for line 2 (A_{IIB}). These signals are to be related to the evolution of various signals characterizing the density profile(Fig.1e) in the plasma bulk ($\bar{n}_{eo}$ and the line average density n_{e4o} measured along a vertical chord located 40 cm away from the plasma center at low field side), the electron temperature (uncalibrated ECE signal) and the edge density (H_α radiation at a toroidal position close to the antenna). One should note the strong effect of sawtoothing on all these signals(in phase with ECE) and the difference in behaviour of A_{IIT} and A_{IIB}. It should be further noted that there is a global correlation between the behaviour of the edge signals and R and ωL : the coupling tends to increase with increasing edge density. No STRICT relation between R and one of the signals of Fig.1e could however be discovered and it must be stressed that Fig. 1 is only exemplative as very different behaviours have been recorded, sometimes showing huge variations or extreme values (up to 4Ω/m) of R.

4. PARAMETRIC DEPENDENCES AND STATISTICAL ANALYSIS.

The aim of a statistical data analysis is to single out the major parametric dependences and to answer the question whether particular modes of operation lead to significant modifications of coupling. Such correlations are obscured by two facts, the first being that drifts are observed over time and the second being the existence, inside the data set, of correlations between the different "independent variables" chosen to make the fits. As to the 1st point, Fig. 2 illustrates typical drifts in coupling, observed after a fresh carbonization[5]during period I where all limiters were in stainless steel. The variations of average and edge densities observed during the same period are also shown. Such a daily drift has no longer been observed with carbon limiters(period II). However, as shown in Fig. 3, significant drift in the voltage stand-off of antennas over long periods of time, has been observed simultaneous with drifts in the coupling parameters. The dependence of the coupling on one major(controllable) parameter, namely $\bar{n}_{eo}$, over period II is shown on Fig. 4, where we have distinguished high and low current operation. During the early period II(up to 10-DEC-85 on Fig. 3)a significant power dependence was observed(Fig.4a,c)which became much fainter later on. Power law fits of the type $R=R_V+A(\bar{n}_{eo})^\alpha$ are also shown (broken line = early period II, solid line = later shots). Systematic parametric studies have been started which indicate a much stronger dependence on n_{e4o} than on $\bar{n}_{eo}$;as can be deduced from Fig.4.The current dependence,if present,is relatively weak.

5. COMPARISON WITH THEORY.

Computation with the model [4] gives R values which are higher by a factor <2. Overall tendencies seem to be well-described by theory, although theoretically predicted effects are often much larger than the ones observed experimentally (such as the effects of phasing shown on Fig. 2). B_T-field reversal experiments have indicated no major difference in coupling with respect to normal operation although the shield blades of the antennas are aligned along the total magnetic field direction in normal operation. Both experiments and theory seem to point to (see also [6]) the crucial influence of the edge plasma.

---

* Senior Research Associate at the NFSR, Belgium.

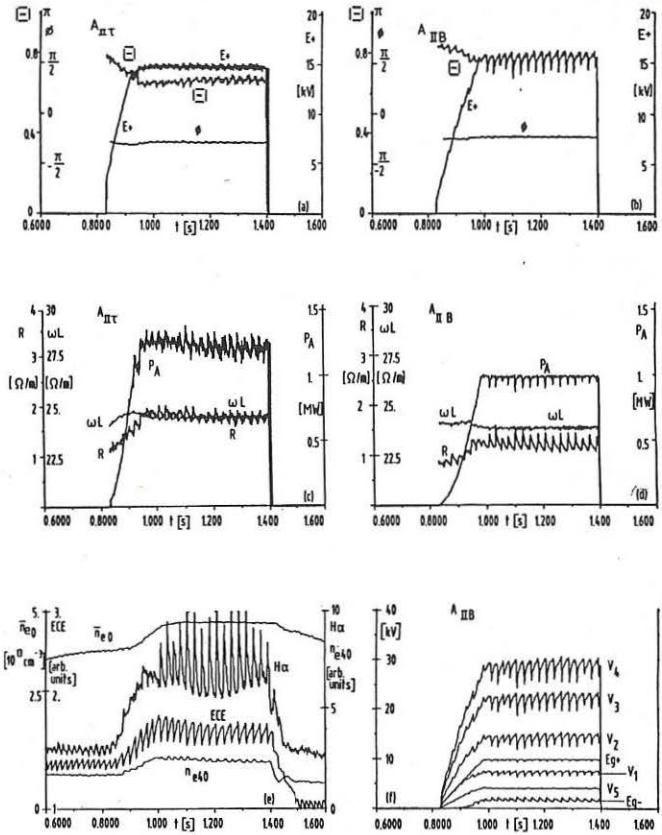

Fig. 1.
Time-evolution of coupling parameters for shot 19161.

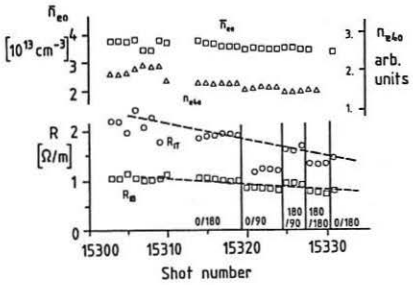

Fig. 2. Evolution of the coupling during a day, after carbonization (period I). The broken lines indicate the drift during the day. Number couples, like 0/180 indicate the phase in degrees of the voltage fed on resp. A_{IT}/A_{IB}.

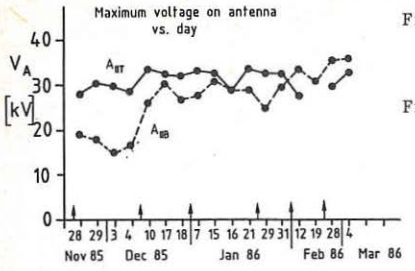

Fig. 3. Drift in voltage stand-off. Arrows indicate carbonization.

Fig. 4. Statistics of R versus density. o and • shots 18571-18967 (full circles : P_A<300 kW);+ shots 18968-19831; x shots 19832-20353; Δ shots 20570-20820. For all shots 45cm < a_p < 47cm and 1.89T < B_T < 2.07T.

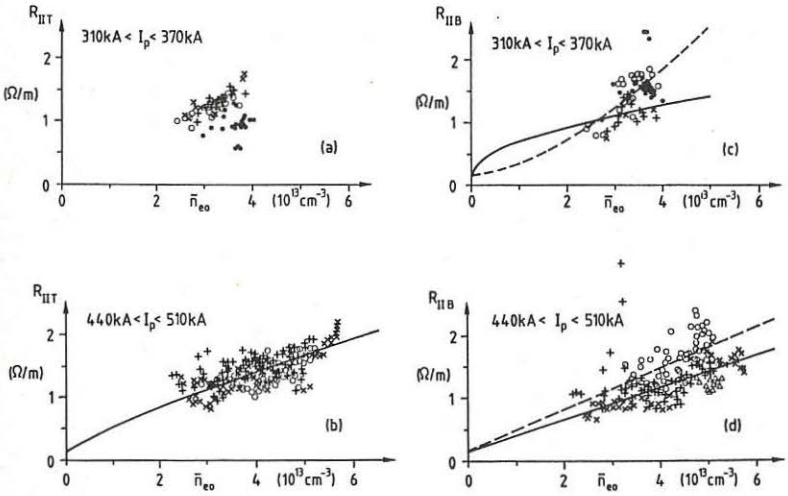

REFERENCES.

[1] V.P. Bhatnagar et al., to be published in Fusion Technology.
[2] A.M. Messiaen et al., Plasma Phys. and Contr. Fusion, Vol. 28,1986,p.71.
[3] G.H. Wolf, Invited paper, this conference.
[4] A.M. Messiaen et al., in "Heating in Toroidal Plasmas", EUR7979EN, 1982, Brussels, Vol. I, p. 243.
[5] J. Winter et al., J. Nucl. Mat., Vol. 128-129, 1984, p. 841.
[6] P. Descamps et al., this conference.

INFLUENCE OF THE WALL-PLASMA DISTANCE ON THE RADIATION OF AN ICRH ANTENNA

A.M. Messiaen+, R. Koch, V.P. Bhatnagar

Laboratoire de Physique des Plasmas - Laboratorium voor Plasmafysica
Association "Euratom-Etat belge" - Associatie "Euratom-Belgische Staat"
Ecole Royale Militaire - B 1040 Brussels - Koninklijke Militaire School

I. INTRODUCTION.

In earlier work [1,2,3,4] it was shown that a part of the power radiated by ICRH launching structures could propagate along the plasma edge either in the form of coaxial modes wherever a vacuum layer exists between the plasma and the metal wall or as surface waves in the outer plasma gradient. An approximate dispersion relation for the coaxial modes is [1] $p^2=k_{//}^2+k_y^2-k_o^2=0$ ($k_{//}$,k_y toroidal and poloidal wavenumber, k_o vacuum wavenumber) while surface modes propagate for positive $k_y > k_o$ [2,3] (B_T is directed along z). In previous models, due to the modelling of the electrostatic screen by an infinite anistotropic plane, the vacuum layer could not be removed to simulate practical situations where the screen is finite and the plasma can come up to the wall. In this paper we investigate the influence of the vacuum layer thickness and, in the limit, of its non existence,on the active radiated power spectrum part related to edge propagation. For this purpose, instead of the conventional strip line antenna, we consider a U-slot excitation in the wall (coplanar line section)[5] giving a similar exciting field configuration when covered by an appropriate electrostatic screen (see Fig.1). The effect of the resonance $k_o^2\varepsilon_1 - k_{//}^2 = o$ (ε_1, ε_2 are the usual cold-plasma dielectric tensor elements [1]), present in the plasma edge in the usual ICRH conditions ($\omega > \omega_{ci}$) when $|k_{//}| < k_o$, on the active power spectrum is also investigated.

2. THEORY.

2.a. U-slot excitation. The boundary conditions imposed by the slot excitation can be expressed in terms of the applied electric field components tangential to the x = o plane. We shall denote by $E_{y,o}$, E_{zo} the spectra of these components which vanish identically at x = o except on the slot itself (Fig. 1) where $E_y = (V_A/e)$ for $2w_y < y < 2w_y + e$, $|z| < w_z$; $E_z = (\text{sign } z)\, V_A \sin \beta y/(e \sin 2\beta y)$ for $o < y < 2w_y$, $w_z < |z| < w_z + e$; with V_A the applied input voltage, β the current propagation factor and we consider the limit $e \to o$. With the usual anisotropic screen model [1,2] located at x = -s, the TE field excitation crossing the screen is given, for small s, by $(E_{y,o})_{TE} = E_{y,o} + k_{//}k_y E_{z,o}/H^2$ (1) with $H^2 = k_o^2 - k_{//}^2$.

2.b. The active radiated power, taking into account poloidal and toroidal periodicities is given by $\mathrm{Re}(P_{TE})$ [2] with

$$P_{TE} = \frac{-1}{8\pi^2\omega\mu_o rR} \iint \sum_n \sum_m \delta(k_{//} - \frac{m}{R})\delta(k_y - \frac{n}{R})\Phi(k_{//},k_y)\,dk_{//}dk_y \quad (2)$$

where $\Phi(k_{//},k_y) = |E_{y,o}|^2_{TE} \left\{ \frac{iH^2}{p} \frac{i\xi_1 H^2 \mathrm{sh}\, pa + p\, \mathrm{ch}\, pa}{i\xi_1 H^2 \mathrm{ch}\, pa + p\, \mathrm{sh}\, pa} \right\}$ * (3) and

---

+ Senior Research Associate at the NFSR, Belgium.

$\xi_1 = (E_y/\omega B_z)_{x=-a}$. The value of ξ_1 is obtained by numerical integration of the fast wave differential equation [6] $\frac{d}{dx}\left|\begin{matrix} i\omega B_z \\ E_y \end{matrix}\right| = \bar{\bar{A}}\left|\begin{matrix} i\omega B_z \\ E_y \end{matrix}\right|$ (4) with $A_{11} = -A_{22} = dk_y/u$, $A_{12} = -u + d^2/u$, $A_{21} = 1 - k_y^2/u$; $d = k_o^2\varepsilon_1$ and $u = k_o^2\varepsilon_1 - k_{//}^2$. Single pass absorption, i.e. no wave reflection at $x = -\infty$ is assumed. The specific resistance due to the loading by the plasma can be deduced from $Re(P_{TE})$ when the coplanar line characteristics are known [5].

2.c. Influence of the singularity. In a neighbourhood of the singularity $u = o$, i.e. near $x = x_o = -a - H^2/(k_o^2\varepsilon_1')$ with $\varepsilon_1' \equiv (d\varepsilon_1/dx)_{x=x_o}$, one can write down [6] an asymptotic solution of the wave equation :

$$\left|\begin{matrix} i\omega B_z \\ E_y \end{matrix}\right| = \left(\bar{\bar{I}} + \frac{\bar{\bar{A}}_o}{k_o^2\varepsilon_1'} \ln\left(\frac{x - x_o}{x_1 - x_o}\right)\right)\left|\begin{matrix} i\omega B_{z1} \\ E_{y1} \end{matrix}\right| \text{ , with } \bar{\bar{A}}_o = \left|\begin{matrix} d & \\ & k_y \end{matrix}\right| \quad (-k_y, d)$$

and the initial condition $(i\omega B_{z1}, E_{y1})$ is given at $x = x_1$. This leads to the following approximate expression : $\xi_1 = (\xi_1)_{x=x_1} + i\frac{k_y^2}{k_o^2\varepsilon_1'} \ln\frac{a - x_o}{x_1 - x_o}$ valid for $|H^2| \to o$, i.e. $x_o \to -a$, and $x_1 < x_o$ close to x_o . A real part (proportional to $\arg[(a - x_o)/(x_1 - x_o)]$) corresponding to additional absorption whenever the singularity is present inside the plasma is thus added to the bulk contribution $(\xi_1)_{x=x_1}$. The ξ_1 values used in the following are obtained from numerical integration of (4) using the density profile shown in Fig. 1, either (i) avoiding the singularity by assuming a sufficiently high edge density N_2 = twice the lower-hybrid density (case $\nu = o$) or (ii) using $\nu/\omega \simeq 10^{-2}$ (case $\nu \neq o$). In this last case, the numerically obtained ξ_1 behaviour for $|k_{//}| \simeq k_o$ agrees with the above formula .

3. RESULTS AND DISCUSSION.

The contour plots of the active power spectrum $Re[\Phi(k_y, k_{//})]$ defined in Eq. (2) are shown in Fig. 2 for the conventional antenna (schematized in Fig. 1). A similar plot is given in Fig. 3a for the slot excitation, exhibiting essentially the same characteristic behaviour dominated by coaxial mode excitation. The sequence of Figs. 3a to 3d shows the effect of approaching, up to contact, the plasma from the wall. This evolution first shows the significant increase in coupling to be expected when approaching the plasma. Second, the coaxial mode locus is seen to deform according to the approximate relation $k_o^2 \simeq k_{//}^2 + k_y^2 a/(a + Im(\xi_1))$, with $Im(\xi_1) > o$, describing the propagation eigenmodes existing in the plasma-vacuum system (denominator in (2) = o). At the limit $a = o$, this locus is $k_o^2 = k_{//}^2$ as clearly seen in Fig. 3d. However, the persistance of a nonvanishing excitation of this limit mode can be seen to follow (eqs. (1) and (3)) from E_z remaining non-zero in the limit $a = o$. In practice, the impedance associated with the excitation of Sect. 2a would vanish with $a \to o$, as the E_z field is short-circuited and real excitation can only lead to eigenmode-free coupling, as seen in making $a \to o$ and $E_z \to o$ in (3). This behaviour is not significantly affected by taking $\nu \neq o$, i.e. by including the edge damping discussed in Sect. 2c. Indeed, the deformation of the contours, in Fig. 4 (to be compared to Fig.3b), around $|k_{//}| = k_o$ indicate that a dissipation mechanism is added at low $k_{//}$ which abruptly disappears for $|k_{//}| > k_o$.

In conclusion we have shown the large sensitivity of the coaxial mode dispersion to the edge density profile (similar to the one of the bulk coupling, as stated in [7]) and the relatively minor effect of the edge singularity. In practice, the excitation of any type of edge eigenmode in the plasma is seen to vanish when a plasma with sufficient density comes in

contact with the wall.

REFERENCES.

[1] A.M.Messiaen et al., Heating in Toroidal Plasmas,Eur 7979EN,Vol.1, p. 243 (1982).
[2] V.P. Bhatnagar et al., Nuclear Fusion suppl. Vol. II, 103 (1983)
[3] A.M. Messiaen et al., Heating in Toroidal Plasmas, Eur 9341EN, Vol. 1, p. 315 (1984).
[4] V. Vdovin and I. Kamenskii, Voprosi atom. nauki in tekhn.-Seriya Term. sintez 2,3 (1985).
[5] A.M. Messiaen and R.R. Weynants, Plasma Phys. and Contr. Fusion, 26 525 (1984).
[6] W. Wasow, Asymptotic expansions for ordinary diff. equations, Interscience, New York 1965.
[7] R. Koch et al., this conference ; P. Descamps et al., this conference.

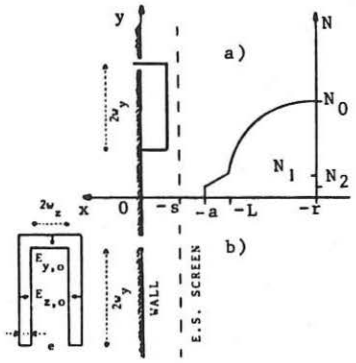

Fig. 1. Conventional strip line antenna (a)) and slot antenna (b)) with the electrostatic screen and the plasma density profile facing it. The shape of the slot antenna is also indicated.

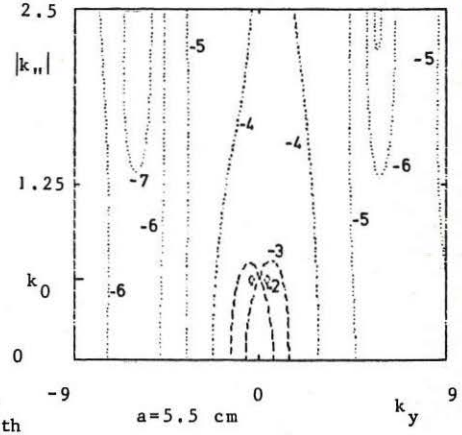

Fig. 2. Contours of $\log_{10}[\mathrm{Re}(\Phi(k_\parallel, k_y))]$ for the conventional antenna (normalized value , MKSA units). The other parameters are : $\omega/2\pi$ = 28.6 MHz, B_T = 2.7 T, w_y = 68.5 cm, w_z = 1 cm, L - a= 2.5 cm, r = 46 cm, $\beta = 1.12 m^{-1}$; $N_0 = 3\times10^{13}$, $N_1 = 5\times10^{11}$, $N_2 = 3.6\times10^{10} cm^{-3}$; a = 5.5 cm.

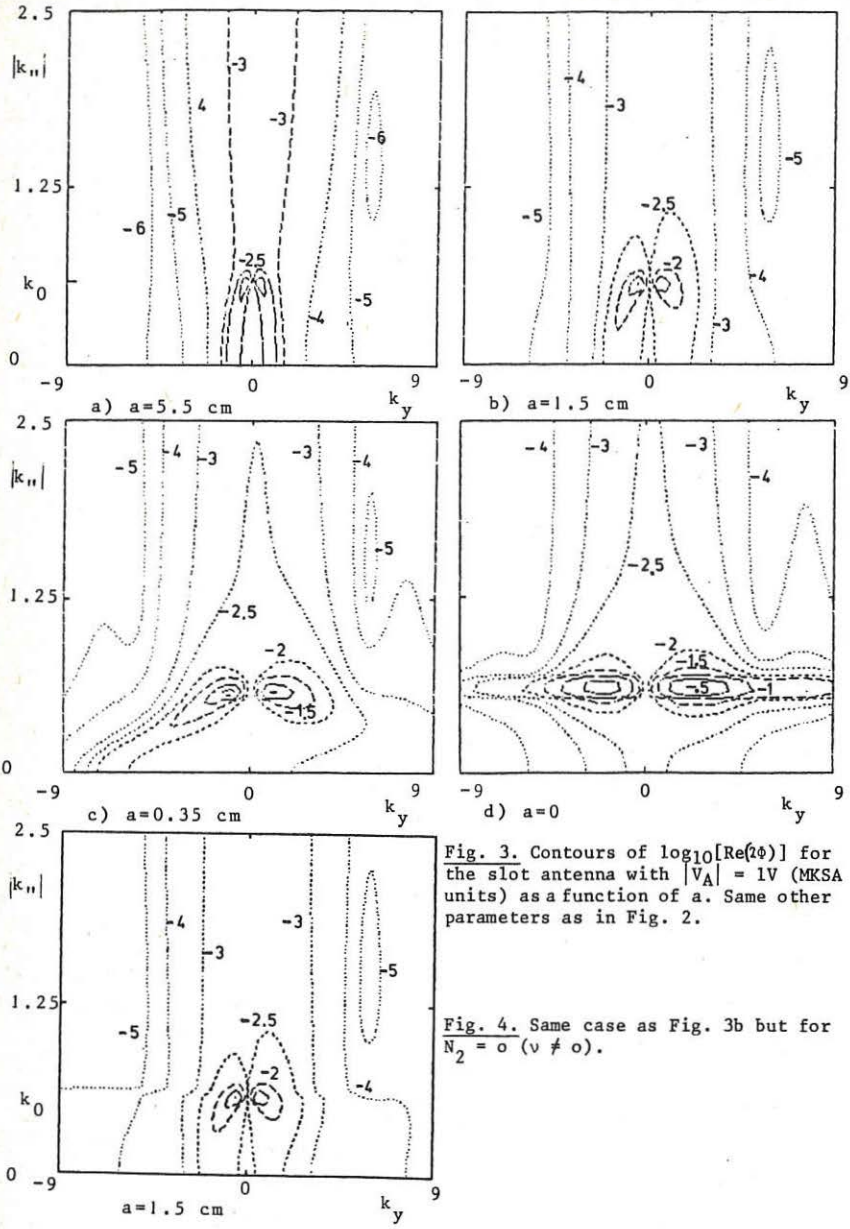

Fig. 3. Contours of $\log_{10}[\mathrm{Re}(2\Phi)]$ for the slot antenna with $|V_A| = 1V$ (MKSA units) as a function of a. Same other parameters as in Fig. 2.

Fig. 4. Same case as Fig. 3b but for $N_2 = o$ ($\nu \neq o$).

COUPLING SPECTRA FOR ION CYCLOTRON HEATING IN LARGE TOKAMAKS IN PRESENCE OF EIGENMODES

T. Hellsten and K. Appert*

JET Joint Undertaking, Abingdon, Oxon. OX14 3EA, UK
*CRPP Ecole Polytechnique, Federale de Lausanne, Switzerland

1. Introduction - The wave spectrum radiated from an antenna during ICRH is of importance for the radiation resistance, current drive efficiency, power deposition and partition to the various species. The wave coupling problem is usually treated by assuming single pass absorption. In general, this is not the case when coupling to the magneto-acoustic wave from the low field side in a tokamak. Instead, the coupling problem is characterised by the presence of eigenmodes. Global codes have recently been developed which can treat the wave coupling problem in presence of reflection [1-3]. In this note we discuss the structure of the wave spectra for some JET scenarios.

2. Characteristics of the Coupling Spectrum - A crude description of the coupling spectrum can be obtained from the dispersion relation for the magneto-acoustic wave in a plane geometry

$$(\varepsilon_\perp - k_z^2)(\varepsilon_\perp - k_x^2 - k_y^2 - k_z^2) - \varepsilon_{xy}^2 = 0. \qquad (1)$$

Here $\varepsilon_\perp$ and ε_{xy} are the diagonal and off-diagonal elements of the perpendicular components of the dielectric tensor. The magnetic field is assumed to be parallel to the z-axis. Let us identify x,y and z with the radial, poloidal and toroidal directions, respectively, in a tokamak of minor radius a and major radius R. Consequently, one has to imagine the components of $\vec{k}$, the wave vector, to be quantized with typical values $n_x\pi/a$, n_y/a and n_z/R where n_x,n_y and n_z designate the quantum numbers. In a calculation k_y and k_z can be chosen whereas k_x or rather n_x, the number of radial nodes of the eigenmode, is obtained as a result when a resonance condition of the form (1) is met. Assume for a moment that k_z could be treated as a continuous variable: a typical coupling spectrum (antenna load versus k_z) then has a structure as schematically shown in Fig.1. Essential for Fig.1 is that $|k_y|, |k_z| << |\varepsilon_\perp|, |\varepsilon_{xy}|$ and $n_x >> 1$. The spacing between modes with different n_x is greater than between modes with the same n_x but different n_y and n_z.

The amplitude and the width of a single resonance peak in Fig.1 are inversely proportional and proportional to the absorption, respectively. The amplitude further depends on the distribution of the current in the antenna, the distance between the antenna and the cut-off, wave frequency, k_y and $k_z$as in the case when single pass absorption is assumed. In general, the coupling with higher k_y and k_z is less effective. As the absorption increases, the resonances corresponding to different eigenmodes start to overlap and compound resonances are the result.

The probability for the antenna to couple to a resonance with a given k_y depends on the width of the resonance and the interval between the discrete k_z modes. A critical value of the absorption coefficient a*, can then be defined for which the width equals the separation of k_z modes. The

absorption coefficient is here defined as the fraction of the wave not reflected back to the antenna. Calculations with the ISMENE code [3] give for JET parameters $a^* \approx 0.25$. For $a<a^*$ the coupling resistance is determined by a single or a few single modes and hence may vary rapidly due to small changes in the plasma equilibrium, i.e. density, magnetic field etc. For $a>a^*$ the antenna couples to a large number of modes and the total resistance varies less when the equilibrium conditions evolve. We further note that since the amplitude and the width of the resonances vary in opposite ways with respect to the absorption, the mean value is independent of the absorption. However, as it falls below a^*, fluctuations will increase around this mean value.

The radiation spectra for antennae like the JET monopole and dipole antennae, which essentially couple to low k_z are characterised by a compound resonance peak in the interval $[0,k_z^*]$ where k_z^* is defined by

$$\pi = \int [k_x(0,0) - k_x(0,k_z^*)]dx. \qquad (2)$$

Typical values of k_z^* in JET are $0.05cm^{-1}$. Eq.(2) applied to Fig.1 implies that the antenna mainly couples to the first group of modes, i.e. $n_x=20$.

Since the wave number k_x is roughly proportional to $\sqrt{n}/B$ the wave spectrum will be sensitive to small variation of the density or the magnetic field strength. If the density increases or the magnetic field decreases the resonances will be displaced towards higher k_z. However, there will in general be one compound resonance peak in the interval $[0,k_z^*]$ which dominates the coupling thus leading to a fluctuation of the radiation spectrum and coupling resistance as the equilibrium parameters evolve. In Fig.2 we show how the radiation spectrum for fundamental heating of hydrogen in deuterium varies for small variation of the density as computed with the ISMENE code. The change due to a finite k_y is also shown. To obtain the spectrum for a finite sized antenna or antennae the spectra shown here have to be weighted with the Fourier components of the antenna current. In Fig.3 we show how the spectrum changes as the toroidal field varies. These calculations can be compared with the measured oscillations of the antenna resistance when the toroidal field was ramped down from 2.6-1.4 tesla in 10s (see Fig.4). The code calculations predict that the compound resonance peak will be localized at the same k_z for a change of B with 0.08T. This corresponds to an oscillation time of 0.67s compared to 0.45s of the experiment.

Predictions of the structure of the coupling spectra can then be based on studying the absorption coefficient. In Fig.5 we show how the absorption coefficient varies with respect to k_z for the case shown in Fig. 2 and for some other heating scenarios in JET:

$\omega=2\omega_{CH}$, $n_H(0)=3x10^{13}cm^3$, $T_H(0)=2.5keV$, $B_o=1.1T$ and $f=33.3MHz$;

$\omega=2\omega_{C^3He}$ in D, $n_{^3He}/n_D=0.15$, $T_D(0)=2.5keV$, $T_{^3He}(0)=5keV$, $B_o=1.7T$ and $f=33.3MHz$;

$\omega=\omega_{C^3He}$ in H, $n_{^3He}/n_H=0.02$, $n_D(0)=3x10^{13}cm^{-3}$, $T_{^3He}(0)=T_H(0)=2.5keV$, $B_o=3.4T$ and $f=33.3MHz$;

$\omega=\omega_{C^3He}$ in D, $n_{^3He}/n_D=0.04$, $n_D(0)=3x10^{13}cm^{-3}$, $T(0)=2.5keV$, $B_o=3.4T$ and $f=33.3$ MHz.

Heating scenarios with "weak" absorption like fundamental heating of ^3He in D will be subjected to sharp resonances as can be seen in Fig.6. Since the resonances for different k_y appears at different k_z the antenna will still see a relatively broad compound resonance.

3. Discussion - Ion cyclotron heating by magneto-acoustic waves being launched from the low field side is characterised by coupling via eigenmodes. When the absorption coefficient, which determines the width and amplitude of the resonances, exceeds a critical value (typical 0.25 for JET) the antenna will couple to a large number of eigenmodes. The average value of the coupling resistance does not depend on the absorption. Antennae which couple to small k_z, will have a narrower radiation spectrum than if single pass absorption is assumed and the spectrum will be characeterised by a compound resonance in the interval $[0,k_z^*]$ whose position is very sensitive to small variations in the equilibrium. This will have consequences on current drive where a prescribed wave spectrum is important for the efficiency. Further, it may affect the partition of power absorbed by electrons and ions.

Acknowledgement - The authors wish to thank Dr M Bures for valuable discussions.

References

[1] S.I. Itoh, et al. Plasma Physics and Controlled Nuclear Fusion Research, IAEA, Vienna, 1985, Vol.1, pp.

[2] S.C. Chiu and T.K. Mau. Nucl. Fus.23 (1983) 1613.

[3] K. Appert, T. Hellsten, J. Vaclavik and L. Villard. 3rd European Workshop on Problems in the Numerical Modelling of Plasmas, NUMOP 85, Varenna, Italy, 1985.

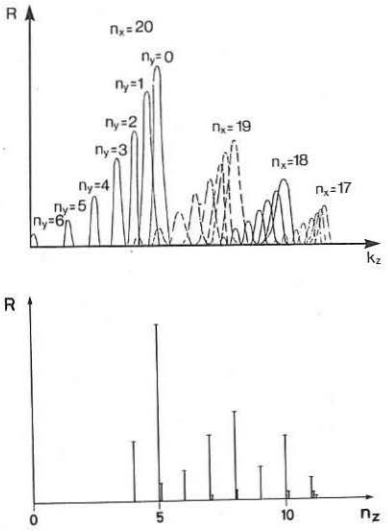

Fig. 1 Schematic picture of the coupling spectrum. Above for a continuous spectrum and below the corresponding one for a discret spectrum.

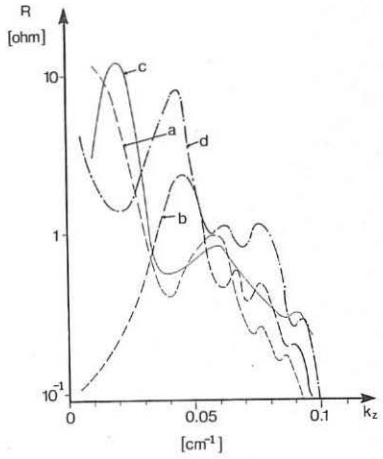

Fig. 2 Computed coupling resistance of the individual Fourier components for $\omega=\omega_{CH}$, $n_H/n_D=0.04$, $B_o=2.3T$, $T(0)=2.15keV$, $k_y=10^{-4}cm^{-1}$ in a-c.
a) $n_D(0)=3.1\times10^{13}cm^{-3}$
b) $n_D(0)=2.8\times10^{13}cm^{-3}$
c) $n_D(0)=2.5\times10^{13}cm^{-3}$
d) as b) except $k_y=0.04cm^{-1}$

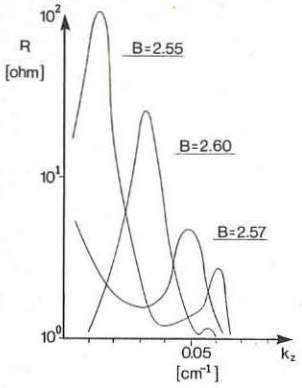

Fig. 3 Computed coupling spectrum for $\omega=\omega_{CH}$ for various magnetic fields.

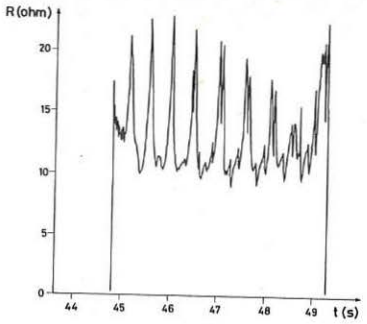

Fig. 4 Measured coupling resistance on a JET antenna during ramp down of the toroidal field. The resistance has been transformed by the short reactive stub close to the antenna.

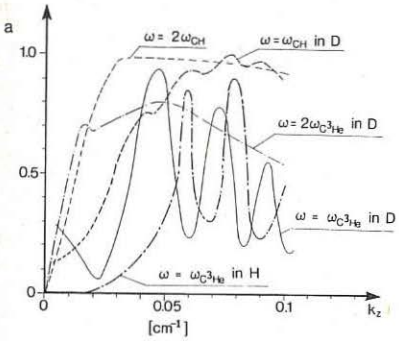

Fig. 5 Absorption coefficient vs. k_z

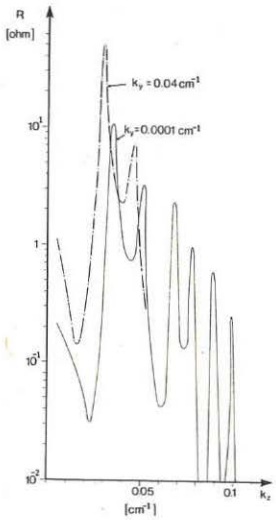

Fig. 6 Computed coupling spectrum for $\omega=\omega_{C^3He}$ in D.

COMPARISON OF THEORETICAL AND EXPERIMENTAL ICRF ANTENNA-PLASMA COUPLING RESISTANCE IN JET

M.P. Evrard*, V.P. Bhatnagar*, M. Bures, F. Sand

*From LPP-ERM/KMS; EUR-EB Association, 1040 Brussels, Belgium

JET Joint Undertaking, Abingdon, Oxon, OX14 3EA, UK

1. Introduction

We present here a comparison of the predictions of different models for antennae coupling resistance with experimental measurements. We discuss the advantages and limitations of each model, and examine the importance of coaxial modes in JET. The influence of the current variation on the coupling resistance is studied and it is shown that a good agreement with experimental values can be found with a simple realistic current profile.

The effects of plasma edge parameters on the coupling resistance have also been investigated.

2. Coupling resistance measurements

The coupling resistance is deduced from voltage measurements made near the generators, 80 m away from the antennae. In the absence of additional fixed stubs, we can link the radiated power to the measurements by

$$\mathrm{Re}\ P = \frac{1}{2} R_c I_{max}^2 = \frac{1}{2} R_{ant} \left| I_{ant} \right|^2 \qquad (1)$$

where I_{max} is the maximum current on the line and I_{ant} is the current at the antenna input. Losses in the line and in the screen have been estimated to contribute to the coupling resistance R_c by about 0.6 Ω at around 33 MHz. In the presence of fixed stubs near the antenna, relation (1) no longer holds. We need phase measurements to reconstruct the voltage pattern along the line, and to deduce the (complex) radiation impedance of the antenna which is at present not available.

3. Theoretical models for antenna impedance

Theoretical models for ICRH antenna impedance have been developed to a highly sophisticated level. Two models [1,2] are presently in use at JET, both allowing for realistic plasmas and using single pass absorption hypothesis in a slab geometry : the induced emf method and the variational method. In the variational method, we derive an equation for the current distribution which is solved, yielding eventually the coupling resistance. The induced emf method is faster and assumes a realistic current distribution and calculates the coupling resistance directly. The variational code takes into account the frame limiter in which the antenna is recessed but only the monopole configuration has been treated. The code based on the induced emf method does not consider the frame limiter but permits to choose between many different current distributions, including the four JET antenna configurations. Both models use the following expression for the radiated power:

$$P = \frac{1}{2} Z_{ant} \left|I_{ant}\right|^2 = \frac{1}{2} \int \frac{dk_{//}}{2\pi} \frac{dk_y}{2\pi} \psi\,(k_{//},k_y) \left|J(k_{//},k_y)\right|^2 \quad (2)$$

where $\psi(k_{//},k_y)$ depends on the boundary conditions and $J(k_{//}, k_y)$ depends on the Fourier transformed components of the current distribution. The code based on induced emf method also takes into account the periodicity of the torus by replacing the integrals in (2) by sums over multiple of $1/R$ and $1/a$ where R and a are the major and minor radius respectively. Due to the complex shape of the actual antenna conductors, the reactive part of the power which is very sensitive to the exact current distribution, specially on the lower conductors, is poorly described in the induced emf method where the antenna currents distribution is an input parameter. To be able to go from the real part of the antenna impedance to the coupling resistance with the help of eqn (1), we require the ratio $I_{max}(ant)/I_{max}$ (line). This has been experimentally measured to be about 1.2 in vacuum and is assumed to be unchanged in the presence of the plasma.

4. Effects of (possible) coaxial modes

Coaxial modes are described by $k_{//}^2 + k_y^2 \leq k_o^2$ and they propagate between the plasma surface and the machine wall. These modes could have adverse effects on the plasma edge conditions, leading to the release of impurities into the plasma. In JET, the geometrical dimensions and the ICRF frequency range permit only a minor contribution within the circle described by $k_{//} + k_y = k_o$ and the importance of coaxial modes depends on the sharpness of the integrand around this circle. For the JET monopole antenna configuration the coaxial modes contribution is largest, but the power spectrum as calculated without taking into account the frame limiter is not very peaked around $k_{//} + k_y = k_o$ (see Fig. 1) and the proportion of the contribution of coaxial modes to the total power is still less than 10%. The presence of the frame limiter should change the situation, and in the torus these modes could be shielded. The presence or absence of coaxial modes in JET has not been assesed experimentally, yet.

5. Influence of the current distribution along the antenna

We describe the current distribution as $I(y) = I_o \cos\gamma y$, where γ is the current propagation constant. To assess the effect of γ, we have studied the evolution of the coupling resistance of all four antenna configurations for a typical plasma ((He_3)-D, $B_o = 3.4$T, f = 33 MHz) where the antennae are nearly resonant. The expected γ for $\frac{\lambda}{\pi}$-resonant antennae of the size of those in JET is around $\gamma \approx 1.35\ m^{-1}$. Although the monopole and the quadrupole seem rather insensitive to changes of γ between $\gamma = 0$ (uniform distribution), and $\gamma = 2\ m^{-1}$, for both dipoles a choice of γ between 0 and $0.9\ m^{-1}$ would fit the experimental results better (Fig. 2). Choosing $\gamma = 0.9\ m^{-1}$ f.i. leads to Fig. 3 where a fairly good agreement with experimental data is found for the monopole, quadrupole and to a lesser extent for the dipoles. This behaviour reflects the fact that the dipole configurations, in which the current in the poloidal sections flow in mutually opposite directions, are difficult to be described by a single value of γ as we attempted in the induced emf method.

The variation of coupling resistance with frequency has been obtained by the variational method. As mentioned above, the induced emf method suffers from the need of redefining a new γ for each frequency, the variational methods is better suited. The resonance of $A\emptyset_1$ antenna in the monopole configuration is found to be at f_{res} = 35 MHz whereas experimentally, it is around 33 MHz.

6. Plasma edge effects on the coupling resistance

We have investigated the effects of the change of the density profile in the edge region of the plasma on the coupling resistance for the different antenna configurations. Variations of the plasma density at the limiter n(a), of the e-folding length in the S.O.L. and of the peaking factor of the bulk plasma density have been considered. The main dependance of the coupling resistance is on the plasma density at the limiter, for all the different antenna configurations. The $A\emptyset_1$ monopole and dipole, together with the $A\emptyset_2$ quadrupole show a marked dependance on the plasma edge density gradient through the peaking factor, the coupling resistance increasing with the steepest profile. But the dependance on the S.O.L. e-folding length is weak. The $A\emptyset_2$ dipole coupling resistance, in addition to show a somewhat lesser sensitivity to the plasma density at limiter than the others, does not seem to depend on the peaking factor. The sensitivity to the S.O.L. e-folding length is comparable to that of the other configurations.

Conclusions

Theoretical determinations of the coupling resistance for all four antenna configurations used in JET have been obtained and compared to experimental measurements. The coaxial modes have been found to be of little importaqnce in JET, and for the monopole antenna contribute less than 10%. Dependance of the coupling resistance on the current distribution has been studied. Though in practice γ may be slightly different for each antenna configuration, theoretically a value of $\gamma = 0.9\ m^{-1}$ gives a good agreement with experiment for all four antenna configurations. The behaviour of R_c with frequency for the monopole antenna has been verified.

The effects of edge conditions on coupling resistance have been investigated for all antenna configurations. R_c depends mainly on the plasma density at the limiter, increasing by about 20% when the edge density doubles.

References

[1] Bhatnagar, V.P., Koch, R., Messiaen, A.M., Weynants, R.E., Nuclear Fusion, 22 (1982) 279, and also Messiaen, A.M., Koch, R., Bhatnagar, V.P., Evrard, M.P., Luwel, M., Vandenplas, P.E., Weynants, R.R., Proc. 3rd Joint Varenna Grenoble Int. Sump. on "Heating in Toroidal Plasmas", Grenoble (1982) Vol 1. 243

[2] Theilhaber, K., Jacquinot, J., Nuclear Fusion, 24 (1984) No 5, p. 541, and Theilhaber, K., Nuclear Fusion, 24 (1984) 1383

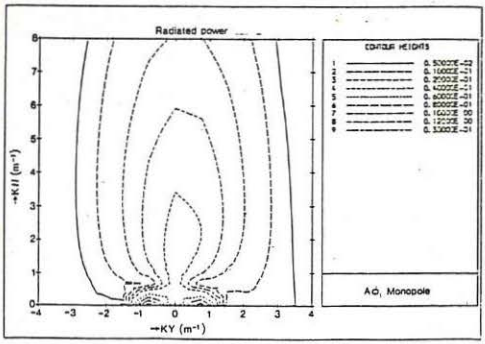

Fig. 1 The spectral density of the real part of the radiated power for a typical plasma (3.4T, He_3 minority, f = 33 MHz)

Fig. 2 Coupling resistance vs the propagation constant. The range of experimental values is indicated by shaded regions. The antenna limiter distance is 5.5 cm.

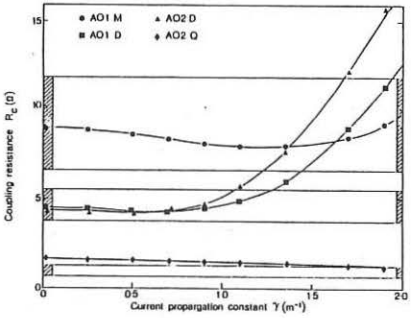

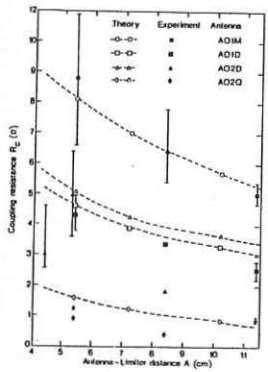

Fig. 3 Coupling resistance vs antenna to limiter distance.

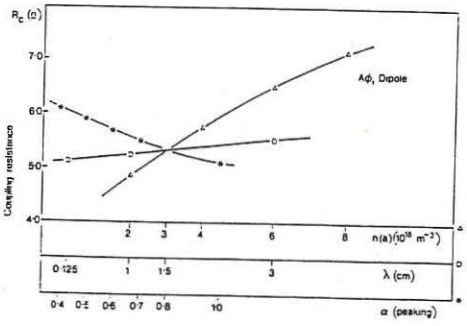

Fig. 4 Effect on coupling resistance of variations of the density at the limiter n(a), S.O.L. e-folding length γ and peaking factor α.

THE ROLE OF THE FARADAY SCREEN IN ICRF ANTENNAE:
Comparison of an optically open and optically closed screen in ASDEX

J.-M. Noterdaeme, R. Ryter*, M. Söll,
J. Bäumler, G. Becker, H.S. Bosch, M. Brambilla, F. Braun, H. Brocken,
A. Eberhagen, R. Fritsch, G. Fussmann, O. Gehre, J. Gernhardt, G. v.Gierke,
E. Glock, O. Gruber, G. Haas, J. Hofmann, F. Hofmeister, A. Izvozchikov[1],
G. Janeschitz, F. Karger, M. Keilhacker [2], O. Klüber, M. Kornherr,
K. Lackner, M. Lenoci[3], G. Lisitano, E. v.Mark, F. Mast, H.M. Mayer,
K. McCormick, D. Meisel, V. Mertens, E.R. Müller[2], H. Murmann,
H. Niedermeyer, A. Pietrzyk[4], W. Poschenrieder, S. Puri, H. Rapp,
H. Riedler, H. Röhr, J. Roth, F. Schneider, C. Setzensack, G. Siller,
P. Smeulders[2], F. Söldner, E. Speth, K. Steinmetz, K.-H. Steuer,
O. Vollmer, F. Wagner, F. Wesner, H. Wedler, D. Zasche

Max-Planck-Institut für Plasmaphysik,
D-8046 Garching, FRG

INTRODUCTION

A Faraday screen has been used on RF antennae since the first days of heating experiments with ICRF waves. Its use on the C-stellarator /1,2/ brought major improvements in the heating efficiency of the plasma. In subsequent heating experiments on other machines the beneficial effect of a Faraday screen, after initial trials without it, was rediscovered on TFR /3/, DIVA /4/ and ERASMUS /5/. Consequently the Faraday screen has become a mandatory component of ICRF antennae, and it has been attributed different functions. To fulfill those functions the screen has become increasingly complicated, and in the next generation of experiments, where the screen has to be cooled, a new round of complexity is added. Can the screen be simplified, and are some of its attributed functions really needed. Those questions were the basis for an experiment on ASDEX.

FUNCTIONS OF THE FARADAY SCREEN

They can be divided in three categories.

A first function is the protection of the antenna against the plasma: the screen should protect the antenna from particles and radiation from the plasma, in order to avoid parasitic loading of the antenna and to increase its voltage stand off. When a ceramic casing covers the antenna, the Faraday screen prevents the metallisation of the ceramic which could occur if Ti gettering is used.

A second function concerns the protection of the plasma: the Faraday screen should act as its name indicates and keep unwanted electric field components away from the plasma. The structure of the screen is chosen so as to allow the fast wave to go through but to short out electric fields along the magnetic field. The Faraday screen also may have a role in suppressing coaxial modes /6/.

A third function, which will not be further discussed is changing the electrical characteristic of the antenna: in order to minimise the voltage

---

[1]Academy of Sciences, Leningrad, USSR; [2]Assigned to JET Joint Undertaking, England; [3]ENEA Frascati, Italy; [4]University of Washington, Seattle, USA; *CEN Grenoble, France

on the transmission line, and to avoid as much as possible currents in the radial direction /7/, the electrical length of the antenna is adapted, by influencing the distributed capacitance, so that a current node appears at the feeding point. The Faraday shield is one component through which the distributed capacitance can be influenced.

ASDEX EXPERIMENT WITH OPEN SCREEN

In ASDEX two ICRH antennae are installed, 180° apart in the torus, on the low field side (Fig. 1). Each antenna is connected to 1.5 MW generator and consists of two /4 loops, fed top and bottom, and short circuited at the midplane (Fig. 2). One of the antennae was covered with an optically open Faraday screen (Fig. 3a), the other one with an optically closed screen (Fig. 3b). Over a large parameter range (300 kW $\leq P_{rf} \leq$ 1200 kW, $\bar{n} = 1.25 - 3.5 \times 10^{19}$ m^{-3}) a systematic comparison was made by firing the antennae alternately in successive shots. The experiments were performed at the second harmonic of hydrogen (67 MHz, 2.2 T) with uncarbonised and later with carbonised walls.

Concerning the first role of the screen (protection of the antenna) we found that we had no voltage stand off problem. The generator was pushed to its maximum power, and a voltage of 12 kV on the antenna was reached. Under some conditions of bad coupling higher voltages (15.5 kV) were reached, but a voltage limit would be encountered in the transmission line. Therefore we cannot say whether or not opening up the screen has changed the voltage standoff capabilities of the antenna voltages above this value. Two points would indicate that there are no problems with plasma getting into the antenna. We found no additional arcing traces on the central conductors after two month of operation, and there is no power dependence of the loading of the antenna. This is to be compared with limiter machines (TFR /3/, TEXTOR /8/) with an antenna crossing the resonance layer which have shown that a closed type Faraday screen is necessary.

The second role of the Faraday screen (protecting the plasma) seems to be sufficiently accomplished by an open type Faraday screen. In earlier experiments, without and with a Faraday screen on DIVA /4/large differences were seen on the plasma parameters. We however see no major systematic difference on the plasma centrum. Curves of β, radiated power, soft X-ray radiation are similar for both antennae. No difference is seen on the flux of fast H^0 /9/. Central electron temperature curves are identical to the point of having the same sawtooth amplitude and frequency (Fig. 4)
The density is feedback controlled but there is a difference in the initial rate of increase of the density at the start of the ICRH. Values of 5 x 10^{20} m^{-3}/s at 900 kW and $n_e = 3.5 \times 10^{19}$ m^{-3} are found for the open screen antenna as compared with 8 x 10^{20} m^{-3}/s for the closed screen antenna. Occasionally, for the antenna with the closed screen this could lead to a different density evolution with larger impurity radiation and impurity lines (Fe XVI). The reason for this is unclear but could be related to the fact that the optically closed screen (originally coated with TiC) was already longer in the machine and may have become contaminated with Fe.

One domain where we have found a systematic difference is on the flux of neutral D particles from the edge. Those fluxes appear and disappear rapidly as the RF is turned off (τ=1-3 ms) showing that these ions are badly confined. A toroidal scan method already used for LH /10/ shows that they are accelerated near the plasma edge. It appears that the fluxes due

to the open screen antenna are much larger than those due to closed screen antenna. It has to be noticed that the actual tail begins for energies higher than 4 keV. For lower energy values the fluxes almost do not depend on ICRH (Fig. 6). Inverted sawteeth are clearly visible on the charge exchange signals: at low energies ($\lesssim 3$ keV) for both antennae, at high energies ($\gtrsim 3$ keV) only for the open screen antenna. The sawtooth modulation is correlated with the H_α/D_α light emitted by the plasma edge and is an effect of neutral density modification. The fact that the high energy channels are modulated only with the open screen antenna indicates, either that the fast ions are further outside the plasma for this antenna or that the mechanism which produces the fast ions for the open screen antenna is sensitive to plasma edge modifictaions.

The following points are further important in analysing the results: The analyser is toroidaly located between both antennae, the plasma current and toroidal magnetic field are parallel, and in the co-direction for the beams. The gas valve is close to open screen antenna. The particles received by the analyser are mostly bananas with large $v_\perp/v_{th}$ ratio and the geometry is such that they cannot be seen just after their acceleration in front of the open screen antenna. Other measurements have shown that the D^o fluxes are very sensitive to the magnetic field and that they can have large fluctuations during one shot, which do not seem to be correlated to any macroscopic parameter of the plasma. There is no indication that the measured D^o fluxes have a direct correlation with the impurity production, but it is clear, that they depend on the plasma capability to absorb the wave /11/.

In conclusion, these fast D^o tail could depend on the kind of Faraday shield used, but in the case of normal absorption of the wave in the plasma, they are only a parasitic effect without consequence on the plasma heating and impurity production.

SUMMARY

We can conclude from our experiment that in our geometry (divertor, antenna not crossing the resonance layer), the function of the Faraday screen as a shield against the plasma is not necessary.
In its function as a shield for the plasma against the unwanted fields from the antenna an open Faraday screen seems to be sufficient. We see no difference on the central plasma parameters and the boundary effect does not seem to be detrimental. We therefore believe that the Faraday shield can be simplified. However, many open questions still remain in this boundary domain between antenna and plasma.

/1/ M.A. Rothman et al., Plasma Physics (J.of Nucl.En., C) 8 (1966) 241
/2/ M.A. Rothman et al., Phys. Fluids 12 (1969) 2211
/3/ J.Jacquinot et al.,Int.Conf.on Plasma Physics, Nagoya 1980, Vol.2, 226
/4/ K. Odajima et al., Nucl. Fusion 20 (1980) 1330
/5/ V.P. Bhatnagar et al., Heat. in Tor. Plasma, Varenna 1978, Vol. 1, 133
/6/ A.M. Messiaen et al., Heat. in Tor. Plasmas, Rome 1984, Vol. 1, 315
/7/ A.M. Messiaen et al., Heat.in Tor.Plasmas, Grenoble 1982, Vol. 1, 243
/8/ R.R. Weynants et al., Radio Frequency Plasma Heating, Callaway Gardens 1985, 40 and private communication
/9/ F. Ryter et al., this conference
/10/ F. Ryter et al., Application of RF Waves to Tokamak Plasmas, Varenna 1985, Vol. 2, 746
/11/ G. Janeschitz et al., this conference

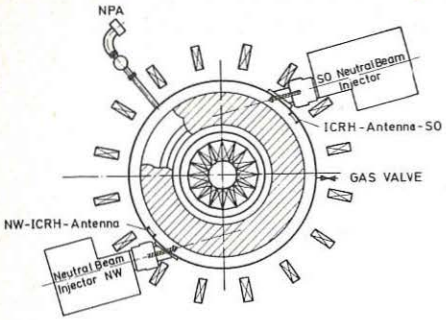

Fig.1: Horizontal cut through ASDEX, indicating the position of the NB-Injectors, the antennae, the neutral particle analyser and the gas valve.

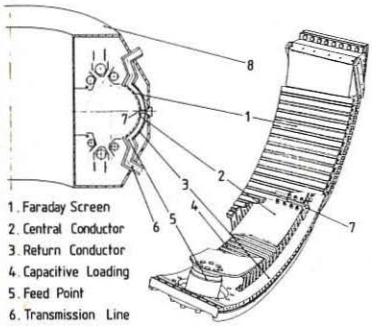

Fig. 2: Geometry of the ASDEX antenna.

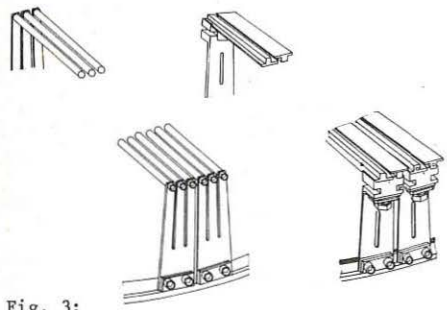

Fig. 3:
a) Optically open screen (SO Antenna)
b) Optically closed screen (NW Antenna).

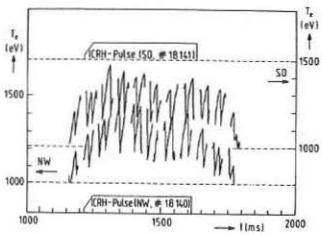

Fig. 4: Central electron temperature evolution. Note: Suppressed null line and its relative displacement for both antennae.

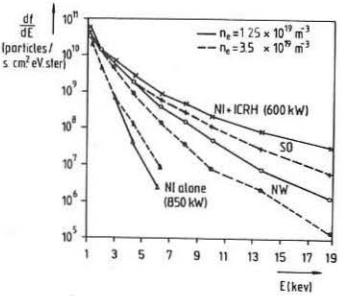

Fig. 5: Flux of D^0 at the edge.

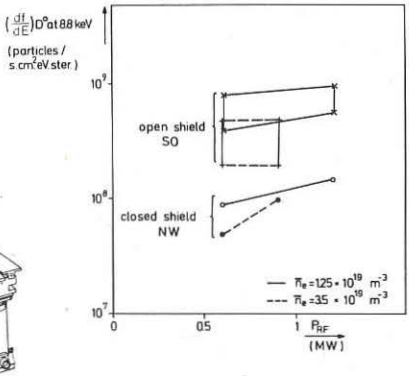

Fig. 6: Dependence of the flux D^0 on power and density. For the open shield the modulation due to sawteeth is shown.

ICRH COUPLING IN DIII-D*

D. J. Hoffman, F. W. Baity, W. E. Bryan, E. F. Jaeger, and T. L. Owens,†
Oak Ridge National Laboratory, Oak Ridge, Tennessee, U.S.A.

D. B. Remsen, J. Luxon, and J. M. Rawls,
GA Technologies, Inc., San Diego, California, U.S.A.

I. INTRODUCTION. A 9-MW ion cyclotron resonant frequency (ICRF) experiment has been proposed to heat the Doublet III-D (DIII-D) plasma. DIII-D is a 2.2-T, 3.5-MA tokamak at GA Technologies with a major radius of 1.67 m and minor radius of 67 cm (elongation ~ 2). The device was recommissioned in early 1986. The initial experimental program includes ohmic plasma and neutral beam studies; high-power rf experiments will follow in later years. Compact loop antennas (which fit completely in a 35- by 50-cm port) have been chosen to convey this power because of their inherent ease of maintenance, high efficiency, and versatility. In order to verify that the antenna will have sufficient loading, a prototype low-power (2-MW) antenna has been designed and installed. Measurements will be made through September 1986. The antenna is a cavity antenna that will operate from approximately 30 to 80 MHz with a 50-Ω match for a load resistance of ~1 Ω. It is surrounded by a fixed graphite-covered frame and can be extended from 3 cm behind this frame to 2 cm in front. This can be used to adjust coupling to the plasma. The electrical, mechanical, and thermal characteristics of this antenna system (and its extrapolation to ignited tokamaks) are discussed. In addition to experimental exploration of coupling, we have investigated wave propagation and absorption in DIII-D by using a cold collisional plasma model in straight tokamak geometry with rotation transform. Loading and power deposition profiles as a function of frequency, density, and species mix are presented.

II. MECHANICAL DESCRIPTION. The antenna for DIII-D is in the cavity configuration (Fig. 1). The main current strap is held by a ground plane at one end and by a vacuum variable capacitor at the other end. The capacitor and strap inductance determine the antenna frequency. At some distance up the current strap, power is fed to the structure. The input impedance is determined by the feed point. The Faraday shield is bolted onto the face of the antenna structure. The antenna is designed to be movable relative to the plasma. Motion of the whole assembly is accomplished by bellows and a remotely controlled drive-motor mechanism shown in Fig. 1. An I-beam frame (not shown in Fig. 1), mounted on the vacuum side of the port, supports the antenna. Both external and vacuum bearings are made of graphalloy—a bronze-impregnated graphite material.

A fundamental problem to the mechanical integrity of the antenna is the thermal/mechanical characteristics of the Faraday shield (Fig. 2). In order to minimize plasma impurities, the Faraday shield, which is composed of 1-cm-diam Inconel rods, is coated with 1.5 mm of graphite on the plasma side; copper plating is used on the antenna side to minimize rf losses. The equivalent disruption pressure at 5 MA is 6 atm (radially inward). At 6 atm, the rods are subject to stresses that are 80% of yield stress (140 ksi) at 1000°F. A finite-element stress analysis of the antenna shows that the rest of the antenna structure has stresses below 11 ksi; consequently, stainless steel is used for the remainder.

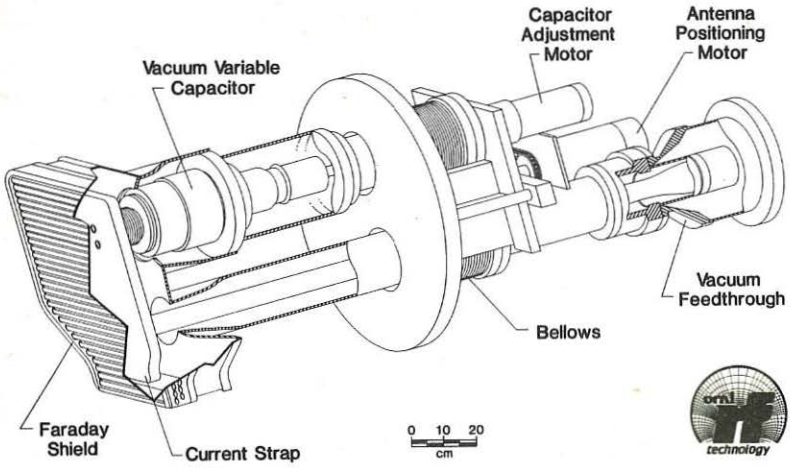

Fig. 1. The cavity antenna designed for DIII-D.

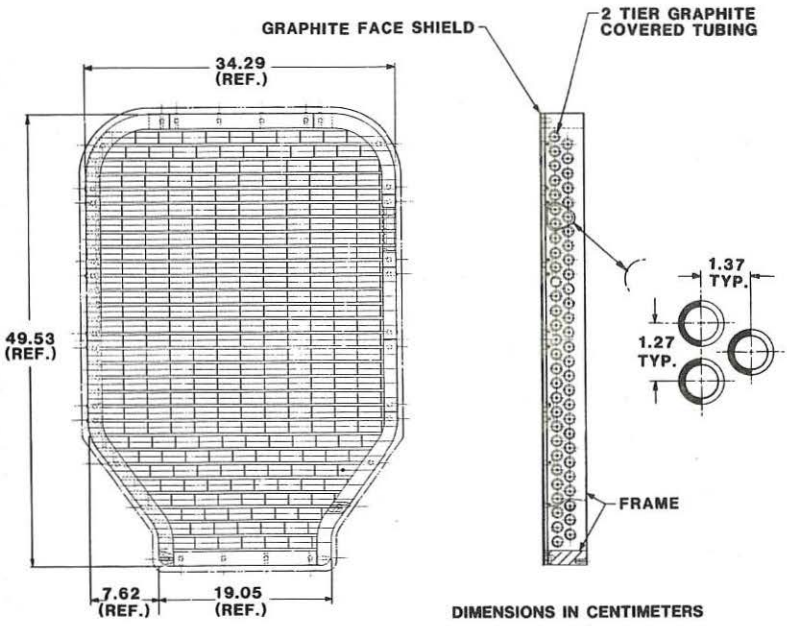

Fig. 2. The Faraday shield configuration for the cavity antenna.

The thermal loads for the exploratory antenna are completely due to the plasma. A total of ~80 W/cm^2 is deposited on the shield for 3 s every 4 min. With radiative cooling only, the graphite heats to 330°C after ten shots, which is 500°C below the braze temperature. When operated at 2 MW, some active cooling is probably required. An actively cooled Faraday shield has been designed and fabricated for use on the Radio-Frequency Test Facility.

The vacuum feedthrough for the cavity antenna is basically the same as the ORNL feedthrough used on TEXTOR. The feedthrough is also illustrated in Fig. 1. The major change is that this feedthrough was designed to bolt to a standard 9 3/16-in. coaxial transmission line. On the vacuum side, the coax has an outer diameter of 4 1/2 in. because there is not enough room for anything larger.

III. ELECTRICAL CHARACTERISTICS. In order to assess power limits, power losses, and plasma coupling, it is necessary to describe the unloaded characteristics of the antenna. The resonant frequency and input impedance are given by

$$f = \frac{1}{2\pi\sqrt{LC}} , \tag{1}$$

$$Z = \frac{\alpha^2 L}{Cr} , \tag{2}$$

where L and C are antenna inductance and capacitance, α is the feed point, and r is the load. The capacitance (including stray) can be varied from 38 to 474 pF. The apparent total inductance ranges from 130 nH at 20 MHz to 115 nH at 74 MHz. This yields a useful frequency range of 20 to 74 MHz.

Measurements, with and without Faraday shields, show that the structure has an equivalent 25 mΩ of load and the shield has 0.1 Ω at 20 MHz. When the apparent decrease of inductance is included, the losses scale as $\sqrt{f}$. Of the 25 mΩ in the structure, approximately 20 mΩ is attributable to the capacitor. While the capacitor clearly needs to be cooled for high-power operation, the body of the antenna does not. If plasma loading is on the order of 1 to 3 Ω, then up to 10% of the rf power will go to the Faraday shield. Therefore, the shield for the high-power version will be cooled.

The power capacity of the antenna depends on the voltage and current limits of the capacitor. An improved, high-current capacitor has been designed and will be tested. However, for 3-s pulses, the power will be limited by the maximum voltage that the capacitor can withstand. Including the decrease of inductance of the current strap and assuming 48-kV peak, the maximum operating power is 1.7 MW/Ω at 30 MHz, 1.0 MW/Ω at 50 MHz, and 0.72 MW/Ω at 70 MHz. Since loading is expected to be 1 to 3 Ω (per 40 cm of current strap), the antenna is nominally a 2-MW antenna.

IV. LOADING CALCULATIONS. As previously discussed, the amount of loading determines power limits and cooling requirements. The antenna design is centered around a 1- to 3-Ω load in the 30- to 50-MHz range. Calculations of coupling in DIII-D were made to support the design point. The method of calculation is as follows.

Global solutions for the ICRF wave fields in a straight tokamak with rotational transform are calculated in the cold plasma limit. The component of the wave field parallel to **B** is assumed

zero. Symmetry allows Fourier decomposition in the toroidal coordinate, and the resulting set of two coupled, two-dimensional partial differential equations is solved by the method of finite difference. Energy absorption and antenna impedance are calculated using a simple collisional absorption model. Resonance can be observed. For the small transforms of DIII-D, only heating at the two-ion hybrid resonance is observed.

The calculations were based on the following parameters: $B_0 \sim 2.2$ T, $n_{central} \sim 3 \times 10^{13}$ cm^{-3}, $n_{edge} \sim 10^{12}$ cm^{-3}, $f \sim 30$ MHz, $R \sim 2.2$ m, $a_p \sim 0.67$ m, and potential antenna extent of 40 cm. The majority of power absorption is seen between the two-ion hybrid resonance and the fundamental resonance. The electric fields on the plasma peak in this region. For some cases, where the resonance is near the edge of the plasma, coax modes dominate with high edge fields. Antenna loading is weakly dependent on species mix, central density, frequency, and magnetic field. However, a variation in edge density from 1 to 6 $\times$ 10^{12} cm^{-2} showed a threefold increase in loading (Fig. 3). Since the antenna can move relative to the plasma, the role of edge plasma in coupling can be explored without perturbing other plasma parameters.

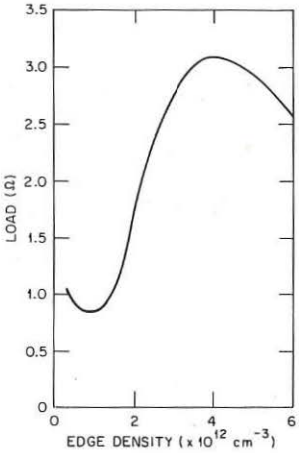

Fig. 3. Coupling for a 40-cm antenna in DIII-D. Central density = 3 $\times$ 10^{13} cm^{-3}, B_0 = 2.2 T, $f \sim$ 30 MHz.

V. SUMMARY. A cavity antenna has been installed on DIII-D to explore coupling. The antenna was designed to operate at 1 to 3 Ω. Calculations show this to be the expected load. Measurements of the coupling will be made first to verify this and then to determine power limits, antenna dissipation, and the efficiency of the antenna.

---

*Research sponsored by the Office of Fusion Energy, U.S. Department of Energy, under Contract No. DE-AC05-85OR21400 with Martin Marietta Energy Systems, Inc., and under Subcontract 54Y-72665 with McDonnell Douglas Astronautics Company.

†McDonnell Douglas Astronautics Company, St. Louis, Missouri, U.S.A.

A FOLDED WAVEGUIDE CAVITY COUPLER FOR ICRF HEATING*

T. L. Owens†

McDonnell Douglas Astronautics Company, St. Louis, Missouri, U.S.A.

I. INTRODUCTION

This paper introduces a new type of waveguide coupler for ion cyclotron range of frequencies (ICRF) heating which is an adaptation of a concept known as a "folded waveguide" reported by Barrow and Schaevitz[1] in connection with low-frequency waveguide transmission systems. The basic idea involves "folding" a simple rectangular waveguide to form a more compact structure as shown in Fig. 1. Cutoff for the folded waveguide occurs when one-half of a free-space wavelength equals the path length around the "folds" of the structure. By adding a large number of folds, the path length around the folds can be made large, leading to very low cutoff frequencies relative to those for simple rectangular waveguides having comparable outside dimensions. Folded waveguide couplers are practical for frequencies as low as 60 MHz for some ports found on present-day experiments.

A polarizing plate is placed at the mouth of the coupler as shown schematically in Fig. 1. The polarizing plate contains rectangular openings at every other fold of the structure. Its purpose is to short out $E_\parallel$ at the mouth of the coupler and to produce unidirectional fields, $E_\perp$ and $H_\parallel$, which are the fields of the fast-magnetosonic wave. A shorting plate is placed at the back of the coupler a distance of approximately one-half of a guide wavelength from the mouth of the coupler. This ensures that the electric field of the wave in the coupling apertures will be small while the $H_\parallel$ field will be near a maximum. Since the plasma surface impedance ($E_\perp/H_\parallel$) is low, a good match to the plasma surface fields will result from this scheme in addition to maintenance of low electric fields within the coupling apertures.

By operating the coupler well above its cutoff frequency (~1.8 times the cutoff frequency to minimize losses to walls), the guide wavelength becomes small enough that reasonably short structures (1-3 m) result.

Fig. 2 shows a variation of the simple folded waveguide coupler in which the internal vanes are tapered between the middle of the cavity and the mouth of the structure. The apertures can thereby be enlarged to nearly fill the entire port. For a constant total power, this has the effect of reducing the power flux at the plasma/coupler interface by nearly one-half of that found for the simple folded waveguide coupler. In addition, the tapered folded waveguide will launch a poloidal mode spectrum which has less power in high poloidal mode numbers at the plasma surface. This should improve penetration of power into the interior of the plasma. A disadvantage of the tapered folded waveguide coupler is that more energy is contained in high-order cavity modes, which are cut off. This will lower the unloaded Q of the cavity and produce somewhat higher peak voltages internal to the cavity compared to the simple folded waveguide coupler.

II. THEORY

A theory for the folded waveguide coupler which yields approximate solutions for the fields within the cavity in the presence of plasma is presented in Ref. 2. More precise 3-D finite element calculations have also been initiated. Preliminary results are presented in Ref. 3. In the approximate calculation in Ref. 2, the folded waveguide is analyzed as an equivalent "unfolded" waveguide with inductive irises at the mouth of the structure to model the shorting diaphrams at the mouth of the

folded waveguide coupler. The region outside the coupler is modeled as a completely enclosed aperture coupled cavity. Fields are calculated assuming perfectly conducting walls. Power absorbed by the plasma is estimated from

$$P = \frac{Z_p}{2} \int_s \int H_\parallel^2 \, ds \, ,$$

where Z_p is an appropriate plasma surface impedance and the integral is evaluated over the plasma surface. An eigenvalue equation is derived by equating complex Poynting flux across the mouth of the coupler.

Using the above procedure theoretical estimates of coupling efficiency and power handling potential can be made. Table 1 summarizes the various quantities of interest for a folded waveguide suitable for use on the Tore Supra tokamak in Cadarache, France. It is found that extremely low electric fields can be maintained at the critical plasma/coupler interface (less than 3.4 kV/cm). Peak voltages occur well back into the coupler where higher electric fields can be tolerated. Coupling efficiencies are quite high (up to 98%) for the examples given. It appears that for a Tore Supra-sized port, folded waveguide couplers are practical even at frequencies of 60 MHz or less, although properties improve as frequency is increased, as seen by comparing the 120-MHz example in Table 1 to the 60-MHz example.

A Faraday shield is not believed to be necessary for shielding electrostatic fields at the coupler mouth nor for heat shielding the inner parts of the structure. A shield may, however, be useful for particle shielding (including photon shielding) to reduce the possibility of breakdown within the coupler.

III. FREE-SPACE TESTS

Cold tests on a small-scale folded waveguide have been performed to verify the predicted free-space field pattern within the structure and to test possible impedance matching schemes.

An example of one of these experimental measurements is shown in Fig. 3. Plotted in the figure is the direction (3a) and magnitude (3b) of the wave magnetic field at the mouth of a simple folded waveguide coupler. Roughly, a half-sine dependence of field is found along the path through the folds of the structure, analogous to the structure of the TE_{01} mode in an equivalent unfolded rectangular waveguide. The frequency of the lowest order mode agrees quite closely with theoretical estimates. Fields at the back of the coupler are equal to those at the mouth of the coupler, indicative of a mode above cutoff rather than evanescent fields.

Full-scale tests of a high-power version of the folded waveguide coupler will be performed on the Radio Frequency Test Facility (RFTF) at the Oak Ridge National Laboratory. These tests will provide some experimental information on folded waveguide coupling to a magnetized plasma.

REFERENCES

[1]W. L. Barrow and H. Schaevitz, AIEE Trans. 60, 119 (March 1941).

[2]T. L. Owens, "A Folded Waveguide Coupler for Plasma Heating in the Ion Cyclotron Range of Frequencies," submitted to IEEE Transactions on Plasma Science.

[3]G. L. Chen, J. H. Whealton, F. W. Baity, and T. L. Owens, "A 3-D Analysis of Arbitrarily Shaped ICRF Antennas and Faraday Shields," Poster No. 17, April 14, 1986, this conference.

*Research sponsored by the Office of Fusion Energy, U.S. Department of Energy, under Contract No. DE-AC05-84OR21400 with Martin Marietta Energy Systems, Inc. and under Subcontract 53Y-72665 with McDonnell Douglas Astronautics Company.

†Currently assigned to the Oak Ridge National Laboratory, Building 9201-2, MS-2, P. O. Box Y, Oak Ridge, TN 37831, U.S.A.

Table 1. Tore Supra folded waveguide coupler parameters at 10 MW of input power and 10-cm plasma/coupler separation (60 cm × 70 cm OD, $Zp = 50\ \Omega$)

	120-MHz coupler (four folds)	60-MHz coupler (eight folds)
Electric field in coupling apertures, kV/cm	3.4	1.9
Peak electric field, kV/cm	31	51
Distance from coupler mouth to field peak, cm	72	145
Plasma loaded quality factor	480	1320
Unloaded quality factor	23,440	9770
Coupling efficiency, %	98	88
Coupler length, cm	144.7	291.45

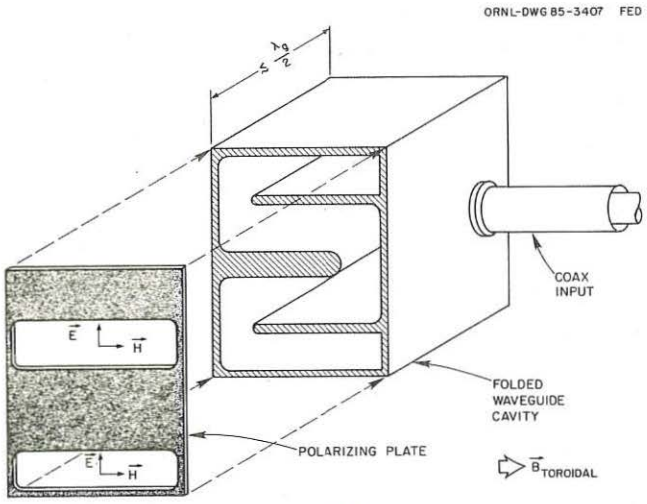

Fig. 1. Standard folded-waveguide coupler.

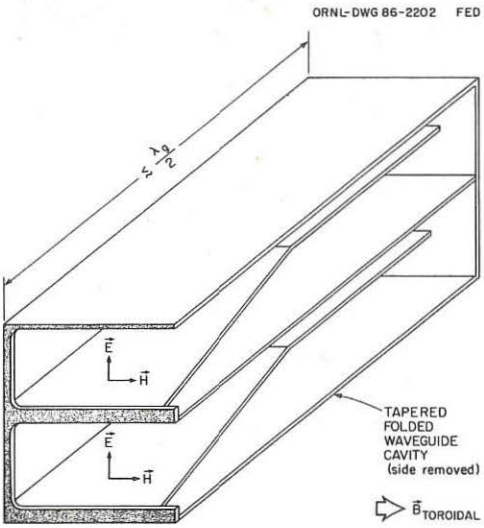

Fig. 2. Tapered folded-waveguide coupler.

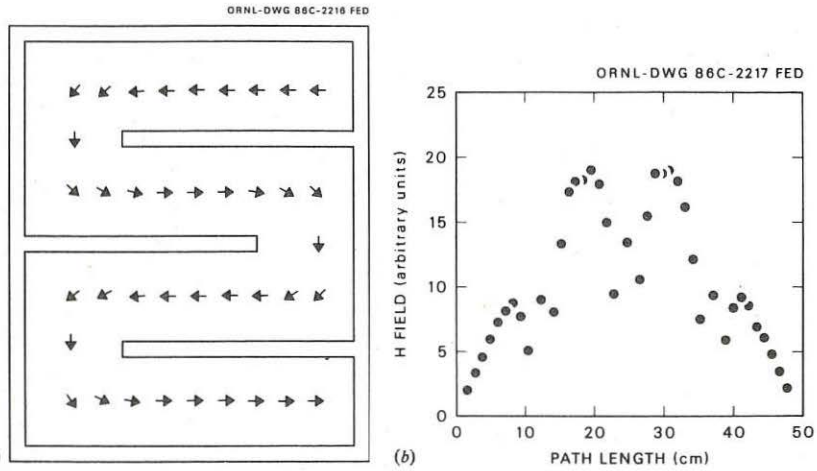

Fig. 3. Measured wave magnetic field at the mouth of a small-scale folded-waveguide model versus position around the folds of the structure. (a) field direction; (b) field magnitude.

VARIATIONAL THEORY APPLIED TO MULTIPOLE AND TO RESONANT ICRH ANTENNAE.

BANNELIER P.

Association Eur-Cea sur la Fusion Contrôlée CEN-FAR BP6 92260 Fontenay-aux-roses France.

I Introduction

Numerous designs of ICRH antennae have been proposed for present and future tokamaks, differing mainly in the number and relative disposition of the conductors and feeders. A realistic calculation of the expected coupling with plasma is necesary to guide the conception, taking into account the possibility of shaping the radiated spectrum by proper choice of current phasing.
A variational principle previously introduced by K.Theilaber /1/ is applied to multipole loop antennae, allowing for arbitrary current phase and amplitude in the feeders.
As an application, we consider a symmetrical resonant antenna such as proposed by Oak Ridge National Laboratory /2/, in which the matching is performed inside the antenna by capacitive elements.The variational principle yields the currents and voltages, the coupling with plasma as well as the values of the capacitors.
Finally we present numerical results for a double resonant antenna proposed for the Tore Supra tokamak. The design is shown to be restricted to a limited range of frequencies.The possibility of arbitrary phasing between the conductors is discussed and spectra are presented for various phasings.

II The Variational Principle

We consider a slab geometry : The toroidal magnetic field is in the Oz direction (no poloidal component), the radial density gradient in the Ox direcion.Effect of the plasma is introduced by the spectral admittance at the edge of plasma :

$$Yp(ky,kz)=Hz(ky,kz)/Ey(ky,kz)$$

Yp(ky,kz) is calculated by integrating from the center of the plasma the coupled equations for Ey(ky,kz) and Hz(ky,kz) for the fast magnetosonic wave in the total radiation limit (i.e. strong absorption). Yp is in general symmetrical regarding kz but not regarding ky.
We consider a loop antenna enclosed by infinite metallic limiters in the Oy and Oz directions and by a Faraday shield acting as a perfect polarizer in the Ox direction.
Let us call $\vec{J}$ and $\vec{K}$ two solutions for the currents flowing in the conductors of the antenna and Ji and Ki the corresponding currents flowing in the feeder n°i.
The variational principle reads /1/:

$$\Sigma_i \; Z_i \; J_i \; K_i = - \int\int_{(S)} \vec{E}(\vec{J}) \; . \; \vec{K} \; ds \qquad (II.1)$$

where $\vec{E}(\vec{J})$ is the electric field induced by $\vec{J}$ and (S) the surface of the inner conductors in the antenna.
Minimization of this integral equation regarding $\vec{K}$ yields the impedances Zi at each feeder and the physical current $\vec{J}$.
The antenna we consider here is plotted on Fig.1 with the geometric dimensions retained for Tore Supra. Note that this compact antenna does not exceed the size of the 60x70 cm port. The calculation can be extended to antenna with any number of conductors and feeding pattern.
We perfom the mode analysis of the fields in the box constituted by the limiters, the return conductor and the Faraday shield. Retaining N modes in the Oy direction and M modes in the Oz direction,

$$Jy(y,z) = \sum_{nm} Jy_{nm} \; f_n(y) \; g_m(z) \qquad Jx(y,z) = \sum_{nm} Jx_{nm} \; f'_n(y) \; g_m(z) \qquad (II.2)$$

where $f_n(y)=\cos \frac{n\pi}{2ly}(ly+y)$ $\quad f'_n(y)=\sin \frac{n\pi}{2ly}(ly+y)$ $\quad g_m(z)=\sin \frac{m\pi}{2lz}(lz+z)$

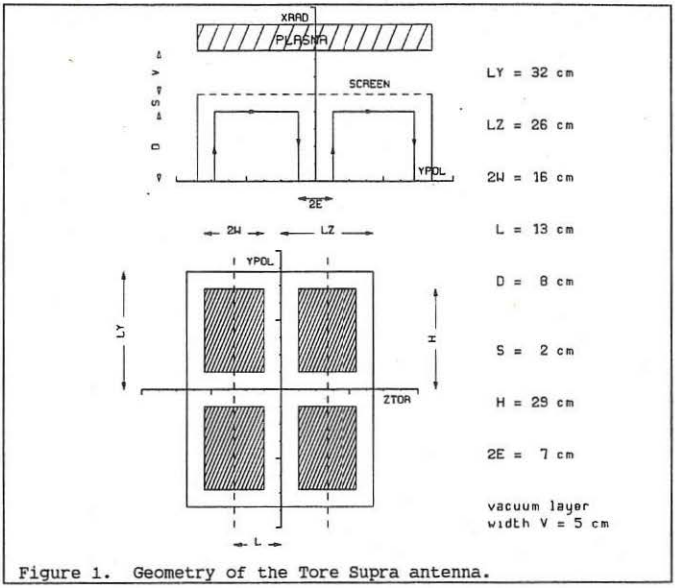

Figure 1. Geometry of the Tore Supra antenna.

Continuity of the currents at the connexions writes :

$$Jx(y,z)=2\,Jy(-h,z)\,\delta(y+h)-2\,Jy(-e,z)\,\delta(y+e)+2\,Jy(e,z)\,\delta(y-e)+2\,Jy(h,z)\,\delta(y-h)$$

so that vector $\underline{Jx}$ can be expressed as a function of $\underline{Jy}$ and J_i as $J_i = \underline{P}_i . \underline{Jy}$.
The variational formula expressed in terms of $\underline{Jy}$ is :

$$\Sigma_i \; Z_i \; (\underline{P}_i . \underline{Jy}) . (\underline{P}_i . \underline{Ky}) = \underline{Ky} \; . \; \underline{\underline{L}} \; . \; \underline{Jy} \qquad \text{(II.3)}$$

We impose the z-dependence of the current distribution :

$$Jy(y,z) = \sum_{n=1}^{N} \left(a_n \; h_1(z) + a_{n+N} \; h_2(z) \right) f_n(y) \qquad \text{(II.4)}$$

where h1(z) and h2(z) are defined on Fig 2. In case of arbitrary number of conductors, care must be taken that the functions hi are orthogonal.

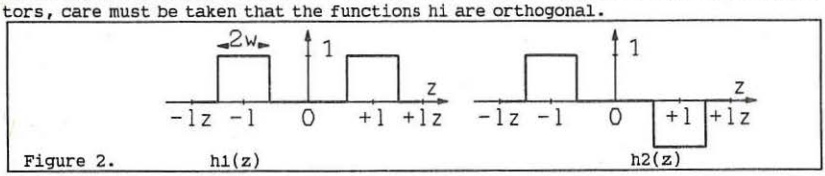

Figure 2.

Finally, the variational principle reads :

$$\Sigma_i \; Z_i \; (\underline{Q}_i . \underline{a}) . (\underline{Q}_i . \underline{b}) = \underline{b} \; . \; \underline{\underline{L}}' \; . \; \underline{a} \qquad \text{(II.5)}$$

where $\underline{a}$ and $\underline{b}$ are 2*N dimensions vectors.

If at several of the connexions the impedance Zi is imposed (for example by a short-circuit or a stub), it can be written :

$$\Sigma_{\text{unknown}} \; Z_i \; (\underline{Q}_i . \underline{a}) . (\underline{Q}_i . \underline{b}) = \underline{b} \; . \; \underline{\underline{L}}'' \; . \; \underline{a} \quad \text{with} \quad \underline{\underline{L}}'' = \underline{\underline{L}}' - \Sigma_{\text{imposed}} \; Z_i \; \underline{Q}_i * \underline{Q}_i \qquad \text{(II.6)}$$

Minimization yields a system of I equations where I is the number of connexions where the impedance is to be determined.

$$\Sigma_{j=1}^{N} C_{ij} (\underline{Q}_j \cdot \underline{a}) Z_j = \underline{Q}_i \cdot \underline{a} \qquad \text{with } C_{ij} = \underline{Q}_i \cdot \underline{\underline{L}}^{-1} \cdot \underline{Q}_j \quad (II.7)$$

Recalling that $\underline{Q}_i \cdot \underline{a}$ is the current in the feeder n°i, it is seen that, for any multipole antenna, it is sufficient to impose the currents in the I feeders to determine the impedances by solving the system which turns out to be linear.

III Resonant antennae

We consider a resonant antenna such as proposed by Oak Ridge National Laboratory for Tore Supra/3/. It is constituted by two identical half antennae, each one fed at the center point by one generator of impedance Z_0. Matching with the generator is realized by adjusting variable capacitors connected at both ends of each antenna (Fig.3).

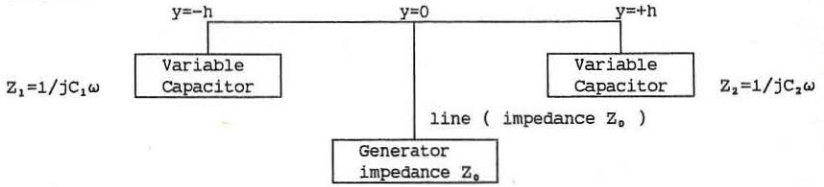

Figure 3. Connecting scheme for one half-antenna.

The geometrical dimensions are indicated Fig.1. Note that the feeding point is approximated by a double current layer instead of a coaxial line in the real design. We impose the impedance to be Z_0 at the feeding points using formula II.6 and state the four unknown impedances insuring matching are purely imaginary. To control accurately the radiated spectrum, we impose the currents at the point $y=\frac{1}{2}(h+e)$ on each half-antenna which yields two equations of same type as II.7.

The resulting system is generally non-linear regarding the four unknown impedances. When the amplitudes of the currents are equal and the phasing 0° or 180°, the values of the capacitors are the same for each half-antenna and are the roots of a mere 2nd-order equation. Results are presented for 0° phasing for the 37 to 80 Mhz frequency range planned for Tore Supra. Plasma is deuterium except at 80 Mhz (helium). Magnetic field is 3.6T(37MHz), 4.2T(43MHz), 3.7T(57MHz), 4.1T(63MHz) ,4.5T(69MHz), 4.5T(69MHz), 3.9T(80MHz) according to the different heating scenarii(Fig.4).

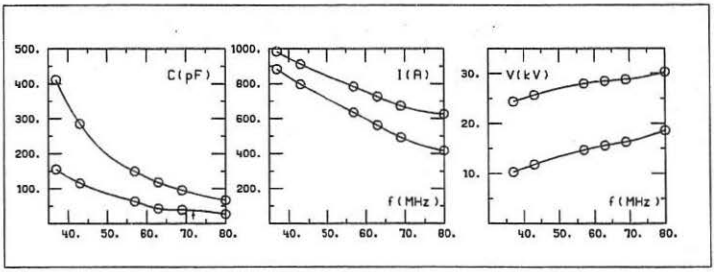

Figure 4. Values of capacitors Currents Voltages
Parabolic density profile from $10^{13}cm^{-3}$ to $8\ 10^{13}cm^{-3}$.
Minor plasma radius 80cm. Major radius 238 cm.
N=20 modes in the Oy direction, M=7 modes in the Oz direction.
Power coupled to plasma normalized to 2 MW for the whole antenna.

Fig.5 shows the current profile at 63 MHz. The design is limited to frequencies where the matching impedances are capacitive which puts an upper limit on frequency.

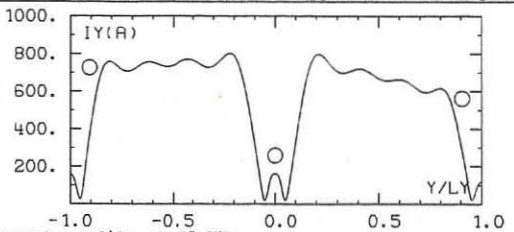

Figure 5. Poloidal current profile at 63 MHz.

This defines the capacitors range necessary for a given coupling with plasma, here 411-67 pF on one side and 155-27 pF on the other for 37 to 80 MHz operation. If the coupling with plasma is decreased, these ranges tend to become more symmetrical. For example, in case of out of phase operation (180° phasing), they become respectively 367-71 and 195-34 pF and without plasma and 0° phasing they are nearly the same (210-35 pF).

For arbitrary currents in each half-antenna, we solve numerically the non-linear system II.7 by a Newton-type method. Starting from 0° or 180° and equal amplitude where we know an exact solution, we change step by step the phasing or the amplitude until reaching the given values.

Let us consider case with currents of equal amplitude and increase the phasing from 0° between antenna n°1 and 2. Due to the mutual coupling, the lineic resistance drops in antenna 2 until the matching is no more possible for a maximum phasing φmax. At 63 MHz, φmax is about 67° for same plasma conditions as above.Appoaching this value, the generator feeding antenna n°2 furnishes almost no power and the matching capacitors have almost the same value (75 pF instead of 48 and 146 pF at each end of conductor n°1).

Still increasing phasing, matching becomes again possible for a phasing greater than φmin=126° at 63 MHz. The range of accessible phasings gets larger when coupling increases. A solution to avoid this limitation would be to separate by a conducting wall the two half-antennae. Spectra of the real part of the impedance as a function of toroidal wavenumber are presented at 63 MHz for 0°,180° and 65°(Fig.6).

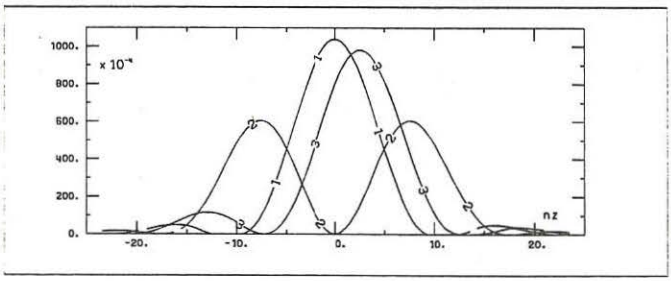

Figure 6. Real part of impedance vs toroidal wavenumber (f=63 MHz).
Curve n°1 : 0° Curve n°2 : 180° Curve n°3 : 65°
Integrated power normalized to 1 W.

References :/1/THEILABER,K., Nuclear Fusion **24** (1984) 1383
/2/OWENS,T.L.,BEATY,F.W.,HOFFMAN,D.J.,Radio Frequency Heating
AIP Conference Proceedings **129** (1985) 95
/3/BECRAFT,W.R.,and al. This Conference

NEW HIGH POWER TETRODES FOR ICRH APPLICATIONS

P. GERLACH - G. SIRE - J.P. ICHAC

THOMSON-CSF Division Tubes Electroniques
38 rue Vauthier - BP 305, 92102 BOULOGNE BILLANCOURT CEDEX - FRANCE

After earlier successful achievements at TFR (France) and Heliotron E (Japan) in ICRH applications, Thomson-CSF Electron Tubes Division has been recently selected to supply a new type of tetrode - the TH 525 - for JET (EURATOM, UK), and complete ICRH amplifiers for Toresupra (France).
These two projects are both typical of the new requirements from physicists working in plasma heating which have appeared during recent years. They show a trend towards increased unit power operating over longer pulses at higher frequencies. The problems, well known to manufacturers of gridded power tubes, which are inherent to such applications become more and more difficult to overcome.
This paper describes the techniques which have been developped at Thomson-CSF to meet these challenges and presents the performances of the new tetrodes that the mastery gained through years of experience in these techniques has allowed to develop.

TECHNOLOGICAL CHALLENGES AND SOLUTIONS

Anode Dissipation

Whatever the design precautions, there is always in ICRH systems a possibility to have temporary overloads or high SWR, and in such a case the anode dissipation increases very rapidly. An efficient liquid-vapor phase cooling technique has been introduced by Thomson-CSF under the name Hypervapotron which has been tested over 2 kW per square centimeter ; but in tubes cooling design, it is used usually far below this limit - say up to 1 kW per square centimeter - allowing a large safety margin. This same technique has also been applied at JET for the cooling of the limiters and beam dumps.

Pyrolytic Graphite Grids

Once the anode dissipation problem solved, the limitations in high power gridded tubes were transfered to the grids ; conventional mesh type grids suffer of the presence of thermal and secondary emission, poor mechanical rigidity at high temperature, lack of dimensional stability in temperature cyclings. The remarkable properties of pyrolytic graphite make it nearly the ideal material to cope with these drawbacks which are still enhanced in tetrodes intended for ICRH applications. Thomson-CSF has developped a technology to manufacture Pyrobloc grids, which are the grids made of this anisotropic crystallized carbon obtained by decomposition of a gazeous hydrocarbon at high temperature and vacuum deposition on a carbon mandrel. Thermal emission of these grids is reduced by the combined effects of a low and constant resistivity in plane (ab) parallel to the plane of deposition and an excellent thermal conductivity in this (ab) plane, resulting in a lower grid temperature. This second property also helps reducing grid deformation as heat transfer to tube terminals is improved.

RF losses are also higher when operating frequency increases, constituting a severe challenge as they lead to an important increase of inner tube temperature which is the source of possible outgassing. This outgassing and the vapor pressure inside the tube vary exponentially with temperature which is an increasing function of the ratio $\sqrt{\rho}/\varepsilon$ where ρ is the resistivity of the material and ε its emissivity ; this ratio is considerably better with Pyrobloc grids, as shown on table 1 below. Another important factor when RF losses are considered is the Q factor, linked to grid material resistivity : this resistivity, as shown on figure 1 is decreasing when temperature increases while that of other materials increase : in hot conditions, the Q factor is of the same order of magnitude for all materials including pyrolytic graphite. Short overloads are also made possible to withstand with these grids due to the material chemical stability at high temperatures without outgassing and the higher resistance to thermal shocks.
Another decisive advantage of the Pyrobloc grids in achieving the larger diameters required for high power as well as the reduced inner interelectrode spacing necessary for high gain is the stability of their diameters due to a negligible thermal expansion factor in the (ab) plane (figure 2). Mechanical strength of this material, improving when temperature increases, and low weight helping a higher resistance to mechanical shocks, are also contributing to the performances of these grids. Furthermore, they come in one piece where mesh, cap and supporting base form a continuous structure without any mechanical assembly or welding point, this enhancing the reliability of the tubes using these grids. More than twenty years experience in designing Pyrobloc grids mounted in tubes operating in large quantities and various types in TV and radio broadcasting as well as in scientific and industrial application worldwide have given Thomson-CSF full expertise in producing them. After having tested through the years several manufacturing processes, Thomson-CSF has selected those offering optimal reproducibility and reliablity the latter being evidenced by recent tests on the screen grid of TH 518, the very same tube already used in ICRH experiments on TFR/France and Heliotron E/Japan : this screen grid rated at 9 kilowatts dissipation was tested at 40 kilowatts dissipation during several minutes without any damage to the tube. It is worth mentioning that the broadcasting version of this TH 518 tetrode, called TH 558 and used in many sockets has been and is operating in a specific design involving a peak dissipation of 64 kilowatts during one microsecond.

Cathode Design

The experience accumulated over the years in producing high power gridded tubes has led Thomson-CSF to select this "cage" type design as the most suitable one for the thoriated tungsten wire cathode used in these tubes. An in-house development of a special manufacturing process has allowed a perfect reproducibility of the cathodes and regularity of their geometry : welding of each cross-over point of the cathode is individually computer-controlled. This process ensures a long and reliable cathode life, already experienced for years in radiobroadcasting applications.

New Developments

A new tetrodes family has been developped to match the latest ICRH requirements. The use of Hypervapotron cooling has allowed a 1.5 MW maximum anode dissipation on the tube TH 525 which shall be operated by JET. Its Pyrobloc grids, as well as the cathode, have been derived from those already field tested for years in radiobroadcasting with the 1 MW AM carrier tetrode TH 539.

The main parameters and the present test status of this new tube are given in table 2 below. The Toresupra project which involves higher operating frequencies - up to 120 MHz - has required to develop another type, the TH 526. This tetrode is very similar in structure to the TH 525, with slightly shorter electrodes allowing operation at this higher frequency. Table 3 below shows the main parameters and the present test status of this TH 526.
The test results mentionned in tables 2 and 3 have been obtained in the Thonon plant of Thomson-CSF where a complete test facility has been installed allowing full development and testing of the tetrodes matching the present and future ICRH requirements. This test facility includes a 5 MW power supply, and a test load for more than 2 MW dissipation capability.
Some of the other tetrodes presently available for ICRH requirements, including the TH 535 which is used as a driver for tubes TH 525 or TH 526, have their main parameters shown on table 4 below.

Circuit Design and Stability Considerations

As gridded tubes dimension become larger to cope with increased power requirements, unwanted circular modes are more likely to occur in the tubes coaxial structure. A special device built inside the Thomson-CSF tubes prohibits the occurence of the fundamental mode TE11. In many applications in open space, the radiation impedance is sufficient to dampen the upper modes. In other ICRH or TV applications the tube is inside a closed resonant cavity circuit which shields this impedance. The strong interaction between the tube and the external circuit on which it is mounted is such that a close cooperation between the amplifier designer and the tube manufacturer is necessary to solve the resulting problems. Thomson-CSF long experience in designing cavities for UHF and VHF TV applications as well as for high power scientific projects, which led to special patented waveguides loading adequately the unwanted frequencies without affecting the operating frequency in coaxial mode, offers an expertise which ranges from the tube design to the corresponding matched circuit. This expertise allows Thomson-CSF either to supply the amplifier with the tube or to assist outside amplifier manufacturers in the most efficient design using the tube. Each of these two situations is encountered with the JET and TORESUPRA projects. The TH 525 shall be used in existing amplifier systems which shall be modified by their designer, HERFURTH GMBH in order to fit this new tube and to attain the increased power of 2 MW per unit instead of the original 1.5 MW only. A positive cooperation is taking place between Thomson-CSF and HERFURTH engineers.
In the case of TORESUPRA, THOMSON-CSF shall supply the 6 complete amplifiers, including each the tetrodes of the 3 stages - TH 526, TH 535 and TH 561 - with their associated coaxial cavities -TH 18525, TH 18535 and TH 18561- operating in grounded grid configuration. Test loads able to dissipate 2 MW in long pulses within the 30-80 MHz frequency range, as well as at 120 MHz with only a small mechanical modification, shall also be supplied by Thomson-CSF.
It is worth to note that the TH 18525 cavity which shall be supplied to TORESUPRA is able to operate at full performance with either TH 525 or TH 526 tubes. A cavity of this type has already been implemented in the test facility presently in service.

CONCLUSION

As the scientific community involved in fusion programs requiring ICRH thinks that the present trend towards higher performance tetrodes able to withstand higher power during longer pulses is likely to continue in the years to come, Thomson-CSF is preparing to develop the next generation of tubes with up to 5 MW target useful RF power. The experience gained in completing the development of TH 525 and TH 526 is a new important step towards this aim.

Material	Resistivity ρ (Ωcm/cm^2)	Total Emissivity ε	$\frac{\sqrt{\rho}}{\varepsilon}$
Pyro	200.10^{-6}	0.9	0.016
W	40.10^{-6}	0.19	0.033
Ta	62.10^{-6}	0.19	0.041
Pt	60.10^{-6}	0.15	0.052

TABLE 1

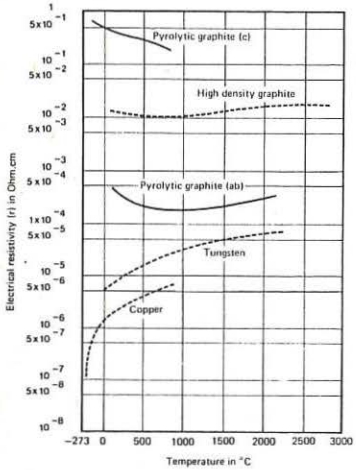

FIGURE 1

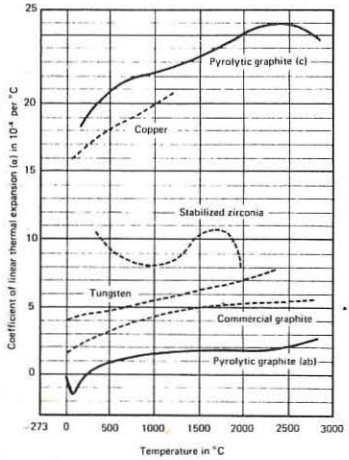

FIGURE 2

TH 525	Max. Ratings	JET operating conditions	Present Test Status
Plate Dissipation (MW)	1.5		1.6
Screen Grid Dissipation (kW)	12		25
Control Grid Dissipation (kW)	4.5		5.5
Plate Voltage (kV)	30	23.7	
Plate Current (A)	180	121	
Screen Grid Voltage (V)	2000	1700	
Control Grid Voltage (V)	−1000	− 450	
POWER OUTPUT (MW)	2.5	2*	2.2
DRIVE POWER REQUIREMENT (kW)	100	<100	
PULSE LENGTH (Sec.)	30	20	50
FREQUENCY (MHz)	90	23 · 57	55
Max. Frequency (MHz)	100		

* SWR≤1.5

TABLE 2

TH 526	Max. Ratings	TORESUPRA operating conditions	Present Test Status
Plate Dissipation (MW)	1.2		1.3
Screen Grid Dissipation (kW)	12		25
Control Grid Dissipation (kW)	4		4.5
Plate Voltage (kV)	27	24 | 18	
Plate Current (A)	150	115 | 120	
Screen Grid Voltage (V)	2000	1750	
Control Grid Voltage (V)	−800	−350	
POWER OUTPUT (on matched load) (MW)	2 | 1.5	2* | 1.4*	2 | 1.8
DRIVE POWER REQUIREMENT (kW)	70 | 60	70 | 60	
PULSE LENGTH (Sec.)	210	210	40 | 90
FREQUENCY (MHz)	80 | 120	80 | 120	55
Max. Frequency (MHz)	130		

* SWR ≤ 1.5

TABLE 3

	TH 535	TH 519	TH 518
Plate Dissipation (kW)	100	700	1200
Screen Grid Dissipation (kW)	0.7	6	9
Control Grid Dissipation (kW)	0.3	2	3
Plate Voltage (kV)	20	18	20
Plate Current (A)	25	70	105
Screen Grid Voltage (V)	1500	1500	1500
Control Grid Voltage (V)	−600	−450	−450
POWER OUTPUT (kW)	100	1000	1500
DRIVE POWER REQUIREMENT (kW)	5	60	90
PULSE LENGTH (Sec.)	cw	30	210
FREQUENCY (MHz)	150	120	60
Max. Frequency (MHz)	300	130	110

TABLE 4

ICRF HEATING TECHNOLOGY DEVELOPMENT ACTIVITIES AT OAK RIDGE NATIONAL LABORATORY*

F. W. Baity, W. E. Bryan, D. J. Hoffman, D. E. Schechter, Oak Ridge National Laboratory, Oak Ridge, Tennessee, U.S.A., and T. L. Owens, McDonnell Douglas Astronautics Company, St. Louis, Missouri, U.S.A.

I. INTRODUCTION. The rf technology program at the Oak Ridge National Laboratory (ORNL) is developing the components needed for heating in the ion cyclotron range of frequencies (ICRF) on future fusion machines, such as the Compact Ignition Tokamak. Components produced in this program are already in use on experiments throughout the world, including Doublet III-D (DIII-D), TMX-U, Alcator-C, and TEXTOR. Designs have been developed for implementation on Tore Supra and ASDEX. Recent developments in vacuum feedthroughs, compact loop antennas, high-current capacitors, and folded waveguides are discussed in this paper.

II. VACUUM FEEDTHROUGHS. The first product of the ORNL rf technology program was the 50-Ω vacuum feedthrough with a cylindrical ceramic. This feedthrough has now received field testing under a variety of operating conditions as a result of its immediate application at several laboratories. Attractive features of this basic design include high voltage and current capability, a demountable ceramic assembly, cooling passages for steady-state operation, low insertion voltage standing-wave ratio, and wide frequency bandwidth.

Figure 1 is a schematic drawing of the feedthrough built for TEXTOR. This design, equipped with 200-mm conflat flanges at both ends, is used at two locations in the coaxial

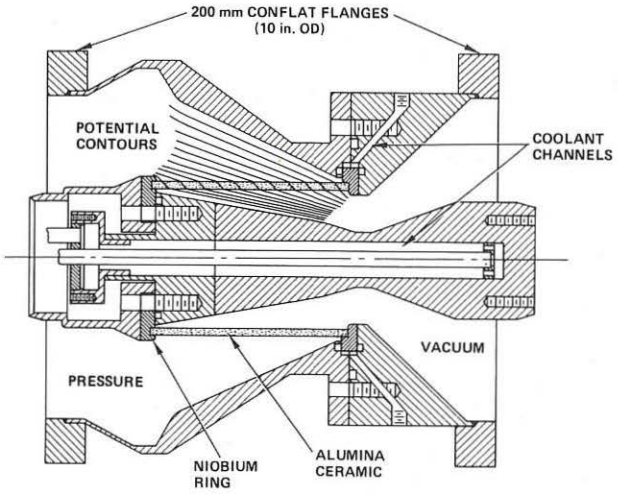

Fig. 1. 50-Ω long-pulse rf feedthrough designed to TEXTOR specifications.

transmission line: near the antenna, with vacuum on both sides of the feedthrough, and at a second position farther from the antenna, operated with nitrogen pressurization on one side. Two versions of this feedthrough were constructed: one with niobium end caps for the ceramic and one with copper end caps. Figure 1 shows the ceramic with the niobium end caps. The niobium proved to be superior in voltage rating, reaching peak voltages greater than 150 kV for 100-ms pulses, but the braze joint could not be made reliably and was somewhat fragile. For subsequent versions of this feedthrough, a tapered copper-to-ceramic braze was used. In both cases, the braze alloy used was Ticusil, and no metalizing of the 96% alumina ceramic was done. For this design, the ultimate voltage rating depends on the pressurization since breakdown always occurs on the pressurized side. For the case of the copper end caps, nickel and gold platings were applied and tested for effects on voltage breakdown, with some improvement. Table 1 summarizes the voltage breakdown limits for the various cases.

Table 1. Feedthrough Voltage Standoff in Kilovolts
(All tests at 25 MHz, 5 s; peak voltage)

Pressure, gauge (atm)	Material brazed to ceramic		
	Niobium	Copper	Nickel
0 (N_2)	80	34	42
1 (N_2)	92	40	57
2 (N_2)		48	75
0 (SF_6)		60	75
1 (SF_6)		80	>88

A prototype 25-Ω feedthrough has been fabricated for ASDEX. This feedthrough incorporates a buffer vacuum between the machine vacuum and the pressurized transmission line. The structure maintains the external dimensions of existing ASDEX feedthroughs. A schematic diagram is shown in Fig. 2. The ceramic is brazed to the hourglass outer conductor. The inner conductor is sealed to the ends of the ceramic cylinder by means of Helicoflex seals. This design should possess greater mechanical strength than the 50-Ω design. A potential disadvantage is that the ceramic cannot be as easily replaced as in the 50-Ω feedthrough in case of a failure in the braze joint.

III. COMPACT LOOP ANTENNAS. A low-power prototype cavity antenna has been installed on DIII-D.[1] The primary purpose of this antenna is to measure plasma loading for a wide range of plasma conditions and frequencies and to compare the results with calculations by GA Technologies and ORNL. The antenna can be moved radially over a small range. The antenna has a Faraday shield consisting of two layers of copper-plated Inconel rods with 1.5-mm-thick graphite plates brazed to the rods on the plasma side. Extensive thermal and stress analysis calculations were performed for this antenna to verify the survivability of the design under the worst-case tokamak conditions, such as major disruptions. The results of this analysis are applicable to other large tokamaks, providing a useful base for other compact loop designs, including Tore Supra. Because the prototype antenna will only operate at low power

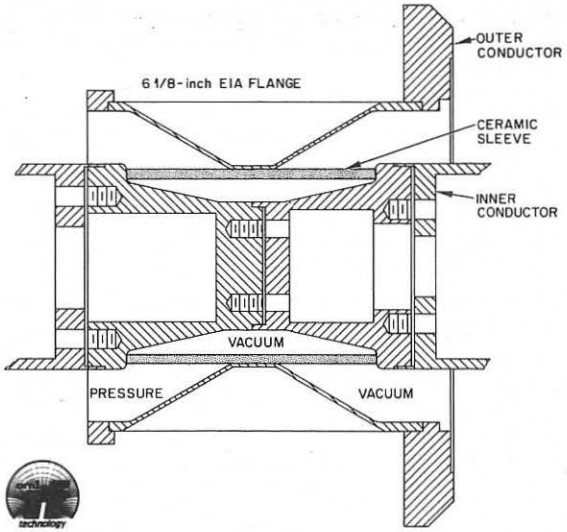

Fig. 2. 25-Ω rf feedthrough designed to ASDEX specifications.

during the first year of DIII-D experiments, inertial cooling was determined to be adequate, and active cooling will not be used.

A development version of a high-power DIII-D cavity antenna is under construction for use in the Radio-Frequency Test Facility at ORNL. It will be operated during the second half of 1986 when the 1.5-MW transmitter becomes operational. This antenna was designed for easy modification so that new antenna components can be easily tested at high power in a plasma environment.

A preliminary engineering design has been done for a resonant double loop (RDL) antenna[2,3] system for Tore Supra. This design consists of two RDL antennas side by side behind a common Faraday shield. The entire structure is mounted in a large port and can be moved radially to couple to plasmas with different minor radii. The antenna incorporates water cooling, allowing operation for 30-s and 210-s plasma pulse lengths. With improved vacuum variable capacitor design, it appears possible to couple 2 MW per loop over the frequency range 35 to 80 MHz.

IV. HIGH-CURRENT CAPACITORS. A key to the success of compact loop antennas in coupling several megawatts of power to a fusion plasma is the development of a vacuum variable capacitor with higher current capacity (~1 kA) than commercially available units. In addition, the internal inductance of the capacitor must be minimized to allow operation at frequencies up to 80 MHz and possibly higher. An improved design was devised based on postmortem analysis of an existing design. The capacitor industry was approached with this new applica-

tion, with the result that both Comet (Bern, Switzerland) and Jennings (San Jose, California, U.S.A.) have agreed to build prototype units which will be tested at full parameters on a test stand at ORNL during 1986.

V. FOLDED WAVEGUIDES. A new waveguide configuration, known as the folded waveguide,[4,5] is a promising candidate for ICRF heating on large, high-field machines where second harmonic heating occurs at frequencies on the order of 100 MHz. The folded waveguide can easily be configured to conform to existing port sizes, which are usually larger in the poloidal dimension than in the toroidal dimension for most tokamaks. An advantage of the folded waveguide over ridged waveguide designs is that the rf electric fields at the mouth of the guide are near a minimum.

The folded waveguide can be envisioned as a rectangular waveguide several times wider than its height which is folded accordion-style several times. The cutoff frequency can be made arbitrarily low for a given envelope by increasing the number of folds. The magnetic field at the mouth of the guide reverses at each fold, so the guide is fitted with an aperture plate to permit only the desired polarization to couple to the plasma.

Measurements on a low-power scale model have confirmed the basic operation of the folded waveguide. Three-dimensional code calculations are in progress.[6]

VI. SUMMARY. Compact loop antennas have been installed on DIII-D and designed for Tore Supra. Two keys to the successful high-power operation of compact loops, enhanced vacuum variable capacitors and low-impedance feedthroughs, are under development. For higher frequency applications ($f > 100$ MHz), the folded waveguide, which offers several advantages over ridged waveguides, is under investigation.

REFERENCES

1. D. J. Hoffman, F. W. Baity, W. E. Bryan, E. F. Jaeger, and T. L. Owens, "ICRH Coupling in DIII-D," Poster No. 27, April 14, 1986, this conference.
2. T. L. Owens, F. W. Baity, and D. J. Hoffman, "ICRF Antenna and Feedthrough Development at the Oak Ridge National Laboratory," *Radiofrequency Plasma Heating: AIP Conf. Proc.* 129, 95–98 (1985).
3. W. R. Becraft, J. Adam, P. Bannelier, F. W. Baity, W. E. Bryan, D. J. Hoffman, and T. L. Owens, "Compact Loop Launcher Design Study for Tore Supra," Poster No. 51, April 14, 1986, this conference.
4. T. L. Owens, "A Folded Waveguide Coupler for Plasma Heating in the Ion Cyclotron Range of Frequencies," submitted to *IEEE Transactions on Plasma Science.*
5. T. L. Owens and G. L. Chen, "The Folded Waveguide Coupler for Plasma Heating in the Ion Cyclotron Range of Frequencies," Poster No. 28, April 14, 1986, this conference.
6. G. L. Chen, J. H. Whealton, D. J. Hoffman, F. W. Baity, and T. L. Owens, "A 3-D Analysis of Arbitrarily Shaped ICRF Antennas and Faraday Shields," Poster No. 17, April 14, 1986, this conference.

---

*Research sponsored by the Office of Fusion Energy, U.S. Department of Energy, under Contract No. DE-AC05-84OR21400 with Martin Marietta Energy Systems, Inc., and under Subcontract 53Y-72665 with McDonnell Douglas Astronautics Company.

COMPACT LOOP LAUNCHER DESIGN STUDY FOR TORE SUPRA

W. R. Becraft
Grumman Aerospace Corporation, Oak Ridge, Tennessee, U.S.A.
J. Adam, P. Bannelier
Centre d'Etudes Nucléaires de Cadarache, St. Paul lez Durance, France
F. W. Baity, W. E. Bryan, D. J. Hoffman
Oak Ridge National Laboratory,* Oak Ridge, Tennessee, U.S.A.
T. L. Owens
McDonnell Douglas Astronautics Company, Oak Ridge, Tennessee, U.S.A.

1. Introduction

A compact antenna is being considered as an alternative to conventional long loop launchers for waves in the ion cyclotron range of frequencies (ICRF) on Tore Supra. A pair of resonant double-loop RDL antennas[1] can be mounted entirely within one of the large horizontal ports. With the expected antenna loading ~6 Ωm, it should be possible to couple the full power (2 MW) of one of the rf power generators through each of the two loops.

A preliminary engineering design of a compact loop launcher for Tore Supra has been completed. The design incorporates active cooling so that the launcher can withstand the nearly steady-state energy flux during the 30 s pulse length of plasma operation. The advantages of the compact loop are threefold: the antenna is easily installed or removed, the antenna can be moved relative to the plasma edge to modify the plasma loading, and there is no need for external matching circuitry. Three such launchers are being considered and would be able to transmit the total (12 MW) power of the six generators. The characteristics of the antenna have been chosen to allow minority heating of deuterium plasmas containing a few percent of H or ^{3}He between 3.5T and 4.5T and for harmonic cyclotron heating of pure ^{3}He at 4T.

Major machine parameters for Tore Supra are listed in Table 1.

Table 1
Tore Supra Machine Parameters

Magnetic field on axis	4.5 T
Major radius	2.38 m
Minor radius	0.8 m
Pulse length	30 s (210 s)
Repetition rate	Every 4 min (10 min)
ICRF port size	60 cm × 70 cm

2. Design Requirements

Each ICRF loop for Tore Supra is required to handle 2 MW for 30 s every 4 min or for 210 s every 10 min over the frequency range from 35 to 80 MHz. Two such loops will be mounted through a single large port on the horizontal midplane. The antenna must be impedance matched to a 30 Ω transmission line. The structure must be able to withstand disruption loads resulting from a rate of change in the magnetic field of 50 T/s.

The entire structure must be designed for radial translation in order to provide good power coupling through a wide range of plasma sizes and positions. The minimum acceptable radial translation is 8 cm. The design goal is 30 cm.

The RDL has several advantages over conventional loops. The capacitors provide both tuning and impedance matching, thus allowing operation over a wide frequency range with no hardware changes. The efficiency is improved by minimizing the high-current path length. The requirements on the feedthrough are reduced because the transmission line is matched at the feedthrough. No high voltages appear in the pressurized transmission line. Finally, the entire antenna structure fits in a port on the machine, facilitating installation and removal.

The Faraday shield of the antenna must be compatible with water cooling. The inlet temperature is 170°C and the inlet pressure is 38 bar, with an 8-bar pressure differential. Other parts of the antenna structure requiring water cooling can use 30°C inlet water temperature at a pressure of 8 bar. The entire structure should be bakeable to 200°C without water cooling.

The materials for the parts of the antenna structure exposed to the plasma are restricted to graphite, stainless steel, or Inconel (in limited quantity).

Maximum expected environmental parameters are as follows. The magnetic field strength in the vicinity of the antenna will be 3.5 T. The neutron flux will not exceed 4×10^{11} (neutrons/cm^2)/s. The particle flux will not exceed 1×10^{19} (particles/cm^2)/s.

3. Design Mechanical Description

The design selected for study at ORNL consists of two asymmetrically fed RDLs, each incorporating two vacuum variable capacitors of advanced design. Figure 1 shows a schematic drawing of the antenna with the mounting flange for the Tore Supra port. The antenna radiating element is supported at each end by the capacitors and in the middle by the coaxial transmission line. The two loops are located side by side in the toroidal direction. Both loops are enclosed in a rectangular box, which is supported by bearings mounted to the sides of the Tore Supra port. A single Faraday shield covers the front of the box. Bellows attached to the port cover provide 30 cm of radial movement of the entire structure. A 30-Ω vacuum feedthrough is attached to the coax from each loop. Each of the capacitors and the antenna position can be adjusted dynamically by remote control. The antenna specifications are summarized in Table 2.

Table 2
Tore Supra RDL Specifications

Length of radiating element	60 cm
Width of radiating element	16.5 cm
Gap between Faraday shield and radiating element	2 cm
Faraday shield type	2 tiers of round tubes
Faraday shield materials	Graphite-coated Inconel
Total inductance	155 nH
Minimum capacitance	40 pF
Maximum capacitance	400 pF
Maximum peak voltage	45 kV
Maximum rms current at 37 MHz (80 MHz)	900 A (750 A)

4. Electrical Design Calculations

The goal for the Tore Supra antenna is 2 MW power operation over the entire frequency range of 35 to 80 MHz with realistic capacitor values. Figure 2 shows the capacitance values needed to tune the antenna and to match the input impedance to 30 Ω as a function of plasma loading resistance for two frequencies: 37 and 80 MHz. The antenna parameters used are those of Table 2. The range of loading resistance shown for each frequency is approximately what is expected based on theoretical calculations of ICRF heating for Tore Supra plasma conditions. The load can be controlled somewhat by adjusting the distance between the plasma and the Faraday shield. The range of capacitance required (40-400 pf) appears reasonable based on existing designs. High-current capacitors are being developed by Comet (Bern, Switzerland) and Jennings (San Jose, U.S.A.) and will be tested at ORNL this year. Based on the specifications supplied by Comet, the maximum power which the antenna can deliver as a function of loading resistance is shown in Figure 3. The curve for 37 MHz is determined by the 900 A rms current limitation for all values of resistance shown. At 80 MHz the maximum voltage limit of 45 kV peak is reached for loads below 3.5 Ω; the maximum current of 750 A rms becomes the limiting parameter for higher loads. The design power level of 2 MW requires 2.5 Ω of loading at 37 MHz and 3.7 Ω at 80 MHz; these values lie in the expected range calculated by ICRF theory.

The calculations shown in Figures 2 and 3 were made assuming the antenna to consist of lumped circuit elements; no correction was made for the variation of the current distribution along the finite length of the antenna radiating element. Calculations of launched wave interactions with the Tore Supra plasma using realistic antenna geometry are addressed by Bannelier[2] at this conference.

5. Summary

A compact ICRF antenna has been designed for Tore Supra. The antenna consists of two RDLs side by side, mounted inside a large midplane port. The antenna structure can be moved radially for operation with plasmas of different minor radius. With upgraded vacuum variable capacitors, the goal of 2 MW per loop over the frequency range from 35 to 80 MHz appears attainable, based on expected plasma loading for Tore Supra conditions.

Reference

[1]T. L. Owens, F. W. Baity, and D. J. Hoffman, "ICRF Antenna and Feedthrough Development at the Oak Ridge National Laboratory," Radiofrequency Plasma Heating: AIP Conf. Proc. 129, 95-98 (1985).

[2]P. Bannelier, ICRF Paper at this conference.

*Operated by Martin Marietta Energy Systems, Inc., under Contract No. DE-AC05-84OR21400 for the U.S. Department of Energy, Office of Fusion Energy.

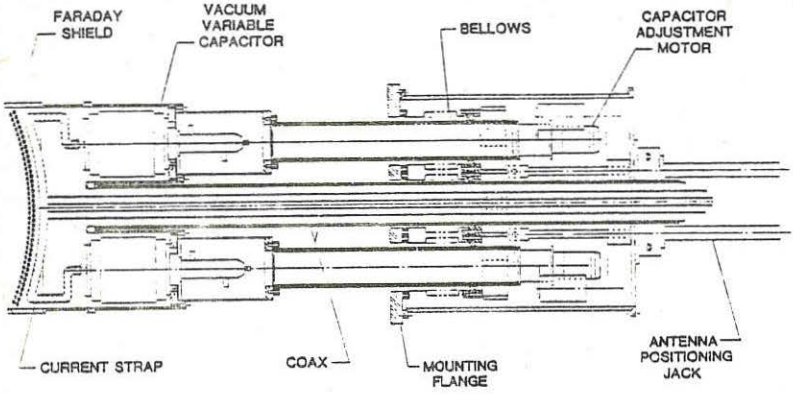

Fig. 1 RESONANT DOUBLE LOOP ANTENNA
(Tore Supra Concept)

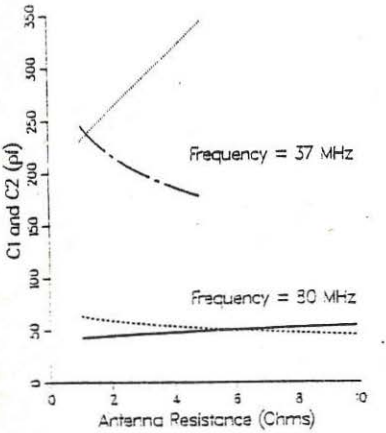

Figure 2. Capacitance values required to match the Tore Supra antenna to 10 ohms as a function of the loading resistance at 37 and 80 MHz. Other antenna parameters are given in Table 2.

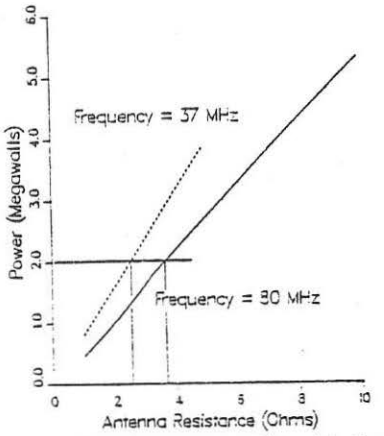

Figure 3. The maximum power capabilities of the Tore Supra antenna as a function of loading resistance at 37 and 80 Mhz. The power limit is determined by the maximum voltage and current specified for a developement capacitor from Comet.

COMPARISON BETWEEN H AND He^3 MINORITY ICRF HEATING EXPERIMENTS IN JET

V.P. Bhatnagar*, S. Corti, J.J. Ellis, J. Jacquinot, P.P. Lallia, F. Sand

JET Joint Undertaking, Abingdon, Oxon, OX14 3EA, UK
* From LPP-ERM/KMS; EUR-EB Association, 1040 Brussels, Belgium

Introduction

In the ion-cyclotron resonance heating (ICRH) experiments in JET, the RF energy is coupled to the plasma via the cold-plasma fast magnetasonic waves which are generated by exciting ICRH antennae located on the low-field side of the takamak. In the minority species heating scheme, the minority ion (e.g. H^+ or ^3He in deuterium plasma) concentration $\eta = Nj/ND$ ($j = H^+$ or ^3He) is required to be below a certain critical concentration η_c [1] for a given k//, minority temperature and plasma density. For $\eta > \eta_c$, significant mode conversion to ion-Bernstein wave takes place. In the minority scheme, the RF power is primarily dumped into minority ions. The energy distribution of the minority ions is characterised by a tail and the distribution function is generally estimated based on the quasi-linear theory developed by Stix [2]. RF accelerated minority ions, which are sufficiently well confined in JET, act as an intermediate energy reservoir and transfer their energy to the background electrons and ions via the drag between minority ions and other plasma species.

In this paper, we analyse and compare the ICRH results obtained in JET with H^+ or ^3He minority in deuterium plasmas. Based on the experimental evidence, the aim is to present the merits and demerits of the heating with the two minority ion species and to establish which minority ion is better suited for plasma heating in JET.

ICRH experiments in JET have been carried out under a wide range of plasma conditions with torodial field (B_T) varying from 2 to 3.4 Tesla and plasma current (I_p) from 2 to 4 MA. But, most of the data for H-minority was taken with an I_p of 2 MA and therefore, for comparison we have selected He^3 data also at I_p = 2 MA. In the case of H-minority the frequency of operation was $\simeq$ 33 MHz and B_T was about 2.3 Tesla whereas in He^3-minority case, f = 25 → 31 MHz and B_T = 2.6 → 3.4 Tesla. A comparison of the efficiency of ion and electron heating, plasma stored energy, asymptotic energy confinement times, change in the radiated power and impurity production are presented.

Results

Figure 1 shows a comparison of bulk-ion (deuterium) heating with H^+ and ^3He minority species. For lower power levels such that $P_{RF}/\langle n_e \rangle \leq 1.5 \times 10^{-13}$ W·m³, the increase in ion-temperature is practically the same in the two cases. However, for the values of $1.5 \leq P_{RF}/\langle n_e \rangle \times 1.0^{13} \leq 2.5$ W·m³, the bulk ion heating in the H-minority case seems to degrade

somewhat in comparison to the He^3 case. Figure 2 shows the corresponding comparison of the central electron temperature. For $1.5 \leq P_{RF}/\langle n_e \rangle \times 10^{13} \leq 2.5$ W·m³, the loss of efficient ion-heating in the case of H-minority is well compensated by the improved electron heating. Note that the T_e and T_i data points were plotted by averaging over the sawteeth.

The above data of plasma heating in JET can be represented by:

$$(\Delta T_{eo} + \Delta T_{io}) \approx \alpha \, P_{RF}/\langle n_e \rangle$$

where $\alpha \approx 1.5$ to 2×10^{13} (keV.W^{-1}m^{-3})

Figure 3 shows plasma stored energy when ICRH power is increased up to 5.5 MW. The slope of a line passing through H^+ data and that through ^{3}He data represent the asymptotic confinement times with values of τ = 0.15 s for H^+ and τ = 0.12 s for ^{3}He.

A comparison of the radiated power normalized by the line-averaged density square ($\langle n_e^2 \rangle$) shows that it is higher at a given power level of 4 MW by a factor of 1.7 in the case of H^+ minority than in the case of He^3-minority (see Fig. 4). Also the increase in metallic (Ni) impurity concentration was higher in the case of H^+-minority by a factor of about 2.5 compared to that with the ^{3}He case [3].

Summary and Conclusions

1. Bulk-ion heating is roughly the same for H^+ and ^{3}He-minority with $\Delta T_D \approx 1$ keV at a normalized RF power $R_{RF}/\langle n_e \rangle \approx 1 \times 10^{-13}$ W m³. At higher power levels, ^{3}He seems to be a little better than H^+ minority from the point of view of ion heating. However, the poor ion-heating at higher power levels in H^+ case is well compensated by a better electron heating. These observations are consistent with the Stix theory [2] in which the strong tail formed in the case of H-minority, relaxes on electrons whereas He^3-minority tail relaxes on bulk-ions at the RF power densities achieved presently in JET. For example for JET parameters, at a minority power density of 0.4 W/cm³, the fraction of power going to electrons is 0.85 and 0.2 in the case of H^+ and H^3 minority respectively. However, when RF heating power will be increased to tens of megawatts resulting in much higher minority power densities, both hydrogen and helium-3 minority are expected to transfer their energy primarily to electrons.

2. The asymptotic energy confinement times with ICRF in JET is marginally better in the case of H^+ than in the case of ^{3}He minority.

3. Both the (Bolometric) radiated power and the metallic impurities are worse in the case of H^+ than in the case for ^{3}He-minority.

References

[1] Equipe TFR, Report EUR-CEA-FC-1046, Fontenay-aux-Roses, France.
[2] T.H. Stix, Nuclear Fusion, 15 (1975) 737.
[3] B. Denne et al, these proceedings.

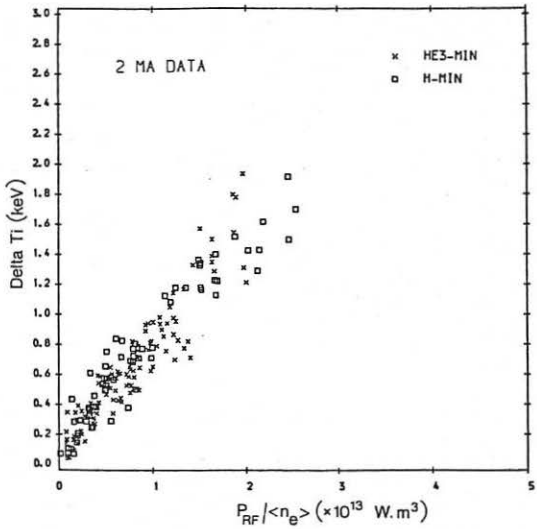

Fig. 1 Increase of bulk-ion (D+) temperature (measured by the neutron diagnostic) is plotted as a function of $P_{RF}/<n_e>$ both for H^+ and He^3 minority where P_{RF} is the ICRF power coupled from the antenna and $<n_e>$ is the line average density.

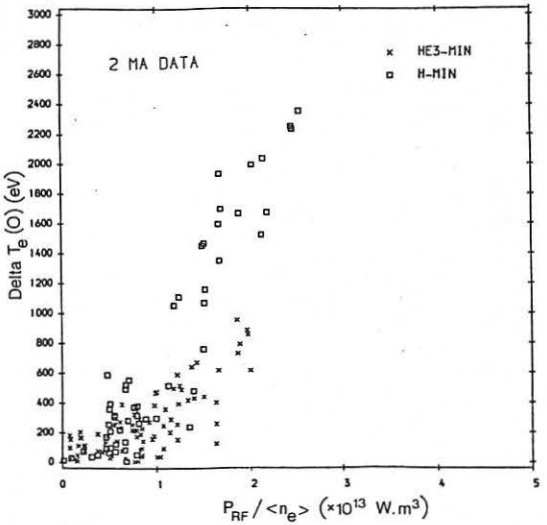

Fig. 2 A similar plot for central electron temperature (ECE) as in Fig. 1.

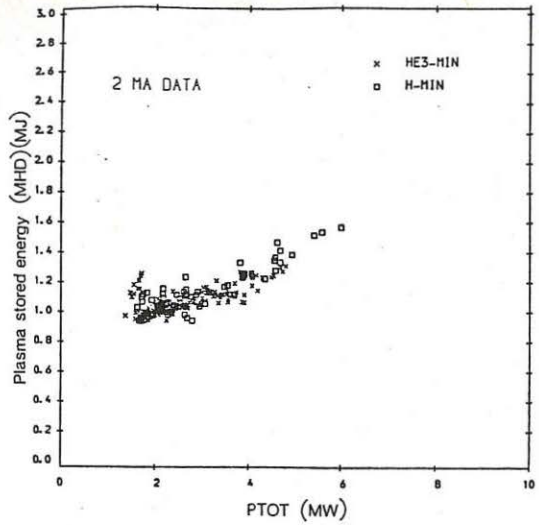

Fig. 3 Plasma stored energy (MHD) plotted as a function of total input power ($P_{RF} + P_{OH}$) for H^+ and He^3-minority cases.

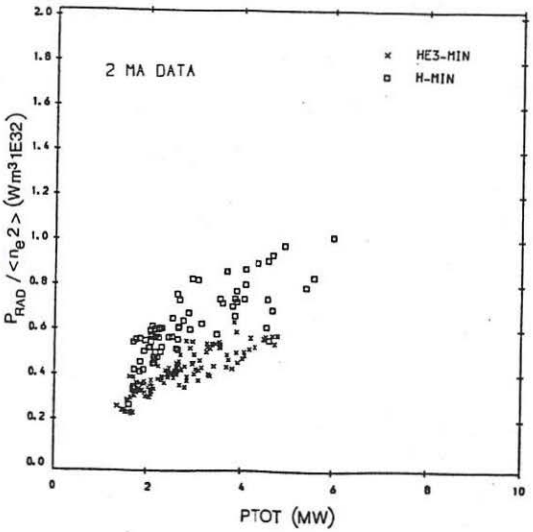

Fig. 4 Radiated power (Bolometer) normalized by $<n_e^2>$ is plotted as a function of total input power ($P_{RF} + P_{OH}$) for H^+ and He^3-minority.

Electron Heating with directly launched Ion Bernstein Waves in JIPP T-IIU Tokamak

K. Kawahata, R. Ando, E. Kako, T. Watari, Y. Hirokura, Y. Kawasumi, S. Morita, Y. Ogawa, K. Sato, S. Tanahashi, Y. Taniguchi, K. Toi,

Institute of Plasma Physics, Nagoya University, Nagoya 464, Japan

Abstract

The directly launched Ion Bernstein Wave (IBW) heating experiments have been carried out on JIPP T-IIU tokamak for two experimental conditions; (a) the IBW-branch between 3rd- and 4th-cyclotron harmonics of the deuterium, called as "Mode-I", and (b) the IBW-branch" between 2nd- and 3rd-cyclotron harmonics, called as "Mode-II". In the "Mode-I" case, the direct hydrogen heating at $\omega=1.5\Omega_H$ has been found. While, in the "Mode-II" case, the remarkable increase of the electron temperature has been observed, especially at the central region of the plasma. To investigate this difference of the heating mode, the power absorption has been calculated with the ray tracing code, taking into account of the effect of the plasma/antenna coupling. It is concluded from the consideration of the electron Landau damping that the transition from the ion heating mode to the electron one would be explained by the difference of the electron temperature at the ohmic phase; i.e., $T_e(0)$ = 0.7 keV for the "Mode-I" and $T_e(0)$ = 1.3 keV for the "Mode-II".

1.Introduction: The IBW heating experiments with the tokamak configuration have been conducted at the JIPP T-IIU device (R/a = 0.91m/0.23m) at the "Mode-I" condition [1,2], and the sub-harmonics ion heating at $\omega=3/2\Omega_H$, which has explored a new window for the nonlinear wave physics, has been observed. Recently, the IBW heating experiments with another branch have been also performed, where the 2nd-branch of the deuterium ions is applied. In this condition, the cyclotron layer at $\omega=2\Omega_D$ locates at the plasma center and the wave couples to the 2nd IBW branch of the deuterium ions; that is called as "Mode-II" experiments. We have observed the remarkable increase of the electron temperature. This is quite different from the result of the "Mode-I" IBW experiments. To explain this discrepancy between "Mode-I and -II" IBW heating experiments, the wave absorption of the IBW by ions and electrons was evaluated with the ray tracing code, taking into account the effect of the plasma/antenna coupling. On Table I parameters for these two modes are presented.

2.Experimental results at the "Mode-II" IBW heating: The IBW heating experiments with the 2nd-branch between 2nd and 3rd cyclotron harmonics of the deuterium ion have been carried out, where the toroidal field is 2.8 T and the deuterium plasma with 10% hydrogen minority are used. The plasma density is roughly the same one to the "Mode-I" IBW experiment, and the plasma current is about 1.8 times as high as that of the "Mode-I", which makes the electron temperature much higher at the ohmic phase; that is, $T_e(0)$ = 0.7 keV for "Mode-I" and $T_e(0)$ = 1.3 keV for "Mode-II". Figure 1 shows the electron temperature measured by Electron Cyclotron Emission (ECE) technique, and ion temperatures with mass separated analyzer, where the input rf power is 90 kW. The electron temperature begins to increase just at the time of the rf switch-on, but the temperature increases of hydrogen and deuterium ions are moderate. Clearly, this shows the remarkable difference from the results of "Mode-I" IBW heating experiments, presented in ref [1,2]. This fast rise of the electron temperature suggests the direct electron heating by

the IBW. We can see from Fig. 1(a) that the electron heating is localized at the central region ($r/a < 0.5$). While, the ion temperature gradually increases with the time constant of about 10 ms, which is roughly equal to the collision time between electrons and ions. The charge-exchange spectra show that the distribution functions of hydrogen and deuterium are almost Maxwellian. Then, it seems that the mechanism of the ion heating is not the direct ion heating by the IBW, but the collisional heating due to electrons heated by the IBW.

In order to examine the partition of the IBW power between electrons and ions, the simulation with zero-dimensional (0-D) transport code has been carried out. We have compared the experimental data with the simulation code by changing the partition of the IBW power for each species, keeping the total wave power constant. It is concluded that, if almost all the wave power is delivered to the electrons, the increase of the electron temperature is consistent with the experimental data, and the ion heating is also explained by the collisional heating through electrons.

3.Discussion: It is very interesting that two kinds of IBW experiments have shown the quite different heating mode; that is, the ion heating at the "Mode-I" IBW experiments and the electron heating at the "Mode-II" one. To understand this phenomenon in more detail, we have calculated the power deposition with the ray tracing code, paying much attension to the plasma/antenna coupling.

First of all, let us discuss the power absorption of the IBW for the "Mode-I" condition. Figure 2(a) shows the power absorption along the ray trajectory calculated with the ray tracing code for the "Mode-I" condition [1]. When the parallel refractive index $N_{\parallel}$ is relatively small (e.g., $N_{\parallel} \sim 4$), the wave can propagate into the plasma center and is strongly absorbed at the cyclotron harmonics layer of $\omega = 3\Omega_D$. When the index $N_{\parallel}$ increases (e.g., $N_{\parallel} > 6$), the wave suffers the electron Landau damping before the wave reaches the cyclotron layer. In Fig. 2(b), the power partition of the IBW between electrons and ions are presented as a function of the refractive index $N_{\parallel}$ for various electron temperatures. We can see the clear transition from the ion heating at the small $N_{\parallel}$ to the electron heating at the large $N_{\parallel}$. Accompanied by the increase of the electron temperature, the region of the electron heating is extending to the small $N_{\parallel}$ regime, as is expected by the Landau damping given by

$$P_{Landau} \propto exp(-(\frac{\omega}{k_{\parallel} v_{th,e}})^2) = exp(-(\frac{c}{N_{\parallel} v_{th,e}})^2) \quad . \qquad (1)$$

In addition to the wave absorption, another key issue is a wave coupling between the antenna and the plasma. This problem has already analyzed by W.N-C. Sy et al. for the Nagoya Type III antenna [3], where the coupling to the 1st branch of the hydrogen ion was analyzed because the dispersion near the antenna is approximated to the 1st branch of the hydrogen. The radiation power coupled to the plasma $P(N_{\parallel})$ is expressed by the product of the electrostatic coupling power $A_{kin}(N_{\parallel})$ and the antenna form factor $f(N_{\parallel})$, as shown in Fig. 2(b) by the dotted line. Comparing the radiation power from the antenna with the absorption rate to the plasma species, we could say that at the low electron temperature plasma the significant part of the IBW power will contribute to the ion heating without suffering the serious electron Landau damping, and the electron heating is enhanced as the electron temperature increases. In the "Mode-I" experimental condition ($T_e(0) = 0.7$ keV), we could see that a significant part of the IBW power is, therefore,

delivered to ions.

Next, it is necessary to evaluate the power absorption for the "Mode-II" experimental condition. Here we should remark that the analysis for the plasma/antenna coupling employed at the 1st-branch IBW is invalid for the 2nd-branch one, because it needs to expand the dispersion relation up to $O((k_\perp \rho_i)^4)$. At the present, we have no formulation to analyze the plasma/antenna coupling for the 2nd-branch IBW. Then, we could not present the wave power coupled to the plasma as a function of the parallel refractive index $N_\parallel$. However, we could expect the strong electron Landau damping from Fig. 2(b), because the electron temperature is relatively high ($T_e(0) = 1.3$ keV). In addition, the central region heating observed experimentally, as shown in Fig. 1(a), will be explained by the characteristics of the electron Landau damping given by eq.(1).

4.Conclusion: The directly launched Ion Bernstein Wave heating experiments have been carried out with JIPP T-IIU tokamak for the 3rd-branch ("Mode-I") and the 2nd-branch ("Mode-II") of the deuterium ions. For the "Mode-II" experiments, the remarkable electron heating has been observed, showing quite difference from the direct ion heating of the "Mode-I" experiments. From the analysis with the global energy balance, it is found that almost all of the wave power should be delivered to the electrons, and the ion is heated by the collision through the electrons.

To explain this difference of the heating mode, the power partition between electrons and ions has been analyzed with the ray tracing code. The result with the ray tracing code shows that at low $N_\parallel$ the ion heating is dominant, and at high $N_\parallel$ the electron heating becomes essential. As the electron temperature increases, this transition occurs at the relatively small $N_\parallel$ value. We could, therefore, say that the experimental evidence (ion heating for "Mode-I" and electron heating for "Mode-II") is attributed to the difference of the electron temperature; that is, $T_e(0) = 0.7$ keV for "Mode-I" and $T_e(0) = 1.3$ keV for "Mode-II".

Acknowledgements: The authors would like to thank members of CS group in IPP, Nagoya Univ., for continuous encouragements and useful discussion. They gratefully acknowledge to Drs R. Sugihara and M. Ono for fruitful comments.

references

[1] Ono, M., Watari, T., Ando, R., Fujita, J., Hirokura, Y., et al., Phys. Rev. Lett., 54 (1985) 2339.

[2] Toi, K., Watari, T., Ohkubo, K., Kawahata, K., Noda, N., et al., in Plasma Physics and Controlled Nuclear Fusion Research (Proc. 10th Int. Conf. London, 1984), Vol. 1, IAEA, Vienna (1985) 523.

[3] Sy, W.N-C., Amano, T., Ando, R., Fukuyama, A., Watari, T., Nucl. Fusion, 25 (1985) 795.

Figure Captions

Fig.1 Time evolutions of the electron and ion temperatures for the "Mode-II" experiment.

Fig. 2(a) Power absorption calculated with the ray tracing code for the situation of the "Mode-I" IBW experiment, where 60% H + 40% D plasma, $B_T(0) = 1.8\ T$, $T_{H,D}(0) = 0.3keV$, $T_e(0) = 0.7keV$ $n_e(0) = 3\times10^{19}m^{-3}$.

Fig. 2(b) Partition of the IBW power between electrons and ions as a function of the parallel refractive index $N_\parallel$ for different electron temperature, corresponding to the result of Fig. 2(a). The coupling power to the plasma expressed by the product of $f(N_\parallel)\cdot A_{kin}(N_\parallel)$ is also presented with the broken line.

Table I. Parameters of IBW heating experiments

	"Mode-I"	"Mode-II"
Frequency (MHz)	40	
RF Power (kW)	60 ~ 90	
Toroidal Field (T)	1.8	2.8
Plasma Current (kA)	120	220
Density ($\bar{n}_e$) ($10^{19}m^{-3}$)	2 ~ 3	
T_e (0)* (keV)	0.7	1.3
T_i (0)* (keV)	0.25	0.4

*) Temperature at the ohmic phase.

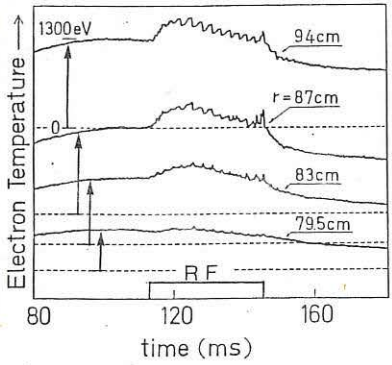

Fig. 1(a)

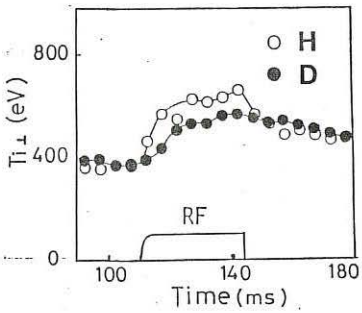

Fig. 1(b)

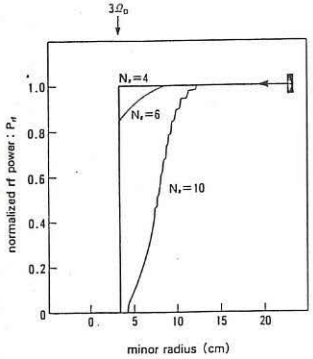

Fig. 2(a)

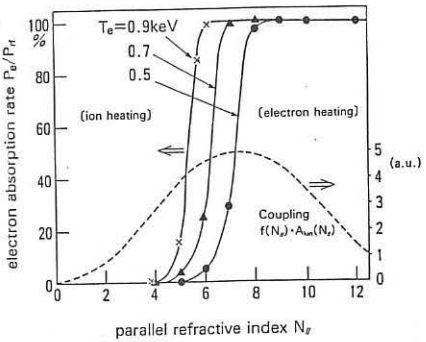

Fig. 2(b)

ICRF HEATING FOR THE ASDEX-UPGRADE TOKAMAK

F. Wesner, J.-M. Noterdaeme
J. Bäumler, F. Braun, F. Hofmeister, H. Wedler,
Max-Planck-Institut für Plasmaphysik,
EURATOM Association, D-8046 Garching, FRG

ABTRACT

The 12 MW of additional power for ASDEX Upgrade will be provided by 6 MW of neutral beam injection and 6 MW of ICRH. Such a combination has proved to be very efficient in ASDEX. In order to enable minority and second harmonic heating schemes, 4 equal RF systems with a frequency range of 30 - 120 MHz and a generator output power of 2 MW each are being built. The water-cooled, wide antennae allow the radiation of waves with different K-spectra by exchangeable central conductor geometries at a moderate voltage level.

INTRODUCTION

The major aim of ASDEX-Upgrade is to investigate a tokamak plasma and its interaction with the walls in a reactor relevant open poloidal divertor configuration and with an energy flux density in the plasma boundary comparable to reactor conditions /1, 2/. To reach this aim a heating power in the plasma of about 12 MW for hydrogen and 8.5 MW for deuterium seems necessary /3/, this estimation being based on a confinement similar to the H-mode found in ASDEX.

The heating power of 12 MW was decided to be supplied partly by Neutral Injection and partly by ICRH. If experimental results call for even more power, the concept of ASDEX-Upgrade allows to add further ICRH or NI devices as well as the application of other RF heating methods.

ICRH GENERAL CONCEPT

To provide 6 MW heating power in the plasma 4 equal systems will be built with a generator power of 2 MW each. This power should be available for standard magnetic field values of ASDEX-Upgrade in the single- and double-null divertor - and the limiter configuration. Heating should be possible, too, up to the maximum magnetic field, a somewhat reduced power being unavoidable.

High field side antennae being nearly impossible due to the poloidal divertors, heating by mode conversion is not practicable. The ICRH application is thus restricted to second harmonic and minority heating. Figure 1 gives the frequency ranges necessary for these heating methods for the main operational regimes of ASDEX-Upgrade.

In view of the still experimental status of ICRH it was decided to build a system providing maximum experimental flexibility:

- A frequency range of 30 - 120 MHz allowing second harmonic heating in D and H as well as minority heating with H or He_3 in D.
- An antenna concept allowing variations of the $k_{\parallel}$-spectrum as well as fitting the antennae to different plasma cross-sections (single- and double-null divertors) by relatively simple modifications.

Every provision has been made for a possible later increase of the heating power by 2 additional systems. If needed, the total number of antennae could even be increased to 8.

EXPERIMENTAL EXPERIENCE

Besides the large experimental experience of PLT and TFR /e.g. 4, 5/, more recent results of ASDEX, JET /6/ and TEXTOR /7/ can now be taken into account. Especially ASDEX results /8, 9/ are highly relevant due to the divertors and the similar heating scenarios. A summary of these results in view of the choice of heating methods for ASDEX-Upgrade show:

- Second harmonic and minority heating are very efficient heating methods, the measured heating efficiencies of 20-25 kJ/MW being larger than for NI in the L-mode.
- A combination with NI improves the available parameter range for ICRH (e.g. the impurity problems being reduced).
- ICRH is accompanied by high-Z impurities leading to about 30 % of power radiation from the plasma centre. This can largely be reduced by low-Z wall material (e.g. carbonization). The physics of the impurity release is still under investigation.
- It is possible to get the H-mode with ICRH /9/. This seems to be somewhat easier with minority heating. Further intense investigtions are necessary in this field.
- Second harmonic heating is largely independent of the gas composition (e.g. for $2\Omega_H$ the content of H ions should only be $\gtrsim 40$ %) allowing a larger experimental flexibility than minority heating.

So the choice of a combination of NI and ICRH as well as the large frequency range allowing second harmonic and minority heating are fully justified by recent results. A restriction to a smaller frequency range and only one ICR-heating scheme, despite of its attractiveness from the economic point of view, seems not yet reasonable for the next generation of experiments.

ANTENNAE

The development of antennae for ASDEX-Upgrade has the following aims:

- Optimization for single-null operation and second harmonic heating (80 MHz). The antenna will be used for minority heating, too, with somewhat worse coupling characteristics.
- The antenna should allow different spectra for $K_\parallel$ by using different centre conductor geometries.
- Fitting to different plasma cross-sections (single-null, double-null divertor and limiter operations) is possible by changing simple side wall elements, the Faraday screen and side limiters being reused.
- The antenna has to be cooled.

The antenna geometry was optimized with respect to the electric field and voltage levels in the antenna and transmission lines. For this purpose the coupling calculations with 2- and 3-dimensional codes were combined with ray-tracing calculations in order to take into account the effect of the geometry on the power absorbed in the plasma, not only on the power radiated by the antenna /10/ (Fig. 2).

A simple loop antenna leads to a $k_\parallel$-spectrum peaked at $K_\parallel = 0$, mainly exciting fast waves with small $k_\parallel$ which are weakly damped by the plasma. It possibly excites coaxial waves, too, which may contribute to the impurity release. Since experimental results are still contradictory concerning these questions, the spectra of the ASDEX-Upgrade antenna will be variable by exchanging the centre conductor array (Fig. 3a,b). 2D- calculations show, that for an antenna wide enough the voltage necessary for radiation

and absorption of a certain power, e.g. in an array like Fig. 3b must not be larger than for a single loop antenna (Fig. 2). It can be seen further in Fig. 2, that for such an array and with a given antenna width there exists an optimum for the widths of the centre conductors and gaps.

Figure 4 shows the principle design of the antenna. It is based on the technology of the ASDEX antenna providing TiC-coated, optically open Faraday screens /11/, carbon protection limiters and water cooling. For single null operation the antennae are asymmetric with respect to the midplane of the experiment in order to utilize the full available space for a large distance between central and return conductor.

LINE AND MATCHING SYSTEM

The antennae are fed at their both ends by 6 1/8" vacuum lines with bellow sections to compensate thermal expansions. They are connected to the pressurized 9" lines by two feedthroughs with intermediate vacuum. First stubs near the upper and lower antenna feeder will reduce the VSWR for the major frequency range ($2\Omega_{CH}$ corresponding to about 80 MHz) and allows cooling of the inner conductor of the vacuum line. The antenna impedance is matched to that of the generator by double stub-tuner systems near the experiment, the distances between the two stubs and between stubs and antennae being adjustable by exchangeable elements.

RF GENERATORS

The 4 RF generators will be very similar to those of ASDEX-W VII /12/. Besides minor modifications based on the operation experiences with ICRH experiments on ASDEX and the extension of the upper frequency limit from 115 to 120 MHz the output power of each generator will be extended from 1.5 to 2 MW up to 80 MHz and up to 1.2 MW at 120 MHz. Special tests with an ASDEX-W VII generator showed that these values can be achieved /13/. At least at lower frequencies a further increase of the power should be possible.

REFERENCES

/1,2/ IPP Garching Reports Nr. 1/197, 1/211 (1982) and 1/217 (1983)
/3/ Additional heating for ASDEX-Upgrade, IPP Garching Rep.1/237 (1985)
/4/ e.g. J. Hosea et al., Proc. of 4th Int. Symp. on Heating in Toroidal Plasmas, Roma 1984, P.261-275
Proc. of 12th European Conference on Controlled Fusion and Plasma Physics, Budapest, 1985
/5/ e.g. J. Adam et al., 4th Int. Symp. on Heating in Toroidal Plasmas, Roma 1984, P.277-290
/6/ J. Jacquinot et al., 12th Europ. Conf. on Controlled Fusion and Plasma Physics, Budapest, 1985, or P.P. Lallia, this conference
/7/ A.M. Messiaen et al., ibid
/8/ K. Steinmetz et al., ibid
/9/ K. Steinmetz et al., this conference
/10/ J.-M. Noterdaeme, M. Söll, 12th Europ. Conf. on Controlled Fusion and Plasma Physics, Budapest, 1985
/11/ F. Wesner et al., 4th Int.Symp. on Heating in Toroidal plasmas, Roma 1984, P.1103, and J.-M. Noterdaeme et al., this conference
/12/ W. Schminke, F. Hofmeister, F. Wesner,10th Symp. on Fusion Engineering, Philadelphia, 1983, p. 1498
/13/ J. Wyss, K.Holm, Applications of RF Waves to Tokamak Plasmas, Varenna, 1985, p.882

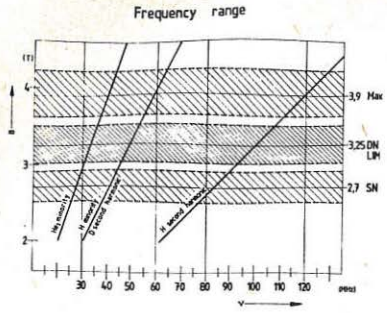

Fig. 1: ASDEX-Upgrade operational regimes and ICRH frequencies

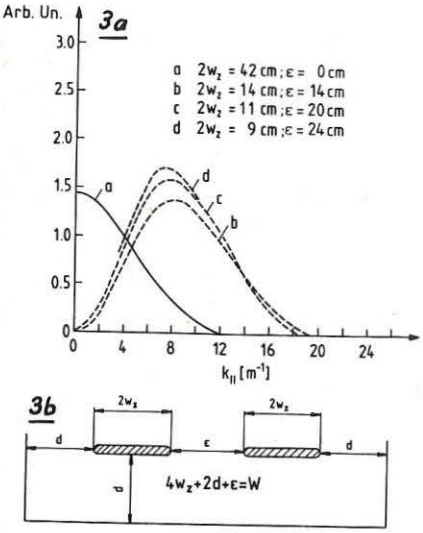

Fig. 3a: Spectra of an antenna array like Fig. 3b for different distances and a total width of 70 cm. Spectrum (a) is for one loop.

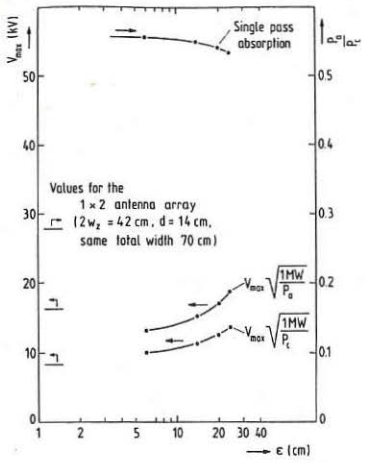

Fig. 2: Power absorption and antenna voltage for an array like Fig. 3b and simple loops

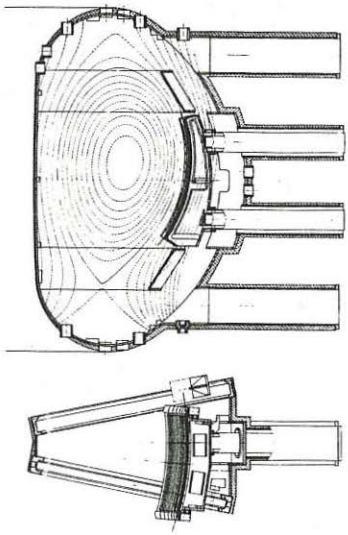

Fig. 4: Cross sectional views of the ICRH antennae in the vacuum vessel.

ANALYSIS ON ICRF HEATING AND CURRENT-DRIVE IN TOKAMAKS

K. Itoh*, A. Fukuyama**, T. Morishita**, Y. Kishimoto†, K. Hamamatsu†, and S.-I. Itoh††

* Plasma Physics Laboratory, Kyoto University, Uji, Kyoto 611, Japan
** School of Engineering, Okayama University, Okayama 700, Japan
† Japan Atomic Energy Research Institute, Naka, Ibaraki 311-02, Japan
†† Institute for Fusion Theory, Hiroshima University, Hiroshima 730, Japan

Abstract

Theoretical model of ICRF wave heating and current-drive in tokamaks is developed. By considering the deformation of the velocity distribution, the wave form, power absorption, tail formation and energy partition are studied simultaneously. This model is applied to JET plasma for example.

Introduction

Recent progress of ICRF heating experiments has shown that the ICRF fast wave is a dependable heating method in the regimes of the mode conversion, minority heating and second cyclotron resonance. The analysis on the heating processes, such as the wave coupling, propagation, energy deposition and high energy particle generation, is an important issue to explain experimental findings and to study the future perspectives of the ICRF waves for plasma heating. We have developed a theoretical model which can study the excitation, propagation and absorption of the ICRF waves in tokamaks [1,2]. The analysis is extended to investigate the thermalization of the absorbed energy, by taking into account the quasilinear diffusion in the velocity space. The wave field structure, tail formation and energy equipartition are analyzed in a selfconsistent manner for a given antenna structure. This model explains, quantitatively, the electron heating rate and profile in the minority heating regime of the JET experiments. The current-drive is discussed separately[3].

Plasma Model

The plasma is composed of electrons, majority ions (D) and minority ions (H). In the case of the minority heating, the major part of the wave energy is firstly absorbed by minority ions through fundamental cyclotron resonance. This causes modification of the distribution function [4]. We assume that the distributions of electrons and deuterons are unaffected (i.e., we do not follow the evolution in the scale of the confinement time), and take into

account the deformation of the velocity distribution of minority ions. The minority ions are treated to be the sum of hot component and cold component. The wave field structure is solved in the one-dimensional model geometry [1], in which the inhomogeneities in the direction of the major radius (x-direction) are kept. The toroidal magnetic field is approximated by the field in the z-direction, which is given as $B_z = B_0/(1+x/R)$. The density and temperature are given as $n_s(x) = n_0(1-x^2/a^2)$ (s = e, D, H) and $T_s(x) = T_0\exp(-3r^2/a^2)$ (s = e, D). The conducting wall is located at $x = \pm b$.

The rf wave equation is given as

$$\nabla\times\nabla\times\vec{E} - \frac{\omega^2}{c^2}\vec{E} = i\omega\mu_0\left(\sum\vec{J}_s + \vec{J}_A\right) \tag{1}$$

where ω is the rf frequency, $\vec{J}_s$ is the induced current (s = e, D, H) and $\vec{J}_A$ is the antenna current. The expression of $\vec{J}_s$ in the presence of the kinetic process is given in Ref.[1]. Antenna, which carries the current in the y-direction, is located at x = d (or -d).

The development of the distribution function of minority ions is given by solving the Fokker-Planck equation. According to Ref.[4], we take the 0th moment of the Legendre expansion of f_H and obtain

$$\frac{\partial f}{\partial t} = \frac{1}{v^2}\frac{\partial}{\partial v}\left(-\alpha v^2 f + \frac{1}{2}\frac{\partial}{\partial v}(\beta v^2 f) + Kv^2\frac{\partial f}{\partial v}\right) \tag{2}$$

where α and β stand for the Coulomb collision with back ground particles, and K indicates the rf heating term (see Ref.[4]). The absorbed power $P_H = \langle\vec{J}_H\cdot\vec{E}\rangle$ is redistributed to electrons and deuterons. The energy partition is calculated by using f_H.

The distribution function of minority ions are approximated by the sum of bulk and tail components, i.e., $f_H = f_{Hb} + f_{Ht}$, where $f_{Hb} = n_b\exp(-mv^2/2T_b)/(2\pi T_b/m)^{1.5}$ and $f_{Ht} = n_t\exp(-mv^2/2T_t)/(2\pi T_t/m)^{1.5}$. This two-temperature distribution is used to estimate $\vec{J}_H$. The constants n_b, T_b, n_t and T_t are given by equating up to 6th order moments of f and f_b+f_t. With this model we can study the stationaly as well as transient phenomena associated with the ICRF heating. Since the wave field is solved in the one-dimensional approximation, the averaging over the magnetic surface is performed by assuming the envelop of P_s in the y-direction. From the result of the two-dimensional analysis[2], we choose the simple envelop $P_s \propto 1-(2y/L)^2$ (L being the antenna length).

Application to JET plasma

We apply this model to JET plasmas. Plasma parameters are R = 3m, a = 1.2m, B = 2T, $n_e(0) = 2.94\times10^{19}/m^3$, $T_e(0) = T_D(0) = 2.5$keV, $n_H/n_D = 4\%$, $\omega/2\pi = 29.8$MHz,

and the elongation ratio is 1.45. The antenna (single monopole) is located in the low-field side of the torus at x = 1.25m.

The figure 1 illustrates the radial distributions of the tail protons (n_{Ht}, T_{Ht} and n_H) and the power to electrons P_e at the saturated stage ($t = \infty$ in Eq.(2)). The total rf power is 1.2MW. About 90% of the rf power is directly absorbed by minority protons (about 10% is absorbed by majority ions through second cyclotron resonance), but electrons absorb more than 60% of P_{rf} through collisions for this power level. The profile and the power level of P_e is in good agreement with JET experiments. The figure 2 shows the temporal evolution of the total heating powers ($\overline{P}_s = 2\pi\int P_s r dr$) to electrons (solid lines) and to deuterons (dashed lines) with the initial condition $n_{Ht}(t=0) = 0$. The rf power is 1.1MW (case-I) and 0.5MW (case-II). Because the high energy ions ($T/T_e \gtrsim 10$) heat electrons, the power to electrons grow much slower than that of majority ions. It is also noted that $\overline{P}_e$ is smaller than $\overline{P}_D$ for the lower heating power, but $\overline{P}_e > \overline{P}_D$ holds for the high power cases. The power partition depends on the energy of tail particles. Note that the delay in the evolution of $\overline{P}_e(t)$ is due to the initial condition of n_{Ht}. If we initiate with condition $n_{Ht}(t=0) = \hat{n}_{Ht}$ and $n_{Hb}(t=0) = n_H - n_{Ht}(t=0)$ ($\hat{n}_{Ht}$ being the saturated value of n_{Ht}), then the heating to electrons occurs without delay. This result explains the fact that the prediction of $P_e(r)$ is in good agreement with the experimental estimation which is evaluated from $\partial T_e/\partial t$ after the internal disruption. If at least half of the generated fast ions remains in q = 1 surface after the onset of the internal disruption, the heating power to electrons does not differ much from the one obtained in the stationary state.

References

[1] A. Fukuyama, et al., Nucl. Fusion 23 (1983) 1005.

[2] S.-I. Itoh, et al., Plasma Physics and Controlled Nuclear Fusion Research (IAEA, Vienna, 1985) Vol.I, p541.

[3] Y. Kishimoto, et al., paper #62 of this conference.

[4] T. H. Stix, Nucl. Fusion 15 (1975) 737.

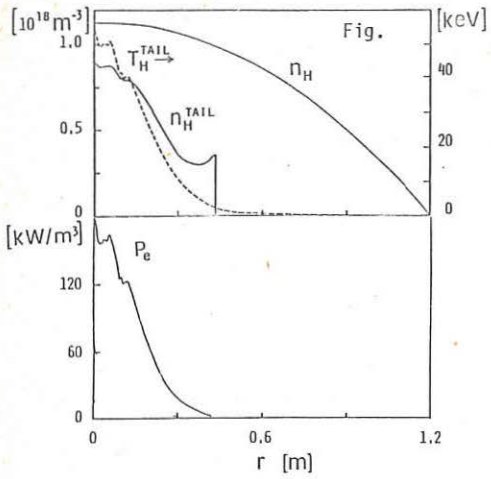

Fig.1
Stationary radial profiles of n_{Ht}, T_{Ht} and P_e for the case of P_{rf}=1.2MW. The power Deposition to electrons are localized in the q = 1 surface (r=0.3m). The temperature of the tail exceeds 40keV near the plasma center.

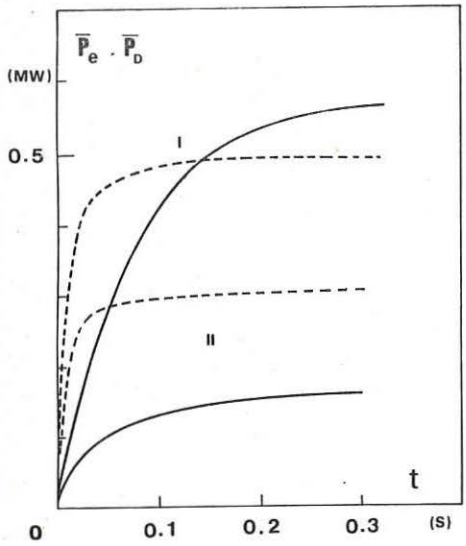

Fig.2
Temporal evolutions of $\bar{P}_e$ and $\bar{P}_D$(dashed line), for P_{rf}=1.1 MW (case I) and 0.5MW (case II). The initial condition is chosen as $n_{Ht} = 0$.

This work is partly supported by the Grant-in-Aid for Fusion Research and the Grant-in-Aid for Scientific Research of MoE Japan.

ION CYCLOTRON HEATING OF A REVERSED FIELD PINCH

G. Cooper and W.N-C. Sy

Research School of Physical Sciences
Australian National University
Canberra, A.C.T.2601, Australia

1. INTRODUCTION

The highly developed ion cyclotron heating technology may well be useful in the operation of a reversed field pinch (RFP) discharge. In order to assess the feasibility of this application, fast wave spectra, eigenmode structures and power coupling characteristics have been investigated for the RFP.

2. THE PLASMA MODEL

The RFP plasma model used in the theoretical calculations is based on the empirically measured HBTX 1A discharge (with a plasma minor radius 0.26m). Detailed experimental measurements[1] show that the plasma equilibrium is well approximated by the force-free condition, but the standard Bessel function model[2] needs to be modified so that the current density vanishes at the edge of the plasma. Toroidal effects lead merely to slight displacements of flux contours and are negligible in the present studies. Accordingly, the cylindrical plasma equilibrium model used in this paper is determined by the condition $\vec{j}_0 = \mu^* \vec{B}_0$, where $\mu^* = \mu^*(r)$ is a chosen profile which vanishes at the plasma boundary. A narrow vacuum layer is assumed to exist between the plasma column and the outer conducting wall. The equilibrium magnetic field profiles for a typical model are illustrated in Fig.1.

3. BASIC EQUATIONS

Unlike most plasma configurations for which wave propagation and ICRF heating studies have been carried out, the RFP has strong magnetic curvature and high magnetic shear. A system of basic equations which takes these effects fully into account has been derived[3] recently; a Fourier decomposition of the form $\exp(im\theta + ikz - i\omega t)$ leads to

$$(A/r)d(rQ)/dr = C_1 Q - C_2 P \ , \qquad (1)$$

$$A dP/dr = C_3 Q - C_1 P \ , \qquad (2)$$

where $P = \vec{B}\cdot\vec{B}_0/\mu_0$, $Q = \vec{E}\cdot(\vec{e}_r \times \vec{B}_0)/i\omega B_0^2$ and A, C_1, C_2, C_3 are a set of equilibrium dependent coefficients. The basic equations can be regarded as high frequency, multiple-ion species generalizations of the Hain-Lüst (ideal MHD) equations, but for a force-free plasma. For numerical modelling, these equations have been slightly generalized by replacing ω by $\omega + i\nu$, to satisfy causality and to simulate dissipative effects.

4. SPECTRAL PROPERTIES

The gross features of the wave spectrum can be partly obtained from a

WKB analysis, which can yield results in qualitative agreement with a full wave solution. In cylindrical geometry, it is convenient to use a uniform asymptotic representation of the form

$$P(r) = J_m\{\int^r k_r(t)dt\} \quad ,$$

where $k_r^2 = (C_2C_3 - C_1^2)/A^2 + m^2/r^2$. The singularities of k_r arise from the zeros of A , which determines the spatial resonances, where mode conversion of the fast waves can occur. In the present model, these spatial resonances include the shear Alfvén continuum and the ion-ion hybrid continuum. If plasma inhomogeneity is weak, such as in a restricted central region of a pinch discharge, the shear Alfvén continuum band is well separated from the ion-ion hybrid continuum as illustrated in Fig.2. In the full RFP plasma, strong inhomogeneity associated with field reversal leads to a coalescence of the two continuous spectra (see Fig.3), even at moderate wavenumbers. It can be seen that resonance absorption is easily obtained in a RFP and in fact, there are only small islands in the spectral space where resonance absorption can be avoided. Figure 4 shows how the radial position of the ion-ion hybrid layer varies with frequency in a H/D plasma for 10%, 30% and 50% H. Figure 5 shows how a plot of k_r^2 can be used to determine quickly the position of the resonance layer.

5. EIGENMODE STRUCTURES AND POWER COUPLING

Full wave solutions to (1) and (2) have been obtained numerically using GEAR's method. Boundary conditions applied are (a) P and Q are continuous at the plasma-vacuum interface, (b) P is finite on the axis and (c) Q vanishes at the conducting wall.

In a H/D plasma with 10% H, a typical eigenmode structure at 1.9 MHz, for the $m = 1$, $k = 0$ mode, is shown in Fig.6, where the "kink" in the P profile is due to partial reflection at the ion-ion hybrid layer. A calculation of the integrated Poynting flux, shown in Fig.7, indicates that power is effectively deposited at the ion-ion hybrid layer by resonant absorption. The corresponding intrinsic spectral resistance, as the frequency is varied, is displayed in Fig.8.

6. CONCLUSIONS

Ion cyclotron heating of a RFP appears promising for the following reasons.

(a) Magnetic isobars, which determine the loci of spatial resonances and the density contours have similar topologies.

(b) Resonance absorption is easily obtained.

(c) Fast wave eigenmode formation is possible in the presence of resonance absorption.

(d) The location of energy deposition, the degree of resonance absorption and the antenna coupling characteristics can all be adjusted by varying the ionic mixtures as well as the usual equilibrium parameters.

REFERENCES

1. D. Brotherton-Ratcliffe and I.H. Hutchinson, Culham Report CLMR246 (1984).

2. N.F. Cramer and I.J. Donnelly, Plasma Phys. Contr. Fusion 27 (1985) 1323.

3. W.N-C. Sy, Austr. J. Phys. 38 (1985) 143.

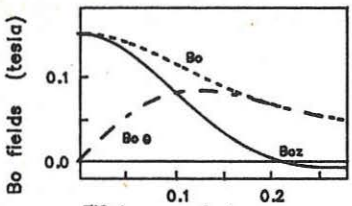

FIG.1.

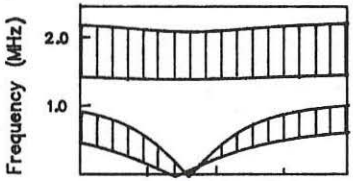

FIG.2.

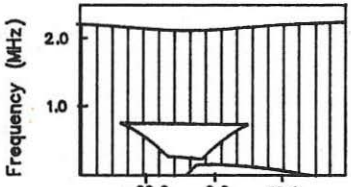

FIG.3.

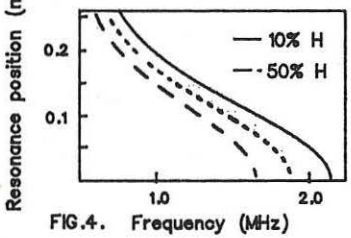

FIG.4.

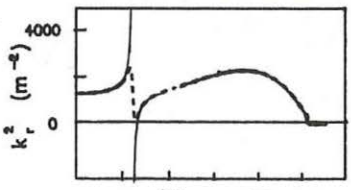

FIG.5.

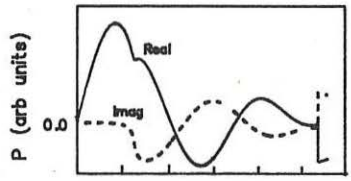

FIG.6.

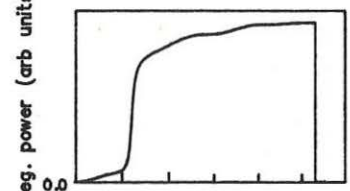

FIG.7.

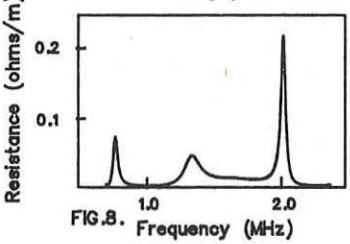

FIG.8.

HIGH-POWER HEAVY-ION MINORITY HEATING

A.V.Longinov, S.S.Pavlov, K.N.Stepanov

Institute of Physics and Technology, the Ukrainian Academy of Sciences, Kharkov 310108, USSR

A possibility of raising essentially the efficiency of heating the toroidal plasmas by the method of heavy-ion minority heating (HIMH) has been substantiated in papers [1,2]. First HIMH experiments performed recently on T-10 [3] and TFR [4] devices have shown that even under non-optimum conditions (especially for TFR [4]) the efficiency of heating increases essentially. In the report presented this method of RF heating is studied using the solution of the kinetic equation for the velocity distribution function of heavy minority ions (HM) [2]. The main features of this equation lie in taking into account the high energy tail cutoff effect and the single pass of a slow wave (SW) through the resonance zone $\omega = 2\omega_c'$.

The RF power absorbed by resonant heavy ions, which is averaged over the magnetic surface with the radius τ, is analysed as a function of some parameters:

$$\langle p\rangle = 3\sqrt{\frac{\pi}{2}}\frac{n_d T_d}{\tau_i}\Delta Z_{eff} F(K_\perp \rho_d, \xi, A, T_d/T_e); \quad \xi = \frac{2\alpha(\omega_{cd}-\omega_c')B_t R}{\pi c L e^3 \omega_c' n_d^2 K_\perp \rho_d \tau} P_{RF} \quad (1)$$

where $\tau_i = \frac{3 T_d^{3/2} m_d^{1/2}}{4\sqrt{\pi} e^4 n_d L}$, $\Delta Z_{eff} = n' Z'^2/n_e$, $n_e = n_d$, $\rho_d = V_{Td}/\omega_{Hd}$, $V_{Td} = \sqrt{2T_d/m_d}$

P_{RF} is the 2π R-averaged kinetic SW energy density flux, A is the atomic number of the HM, the F function is calculated using the solution of the kinetic equation, $\alpha = 2$ for $\tau = \int \mathrm{Im}\, K_\perp dR \ll 1$ and $\alpha = 1$ for $\tau = 1$. Besides, we also determined the power fraction imparted from HM to electrons $P_e = \langle P_e\rangle/\langle P\rangle$ and deuterons $P_d = \langle P_d\rangle/\langle P\rangle$; the relative HM energy $\overline{W} = m'\overline{V'^2}/m_d V_{Td}^2$; the relative HM pressure $\beta'/\beta_p = n' T_d \overline{W}/(n_d T_d + n_e T_e)$; and $\Delta Z_{min}(\xi)$ corresponding to the ΔZ_{eff} value, at which almost a complete (90%) SW absorption in the $\omega = 2\omega_c'$ zone is ensured. The value of $K_\perp \rho_d = 0.35\,\omega_c'/\omega_{cd}$ used in the calculations (Fig.1) is typical of the HIMH. The $K_\perp \rho_d$ value is changed (Figs. 3,4) by the variation of plasma and wave parameters, $F(A)$ is independent of the degree of ionization Z' of the heavy atom with a given A. Fur-

ther, we put $T_d = T_e$.

1. Optimization of the HM species. Fig. 1a shows F versus ξ for different HM species (Li^7, Ne^{22}, V^{51}). The analysis of curves in Fig.1 shows that the ξ values, at which $P_d = P_e(\xi = \xi'_{cr})$ or the SW damping factor is maximum ($\xi = \xi''_{cr}$), are essentially dependent on A. Let A'_{opt}(or A''_{opt}) denote the A value, at which $\xi = \xi'_{cr}$(or $\xi = \xi''_{cr}$). It is obvious that for $A > A'_{opt}$ the resonant ion energy is imparted mainly to deuterons, whereas at $A < A'_{opt}$ it goes to electrons irrespective of the HM concentration. And here lies the important difference between the HIMH and the method of light ion minority heating. Using Eq.(1) and the values of $F(\xi)$ from Fig. 1 one can obtain $\Delta Z_{min} = C(\xi)A^2 \rho_d \omega'^2_c / (\omega_{cd} - \omega'_c)\omega_{cd} R$, where the $C(\xi)$ functions for different A are shown in Fig. 1b. It is obvious that at $A = A''_{opt}$ there is almost a complete SW absorption at a lowest HM concentration ($\Delta Z_{eff} = \Delta Z^*_{min} = \min[\Delta Z_{min}(\xi)]$). Thus, to attain a high HIMH efficiency, especially in the regimes with a preferential ion heating, for the lowest ΔZ_{eff} value it is necessary to choose the optimum HM species. For $K_\perp \rho_d = 0.35\omega'_c/\omega_{cd}$ we obtain $A''_{opt} = \sqrt{0.7\xi'}$. For example, for TFR conditions $n_d = 10^{14}$ cm^{-3}, $r/R = 0.05$, $P_{RF} = 45$ w/cm^2 we have $\xi = 500$ and $A''_{opt} = 18$ (O^{18} isotope). For the same parameters and $\rho_d/R = 0.0015$ we have $\Delta Z^*_{min}(O^{18}) = 0.15$. For regimes with non-optimum A values: i) if $A \gg A''_{opt}$, it is necessary to use high ΔZ_{eff} values, which may appear inadmissible (in particular, under TFR conditions, on using V^{51} at $K_\perp \rho_d = 0.35\omega'_c/\omega_{cd}$ we have $\Delta Z_{min} = 4.5$(!), i.e., for actual V^{51} concentration the SW absorption is weak ($2\Delta Z_{eff}/\Delta Z_{min} \approx 0.07$) which explains the results of [4]); ii) if $A \ll A''_{opt}$ (the electron heating regime) the value of $\beta'/\beta_p = \beta(\xi)\rho_d \omega'_c A^3/R(\omega_{cd} - \omega'_c)Z'^2$ can appear to be too high (see Fig. 1c for the $\beta(\xi)$ function).

2. Effects of banana losses. Fig.2 illustrates the qualitative behaviour of $f'(V)$=const lines at point B in the equatorial plane on the outer side of the torus ignoring losses. It is seen that in the cases typical of $\xi \gtrsim \xi''_{cr}$ regimes, the ions (especially with high A) are concentrated in the zone with lowest V_o values ($f'(V) = 0$ in the banana trajectory region $V > V_o$). We have studied the role of the banana losses. The behaviour of the basic

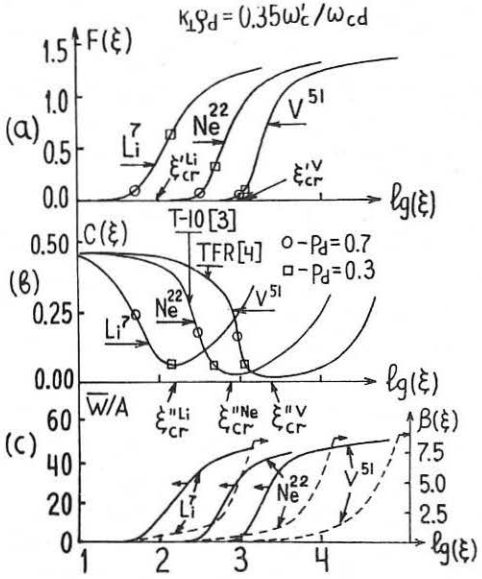

Fig. 1

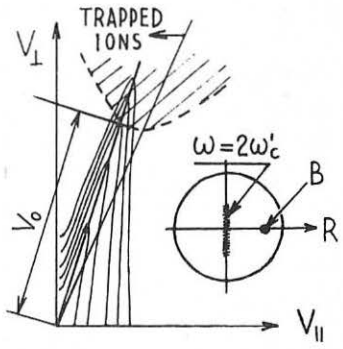

Fig. 2

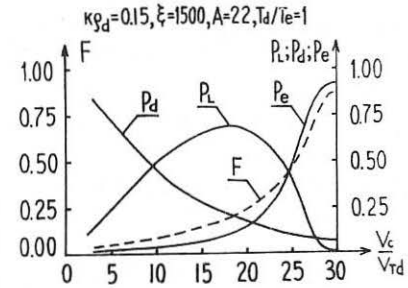

Fig. 3

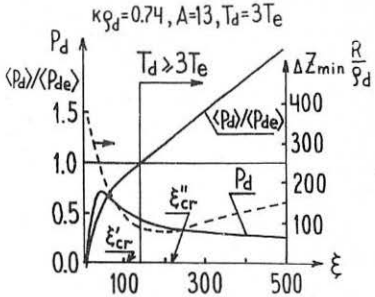

Fig. 4

functions versus V_0/V_{Td} is presented in Fig. 3 for the low value of $K_\perp \rho_d = 0.17 \omega_c'/\omega_{cd}$ when the losses become higher (the resonant zone is close to the mode conversion zone). Main conclusions are: 1) the maximum energy losses $P_L = P_{loss}/P_{RF}$ occur at appreciably high V_0/V_{Td} values and the P_L value decreases (!) as V_0 decreases; 2) the low V_0 regime requires higher ΔZ_{eff} values; 3) the power value for the deuteron heating remains practically the same even at low V_0; 4) according to items 1) and 2) it follows that the HIMH can efficiently be used in low V_0 devices (e.g., in stellarators or low magnetic field tokamaks); 5) regimes with high $K_\perp \rho_d$ are most effective to reduce losses.

3. Feasibility of the $T_d \gg T_e$ regime. The HIMH advantages especially show up in the $T_d \gg T_e$ regime. For example, if $\tau_{Ed} \gg \tau_{de}$ this regime is attainable for $\langle P_d \rangle / \langle P_{de} \rangle \gtrsim 1$, where τ_{Ed} is the deuteron energy-confinement time, τ_{de} and $\langle P_{de} \rangle$ are, respectively, the e-d energy equipartition time and power. $\langle P_d \rangle / \langle P_{de} \rangle = (\sqrt{\pi}/2)(m_d/m_e)^{1/2} T_e^{3/2} \Delta Z_{min} F(\xi) \rho_d / (T_d - T_e) T_d^{1/2}$ To illustrate, Fig. 4 shows $\langle P_d \rangle / \langle P_{de} \rangle$, ρ_d and ΔZ_{min} versus ξ at $T_d = 3T_e$ and $K_\perp \rho_d = 0.74$ for the C^{13} isotope used. The $T_d \gtrsim 3T_e$ regime is attainable at $\xi \gtrsim 140$ even if the HM used has a relatively low A. In this case, about 60% of the RF power goes to electrons. For example, in T-10 ($n_e(0) = 5 \cdot 10^{13}$ cm^{-3}, $B_t = 3$T, $T_d(0) = 6$ keV, $T_e(0) = 2$ keV, the regime $T_d \gtrsim 3T_e$ is attainable in the region of $r/R \lesssim 0.05$ for $\tau_{Ed} \gg \tau_{de}$ and $P_{RF} = 23$ W/cm^2 ($P_{input}^{SW} \approx 500$ kW). Note that the $T_d = 3T_e$ regime is unattainable for H-minority heating at $n_H/n_d = 0.1$ because one has $\langle P_d \rangle / \langle P_{de} \rangle \ll 1$ in this case.

The presented HIMH picture may change essentially in some cases because of ionization-recombination phenomena.

Thus, the HIMH has some specific properties which must be taken into account in order to attain a high plasma heating efficiency.

References

1. A.V.Longinov, K.N.Stepanov, Proc. IV Intern. Symp. on Plasma Heating in Toroidal Systems (Rome, 1984) Part 1, p. 486.
2. A.V.Longinov, S.S.Pavlov, K.N.Stepanov, Proc. 12th European Conf. on Contr. Fusion and Plasma Physics (Budapest, 1985) Part 2, p.132.
3. V.V.Alikaev et al., Ibid., Part 2, p.156.
4. TFR Group, Ibid., Part 2, p.112.

FEATURES OF FAST MAGNETOSONIC WAVE EXCITATION IN T-10 TOKAMAK USING ANTENNAE WITH DIFFERENT $K_{\parallel}$ SPECTRA

A.V. Longinov and V.A. Tsurikov

Kharkov Institute of Physics and Technology, Ukrainian SSR Academy of Sciences, 310108 Kharkov, USSR

An important problem of ICRF heating in tokamaks and stellarators is the excitation of fast magnetosonic waves (FMSW) in a plasma with complex antenna systems. To design such antenna systems one has, alongside with the technical aspects, to study the phenomena accompanying the FMSW excitation in a plasma, in particular, in the scrape-off layer.

This report is devoted to the investigation of certain features of the FMSW excitation in the toroidal plasma with the antenna employed in experiments on T-10 [1]. The model similar to that adopted previously [2] describes the fast mode excitation and propagation in the inhomogeneous deuterium plasma in the straight-cylinder approximation [3]. The principal parameters used in the calculations are: $n_e(0)=7.1\times10^{13}\,cm^{-3}$, B=4 T, R=150 cm, radius of the chamber a_c=39 cm, and plasma column radius a_p=35.5 cm. The antenna (current layer) with a width $L_{\parallel}$= 52 cm and radius a_{cl}=36.5 cm covers a poloidal angle $\vartheta_0=110^{\circ}$ ($L_{\vartheta}\approx$ 71 cm), with the exciting unipolar current on the antenna surface uniformly distributed along the z-axis. The density profile is assumed to be parabolic. Some features of the excitation of the nonaxisymmetric modes are discussed below (for details see Ref. [3]). The wave damping satisfies the condition $\tau \lesssim 1$ (resonance overlapping).

Fig.1 shows the distribution of the $E_{\vartheta}^{l,m}$ and $E_r^{l,m}$ field components along the radius r for two modes with wave numbers m =1 and m=-1 and rather low toroidal numbers l ($l=k_{\parallel}R$=3) corresponding to the major-azimuth Fourier expansion. Typically, for $r>a_p$ where the plasma density n_e is assumed to be zero (scrape-off layer), the radial field component E_r increases considerably. The increase in E_r is found to be characteristic of the non-

axisymmetric modes with low ℓ, though these are not surface-wave modes.

Another feature is that the field components for the modes with m signs reversed have practically similar amplitudes and positions of nodes and antinodes all over the plasma column cross section, except in the vicinity of the axis. Hence the interference at $\vartheta = 90^{\circ}$ can result in the field decreasing all over the cross section except near the axis. This feature which is in fact due to the focalization, manifests itself under both strong and weak wave damping when the wave is absorbed after being many times reflected from the walls. An important consequence of this effect can be a peaked energy-deposition profile when the cyclotron absorption zone is located at $\vartheta = 90^{\circ}$.

Fig.2 shows the position of Section 1 ($\vartheta = 90^{\circ}$) with a length along the z-axis being one-eighth that of the torus. Figs.3 and 4 represent the distributions of the $|E_{\vartheta}|$ and $|E_r|$ fields summed up over the m, ℓ harmonics for the given antenna in Section 1. Here a pronounced focalization effect can be observed for the total field. The field amplitudes correspond to the power of 5 MW coupled to the plasma. As seen in Fig.4, $|E_r|$ increases essentially in the scrape-off layer, being well in excess of the $|E_r|$ value in the plasma. The high radial field at the wall can lead to the electric potential increasing in the Debye layer and hence, to greater sputtering of the wall material, arcing, etc. Therefore one has to consider the possibility of reducing the value of the radial field in the scrape-off layer. Thus, for example, the antenna systems can be used without (or with decreased) low $k_{\parallel}$ harmonics. Fig.5 shows $|E_r|$ values calculated for the same plasma column cross section and parameters as in Fig.3, but for the antenna with a shorter wavelength spectrum provided by the bipolar exciting current distribution along the z-axis. As can be seen in Fig.5, the radial field is essentially lower in the scrape-off layer (by a factor of ~ 15), with the focalization effect retained.

In the above cases the plasma density in the scrape-off layer is assumed to be zero. In reality, however, the field formation in the scrape-off layer can be influenced by the fi-

nite plasma density. Figs.6,7 and 8 present the calculations of the $|E_r|$ field on the cylinder surface of radius $r = a_{cl}$ (Surface II in Fig.2) for the antenna with the unipolar exciting current. The plasma parameters are similar to those mentioned above, but the plasma densities (n_e') in the scrape-off layer are different. Fig.6: $n_e'/n_e(0)=0$ (the above case), Fig.7: $n_e'/n_e(0)=1\%$, and Fig.8: $n_e'/n_e(0)=5\%$; $n_e(r)=\text{const}$. As is shown in Fig.6, the $|E_r|$ field reaches its maximum value at the antenna edges ($|E_{r\max}|=2.5$ kV/cm), the region of the higher field along the z-axis exceeding the antenna length. It is evident from Fig.7 that even at a rather low density $n_e'=7.1\times10^{11}\,cm^{-3}$ $|E_r|$ is essentially decreased, and at $n_e=3.5\times10^{12}\,cm^{-3}$ (Fig.8) it decreases still further, with the region of higher field values being found at the antenna edges only. It should be noted, however, that immediately at the wall (in the Debye layer) the increased value of the radial field is always retained. Yet, as the Debye layer decreases in thickness with the increasing density while E_r remains constant, the potential in the Debye layer drops and hence, the energy of particles impinging on the wall is decreased.

Conclusions:

1. In the case of using the antennae covering limited poloidal angles, the focalization effect is essentially retained even under weak FMSW damping (the wave propagating through the cyclotron resonance region is partially absorbed).
2. The antennae with long wavelength spectra covering limited poloidal angles are capable of generating high radial electric fields in the regions extending far beyond the antenna length.
3. The radial electric field at the wall can be decreased essentially through the use of short wavelength spectrum antennae.
4. The density increase observed in the scrape-off layer results in the RF potentials dropping in the Debye layer at the wall.

1. A.V. Longinov et al. Proc.Nat.Conf.Fusion Reactor Techn. (Russ), Leningrad, 23-25 June 1981, 1, p.381.
2. A.V. Longinov et al. Proc.7th Int.Conf.Plasma Phys.Contr. Nucl.Fusion Res., Vienna, 1979, 2, p.583.
3. A.V. Longinov, V.A. Tsurikov, Preprint KFTI 85-33.

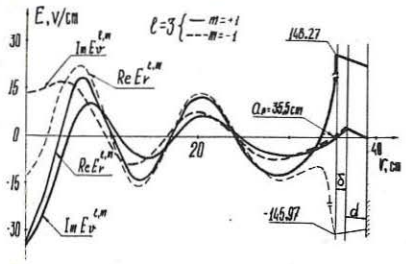

Fig.1

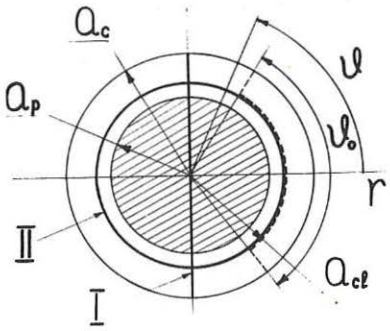

Fig.2

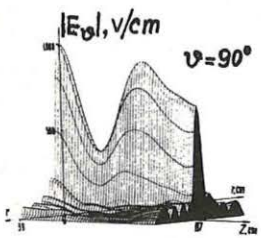

Fig.3

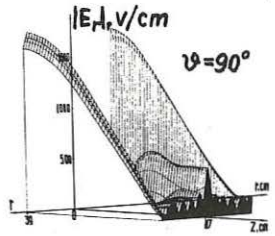

Fig.4

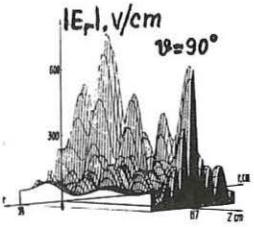

Fig.5

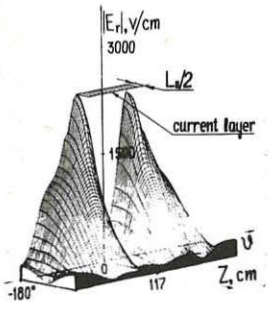

Fig.6

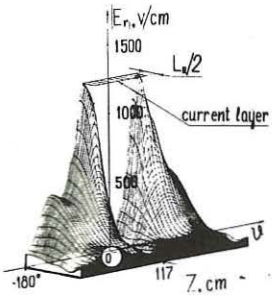

Fig.7

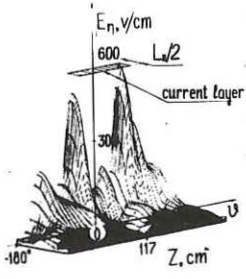

Fig.8

EXPERIMENTAL DETERMINATION OF THE ICRF POWER DEPOSITION PROFILE AND COMPARISON WITH RAY TRACING CALCULATIONS

V.P. Bhatnagar*, E. Barbato⊛, G. Bosia, M.P. Evrard*, D. Gambier**, R. Giannella***, J. Jacquinot, P.P. Lallia, M. Malacarne, K. Thomsen#, B. Tubbing+, V. Zanza⊛

JET Joint Undertaking, Abingdon, Oxon, OX14 3EA, UK
*From LPP-ERM/KMS; EUR-EB Association, 1040 Brussels, Belgium
**From EUR-CEA Association, Fontenay-aux-Roses, France
***From EUR-ENEA Association, Frascati/Roma, Italy
#From Risó National Laboratory, Roskilde, Denmark
+From EUR-FOM Association, "Rijnhuizen", The Netherlands
⊛EUR-ENEA Association, Frascati/Roma, Italy

I INTRODUCTION

A detailed knowledge of the ion-cyclotron resonance heating (ICRH) power-deposition profile is a prerequisite in carrying out a meaningful power balance in the plasma. It is also an essential input to the tokamak transport codes which predict the evolution of plasma heating.

Three ICRH antennae located on the low-field side have been energised in JET which couple power to the fast magnetosonic waves in a deuterium plasma with H+ or He^3 minority species. In this paper, ICRH power deposition profiles in JET determined both theoretically (ray-tracing) and experimentally (several methods; see below) are compared.

(i) Ray Tracing : A sophisticated ray-tracing code [1], which includes the effects of poloidal field, has been used to generate the ICRH power-deposition profiles in the D-shaped JET plasmas. The initial conditions of ray tracing are obtained by the full-wave solution of a realistic antenna plasma coupling model. The ray-tracing analysis shows that the ICRH power-deposition profiles are narrow and that the energy is deposited somewhat locally due to the large plasma parameters and large damping per pass.

(ii) Change of Slopes of Sawteeth : The RF power deposition in electrons can be estimated from [2,3]

$$P^e_{RF} = \frac{\partial W_e}{\partial t}\bigg|_{+\varepsilon} - \frac{\partial W_e}{\partial t}\bigg|_{-\varepsilon} \qquad (1)$$

where $\pm\varepsilon$ represent an infinitesimal time difference just after and before the application of a square wave RF pulse. Such a procedure assumes that the other source and sink terms (such as P_Ω, $-P_{ei}$, $-P_{rad}$ etc) remain unchanged at such short time intervals. Experimentally, the RF is square wave modulated and the difference of the slopes of a sawtooth in the electron-cyclotron emission (ECE) diagnostic of the 12-channel grating polychrometer [4] allows the determination of electron power deposition profile.

(iii) Modulation Experiments : When the antenna radiated power is amplitude modulated, the bulk temperatures in the plasma where RF power is deposited oscillate at the modulation frequency. The amplitude and phase of the oscillating signal of a temperature diagnostic at different radial positions lead to the knowledge of the power deposition profile of the additional heating [5,6]. The presence of large sawteeth in JET renders the signal analysis by correlation technique difficult especially when $\nu_m \approx \nu_{st}$, where ν_m is the RF modulation frequency and ν_{st} is the average sawtooth frequency. For $\nu_m > \nu_{st}$ or ν_m close to a harmonic of ν_{st}, the

ratio of signal to this extraneous disturbance is poor. However, when $\nu_m < \nu_{st}$, this technique gives useful results.

(a) Correlation function technique Consider the equation, $c(\tau) = \int \bar{f}(t)\, g(t+\tau)\, dt$. If $\bar{f}(\omega)$ and $\bar{g}(\omega)$ are the Fourier transforms of f and g respectively then $\bar{c} = \bar{f}^* \cdot \bar{g}$ is the Fourier transform of c. We use the discrete Fourier Transform for the data sampled at a given number of points during the time interval of interest. The analysis program computes the auto-correlation spectra and the index m of the maximum modulus of the correlation function transform. It also displays the frequency ν_m as well as the values $2\left|\bar{f}_m\right|$ and $2\left|\bar{g}_m\right|$ that are the amplitudes of the two signals oscillating at that frequency and their relative phase θ_m.

(b) BOXCAR Technique : The "Boxcar" method is used to analyse non-Gaussian random signals. In this method, each period of RF modulation is treated as an independent event and the signal behaviour on many successive events is averaged. As the sawteeth and the RF modulation are not synchronous and as the sawtooth amplitude is greater than the RF-modulated amplitude by an order of magnitude, it is necessary to eliminate the effect of the sawteeth. First, the sawteeth crashes are suppressed, and we build a long period, high amplitude single sawtooth. Then, the linear trend is removed and the remaining signal is analyzed.

II. Plasma Response to RF Modulation

If sawteeth do not change the power balance, the modulated quantities in the power balance equation can be written as

$$\begin{aligned} i\omega \tfrac{3}{2} n_e \bar{T}_e &= \bar{P}_{HF}^{(e)} + \bar{P}_e - \frac{1}{\tau_e} \tfrac{3}{2} n_e \bar{T}_e \\ i\omega \tfrac{3}{2} n_D \bar{T}_D &= \bar{P}_D - \frac{1}{\tau_D} \tfrac{3}{2} n_D \bar{T}_D \end{aligned} \qquad (2)$$

where we have neglected $\bar{P}_Q$, $\bar{P}_{rad}$ and $\bar{P}_{cx}$ (localized at the edge), $\bar{P}_{HF}^{D}$ (mainly minority heating), $\bar{P}_{ei}$ ($\tau_{ei} \approx 150$ ms $>> \tau_e, \tau_i$) and $\bar{n}_j/n_j << \bar{T}_j/T_j, j=e,i$. $\bar{P}_{tot} = \bar{P}_{HF}^{(e)} + \bar{P}_e$ is the total (modulated) power going to the electrons through the minority and by direct mode conversion. Using the modulus/ phase representation of the complex modulated quantities, we write

$$\bar{T}_e = T_{oe}\, e^{-i\theta_e} \; ; \; \bar{P}_{tot} = P_{oe}\, e^{-\Psi_e} \qquad (3)$$

Where θ_e and ψ_e are the relative phases $\omega.\tau.$ to the RF power signal at the generator. This leads to the following expressions for amplitude and phase relating the measured quantities T_{oe} and θ_e to the power density in the electrons

$$P_{oe} = \tfrac{3}{2} n_e T_{oe} \frac{\omega}{\sin \phi_e} \quad \text{and} \quad \phi_e - \theta_e = -\Psi_e \qquad (4)$$

where we have defined a phase angle ϕ_e such that $\tan \phi_e = \omega\tau_e$ (5)

The local electron energy confinement time is estimated from the local plasma transport considerations to be as

$$\tau_e = \langle R \rangle^2 / \left(j^2_{0,1} \cdot D_e\right) \qquad (6)$$

where $j_{0,1}$ is the first zero of Bessel function $J_o(r)$, D_e is the electron diffusion coefficient (at the centre of the plasma) and $\langle R \rangle$ is an average radius of the zone of interest. For the ions, we obtain similarly

$$P_{oD} = \tfrac{3}{2} n_D T_{oD} \omega / \sin\phi_D \quad \text{with } \tan \phi_D = \omega\tau_D \text{ and } \tau_D = \frac{\langle R \rangle^2}{j^2_{0,1} D_D} \qquad (7)$$

III. Results

We present results of analysis of modulation experiments in which the antenna radiated power was square wave modulated at 5 Hz. The electron cyclotron emission (ECE) from the plasma was used as the T_e diagnostic by detecting the signal by Michelson interferometer [7] and a 12 channel polychrometer [4]. The correlation technique has been applied to the two diagnostics and the signal amplitude and phase for the two is plotted in Fig. 1 as a function of the major radius. The signal for the same shot was also analysed by using the boxcar technique outlined above and the peak amplitude of the temperature signal is plotted against the major radius at different time interval in a 3-D plot shown in Fig. 2.

Using the formulation presented in Section 2, the estimated e-power deposition profile points deduced from the correlation technique are shown in Fig. 3 for the two processing of the ECE signals. The power density points were obtained by estimating the value of the ϕ_e (from eq. 5) in which $\langle R \rangle$ and D_e were taken to be 0.25 m and 1 m^2/s respectively) which is found to be nearly the same as θ_e measured at the centre with its value $\theta_e = 0.36$ rad. The points derived from the change of slope of sawteeth at a switch ON/OFF phase of the modulation are also shown. For the same shot in which the power coupled by the antenna was 1.25 MW with He^3-minority, prediction of the p-d-profile from ray-tracing are also shown where the predominantly absorbed power by the minority species is redistributed to electrons and background ions based on the Stix model [8]. In this case, at the low He^3-minority power density, a significant fraction of the power is transferred to the ions. The correlation technique performed on the neutron diagnostic signal gave the central ion-power density which has relatively large error bars. The value of central ion diffusion coefficient is estimated to be 3 m^2/s. Experimentally derived e-power deposition profiles by several methods are found to be in good agreement among each other as well as with ray tracing.

IV. Summary and Conclusions

ICRH power-deposition profiles determined by (a) Ray tracing, (b) Change of slopes of a sawtooth of an ECE signal and (c) Modulation experiments analysed by correlation technique and Boxcar technique, have been compared for a JET deuterium plasma in the minority heating scheme. The results of power densities obtained by different methods are found to be in good agreement . The RF power-deposition profile are found to be well localized and are relatively narrow with respect to the size of the plasma. When the modulation frequency is increased from 5 to 25 Hz, the plasma temperature response goes down and the signal to noise ratio is worse. The presence of the strong sawteeth complicates the data analysis. The power-deposition profile presented have been obtained from the data when the modulation frequency was 5 Hz. These results suffer from the effect of energy diffusion which broadens the deposition profile. The effect of sawteething, equipartition etc have been ignored.

References

[1] V.P. Bhatnagar et al, Nuclear Fusion, 24 (1984) 955
[2] Equipe TFR, Report EUR-CEA-FC-1046 (1980), Fontenay-aux-Rose, France
[3] D.J. Gambier et al, 12th Conf. Plasma Phys., Budapest, (1985) ppr. 394
[4] B.D.J. Tubbing, ibid, paper 142
[5] E. Barbato, R. Giannella, Physics Letters, 110A, No. 6 (1985) 309
[6] G.L. Johns et al, Nuclear Fusion, 26 (1986) 226
[7] A.E. Costley et al, 12th Conf. Plasma Phys., Budapest, (1985) ppr. 186
[8] T.H. Stix, Nucl. Fusion, 15 (1975) 737

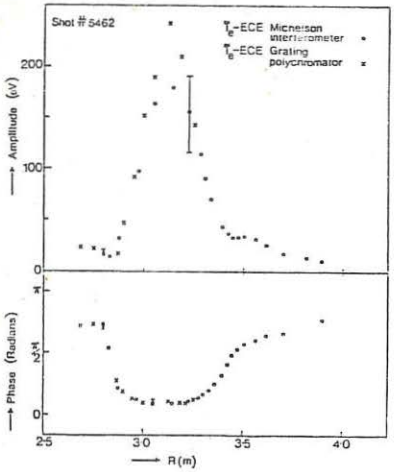

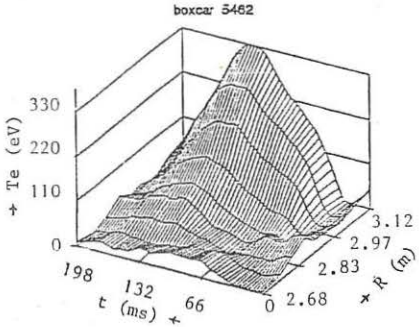

Fig. 2 The modulated electron temperature obtained from the boxcar technique is shown as a function of time for different positions along the major radius in a 3-D plot.

Fig. 1 Amplitude and phase θ_e of the Fourier transform at the modulation frequency for signals from two different ECE electron temperature diagnostics versus the major radius.

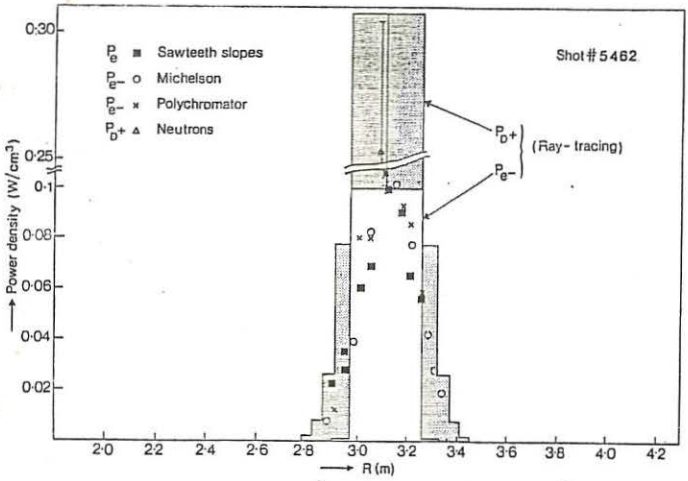

Fig. 3 Profiles of the RF power delivered to electrons as measured from sawteeth slopes (■) and from the correllation technique (o and x). An estimated value for the RF central power density to the ions deduced from the neutron signals is also shown (Δ). The slab deposition profiles shown are computed by the ray-tracing code.
$NH_e^3/N_D = 0.18$, $B_o = 3.08$ T, $I_p = 2.7$ MA, $f = 29.9$ MHz, $T_{eo} = 3.2$ keV, $T_{io} = 2.2$ keV, $N_{eo} = 2.15 \times 10^{13}$ cm^{-3}, $P_{RF} = 1.25$, $P_e = 0.21$, $P_D = 0.79$ MW, 0.25 MW is assumed not to be absorbed in the centre of the plasma.

EFFECT OF OFF AXIS ICRF POWER DEPOSITION IN JET

F. Sand, **B. Beaumont, *V.P. Bhatnagar, M. Bures, S. Corti
J. Jacquinot, P.P. Lallia, A. Tanga

JET Joint Undertaking, Abingdon, Oxon, OX14 3EA, UK
** From EUR-CEA, Fontenay-aux-Roses, France
* From LPP-ERM/KMS; EUR-EB Association, 1040 Brussels, Belgium

1. Introduction

First tests were made in JET to assess off axis power effects on:
- confinement (including possible heating optimization q = 2 stabilization)
- sawteeth behaviour
- profile control.

The large dimension of the plasma cross section (2.50 m x 4 m) compared to the antennae dimensions and to the perpendicular wavelength of the wave together with a significant focalisation provide good localisation of the power deposition. The parameter range provided single pass absorption and little reflection.

2. Description of the Method

The JET RF system can cover a broad band in frequency (25-55 MHz) but in discrete steps requiring time consuming adjustments. It was therefore decided to alterna tively fix the frequency at a given value (~33 MHz) and to slip the resonant layer through the plasma cross section by a continuous change of the main toroidal magnetic field. The ramp duration is 10s and the magnetic value decreases either from 3.4 T to 2.1T (Case A, He^3 minority, 3 MA) or from 2.6 to 1.4T (Case B, H minority, 2 MA). The 4s RF pulse is superimposed at various times (45-49 or 48-52 or 51-55) to cover the full plasma cross section (Fig. 1).

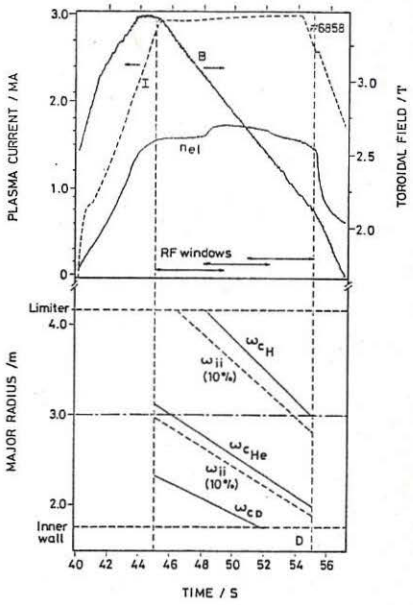

Fig. 1 Evolution during the ramping of the field of resonnant layer position for case A-(3.4—2.1T)

3. Localisation expected

The elements playing a role in the broadening of the power deposition are mainly

(a) the natural thickness of the absorption zone.

(b) the difference in frequency at which each antenna is tuned (32.4 to 33.5 MHz) which scatter the resonant layers over 10 cm approximately.

(c) the vertical spread which, despite the focalisation, distribute the power on several successive magnetic surfaces.

The final distribution extends therefore over a domain whose thickness along R is typically between 30 and 50 cm and the expected effects are smoothed accordingly.

4. Experimental results

4.1 We have already reported /1/ that the dimensions of the sawteeth are dramatically increased when we heat the plasma inside the q = 1 cross section. This effect disappears when the resonant layer is moved outside q = 1.

4.2 Fig. 2 gives the $\Delta T/\Delta P$ plotted versus the position of the resonance layer.

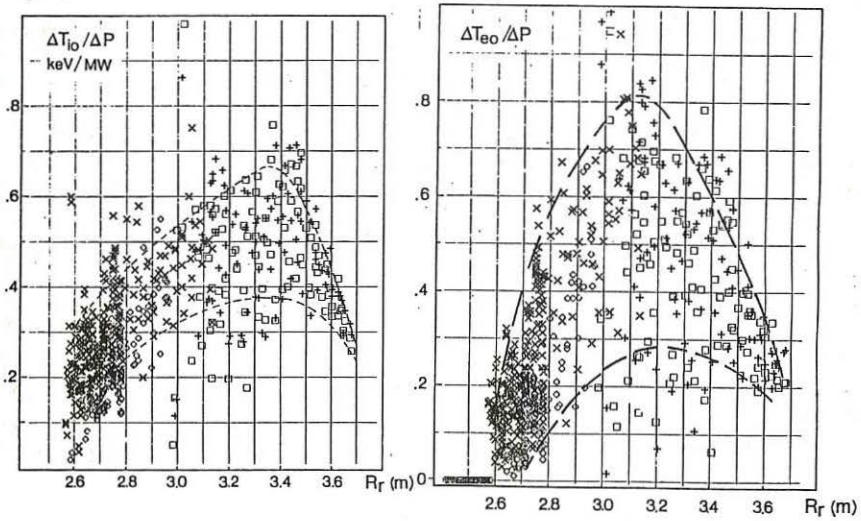

Fig. 2 : Ion and Electron temperature variation versus the position of the resonance layer

When plotting the total energy content of the plasma versus total power $P_{TOT} = P_{ohmic} + P_{RF}$ we find a linear dependence which could be described by : $W_{TOT} = \tau_{Eo} P_{\Omega o} + \tau_a (P_{TOT} - P_{\Omega})$. We have reported (Fig. 3) for different conditions the τ_a-value versus the position of the resonance

layer. The resulting distribution exhibits a broad maximum in the central region (~ q < 1) and decreases outwards significantly. When moving from condition A (3.4 → 2.1 T, He^3 minority and I_p = 3 MA) to condition B (2.6 → 1.4 T, H minority and I_p = 2 MA), it is a striking result to find all the values merging in the same general curve.

Fig. 3 τ_a versus position of the resonnant layer

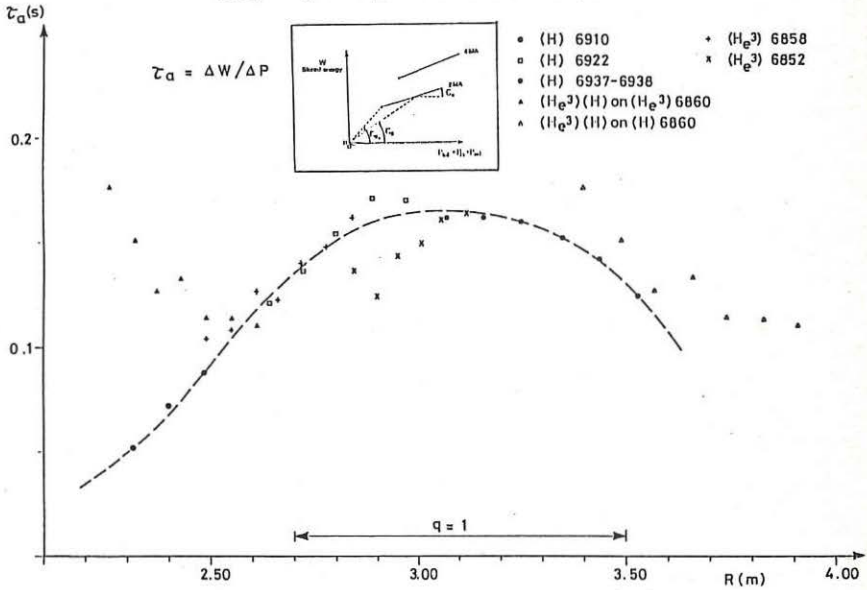

Several factors complicate the interpretation namely:

(a) The minimum mean hydrogen content in JET is around 5% of the Deuterium majority. Accordingly when the He^3 heating takes place at radius smaller than 2.8 m a second minority heating zone (H minority) enters the plasma from the LFS. Consequenly, when the magnetic field decreases an increasing heating efficiency on (H) competes with the decreasing heating efficiency on He^3.
(b) An adverse consequence of the RF heating is a moderate release of impurities increasing the radiated power which is thus more pronounced at the end of the RF pulse. Together with the density increase, this results in a decrease on τ_a at the later times and complicates the interpretation.

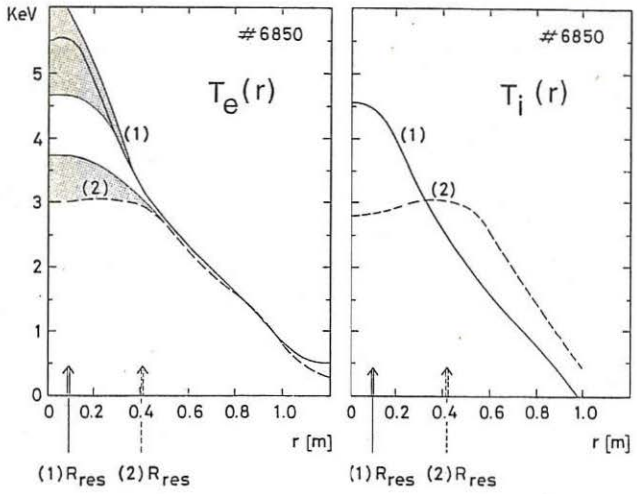

Fig. 4 Electron and Ion temperature profiles with on axis (1) and off axis (2) RF heating

4.3 Significant effect on off axis heating on T_i -profile have been identified (Fig. 4). On the other hand, no change in T_e-profile outside q = 1 could be attributed to off axis heating despite the obvious mean increase observed in this case. This is in agreement with the so-called "profile consistency" observed on JET.

4.4 No evidence of any beneficial effects can yet be reported when heating around q = 2 surface. One could even discern an increased sensitivity to disruption possibly connected to impurity release when heating on the HFS q = 2 surface. This should however be reconsidered carefully with steady state condition before definite conclusions could be drawn.

Conclusion

So far, off axis heating did not achieve any major favourable results. The best heating efficiency has been obtained when the resonance zone is located close to the magnetic axis.

Reference:

/1/ ICRF Studies on JET - J. Jacquinot et al. 12th Eur. Conf. on Controlled Fusion and Plasma Physics, Budapest Sept. 1985

A SHORTWAVE FIR-TREE ANTENNA FOR ICRF HEATING OF PLASMA IN THE T-10 TOKAMAK

A.V.Longinov, E.I.Kolosenko, G.A.Miroshnichenko, G.Ya.Nizhnik, V.A.Tsurikov, A.A.Chmyga

Institute of Physics and Technology, the Ukrainian Academy of Sciences, Kharkov 310108, USSR

A fir-tree type of an antenna has been used in ICRF plasma heating experiments in the T-10 tokamak [1,2]. The peculiar feature of this antenna is its low impedance and a large radiating surface, which makes feasible high RF power regimes. The unipolar distribution of the exciting current on the radiating surface ensures a wide K spectrum. As shown in [3,4], the employment of the antenna with this spectrum enhances the role of the conversion of fast waves into slow ones when fast magnetosonic waves (FMSW) are excited on the low magnetic field side (LFS), and also causes an essential radial electric field increase at the chamber walls which may lead to an enhanced impurity influx in the discharge.

This report is concerned with the main characteristics of a new fir-tree antenna that differs from the previous one in a narrower and, which is very essential, a shorter K spectrum. The antenna with a partially removed electrostatic screen located in the T-10 vacuum chamber dummy is shown in Fig. 1, and its arrangement (as viewed from the plasma side) is shown schematically in Fig. 2. The antenna consists of the basic 1 and additional 2 radiating surfaces and an electrostatic screen 3, the screen conductors being parallel to the magnetic field [1]. The conductors of the surfaces 1 and 2 are inclined at $\sim 20^{\circ}$ to the chamber axis. The shortwave $K_{\parallel}$ spectrum results from the variation of this angle of inclination along the chamber axis. For the bipolar distribution the amplitudes of the harmonics with low toroidal numbers $\ell = K_{\parallel} R$ are small. This results in the decrease of the radial electric field near the chamber wall by a factor of 15 [4] as compared with a unipolar current distribution in the antenna [1].

Because of a relatively small width of the antenna ($\sim$ 50cm),

the $K_{\parallel}$ spectrum of the exciting current I_{ϑ}^{ℓ} appears to be excessively shifted to the region of larger $K_{\parallel}$ (Fig. 3). Therefore the intense harmonics lie in the region where the active impedance $Z_a(\ell)=\sum Z_a(m,\ell)$ (m is the poloidal number) is essentially decreased. As calculations show, this causes the active impedance decrease, especially for low plasma densities. This is seen from Fig. 4 which shows the average local impedance $\overline{Z}_a$ as a function of the plasma density for the unipolar (curve 1) and bipolar (curve 2) antennas. Therefore, to keep a high efficiency of the antenna, we have used a new design of the radiating surface, namely, a double current-carrying surface (Figs. 1,2). The main (1) and additional (2) surfaces are formed by a set of inclined conductors. Now that the current components I_{ϑ} responsible for FMSW excitation are directed in a consistent manner on each surface, it is possible to increase the excitation efficiency by a factor of 4.

Distributions of the local active impedance Z_a on the antenna surface have been studied for the conductor shape shown in Fig. 2. Figure 5a shows the unfolded current surface with the local impedance isolines. The variation of the radiating surface conductor inclination illustrated in Fig. 2 is not optimum because the contribution to the impedance of some part of the current surface, where the direction of the conductors changes, is low and can even be negative. The optimization of the current distribution has allowed us to eliminate the regions with $Z_a<0$ and to increase the antenna efficiency by>25% (Fig. 5b). The current distribution has been optimized by changing the shape of the conductors (Fig. 6).

Other elements of the new antenna (the transmission line, matching circuit, etc.) remained the same as in [1], frequency and power characteristics also being similar to those of the previous antenna. Thus, the employment of the new shortwave antenna allows one:

a) to suppress the excitation of asymmetric modes with a low toroidal number ℓ which are responsible for the radial electric field increase at the chamber wall;

b) to eliminate or essentially diminish the fast-to-slow wave

conversion effects which lead to heating efficiency reduction and to the enhanced influx of impurities due to the arrival of the slow wave to the chamber surface on the inner side of the torus [2,3] (this conclusion follows from Fig. 3 which gives a plot of the ratio of the RF slow wave power $P_s(\ell)$ generated in the conversion region to the RF power $P_{in}(\ell)$ radiated by the antenna [3]; as is seen from the figure, the conversion effects are essential both for D and D+H plasmas only for the antenna [1] with a long wavelength spectrum);

c) to confirm or to reject the theoretically predicted important role of conversion effects in the wave excitation on the low magnetic field side basing on the analysis of experimental results obtained with different antennas.

It should be noted that for the antenna presented the heating method with heavy-ion admixtures [2,3] becomes, according to theory, inefficient because of the suppression of the conversion effects in the LFS case.

References

1. A.V. Longinov et al., Trudy II Vsesoyuznoj konferentsii po inzhenernym problemam termoyadernykh reaktorov (Proc. Nat. Conf. Fusion Reactor Techn.) (Russ) Leningrad, 23-25 June (1981) Vol. 1, p.381.
2. A.V. Longinov, K.N. Stepanov, In:"Vysokochastotnyj nagrev plazmy" (RF heating of plasma) (Russ), Gorky, Institute of Applied Physics, the USSR Academy of Sciences (1983) p.105-210.
3. A.V. Longinov, S.S. Pavlov, K.N. Stepanov, XII European Conference on Controlled Fusion and Plasma Physics, Budapest, 2-6 September 1985, Vol.2, p.156.
4. A.V. Longinov, V.A. Tsurikov, Preprint KFTI 85-33 (1985).

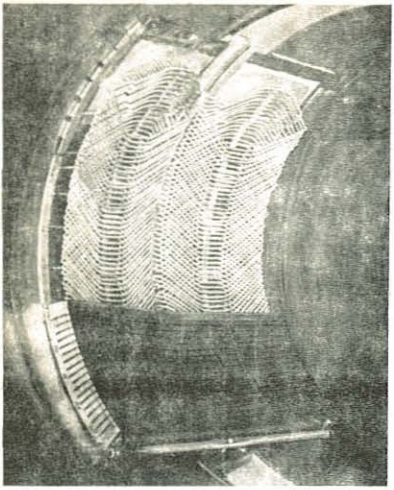

Fig.1

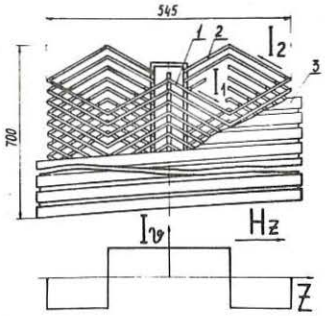

Fig.2

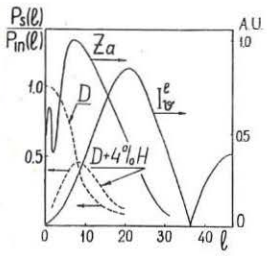

Fig.3

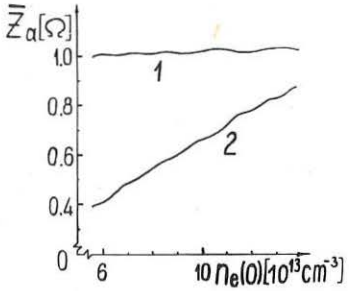

Fig.4

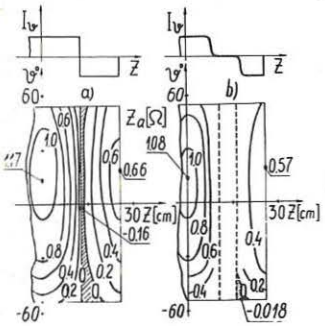

Fig.5

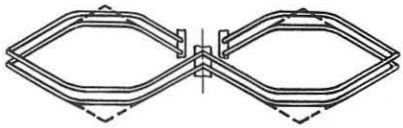

Fig.6

Electron Cyclotron Heating

ELECTRON CYCLOTRON HEATING ON TFR

TFR Group & FOM ECRH Team, presented by J. Tachon
TFR Group, Association EURATOM-CEA sur la Fusion, DRFC CEN,
BP 6, 92260 Fontenay aux Roses, France
FOM-Instituut voor Plasmafysica, Rijnhuizen, Nieuwegein, The Neterlands

ABSTRACT

We present the results of the ECR experiment with emphasis on electron heating. Up to 500 kW were coupled to the plasma at 60 GHz. Scans in electron density, plasma current and toroidal field are presented along with energy balance and transport analysis. The effect on sawtooth behaviour is also presented.

INTRODUCTION

The full ECRH power, 3 x 200 kW at 60 GHz, 100 ms pulses has been routinely injected into TFR (R=98 cm, a=18 to 20 cm, carbon limiters) from september 1985. Microwave power is launched in O-mode from the outside; one of the antennas has an 84° toroidal angle, the two others face a twist reflector which converts the transmitted power into X-mode <1a,1b>. Although MHD control and suprathermal behaviour have been studied <1b,2>, we will present here only heating and transport studies. As will be discussed later, technical modifications inside the vacuum vessel have led to a different behaviour, even in the ohmic regime, since the end of 1985.

CENTRAL HEATING

With a toroidal field on the axis equal to 21.4 kG, the central electron temperature is sharply peaked inside q=1. Fig 1 shows the dependance with central electron density of Te. The lower values given by the Si-Li detector and the superheterodyne 2ωce measurements can be linked to the fact that they measure one point which, due to the large plasma displacements, is not necessarily the maximum, whereas the Michelson gives the whole profile . Below $Ne(0)=1.7\ 10^{13}\ cm^{-3}$ the electron distribution function becomes non maxwellian and 2ωce temperature measurements are therefore uncertain. At high density diffraction becomes important, and heating is less localised.

Fig 2 shows the variation of the global energy confinement time with

average density at full power. The weight of the central temperature peak is negligible. An increase of τe with Ne is observed, although smaller with ECRH than in the ohmic regime. Results with one or two gyrotrons only are close to this curve Energy balance and transport studies have been done routinely using a simple NxOD code and, for a few shots, the more elaborate MAKOKOT simulation code. The power deposition profile calculated at the first pass ‹3› has been used in the simulation to study the profile evolution. The main result is that the anomalous electron conductivity Xe which in ohmic regime scales as $Xe \approx 1/Ne.q.Te^{3/4}$ ‹4› has a different temperature dependance in ECRH namely $Xe \approx r.Te^{1/2}/R.Ne.q$ ‹5› : see Fig 3. The simulations also show that the central density pump-out is explained by the decrease of the neo-classical pinch velocity as mentionned previously ‹6› and by the $Te^{1/2}$ dependance of the particle diffusion coefficient (D=2.Xe/3). However enhanced recycling due to power losses on the vessel partially cancels this effect, leading to quasi constant average density.

Dependance with plasma current was striking in 1985 (before the installation of a stainless steel calorimeter on the inner wall) and much less obvious since then. Previously two regimes were observed in ohmic plasmas at 21.4 kG: below 105 kA, no MHD activity was observed, and the confinement time was ≈ 8 ms, whereas strong saturated m=2, n=1 and m=3, n=1 MHD activity appeared above this limit, leading to confinement times of the order of 4 ms. With ECRH, confinement times fell even with 100 kW in the low current case, whereas they stood essentially unchanged in the MHD regime. Since the beginning of 1986, the good ohmic confinement regime has disappeared, as well as the high current regime with saturated MHD: modes tend to be either absent or explosively growing, the ohmic as well the ECRH confinement time are roughly independent from the plasma current between 80 and 130 kA, respectively τe = 6 ms and τe = 3 ms for an average density of 1.5 10^{13} cm^{-3}.

NON CENTRAL HEATING AND SAWTOOTH BEHAVIOUR

Although central temperature is sharply maximum for precisely central heating, τe dependance is much weaker as has been previously found in T10 ‹7› although the "flat top" reaches only r=a/4. Fig 4 shows τe as a function of $B\varphi$, made with central density of 2. 10^{13} cm^{-3}, and Ip=87 kA. The low density insures that the dependance is not mainly due to absorption and refraction problems. Moreover at this values of plasma current, MHD activity is negligible and an extended stochastic edge region is unlikely to explain the sharp drop observed when heating is applied off center by more than 6 cm.

Sawtooth behaviour has been studied in detail for ohmic plasmas, with Ne=1.5 10^{13} cm^{-3}, the period is typically 0.7 ms with an m=1, n=1 precursor at 10 kHz growing during 0.3 ms. When the power deposition is away from the q=1 surface, either inside (central heating) or outside, no modification of the sawtooth behaviour is observed, in sharp contrast with T10 and PDX observations. Conversely, when the power is deposited at the q=1 radius, strong changes are seen: with one gyrotron (200 kW) the q=1 island grows more slowly; with three gyrotrons, the m=1 oscillation reaches a nearly saturated state, and the sawtooth lengthens to about 2 ms, with an erratic behaviour reminiscent of complex sawteeth observed in larger Tokamaks ‹8› (see Fig. 5). It seems that triggering of the internal disruptions is strongly affected by local modifications of profiles near the q=1 surface.

CONCLUSION

It is striking to note that the degradation of confinement time with ECRH is nearly maximum already at low power. Subsequent increases of ECRH power do not degrade τ_e much further. The R.grad(Te) ‹ 13 keV limit ‹9› is fulfilled outside the q=1 surface, although much larger gradients are observed inside.

REFERENCES

‹1› FOM ECRH Team & TFR Group, 12th ECCFPP, Budapest 1985, EPS Vol2 60 (1985).
TFR Group, J. Hoekzema et al., "Experimental results of ECRH in TFR", 5th Int. Workshop on ECE and ECRH, San Diego, 1985.

‹2› TFR Group, FOM ECRH Team presented by L. Jacquet and M. Pain, "Numerical and experimental study of the electron distribution function in TFR with and without ECRH", this conference.

‹3› R. CANO et al., EUR CEA FC1170 (1983).

‹4› C. MERCIER et al., Nucl. Fus. 21 291 (1981).

‹5› B. KADOMTSEV, O. POGUTSE, JETP Letter 39 269 (1984).

‹6› Y. DNESTROVSKII et al., Sov J Plasma Phys 10 137 (1984).

‹7› V. ALIKAEV et al., 10th PPCNRF, London 1984, IAEA Vol1 419 (1985).

‹8› D. CAMPBELL et al., 12th ECCFPP, Budapest 1985, EPS, Vol1 131 (1985).

‹9› TFR Group presented by L. Laurent, 12th ECCFPP, Budapest 1985, in Plasma Phys., Vol 28 Num 1A 85 (1986).

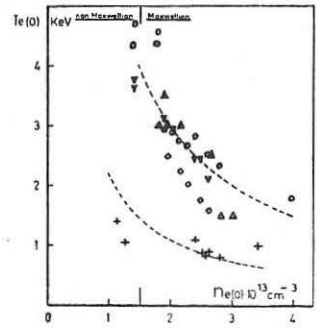

FIGURE 1: Temperature on magnetic axis versus central density
-Ohmic regime: Thomson scattering +
-460 kW ECRH: Michelson interferometer ○
Superheterodyne (2ωce) ▽
Soft X-rays with absorber △
Si-Li detector off center ◇

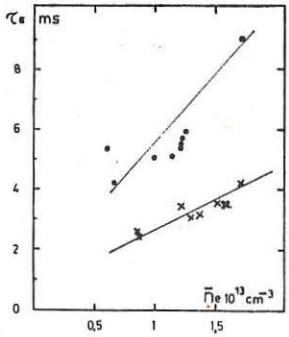

FIGURE 2: τe versus average density Ne
-Ohmic regime: ●
-460 kW ECRH : ×

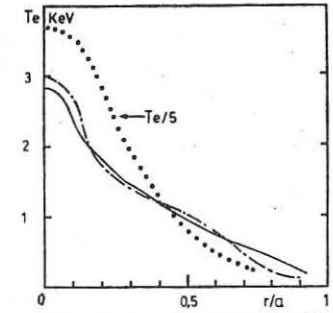

FIGURE 3: Electron temperature profile computed 40 ms after the beginning of ECRH pulse:
-with $\tau e = 1/Ne_{\alpha}.Te^{3/4}$: • • • •
-with $\tau e = r.Te^{1/2}/Ne.q$: ——————
-from Thomson scattering: —·—·—·—

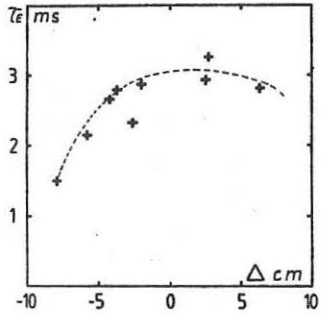

FIGURE 4: τe versus ECRH shift
Δ = Rresonance - Rmagn. axis
(Pecrh=460 kW, PΩ=100 kW)

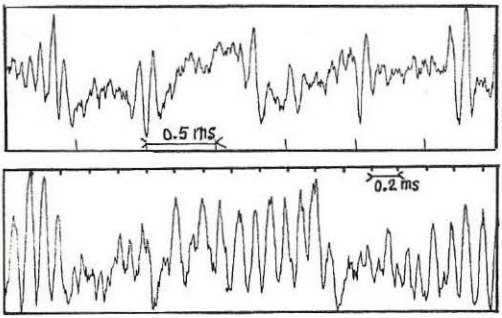

FIGURE 5: Sawteeth on soft X-rays

-at r=3 cm in the ohmic regime

-at r=3 cm with 460 kW ECRH on q=1

PERFORMANCE OF THE 70 GHz ECRH SYSTEM ON W VII-A

R. Wilhelm, V. Erckmann, G. Janzen, W. Kasparek,
G.A. Müller. P.G. Schüller, M. Thumm
Institut für Plasmaforschung, Universität Stuttgart, Stuttgart, W. Germany

W VII-A Team*
Max-Planck-Institut für Plasmaphysik, EURATOM-Assoc., Garching, W. Germany

1. Introduction

During a three year period, extensive ECRH investigations were performed on the Garching W VII-A stellarator. The experiments were started in 1983 using a single 28 GHz/200 kW/40 ms pulse gyrotron and were continued with a 70 GHz/200 kW/100 ms system until November 1985. In both cases, initial experiments were started by radiating the unpolarized gyrotron waves (mainly the TE02 mode) through an oversized circular waveguide (length almost 30m, including one 90°-bend) directly into the torus. In further steps, the TE02 wave was transformed into the almost perfectly linearly polarized HE11 hybrid mode in the conversion sequence TE02→TE01→TE11→HE11 [1,2]. The resulting narrow millimetre-wave beam was launched perpendicularly to the magnetic field from the low-field side in O-mode orientation ($\vec{E} \parallel \vec{B}$) for heating at the fundamental frequency and in X-mode polarization ($\vec{E} \perp \vec{B}$) for harmonic heating [3]. Almost 20,000 plasma discharges (approximately 8,000 at 28 GHz and about 11,000 at 70 GHz) resulted in a lot of information concerning physics and techniques of ECRH applications. A summary of the recent physical results is given at this conference*, while the following sections describe the technical features and the performance of the 70 GHz system.

2. Microwave Source

At either frequencies (28 GHz, 70 GHz) commercial pulse gyrotrons were used. Careful control of the various parameters (magnetic field geometry, gun anode voltage, collector voltage and current of the electron beam) turned out to be the basic requirement for stable tube operation at the ultimate parameter set for maximum output power at highest achievable mode purity. The instability of the parameter settings has to be in the range of $\leq 10^{-3}$. High precision high voltage supplies for the collector voltage (80 kV) (developed at IPP Garching) and the gun anode voltage (developed by IPF Stuttgart) were used [4]. Programming the gun anode voltage allows a fast modulation of the gyrotron microwave power (0-10 kHz). Square wave modulation of the gyrotron output power (frequency range 100 to 600 Hz at 10-30% modulation degree) allowed heat wave experiments on the plasma to analyze thermal transport [5].

3. Transmission Line Components

Low-loss power transmission from the microwave source to the plasma device and mode transformation to achieve a narrow and linearly polarized beam are basic requests for optimum ECRH applications. For this purpose various waveguide components are required, which were developed and systematically improved by the IPF Stuttgart. The following table gives an overview of the

---

*) see V. Erckmann et al.: "ECRH in the Wendelstein VII-A Stellarator", invited paper at this conference.

basic components in the 70 GHz transmission line and their purpose.

component	waveguide mode	purpose	typical losses
(gyrotron)	≈ 95% TE02	(power source)	≤ 5% TE03,TE13
down-taper	TE02	reduction of gyrotron output waveguide diameter from 63.5 mm to 27.8 mm	< 0.1%
corrugated bend	TE02	gradual 90°-bend with sinusoidal curvature	≤ 1.5%
mode converter	TE02→TE01	transformation into low-loss transmission mode	0.5%
mode filter	TE01	attenuation of spurious TEmn (m≠0) modes by 90-99%	≤ 2%
mode converter	TE01→TE11	transf. into almost linearly polarized mode	≤ 6%
mode converter	TE11→HE11	transf. into optimum lin. pol. hybrid mode	1.7%
corrugated up-taper	HE11	enlargement of waveguide diam. from 27.8 to 63.5 mm	≤ 0.3%
(barrier window)	HE11	(torus window)	
antenna waveguide	HE11	corrugated stainless steel w.guide for HE11 launching	< 0.1%

The losses indicated in the table were determined experimentally for the individual components in specific low-power tests. All experimental values were found to be in very good agreement with the theoretical calculations [1,2].

According to the table there are still two major contributions to the overall power loss: the content of spurious modes of the gyrotron (which can not be reconverted) and the losses of the TE01→TE11 mode converter. With respect to the first point, improvements can be expected for future gyrotrons. The most critical converter, on the other hand, has been remarkably improved by a new computer-aided design [6]. The measured losses of 2.7% essentially result from the ohmic attenuation in the transducer. Besides a further conservation of microwave power the reduction of the spurious-modes level in the most critical last section of the transmission line will be the main advantage of the new component. This novel TE01→TE11 mode transformer will be used in the transmission lines of the 70 GHz/1 MW ECRH system on the future W VII-AS stellarator.

4. Mode Measurements and Power Calibration

Fast real time power measurements in the various waveguide modes are indispensable for gyrotron tuning (with respect to maximum power at highest obtainable mode purity) and for ECRH experiments. This open problem was solved by a novel instrument ("k-spectrometer" [7]), which indicates the different modes and their direction of propagation in the form of an optical spectrum.

As an example Fig. 1 shows the wavenumber spectrum of the first three axisymmetric modes TE01 to TE03 produced in a low-power component test line. The logarithmic plot simultaneously demonstrates the high resolution of thespectrometer as well as the high quality of the inserted mode converters.

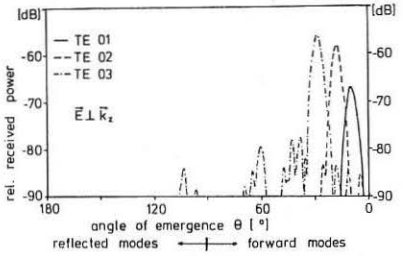

Fig.1: Spectra of TE01, TE02 and TE03 modes measured with the k-spectrometer at 70 GHz (low-power measurement).

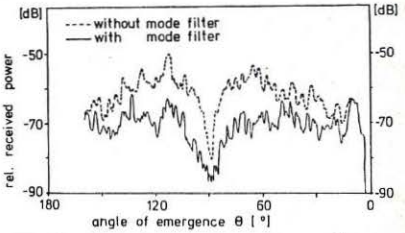

Fig.2: Multi-mode spectrum (dashed curve) of both forward and backward travelling waves produced by reflection of a TE01 wave from a crumpled aluminium foil. Attenuation of asymmetric modes by insertion of a corrugated-wall mode filter (solid curve).

Further applications of the instrument are shown in Fig. 2: Reflections of a low power TE01 wave incident on a crumpled aluminium foil in the waveguide generate a dense spectrum of forward and backward travelling waves (dashed curve). These waves – except the one in the original TE01 mode – are strongly damped after insertion of a mode selective filter as used in the high-power transmission line (solid curve). During the high power ECRH experiments a k-spectrometer was inserted in the TE01 section of the transmission line. This instrument served as a TE01 power monitor in the forward direction and allowed the optimization of the gyrotron operational parameters. A second receiver horn mounted to the spectrometer was positioned to measure reflected high order modes giving a safety switch-off signal in cases of too strong plasma reflections and/or waveguide arcing.

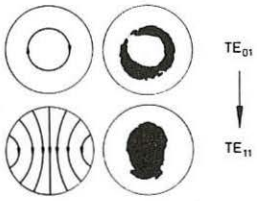

Fig.3: Thermographic burn patterns produced by the TE01 and TE11 modes which were successively generated from the TE02 gyrotron output mode (mode purity ≈ 95%) at 70 GHz (170 kW, 1ms).

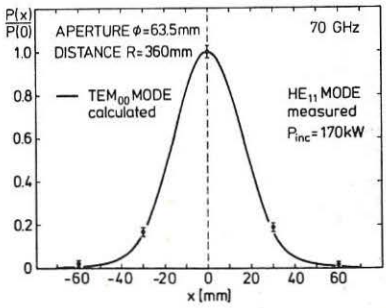

Fig.4: High-power measurement (170kW) of the HE11 mode H-plane near-field pattern at 70 GHz compared with the theoretical Gaussian mode.

During high-power operation the rather pure mode composition can be deduced from burn patterns of thermographic paper. Fig. 3 shows patterns obtained after the TE02→TE01 converter and at the output of the TE01→TE11 transducer, respectively. Besides the characteristic shapes of the main modes the presence of small fractions of asymmetric modes can be seen in both cases. Measurements with the k-spektrometer and with stacked thermographic papers revealed some content (≈5%) of TE03 and TE13 modes at the gyrotron output. Nevertheless, the resulting microwave beam radiated into the torus is of high quality as verified by direct measurements inside the torus vessel. The incident power was measured by 5 pick-up antennas mounted to the inner torus wall opposite to the incoming waveguide. Fig.4 gives a comparison of experimental values with the corresponding theoretical TEM00 wave power distribution indicating the very good agreement. The measurements also show the small spread of the polarized HE11 beam at a distance of 360 mm from the aperture.

Absolute power calibration was performed using newly developed calorimetric loads [8]. In these loads an organic absorber fluid (octanol) is used, which has an appropriate power absorption length in the cm-range (compared to only 0.15 mm at 70 GHz for water). Combining this with an optimized geometry power reflections could be reduced to about −30 dB. This new absorber also allowed for the first time absorption and calibration of the concentrated HE11 output beam. In very good agreement with the previous low-power calibrations of the individual waveguide components (table in section 2) an overall efficiency of almost 90% was measured for the entire transmission system.

5. Conclusions

Safe and reliable operation of a 70 GHz ECRH system has been demonstrated in a large number of plasma discharges. The optimized high-power microwave components (tapers, bend, mode transformers, mode selective filters) allow a highly efficient mode transmission and plasma irradiation with a narrow, linearly polarized beam. The overall efficiency was almost 90%. The available power at the antenna mouth in the HE11 mode was 170 kW (at approx. 190 kW gyrotron output). Specific microwave diagnostic instruments (k-spectrometer, calorimetric loads) turned out to be indispensable tools for test purposes and ECRH experiments as well. The present 70 GHz/100 ms system is now being upgraded by another four long-pulse transmission lines, each containing two further corrugated bends with a total of approximately 3% additional conversion losses. The new system with 1 MW total microwave power is expected to have a similar efficiency as the described W VII-A transmission line due to the improvement of the efficiency of the TE01→TE11 mode converters.

References

[1] M. Thumm et al., Proc. 4th Int. Symp. Heating in Toroidal Plasmas, Rome, 1984, Vol. II, p. 1461.
[2] M. Thumm et al., Int. J. Infrared and Millimeter Waves, 6 (1985) 459.
[3] V. Erckmann et al., Proc. 12th European Conf. Plasma Physics and Nuclear Fusion, Budapest 1985, Contr. papers, Part I, p. 385.
[4] G. Müller et al., Proc. 13th SOFT, Varese, 1984, Vol. II, p. 811.
[5] H.J. Hartfuß et al., Proc. EC-5 Int. Workshop on ECE and ECRH, San Diego, 1985, in press.
[6] M. Thumm et al., Proc. EC-5 Int. Workshop on ECE and ECRH and Gyrotron User/Developer Meeting, San Diego 1985, in press.
[7] W. Kasparek and G.A. Müller, Conf. Digest 10th Int. Conf. Infrared and Millimeter Waves, Lake Buena Vista, 1985, p. 238.
[8] P.G. Schüller et al., Conf. Digest 10th Int. Conf. Infrared and Millimeter Waves, Lake Buena Vista, 1985, p. 160.

NUMERICAL AND EXPERIMENTAL STUDY OF THE ELECTRON DISTRIBUTION FUNCTION IN T.F.R WITH AND WITHOUT E.C.R.H.

TFR - Group
FOM ECRH Group

Presented by L. JACQUET and M. PAIN

The suprathermal part of the electron distribution function in Tokamak discharges with and without ECRH is analysed. The experimental spectra of the electron distribution function measured from a S_i-Li detector are compared to that deduced from a numerical computation [1].

The code which is Monte-Carlo like, simulates the evolution of a set of particles in velocity space ($v_{\parallel}, v_{\perp}$). Computation is carried out between the initial velocity $v = v_I$ and the Dreicer velocity $v = v_D$ (fig. 1). The initial velocity is determined by the energy interval to be studied. At each time step, a test particle is submitted to :

- the electric acceleration $q\vec{E}/m_e$, where $\vec{E}$ is the electrical toroidal field.
- an average drag - $< v_{\parallel} > \vec{v}/||\vec{v}||$ with $v_{\parallel} = A_D/2v^2$
- an average randomly directed acceleration given by

  $< \vec{v}^2 > = \varepsilon_1 \frac{A_D}{v^2} V_o + \varepsilon_2 \frac{A_D}{v^2}$ where ε_1 and ε_2 are random coefficients $\varepsilon_1^2 + \varepsilon_2^2 = 1$.

  and

$$A_D = 8 \; N_e \; e^4 \; Z_e \; Z_i \; \log \Lambda / m_e^2$$

- with ECRH, a perpendicular acceleration given by :

$$\frac{d}{dt}\left(m\frac{v_{\perp}^2}{2}\right) = \frac{\pi e^2}{4m_e} |E_{\perp}|^2 \sum_{n=-\infty}^{\infty} J_{n-1}\left(\frac{k_{\perp} v_{\perp}}{\omega}\right) . \delta(\omega - n\omega_{ce} - k_{\parallel} v_{\parallel}) \quad [2]$$

In each element of the velocity space grid, the distribution function is proportional to $\sum_i \tau_i$ where τ_i is the time spent by the i^{th} particle in that element. From this distribution function, the code computes the continuum part of the soft X-ray spectrum emitted by the plasma.

Taking impurities into account, the bremmstrahlung emission in 4 sterradian in the $(\omega, \omega + d\omega)$ range,

$$\frac{d^3W}{dt \; dV \; d\omega} = \int_{V_{min}}^{\infty} \frac{16\pi e^6 \; Zeff}{3\sqrt{3} \; m_e^2} n_e \frac{1}{v} f(v) \; dv$$

where $\frac{16\pi e^2 \; Zeff \; n_e^2}{3\sqrt{3} \; m_e^2 \; c^3}$ is the total power radiated by the electrons

with velocity v [3] , f (v) is the electron distribution function and

$$\frac{1}{2} m_e v_{min}^2 = \hbar\omega$$

We obtain the X ray sepctrum as

$$\frac{E\, d^3 N}{dE\, dV\, dt} = \frac{32\pi^3 e^6 Zeff}{3\sqrt{3}\, m_e^2 c^3 h} n_e^2 \int_{E_{min}}^{\infty} \int_{-\pi/2}^{\pi/2} \cos\theta\, f(E,\theta)\, dE\, d\theta \; [cm^{-3}, s^{-1}]$$

with $E_{min} = \frac{1}{2} m_e v_{min}^2$

If we assume that radiative recombination rates are close of those we would find if f (v) was maxwellian distribution, the continuum spectrum can be written

$$\frac{E\, d^3 N}{dE\, dV\, dt} = \frac{32\pi^3 e^6 (Zeff+\xi)}{3\sqrt{3}\, c^3 m_e^2 h} n_e^2 \int_{E_{min}}^{\infty} dE \int_{-\pi/2}^{\pi/2} \cos\theta\, f(E,\theta)\, d\theta \; [cm^{-3}, s^{1}]$$

where ξ is a numerical factor taking into account the radiative recombination.

The experimental apparatus consists of a S_i-Li detector with a multichannel analyser. It measures the X-ray spectra in the energy interval of [1.5,30] keV. It has a spatial resolution of 1 cm and a temporal resolution of 20 ms. An in-situ calibration is done with an A_m^{241} souce in iron substrate.

The plasma studied has the following parameters :

- central density : $1.5\ 10^{13}\ cm^{-3}$
- Plasma current : 100 - 110 kA
- Toroidal field : 21.4 - 27 kG

an experimental spectrum is shown in (fig.2). Both the simulated and the experimental spectra are shown in logarithmic scale. We note the spectra can be fitted by two straight lines appropriate for the energy intervals [1.5,10] keV and [10,30] keV. For ohmic discharges (fig.3) there exists a good agreement between the measured and the computed slopes of the suprathermal ([10,30] keV) part of the distribution function.

B_T (kG)	Experimental slope (kev^{-1})	Computed slope (kev^{-1})
21.4	$- 2.5\ 10^{-2}$	$- 3\ 10^{-2}$
24	$- 3.1\ 10^{-2}$	$- 3\ 10^{-2}$
27	$- 3.2\ 10^{-2}$	$- 3\ 10^{-2}$

In the presence of ECRH, the code predicts a depletion of the suprathermal part (i.e a decrease of the slope in the [10,30] keV interval). The depletion is stronger for a central heating (B_T = 21.4 kG with f_{ECRH} = 60 GHz). Computation gives a slope of $3.8\ 10^{-2}\ keV^{-1}$.

This prediction is confirmed by the experiment

B_T (kG)	Experimental slope (kev^{-1})	Computed slope (kev^{-1})
21.4	$-5\ 10^{-2}$	$-3.8\ 10^{-2}$
24	$-3.9\ 10^{-2}$	$-3\ 10^{-2}$
27	$-3.4\ 10^{-2}$	$-3\ 10^{-2}$

For ECRH - heated discharges, both the code and the experimental spectra show a depletion effect of the suprathermal part of the distribution function. We believe that the depletion is a consequence of the particle "shift" in the energy diagram caused by ECRH. In fact, this shift is less efficient when collisions dominate, because shifted particles are thermalised. But collisions become rare at high energy, making the ECRH energy shift more efficient. ECRH increases the suprathermal population close to the bulk. But for high energies ECRH allows many particles to run across the Dreicer limit and become runaway depleting the high energy portion of the distribution function.

In summary, our simple numerical model gives good predictions. The representation of the distribution functions by two maxwellian is satisfactory as indicated by the experimental and the numerical results.

Référence

[1] L. Jacquet, M. Pain, M.A. Dubois, A.L. Pecquet "Analyse des Spectres X-Mous obtenus à l'aide d'un détecteur $S_i - L_i$ et comparaison avec les formes calculées de la fonction de distribution en présence et en absence de chauffage cyclotronique électronique", Rapport Euratom-CEA n°1289

[2] O. Eldridge, "Electron Cyclotron Heating as Resonant Diffusion", Phys. of Fluids, Vol. 15 4679 (1972)

[3] G. Ribiki, F.Lightman, "Radiative Processes in Astrophysics", Mc Graw Hill, 1966.

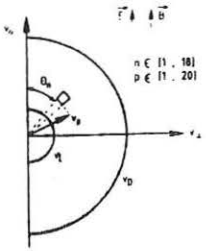

Fig. 1 : Velocity space grid used by the code

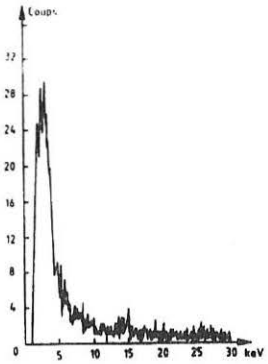

Fig 2 : Experimental spectrum with B_T=21.4 kg and 400 kW of ECRH power

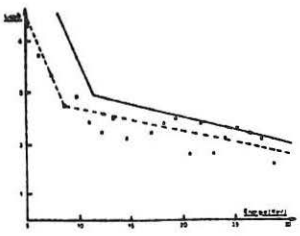

Fig 3

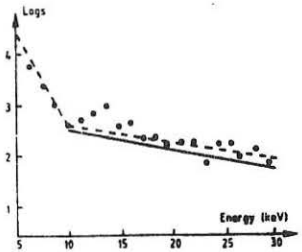

Fig 4 Logarithmic scale of a spectrum with B_T = 21.4 kg and 400 kW o ECRH power : cross and dashec curves : experimental data solid curve results of the simulation

ELECTRON CYCLOTRON RESONANCE HEATING AND CURRENT DRIVE EXPERIMENTS ON THE CLEO DEVICE.

T Edlington, M W Alcock, D Atkinson, S G Blewett, B J Parham, P R Collins, A N Dellis, B Lloyd, M O'Brien, J Riley, A C Riviere, D C Robinson, D F H Start and T N Todd

Culham Laboratory, Abingdon, Oxon, OX14 3DB, UK
(Euratom/UKAEA Fusion Association)

1. INTRODUCTION

The CLEO experiment has been used to study electron cyclotron resonance heating utilising both fundamental and second harmonic resonances. Two high-power gyrotrons are installed, each providing 200 kW of RF power at 28 GHz and 60 GHz respectively. The machine can be operated either as a conventional tokamak with a relatively high aspect ratio (R/a ~7), as a pure stellarator with an ℓ=3 m=7 helical winding or in a variety of hybrid configurations.

For 60 GHz heating experiments, the TE_{01} circular mode was radiated from the low field side of the torus through open-ended, oversized waveguide aligned along a major radius in the horizontal mid-plane. For 28 GHz experiments both circular and linear polarisation have been studied. The circularly polarised launch is comparable with that of the 60 GHz whilst for the linearly polarised launch a TE_{01} to TE_{11} mode converter is introduced into the transmission line close to the torus. With this arrangement both X mode second harmonic and O mode fundamental heating have been studied. In the case of second harmonic, the heating efficiency was independent of the launch polarisation which may indicate that single path absorption is not necessary for good heating efficiency.

By removing sections of the TE_{01} to TE_{11} mode converter to obtain incomplete conversion and varying the position of the converter with respect to the end of the launch antenna, the angle at which the power is launched can be varied. High power tests in which microwaves were launched into free space and the antenna pattern recorded on heat sensitive paper demonstrate that asymmetric launch with an angle up to 11° from the waveguide axis is possible. By rotating the antenna through 180° the rf power can be launched with $k_{\parallel}$ in the same direction as the plasma current or in the opposite direction. This technique has been used to look for evidence of ECRH driven current. Preliminary experiments in tokamak geometry with 28 GHz second harmonic heating have been completed and indicate very low efficiency. Numerical calculations of the expected current drive for the CLEO experimental conditions are compared with the experimental results.

2. 60 GHz HEATING

Efficient, bulk electron heating of tokamak discharges using high power microwaves at the 2nd harmonic of the electron cyclotron resonance has been previously demonstrated in the CLEO experiment [1]. In CLEO 140 kW of rf at 60 GHz injected from the low field side of the torus with mixed polarisation increased the central electron temperature from 0.43 keV to 1.25 keV. In contrast to similar experiments at lower densities using 28 GHz microwaves,

no high energy non-Maxwellian tail is produced by the rf heating. It is therefore particularly interesting to study the effect of this form of heating on tokamak confinement and to compare it with scaling laws derived from other heating methods. Figure 1 shows how the global energy confinement time varies with line averaged electron density along a central vertical chord through the plasma. Values are plotted for both the ohmic and ECRH phases of the discharge. In CLEO for both fundamental and second harmonic, the heating is invariably accompanied by a fall in $\bar{n}_e$ for constant gas flux becoming more pronounced as the cut-off density is approached. As a result the range of densities covered in Fig.1 is greater for the ohmic data than for the ECRH data. In calculating τ_E during heating we have taken the rf optical depth for each density from a ray tracing code in toroidal geometry which includes a realistic model of the antenna pattern and the effect of multiple reflections from the torus wall. For the range of densities covered the absorption coefficient varies from ~0.5 to 0.9. Based on these values there is a fall in confinement comparing the two phases of the same discharge and a somewhat smaller drop when the comparison is made at the same $\bar{n}_e$. Figure 1 also shows the so-called neo-Alcator and L mode confinement scaling laws as formulated by Goldston in [2]. The L mode line is plotted for a constant input power which is approximately valid here when P_{ohmic} is included. For CLEO parameters, in this low density regime, the

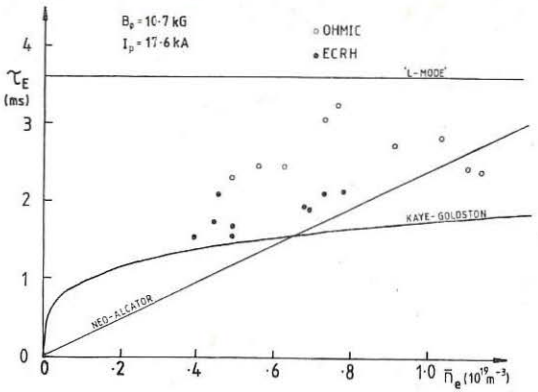

Fig.1 Scaling of energy confinement time with line-averaged electron density for 60 GHz 2nd harmonic ECRH.

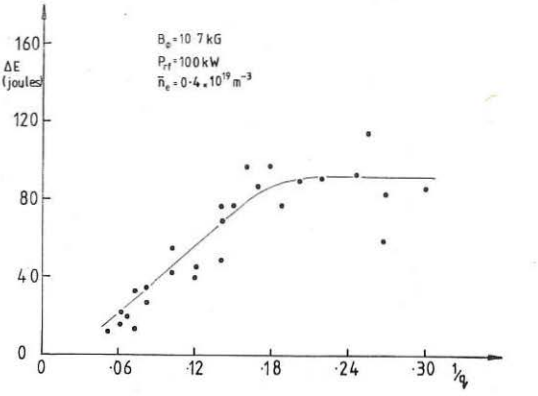

Fig.2 Increase in plasma stored energy as a function of plasma current for 60 GHz 2nd harmonic heating.

predicted L mode confinement is higher than the ohmic confinement based on the neo-Alcator scaling. The more recent Kaye-Goldston scaling [3] is numerically closer to the data than the L mode but is a no more accurate description of the experimental scaling than the neo-Alcator scaling.

Figure 2 shows the scaling of the stored energy increase during ECRH with plasma current and suggests a possible saturation in the plasma current scaling of confinement at low q_a. Energy confinement time is not plotted for this data since neither the ohmic stored energy nor the variation of the optical depth of the microwaves with plasma current are known to sufficient accuracy. Calculating the ohmic stored energy from conductivity suggests that $\Delta E/E_{ohmic}$ is relatively constant for this data and in the range 2→3.

3. 28GHz HEATING

The effect of varying the axial toroidal field in 2nd harmonic heating experiments with 28 GHz ECRH is shown in Fig.3. For these experiments and for similar ones at the fundamental resonance a significant asymmetry in heating efficiency with respect to resonance position is observed which is not predicted by ray tracing studies. With the resonance on the high field side of the axis the heating is rather insensitive to resonance position and some increase in stored energy is observed even with the resonance less than 1 cm from the limiter. When the resonance is moved to the low field side of the axis, the heating efficiency falls off more rapidly. The change in loop voltage associated with the heating reverses sign for $X_{res} \gtrsim 5.4$ cm even though $\Delta\beta_p$ remains positive. This suggests that part of the rf power produces an increase in the trapped electron population in this region, resulting in an enhanced plasma resistivity via neo-classical effects.

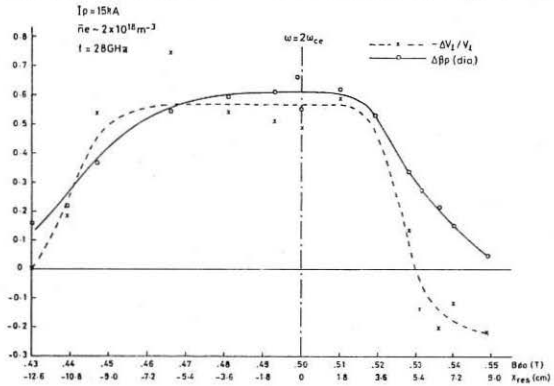

Fig.3 Poloidal beta increase and relative loop voltage change as a function of resonance position for 2nd harmonic heating at 28 GHz.

4. CURRENT DRIVE

The creation of an asymmetric resistivity with rf waves was proposed by Fisch and Boozer [4] as a possible mechanism for non-inductive current drive and an experimental verification of the theory was provided in [5]. Numerical calculations of Cordey et al [6] show that ECRH should be almost as efficient as lower hybrid waves in driving current.

The open end of a circular waveguide excited in the TE_{11} mode radiates a linearly polarised beam with its peak intensity on the waveguide axis. For 28 GHz and a waveguide diameter of 40 mm the H-plane antenna pattern has 10dB points at ± 17°. When the same waveguide is excited in the TE_{01} mode the

antenna pattern is a hollow cone with its maximum at 13° from the axis. The polarisation is azimuthal and therefore the electric fields have opposite signs on either side of the axis. If the two modes are combined, the TE_{11} wave will increase the TE_{01} field on one side of the axis and decrease it on the other side. A mixture of TE_{01} and TE_{11} was produced by removing one period from a 4 period mode converter designed for complete $TE_{01} \rightarrow TE_{11}$ conversion. The relative phase of the two modes varies continuously in the plain waveguide following the converter. The deflection of the wavefront was optimised empirically by varying the length of plain 40 mm diameter waveguide between the converter and the plasma. The angle of deflection was measured by launching the wave at high power into free space and measuring the antenna pattern with heat sensitive paper. The beam can then be directed either parallel or anti-parallel to the plasma current by rotating the converter by 180°. In the best case angles of +11.3° and -8.0° with respect to the waveguide axis in the horizontal plane were achieved, the asymmetry being due to residual spurious modes. The numerical results described in [6] have been included in a ray tracing code. For CLEO parameters the predicted ECRH current drive is optimised for a launch angle of 15°. Figure 4 shows the voltage and current waveforms for two tokamak discharges in CLEO into which 135 kW of 28GHz was injected. In one case the wave was launched predominantly in the direction of the electron drift and in the other case in the opposite direction. If the plasma parameters for these shots and the real antenna geometry are included in the ray tracing code the predicted current drive efficiencies are approximately 12 A/kW (incident) for the parameters of the ohmic target and 90 A/kW for the parameters of the heated discharges. These figures suggest that a substantial proportion of the total current should be replaced by rf driven current, however within the experimental errors there is no systematic difference between discharges with co- and counter-injection . Analysis of this type of discharge with a non-linear Fokker Planck code suggests that the electron distribution function is strongly distorted with the electric field calculated to be approximately 1/8 of the Dreicer critical field. The current density calculated with this code is dominated by the DC electric field and the difference between calculated driven current densities for the two cases in Fig.4 is small.

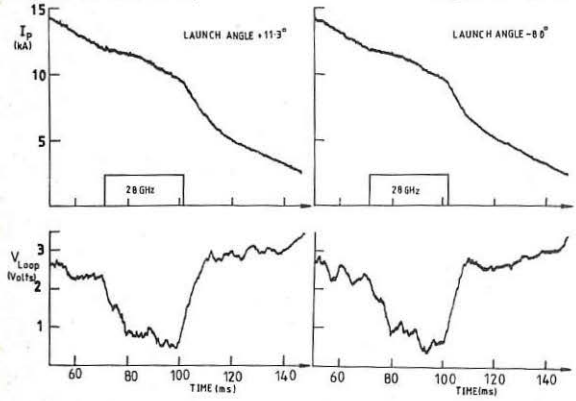

Fig.4 Plasma current and loop voltage waveforms during rf injection with angled launch antenna.

REFERENCES

[1] T Edlington et al, 12th Euro Conf on Contr Fus and Plasma Physics, Budapest, Vol.II (1985) p.80.

[2] R J Goldston, Proc. 11th Euro Conf on Plasma Physics and Contr Fusion, Aachen, Vol.26 (1984) p.87.

[3] S M Kaye and R J Goldston, Nuclear Fusion Vol.25, No.1 (1985)

[4] N J Fisch and A H Boozer, Phys Rev Lett 45, 720 (1980)

[5] D F H Start et al, Phys Rev Letts Vol.48, No.9 (1982) 624.

[6] J G Cordey et al, Plasma Physics, 24, No.1 pp73-89, (1982).

Longitudinal Launching of EC and LH Waves in Toroidal and in Mirrors Devices

T.Consoli
C.E.C.

Abstract:

It has been shown that dense and energetic plasma beams can be accelerated by the combine action of EC and LH waves, launched with a "special multicoaxial grill"/1/. The first wave generates or/and heats any plasma target whose electron density and temperature are controlled by means of the power and frequency of the RF sources. Thus the conditions for converting $W_{\perp e}$ in $W_{// e}$ by the $\mu\nabla B$ force or/and by electron Landau damping (when v_φ of the travelling LHW is equal to $v_{// e}$) are satisfied. The two phenomenon have been separately and already demonstrated experimentally, /2/.

This paper is concerned with two applications of the simultaneous launching of EC and LH waves with a special launcher:

a-The first application is the control of the "border plasma "characteristics and of the toroidally driven current, by the RF fields in view to improve the τ_E energy confinement time.

b-The second application is a new approach for filling with a hot and dense plasma a mirror device and for suppressing its losses.

Concerning the first application, the Tokamak results on the degradation of τ_E, have focalized the attention on the role played by the plasma edge on the transport coefficients. A solution for reducing this degradation may be the control of the plasma edge parameters by RF fields or also and rather preferably by the generation of a controllable and protecting "plasma mantle". On fig 1, a schematic view of the proposed system and applied on JET is shown. The EC and LH travelling waves are launched tangentially to the toroidal field with a multicoaxial grill. Here contrarily to the conventional grill launching case, the waves propagate in one direction with the required $N_{//}$; they heat the electrons and induce current When in addition a gas is fed in the central guide, a hot and dense plasma mantle is generated. Its parameters n_e, T_e, can be controlled in the range of 10^{12} to 10^{14} cm^{-3} and 0,1 to 10 keV and above .

Concerning the second application ,the coaxial grill appears to be more suitable to axisymetric open devices,as for example a magnetic cuspide field with RF grills located at the cusps fig 2./3/.In this case the grills at the spindle cusps are of the multicoaxial type and those around the circular mirror are conventional grills set toroidally.Thus EC and LH waves are launched on the axis and LH waves along the circular cusp.The launchers on the axis drive dense and hot plasma jets in opposite directions and those in the middle plane radial jets.The converging axial and radial plasma flows are thermalized in the center of the device where a hot and dense plasma is accumulated and confined.The confinement is therefore resulting from the combine effects of the magnetic field and of the "kinetic pressure"exerced by the convergent plasma jets. The launchers acting as"injector and stoppers"when they are correctly phased,matched and loaded,convert the RF energy into kinetic energy with an efficiency higher than in resonant adiabatic plugs/4/.Finally as an example of this second application,a thermonuclear plasma core with $n_e \sim 10^{14} cm^{-3}$, $T_e = T_i \sim 10$ keV,might be obtained in the following conditions : P_1=1 Mw, F_1=140 GHz, F_2=4 GHz, P_2= 5 Mw, V_{core}=30 l,magnetic field at the mirrors B_{max}=5 T.

References:

/1/Consoli T.,Proc.of the 13th Europ.Conf.on Contr.Fusion and Plas. Heating.Schliersee April(1986).
/2/ Consoli T.,Proc.4th Int.Symp.on Heat.in Tor.Plas.Roma(1984)
/3/Consoli T.,Phys.Letters 7(1963) 237. Vol 2,733.
/4/ Hatori T.,et al.,Proc.Vth IAEA Conf.Tokyo(1974)Vol.2,663.

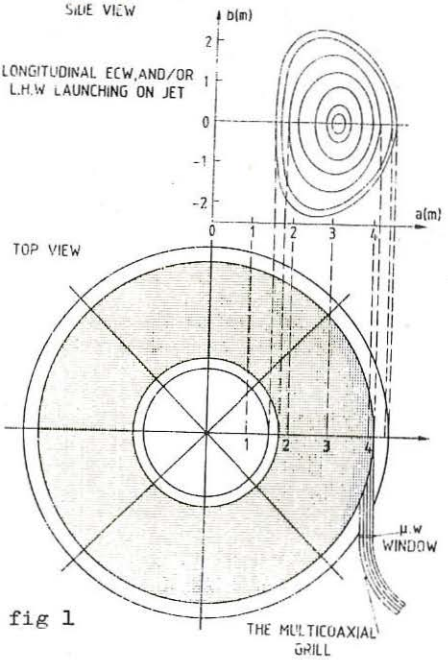
SIDE VIEW
b(m)
2
1
0
-1
-2
LONGITUDINAL ECW AND/OR
L.H.W LAUNCHING ON JET
0
1
2
3
4
a(m)
TOP VIEW
1
2
3
4
μ.w
WINDOW
THE MULTICOAXIAL
GRILL

fig 1

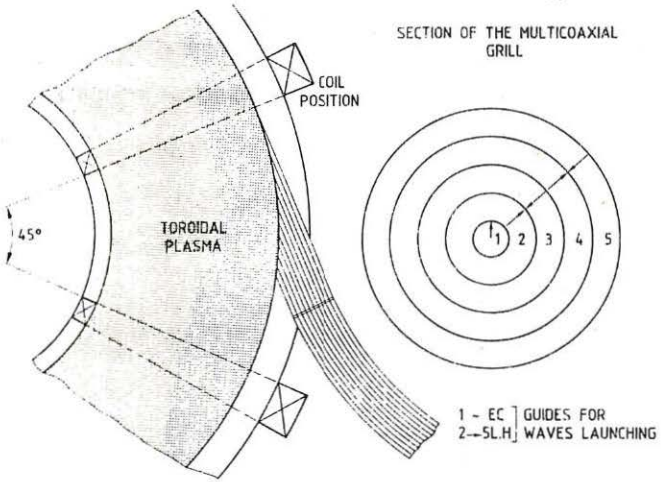
SECTION OF THE MULTICOAXIAL
GRILL
COIL
POSITION
45°
TOROIDAL
PLASMA
1
2
3
4
5
1 - EC
2 - SL.H.
GUIDES FOR
WAVES LAUNCHING

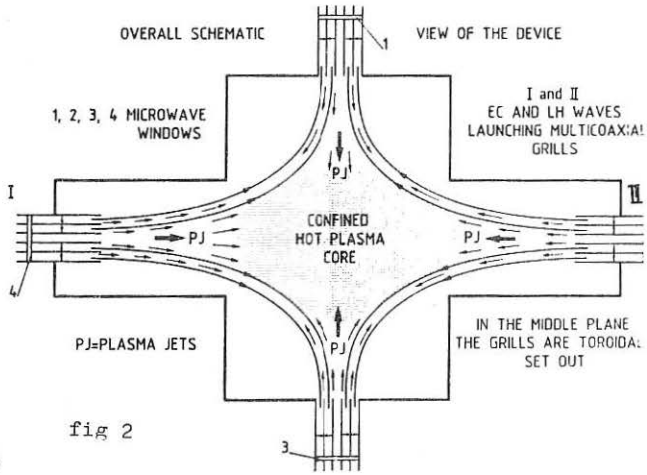
OVERALL SCHEMATIC
VIEW OF THE DEVICE
1, 2, 3, 4 MICROWAVE WINDOWS
I and II EC AND LH WAVES LAUNCHING MULTICOAXIAL GRILLS
I
II
PJ
CONFINED HOT PLASMA CORE
PJ=PLASMA JETS
IN THE MIDDLE PLANE THE GRILLS ARE TOROIDAL SET OUT
1
2
3
4

fig 2

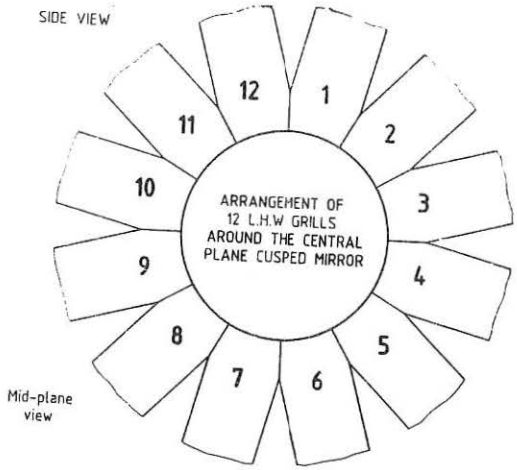
SIDE VIEW
12
1
2
3
4
5
6
7
8
9
10
11
ARRANGEMENT OF 12 L.H.W GRILLS AROUND THE CENTRAL PLANE CUSPED MIRROR
Mid-plane view

PLASMA BEAM ACCELERATION BY EC AND IC SLOW WAVES OR BY LH FAST WAVES

T. Consoli

Expert with the Commission of the European Communities
DG XII - Fusion Programme, 1049 Brussels, Belgium

Abstract : The combination of ECW and LHW launched by a "special" coaxial guide improves the performance of ECR plasma beam accelerators and opens a wide domain of thermonuclear applications.

It has been shown that, in a longitudinal magnetic field gradient, the $\mu\vec{\nabla}B_z$ force magnified by ECR accelerates a plasma beam /1/, which is confined and stabilized by an additional radial magnetic field produced by a multipolar coil. The energy gained by the electrons $W_{\perp e}$ is converted into parallel energy $W_{//e}$ /2/. The ions when $\nu_{ei} < \omega_{ce}$ are mainly dragged along by the space charge electrostatic potential V_s. Experimentally it has been proved that when the conditions assumed by the theory /3/,/4/ are satisfied, the characteristics of the accelerated beam are : $(\omega_{pe})_{beam} < \omega_{rf} \cong \omega_{ce}$, $\langle W_{\perp e}\rangle \cong \langle W_{//i}\rangle$, $\langle v_{//e}\rangle \cong \langle v_{//i}\rangle$, $\eta = P_{beam}/P_{rf} \sim 50\%$. The equivalent current density J_e, which is a function of $W_{\perp e}$, P_{rf}, and f_{rf}, is limited by the feasible ∇B_z. This limitation can be overcome by using two waves - ECW and LHW - the former for the production of the required (n_e, T_e, $W_{\perp e}$) hot electron plasma target. The second wave drives when $(v_\phi)_{wave} \geq (v_{//e})$ or $N_{//} > 1$ by Cherenkov-Landau damping an intense electronic current if the necessary f_{rf} and P_{rf} are chosen /5/, /6/. The same waves according to their nature (stationary or travelling) their f_{rf} and $N_{//}$, can heat the ions or the electrons or drive a current.

This paper is concerned with this last application. For this purpose the special launching structures described hereafter can be used. A first solution consists in a coaxial guide (Fig.1), whose central hollow cylinder is used as an oversize guide for launching circularly polarized right hand waves. The external guide contains a number p of metal irises, periodically distributed each d cm along its length. In this guide, the wave's v_ϕ is slowed down by the outphasing ψ due to the iris and accordingly $N_{//} = \frac{c}{v_\phi} = \frac{\lambda_{vac}}{2d} \cdot \frac{\psi}{\pi}$, where $\psi = f\ (f_{rf}, r_1 - r_2, e, p)$, $r_1 - r_2 = l$ is the radial dimension and e the thickness of the iris. The equivalent electrical circuit of this structure behaves as a transmission line without a cut off /7/. A better solution is a multicoaxial guide formed by a set of p superposed metal cylinders as

shown in Fig.2 (3-guide case) and Fig.3 (5-guide case). In both, the inner guide is used for launching the ECW and the outers for the TEM propagation mode of LHW. The ratio a_p/b of the guides' radii (p = 1,2,3...), is chosen so as to minimize the resistive losses. These guides are connected to one or more klystrons emitting waves at the same frequency but with different phases $\phi_1, \phi_2, \ldots \phi_p$. The phasers are an integral part of each guide or a separate component. The launcher as a whole behaves as a "coaxial grill" and launches, according to the applied frequencies and phases, a travelling wave with the necessary $N_{//}$ spectrum. Exact solution of this multicoaxial launcher calls for theoretical treatment, not included in this paper. Nevertheless, its behaviour as a conventional grill is obvious and can be understood from Fig. 3. Indeed in the case of a rectangular guide array, the Brambilla grill theory /8/ assumes infinite and parallel faces, that is $h \gg e$ (height $\gg$ aperture). In our case, in a first approximation, we can assume that $N_{//}$ is not appreciably changed if $h_1 > h_2 > h_3 > h_4 > e$, the faces remaining parallel as shown in Fig. 3A. Some change occurs if the facing walls are curved but equidistant (Fig. 3B). Thus the multicoaxial grill can be considered as a succession of a large number of "canted grills" (5 in Fig. 3C). Finally, as the radial metal dividing walls in Fig. 3C are parallel to the radial electric field $\vec{E}_r$, they can be suppressed; we thus come back to a superposition of coaxial guides. These considerations allow us to write, in a first approximation, $N_{//} = \frac{\lambda}{2d} \cdot \frac{\phi}{\pi}$ where ϕ and d are respectively the phase and the gap between two adjacent guides ($d = a_p - a_{p-1} - \delta$) (here δ is the thickness of the walls). The propagation of the LHW launched by a coaxial grill lies in the field of wave propagation in the cylindrical non-homogeneous magnetoplasma which was treated in detail particularly by Rebut /9/.If we also assume that the density gradient dn_e/dz just behind the microwave window satisfies Brambilla's conditions for LH slow waves at the plasma edge (see Ref. /8/), we can improve the ECRW plasma accelerators as follows .

Proposed experimental device: It is schematized in Fig. 4, where the launching structure is of the first type. It is obvious that the second solution is more appropriate. The ionization of the gas and the perpendicular energy gain by the electrons occur just behind the microwave window, where the neutral gas is injected. The density n_e and the perpendicular energy $W_{\perp_e}$ of the ECR generated hot electron plasma target are controlled through the neutral gas pressure and the rf power level, so as to reach the required experimental conditions for coupling LH travelling waves to the electrons

and thus drive a current. This needs an $N_{//} \simeq 6.3/T_e^{1/2}$ keV. The characteristic parameters are : B_z = 1 tesla (produced by circular coils), B_r = 0.3 tesla (produced by a permanent magnet hexapol). In the case of 5 guides, the multicoaxial grill's radial dimensions are: 3, 6, 9, 12, 15 cm. The plasma column length is 200 cm. The central guide is fed by two gyrotrons f = 28 GHz, P_{rf} = 250 kW for 10 msec. The 4 external guides are supplied by an f = 2.45 GHz, P_{rf} = 500 kW klystron. The $N_{//}$ can be varied from 1.5 to 6 by changing the ϕ_p phases. The expected plasma beam characteristics will be analyzed with the diagnostics already used currently /4/ and shown in Fig.4. The plasma density in these conditions must be maintained around 10^{12} e/cm^3 so as to get an f_{pe}^2/f_{ce}^2 ratio of the order of 10^{-1} which favours a high efficiency $\eta = P_{beam}/P_{rf}$ of the current drive mechanism. The expected values for η (from 20 to 30%) allow a plasma flow of 10^{22} p/sec, corresponding to energies $W_{\perp e} \simeq W_{//i}$ of the order of 10 keV.

Conclusions : Improvement of the ECR plasma beam accelerator device described in this paper is realistic and feasible when EC and IC waves are launched. As an application, it is possible to build another device in which two similar systems are opposed. The collision of the two opposed hot plasma beams produces a thermalized plasma which is trapped and confined in the magnetic well formed at the junction of the two inverse linear magnetic fields. When deuterium is the gas used for the beams, 10^{13} neutrons can be obtained. The multicoaxial structure can also be used for longitudinal launching of EC and IC waves in Tokamaks. As far as LH waves are concerned the resulting situation is unfavourable : only LH fast waves can be coupled to the plasma.

References

/1/ Consoli, T., Proc. 4th Internat. Symp., Heating in Toroidal Plasmas, Roma, March 1984, EUR 9341 EN, Monotypia Franchi, Città di Castello (PG) Italy, Vol. II, 733

/2/ Consoli, T., Proc. 8th CIPIG, Vienna, July 1967, 611

/3/ Canobbio, E., Nucl Fusion 9 (1969) 27

/4/ Finzi, U., C R Acad Sci 269 (1969) 1293 and
Geller, R., et al., Proc. 4th Internat. Conf. Plasma Physics and Controlled Nuclear Fusion Research, Madison, June 1971, IAEA-CN-28/Vienna, Vol. 2, 631

/5/ Brambilla, M., Nucl Fusion 16 (1976) 47 and
Gormezano, C., Proc. 4th Internat. Symp., Heating in Toroidal Plasmas, Roma, March 1984, EUR 9341 EN, Monotypia Franchi, Città di Castello (PG) Italy, Vol. II, 1255.

/6/ Fisch, N.J., Phys Rev Letters 13 (1978) 41

/7/ Consoli, T., Revue Faculté des Sciences, Université d'Istanbul, Tome VI Fasc. 1, janvier 1943, pp.40-63

/8/ Brambilla, M., Nucl Fusion 18 (1978) 493

/9/ Rebut, P., Ondes dans les plasmas inhomogènes en géométrie cylindrique. Thèse de l'Université de Paris, janvier 1966.

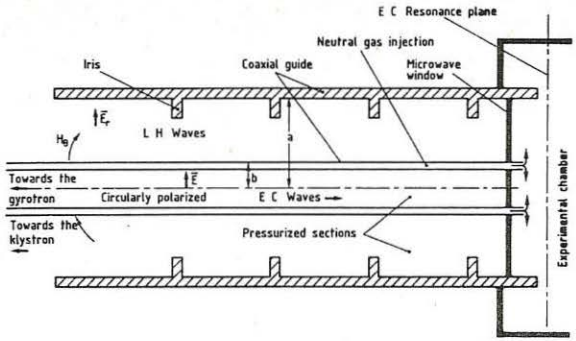

Fig. 1 - Schematization of the coaxial launching structure for IC or LH and EC waves

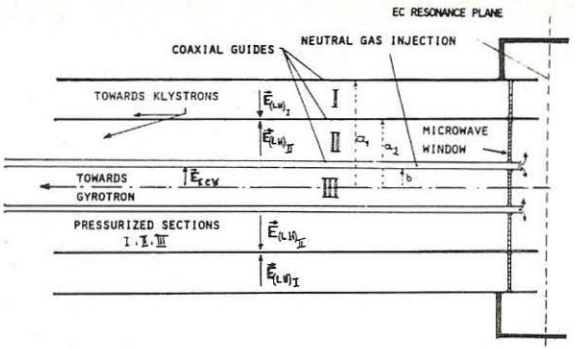

Fig. 2 - Multicoaxial grill (two external outphased cylindrical guides in this case).

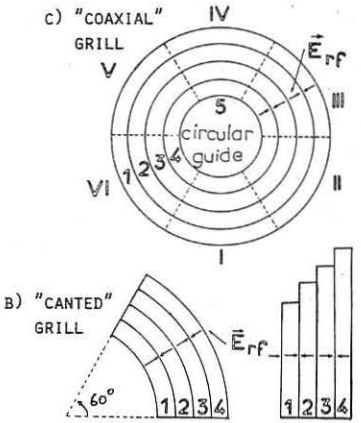

Fig. 3 - Multicoaxial guide behaves as an infinite set of "canted grills" in series.

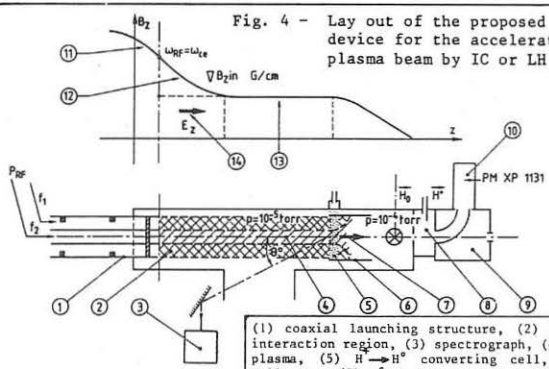

Fig. 4 - Lay out of the proposed experimental device for the acceleration of a plasma beam by IC or LH and EC waves.

(1) coaxial launching structure, (2) LH wave-plasma interaction region, (3) spectrograph, (4) hot electron plasma, (5) $H^- \rightarrow H^\circ$ converting cell, (6) electron collector, (7) H° fast neutral beam, (8) $H^\circ \rightarrow H^+$, (9) electrostatic analyser, (10) X-ray detector, (11) profile of the axial magnetic field, (12) and (13) IC or LH and EC interaction magnetic field regions, (14) charge separation electrostatic field.

ELECTRON CYCLOTRON HEATING BY THE EXTRAORDINARY MODE IN THE T-15 TOKAMAK

H. Capes, I. Fidone, G. Giruzzi and V. Krivenski

Association Euratom-CEA sur la Fusion
Centre d'Etudes Nucléaires
92265 Fontenay-aux-Roses (France)

Abstract

Electron Cyclotron Heating by the extraordinary mode for oblique propagation at down-shifted frequency and external launching is investigated using the relativistic theory of wave absorption. For this purpose, the transport code Makokot has been coupled to a ray-tracing code which evaluates the power deposition along the wave-packet trajectories. It is shown that, for a toroidal magnetic field B(0) = 43 kG, frequency f = 83 GHz, and nearly top launching, efficient plasma heating and control of temperature profiles may be achieved.

Auxiliary heating by EC wave absorption is planned in the T-15 tokamak. In view of the promising results obtained with the O-mode /1/ for normal propagation from the low-magnetic-field-side, it is natural to consider this method as the most attractive candidate for electron heating However, the use of E-mode at down-shifted frequencies for low-magnetic-field-side launching and large oblique propagation /2,3,4/, presents several attractive features. The value of the magnetic field can be significantly higher than the maximum value allowed by the O-mode wave, which for a frequency f = 83 GHz is B(0) ≃ 33 kG. The E-mode cut-off density is higher. Superthermal electrons may be produced.

In the present paper we wish to show the potential of the E-mode heating method by investigating the electron temperature evolution in the T-15 device. A ray-tracing code, which follows the trajectories of a finite wave-packet and evaluates the relativistic wave damping, is coupled to the transport code Makokot /5/. The Mercier scaling /6/ has been used to obtain an ohmic stationary plasma. However to take into account the numerical simulation of TFR and T-10 experiments, the Kadomsev-Potguse scaling /7/ has been choosen to study the EC heated plasma,

$\chi_e = 1.58 \times 10^{20}\ (r/R) T_e^{1/2}/nq$, where the numerical constant is adjusted in order to recover in a purely ohmic plasma the central electron temperature profile calculated according to /5/. The electrical resistivity includes neoclassical corrections, the ion heat flux is assumed to be neoclassical and Zeff = 1.

ECH is applied to the plasma after reaching an ohmic steady-state. The basic plasma parameters are B(0) = 43 kG, I = 1.5 MA, $< n_e > = 4 \times 10^{19}\ m^{-3}$. The density has a parabolic like profile with $n_e\ (o) = 6 \times 10^{19}\ m^{-3}$. The electron temperature at the end of the ohmic phase is shown in Fig.1 (t = 0). The wave launching direction is given by the parameters ($\theta, \Delta\theta, \psi$), where θ is the poloidal angle at the launching position, $\Delta\theta$ is the angle between the wave direction in the poloidal section and the inner normal, ψ is the injection angle in the toroidal section with respect to the normal of the magnetic field.

In Fig. 1 we show the time evolution of the electron temperature profile vs the normalized radial position. The initial launching conditions (t = 0) are $\theta = 70°$, $\Delta\theta = 5°$, $\psi = -85°$, the wave power $P_o = 5$ MW. In order to model the temperature profile the injection angles have been changed in the course of the time : the two temperatures profiles at time t = 175 ms correspond to the same state at time t = 75 ms (with angles $\Delta\theta = 0°$, $\theta = -55°$) but $\theta = -45°$ for t > 125 ms (full) while $\Delta\theta = 10°$, $\theta = -85°$ (dotted). The further evolution passing at t = 175 ms from $\theta = -45°$ to $\theta = -35°$ is shown at t = 250 ms. In Fig. 2 we show the central electron temperature $T_e(o)$ and the mean electron energy $<T>$ vs the time for the same initial conditions as in Fig.1, but keeping the injection angles $\Delta\theta = 0°$, $\theta = -55°$ constant for t > 25 ms. Two powers are considered $P_o = 5$ MW (full) and $P_o = 10$ MW (dashed). We observe that the central electron temperature saturates at a value independent of the injected power, the increasing power affecting only the profile broadening. Energy confinement time deteriorates passing from 230 ms ($P_o = 5$ MW) to 160 ms ($P_o = 10$ MW). The broadening may be explained by the $T_e^{1/2}$ heat conduction coefficient scaling and by the low-magnetic- field-side launching position. More peaked profiles can be obtained, changing slightly the antenna position as shown in Fig.3, where $\theta = 110°$ and the other parameters are similar to those of Fig.1. In Fig. 4, we present for comparison the temperature profile evolution in the case of standard O-mode heating, with

B(o) = 32.5 kG and P_o = 5 MW. Note that this scheme does not allow to model the temperature profile and to adjust power deposition region during the heating phase.

We have shown the potential interest of E-mode heating scheme, which is an alternative to the usual O-mode method for high density, high magnetic field tokamak plasmas.

It is a pleasure to acknowledge the co-operation of J.P. Morera and Ha Quang for coupling the ECH code to the Makokot transport code.

/1/ V.V. Alikaev et al, London, UK, 12-19 September (1984)

/2/ I. Fidone, G. Giruzzi, E. Mazzucato, Phys. Fluids 28, 1224 (1985)

/3/ E. Mazzucato, I. Fidone, G. Giruzzi, V. Krivenski, Nucl. Fusion 26, 3 (1986)

/4/ I. Fidone et al, Phys. Fluids 29, March (1986)

/5/ C. Mercier et al, Nucl. Fusion 21, 291 (1981)

/6/ H. Capes, C. Mercier, Report EUR-CEA-FC-1148 (1982)

/7/ B.B. Kadomsev, O.P. Potguse, JETP Lett. 39, 269 (1984).

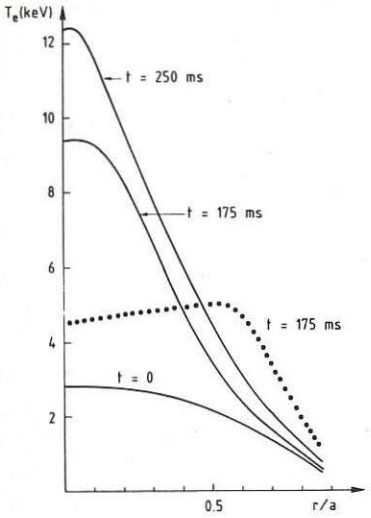

Fig. 1

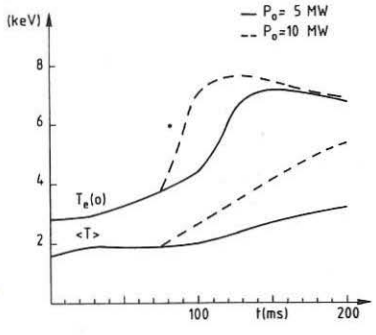

Fig. 2

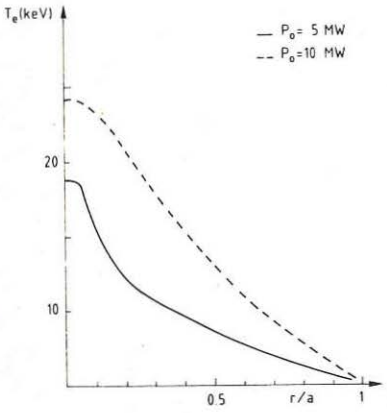

Fig. 3

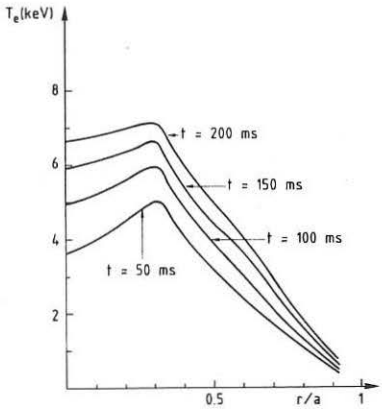

Fig. 4

ELECTRON CYCLOTRON DAMPING FOR LARGE WAVE POWER IN TOKAMAK PLASMAS

V. Krivenski, I. Fidone, G. Giruzzi, R.L. Meyer [a], and L.F. Ziebell [b]

Association Euratom-CEA sur la Fusion
Centre d'Etudes Nucléaires
92265 FONTENAY-AUX-ROSES (FRANCE)

Abstract

The power dependence of the wave damping in a tokamak plasma for arbitrary direction of propagation, mode of polarization, and wave frequency is investigated. Using a 2-D Fokker-Planck code, it is shown that the wave damping increases or decreases with the rf power depending on the velocity range of the absorbing electrons.

Several experiments have demonstrated the attractiveness of ECH in tokamak plasmas. Up to now relatively modest powers ($P_o \leqslant 1$ MW) have been employed and only the next stage, high power, experiments will show if ECH method is a good candidate for heating a tokamak reactor. In this kind of tests a large modification of the plasma absorption properties may be expected, due to the strong deformation of the electron distribution function, and a crucial problem will be the determination of the optimal experimental conditions.

In this paper we examine the role that wave parameters such as power P_o, frequency ω, mean value of the parallel refractives index $\bar{N}_\parallel$ and parallel half-width of the wave packed $\Delta N_\parallel$, play in the quasilinear evolution of the wave damping. This problem, in contrast with the linear problem of EC wave absorption in a tokamak, has received little attention. To our best knowledge, the only case considered is the ordinary mode for propagation normal to the tokamak magnetic field $\vec{B}$. In this case the result obtained shows [1] that the maximum value of the wave damping decreases for increasing values of the wave power. This result is not however generally valid for arbitrary mode of polarization, direction of propagation and resonant frequency. As shown below, for resonant velocities above the thermal speed, the wave damping can significantly increase or at least not deteriorate for wave powers of interest for plasma heating.

Some remarks on the method used :the wave amplitude is evaluated at any instant and any point in space according to the actual damping. The electron distribution function f is obtained from the solution of the kinetic equation including both the relativistic EC diffusion term [2] and the high velocity form of the Fokker-Planck collision operator, which describes the velocity slow-down and the pitch-angle scattering of the resonant electrons. A Gaussian parallel wave packet is assumed at the antenna location.

We first consider the ordinary mode damping. For $N_{\parallel} \simeq 0$ the initial change of the wave damping k_o'' is given by

$$\left(\frac{\partial k_o''}{\partial t}\right)_{t=0} \propto P_o \left[\frac{\phi}{4} - 1 - \frac{T_e (\omega/\omega_c)^2}{m_e c^2 (\Delta N_{\parallel})^2}\right] \phi^3 \exp(-\phi),$$

where $\phi = mc^2 (\omega_c^2 - \omega^2)/2T_e \omega^2$, ω_c is the cyclotron frequency, c the speed of the light, m_e and T_e the electron mass and temperature. In particular this relation shows that initially, for ω such that k_o'' is near its maximum [1] ($\phi \simeq 5/2$), the wave damping always decreases. For different values of ω_c / ω and $\Delta N_{\parallel}$ however (for example those of Fig.1), the ordinary wave damping may increase with time.

This initial condition is not sufficient for asserting that at steady state the damping will be larger than the Maxwellian one. As known, in the absence of collisions the wave damping tends to zero asymptotically. The possibility of a wave absorption enhancement at steady state is demonstrated by Figs. 1 and 2. T-10 parameters and typical temperature and density profiles are used, with central density $n_e(0) = 5 \times 10^{13}$ cm^{-3}, equal ion and electron temperatures, $Z_{eff} = 2$, $P_o = 1$ MW. In Fig. 1 we show k_o'', the wave damping corresponding to $N_{\parallel} = \bar{N}_{\parallel}$, for a Maxwellian distribution function (t = 0) and at steady-state. The case of ordinary mode, vertically injected, is considered for $\bar{N}_{\parallel} = 0$, $\Delta N_{\parallel} = 0.1$, $\omega_c/\omega = 1.017$, T_e (o) = 1 keV. The total power absorbed in the transit from the plasma edge to the plasma axis passes from 50 % (t= 0) to 90 % (t=∞), i.e. quasilinear effects make the plasma nearly black-body. In Fig.2 the interesting case of extraordinary mode, injected from the low-magnetic-field-side at down-shifted frequency [3] is presented. The fraction η (x) of the wave power deposited between the plasma edge and the radial location x is plotted, for propagation in the equatorial plane, $\bar{N}_{\parallel} \simeq 0.66$, $\Delta N_{\parallel} \simeq 0.12$, frequency f = 83 GHz, B(o) = 39 kG, T_e (o) = 2.5 keV.

The physical reasons of the variation of the wave damping may be understood considering Fig.3, where the contours of constant f at steady-state are plotted vs $\vec{u} = \vec{p} / (mTe)^{1/2}$, for x = 20 cm and the conditions of Fig.2. It appears that for large $u_\perp$ the distribution function is greater than the initial Maxwellian. In this case, at steady-state, the overall population of the resonant electrons is much greater than at t = 0 The increased value of f can easily overcome the quasilinear perpendicular flattening and explains the increase of k''_o. In contrast, for resonant velocities in the thermal range, as it occurs for wave absorption at $\omega = \omega_c$ the increase of the resonant electron population is negligible and the wave damping decreases.

The wave damping dependence on the parallel angular width $\Delta\psi$ of the wave spectrum and on the magnitude of the resonant velocity is examined in Fig.4. The launching conditions and the other parameters are as in Fig.3, but we assume the wave power to be P = 0.5 MW at x = 20 cm. The electrons, resonating with the center of the spectrum, have a parallel momentum near $u_\parallel$ = - 3.4, - 3.7, - 4 (for B(o) = 38.5, 39, 39.5 kG respectively). Fig.4 shows the importance of the down-shifted frequency [3] as a factor of the wave damping enhancement over the Maxwellian value.

a) permanent address : Laboratoire de Physique des Milieux Ionisés, Université de NANCY I, Nancy, France

b) Permanent address : Instituto de Fisica, Universidade Federal do Rio Grande do Sul, 90049 Porto Alegre, RS, Brazil.

1 I. Fidone, R.L. Meyer, and G. Granata, Phys. Fluids 26, 3292 (1983)

2 I. Fidone, G. Granata, and R.L. Meyer, Phys Fluids 25, 2249 (1982)

3 I. Fidone, G. Giruzzi, and E. Mazzucato, Phys. Fluids 28, 1224 (1985).

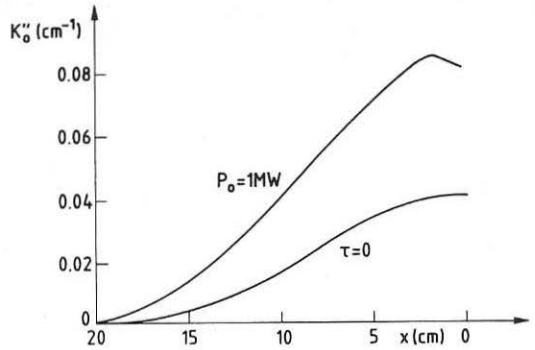

Fig. 1

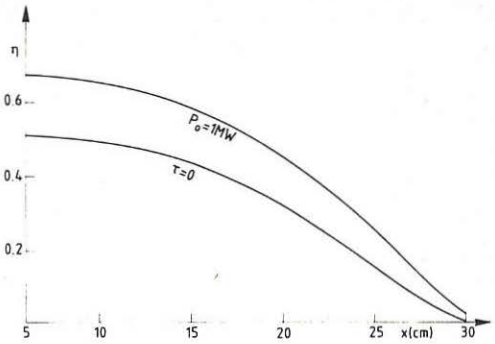

Fig. 2

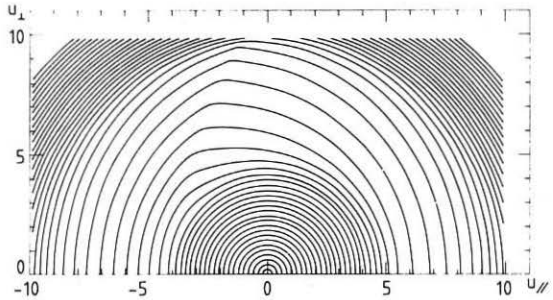

Fig. 3

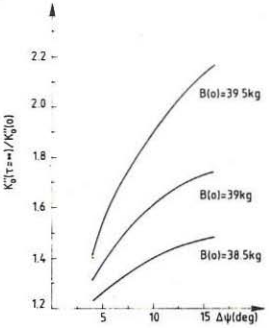

Fig. 4

TAIL MODE STABILIZATION BY ELECTRON CYCLOTRON WAVES IN A LOWER HYBRID SUSTAINED PLASMA

D.Farina, M.Lontano, R. Pozzoli(+)
Istituto di Fisica del Plasma, Associazione CNR/EURATOM
MILANO, Italy
(+)Dipartimento di Fisica, Università degli Studi di Milano, MILANO, Italy

In Lower Hybrid (LH) sustained plasmas the occurrence of tail mode activity has been shown to deteriorate the particle and energy transport /1/. This mode can be stabilized by the injection of Electron Cyclotron (EC) waves interacting with suprathermal electrons /2,3/.

The aim of this paper is to provide a theoretical basis for the understanding of this process. First, we compute the stationary electron distribution under the action of LH and EC waves; then, we analyze the stability condition of the tail mode.

In the frame of the quasilinear approach, the electron distribution function $f(u_\parallel, u_\perp)$ in the stationary state satisfies the following equation:

$$D_{lh}(f) + D_{ec}(f) + C(f) = 0, \qquad (1)$$

with $u_\parallel = v_\parallel / v_t$, $u_\perp = v_\perp / v_t$, $v_t = \sqrt{2T_o/m}$ and T_o is the bulk temperature. Here D_{lh} is the q.l. diffusion term due to LH waves, characterized by the spectrum $k_{\parallel 2} < k_\parallel < k_{\parallel 1}$. This term, localized in the resonant region $u_1 < u_\parallel < u_2$, writes:

$$D_{lh} = \frac{\partial}{\partial u_\parallel}\left[D_o \frac{\partial f}{\partial u_\parallel} \right]; \qquad (2)$$

D_{ec} represents the q.l. diffusion due to EC waves; for an ordinary mode (OM) in perpendicular propagation it is given by

$$D_{ec} = \frac{u_\parallel^2}{u_\perp} \frac{\partial}{\partial u_\perp}\left[u_\perp D \frac{\partial f}{\partial u_\perp} \right]; \qquad (3)$$

C is the collisional term. For suprathermal electrons it writes

$$C = \frac{\partial S_\parallel^c}{\partial u_\parallel} + \frac{1}{u_\perp} \frac{\partial}{\partial u_\perp}\left(u_\perp S_\perp^c \right) \qquad (4)$$

where $$S_{\parallel}^{c} = \frac{u_\perp}{u^3}\left(u_\perp \frac{\partial f}{\partial u_\parallel} - u_\parallel \frac{\partial f}{\partial u_\perp}\right) + \frac{u_\parallel}{u^3}\left(\frac{u_\parallel}{2u^2}\frac{\partial f}{\partial u_\parallel} + \frac{u_\perp}{2u^2}\frac{\partial f}{\partial u_\perp} + f\right)$$

$$S_{\perp}^{c} = -\frac{u_\parallel}{u^3}\left(u_\perp \frac{\partial f}{\partial u_\parallel} - u_\parallel \frac{\partial f}{\partial u_\perp}\right) + \frac{u_\perp}{u^3}\left(\frac{u_\parallel}{2u^2}\frac{\partial f}{\partial u_\parallel} + \frac{u_\perp}{2u^2}\frac{\partial f}{\partial u_\perp} + f\right).$$

Note that the terms D_o and D in Eqs(2),(3) are normalized to the thermal collision frequency $\nu(v_t) = 4\pi e^4 n \Lambda / m^2 v_t^2$.

We follow here the method developed by D. Hewett et al./4/ for the analysis of the electron distribution in the presence of LH waves.

With the assumption $D_o >> 1$, we put $f = \varphi(u_\perp)\exp\{\psi(u_\parallel, u_\perp)/D\}$. Taking the leading order terms in Eq.(1), we obtain

$$\frac{\partial \psi}{\partial u_\parallel} \cong -\frac{u_\perp}{(u_\perp^2+x)^{3/2}}\left(x + \frac{u_\perp^2}{x+u_\perp^2}\right) - \frac{4}{\varphi}\frac{d}{dx}(x\varphi')\chi(u_\parallel, x) + \\ - \frac{4}{\varphi}\frac{\partial}{\partial x}\left[x\varphi' d(u_\parallel)\right] \qquad (5)$$

where $x = u_\perp^2$, $\chi(u_\parallel, x) = \ln\frac{u_\parallel + \sqrt{x+u_\parallel^2}}{u_\perp + \sqrt{x+u_\perp^2}} - \frac{u_\parallel}{\sqrt{x+u_\parallel^2}} + \frac{u_\perp}{\sqrt{x+u_\perp^2}}$; $d(u_\parallel) = \int_{u_\perp}^{u_\parallel} dt\, t^2 \Delta$.

Requiring that the parallel flux be continuous at the boundaries $u_\parallel = u_1, u_2$ and retaining that on the boundary the function f be Maxwellian with respect to $u_\parallel$: $\partial f/\partial u_\parallel = -2u_\parallel f$, we obtain the following equation for φ :

$$\frac{d}{dx}(x\varphi') + \frac{R}{4\chi + d}\varphi = 0 \qquad (6)$$

where $d = d(u_2)$, $R = 2x\left[\frac{u_\perp}{(x+u_1^2)^{3/2}} - \frac{u_2}{(x+u_2^2)^{3/2}}\right] + \frac{u_1^3}{(x+u_1^2)^{5/2}} - \frac{u_2^3}{(x+u_2^2)^{5/2}}$.

From the numerical solution of Eq.(6) the distribution φ can be computed. Here we use an analytical model of φ, which contains the essential behaviour of the numerical solution, to analyze the tail instability in the presence of EC waves. We assume, in the resonant region

$$\varphi(x) = A \exp(-\alpha x) \qquad (7)$$

where $\alpha = \left(\frac{1}{u_1^2} - \frac{1}{u_2^2}\right)\Big/\left(4\ln\frac{u_2}{u_1} + d\right)$.

The imaginary part ε_i of the scalar dielectric permittivity for the modes characterized by $\varepsilon_r \simeq 1 - \frac{\omega_{pe}^2}{\omega^2}\frac{k_\parallel^2}{k^2} \simeq 0$ is given by

$$\varepsilon_i \simeq A\frac{\pi}{2n_0}\frac{\omega_{pe}^2}{k^2}v_t\left\{\frac{2\sqrt{\pi}}{D_0\alpha^{1/2}}u_1 + \frac{1}{8D_0}\left[\frac{\sqrt{\pi}}{\alpha^{3/2}}u_1 + \frac{3}{\alpha^{5/2}}\frac{u_r+u_1}{u_2(u_2+u_1)}\right] + \right.$$

$$\left. - \frac{1}{4}\frac{k_\perp}{k_\parallel}\frac{1}{\alpha}\frac{k_\perp v_t}{\omega_{ce}}\right\}, \qquad (8)$$

where $u_r = (\omega+\omega_{ce})/k_\parallel v_t$, and only the leading contributions in $1/\alpha$ have been written. This expression is valid when both $\omega/k_\parallel v_t$ and $(\omega+\omega_{ce})/k_\parallel v_t$ belong to the interval u_1, u_2; otherwise the distribution is stable.

From the Eq.(8) we obtain the marginal stability condition for the perpendicular temperature of the tail $T_\perp$:

$$\frac{1}{\alpha} = \frac{T_\perp}{T_0} \gtrsim D_0^{2/3}\left[\frac{2}{3}\frac{u_2}{k_\perp \lambda_D}\frac{\omega_{ce}}{\omega_{pe}}\right]^{2/3}. \qquad (9)$$

Taking into account the relation (7), between $T_\perp$ and D, and that between the injected power P_{in} and the local electric field E_{ec} of the EC waves, with frequency ω_o ,

$$D = \frac{\pi}{4}E_{ec}^2\frac{e^2}{m^2c^2}\frac{\omega_o}{\omega_{ce}^2}\left(1-\frac{\omega_{pe}^2}{\omega_o^2}\right)\frac{1}{\Delta n_\parallel}\frac{1}{\nu} \qquad (10)$$

($\Delta n_\parallel$ is the $n_\parallel$-spread around the perpendicular propagation) where, from the Poynting theorem,

$$P_{in} = \frac{1}{8\pi}E_{ec}^2 \cdot c \cdot S\left(1-\frac{\omega_{pe}^2}{\omega_o^2}\right)^{1/2}, \qquad (11)$$

we can correlate the stability condition to the required EC power. S is the illumination surface.

A condition favourable to stabilization occurs when the non relativistic EC resonance is outside the plasma and the whole power of the EC waves can be absorbed by the electrons of the tail. This is the case, for instance, of the FTU tokamak, su-

stained by 8 Ghz LH waves, operating with a 7T magnetic field on the axis, with a peak electron density $\hat{n} < 2 \times 10^{14} cm^{-3}$, under the irradiation of 140 Ghz EC waves.

References

/1/ - S.C. Luckardt, K.I. Chen et al., Internal Report PFC/JA-84-42 MIT-PFC (1984);

/2/ - S.C. Luckardt, G. Bekefi et al., Proc. 3rd International Symposium on Heating in Toroidal Plasmas, Vol.2, 529 (Brussels,1982);

/3/ - T. Maekawa, T. Cho et al., Nuclear Fusion, 23,242 (1983);

/4/ - D. Hewett, K. Hizanidis et al., Proc. IAEA Techn. Comm. Meeting on Non-Inductive Current Drive in Tokamaks, Vol. 1, 124 (Culham, 1983).

WAVE DYNAMICAL ANALYSIS OF EC WAVES PROPAGATING IN A PLASMA SLAB ACROSS BOTH EC AND UH RESONANCES

G. Lampis, C. Maroli, V. Petrillo

Associazione CNR-EURATOM
Istituto di Fisica del Plasma del CNR,
Via Bassini,15 20133 MILANO (ITALY)

Istituto di Scienze Fisiche dell'Università
Via Celoria,16 20133 MILANO (ITALY)

A wave dynamical analysis is given of the propagation and absorption of extraordinary waves in a plasma slab, across both electron-cyclotron (EC) and upper-hybrid (UH) resonances.

The confining magnetic field is directed along the z-direction with $B_z(x) = B_0(1+x/R_0)$ (R_0 is the tokamak major radius). The density gradient is along the x-direction.

The electric field components of an e.m. wave injected in the equatorial plane with an arbitrary angle with respect to the magnetic field B_z, satisfy the Maxwell system:

$$ik_z E_z' + (k_z^2 - \omega^2/c^2) E_x - i(4\pi\omega/c^2) J_x = 0 \qquad (1)$$

$$-E_y'' + (k_z^2 - \omega^2/c^2) E_y - i(4\pi\omega/c^2) J_y = 0 \qquad (2)$$

$$-E_z'' + ik_z E_x' - (\omega^2/c^2) E_z - i(4\pi\omega/c^2) J_z = 0 \qquad (3)$$

The current density is obtained from the linearized relativistic Vlasov equation /1/ and the undisturbed electron distribution is maxwellian.

The Vlasov equation is solved along the characteristics and, for the current density one finds:

$$J_x = F \int d\underline{\pi} \int_{-\infty}^{\phi} d\phi' \, \frac{\pi_\perp \cos\phi \, e^{\psi} \, n(x')}{(1+\pi^2)^{\frac{1}{2}} \omega_c(x')} \, R(\phi', x') \qquad (4)$$

$$J_y = F \int d\underline{\pi} \int_{-\infty}^{\phi} d\phi' \, \frac{\pi_\perp \sin\phi \, e^{\psi} \, n(x')}{(1+\pi^2)^{\frac{1}{2}} \omega_c(x')} \, R(\phi', x') \qquad (5)$$

$$J_z = F \int d\underline{\pi} \int_{-\infty}^{\phi} d\phi' \, \frac{\pi_\parallel \, e^{\psi} \, n(x')}{(1+\pi^2)^{\frac{1}{2}} \omega_c(x')} \, R(\phi', x') \qquad (6)$$

where:

$$F = -\omega_p^2 \mu^2 / (16\pi^2 n(x) K_2)$$

$$R(\phi',x') = \pi_\perp \cos\phi' E_x(x') + \pi_\perp \sin\phi' E_y(x') + \pi_\parallel E_z(x')$$

$$\psi = (-\mu(1+\pi^2)^{\frac{1}{2}} + i(\omega(1+\pi^2)^{\frac{1}{2}}/\omega_c(x) - k_z c\pi_\parallel/\omega_c(x)) \times \int_\phi^{\phi'} d\phi'' \exp(c\pi_\perp(\sin\phi - \sin\phi'')/(R_0\omega_c(0))$$

$$x' = (R_0 + x)\exp(s(\sin\phi - \sin\phi')) - R_0 \; ; \quad s = c\pi_\perp/(R_0\omega_c(0))$$

$$\mu = c^2/v_{th}^2 \; ; \quad \underline{\pi} = \underline{p}/m_0 c$$

where ϕ is the azimutal angle of $\underline{p}$. $K_2(\mu)$ is the McDonald function.

By introducing (4),(5),(6) respectively into (1),(2),(3) a system of three coupled integrodifferential equations is obtained. This system is transformed into a differential one by expanding $x' = x + O(s)$ around $s=0$.

In order to simplify the final equations, one has to assume: i) $\lambda_0/R_0 \ll 1$, which is the usual WKB limit; ii) $\mu \gg 1$, which is the weakly relativistic limit; iii) $\lambda_0 \mu^{\frac{1}{2}}/R_0 \lesssim 1$, satisfied in nearly all cases of practical interest. λ_0 is the vacuum wave length.

With these limitations the current vector is:

$$\underline{J}(x) = \sum_{k=0,\ldots,4} \underline{\underline{g}}_k(x) \cdot (d^k \underline{E}(x)/dx^k). \qquad (7)$$

In the construction of the elements of the generalized conductivity tensors $\underline{\underline{g}}_k(x)$, only the terms $O(1)$, $O(\mu)$, $O(\lambda_0\mu/R_0)$ and $O(\lambda_0\mu^2/R_0)$ are kept into account.

The matrix elements are expressed in terms of the Shkarovsky functions. (/2/)

By inserting $\underline{J}$ into the propagation equations, a system of the tenth order is found for E_x, E_y, E_z.

Numerical results

The boundary value problem associated to this system is solved by applying the numerical routine COLSYS(/3/), which is based on spline collocation method.

The solutions give a global-wave description of the conversion of the incoming extraordinary wave into electron Bernstein waves at the upper-hybrid layer as well as of the damping of these waves in the region between the EC and UH layers.

Both purely relativistic ($n_\parallel = 0$) and classical ($n_\parallel > v_{th}/c$) cases are examined in detail.

Fig. (1) shows the real part of the electric field x-component and the Poynting vector $\langle P_x \rangle$ for purely perpendicular injection and $\mu = 1000$ for various density values.

At very low densities, the plasma is transparent and no Bernstein waves are present.

Increasing the density, short wave-length oscillations begin to appear, and for $X = \omega_{pe}^2/\omega^2 \geq 2.5\ 10^{-2}$ Bernstein waves between the EC and UH resonances are clearly recognizable.

The cyclotron damping of these waves is located at the left of the ECR.

Increasing the angle θ between $\underline{k}$ and the direction perpendicular to B_z for fixed density ($X = 10^{-2}$) the Bernstein waves gradually disappear, because the density threshold for B-waves generation raises with the angle (Fig. (2)).

For oblique propagation, the wave is strongly damped inside the EC layer in the XM polarization.

Fig.(3) shows the absorption coefficient versus X for three values of the injection angle.

These curves are totally independent upon the electron temperature, while the electric field shape and the conversion efficiency are very much sensitive to such parameter.

Fig. (4) shows the absorption and transmission coefficients as a function of the injection angle.

A very simple analytical formula fits very well the transmission coefficient numerical values:

$$T = \exp(-\phi) \qquad (8)$$

where:

$$\phi = (\omega a \pi R X)/(2c Y^2) \qquad \text{for } \theta = 0^\circ \quad (9)$$

$$\phi = \frac{\omega a \pi X R (1+n_\parallel^2)\, \mathrm{erf}(\sqrt{\mu}/(n_\parallel R))}{2c\ (1-n_\parallel^2)^{1/2}} \qquad \text{for } \theta > 0^\circ \quad (10).$$

For the high field side injection the reflection coefficient is zero, and :

$$A = 1 - \exp(-\phi). \qquad (11)$$

R is the aspect ratio, and $Y = \omega_c(x)/\omega$.

The absorption coefficient (11) accounts for the contribution of both X and Bernstein modes.

REFERENCES

/1/ C. Maroli, V.Petrillo,G.Lampis,F.Engelmann;Plasma Phys.&C.F. (in press)

/2/ Y.P. Shkarovsky: Phys. Fluids 9,570 (1966)

/3/ U.Asher,J.Christiansen,R.D.Russell: Math.Comp.33,659(1979)

Fig.1 - $\mathrm{Re}(E_x)$, $\langle P_x \rangle$ in arbitrary units, for $-0.2 \leq x \leq 0.2$; $\mu = 1000$; $\theta = 0^\circ$; $B_0 = 5$kG; $R_0 = 51$ cm; a = 17 cm; XM from inside and X = 0.002 , 0.012 , 0.025 , 0.1 from top to bottom.

Fig.2 - $\mathrm{Re}(E_x)$, $|\underline{E}|$ in arbitrary units, for $-1 \leq x \leq 1$;

μ = 1000; X = 0.01; B_0 = 5 kG; XM from inside and $\theta = 10^o, 30^o, 45^o, 80^o$ from top to bottom.

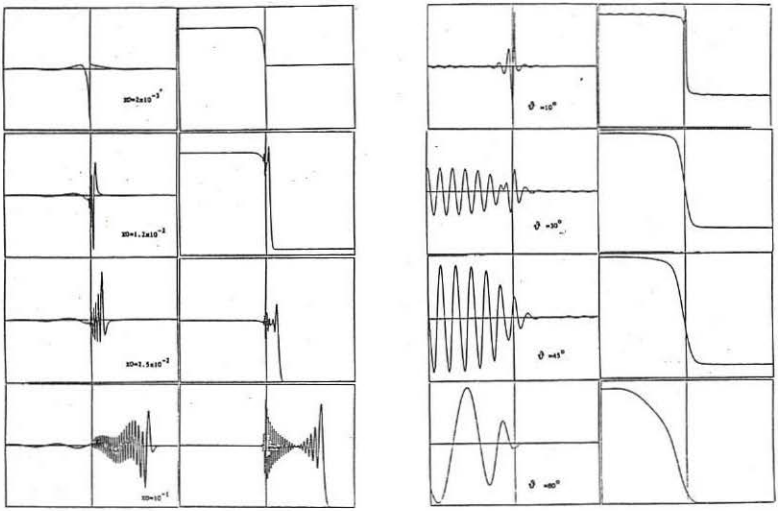

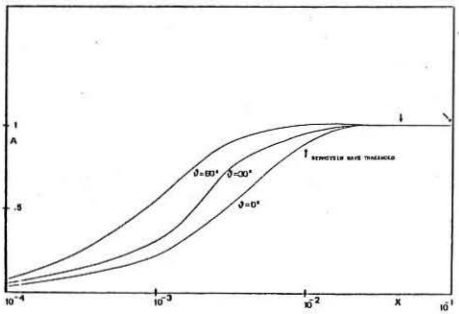

Fig.3 - Absorption factor vs X, for $\theta = 60^o, 30^o 0^o$; μ = 1000; B_o=5kG. The arrows show the thresholds for Bernstein waves excitation.

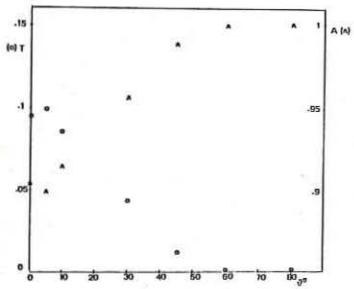

Fig.4 - Transmission and absorption factors vs θ, for X = 0.01; μ = 1000; B_o = 5 kG.

WAVE ABSORPTION NEAR THE SECOND ELECTRON CYCLOTRON HARMONIC IN NON-MAXWELLIAN PLASMAS

S.Pešić

Laboratory for Physics, Institute "B.Kidrič" - Vinča,
P.O.Box 522, 11001 Belgrade, Yugoslavia

Previous theoretical studies of wave absorption near the second electron cyclotron harmonic (SECH) have usually considered the case in which the plasma is characterized by isotropic Maxwellian distribution /1-4/. In order to gain an insight into the wave damping under nonequilibrium conditions which frequently exist in real plasmas, in the present paper we extend our earlier work /4/ and examine the linear wave propagation and spatial wave damping around the SECH in presence of thermal anisotropy and longitudinal drift motion.

We consider a high-temperature magnetically confined plasma in which the electron distribution function is close to the model distribution,

$$F(p_\perp, p_{//}) = \frac{1}{\pi^{3/2} m_0^3 v_{t\perp}^2 v_{t//}} \exp\{-\frac{(p_{//}-p_0)^2}{m_0^2 v_{t//}^2} - \frac{p_\perp^2}{m_0^2 v_{t\perp}^2}\} . \qquad (1)$$

Starting from the general expression for the dielectric tensor and carrying out the corresponding momentum space integration within the weakly relativistic approximation ($\gamma = \{1 + p^2/m_0^2c^2\}^{1/2} \cong 1 + p^2/2m_0^2c^2$) one obtains,

$$\varepsilon_{ij} = \delta_{ij} - i2X\mu_{//} \sum_{n=-\infty}^{\infty} \int_0^\infty d\tau\, M_{ij} \frac{\exp(-\Lambda) I_n(\Lambda)}{(1-i\tau)^{1/2}(1-i\alpha\tau)}$$

$$\times \exp\{i\tau[V\sqrt{2}(1-i\tau)^{-1} + \mu_{//}(1-n\Upsilon) - N_{//}^2 c^2/v_{t//}^2]\}, \qquad (2)$$

where $X = \omega_p^2/\omega^2$, $\Upsilon = \omega_c/\omega$, ω_p and ω_c being, respectively, the electron plasma and cyclotron frequency, $\mu_{\perp//} = 2c^2/v_{t\perp//}^2$, v_t is the electron thermal velocity, $\Lambda = \lambda/(1-i\alpha\tau)$, $\lambda = N_\perp^2/\mu_\perp \Upsilon^2$, $\vec{N} = \vec{k}c/\omega$ is the wave refractive index, $\alpha = T_\perp/T_{//}$, $V = (u - N_{//}c)/v_{t//}$, u is the electron drift velocity and the indices $\perp$ and // refer to the direction respectively, perpendicular and parallel to the applied magnetic field. The complete expressions for the

elements of the matrix M_{ij} are given in /5/. In evaluating the dielectric tensor ε_{ij} the ion dynamics is ignored since it is negligible in the frequency range of interest ($\omega \cong 2\omega_c$). Furthermore, in the integration over $p_\perp$ and $p_{//}$ the relativistic factor γ is retained only in the exponential part of the integrand /5/. It should be pointed out here that the previous approximation is justified only when the short-time ($\omega t < \mu_{//}$) behaviour of the phase is dominant or more precisely, for $\mu_{//}N_{//}^2 >> 1$. This conclusion is further verified by comparing the calculated values of the complete weakly-relativistic dispersion function of Shkarofsky /6/ with the corresponding integral in (2) for an isotropic plasma without drift.

The wave propagation and spatial damping in the considered plasma are analysed within the local wave dispersion description. The complete dispersion equation governing electromagnetic waves in a plasma confined by a magnetic field whose direction is perpendicular to that of the gradients (see, for instance /4/) is solved numerically for a wide range of plasma parameters and wave propagation conditions. In the numerical analysis of this equation the finite Larmor radius effects are retained up to the second order in λ. The parallel component of the wave refractive index is assumed to be real and determined by the direction of the wave vector of the incident electromagnetic waves at the plasma-vacuum interface, $N_{//} = \cos\theta_i$. In order to simulate the toroidal discharge conditions we took $\vec{B} = B(0)\vec{e}_z/(1 + x/A)$ with $x = r\cos\phi/a$, $\phi = 0$ or $\phi=\pi$ and an aspect ratio $A = 3$. Furthermore, the electron density and temperature are allowed to have a parabolic radial profile.

First we present the results concerning the propagation and spatial damping of the extraordinary (X) mode in the considered nonthermal plasma. We recall that at large propagation angles mode splitting and coupling of the extraordinary and fast quasi-longitudinal modes occurs /4/. The thermal anisotropy enhances the mode coupling. Namely, the range in the parameter plane $\{(\omega_p/\omega_c)^2, c/v_{t//}\}$ in which mode coupling occurs, enlarges significantly for increasing the temperature-anisotropy ratio α. In general, the thermal anisotropy causes a pronounced deviation of $ReN_{\perp x}$ from the corresponding cold plasma values and a strong assymetry of the absorption line profiles about the resonance. To illustrate the wave behaviour around the SECH we present in Fig. 1. the variation of the real and imaginary part of $N_{\perp x}$ with the dimensionless space coordinate x for $\omega_p^2(0)/\omega_c^2(0) = 1.4$, $\theta_i = 60^0$, $c/v_{t//}(0) =$

= 16 and several values of α. Here and in Figs. 2.-3. we took a driving frequency equal to the second harmonic of the "central" electron cyclotron frequency. We see that the increase of α leads to an important enlargement of the wave damping region towards the high-magnetic field side. This suggests the use of wave launching at downshifted frequencies ($f < f_c(0)$) in small size plasmas with a strong thermal anisotropy. Besides, in the considered parameters range ($\theta_i \geq 60^o$, $c/v_{t//}(0) \geq 8$, $\alpha = 0.5\text{-}8.$) it is found that $\mathrm{Max}(\mathrm{Im}N_{\perp x})$ scales with $(\omega_p/\omega_c)^2 \alpha c/v_{t//}$ while the dependence on $N_{//}$ is stronger than $N_{//}^{-1}$. The spatial deposition of the wave energy for launching from the low magnetic field side is presented in Fig. 2. where we plot the variation with x of the normalized optical depth $\eta_x/k_0 a = \int_a^x dx' \, \mathrm{Im}N_\perp(x')$ for $\omega_p^2(0)/\omega_c^2(0) = 1.4$, $\theta_i = 70^o$, $c/v_{t//}(0) = 16$ and several values of α. As one can see, for $\alpha > 0.1$ complete absorption in a single pass takes place. Large values of the normalized optical depth of the X-mode ($\eta_x/k_0 a = O(10^{-3})$) are reached only in the vicinity of the resonance position. Therefrom, for wave launching from the low magnetic field side in large size plasmas ($k_0 a \geq \geq 10^3$), the interaction between the X-mode and energetic electrons on the far tail of the

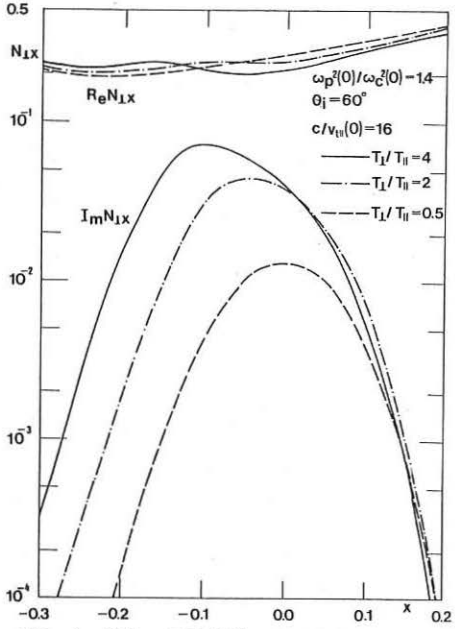

Fig. 1. $\mathrm{Re}N_{\perp x}$ and $\mathrm{Im}N_{\perp x}$ versus x.

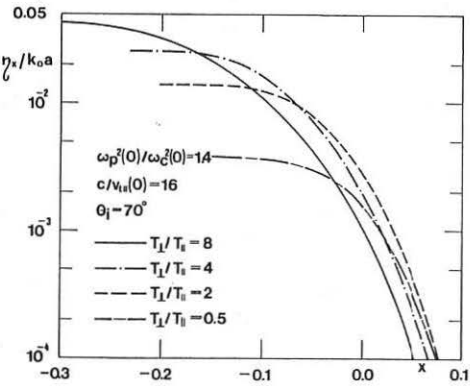

Fig. 2. The normalized optical depth vs x.

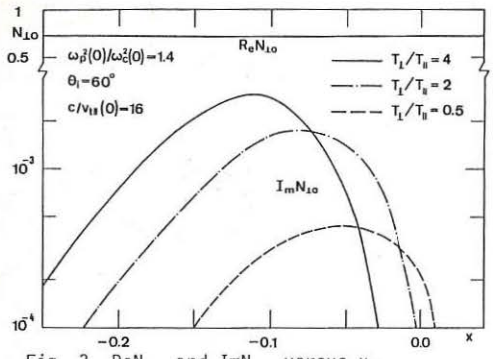

Fig. 3. $ReN_{\perp O}$ and $ImN_{\perp O}$ versus x.

absorption line profile is weak.

The presence of longitudinal drift motion displaces the absorption line profiles towards the low magnetic field side (for $k_{\parallel}>0$). The assymetry of the absorption line profiles reduces and the maximum of $ImN_{\perp X}$ somewhat increases for increasing $u/v_{t\parallel}$. For $u/v_{t\parallel}\leq 2$ the total optical depth of the X-mode is slightly affected by the electron drift motion. However, the region of maximum absorption shifts towards the plasma edge.

Let us now discuss briefly the spatial damping of the ordinary (O) mode around the SECH. In Fig. 3. we show the variation of the real and imaginary part of $N_{\perp O}$ with the dimensionless space coordinate x for $\omega_p^2(0)/\omega_c^2(0)=1.4$, $\theta_i=60^0$, $c/v_{t\parallel}(0)=16$ and several values of α. As one might guess the spatial damping of the O-mode is much weaker than the X-mode damping. In the considered parameters range the maximum value of the normalized optical depth is $\eta_O/k_0a=\mathcal{O}(10^{-4})$. One concludes that in spite of the enhancement of the spatial damping caused by the increase of the perpendicular temperature, the O-mode is absorbed completely in one pass through the resonance only in very large size plasmas.

References

1. Hui,B. et al., Phys. Fluids 23,822(1980).
2. Bornatici,M. et al., Plasma Physics 23,89(1981).
3. Hsu,J.Y. et al.,Phys. Fluids 26,3300(1983).
4. Pešić,S.,Contributed Papers of the 12th ECCFPP,part II,p.88(1985).
5. Tsai,S.T. et al.,Phys. Fluids 24,2186(1981).
6. Shkarofsky,I.P.,Phys. Fluids 9,591(1966).

PARAMETRIC INSTABILITIES OF ELECTRON CYCLOTRON WAVES

P.K. Shukla and M.Y. Yu
Institut für Theoretische Physik, Ruhr-Universität Bochum,
D-4630 Bochum, FRG

L. Stenflo
Department of Plasma Physics, Umea University,
S-90187 Umea, Sweden

During high frequency wave heating experiments, intense electron cyclotron waves may be generated in the plasma. It is thus of interest to understand the behavior of such waves. In this paper, a set of nonlinear equations describing the interaction of large amplitude electron cyclotron waves with low-frequency electrostatic fluctuations in a non-uniform magnetized plasma is derived. The ponderomotive force as well as differential Ohmic heating nonlinearities are included. General dispersion relations describing parametric processes are discussed, and modulational as well as filamentational instabilities are studied. Application of our results to electron cyclotron resonance heating of fusion plasmas shall be discussed.

We consider weakly damped right-hand circularly polarized electromagnetic waves propagating along the ambient magnetic field $B_o\hat{z}$. The frequency ω and wave number k_z satisfy the dispersion relation

$$\omega^2 = k_z^2c^2 + \omega\omega_{pe}^2(\omega - \omega_{ce})^{-1}, \qquad (1)$$

which is valid for $|\omega - \omega_{ce}| \gg k_z v_{te}, k_z v_{dez}$, and $\omega \gg (\omega_{ci}\omega_{ce})^{1/2}$. Here, v_{te} is the electron thermal velocity, v_{dez} is the electron drift velocity along z, ω_{ci} $(= q_iB_o/m_i)$ is the ion gyrofrequency, ω_{ce} is the electron gyrofrequency, and $\omega_{pe} = (n_oq_e/\varepsilon_om_e)^{1/2}$ is the electron plasma frequency. The unperturbed average plasma density is denoted by n_o.

The nonlinear interaction of the electromagnetic waves with the background slow plasma motion gives rise to an envelope of high-frequency waves whose amplitude E obeys the equation [1,2]

$$i(\partial_t + \gamma + v_{gz}\partial_z)E + \frac{v'_{gz}}{2}\partial_z^2E + \frac{v'_{g\perp}}{2}\nabla_\perp^2E - \Delta E = 0 , \qquad (2)$$

where $v_{gz} = \partial\omega/\partial k_z = 2k_zc^2/[2\omega + \omega_{ce}\omega_{pe}^2/(\omega - \omega_{ce})^2]$,

$v'_{gz} = \partial^2\omega/\partial k_z^2 = \{1 - (v_g^2/c^2)[1 - \omega_{ce}\omega_{pe}^2/(\omega - \omega_{ce})^3]\}v_{gz}/k_z$,

$v'_{g\perp} = \partial^2\omega/\partial k_\perp^2|_{k_\perp=o} = [1 - \omega_{pe}^2/2(\omega_{pe}^2 - \omega^2)(1 - \omega/\omega_{ce})]v_{gz}/k_z$,

$\gamma = (\nu_e/2)[\omega_{pe}^2/(\omega - \omega_{ce})^2]\omega v_{gz}/k_zc^2$, and ν_e is the electron collision frequency. The nonlinear frequency shift Δ is [1,2]

$$\Delta = \frac{\omega\,\omega_{pe}^2}{2(\omega-\omega_{ce})}\,\frac{v_{gz}}{k_z c^2}\left[N + \frac{\omega_{ce}k_z v_{ez}}{\omega(\omega-\omega_{ce})} + \frac{\omega_{ce}b}{\omega-\omega_{ce}}\right], \qquad (3)$$

where $N=n_e/n_o$ and $b = B_z/B_o$ are the normalized slowly varying density and parallel magnetic fields, and v_{ez} is the parallel component of the electron flow velocity associated with the slow motion.

In order to derive the equations governing the dynamics of the low-frequency fluctuations $(\Omega, \vec{K})$, we start with the continuity, momentum, and energy equations for each particle species, together with the Maxwell equations. These equations are given in, for example, Stenflo [3].

We shall consider here low-frequency electrostatic modulations. By linearizing the basic equations [3] but keeping the ponderomotive force $(-\vec{F}_p)$ in the electron momentum equation as well as the differential Ohmic heating nonlinearity in the electron energy equation, and following closely the derivation of Stenflo [3], one can derive the electron density perturbation which in Fourier analyzed form is given by

$$-i\omega_{pe}^2\varepsilon(\Omega,\vec{K})N/(1+\chi_i) = \vec{K}\cdot\underset{\approx}{\chi}_e(\Omega,\vec{K})\cdot(\vec{F}_p+\vec{F}_H), \qquad (4)$$

where $\varepsilon = 1+\chi_i+\chi_e$, $\underset{\approx}{\chi}_e$ is the susceptibility tensor for the electrons, and $\chi_e \equiv \vec{K}\cdot\underset{\approx}{\chi}_e\cdot\vec{K}/K^2$ and $\chi_i = \chi_i(\Omega,\vec{K})$ are the scalar susceptibilities for the electrons and ions, respectively. The latter are given by

$$\chi_j = K^2\left\{\lambda_{Dj}^2 - A(\omega-\vec{k}\cdot\vec{v}_{dj})(\omega-\vec{k}\cdot\vec{v}_{dj}+i\nu_j)[1-\omega_{cj}^2/(\omega-\vec{k}\cdot\vec{v}_{dj}+i\nu_j)^2]\right\}^{-1},$$

where $(\omega_{pj}^2 A)^{-1} \approx K^2 + \dfrac{q_j\vec{K}\cdot(\vec{B}_o\times\nabla n_o)}{m_j n_o(\omega-\vec{K}\cdot\vec{v}_{dj}+i\nu_j)} - \dfrac{q_j^2(\vec{K}\cdot\vec{B}_o)^2}{m_j^2(\omega-\vec{K}\cdot\vec{v}_{dj}+i\nu_j)^2}$

and λ_{Dj} is the Debye length.

The ponderomotive force $-\vec{F}_p$ is given by [1]

$$\vec{F}_p = i\frac{v_h^2}{2}\vec{K}_\perp + \frac{i(\omega-\omega_{ce})}{2\omega}\left(K_z + \frac{\omega_{ce}\Omega k_z}{\omega(\omega-\omega_{ce})}\right)v_h^2\hat{z}\,, \qquad (5)$$

where $v_h^2/2 = (q_e/m_e)^2|E|^2/(\omega-\omega_{ce})^2$.

The nonlinear heating force is

$$\vec{F}_H = -2\nu_e v_h^2\vec{K}/3\tilde{\Omega}\,, \qquad (6)$$

where $\tilde{\Omega} \equiv \Omega - \vec{K}\cdot\vec{v}_{de} + i/\tau + (2i/3n_o)(K_z^2 R_z + K_\perp^2 R_\perp)$, and τ is the electron energy relaxation time, R_z and $R_\perp$ are the heat diffusion coefficients along and across the external magnetic field, respectively. We have assumed that the density gradient scalelength is larger than the wavelength of the perturbations. In an analogous manner, we obtain

$$v_{ez} = - N v_{dez} - \frac{\Omega}{K^2} \frac{(\underset{\sim}{\chi}_e \cdot \vec{K})_z}{(1 + \chi_i)} N + \frac{i}{\omega_{pe}^2} \Omega [\underset{\sim}{\chi}_e \cdot (\vec{F}_p + \vec{F}_H)]_z \quad . \qquad (7)$$

Equation (2) combined with (3) and (7), and Eq. (4) combined with (5) and (6), form two coupled equations for the interaction between the high-frequency electromagnetic waves and the low-frequency collisional modes. The linear properties of these low-frequency electrostatic modes have been considered in detail by many authors. It is, however, of interest to note that the nonlinear heating force $\vec{F}_H$ can be much larger than the usual ponderomotive force $\vec{F}_p$.

Eliminating v_{ez} and N in (3) by means of (7) and (4), we obtain Δ in terms of $|E|^2$. Since the Fourier transformed version of the nonlinear frequency shift Δ has now been represented as $\alpha(\Omega,\vec{K})|E|^2$, Eq. (2) can be cast in the form of the cubic nonlinear Schrödinger equation. Following standard techniques [1], one can analyze the latter in order to derive the dispersion relation for the modulational instability of a whistler pump with amplitude E_o. The growth rate γ is then proportional to $[\alpha(K_z v_g, \vec{K})|E_o|^2]^{1/2}$. Clearly, γ involves the coupling factor α which depends on the dielectric susceptibilities (χ_i, χ_e) of the low-frequency electrostatic fluctuations. It is thus possible that the electron cyclotron waves can be modulationally unstable against long wavelength electrostatic perturbations whose spectra may depend on the choice of the frequency regime. As an illustration, we mention that in the frequency regimes $\Omega >> \omega_{ci}$, $|\Omega - \vec{K}\cdot\vec{v}_{de}| \ll \nu_e \ll \omega_{ce}$, one encounters collisional gradient drift modes which are essentially supported by unmagnetized ions and magnetized electrons. Our result shows that these convective plasma fluid modes could be excited by the electron cyclotron heater waves. It is then natural to expect an enhanced level of electrostatic fluctuations which may affect the plasma properties, as well as the propagation of electromagnetic waves in the magnetic fusion devices.

This work was supported by the Sonderforschungsbereich Plasmaphysik Bochum/Jülich.

References

[1] V.I. Karpman and H. Washimi, J. Plasma Phys. 18, 173 (1977).

[2] P.K. Shukla and L. Stenflo, Phys. Rev.A 30, 2110 (1984).

[3] L. Stenflo, J. Plasma Phys. 34, 95 (1985).

ELECTRON CYCLOTRON EMISSION FOR A RELATIVISTIC LOSS-CONE TYPE DISTRIBUTION FOR ARBITRARY PROPAGATION

M. Bornatici and U. Ruffina

Physics Department "A. Volta", University of Pavia, Pavia, Italy

Abstract. The fully relativistic electron cyclotron emission of both the extraordinary and ordinary mode is calculated analytically for a relativistic loss-cone type distribution for propagation at an arbitrary angle with respect to the magnetic field, accounting for both finite-density and finite Larmor radius effects. Numerical results are shown and discussed for the extraordinary mode.

The fully relativistic emissivity for arbitrary propagation. The electron cyclotron emissivity for an arbitrary electron distribution $f_o(p_\perp, p_\parallel)$, around the n-th harmonic of the electron cyclotron frequency, j_n, $n \geq 1$, can be written as [1]

$$\frac{j_n}{j_o} \equiv \left(\frac{N}{N_r}\right)^2 \cos\beta \, \frac{\rho \pm \sin^2\theta}{2\rho} \, \frac{\omega}{\omega_c} \, \frac{N}{N_\perp^2} \left(\frac{n\omega_c}{\omega}\right)^2 \times$$

$$\int \frac{d^3p}{\gamma} \, f_o(p_\perp, p_\parallel) \left| \left(\frac{E_x - iE_y}{E_y} + \frac{\omega}{n\omega_c} N_\perp \frac{p_\parallel}{mc} \frac{E_z}{E_y} \right) J_n + i \frac{b}{n} J_{n+1} \right|^2 \delta\left(\gamma - N_\parallel \frac{p_\parallel}{mc} - \frac{n\omega_c}{\omega}\right) \quad (1)$$

where $j_o \equiv \omega_p^2 \omega_c m/8\pi^2 c$; $N = N^{(i)}$ and $N_r = N_r^{(i)}$, i = X,O, are, respectively, the (cold) refractive and ray refractive index of the extraordinary (X) and ordinary (O) mode, with $N_\perp = N \sin\theta$ and $N_\parallel = N\cos\theta$, θ being the angle between the equilibrium magnetic field $B_o = B_o \hat{z}$ and the wave vector $\underline{k} = k_\perp \hat{x} + k_\parallel \hat{z}$; the angle β is such that $\beta = \sphericalangle(\underline{k}, \underline{S})$, with $\underline{S}$ the electromagnetic power flux density, which, in the cold plasma limit, reduces to the Poynting vector so that $4\pi |\underline{S}|/c|E_y|^2 = (N/\cos\beta)(2\rho/(\rho \pm \sin^2\theta))$, the plus (minus) sign referring to the X-mode (O-mode), with $\rho \equiv (\sin^4\theta + 4(\omega/\omega_c)^2[1-(\omega_p/\omega)^2]^2\cos^2\theta)^{1/2}$.
With reference to the integral over the momentum $\underline{p} = (p_\perp, p_\parallel)$, it has to be noted that i) the Bessel functions J_ν of argument $b \equiv (\omega/\omega_c) N_\perp (p_\perp/mc)$ account for finite Larmor radius (FLR) effects; ii) the coefficient of J_n has to do with the mode polarization, and ii) the δ-function accounts for the fully relativistic cyclotron resonance, with $\gamma \equiv [1 + (p/mc)^2]^{1/2}$.

To carry out the integration in (1), we use γ, $p_\parallel$ and the azimuthal angle of $\underline{p}$ as coordinates, the latter integration being readily carried out, whereas the $p_\parallel$-integration is performed simply by using the δ-function. For the γ-integration, it is convenient to change variable of integration [2,3], namely $\gamma = (1-N_\parallel^2)^{-1}[(n\omega_c/\omega) + |N_\parallel|(N_\parallel^2 + (n\omega_c/\omega)^2 - 1)^{1/2} t] \equiv \gamma(t)$, with $N_\parallel^2 < 1$ and $N_\parallel^2 + (n\omega_c/\omega)^2 - 1 \geq 0$. One thus obtains

$$\int \frac{d^3p}{\gamma} H(p_\perp, p_\parallel) = 2\pi (1-N_\parallel^2)^{-1} \left[N_\parallel^2 + \left(\frac{n\omega_c}{\omega}\right)^2 - 1\right]^{1/2} (mc)^3 \int_{-1}^{1} dt \, H\left(p_\perp = p_\perp^{(res)}(t), p_\parallel = p_\parallel^{(res)}(t)\right) \quad (2)$$

where $p_{\parallel}^{(res)}(t) \equiv (1/N_{\parallel})[\gamma(t) - n\omega_c/\omega]mc$ and $p_{\perp}^{(res)}(t) \equiv ([\gamma(t)]^2 - [1+(p_{\parallel}^{(res)}/mc)^2])^{1/2}$.

We consider explicitly a relativistic loss-cone distribution with loss-cone index ℓ. By making use of the series representation of the Bessel functions occurring in (1), the corresponding integration in (2) can be carried out analytically term by term by noting that

$$\int_{-1}^{1} dt\ (1-t^2)^m\ e^{-xt} = \sqrt{\pi}\ m!\ \left(\frac{2}{x}\right)^{m+1/2} I_{m+1/2}(x)$$

with I_ν the modified Bessel functions of the first kind. The resulting expression for the emissivity (1) is

$$\frac{j_n(X,O)}{j_O} = \left[\left(\frac{N_r}{N}\right)^2 \cos\theta\right] N\ \frac{\rho \pm \sin^2\theta}{2\rho}\ \left[\left(\frac{\pi}{2\mu}\right)^{1/2} \frac{e^{-\mu}}{K_{2+\ell}(\mu)}\right] \frac{n^2}{2^n (n-1)!}\ \left[(nN_\perp)^2 \frac{T}{mc^2}\right]^{n-1} \times$$

$$\times \sum_{k=0}^{\infty} C_{n,k}\ \frac{(n+k+\ell)!}{(n+k)!\,\ell!}\ \left[(nN_\perp)^2\ \frac{T}{mc^2}\right]^k F_{n,k}^{(X,O)}(\omega,\theta;\ell) \qquad (3)$$

where $\mu \equiv mc^2/T$; K_ν is the modified Bessel function of the second kind; the factor $C_{n,k}$ originates from the series representation of the Bessel functions,

$$C_{n,k} = (-1)^k\ \frac{n![2(n+k)]!}{2^k k!(2n+k)!(n+k)!}\ (=1 \text{ for } k=0)$$

The function $F^{(X,O)}$ describes the contribution from the mode polarization as well as the frequency dependence of the emissivity and is defined by

$$F_{n,k}^{(X,O)}(\omega,\theta;\ell) \equiv \left[(1+A)^2 + \frac{2k}{n}(1+A) + \frac{2k(k-1)(n+k)}{n^2[2(n+k)-1]}\right] G_{n+k-1,\ell} +$$

$$B\left\{\left[\frac{1-N_{\parallel}^2}{\mu N_{\parallel}^2} B + 2\left(1+A+\frac{k}{n}\right)\right] \left(\frac{n\omega}{\omega}\right)^2 G_{n+k,\ell} + B\left(\frac{n\omega}{\omega}\right)^4 G_{n+k+1,\ell}\right\} \qquad (4)$$

$$1+A \equiv i\left(\frac{E_x - iE_y}{E_y} + \frac{N_\perp N_\parallel}{1-N_\parallel^2}\ \frac{E_z}{E_y}\right) = 1+2\ \frac{\omega}{\omega_c}\ \frac{1-(\omega_p/\omega)^2}{\sin^2\theta \pm \rho} - \frac{n\omega_c}{\omega} B^{(X,O)} \qquad (5)$$

$$B \equiv -i\ \frac{\omega}{n\omega_c}\ \frac{N_\perp N_\parallel}{1-N_\parallel^2}\ \frac{E_z}{E_y} = 2n\left(\frac{\omega}{n\omega_c}\right)^2 \frac{N_\perp^2 N_\parallel^2}{1-N_\parallel^2}\ \frac{1}{\sin^2\theta \pm \rho} \equiv N_\parallel^2 B^{(X,O)} \qquad (6)$$

the results (5) and (6) being obtained by taking the mode polarization in the cold plasma limit (in particular, note that $B^{(X)} > 0$ whereas $B^{(O)} < 0$). Furthermore, the profile function $G_{q,\ell}$ in (4) is defined by

$$G_{q,\ell} \equiv \left(\frac{\omega}{n\omega_c}\right)^{2q+1}\ \frac{1}{(1-N_\parallel^2)^{1/2}}\ \left(\frac{1-N_\parallel^2}{\mu N_\parallel^2}\right)^{q+\ell+3/2} z_n^{\,} I_{q+\ell+3/2}(z_n) e^{-\mu \frac{n\omega_c/\omega - 1 + N_\parallel^2}{1-N_\parallel^2}} \qquad (7)$$

with $z_n \equiv \mu |N_\parallel| (1-N_\parallel^2)^{-1} [N_\parallel^2 + (n\omega_c/\omega)^2 - 1]^{1/2}$. In (3)-(6), the plus (minus) sign refers to the X mode (O mode).

With reference to the emissivity (3), it has to be noted that i) the summation over k originates from the series representation of the Bessel functions occurring in (1) and fully accounts for FLR effects, which are measured by the parameter $[(nN_\perp)^2 T/mc^2]$; ii) the loss-cone feature of the distribution affects both the profile and the strength of the emissivity, the former ef-

fect is due to the dependence of the profile function (7) on the loss-cone index ℓ, whereas the latter one is described by the factor $(n+k+\ell)!/[(n+k)!\ell!]$ that is an increasing function of ℓ.

Numerical Analysis and Discussion. Sample results of the numerical evaluation of the (total) emissivity $j = \sum_{n=1}^{\infty} j_n$ of the (fast) X mode are shown in Fig.1 for propagation at an angle $\theta=30°$, and in Fig.2 for $\theta=60°$ for $(\omega_p/\omega_c)^2=0.1$, $T=100keV(\approx 2(\omega_p/\omega_c)^2 mc^2)$ and loss-cone index $\ell=0;1;2$, and 3. The emission profile is the result of the overlap of (single peaked) contributions from different harmonics and, for the parameters considered, tends to pile up near the (cold) right-hand cutoff ($\omega/\omega_c \approx 1.1$) of the X mode. More specifically, the dominant contribution to the emissivity is due to the 2.nd harmonic, the weight of the $n \geq 3$-harmonics tending to increase as either the loss-cone index ℓ increases or θ tends to 90°, so that FLR effects are enhanced in either case. Furthermore, as ℓ increases and/or the propagation tends to perpendicular, the n-th harmonic contribution is such that its peak shifts to lower frequencies, i.e., towards the right-hand cutoff, whereas the corresponding height increases in so far as the (opposite) effect arising as one approaches the right-hand cutoff does not prevail. These two effects are displayed for the 2.nd harmonic in Fig. 3, where the non-monotonous dependence of the maximum (with respect to frequency) of $j_2^{(X)}$ with respect to both the loss-cone index ℓ and the propagation angle θ is shown together with the corresponding dependence of the frequency connected with the peak itself.

With respect to the value corresponding to the Maxwellian distribution, i.e., for $\ell=0$, the emissivity is enhanced by the loss-cone, except for propagation at small angles as in Fig. 1, for which there is a sharply peaked contribution from the 1.st harmonic, brought about by both the significant frequency upshift and the increase of the line width due to the longitudinal Doppler effect; such a contribution decreases as either θ or ℓ increases. Finally, with respect to the emission profile for perpendicular propagation [4], the line structure becomes less pronounced with decreasing θ, and the emissivity tends to be single peaked for propagation at small angles and for moderately high values of ℓ, as it appears from Fig.1 for the curves corresponding to $\ell=2$ and $\ell=3$.

References

1. M. Bornatici, R. Cano, O. De Barbieri, and F. Engelmann, Nucl. Fusion 23, 1153 (1983)
2. S. Tamor, Nucl. Fusion 18, 229 (1978)
3. M. Bornatici, and U. Ruffina, Nuovo Cimento 6D, 231 (1985)
4. M. Bornatici, and U. Ruffina, FOM-Instituut voor Plasmafysica, Rijnhuizen, Nieuwegein, I.R. 86/004 (submitted to Plasma Phys.)

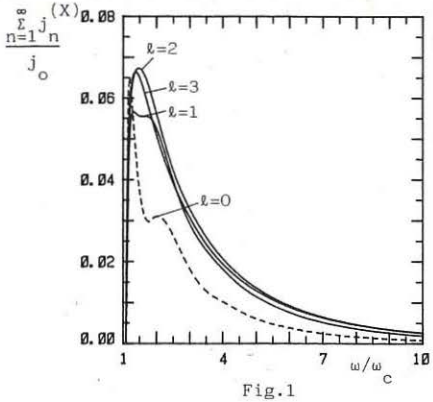

Fig.1

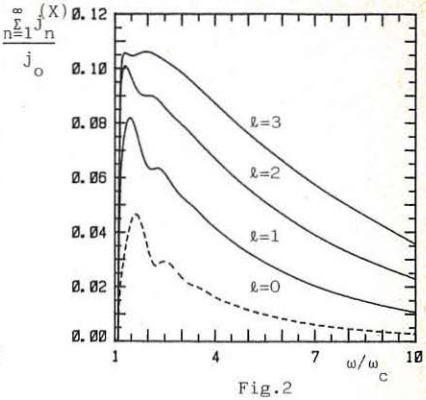

Fig.2

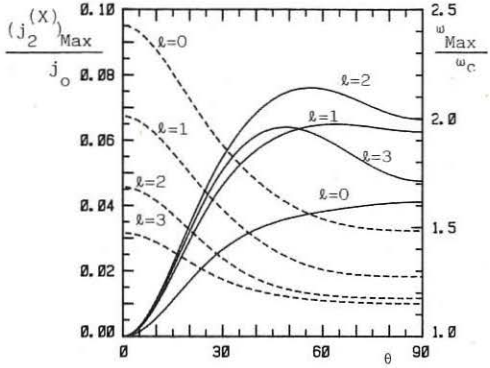

Fig.3

Figure Captions

Fig.1. The dimensionless emissivity of the (fast) extraordinary mode as a function of frequency for $(\omega_p/\omega_c)^2=0.1$, T=100keV, loss-cone index ℓ=1;2;3, and propagation angle θ=30°. The dashed curve refers to the Maxwellian distribution (ℓ=0).

Fig.2. Same as Fig. 1 for θ=60°.

Fig.3. Peak value of the emissivity (solid line) and frequency corresponding to the peak emissivity (dashed line) of the 2.nd harmonic extraordinary mode as a function of the propagation angle for $(\omega_p/\omega_c)^2=0.1$, T=100keV and loss-cone index ℓ=0;1;2, and 3.

THEORY OF LINEAR MODE CONVERSION

R.A.Cairns[a] and C.N.Lashmore-Davies[b]

(a)Department of Applied Mathematics,
University of St.Andrews,St.Andrews,Fife, Scotland
(b)UKAEA, Culham Laboratory, Abingdon, Oxon U.K.
(Euratom/UKAEA Fusion Association)

In a previous paper[1] we described a method of treating a class of mode conversion problems using a simple technique involving only algebraic manipulations of the local dispersion relation. A number of examples showed that existing results could be obtained in a very simple way. While there is ample evidence that the technique works, a number of questions remain concerning its derivation and the way in which the wave amplitudes which it introduces are related to the electromagnetic field in the plasma. The aim of the present paper is to resolve at least some of these questions by developing in more detail the theory for the case in which one of the modes is a localized non-propagating disturbance. Many of the examples which we have analyzed previously are of this type.[1]

We begin with a very brief review of our earlier theory which deals with systems whose dispersion relation is of the form shown in fig.1. Near a point such as A the two branches of the dispersion relation become coupled and the usual WKB approximation for an inhomogeneous system breaks down. In the vicinity of A we approximate the dispersion relation by

$$(\omega - \omega_1)(\omega - \omega_2) = \eta \qquad (1)$$

where $\omega_1(k,x)$, $\omega_2(k,x)$ are given by the dotted lines in fig.1 and are required to be slowly varying functions of k and x, asymptotic to the exact dispersion curves far from the crossing point at A.

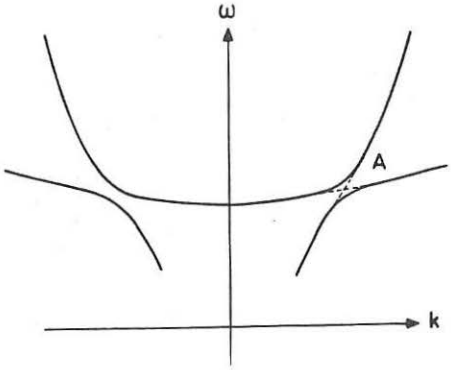

Fig. 1
Typical dispersion curves in a mode-coupling problem

relation is then converted to two coupled first order differential equations by associating a separate amplitude with each wave giving

$$\frac{d\phi_1}{d\xi} - i(k_o - \frac{b}{a}\xi)\,\phi_1 = i\lambda\,\phi_2 \qquad (2)$$

$$\frac{d\phi_2}{d\xi} - i(k_o - \frac{g}{f}\xi)\phi_2 = i\lambda\,\phi_1 \qquad (3)$$

where a and f are the group velocities of the two modes and b and g are given by $\partial\omega_{1,2}/\partial\xi$ respectively. The quantity λ is $\lambda = (\eta_0/af)^{1/2}$. If $|\phi_1|^2$ and $|\phi_2|^2$ are regarded as the energy fluxes in the two modes, equations (2) and (3) give energy conservation. The asymptotic solution of the equations yields the mode conversion information. However, the question remains of what ϕ_1 and ϕ_2 are in terms of the electromagnetic fields in the plasma. We shall now justify the use of equations (2) and (3) for the special case where one of the modes is non-propagating i.e. the group velocity of one of the waves is zero (e.g. f = 0). It can be seen from equations (2) and (3) that under these conditions the local dispersion relation is $g\xi[a(k-k_0) + b\xi] = \eta$. This situation occurs very often in practice.

We now begin from Maxwells equations applied to a uniform plasma

$$\underline{k} \times (\underline{k} \times \underline{E}) = -i\omega\mu_0\underline{J} - \frac{\omega^2}{c^2}\underline{E} \qquad (4)$$

where $J_i = \sigma_{ij}E_j$, σ_{ij} is the conductivity tensor and we have assumed fields varying as $\exp i(\underline{k}.\underline{r}-\omega t)$. We now suppose that σ_{ij} can be split into two parts

$$\sigma_{ij} = \sigma_{ij}^{(1)} + \sigma_{ij}^{(2)}\,, \qquad (5)$$

with, correspondingly,

$$\underline{J} = \underline{J}^{(1)} + \underline{J}^{(2)} \qquad (6)$$

We can now write (4) as

$$\underline{k} \times (\underline{k} \times \underline{E}) - i\omega\mu_0\,\underline{g}^{(1)}\underline{E} + \frac{\omega^2}{c^2}\underline{E} = -i\omega\mu_0\,\underline{J}^{(2)} \qquad (7)$$

and if $\underline{J}^{(2)}$ is neglected we obtain an equation $K_{ij}E_j = 0$, with K_{ij} the appropriate tensor constructed from $\sigma_{ij}^{(1)}$. This then leads to the dispersion relation for the propagating mode e.g. a cold plasma mode. The current $\underline{J}^{(2)}$ might then refer to a thermal mode which will eventually be identified with the non-propagating wave.

In an inhomogeneous system we write

$$\underline{E} = \underline{E}_0(x)e^{i\int k_1(x)dx} \qquad (8)$$

where k_1 is the wavenumber obtained from the dispersion relation $\omega=\omega_1(k,x)$. Assuming that k_1 is a smoothly varying function of x, we expand $K_{ij}E_j=0$ to obtain[2]

$$i\left[\frac{\partial K_{ij}}{\partial k_1}\frac{dE_{oj}}{dx} + \frac{1}{2}\frac{d}{dx}\left(\frac{\partial K_{ij}}{\partial k_1}\right)E_{oj}\right] = 0 \qquad (9)$$

Using the fact that for a non-dissipative system K_{ij} is hermitian we can easily obtain

$$\frac{d}{dx}\left(E_{oi}^{*}\frac{\partial K_{ij}}{\partial k_1}E_{oj}\right) = 0 \qquad (10)$$

which represents conservation of energy flux[3] for wave 1 in a regime where it is uncoupled to mode 2.

Now consider the effect of $\underline{J}^{(2)}$. We take

$$\underline{E}(x) = \phi_1 x)\underline{\varepsilon}(x)e^{i\int k_1(x)dx} \qquad (11)$$

where the vector $\underline{\varepsilon}(x)$ is a (local) solution of $K_{ij}\varepsilon_j = 0$ normalized so that

$$\varepsilon_i^* \frac{\partial K_{ij}}{\partial k_1} \varepsilon_j = -1 \qquad (12)$$

i.e. $\underline{\varepsilon}$ is the eigenvector of the local electric field of the propagating mode. Expanding (7) as before, we obtain

$$i\left[\frac{\partial K_{ij}}{\partial k_1}\frac{d}{dx}(\psi_1\varepsilon_j) + \frac{1}{2}\frac{d}{dx}\left(\frac{\partial K_{ij}}{\partial k_1}\right)\psi_1\varepsilon_j\right] e^{i\int k_1(x)dx} = -i\omega\mu_0 J_i^{(2)} \qquad (13)$$

Taking the scalar product of (13) with $\underline{\varepsilon}^*$, the hermitian property of K_{ij}, equation (12) and the fact that $\varepsilon_i^* \frac{\partial K_{ij}}{\partial k_1}\frac{d\varepsilon_j}{dx}$ may be taken as real we eventually obtain

$$\frac{d\phi_1}{dx} - ik_1(x)\,\phi_1 = \omega\mu_0\varepsilon_i^* J_i^{(2)} \qquad (14)$$

where $\phi_1 = \psi_1 e^{i\int k_1(x)dx}$. Equation (14) describes the coupling of the propagating mode ω_1 to the current component $J_2^{(2)}$ associated with the non-propagating resonant mode.

We exhibit the resonant nature of mode 2 explicitly by writing

$$J_i^{(2)} = \sigma_{ij}^{(2)} E_j = \frac{C_{ij}}{(\omega-\omega_2)} E_j \qquad (15)$$

where ω_2 is independent of k depending only on x. We suppose that $\omega = \omega_2$ at x = 0 so that near this point

$$J_i^{(2)} = \frac{d_{ij}}{x} E_j \qquad (16)$$

The singularity resulting from the resonant response of mode 2 can be resolved in the usual way, either by introducing a little damping or by treating the problem as an initial value problem. Using (16) in (14) we finally obtain the equation for the propagating mode coupled to the resonant mode

$$\frac{d\phi_1}{dx} - i\,k_1(x)\,\phi_1 = \omega\mu_0 \frac{\varepsilon_i^* d_{ij}\varepsilon_j}{x}\,\phi_1 \qquad (17)$$

The solution of (17) is

$$\phi_1 = A\exp(ik_0x + i\eta\log x) \qquad (18)$$

where $i\eta = \omega\mu_0\,\varepsilon_i^* d_{ij}\varepsilon_j$ and η is real since $\sigma_{ij}^{(2)}$ is anti-hermitian. On passing through the resonance ϕ_1 decreases by a factor $\exp(-\pi\eta)$, the argument of logx being prescribed, as already pointed out, by causality arguments or the introduction of damping. This decrease is precisely what is obtained from our previous theory in the case when the group velocity of one of the waves is zero. We have therefore justified our previous theory for this special, although commonly occurring, case.

We conclude by applying the above analysis to the coupling of the cold extraordinary mode to a Bernstein mode at the second harmonic of the electron cyclotron frequency. For propagation exactly perpendicular to the magnetic field using the hot plasma dispersion relation we easily obtain the splitting of the cold and hot modes corresponding to equations (5) and (6). Thus

$$\begin{bmatrix} 1 - \frac{\omega_p^2}{\omega^2-\Omega^2} & i\,\frac{\omega_p^2\Omega}{\omega(\omega^2-\Omega^2)} \\ -i\,\frac{\omega_p^2\Omega}{\omega(\omega^2-\Omega^2)} & 1 - \frac{c^2k^2}{\omega^2} - \frac{\omega_p^2}{\omega^2-\Omega^2} \end{bmatrix} \begin{bmatrix} E_x \\ E_y \end{bmatrix} = -i\omega\mu_0 \underline{J}^{(2)} \qquad (19)$$

$$-i\omega\mu_0 \underline{J}^{(2)} = \frac{\omega_p^2}{\omega(\omega-2\Omega)} \frac{\lambda}{2} \begin{bmatrix} 1 & -i \\ i & 1 \end{bmatrix} \begin{bmatrix} E_x \\ E_y \end{bmatrix} \qquad (20)$$

where we have only included the warm plasma corrections in the n = 2 term to lowest order in $\lambda(\equiv k^2 v_T^2/\Omega^2)$. Note the resonant response of $\underline{J}^{(2)}$ at $\omega = 2\Omega$. The polarization of the cold X-mode is obtained from equation (19) by putting $\underline{J}^{(2)} = 0$ giving $E_x = -i\omega_p^2\Omega E_y/\omega(\omega^2-\Omega^2-\omega_p^2)$ thus determining the eigenvector $\underline{\varepsilon}$

$$\underline{\varepsilon} = \left(\frac{\omega^2}{2kc^2}\right)^{1/2} \begin{bmatrix} -i\ \omega_p^2\Omega/\omega(\omega^2-\Omega^2-\omega_p^2) \\ 1 \end{bmatrix}$$

where the normalization condition, eqn.(12), has been used. Again assuming $\underline{E} = \psi_1(x)\underline{\varepsilon}\, e^{i\int k(x)dx}$ and expanding (19) in the way outlined above we obtain

$$\frac{d\phi_1}{dx} - ik\phi_1 = \omega\mu_0 \underline{\varepsilon}^* \cdot \underline{J}^{(2)} \qquad (21)$$

Substituting for $J^{(2)}$ from (20) into (21) gives

$$\frac{d\phi_1}{dx} - ik\phi_1 = i \frac{\omega_p^2}{2\Omega\omega} \frac{R}{x} \frac{\lambda}{2} \varepsilon_i^* a_{ij} \varepsilon_j \phi_1 \qquad (22)$$

where a_{ij} is the matrix appearing in (20) and we have put $\omega = 2\Omega = 2\Omega x/R$ where R is the magnetic field gradient scale length. The solution of equation (22) is again

$$\phi_1 = A\exp(ikx - i\, \omega_p^2 \frac{R\lambda}{8\Omega^2} \varepsilon_i^* a_{ij} \varepsilon_j \log x) \qquad (23)$$

By the previous argument the wave amplitude decreases by the factor $\exp(\pi\omega_p^2 R\lambda \varepsilon_i^* a_{ij} \varepsilon_j/8\Omega^2)$ in crossing the resonance. This is easily shown to reduce to the transmission coefficient obtained in our previous work.[1]

In this paper we have provided a justification for our previous theory of mode conversion for the case where one of the two coupled modes is non-propagating and have shown explicitly the relation of the amplitude of the propagating wave to the fields in the plasma. From the viewpoint of the incident wave it is immaterial whether the energy is dissipated locally, as for a resonant mode, or carried away by a wave of small but finite group velocity. Of course, from the viewpoint of the power deposition profile, such a difference may be significant.

References

(1) R.A.Cairns and C.N.Lashmore-Davies, Phys.Fluids 26, 1268 (1983).
(2) H.L.Berk and D.L.Book, Phys. Fluids, 12, 649 (1969).
(3) T.H.Stix, The Theory of Plasma Waves, McGraw-Hill, New York, 1962.

ELECTRON CYCLOTRON EMISSION DURING PULSED CYCLOTRON HEATING IN TOKAMAK PLASMAS

G. Giruzzi, I. Fidone, G. Granata and V. Krivenski

Association Euratom-CEA sur la Fusion
Centre d'Etudes Nucléaires
92265 FONTENAY-AUX-ROSES (FRANCE)

Very often the tokamak plasma exhibits a strongly non-Maxwellian electron distribution which affects the plasma discharge, especially in low-density regimes. The momentum distribution of the electron tail is determined by various kinetic processes as, for instance, the parallel acceleration of the dc electric field, diffusion due to rf waves, the collisional velocity slow-down and pitch-angle scattering, and eventually other dissipation mechanisms. For a better understanding of the dynamics of the electron population in plasma confinement and heating experiments, it is of interest to investigate the relative roles of those processes in the tail formation. A simple method is based on electron cyclotron emission. As known, the fast electron tail copiously emits cyclotron radiation at frequencies significantly smaller than the electron gyrofrequency ω_c and its harmonics. The frequency distribution and the magnitude of the emitted spectrum are determined by the parallel and perpendicular momentum distributions of the superthermal tail. The emitted radiation is then well suited for accurate investigations of the transient phase of the tail distribution. Using a 2D initial value Fokker-Planck numerical code, we compute the electron distribution and the related second harmonic emission before, during and after a pulse of electron cyclotron heating in the case of a low density plasma with a strong dc electric field. The electron tail distribution $f\ (p_\perp, p_\parallel, t)$ is obtained from the solution of the kinetic equation

$$\frac{\partial f}{\partial \tau} = \left(\frac{\partial f}{\partial \tau}\right)_{cy} + \left(\frac{\partial f}{\partial \tau}\right)_{coll} + \left(\frac{\partial f}{\partial \tau}\right)_{E_\parallel} \qquad (1)$$

where $\tau = \nu_e t$, $\nu_e = 2\pi e^4 n_e \Lambda / m^{1/2} T_e^{3/2}$, $-e$ is the electron charge, n_e is the electron density, m is the electron rest mass, T_e is the body tempe-

rature, Λ is the Coulomb logarithm, and the three terms at the right-hand-side represent respectively the electron diffusion term [1], the high velocity limit of the Coulomb collision term and the parallel dc electric field $E_{\parallel}$ term.

We consider a tokamak device with small radius a = 20 cm, major radius R = 100 cm, medium magnetic field B = 25 kG, central electron density and temperature $n_e = 2 \times 10^{13}$ cm^{-3} and $T_e = 1.5$ keV, $E_{\parallel} = 2.7 \times 10^{-3}$ V/cm and $E_{\parallel} T_e / 2\pi n_e e^3 \Lambda = 0.1$. We also consider an electron cyclotron wave-packet polarized in the extraordinary mode propagating from the high magnetic field side at an angle $\psi = 70°$ with respect to the direction of $\vec{B}$. The wave-packet has a Gaussian $N_{\parallel} = \sin\psi$ spectrum of half-width $\Delta N_{\parallel} \simeq \Delta\psi = 10°$, and a frequency $f = \omega/2\pi = 60$ GHz.

We first solve Eq.(1) for $(\partial f/\partial\tau)_{cy} = 0$. A steady-state is attained for $\tau \simeq 400$ in which a near flat parallel tail is established in a wide region of space [2]. This electron tail is a good absorber of cyclotron waves and for the wave-packet in the extraordinary mode nearly total absorption occurs in the first transit [2]. We find that for a 70 kW pulse of electron cyclotron energy, nearly 50 kW reach the plasma center. The pulse is applied for $400 < \tau < 700$, followed by a transient relaxation phase The tail momentum distribution and the radiation temperature at the second harmonic are shown in the following figures, which refer to the central region of the plasma column. In Fig.1, we present $f_{\parallel} = 2\pi \int_0^{\infty} u_{\perp} f \, du_{\perp}$ versus $u_{\parallel}^2$ at τ = 400,700 and 870 ($\vec{u} = \vec{p}/(mT_e)^{1/2}$). It appears that the effect of the electron cyclotron wave energy ($\tau \lesssim 700$) is a raise of the parallel tail population. This results from the combined effects of pitch-angle scattering and more efficient parallel acceleration due to the increase of the perpendicular energy of the electrons in the low energy side of the tail. This is also seen in Fig. 2 in which we show $T_{\perp}(u_{\parallel}) = 2\pi T_e \int_0^{\infty} du \, (f u_{\perp}^3 / 2 f_{\parallel})$ versus $u_{\parallel}$. It appears that $T_{\perp}(u_{\parallel})$ at $\tau = 700$ (ECRH on) is greater than $T_{\perp}(u_{\parallel})$ at $\tau \lesssim 400$ (no ECRH). Furthermore, the perpendicular distribution for $\tau = 400$ is very close to a Maxwellian distribution at temperature $T_{\perp}(u_{\parallel})$ whereas for $\tau = 700$ it deviates considerably from the Maxwellian shape, as shown for $u_{\parallel} = -6$ in Fig.3. We now discuss the transient phase for $\tau > 700$. After the pulse duration, the electron tail tends to the initial configuration, i.e., the tail distribution for $\tau = 400$. The process starts with a decrease of the perpendicular energy of the tail electrons for parallel velocities near $u_{\parallel} = -5$ which resonate with the cyclotron

wave-packet (see Fig.2, τ = 870). This increases the parallel velocity slow-down and results in a depletion of the parallel distribution in the low $u_\parallel$ side of the tail (see Fig.1, τ = 870). This slow-down is accompanied by a redistribution of the tail energy and may result in a transient increase of $T_\perp(u_\parallel)$ for large $u_\parallel$ due to the predominant effect of pitch-angle scattering. In the long run, of course the final state coincides with the initial one at τ = 400.

The three phases of the tail distribution can be investigated by the cyclotron emission near the second harmonic. In Fig.4, we present the radiation temperature $T_r(\omega)$, defined by the ratio of the emission and absorption coefficients, versus $\omega/2\omega_c$ for τ = 400, 700 and 870. For $\omega/2\omega_c \simeq 1$, the familiar thermal emission is found and $T_r(\omega) \simeq T_e$. The effect of electron heating at τ = 700 is shown by the sharp maximum near $\omega/2\omega_c = 0.9$. It is of interest to note that in this case T_r differs significantly form $T_\perp(u_\parallel)$. This illustrates the difference between the mean kinetic energy and the actual energy of the resonant electrons in the perpendicular electron tail, i.e., the deviation from Kirchhoff's law for non-Maxwellian distributions. For later times, we obtain a similar picture with the maximum displaced towards lower values of $\omega/2\omega_c$ (Fig.4, τ = 870) until the same distribution as at τ = 400 is attained.

Recent experiments on electron cyclotron heating by X-mode in low density plasmas [3-5] have displayed an increase of the second harmonic emission after the gyrotron pulse. It is of course premature to relate this increase of the radiation temperature with the results of Fig.4 but the qualitative agreement between the theory and the experiments gives some confidence on the potential of the method. It is also worth mentioning that, in the case of the lower-hybrid sustained discharge with no assist from the OH transformer we find no significant increase of T_r after the gyrotron pulse, in agreement with recent results on rf current enhancement by ECRH [6].

1 Fidone, I., Granata, G., and Meyer R.L., Phys. Fluids 25 (1982) 2249
2 Giruzzi, G., Krivenski, V., Fidone, I., and Ziebell, L.F., Plasma Phys. 27 (1985) 1151
3 Elder, G.B., et al ORNL/TM 8403 (1983)
4 Argenti, L., et al , Budapest, September 2-6, 1985 (EPS, Geneva, 1985) 9F II, 300
5 Mazzucato, E., private communication
6 Hoshino, K., et al Budapest September 2-6, 1985 (EPS Geneva, 1985) 9F II, 184

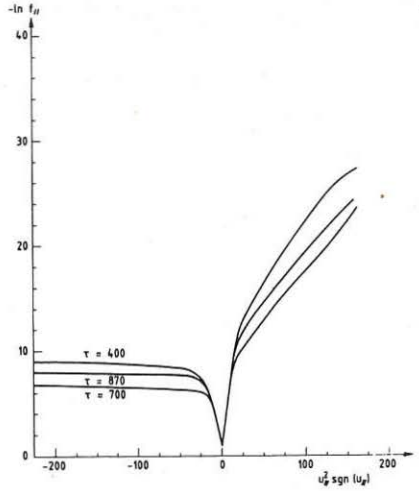

Fig. 1

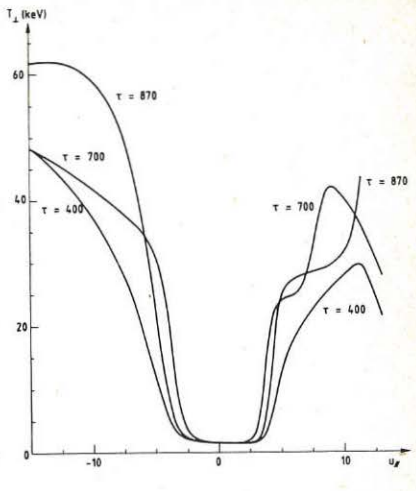

Fig. 2

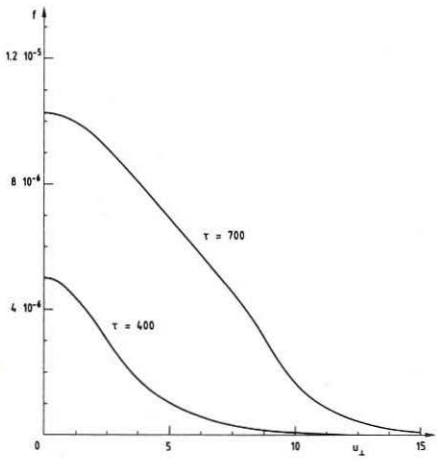

Fig. 3

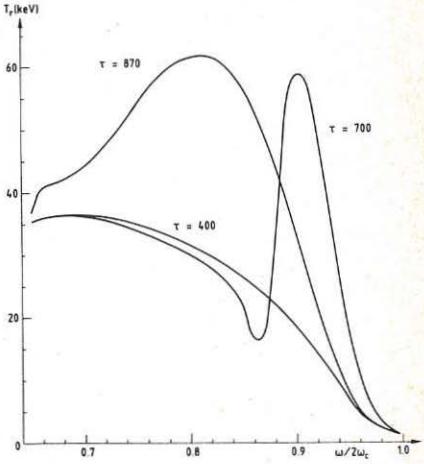

Fig. 4

LOW-VOLTAGE START-UP IN THE CLEO TOKAMAK USING ECRH

B Lloyd, T Edlington, M W Alcock, D Atkinson, B J Parham, P R Collins, A N Dellis, J Riley, A C Riviere, D C Robinson and T N Todd

Culham Laboratory, Abingdon, Oxon OX14 3DB, UK
(UKAEA/Euratom Fusion Association)

Introduction

There is considerable interest in the development of low-voltage start-up scenarios for tokamak devices because of the engineering design simplifications which can result, particularly with respect to the poloidal field system and the vacuum vessel. Furthermore, a reduction in the applied voltage necessary for start-up can lead to a decrease in the initial runaway electron population in the plasma. The use of ECRH-assisted start-up permits greater control over the location of the initial breakdown thereby reducing plasma-wall interaction and the impurity line radiation losses arising from this.

Studies of ECRH-assisted start-up have been carried out in CLEO tokamak (R_o = 0.9m, a = 0.13m) at both the fundamental and second harmonic cyclotron resonance with the aid of an EMI-Varian 28 GHz gyrotron capable of providing 200 kW of rf power for pulse lengths of up to 40ms. The radiation was injected along a major radius from the low-field side of the torus through open-ended oversized circular waveguide. The power was transmitted to the antenna in the form of the circularly polarised TE_{01} mode (for $\omega = \omega_{ce}$) and in the TE_{11} mode orientated to excite primarily the O-mode (for $\omega = \omega_{ce}$) and primarily the X-mode (for both $\omega = \omega_{ce}$ and $\omega = 2\omega_{ce}$).

Feedback control of plasma current, line-averaged electron density and both vertical and horizontal plasma position allow well-controlled reproducible plasmas to be established. With ECRH-assisted start-up it has been possible to produce discharges with $V_\ell < 2V$ throughout.

Fundamental ECRH

The beneficial effects of ECRH-assisted start-up are clearly illustrated in Fig 1. An 80kW, 20ms pulse of rf power (TE_{01} launch; both O-mode and X-mode excited in the plasma) is injected at a time t = 4ms and breaks down an initial prefill of deuterium to a central line-averaged electron density of $\bar{n}_e \sim 0.9 \times 10^{18} m^{-3}$ in a toroidal magnetic field on axis of $B_{\phi o}$ = 0.895T. For this field the fundamental cyclotron resonance is inwardly displaced ~ 0.09m from the minor axis. The plasma current feedback system is triggered at t = 13ms and provides the initial rate of current rise of 0.75MA/s. Capacitor banks are discharged into a separate primary winding at 22, 51 and 81ms in order to assist the feedback system. The plasma current reaches its programmed flat-top level of 13.2kA at 42.8ms (ie 29.8ms after initiation)

representing an average rate of current rise of 0.44MA/s during the start-up phase of the discharge. Throughout this phase the loop voltage is typically ~ 1.1V corresponding to an electric field of $E \sim 0.19V/m$. The flux consumption during the plasma current rise is $\Delta\Phi = \int V_\ell dt \sim 0.033Vs$.

Estimates of the efficiency of conversion of electromagnetic energy from the poloidal field system into stored magnetic energy during start-up give 32-46% depending on the central q assumed ($1 \leq q_o \leq 2$).

In Fig 2 the discharge under consideration is compared with the best (ie lowest voltage at breakdown) yet achieved in the absence of rf power. The final current level and the rate of current rise are the same in the two cases. Preionisation results in a ~ 50% reduction in the volt-second consumption and a ~ 50% increase in the fraction of electromagnetic energy input from the poloidal field system which is converted to stored magnetic energy. The voltage required at the initiation of the current ramp is reduced by a factor of 5.

With the TE_{01} launch it was not possible to investigate the effects of toroidal field variations because for $B_{\phi o} \geq 1T$ there was excessive reflection of microwave power leading to enforced termination of the rf pulse. The reflection arises when the low density X-mode cut-off layer is located too close to the antenna. This problem was overcome by transmitting the TE_{11} mode to the antenna with the waveguide orientated to predominantly excite the O-mode in the plasma. Provided that the cyclotron layer was located inside the vacuum vessel the initial loop voltage V_ℓ^i and rate of current rise $\dot{I}_p^i$ were found to be almost independent of B_ϕ (Fig 3) except at the highest fields in which case the cyclotron layer was located close to the antenna leading to a deterioration in the coupling of the rf power. Furthermore, under these circumstances electrons produced in the initial preionisation phase would be swept immediately into the wall by the $\underline{E \times B}$ drift. The volt-second consumption $\int V_\ell dt$ and the average rate of current rise $\langle \dot{I}_p \rangle$ evaluated over the start-up phase exhibit a similar B_ϕ dependence to V_ℓ^i and $\dot{I}_p^i$ respectively.

The power dependence of $\langle \dot{I}_p \rangle$ and $\int V_\ell dt$ for TE_{11} O-mode injection was investigated. There was a deterioration in these parameters with increasing P_{rf} which may be associated with the increasing difficulty which was experienced in controlling $\bar{n}_e$ to a low level during the current rise as the rf power was raised. At the highest powers the discharge was not sustained adequately after the rf pulse. V_ℓ and $\dot{I}_p^i$ were essentially $\underline{\text{independent}}$ of P_{rf} in the range 60→135 kW, similar to results obtained in ISX-B[1].

During the preionisation phase small plasma currents were often detected. Such plasma currents have been observed previously [2] and may be associated with an asymmetric loss of particles in the presence of toroidal and vertical magnetic fields [3,4]. The magnitude of the currents observed in CLEO were not reproducible or predictable but generally increased with rf power. At

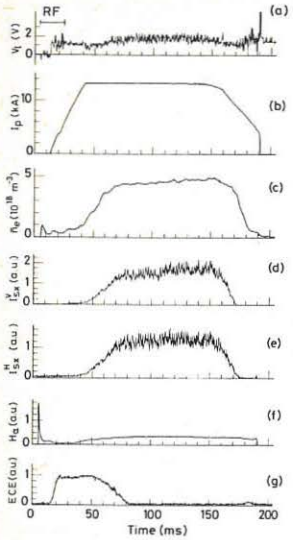

Fig 1 Low voltage ECRH-assisted start-up at the fundamental (TE_{01} launch): (a) loop voltage, (b) plasma current, (c) line-averaged electron density, (d) vertical soft X-ray emission (r=0), (e) horizontal soft X-ray emission (r=0), (f) H_α emission, (g) ECE at 36.3GHz.

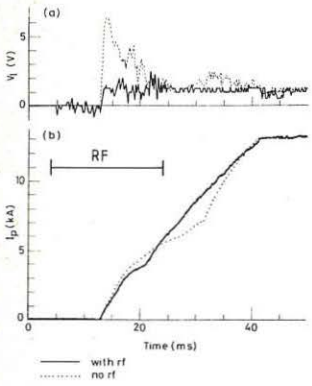

Fig 2 Comparison of ohmic and ECRH-assisted (fundamental, TE_{01} launch) start-up: (a) loop voltage, (b) plasma current.

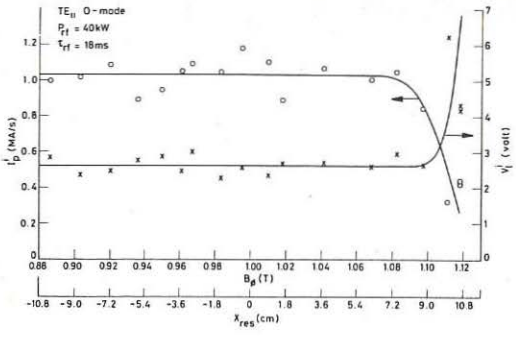

Fig 3 Variation of initial loop voltage and rate of current rise with B_ϕ during ECRH-assisted start-up at the fundamental (TE_{11}, O-mode launch).

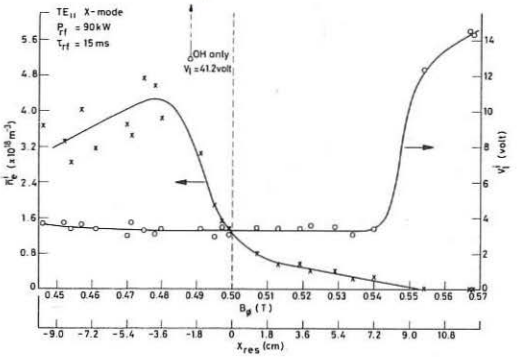

Fig 4 Variation of initial loop voltage and line-averaged density with B_ϕ during ECRH assisted start-up at the second harmonic (TE_{11}, X-mode launch).

P_{rf} = 120kW currents up to 0.6kA were measured with dI_p/dt still ~ 230kA/s when the plasma current feedback system was initiated.

The results obtained with the TE_{11} O-mode launch were not as impressive as those with the TE_{01} launch. Whether this is related directly to the mode of launch or arises because of inferior discharge optimisation in the former case is not absolutely certain. Similarly, experiments with a TE_{11} X-mode launch yielded yet worse results. As expected, in this case, one was much more susceptible to excessive reflection associated with the X-mode cut-off layer.

Second harmonic ECRH

Experiments at the second harmonic with a TE_{11} X-mode launch yielded qualitatively similar results to the fundamental TE_{11} O-mode launch. This is illustrated by the B_ϕ dependence of V_ℓ^i shown in Fig 4. Also shown in this case is the variation of the central line-averaged density during the preionisation phase, $\bar{n}_e^i$, which exhibits a very strong dependence. This variation is probably a function of the relative positions of the cyclotron layer and the central vertical chord along which the density is measured, bearing in mind the outward ExB drift. Note that the highest line-averaged density achieved in the preionisation phase is approximately equal to the X-mode cut-off value implying a peak density which exceeds this figure. This suggests that the O-mode component (generated after polarization scrambling due to repeated reflections from the vacuum vessel) may play a role.

V_ℓ and I_p^i were essentially independent of rf power in the range 60→135kW as were $\langle I_p \rangle$ and $\int V_\ell dt$ since during the power scan no difficulties were encountered in controlling $\bar{n}_e$.

The effects of varying the rf pulse duration and timing were also investigated. Within the range of study only very weak dependences were encountered. Similar observations were made in ISX-B [1] during preionisation at the fundamental.

Summary

The effectiveness and reliability of low voltage ECRH-assisted start-up has been demonstrated by conducting experiments over a wide range of parameters and launching conditions. Well-controlled discharges with V_ℓ < 2V throughout have been established. The effective use of second harmonic heating in the start-up phase has been demonstrated.

References

[1] Kulchar A G et al (1984) Phys Fluids 27, 1869
[2] Kubo S et al (1983) Phys Rev Lett, 50, 1994
[3] Tanaka S et al (1985) Plasma Phys and Contr Nuc Fus Res, 1984, Proc 10th Int Conf, London, I, 623, IAEA Vienna
[4] Wilhelm R et al (1984) Plasma Phys and Contr Nuc Fus 26, 1A, 259

CURRENT DENSITY PROFILE CONTROL ON JET USING ECRH CURRENT DRIVE

M R O'Brien, M Cox, T C Hender, D C Robinson and D F H Start

Culham Laboratory, Abingdon, Oxon, OX14 3DB
(UKAEA/Euratom Fusion Association)

Introduction

The localised nature of electron cyclotron resonance heating (ECRH) has been successfully exploited on several tokamak experiments (CLEO, T-10, Doublet III, PDX) to reduce the amplitude of, and in some cases completely suppress, the sawteeth and m=2 MHD instabilities. The necessary current density profile control was achieved by modifying the electron temperature profile and in each case the ECRH power was a substantial fraction of the total heating power. In tokamaks with large, broadly distributed additional heating, as in the case of neutral beam injection, a possibly more effective method is to control the current density profile directly using ECRH current drive. We have studied this possibility for the JET tokamak by ray tracing and Fokker-Planck calculations applied to the downshifted frequency scheme suggested by Fidone, Giruzzi and Mazzucato [1]. Calculations have been made for fundamental X-mode ECRH at 60 GHz and 70 GHz and for second harmonic X-mode at 140 GHz, these frequencies being available at present or in the near future. The predicted current densities are compared with calculations of the currents required to stabilise the m=2 resistive mode.

Current drive calculations

The geometry of the method is depicted in the poloidal cross section in Fig 1. In this example the magnetic field on axis is 3.2T so that the resonance for 60 GHz lies outside the plasma at R=4.43m. A ray tracing code [2] is used to follow rays launched outwards from the top of the torus towards the resonance surface. The rays are given a toroidal component to achieve current drive and the launch angle is chosen to localise the absorption and optimise the current at 1m from the plasma centre where we assume the q=2 surface to be for the purpose of this study. For the X-mode fundamental the k vector at launch has components $(k_z, k_R, k_\phi) = k(-0.64, 0.38, 0.66)$ where ϕ is the toroidal angle. We follow a cone of rays with a 5° semi angle about this central ray corresponding to HE_{11} mode launch from a 3cm wide antenna [3]. The rays in Fig.1 are extreme rays on this cone and the shaded section shows where absorption occurs.

Typical current and power deposition profiles, which are almost identical due to the strong localisation, are shown in Fig.2. In this particular case ($\hat{n}_e = 4 \times 10^{13}$, $\hat{T}_e = 5$keV) the absorption is 100% and the current driven is 112 amps per kilowatt of injected power. The temperature and density profiles are taken to have the form $n_e = \hat{n}_e(1-\psi)$ where ψ is the poloidal flux function. In the absorption region the temperature and density have values $T_e \approx 1.3$keV and $n_e \approx 1 \times 10^{19} m^{-3}$ respectively.

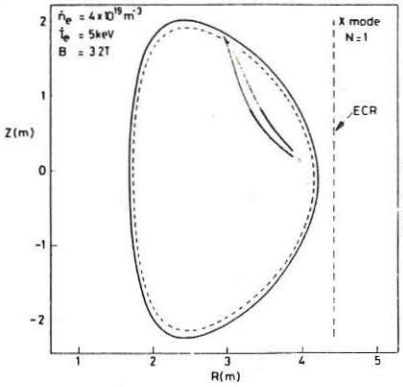

Fig 1 RF injection geometry and ray tracing for 60 GHz ECRH

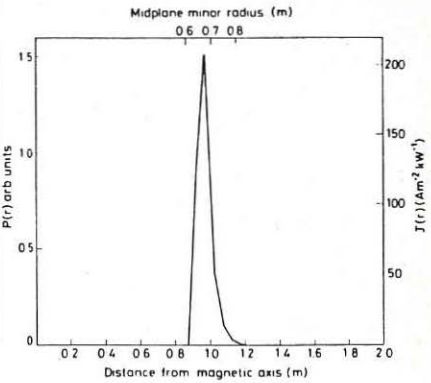

Fig 2 Power deposition and current density profiles

The scaling of the current per kilowatt of injected power, P_{inj}, with central density is shown in Fig.3 for 60GHz and for central magnetic fields of 3.0T and 3.2T and central temperatures of 5keV and 6keV. The dashed sections of the curves show where the absorption has fallen to less than 50%. Where full absorption occurs the current is almost exactly proportional to $\hat{n}_e^{-1}$, with a value ~ 240A/kW at $\hat{n}_e$ = 2 x $10^{19}m^{-3}$ falling to ~ 70A/kW at $\hat{n}_e$ = 6 x $10^{19}m^{-3}$.

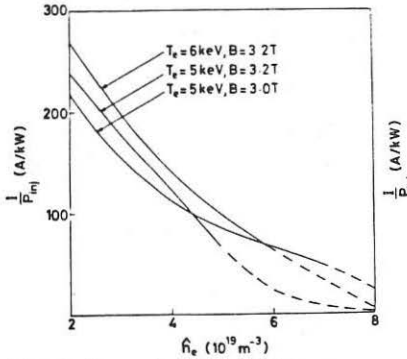

Fig 3 Current drive efficiency versus central density for 60 GHz RF

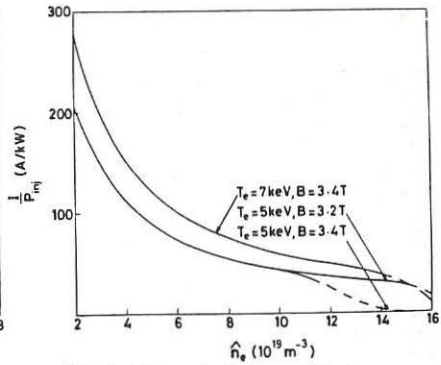

Fig 4 Current drive efficiency versus central density for 70 GHz RF

Similar values are obtained with 70GHz waves as shown in Fig.4. Note that for a given magnetic field and temperature the higher frequency allows total single pass absorption at higher density ($n_e(max) \alpha f^2$). For total absorption the current is closely proportional to T_e.

In the case of 140 GHz second harmonic heating, the current drive efficiency is substantially less than for fundamental, principally because

the resonance condition is influenced as much by the relativistic mass shift as by the Doppler shift and this allows electrons circulating in both directions around the torus to come into resonance. For example, at $\hat{n}_e=4\times10^{19}m^{-3}$, $\hat{T}_e=7keV$, B=3.4T, the efficiency $\eta(=I/P_{inj})$ is 23 A/kW compared with η=150A/kW for 70 GHz fundamental heating.

The above calculations ignored electron trapping and to study these effects we have made Fokker-Planck calculations using the code described in ref 4. The results are given in Fig.5 for fixed local density and temperature ($n_e = 4 \times 10^{19}m^{-3}, T_e = 3keV$) and for conditions pertaining to the ray tracing calculations, namely absorption at a poloidal angle ~ 60° (from the outer midplane) and by electrons with $v_\parallel \sim 3v_e$. As can be seen from Fig.5 the current is reduced as the flux surface radius is increased and even reverses direction for ε>0.33. This effect has been derived analytically in ref.5 and is due to a cancellation of the Fisch-Boozer current [6] by a reverse current component arising from the depletion of passing electrons in the resonance region [7].

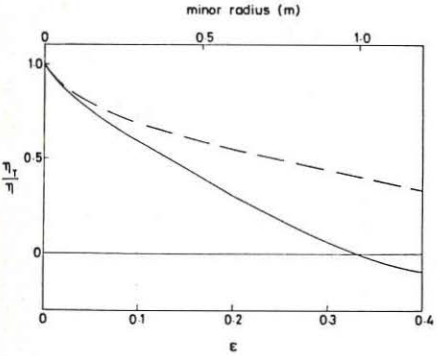

Fig 5 Ratio of current drive efficiencies in the presence (η_T) and absence (η) of electron trapping versus inverse aspect ratio ε. The dashed curve is for absorption of 90GHz RF at a poloidal angle of 135°. Other parameters are the same as those for the solid curve.

A smaller reduction in current is obtained if the power is absorbed on the inside of the flux surface[5] which might be achieved by using higher frequency (~ 90 GHz) and a central resonance (see fig 5). Access to the inside of the flux surfaces becomes easier as they move outwards as β increases. Note that for sawtooth (m=1) stabilisation in the region ε<0.1 the trapping effect is much less of a problem.

Tearing mode calculations

The current profile modifications needed to stabilize the m=2, n=1 tearing mode have been calculated using the FAR[8] code which solves the incompressible linear resistive MHD equations in full toroidal geometry. The equilibrium is specified by $FdF/d\psi = (1-\psi)^2 + be^{-a(\psi-\psi_0)^2}$, $q_0 = 1.1$ and the pressure $P \alpha (1-\psi)^2$. The Gaussian term represents the stabilising perturbation and F is the toroidal magnetic field. The profile of $FdF/d\psi$ for a=100, b=0.05 is shown in Fig.6 as a function of midplane radius.

The growth rate for β=0 and $\delta I/I$ = 6.7% is plotted against ψ_0 in Fig.7 and shows that stability can be achieved by suitable positioning of the perturbation. At the optimum radius the stability requirement is $\delta I/I$~3.5%.

At finite β the favourable average curvature has a strong stabilising influence[9] such that, for example, at $\beta_{poloidal} = 0.12$ the stabilising current is only $\delta I/I \sim 2.6\%$.

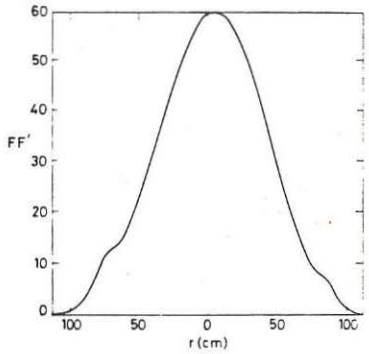

Fig 6 Perturbed current profile across the horizontal midplane

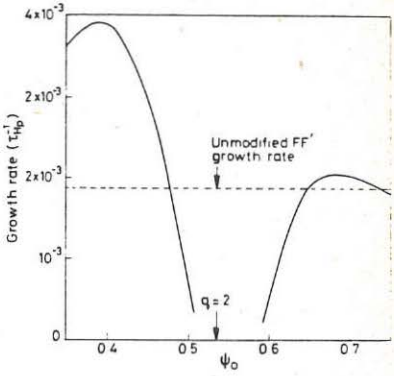

Fig 7 Growth rate of n=1 tearing mode versus position for $\delta I/I = 6.7\%$

Conclusions

The tearing mode calculations suggest that the m=2 mode can be stabilised with $\delta I/I \sim 3\%$ corresponding to 150 KA for 5 MA discharges. The current drive calculations show, in the absence of trapping that efficiencies in excess of 70 A/kW for $n_e \lesssim 6 \times 10^{19} m^{-3}$ can be achieved with fundamental heating. Thus in this density range the tearing mode could be stablisied with 2MW of ECRH power. In addition the non-inductive current will be supplemented by the locally increased ohmic current due to the plasma heating by the RF. However it should be noted that the scheme requires precise positioning of the current perturbation and is susceptible to trapped electron effects. The latter can be ameliorated by absorption on the inside of the flux surfaces.

References

[1] I Fidone, G Giruzzi and E Mazzucato Phys Fluids 28(1985)1224
[2] T Edlington, J G Cordey, M R O'Brien and DFH Start, Proc of 3rd Varenna Grenoble Int Symp on Heating in Toroidal Plasmas 1982 Vol III p 869.
[3] A N Dellis, private communication.
[4] M R O'Brien, M Cox and D F H Start, to be published in Nuclear Fusion
[5] D F H Start, J G Cordey and T Edlington Plasma Physics 25(1983)447
[6] N J Fisch and A H Boozer Phys Rev lett 45(1980)720
[7] T Ohkawa General Atomic Company report GA-A13847
[8] L A Charlton et al, to appear in Journal of Computational Physics.
[9] T Hender, R J Hastie and D C Robinson, this conference

GYROTRON POWER SOURCES FOR ELECTRON CYCLOTRON HEATING*

K. Felch, R. Bier, L.J. Craig, L. Ives, H. Jory, and S. Spang

Varian Associates, Inc., 611 Hansen Way, Palo Alto, CA 94303
USA

ABSTRACT

Previous publications have dealt with Varian gyrotrons for long-pulse or CW output at frequencies of 28, 35, 53, 56, 60, and 70 GHz. Currently a development program is in progress to produce a 100 kW CW gyrotron at 140 GHz. The first experimental 140 GHz gyrotron achieved CW power levels of up to 75 kW at 31% efficiency. This is the highest CW power level ever obtained in a microwave tube at a frequency above 100 GHz. Recently, in pulse tests on the second experimental 140 GHz gyrotron, a power level of 155 kW at 29% efficiency was achieved. Various measurements made during tests on the first experimental 140 GHz tube are summarized and the results of parameter variation studies carried out during pulse tests on the second experimental 140 GHz tube are presented. CW tests on the second experimental tube are currently underway.

I. INTRODUCTION

Varian 140 GHz gyrotrons are being developed for use in electron cyclotron resonance heating (ECRH) of plasmas. The present goal of the program is to develop 140 GHz gyrotrons capable of generating 100 kW CW. The 140 GHz tubes are similar to previous 200 kW CW gyrotron oscillators developed by Varian at frequencies of 28 GHz, 35 GHz, 56 GHz, and 60 GHz.[1] In addition, 200 kW, 40-100 ms pulse tubes at 28 GHz, 53 GHz, 60 GHz, and 70 GHz have been delivered to various fusion laboratories. In the following we begin by describing the basic design features of the 140 GHz gyrotron. Next we summarize the test results obtained on the first experimental 140 GHz gyrotron and then present the most recent results obtained during pulse tests of the second experimental tube. A more detailed discussion of the 140 GHz gyrotron design and initial tests made on the first experimental tube may be found in the references.[2, 3, 4]

II. 140 GHz GYROTRON DESIGN

The design of the 140 GHz gyrotron is centered around an interaction cavity which is resonant in the TE^{o}_{031} mode at 140 GHz. Both simple, tapered TE^{o}_{031} cavities and $TE^{o}_{021}/TE^{o}_{031}$ complex cavities have been tested thus far on the first two experimental 140 GHz tubes. The hollow electron beam is formed by a magnetron injection electron gun. The beam is located

---

* The 140 GHz gyrotron oscillator is being developed under contract with Lawrence Livermore National Laboratory, operated by the University of California for the U.S. Department of Energy, under Prime Contract W-7405-eng-48.

at the second radial maximum of the electric field in the cavity. The electron gun is designed for operation at voltages between 50 kV and 70 kV at beam currents up to 8 A. The beam has a calculated perpendicular to parallel velocity ratio, α, of 1.5 to 2.0 in the interaction cavity.

The microwave power generated in the interaction circuit diffracts into the output waveguide and propagates in the TE^{o}_{03} waveguide mode through a vacuum window and into the external transmission system. The electron beam is collected on the walls of the output waveguide as it follows the diverging magnetic field lines of the superconducting gyrotron magnet. The uptaper between the interaction cavity and the electron beam collector on the first experimental 140 GHz gyrotron has a linear radial profile, while the second experimental gyrotron and all succeeding 140 GHz tubes employ a nonlinear uptaper which has a calculated mode purity of 98% in the desired TE^{o}_{03} mode. The output window is a double-disc design which is cooled by a low-loss dielectric fluid flowing between the discs. A superconducting magnet provides the 50-56 kG magnetic field required for operation at 140 GHz.

III. 140 GHz GYROTRON TEST RESULTS

A. First Experimental 140 GHz Gyrotron

The first experimental 140 GHz gyrotron employed a simple, tapered TE^{o}_{031} interaction cavity. During pulse tests on the first experimental tube, an output power of 100 kW at 28% efficiency was achieved when employing a beam voltage of 60 kV and a beam current of 6 A. Mode competition with the TE^{o}_{231} mode at 137.0 GHz and the TE^{o}_{521} mode at 144.6 GHz and the apparent mirroring of beam electrons served to preclude the achievement of higher powers and efficiencies. Mode competition increased significantly at beam voltages above 60 kV, and electron beam mirroring occurred when operating at high values of α at high values of beam current.

In CW tests on the first experimental 140 GHz tube, an output power level of 75 kW was achieved at 31% efficiency in the desired TE_{031} mode. At this power level, the measured temperature of the output window was 108°C, well within the safe operating range for the window. During the CW tests, measurements of the microwave losses in the cavity, window and various other portions of the tube were made. While operating at 75 kW CW, 6.6 kW were measured in the cavity cooling circuit and 3.5 kW were observed in the window and other parts of the tube that absorb rf power. The power losses measured in the cavity are in agreement with theoretical predictions when the effects of surface roughness and temperature are taken into account.

B. Second Experimental 140 GHz Gyrotron

Following the CW tests on the first experimental tube, pulse tests on the second experimental tube were initiated. The major design change made in the second experimental tube was the use of a $TE^{o}_{021}/TE^{o}_{031}$ complex cavity design instead of the simple, tapered TE^{o}_{031} design employed on the first tube. The complex cavity design was chosen to try to reduce the effects of mode competition observed during tests on the first experimental tube.

Some of the results of an extensive series of parameter variation studies on the tube are shown in Figures 1 and 2. In Figure 1a we have plotted output power vs beam current for different beam voltages. The cavity magnetic field has been set for optimum output power for each beam voltage. At a beam voltage of 70 kV, an output power of 155 kW was obtained at 29% efficiency. In general, mode competition with the TE^{o}_{231}

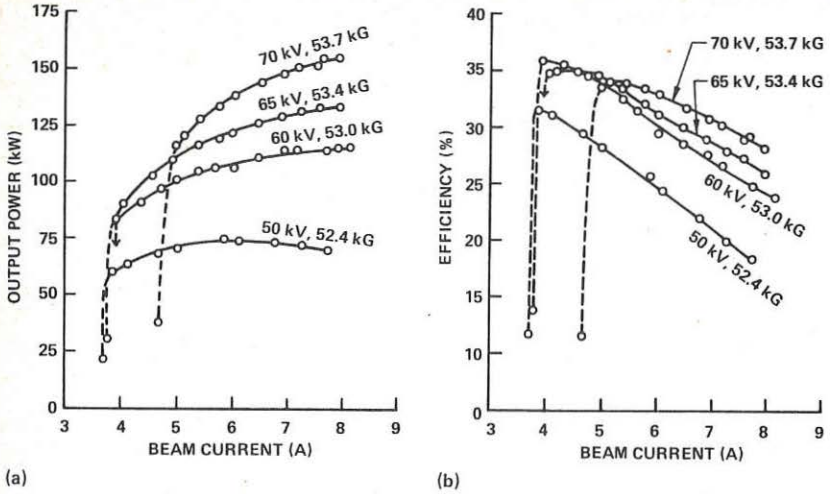

FIGURE 1. OUTPUT POWER (a) AND OUTPUT EFFICIENCY (b) vs BEAM CURRENT DURING PULSE TESTS ON THE SECOND EXPERIMENTAL 140 GHz GYROTRON FOR DIFFERENT BEAM VOLTAGES. THE CAVITY MAGNETIC FIELD HAS BEEN SET FOR OPTIMUM POWER FOR EACH BEAM VOLTAGE. THE PULSE REPETITION RATE AND PULSE DURATION WERE 10 PPS AND 0.8 TO 1.0 ms, RESPECTIVELY.

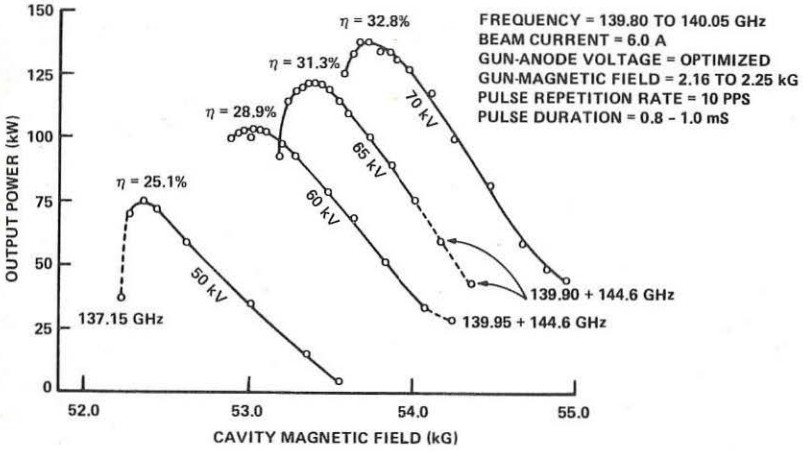

FIGURE 2. OUTPUT POWER vs CAVITY MAGNETIC FIELD DURING PULSE TESTS ON THE SECOND EXPERIMENTAL 140 GHz TUBE FOR DIFFERENT BEAM VOLTAGES.

and TE^{o}_{521} modes was no greater at 70 kV than it was at 60 kV, in contrast to the results obtained on the first experimental tube. In fact, output efficiency at the maximum power for each voltage actually increased with increasing voltage, as shown in Figure 1b.

The variation of output power with cavity magnetic field is shown in Figure 2 for operation at a beam current of 6 A. Optimum efficiencies, η, are shown for each value of beam voltage. Again we note the improved performance at higher voltages. Higher power levels than those shown in the figures were measured when the gun-anode voltage was increased past the point where mirroring electrons caused small amounts of current to be drawn to the body and gun-anode portions of the tube. As an example, 170 kW of output power was measured at a beam voltage of 70 kV and a beam current of 7.5 A when the gun-anode voltage was raised in this manner, while a power level of 155 kW was measured for the same beam voltage and current but with the gun-anode voltage set such that no body or gun-anode current were observed. Though such operation is possible under pulse conditions, the body and gun-anode current would cause excessive heating in CW operation.

IV. CONCLUSION

In general, the initial pulse tests on the second experimental 140 GHz gyrotron indicate that the $TE^{o}_{021}/TE^{o}_{031}$ complex cavity has significant advantages over the TE^{o}_{031} simple, tapered cavity design employed on the first experimental tube. Higher power levels were achievable, and the range of parameter space available to the desired TE^{o}_{031} mode was much greater for the $TE^{o}_{021}/TE^{o}_{031}$ cavity. Evaluation of the second experimental tube under CW operating conditions is currently underway.

Both the first and second tubes employed electron guns of the same design. In both tubes the apparent mirroring of beam electrons appeared to limit output efficiencies, especially at high values of beam current. A second electron gun design that should provide a higher quality electron beam,[4] thereby reducing electron beam mirroring problems, will be tested on the next experimental 140 GHz tube.

The results obtained thus far on the first two experimental 140 GHz gyrotrons represent an important step in providing high-power, high-frequency microwave power for a variety of applications. The 75 kW CW power level measured on the first 140 GHz tube is the highest CW power level ever achieved in a microwave tube at a frequency above 100 GHz. The improvements in efficiency and output power levels observed during pulse tests on the second experimental tube indicate that further advances in the performance of Varian 140 GHz gyrotrons are still forthcoming.

REFERENCES

1. H. Jory, "Status of Gyrotron Developments at Varian Associates", Proc. 4th Int. Symp. on Heating in Toroidal Plasmas, Vol 2, pp. 1424-1430, 1984.

2. K. Felch, R. Bier, L. Fox, H. Huey, L. Ives, H. Jory and S. Spang, "Design Considerations for a 100 kW CW, 140 GHz Gyrotron Oscillator", Technical Digest - IEEE IEDM, pp. 834-837, Dec. 1984.

3. K. Felch, R. Bier, L. Fox, H. Huey, L. Ives, H. Jory, N. Lopez, J. Shively, and S. Spang, "Recent Operating Experience with Varian 70 GHz and 140 GHz Gyrotrons", Course and Workshop on Applications of RF Waves to Tokamak Plasmas, Vol. 2, pp. 842-847, 1985.

4. K. Felch, R. Bier, L.J. Craig, L. Ives, H. Jory, and S. Spang, "CW Operation of a 140 GHz Gyrotron," Submitted for publication in the 4th Special Topics Issue on Gyrotrons of Int. J. Electronics, 1986.

Neutral Injection Heating

NEUTRAL BEAM DEPOSITION EXPERIMENTS AT ELEVATED DENSITIES IN ASDEX

E. Speth, O. Gruber, G. Janeschitz, H. Murmann, H. Niedermeyer, F. Wagner, O. Vollmer, G. Becker, H.S. Bosch, H. Brocken, A. Eberhagen, G. Fussmann, O. Gehre, J. Gernhardt, G. v.Gierke, E. Glock, G. Haas, J. Hofmann, A. Izvozchikov[1], F. Karger, M. Keilhacker[2], O. Klüber, M. Kornherr, K. Lackner, M. Lenoci[3], G. Lisitano, F. Mast, H.M. Mayer, K. McCormick, D. Meisel, V. Mertens, E.R. Müller, A. Pietrzyk[4], W. Poschenrieder, H. Rapp, H. Riedler[5], H. Röhr, J. Roth, F. Ryter[6], J. Schneider, C. Setzensack, G. Siller, P. Smeulders, F. Söldner, K.H. Steuer, D. Zasche.

Max-Planck-Institut für Plasmaphysik,
EURATOM-Association, D-8046 Garching, FRG

INTRODUCTION

In the past the penetration requirements for neutral beams have been derived from the postulate that the beam power should be deposited near the plasma axis. It has been demonstrated theoretically that the shape of the deposition profile is governed by the parameter a/λ (a = minor plasma radius, λ = mean free path of the injected neutrals at line-averaged density). Assuming constant electron thermal conductivity, it can be shown theoretically, that decreasing penetration (i.e. increasing a/λ)of the beam results in decreasing global energy confinement time and decreasing attainable central electron temperature, values of a/λ in excess of 2 being considered as critical /1/. Consequently the beam energies necessary to penetrate large plasmas in order to heat the plasma centre lie in the range of several 100 keV /2/, which leads to serious difficulties for positive-ion-based neutral beams due to the decreasing neutralisation efficiency. As a solution negative-ion-based systems have been proposed, which would offer reasonable efficiency, but require the development of a new technology.

In order to make an experimental assessment of the required beam penetration a series of experiments were started in 1984 in ASDEX, in which neutral beam deposition was varied systematically. The first results reported at Budapest /3/ showed (in agreement with other experiments /4/) no degradation of heating and confinement within the parameter range accessible, but suffered from following drawbacks: the plasma density was too low ($\bar{n}_e = 6 \times 10^{13}$ cm^{-3}) for extremely hollow deposition profiles to be produced and the power level was only moderate (1.3 MW). This paper describes the continuation of the experiments at almost twice the density and three times higher power.

EXPERIMENTAL PARAMETERS AND RESULTS

The experiments were carried out under the following conditions: $I_{pl} = 420$ kA, $B_T = 2.2$ T, $\bar{n}_e = 1.15 \times 10^{14}$ cm^{-3}, D_2-plasma, double-null, diverted. The density was built up with D_2 gas-puffing before and during the injection pulse ($\tau = 400$ msec), and reached a stationary state towards the end of the pulse. Comparison was made between shots of different beam

---

[1]Academy of Sciences, Leningrad, USSR; [2]Assigned to JET Joint Undertaking, England; [3]ENEA Frascati, Italy; [4]University of Washington, Seattle, USA; [5]Fellow of the Schiedel-Stiftung, Austria; [6]CEN Grenoble, France

energy per nucleon, i.e. 40 kV acceleration voltage, H^o-injection, <E> = 25 keV/AMU (P_N = 3.6 MW) and 44 kV acceleration voltage, D^o-injection, < E> = 13 KeV/AMU (P_N = 4.1 MW), keeping everything else identical. All the shots were L-type discharges.

The global energy confinement time, evaluated from the diagmagnetic β_{pol} during the stationary phase, does not show a significant difference (see Fig. 1). The value of τ_E = 35 msec is consistent with ASDEX L-scaling. The electron temperature profiles during the stationary phase (taken from YAG-laser scattering and ß-shift corrected) are shown in Fig. 2. As can be seen, there is a reduction of about 10 % in $T_e(0)$ for the low-energy case (44 kV D^o) inspite of the somewhat higher power. The corresponding power deposition profiles are shown in Fig. 3.

DISCUSSION

If one interprets this reduction of $T_e(0)$ for the 44 kV D^o-case as the onset of degradation of heating, one may identify the corresponding profile parameter $a/\lambda = 6$ with the limit for off-axis deposition in tokamaks ($\lambda = (\bar{n}_e \sigma_{TOT})^{-1}$; $\bar{n}_e$ = line-averaged density, σ_{TOT} = total trapping cross-section).

In calculating $a/\lambda = 6$ a correction for steeper injection angles (15 - 20° on large machines instead of 45° on ASDEX) has been applied. Applying this scaling law to larger plasmas yields the curve shown in Fig. 4. It can be seen that e.g. 70 keV D^o in JET or 120 keV D^o in NET would be sufficient to produce deposition profiles of the same relative shape as in Fig. 3b and would hence result in non-degraded heating.

At low energy (E < 20 keV/AMU) the deposition limit may not be determined by heating but by impurity radiation due to enhanced charge-exchange wall erosion. Enhanced impurity (iron) influx was e.g. observed in the 44 kV D^o-case at the end of a 400 msec-pulse, but was absent in the 40 kV H^o-case. Low energy injection at $a/\lambda = 6$ may therefore be limited by an additional constraint, namely to E > 20 keV/AMU independently of plasma size and calls for a high proton ratio from the ion sources. From the present data it cannot be entirely excluded that this limit may even be higher ($\sim$ 30 keV/AMU).

It is important to note, that hollow deposition profiles as shown in Fig. 3b are sensitive to central impurity radiation leading to radiation collapse. The viability of hollow deposition profils must therefore be confirmed in long pulse experiments.

If the principle of "profile consistency", i.e. the invariance of the temperature profile with respect to power deposition /3,5,6/ will persist in larger tokamaks, it may even not be required to obey a/λ = const. in order to produce heating and confinement without degradation. Other scaling laws may have to be considered, e.g. relating λ to the width of the toroidal shell outside q = 2 /6/, or possibly λ = const., suggesting that it may be sufficient to deposit the power independently of plasma size at constant depth measured from the plasma edge and λ chosen just large enough to avoid enhanced charge exchange wall sputtering (see above).

It should be noted, that the conclusions contained in this paper are valid for injection into tokamaks and do not necessarily apply to stellarators.

Finally it may be appropriate to reconsider the development of power recovery and plasma sources with high atomic ion yield in comparison with negative ions.

REFERENCES

/1/ J.G. Cordey, Applied Atomic Collision Phyics, Vol. 2, Plasmas, Academic Press (1984), p. 327
/2/ J.W. Willis et al., ERDA-report 76-77
/3/ E. Speth et al., Proc. of the 12th Europ. Conf. on Contr. Fusion and Plasma Physics, Budapest (1985), part II, p. 284
/4/ M. Murakami et al., Plasma Physics and Controlled Fusion, Vol. 28, 1A (1986), 17/5/F. Wagner et al., to be published in Nucl. Fusion
/6/ G.L. Schmidt et al., Proc. of the 12th Europ. Conf. on Contr. Fusion and Plasma Physics, Budapest (1985), part II, p. 674.

FIGURE CAPTIONS

Fig. 1: Global energy confinement time τ_E vs. species-averaged beam energy <E> and full beam energy E_o respectively

Fig. 2: Electron temperature profiles

Fig. 3: Power deposition profiles for ohmic power (p_Ω), electrons (p_e), ions (p_i) and total power (Σ).
a) for 40 KV H^o, 3.6 MW
b) for 44 kV D^o, 4.1 MW

Fig. 4: Opacity $\bar{n}_e \cdot a$ vs. species-averaged beam energy <E> ; injection angle < 20°,
$\bar{\sigma}_{TOT}$ = total trapping cross section,
$\bar{T}$ = average plasma temperature

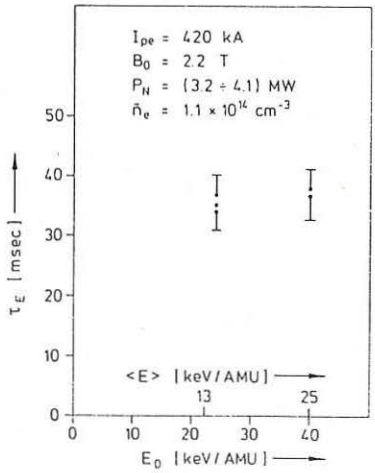

Fig. 1

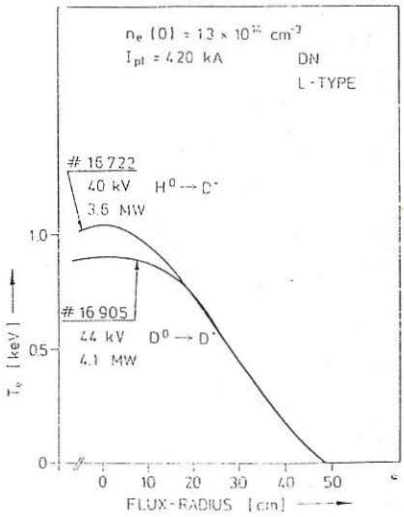

Fig. 2

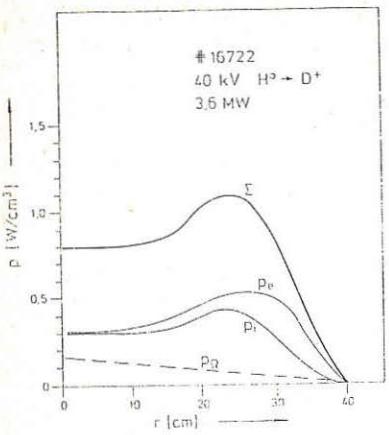

Fig. 3a

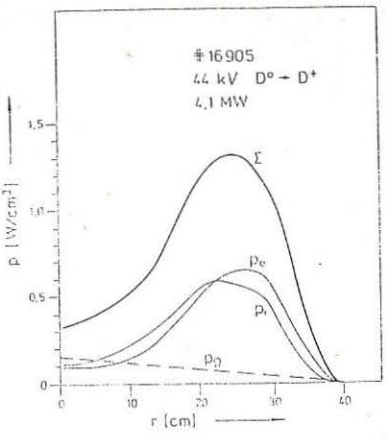

Fig. 3b

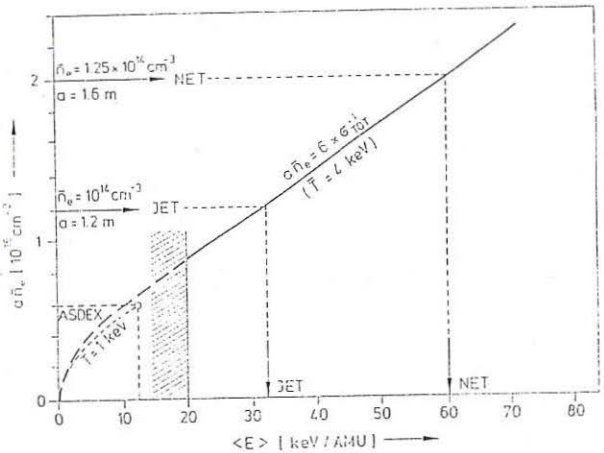

Fig. 4

FAST ION BEHAVIOUR DURING NBI IN TFR FROM NEUTRON FLUX MEASUREMENTS

Equipe TFR, presented by M.Fois
Ass. EURATOM-CEA sur la FUSION CONTROLEE
DRFC CEN, BP n. 6, 92260 FONTENAY-AUX-ROSES

Introduction

With the injection lines installed on TFR in 1984 and graphite limiters, the heating efficiency was shown in [1] to be less than in previous experiments reported in [3] ; furthermore, ion temperature saturates with additional power and electron heating is poor.

One or the other of these features are shared with most NBI experiments in Tokomaks (H regimes excepted) and are currently reworded as "confinement deterioration" but, in order to quantify confinement statements, one has to assume a classically computed power deposition profile.

In NBI, transmission into the torus, capture by the plasma, confinement and slowing down of the captured fast ion population are the successive steps where power coupling problems might arise and we decided to start from a systematic experimental check on all of these points: by neutral beam shine-through calorimetry for transmission and capture, by charge exchange and neutron emission for fast ions.

This contribution reports on one particular experiment in this line: neutron flux probing of the injected fast D^+ population.

Theory and description of the experiment

When D^0 beams are injected into D^+ plasmas three components add up to the total neutron flux, labeled as beam-beam, beam-plasma and plasma-plasma:

$$\Phi_{bb} = \int_V d^3\vec{r} \int_{E_1}\int_{E_2} \frac{1}{2} f(E_1,r)\, f(E_2,r)\, \langle \sigma_{DD} v_r \rangle \, dE_1 \, dE_2$$

$$\Phi_{bp} = \int_V d^3\vec{r} \int_E f(E,r)\, n_D(r)\, \langle \sigma_{DD} v_r \rangle \, dE$$

$$\Phi_{pp} = \int_V d^3\vec{r}\, \frac{1}{2}\, n_D^2(r)\, \langle \sigma_{DD} v_r \rangle$$

f stands for the average radial distribution function of the injected fast ions, n_D for the bulk ion density and $\langle \sigma_{DD} v_r \rangle$ are the appropriate average reaction rates.

Owing to the very strong E dependence of σ_{DD}, only the high energy part of f (corresponding to the beginning of the slow down process) will significantly contribute to neutron fluxes; hence, collisional radial diffusion and charge exchange of the fast ions (with the central neutral

density measured in [2]) can here be neglected and we can write:

$$f(E,r) = I(r) \left[- \frac{dE}{dt} (E,r) \right]^{-1}$$

where I(r) is the radial source term of fast ions, both poloidally and toroidally integrated, as calculated by a capture code and

$$\frac{dE}{dt} = - n_e(r) \, T_e^{-3/2}(r) \, G(E)$$

classically describes the collisional energy loss of fast ions.

Typical values, with 4 sources injecting 600 kW on TFR, are:

$$\langle n \rangle \approx 8 \, 10^{13} \text{ cm}^{-3} \, , \; T_e(0) \approx 1.4 \text{ keV} \, , \; I_{inj}(E_o) \approx 10 \text{ A} \, , \; E_o \approx 34 \text{ keV} \, ,$$

for these values, the calculated neutron fluxes are:

$$\phi_{bb} \approx 3 \, 10^{11} \text{ s}^{-1} \, , \; \phi_{bp} \approx 3 \, 10^{12} \text{ s}^{-1} \, , \; \phi_{pp} \approx 10^{10} - 10^{11} \text{ s}^{-1}$$

One important remark has to be made at this point: the dominant flux ϕ_{bp} depends on the power deposition profile through f(E,r): in more detail, ϕ_{bp} depends on the capture process through I(r) and on the slowing down process through dE/dt, that is information on <u>both</u> capture <u>and</u> energy transfer are coded into ϕ_{bp}.

Now, if slowing down is assumed to be classical (or actually measured to be, as we have done and will elsewhere publish), then $\phi_{bp} = \phi_{bp}(\delta)$ just reflects the actual power deposition profile through any geometrical parameter δ characterizing its broadness or radial shape (see Fig.1 for the actual δ).

In particular, concerning saturation problems, the functional dependence $\phi_{bp}(\delta)$ should not change with P_{add} if only bulk energy confinement deteriorates and the $T_e(r)$ profile only negligibly changes with P_{add} as in TFR.

Hence, the basic principle of the here reported experiment is to explore the functional dependence $\phi_{bp}(\delta)$ for different values of P_{add}; in order to make conclusions as direct as possible, purely geometrical action on power deposition was preferred rather than changing either injection energy or line density.

This was possible because allowance for easy mechanical tilting of the ion sources in the vertical plane had been provided on TFR, as can be seen on Fig. 1, where the actual δ parameter is also defined.

As numerical simulations show in Fig.2a, fast ion profiles can thus be modified from "central" to rather "peripheral" by changing δ from 0 to 12 cm; Fig.2b shows the corresponding neutron emission radial profiles.

Experimental results and interpretation

The experimental procedure was as follows. First, "δ scans" were measured for each source of one injection line; this enabled us to check the neutron yield of each source for a given set of operating parameters and to center the δ scale on the plasma axis within $\pm$ 0.5 cm. Second, "δ scans" were repeated with 2 and 4 sources operating together, thus varying P_{add}.

For single source operation, the absolute neutron yields were lower than calculated ($\approx$ 40%), but within the absolute calibration uncertainty of the neutron detectors. On the other hand, as shown in Fig.3a, 4 sources

yields were less than 4 times the single source ones, but not by a constant factor throughout the δ range; 2 sources results were intermediate.

The relative comparison between normalized 1 and 4 sources "δ scans" is shown in Fig.3b, together with simulations: the 1 source results fit remarkably well the simulation calculated with the actual experimental line density: $nl=3.3\ cm^{-2}$, while the 4 sources scan is significantly broader.

This undoubtedly implies a radially broader fast ion profile at high energy, that can be simulated by multiplying by 2.5 the actual nl value, as also shown in Fig.3b; this is just a practical trick to simulate a broadened fast ion profile and we don't mean that capture is actually enhanced, but this also means that if ion heating saturation had to be entirely explained in terms of "enhanced" or "abnormal" capture, an incredibly high enhancement factor would be required.

Therefore, rather than look for exotic capture schemes, we decided to provide an independent experimental determination of the capture by neutral beam shine-through calorimetry: preliminary results show indeed that capture is quite "normal" and insensitive to P_{add} as it should be.

Conclusion

Instead of hypothesis, we are now left with a few experimental facts:

1) Central fast ion density saturates with P_{add} (charge exchange with modulated beam,[2] and neutrons, this paper).
2) Fast ion profile broadens with P_{add} (neutrons,this paper).
3) Slowing down and capture are normal (charge exchange and calorimetry, to be published).

Therefore the present conclusion is that ion heating in TFR is at least partly limited by fast ion radial broadening and two further questions may be raised:

1) Can bulk ion energy confinement deterioration be entirely excluded? We would say not, because absolute fast ion densities cannot be measured on TFR with sufficient accuracy.
2) What mechanism induces fast ion losses and broadening? We don't know at present, but the fact that neutrons are produced at high fast ion energy implies that this mechanism has to act at the very beginning of the slow-down process, which is the same conclusion obtained by active charge-exchange and reported in [2].

References

[1] Transport investigations on TFR... Equipe TFR, in Plasma Physics and Controlled Nuclear Fusion Research (Proc. 10th Intern. Conf. London 1984), Vol.1,103.
[2] Fast ion behaviour in TFR from auxiliary modulated beam measurements. Equipe TFR. Proc. 12th Europ. Conf. Budapest 1985, Vol.2,308.
[3] TFR 600 neutral-beam heating results. Equipe TFR, in Plasma Physics and Controlled Nuclear Fusion Research (Proc. 8th Intern. Conf. Brussels 1980), Vol.2,547.

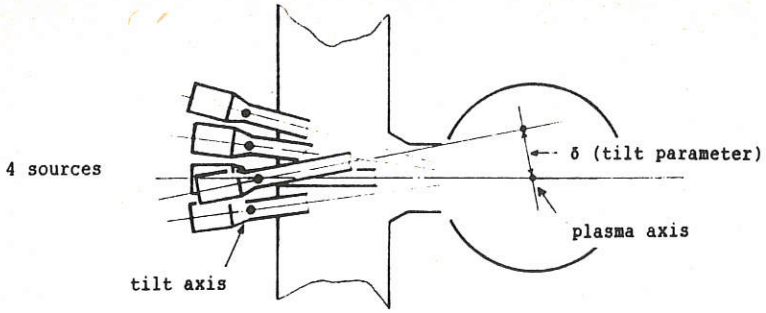

Fig.1 : Neutral beam injection line and definition of δ parameter.

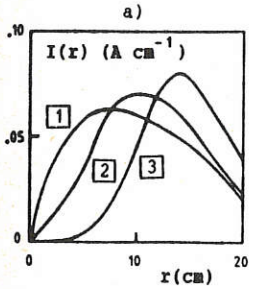

Fig.2 :
for 1 A injected,
a) Source term I(r)
b) Neutron emission radial profile
[1] δ= 0 cm
[2] δ= 6 cm
[3] δ=12 cm

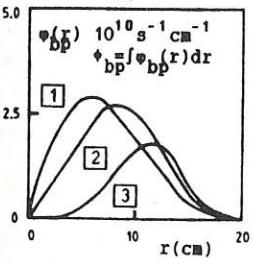

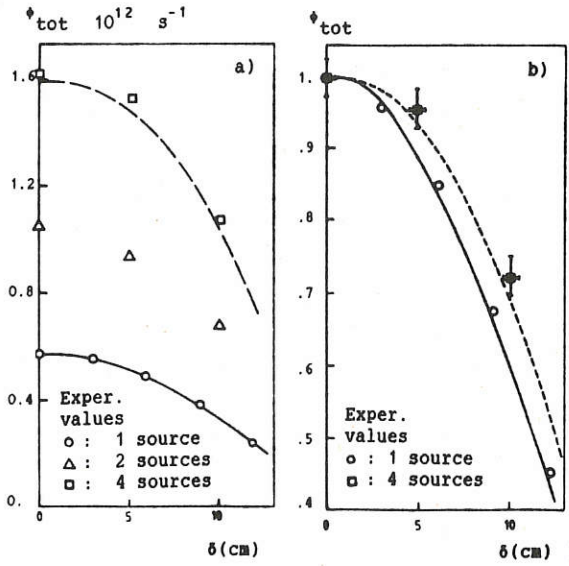

Fig.3 : Experimental results and comparison with simulations for 1,2 and 4 sources.
a) ϕ_{tot} versus δ.
b) $\frac{\phi_{tot}}{\phi_{tot}}$ normalized for δ=0 versus δ.

Simulations: —— Experimental n_e
– – – Exper. n_e * 2.5

VELOCITY-RELAXIATION OF INJECTED H^0-PARTICLES IN A HIGH TEMPERATURE HYDROGEN PLASMA

Ichiro MORI, Technical College,
Kaoru Ohya* Faculty of Engineering*
Tokushima university, Minami-Josanjima 770 Tokushima Japan

1. INTRODUCTION

Recently, in the neutral beam injection (NBI) and the temperature measurement by using H^0-beam have been performed extensively. However, the analysis with a exact cross-section of elastic scattering has not been appeared. In this paper, relaxations of H^0-beam spectrum after the interaction with a hot plasma are analyzed theoretically by solving a Fokker-Planck equation (FP E). In the following, the results of calculation for the exact cross-section and the method to get the Fokker-Planck coefficients are stated.

2. CROSS-SECTION

A cross-section of H^0-H^+ elastic scattering is calculated by making use of a partial wave method. Figure 1 shows an angular dependence of the exact cross-section /1/. The cross-section of elastic scattering, σ_{es}, is compared with that of charge exchange and the ionization, σ_{cx} and σ_{ion}, obtained by Riviere /2/ as shown in Fig.2.

The results of the calculation show that the exact cross-section approaches to that of a Born-approximation in high energy region such as 100 KeV. The Born-approximatin can then be used to obtain the Fokker-Planck coefficients. For the analysis of H^0-beam, effects of the charge exchange and the ionization by H^+-particles are included by consideration of Riviere's cross-sections.

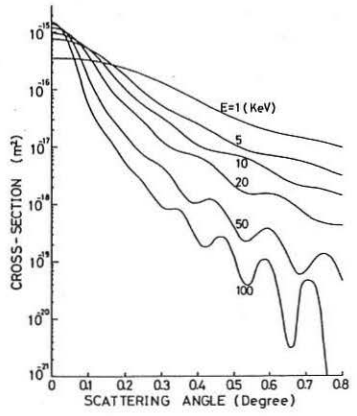

Fig.1 Angular dependences of H^0-H^+ elastic scattering cross-section

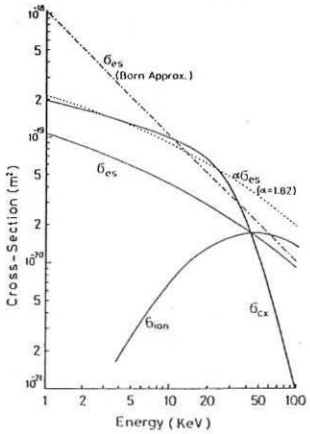

Fig.2 Elastic scattering cross-section and its comparison with charge-echange and ionization cross-sections

It is pointed out that there is a cross-point formed by three curves, σ_{es}, σ_{cx} and σ_{ion} in Fig.2. If a particle energy exceeds the cross-point energy, 47 KeV, loss mechanism of H^0-particles depends mainly on ionization by H^+-particles. Conversely, if the particle energy is smaller than cross-point energy, the mechanism will be decided by charge-exchange.

3. FOKKER-PLANCK EQUATION

Let us consider first an effect of elastic scattering to calculate the coefficients of Fokker-Planck equation (FPE). We can obtain the friction and difffusion coefficients by using the calculating method studied by Rosenbluth et al./3/. Results are as in the following.

$$\frac{\langle \Delta v_\mu \rangle}{\Delta t} = -\frac{e^4}{8\pi\varepsilon_0^2 m_p^2}\left[\ell n\left\{\frac{4\pi\varepsilon_0 aE}{e^2}\left(\frac{m_p}{2m_e}\right)\right\} + (1/6)\right]\cdot\frac{\partial}{\partial v_\mu}\{h(v)\} \tag{1}$$

$$\frac{\langle \Delta v_\mu \Delta v_\nu \rangle}{\Delta t} = \frac{e^4}{8\pi\varepsilon_0^2 m_p^2}\left[h(v)\delta_{\mu\nu} + \left\{\ell n\left(\frac{4\pi\varepsilon_0 aE}{e^2}\cdot\frac{m_p}{2m_e}\right) - \frac{17}{6}\right\}\frac{\partial^2 g(v)}{\partial v_\mu \partial v_\nu}\right] \tag{2}$$

where m_p, m_e, a, ε_0, e and E the proton mass, the electron mass, the Bohr-radius, the dielectric constant in vacuum, the electric charge and the relative energy respectively. If we assume that the plasma has a Maxwellian distribution with density of n_0 and temperature of T, then the above functions h(v) and g(v) are written as follows.

$$h(v) = 2n_0\Phi(\beta^{1/2}v)/v \simeq 2n_0 v^{-1} \tag{3}$$

$$g(v) = n_0\beta^{-1/2}[(\beta^{1/2}v)\Phi(\beta^{1/2}v) + (2\beta^{1/2}v)^{-1}\Phi(\beta^{1/2}v)\} + \pi^{1/2}\exp\{-(\beta^{1/2}v)^2\}] \simeq n_0(v+\beta^{-1}v^{-1}/2) \tag{4}$$

where $\Phi(\beta^{1/2}v)$ represents an error function with an argument of $\beta^{1/2}v$ and the relates to a plasma temperature with a formula $\beta=(m_p/2kT)$.

The Fokker-Planck equation can be described as

$$\left.\begin{aligned}\frac{\partial f}{\partial t} &= \frac{n_0\Gamma}{2}\left[\beta^{-1}v^{-3}\frac{\partial^2 f}{\partial v^2} + (2v^{-2}-\beta^{-1}v^{-4})\frac{\partial f}{\partial v} + (v^{-3}-\frac{\beta^{-1}}{2}v^{-5})\{(1-\mu^2)\frac{\partial^2 f}{\partial \mu^2} - 2\mu\frac{\partial f}{\partial \mu}\}\right] \\ \Gamma &= \frac{e^4}{8\pi\varepsilon_0^2 m_p}\ \ell n\left(\frac{4\pi\varepsilon_0 aE}{e^2}\cdot\frac{m_p}{2m_e}\right)\end{aligned}\right\} \tag{5}$$

where $\mu=\cos\theta$ and θ is an angle between the velocity vector $\vec{v}$ and the axis, i.e., beam direction in velocity space. The equation (5) can be solved by a variables-separation method. Angular part of solution, $\Theta(\mu)$, is given by Legendre function with index n, $\Theta(\mu) = P_n(\mu)$, while a velocity distribution, F(v,t), depends on the following equation.

$$\frac{\partial F}{\partial t} = \frac{n_0\Gamma}{2}\left[\beta^{-1}v^{-3}\frac{\partial^2 F}{\partial v^2} + (2-\beta^{-1}v^{-2})v^{-2}\frac{\partial F}{\partial v} - (1-\frac{\beta^{-1}}{2}v^{-2})v^{-3}n(n+1)F\right] \tag{6}$$

In addition to the effect of elastic scattering represented by the right hand side of Eq.(6), let us introduce the terms which describe the effects of charge exchange and ionization. These terms are represented as $-F(v,t)n_0\langle\sigma_{cx}v\rangle$ and $-F(v,t)n_0\langle\sigma_{ion}v\rangle$, where the brakets stand for the mean with respect to the distribution of ions, i.e., Maxwellian and we can use the Riviere's expressions for σ_{cx} and σ_{ion}. The final equation becomes as follows

$$\frac{\partial F}{\partial t} = \frac{n_0\Gamma}{2}\beta^{-1}v^{-3}\frac{\partial^2 F}{\partial v^2} + \frac{n_0\Gamma}{2}(2-\beta^{-1}v^{-2})v^{-2}\frac{\partial F}{\partial v} - \left\{\frac{n_0\Gamma}{2}(1-\frac{1}{2}\beta^{-1}v^{-2})v^{-3}n(n+1) + n_0\langle\sigma_{cx}v\rangle + n_0\langle\sigma_{ion}v\rangle\right\}F + S \qquad (7)$$

where the last term, S, represents a source term.

The most important feature in Eq.(6) or in Eq.(7) is the fact that the diffusion rate in velocity space of the H^0-particles is directly proportionl to the plasma temperature itself, i.e., the coefficients of second derivatives in Eqs. (6) and (7) include a factor $\beta^{-1}$where the β^{-1}means $2kT/m_p$ as in the above notation. Therefore the effective energy relaxation of H^0-beam in the NBI-experiments and also effective contribution on the temperature measurements would be expected with an increase of the plasma temperature.

4. SOLUTION OF FOKKER-PLANCK EQUATION

Now from here on we solve numerically the Fokker-Planck equation by using a computer. A solution of Eq.(6) as an initial value problems is shown in Fig.3 in which an initial function is assumed to be a rectangular distribution whose normalized value was taken as 10^3, i.e.,

$$\left.\begin{aligned} &F(0.98 \leqq (v/v_0) \leqq 1.02;\ t=0) = 10^3\ , \\ &F(v/v_0\ ,\ t\ ) = 0 \quad \text{for other value of } v/v_0\ , \end{aligned}\right\} \qquad (8)$$

where v/v_0 is an normalized velocity with v_0, the injecting H^0-velocity. In Fig.3, v is taken as the velocity corresponding to the energy of 100 KeV. In the figure the plasma temperature and the density are assumed to be 10 keV and 10^{20} m^{-3} respectively.

Solution for initial value problem in the presence of ionization and charge exchange reaction is shown in Fig.4. In this figure, plasma temperature and density have the same value as in the Fig.3, however, we must notice that the time scale is different from that of the Fig.3.

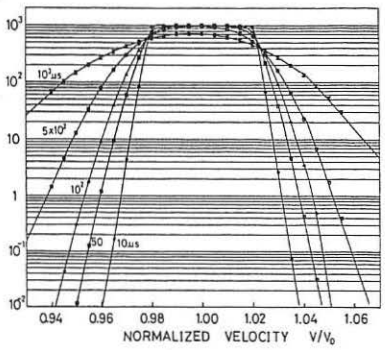

Fig.3 Solution of initial value problem of Fokker-Planck equation. The figure shows the relaxation of distribution without cgarge-exchange and ionization. Initial value is assumed to be $F(0.98 \leqq (v/v_0) \leqq 1.02;\ t=0)=10^3$.

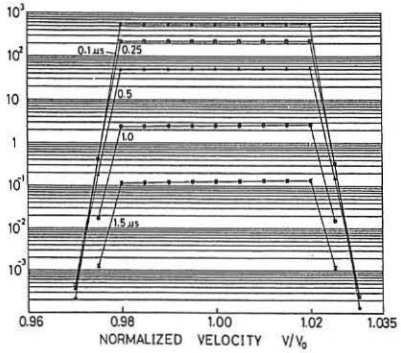

Fig.4 Solution of initial value problems. Figure shows the rerax-ation of distribution with the presence of charge-exchange and ionization.

Figure 5 shows the velocity distribution at 0.23 μs after the start up with a equivalent current of one ampere in continuous injection of H^0-beams. The plasma density of 10^{20} m^{-3} and the temperature of 10 keV were assumed in this figure.

It is seen from the figure that a relaxation or a diffusion in a velocity-space is not effective in the high energy injection. In the low energy injection, however, it is much more effective.

Spectral spreading or the relaxation of distribution function with increase of plasma temperature are shown in Fig.6 where the time is fixed also at 0.23 μs after the start up of the injection. Increase of the relaxiation with the plasma temperature certisfies the relation between the diffusion coefficient and the plasma temperature.

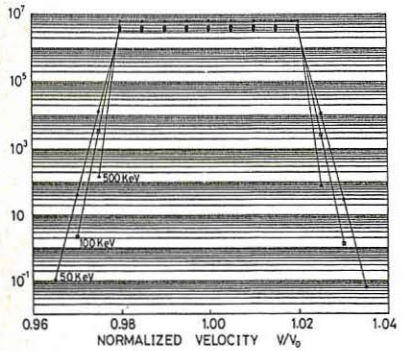

Fig.5 Effect of injecting energy on the distribution. Figure shows the distribution at 0.23 μs after start up of one ampare continuous injection. Parameter is the injecting energy.

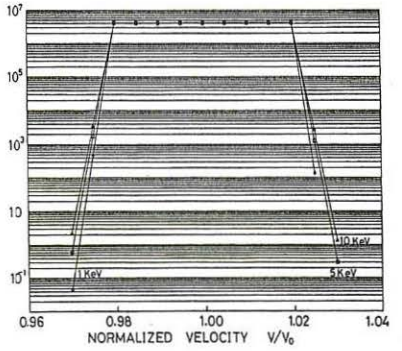

Fig.6 Effect of plasma temperature on the distribution. Figure shows the distribution at 0.23 μs after the start up of one ampare continuous injection. Parameter is the plasma-temperature.

REFERENCES

/1/ I. Mori, J. Mori and K. Ohya, To be appear in Journal of Physics B

/2/ A. C. Riviere, Nuclear Fusion 11, 363 (1971)

/3/ M. N. Rosenbluth, W. M. MacDonald and D. L. Judd, Phys. Rev. 107, 1 (1957)

FUSION PRODUCT ENERGY SPECTRA IN BEAM HEATED D-D, D-T, AND D-^{3}HE PLASMAS*

Dennis Slaughter
University of California Lawrence Livermore
National Laboratory, Livermore, California, 94550

INTRODUCTION

One of the critical parameters in large scale fusion experiments is the ion speed distribution and its variation with changes in confinement and heating. Large plasma dimensions and high densities complicate direct measurement of this distribution since ions escaping to the wall are primarily those which undergo charge exchange in the outer plasma or those which have suffered many collisions and significant energy loss during their migration from the central plasma. Several previous works[1-5] have shown that neutron and proton fusion reaction products generate a spectral line which is fairly broad due to Doppler broadening. For Maxwellian reacting ions, the Doppler width is related to the mean ion energy by eq. 1 below.

$$\Delta E_3 = \sqrt{\frac{16 \ln 2 \, m_3 m_4 QT}{\left(m_3 + m_4\right)^2}} \qquad (1)$$

where ΔE_3 is the full width at half maximum (FWHM) of the lighter reaction product, Q the energy released in the reaction, T the plasma temperature, m_3 and m_4 are the masses of the light and heavy reaction products respectively. Predictions of spectral shape and fusion product line width have been extended to non-Maxwellian plasmas by Boggdanov[2], Lehner and Poh[16], to beam driven plasmas by Elevant[4], Scheffel[15] and Heidbrink[7] and to rotating plasmas by Scheffel[15].

Neutron spectrum measurements have confirmed the above model in experiments with Maxwellian deuterium plasmas[8,9] as well as deuterium-tritium plasmas[10-11]. Proton spectra due to the D-^{3}He reaction have also been determined experimentally[12-13], and measurements in non-Maxwellian plasmas have been reported[14-19].

*Work performed by the University of California, Lawrence Livermore National Laboratory under the auspices of the U. S. Department of Energy, contract number W-7405-ENG-48.

SPECTRUM SIMULATIONS

The results reported here are based on a Monte Carlo simulation of reactions[20] in which a variety of ion speed distributions and angular distributions were considered. In all cases the appropriate differential cross sections, based on the model of Peres[21], were used to weight each reaction during the accumulation of a simulated fusion product energy spectrum. In the case of D-D fusion the reaction was assumed anisotropic in the center-of-mass system (CMCS) and used the angular distribution from reference 6. In the other cases the reaction was assumed isotropic in the CMCS. Typically 10^5 to 10^6 simulated reactions were sampled in order to compile each fusion product energy spectrum. Details of the calculations and a more complete presentation of the results will be published elsewhere.

Several generic ion speed distribution functions were considered for plausible beam heated plasmas and the four whose results will be reported here are: 1) isotropic Maxwellian, 2) isotropic, monoenergetic, 3) monoenergetic beam incident on a Maxwellian target viewed at 0 degrees relative to the beam, and 4) a three component Gaussian distribution characteristic of injected neutral species whose atomic, diatomic, and triatomic components are broken up in the plasma into ions with energies equal to full, half, and one third energy components, respectively. In the latter case energy diffusion produces three Gaussian components in the speed distribution.

The three component Gaussian distribution function is described by the form given in eq. 2 below.

$$f(v) = \sum_{i=1}^{3} \frac{Bi}{Wi} e^{-1/2 \left(\frac{v-v_i}{W_i}\right)^2} \qquad (2)$$

where v_i are the speeds corresponding to the acceleration energy, Eb, and the partial energy components $E_b/2$ and $E_b/3$. B_i and w_i are parameters describing the relative populations of the injected species and their width due to energy diffusion. In all of the results presented the width parameters are constrained by eq. 3 below

$$W_i = \gamma V_i \qquad (3)$$

so that the speed distribution function is described completely by the parameters E_b, B_i and γ. All of the results summarized below were carried out with γ=.0425, based on experiments with injection into mirror confined plasmas, and B_i corresponding to injected species with 50% at full energy, 40% at half energy and 10% at one third energy.

RESULTS

Results of the simulations were compiled for a wide variety of mean ion energies and for all of the reaction types and ion speed distribution functions. Mean energy of the fusion reaction product energy spectrum was calculated in each case and the full-width-at-half-maximum (FWHM) determined. In addition, all moments about the mean up to order ten were calculated to determine the extent to which the result spectra were non-Gaussian. The Doppler width results may be approximated by a simple power law given by eq. 4 below

$$\Delta E = a \left(\bar{E}\right)^b \qquad (4)$$

This approximation is simpler than those of Elevant[4] and Scheffel[5] and slightly less accurate. Nevertheless, this power law, together with the values of the constants given in Table I represent the data in these simulations within 3 % over most of the energy range 1-100 keV, and within 7 % in all cases.

Table I
Parameters used to describe Doppler width in eq. 4

Reaction	D(d,n)		T(d,n)		3He(d,p)	
	a	b	a	b	a	b
Maxwellian	64.5	.515	134.8	.512	116.4	.554
Monoenergetic	22.3	.676	55.0	.717	53.8	.620
Gaussian	33.3	.625	73.1	.650	67.8	.609
80 keV beam on Maxwellian	48.6	.548	118.2	.504	117.5	.524

Examination of the table shows that the square root dependence of the Doppler width on mean ion energy is a good approximation in most cases. In addition, the moments about the mean for the result spectra were compared to the moments for a Gaussian distribution and it was found that all of the result spectra are Gaussian to order ten at low ion energies (<20 keV) and are very nearly Gaussian to the highest energy considered.

CONCLUSIONS

Examination of the results and the constants in Table I indicate the Doppler width is proportional to the square root of mean ion energy, but the constant of proportionality varies widely among different generic speed distribution types. For example a line width for D-D neutrons of 75 keV corresponds to a 1.2 keV Maxwellian ion distribution but also to a 6 keV monoenergetic ion distribution. These variations are reduced at the highest ion energies but are substantial in every case. Consequently, a measured Doppler width for the fusion products of these reactions may not be used alone to infer the mean energy of reacting

ions. The functional form of the ion speed distribution must be known apriori or through independent measurement in order to infer a mean ion energy from a fusion product spectrum measurement. Detailed spectroscopy is not helpful since all of the reaction product spectra in these simulations were found to be Gaussian to high order. Consequently additional parameters in the ion distribution function may not be obtained from the details of the fusion product energy spectrum in the cases considered here. This is unfortunate in some cases, but the resulting simplicity may be helpful in interpreting some fusion product spectra with poor statistics when the form of the ion speed distribution is known with confidence. Nevertheless, there are many other cases, not considered here, where anisotropic ion angular distributions produce fusion spectral lines which are not Gaussian[7]. In those cases, detailed spectroscopy may provide information on scattering of injected neutrals and beam slowing down.

REFERENCES

1. M. M. R. Williams, J. Nuc. Energy 25, 489 (1971).
2. S. P. Bogdanov, V. I. Volosov, Recent Advances in Plasma Diagnostics, Vol. 3, V. T. Tolok, Ed., (1971).
3. H. Brysk, Plasma Physics 15, 611 (1973).
4. T. Elevant, Nuc. Inst. Meth. 185, 313 (1981).
5. J. Scheffel, Nuc. Inst. Meth. 224, 519 (1984).
6. G. Lehner, F. Pohl, Zeitschrift fur Physik 207, 83 (1967).
7. W. W. Heidbrink, Nuc. Inst. Meth. A236, 380 (1985).
8. W. A. Fisher, S. H. Chen, D. Gwinn, R. R. Parker, Nuc. Inst. Meth. 219, 179 (1984).
9. J. D. Strachan, P. Colestock, H. Eubank, L. Grisham, J. Hovey, G. Schilling, L. Stewart, W. Stodiek, R. Stooksberry, K. M. Young, Nature 279, 626 (1979).
10. V. W. Slivinsky, H. G. Ahlstrom, K. G. Tirsell, J. Larsen, S. Glaros, G. Zimmerman, H. Shay, Phys. Rev. Lett. 35, 1083 (1975).
11. R. A. Lerche, L. W. Coleman, J. W. Houghton, D. R. Speck, E. K. Storm, Appl. Phys. Lett. 31, 645 (1977).
12. W. W. Heidbrink, Nuc. Fusion 24, 636 (1984).
13. J. H. Foote, Nuc. Fusion 19, 1215 (1979).
14. B. Rose, A. E. Taylor, E. Wood, Nature 181, 1630 (1958).
15. R. A. Coombe, B. A. Ward, Plasma Physics 5, 273 (1963).
16. M. J. Bernstein, F. Hai, Phys. Lett. 31A, 317 (1970).
17. F. Pecorella, M. Samuelli, A. Messina, C. Strangio, Phys. Fluids 20, 675 (1977).
18. K. Hubner, J. P. Rager, K. Steinmetz, "Space Resolved Investigations on the Plasma Focus Neutron Emission", Tenth European Conference on Controlled Fusion and Plasma Physics I, 265 (1981).
19. J. S. Brzosko, H. Conrads, J. P. Rager, B. V. Robouch, K. Steinmetz, Nuc. Tech. Fusion 5, 209 (1984).
20. Dennis Slaughter, LINE: A Code Which Simulates Spectral Line Shapes for Fusion Reaction Products Generated by Various Speed Distributions, LLNL Report no. UCID-20374 (1985).
21. Asher Peres, J. Appl. Phys. 50, 5569 (1979).

NEUTRALISATION MEASUREMENTS FOR THE JET INJECTOR

R S Hemsworth, *A Stäbler, H D Falter, P Massmann, G H Deschamps, and A P H Goede

JET Joint Undertaking, Abingdon, Oxon, UK. *Attached from I.P.P. Garching

Introduction

Neutralisation of the extracted beam is, of course, an essential part of any neutral injection system. During testing of the first JET injector in the Neutral Injection Test Bed, extensive measurements have been made of the neutralisation efficiency with both H_2 and D_2 as the working gas, for extraction voltages of up to 80kV. Careful measurements of the neutralisation target present in the absence of the beam enable an accurate comparison to be made between predicted and measured neutralisation efficiencies. The variation in the power in the fractional energy ions is independently determined and shown to support the conclusions from the neutralisation measurements.

Gas Target Measurements

The JET beam source (PINI) is equipped with a close coupled neutraliser consisting of two equally long stages with an overall length of 1.8m. The cross section is racetrack shape of typical dimensions 0.43m x 0.18m. The gas is fed into both the plasma source (Qs) and the neutraliser (Qn), in the latter case via the gap between the two stages. The line density with the nominal neutraliser gas flow (Qn = 18 Torr.1.sec^{-1}) has been measured by tracking a nude high pressure ionisation gauge along the centreline of the neutraliser (see Fig.1). The gauge was calibrated for H_2, in situ, against a Baratron capacitance manometer. For the case where Qs=0, there is no gas flow in the first stage neutraliser, so that the pressure is constant in this region. This pressure has been measured as a function of Qn; it is not linear as the system operates in the transition flow regime. The pressure profile due to Qs has not been measured, but it is assumed to be identical to that due to Qn along the second stage neutraliser and to extrapolate linearly back to the extraction grids. The pressure at the junction between the two neutraliser stages (Qs only, Qn=0) is consistent with this assumption. The gas pressure profile from combined flows of Qs and Qn is taken as a simple addition of the individual profiles.

It is worth noting that Qs is normally approximately equal to the equivalent flow due to the extracted current, so that the net flow from the source to the neutraliser is usually very small, hence the gas target due to Qs is also small.

Neutralisation Measurements

The experimental set-up consisted of the PINI and neutraliser connected to the Neutral Injector Box containing the deflection magnet, the beamline calorimeter, the various ion dumps and the Test Bed Box Scrapers. The NIB was connected to the Target Tank containing a simulation of the torus duct and the Test Bed Beam Dump. This set-up is shown schematically in Fig.2.

Most of the measurements of neutralisation consisted of simply comparing the power to either the TBBD or the Target Tank plus the

TBBS from similar, usually sequential, shots with and without the deflection magnet energised. The power to the TBBD and the Target Tank plus TBBS were determined by water flow calorimetry, the flow and water temperature rise being independently determined for the two sets of components. The neutralisation efficiency is calculated as:

$$\eta = \frac{\{E_{tbbd} / E_o\}\ \text{on}}{\{E_{tbbd} / E_o\}\ \text{off}} \quad \text{and/or} \quad \eta = \frac{\{E_{tt} / E_o\}\ \text{on}}{\{E_{tt} / E_o\}\ \text{off}}$$

where $\{E_{tbbd} / E_o\}$on is the energy to the TBBD with the deflection magnet energised, normalised to the extracted energy, E_o etc. (In practice the extracted energy was usually the same for both shots.) The agreement between the measurements was generally very good. Since the determination of ε involves the ratio of energies, and as the water flow was held constant, this frequently reduced to simply the ratio of the integrals under the water temperature rise versus time curve, such as shown in Fig.3. Overall the accuracy of this measurement is high $<\pm 5\%$.

The method described above could not generally be used when the beam was intercepted by the beamline calorimeter, since this is designed to accept only $\leq$1.4MW per beam. With the magnet energised and the beamline calorimeter intercepting the neutral beam, the total power leaving the neutraliser is deposited on the calorimeter and the components connected to the Central Support Column, i.e. the various ion dumps and the magnet liners. Thus the neutralisation efficiency is calculated as:

$$\eta = \frac{Ecal}{Ecal + Ecsc}$$

where Ecal is the energy deposited on the calorimeter etc. Again water flow calorimetry was used to determine the deposited energy, except this time absolute measurements of water flow and temperature were necessary. The error in these measurements is estimated to be $\sim\pm 10\%$.

Predicted Neutralisation Efficiencies

In order to predict the neutralisation efficiency from known charge transfer cross sections, the extracted species mix must be known. Extensive species measurements for the JET PINIs have been made with H_2 as the working gas([1]). Measurements of the extracted species with D_2 as the working gas have recently been made, both at Culham and during the course of this work ([2]), these two measurements being in good agreement.

Account must, of course, be taken of reionisation losses in the magnet region. It is estimated that ~ 5% of the neutral beam is reionised with a gas flow of 18 Torr.1.sec^{-1}.

Comparison of Measured and Predicted Neutralisation

The measured and predicted neutral power fraction versus the target gas density for extraction voltages of 60kV and 80kV with H_2 as the working gas and for 80kV with D_2 as the working gas are shown in Figs 4 to 6. Spot points are also shown at 60kV and 70kV with D_2 as the working gas. It is obvious that there is very poor agreement between measurement and prediction. Reasonable agreement can only be achieved by multiplying the n.l scale by a factor <1.

As the species extracted from the JET PINI is well known, as are the relevant cross sections, the neutralisation measurement is in fact a measure of the gas target, n.l, in the presence of the beam, i.e.

for the JET system the gas target in the presence of the beam is of the order of half that in the absence of the beam.

Supporting evidence for the conclusion that the gas target is reduced in the presence of the beam can be obtained from the independent measurement of the power in the deflected, dumped, fractional energy ions. Because of the complexity of the system, accurate absolute measurements of this power were not possible and the experimental data shown in Fig.7 have been 'normalised' for the purpose of comparison. It is clear that the variation in the power in the deflected fractional ions strongly supports the conclusion that the gas target in the presence of the beam is indeed 'thin': The power to the fractional energy ion dumps actually increases with the gas flow, whereas a decrease is expected. As substantial re-neutralisation of these ions occurs as they traverse the magnet the accuracy of determining the reduction in the gas target is poor and no significance is attached to the discrepancy between the reduction factor determined from these data c.f. that from the neutralisation measurement.

A likely explanation for the reduction in the gas target is significant heating of the gas, as recently suggested by Paméla ([3]). This is supported by another experimental observation: The Baratron capacitance manometer attached to the neutraliser at the gap between the first and second stages shows an increase in the pressure when the beam is turned on (see Fig.10). This is precisely the opposite of expectations. The beam transports particles from the source, effectively reducing the net flow into the neutraliser, so that a reduction in the neutraliser pressure is expected, typically of the order of 0.5m Torr. An increase in the measured pressure is expected if the neutraliser gas is heated because the system is set up for constant gas flow and it operates in the transition flow regime. (As the Baratron is at room temperature, at the end of a piece of relatively narrow bore tube, no pressure change would result from a temperature increase of the gas in the neutraliser if the system operated entirely in the molecular flow regime due to thermal transpiration effects between the gauge and the neutraliser.) In order to explain a reduction in the gas target by a factor of two, the gas temperature would need to be increased to approximately 1400°C.

Conclusion

The obvious consequence of the low neutralisation efficiency is that the neutral power to JET will be lower than predicted. This can be ameliorated to some extent by increasing the gas flow. The measured gas flow to create the design gas target in the absence of the beam is 18 Torr.l.sec^{-1}. This can be increased to 25 Torr.l.sec^{-1} without exceeding limits such as the power lost due to reionisation or the power loading to the extraction grids. Nevertheless the gas target in the presence of the beam will be substantially below the design figure of 10^{16}cms^{-2}. The reason for the low neutralisation is likely to be heating of the neutraliser gas by the beam. It is probable that the size of the neutraliser c.f. the mean free path of the molecules is significant in determining the equilibrium temperature of the gas and thus should be taken into account in the design of the future systems.

References

1. T.S.Green et al, Proc. 10th Int. Conf. on Plasma Physics & Contr. Fus. Res., London, 1984.
2. A.R.Martin, Culham Neutral Beam Development Grp., unpublished data.
3. J.Paméla, EUR-CEA-FC-1279, 1985.

Fig.1 MEASURED PRESSURE PROFILE ALONG BEAM PATH

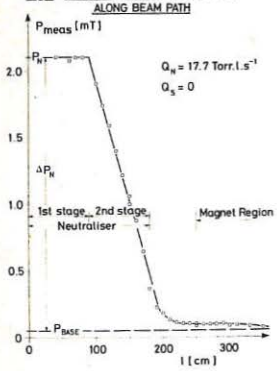

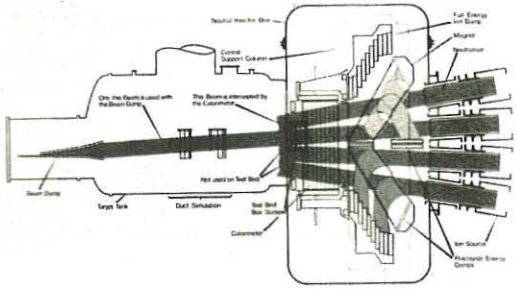

Fig.3 TEST BED TARGET TANK WATER TEMPERATURE WAVEFORM

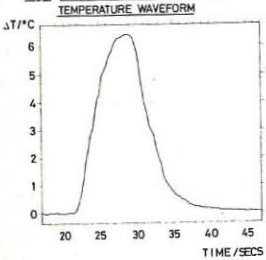

Fig.4 NEUTRALISATION DATA : 60kV/H_2

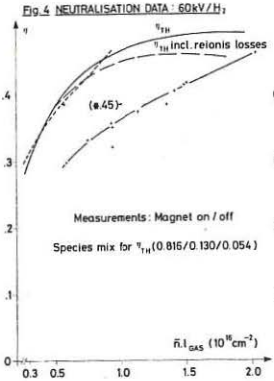

Fig.5 NEUTRALISATION DATA : 80kV/H_2

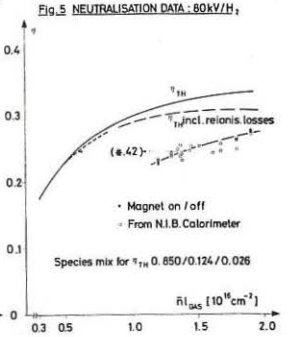

Fig.6 NEUTRALISATION DATA : D^0 BEAMS

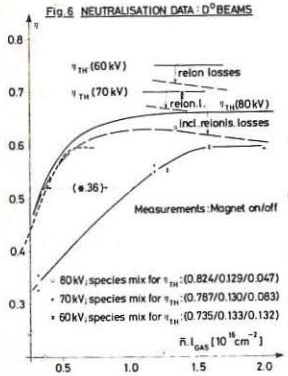

Fig.7 POWER IN DUMPED FRACTIONAL ENERGY IONS FOR 60 kV (H_2) OPERATION

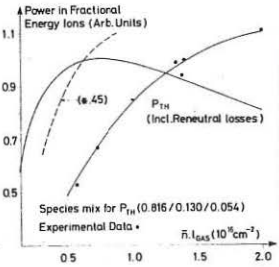

Fig.8

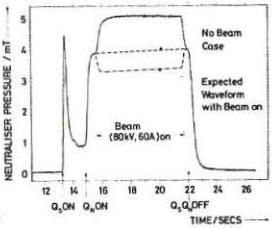

EXTRACTION OF INTENSE H^- BEAMS FROM VOLUME SOURCES

A. J. T. Holmes and M. P. S. Nightingale

UKAEA Culham Laboratory, Abingdon, Oxon, England.
(UKAEA/Euratom Fusion Association)

1. Introduction

Volume H^- plasma sources offer many advantages when used as the ion sources for future neutral beam injectors. In these sources the H^- ions are formed by dissociative attachment collisions between vibrationally excited molecules and cold electrons[1], resulting in a large plasma region from which many H^- beamlets could be extracted in a manner closely analogous to positive ion sources. These volume H^- sources have the additional advantage in that their mode of operation is similar to magnetic multipole sources such as those used on the JET neutral beam injectors[2]. An H^- ion source of this type is described by Nightingale[3].

The H^- ions and electrons in these H^- ion sources have the same temperature and plasma potential, consequently an applied potential to extract H^- ions would also extract a much larger flux of electrons. We describe here an accelerator which can suppress these extracted electrons using transverse magnetic fields. This accelerator is also capable of forming a highly collimated H^- beam by adjustment of the potential of an intermediate electrode.

2. Accelerator Design

The H^- source used in these experiments is described in the companion paper by Nightingale[3] and we restrict the description of the experiment to the accelerator alone. The accelerator has three planar electrodes and two beam accelerating gaps and the electrodes are supported on water cooled flanges separated by araldite insulators. The maximum operating potential is 50 kV. The beam envelope is determined by the extraction electrode profiles which are shown in Fig. 1. The beam forming electrode faces the H^- plasma generator as in positive ion sources and has a pierce profile. However, it also contains two bar magnets orientated to give two field maxima of 80 gauss which suppress the plasma electron flux. The net magnetic flux encountered by the H^- ions is zero so that it remains undeflected.

However, the electrons can also cross the field by pitch angle collisions and hence can diffuse into the first accelerating gap, where they can be accelerated to several keV. These electrons are trapped by a second dipole field at the front edge of the second electrode whose peak value is 340 gauss. This deflects the electrons into the recess in the second electrode, where they are dumped at an energy equal to the first gap potential. The H^- beam is also steered by this field and drifts through the electrode to the rear edge, where it is steered in the opposite direction by an oppositely directed dipole field.

The H^- beam and less than 1% of the electron flux are then accelerated to the full beam energy across the second gap, and the H^- beam is steered back on to its original axis by a final dipole field in the third electrode. In this way the H^- beam is exactly on axis and unsteered by magnetic or electrostatic lens effects. Experimental observations have shown that the residual steering arising from misalignment is less than 0.25°.

3. Experimental Results

3.1 Beam optics

A typical beam profile at minimum divergence is shown in Fig. 2. It can be seen that the beam has an approximately gaussian profile but is significantly narrower than the extraction aperture radius. This point will be discussed in section 3.2, but it causes the concept of beam divergence to become meaningless. Instead we use beam radius at 1.2 m from the source as a measure of the beam envelope.

The beam is focussed by varying the potential of the second electrode in the accelerator. Fig. 3 shows the variation in the beam diameter with first gap potential. A broad minimum is observed at approximately half the beam forming aperture radius when the first gap potential is about 10% of the beam energy.

The voltage ratio of the first gap to total beam energy for a collimated beam is also virtually independent of H^- current density, as seen in Fig. 4. This data was taken at a virtually constant beam energy and shows that a variable current density H^- beam can be extracted at constant beam energy, although there is a lower minimum in beam energy for any given beam current. This is seen more clearly in Fig. 5, which shows the beam current density for various discharge currents and total beam energies. All points in this diagram correspond to a focussed beam whose radius is virtually constant (the source gas flow is constant in this experiment).

These results indicate that the accelerator behaves in a manner analogous to an electron gun, having an essentially rigid ion emitting surface[4]. As the electrostatic lenses forming the accelerating column will have constant focal properties for a given geometry and voltage ratio then the beam envelope will have a fixed shape if the ion emitting surface does not move as a result of increasing the plasma density. This behaviour has not been seen in positive ion sources and is possibly a result of the magnetic field parallel to the plasma boundary.

3.2 Beam transport

The beam radius at 1.2 metres from the source is virtually independent of beam current and beam energy, but it is a very strong function of gas pressure in the drift region, originating from the source. This dependence is seen in Fig. 6, where at low pressures a very divergent beam is observed.

A probable explanation of this effect is that the beam space charge is over neutralised to give a positive space potential relative to the external electrodes so that slow positive ions formed by ionisation can be expelled from the beam. This result has been seen experimentally by Goretskii & Naida[5]. If this is so then the beam envelope is subject to a force which reduces its diameter until the emittance "pressure" establishes a new

equilibrium. A simple model for this process indicates that the potential should vary quadratically with radius with a coefficient which is virtually independent of beam current and energy. Consequently the electrostatic force is stronger for large diameter beams of constant ion density, hence resulting in more beam compression, which is in qualitative agreement with earlier measurements on an 8 mm extraction aperture where a larger beam diameter of 16 mm was seen[4].

References

(1) M.Bacal, G.W.Hamilton, A.M.Bruneteau, H.J.Doucet, J.Taillet. Rev. Sci. Instrum., 50, p719, 1979.
(2) A.J.T.Holmes, T.S.Green, A.R.Martin, R.S.Hemsworth and E.Thompson. 4 Inst. Symp. on Heating in Toroidal Plasmas, p1065, Rome 1984.
(3) M.P.S.Nightingale and A.J.T.Holmes: this conference.
(4) A.J.T.Holmes, G.Dammertz and T.S.Green. Rev. Sci. Instrum., 56, p1697, 1985.
(5) V.P.Goretskii and A.P.Naida. Soc. J. Plasma Phys., 11, p227, 1985.

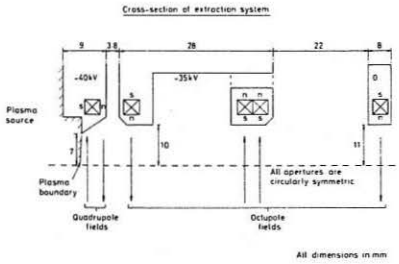

Fig. 1 A Diagram of the Accelerator Geometry.

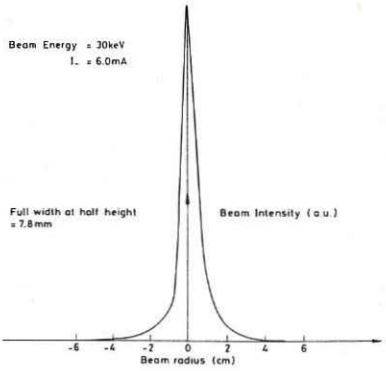

Fig. 2 The Beam Profile at 1.2 metres from the source, showing the beam diameter contraction.

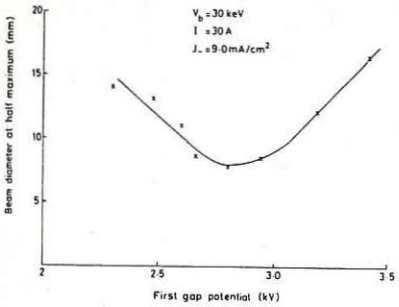

Fig. 3 Variation in Beam Radius with First Gap Potential.

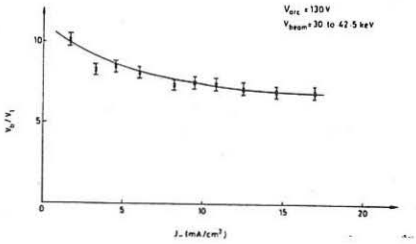

Fig. 4 Accelerator Gap Voltage Ratio as a function of H^- Current Density.

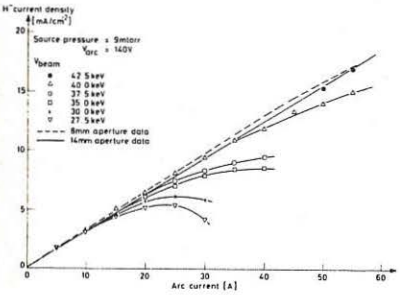

Fig. 5 Variation in H^- Current Density with Arc Current and Beam Energy.

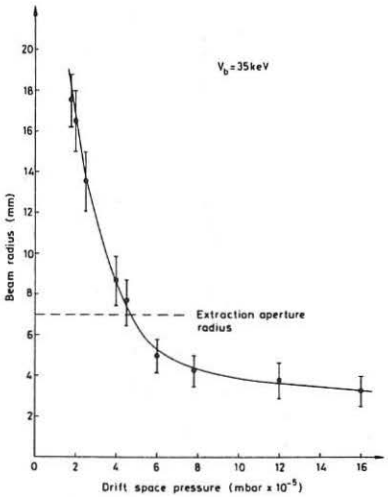

Fig. 6 Dependence of the Beam Radius on the Pressure in the Drift Space between Accelerator and Target.

PROGRESS IN THE DEVELOPMENT OF A NEGATIVE ION SOURCE FOR USE IN NEUTRAL BEAM HEATING

M. P. S. Nightingale and A. J. T. Holmes

UKAEA Culham Laboratory, Abingdon, Oxon, England.
(UKAEA/Euratom Fusion Association)

A. Aims

The use of intense negative hydrogen and deuterium ion sources in neutral beam injection for fusion plasma heating at high beam energies has been proposed for many years, since negative ions offer the possibility of high neutralisation efficiencies, and should produce beams with 100% full energy component. It is expected that future neutral beam heating of large tokamaks will require DC negative ion currents of more than 10A per source at beam energies of more than 100 keV. This corresponds to extracted current densities of approximately 30 mA cm^{-2} given the typical source dimensions presently envisaged.

Several source designs have been considered for negative ion production, of which the most promising appears to be the so called 'volume' source, two of which are in use at Culham Laboratory. It is now widely accepted that in these sources H^- ions are produced via the production of vibrationally-excited hydrogen molecules in one section of the source (the discharge volume) by fast electron impact on molecules at electron energies of more than 10 eV. The reaction is:

$$H_2(v=0) + e(\text{fast}) \rightarrow H_2^* + e \rightarrow H_2(v^*) + e + h\nu$$

where $H_2(v^*)$ refers to a vibrationally excited molecule of v^* of between six and thirteen. This is followed by the diffusion of these molecules into a region (the extraction volume) of lower electron temperature (0.5 - 2 eV) where the dissociative attachment reaction:

$$H_2(v^*) + e(\text{slow}) \rightarrow H^- + H$$

takes place without the subsequent substantial destruction of H^- that would occur at higher electron temperatures. The H^- ions so produced are then extracted and accelerated in a similar manner to existing positive ion sources.

B. The Large Culham H^- Source

The large H^- source shown in Fig. 1 has been used at Culham Laboratory to demonstrate the level of ion current density extractable from sources of approximately the size and power required for a practical neutral beam injector. Using a 6 kV triode accelerator with a 1.5 mm diameter aperture, probe ion beams have been extracted, and the results for H^- and D^- extraction are shown in Figs. 2 and 3. These demonstrate that current densities of 60 mA/cm^2 and 25 mA/cm^2 can be extracted in the two cases -

values which are of the order required for neutral beam injection. The functional dependence of extracted H^- current on discharge parameters is described below, but the maximum observed in the corresponding extracted D^- current has not yet been explained.

In addition, Langmuir probe measurements have shown that the extractable current density should be uniform to within ± 20% over the central 1000 cm^2 of the source. The Langmuir probes have also been used to investigate the axial variation of H^- density within the source. These have shown that even higher extractable currents may be obtainable by moving the extraction aperture further into the source.

The manufacture of a 100 kV triode accelerator is nearing completion at Culham Laboratory, using a design based upon the work of Holmes and Nightingale (this conference). This should allow a single beamlet of more than 100 mA to be extracted for the first time from such a source.

C. The Small Culham H^- Source

A smaller (10 kW) source (Fig. 4) has been developed at Culham for use in source and accelerator design. Using a triode accelerator similar to that described by Holmes & Nightingale (this conference) an H^- beam has been extracted from an 8 mm diameter aperture, accelerated to 27 kV, and focussed onto a target 2.2 metres from the accelerator. The resulting measured H^- current density and simultaneously extracted electron current are shown in Figs. 5 and 6. These results demonstrate that the ion current density saturates with increasing arc current at a value that increases with pressure, whereas the electron current increases with arc current but decreases with pressure. Note that this behaviour is identical in form to that observed in the large source (Fig. 2).

A simple analytical model has been developed at Culham to describe the source operation in the high current 'saturation' mode. This assumes that the saturation occurs because destruction of vibrationally-excited molecules by fast electron collisions occurs at high arc currents. When this occurs it can be shown that

$$n_- \propto \left(\frac{n_e\, n_o}{n_+}\right)$$

Langmuir probe measurements have been used to derive the n_+, n_e and n_- densities, using the model of Lea & Allen, which show that the model does indeed predict the correct n_- scaling. It is now believed that this pressure dependent saturation may apply universally for sources run at the discharge powers required for a neutral beam source. Although this saturation does affect the achievable power and gas efficiency of the source, it does not preclude such sources providing ion current densities of the required magnitudes.

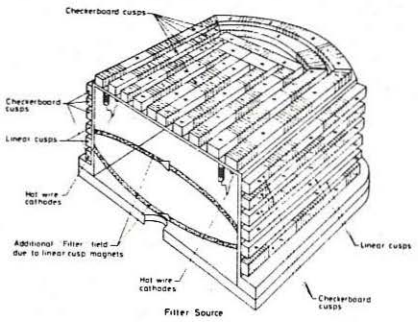

Figure 1 The Culham Large Negative Ion Source

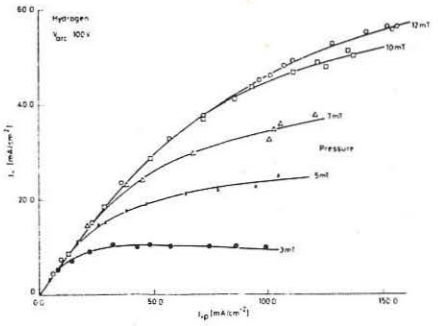

Figure 2 The H^- current densities extracted from the large source

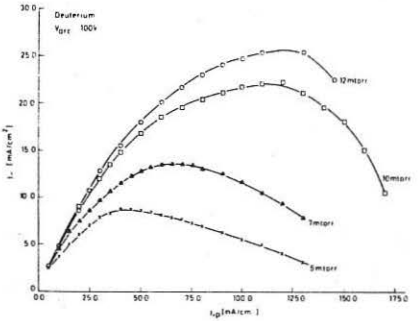

Figure 3 The D^- current densities extracted from the large source

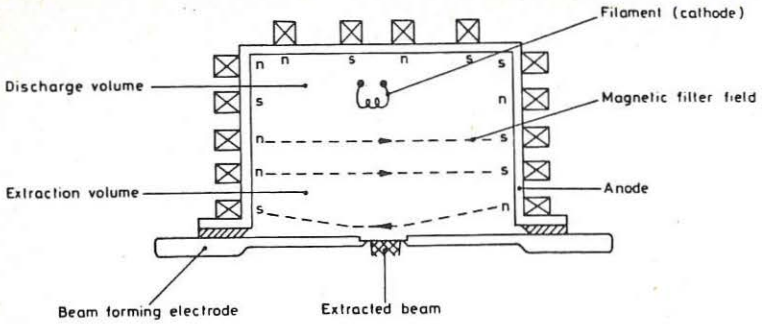

Figure 4 The Culham Small Negative Ion Source

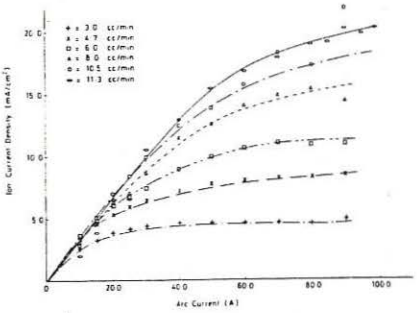

Figure 5 The H^- current densities extracted from the small source

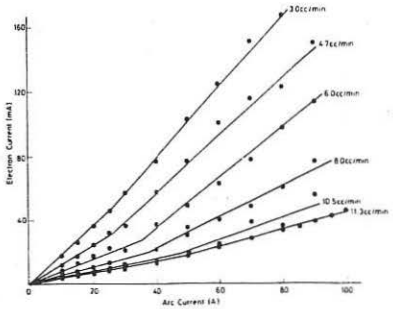

Figure 6 The electron current extracted from the small source

Lower Hybrid Heating and Current Drive

LOWER HYBRID CURRENT DRIVE EFFICIENCY ON THE PETULA-B TOKAMAK AT f = 1.3 GHz AND AT f = 3.7 GHz

C. Gormezano, G.T. Hoang, G. Agarici, H. Bottollier-Curtet, P. Briand, G. Briffod, P. Chabert, M. Clément, C. David, A. Girard, M. Goniche, P. Grelot, W. Hess, M. Hesse, G. Ichtchenko, A. Panzarella, F. Parlange, F. Ryter, G. Tonon, J-C. Vallet, D. van Houtte.

ASSOCIATION EURATOM - C.E.A. - Département de Recherches sur la Fusion Contrôlée - C.E.N.G. - 85 X - 38041 GRENOBLE Cédex (France)

Current Drive experiments are made in the Petula-B tokamak (R = .72 m, a = .16 m, B = 2.7 T, Ip ≃ 150 kA) by means of a 1.3 GHz generator (P< 400 kW, Δt = 150 ms) and of a 3.7 GHz generator (P < 400 kW, Δt ≃ 10-40 ms). Experiments at 1.3 GHz have already been reported /1/. The grill at 3.7 GHz is composed of 18 waveguides, 9 in a row, made of 3 juxtaposed multijunctions allowing the central value of the parallel wave spectrum, $N_{//}$, to be varied between 1.5 and 2.7 depending upon the phasing between multijunctions. As compared to the 4 waveguide grill at 1.3 GHz ($1.4 < N_{//} < 4.5$), the wave spectrum is much narrower, 50 % of the launched power being in the main lobe ($< N_{//} > \pm 0.8$).

At f = 1.3 GHz, the usual operating density for L.H.C.D. is $\sim 10^{13}$ cm^{-3} so that accessible values of $N_{//}$ are about 1.4. Then, the main part of the wave spectrum can reach the plasma center. At f = 3.7 GHz with a narrow spectrum, accessibility can be a severe problem. Maximum values of $N_{//acc}$ are 1.6 at $\bar{n}_e = 1.4\ 10^{13}\ cm^{-3}$, 2 at $\bar{n}_e = 2\ 10^{13}\ cm^{-3}$ and 2.4 at $\bar{n}_e = 5\ 10^{13}\ cm^{-3}$. Most part of a typical wave spectrum centered at $N_{//} = 1.7$ will then be inacessible to the plasma center. Moreover, the corresponding energy of HF resonant electrons is low (80 keV for $N_{//} = 2$, 40 keV for $N_{//} = 2.7$) as compared to usual energies (150 keV at $N_{//} = 1.4$) in other L.H.C.D. experiments.

Density limit : at f = 1.3 GHz, the density limit occurs at $\bar{n}_e = 2\ 10^{13}\ cm^{-3}$ /2/ /3/ as shown in fig. 1. At 3.7 GHz, the maximum density for which zero loop voltage operation is obtained is $\bar{n}_e = 2.1\ 10^{13}\ cm^{-3}$ for $P_{h.f.} = 300$ kW. At higher H.F. power, a m=2 tearing mode develop preventing stable discharges to be obtained. For $\bar{n}_e > 3.5\ 10^{13}\ cm^{-3}$, such a mode disappear, but the HF power is then too low in order to obtain V = 0. It is not therefore possible to assess the value of the density for which zero loop voltage operation is still possible by lack of HF power.

Density dependence of parametric decay waves indicates a threshold at $\bar{n}_e = 8\ 10^{13}\ cm^{-3}$ which is usually observed at the density transition. As compared to the corresponding threshold at f = 1.3 GHz ($\bar{n}_e = 1\text{-}1.2\ 10^{13}\ cm^{-3}$), an increase by a factor of 6 to 8 of the density transition can be tentatively inferred. This is in agreement with a scaling such as $n_t = f^{\alpha}$ with α ranging from 1.7 /4/ to 2 as suggested in /5/.

At higher densities ($\bar{n}_e \sim 10^{14}\ cm^{-3}$), a large loop voltage drop is still observed ($\Delta V/V \simeq 20$ % for $P_{h.f.} = 400$ kW) with a corresponding slight increase in Te ($\sim$ 200 eV), a decrease of the m = 2 tearing mode and a change in the behaviour of the scrappe-off plasma. At such high densities, fast ion tails cannot be detected and the increase in neutrons is rather weak.

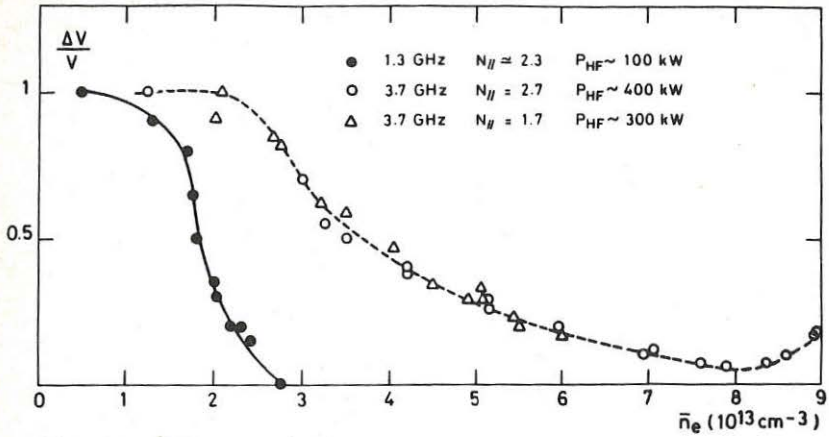

Fig. 1 : ΔV/V versus density

Comparison between efficiencies at f = 1.3 GHz and at f = 3.7 GHz : The power dependence of the loop voltage drop is plotted in fig. 2 at $\bar{n}_e \simeq 10^{13}$ cm^{-3}, for which accessibility plays a little role. Total replacement of the plasma current is obtained for the same HF power at f = 1.3 GHz and at f = 3.7 GHz for $N_{//} = 1.7$. It is to be noted that, at f = 3.7 GHz, 10 % of the HF power is absorbed into the waveguides due to their small width and the HF power plotted in fig. 2 should be corrected accordingly.

In fact, higher efficiency was expected from theoretical considerations /4/ at f = 3.7 GHz : $\eta = \bar{n}$ RI/P = 1.1 instead of 0.75 at $N_{//} = 1.7$. An upshift of $N_{//}$ up to 2.1 would explain the difference although ray tracing codes indicate a possible upshift of only 10 %. Lack of efficiency can be due to the "gap" problem.

Dependences of efficiency at f = 3.7 GHz : from fig. 2, it can be inferred than an HF power of 400 kW would have been required for a total replacement of the plasma current for $N_{//} = 2.7$, in agreement with a $N_{//}^{-2}$ dependence from theory. At higher densities, $\bar{n}_e > 3\ 10^{13}$ cm^{-3}, the same loop voltage drop is observed for the two indices. It is to be noted that when the central multi-junction is fed alone, a broad wave spectrum is launched ($1 < N_{//} < 5$). The resulting efficiency is much lower, by a factor of about 3.

Typical power dependence of the loop voltage drop for different densities are shown in fig.2. ΔV/V is a function of the DC electric field, E, which results in an additional H.F. current /6/ so that :

$$I_p \frac{\Delta V}{V} = I_p - I_{oh} = I_{hf} + \sigma(I_{hf}).E$$

$\sigma(I_{h.f.})$ being the HF conductivity and $I_{h.f.}$ the HF current that results in absence of E field. The enhanced conductivity becomes negligeable at high density. It is to be noted that this effect is important at low density due to the small size of PETULA.

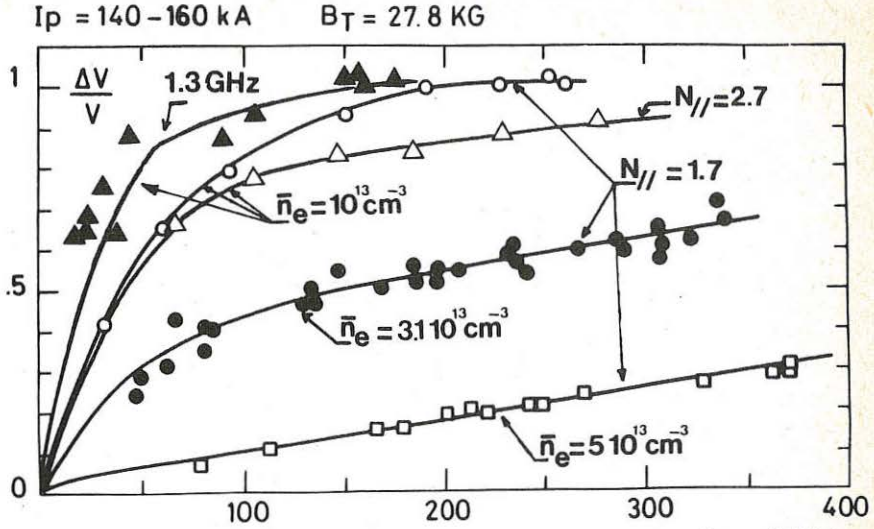

Fig. 2 : $\Delta V/V = f(\bar{n}_e)$ - At f = 3.7 GHz with one exception

If the behaviour of V is well explained at $N_{//} = 2.7$, the main part of the wave cannot reach the plasma center at $N_{//} = 1.7$ for $\bar{n}_e > 5\ 10^{13}\ cm^{-3}$ due to accessibility criterion. But a significative loop voltage drop is observed : ∿25 % for $P_{h.f.} = 300$ kW together with a modification of the plasma current such that sawteeth are stabilized, indicating that a substantial amount of the current is driven by the H.F. Moreover, a downshift of the wave spectrum is expected from ray tracing code at these densities. Then, part of the wave has to be absorbed in the outer part of the plasma where the gap problem is important due to the low electron temperature. At high H.F. power, saturation may appear depending upon the density. This is discussed in /7/. At f = 3.7 GHz, the signal $\Lambda = \beta_\theta + li/2$ which is deduced from equilibrium equations, increases by a large factor, up to 25 %. The main part of this increase can be attributed to the increase in poloidal beta. Magnetic field dependence of Λ and of the relative current drive efficiency (fig. 3) shows that poloidal beta is indicative of the HF current.

As shown in fig.4, V is constant when the plasma current is increased from 90 kA to 150 kA, indicating an increase of the efficiency. But, radial electron temperature profiles exhibit a more peaked profile at low plasma current, the central value of Te being roughly constant. This difference can explain an improved efficiency at high Ip via the gap problem.

Conclusions : the gross behaviour of current drive at f = 3.7 GHz, taking into account the limited available power, corresponds to expectations from previous experiments at f = 1.3 GHz. At high densities, a significative part of the HF current has to be driven in the outer part of the plasma where efficiency is rather low. Improved performances can then be expected on larger machines.

References :

/1/ Parlange, F., et al, Proc. 12th. Eur. Cont. Cont. Fus. Plasma Phys. Budapest (1985).
/2/ Van Houtte, D., et al, Proc. 4th. Symp. Heating in Toroidal Plasmas Roma I (1984) 554.
/3/ Leuterer, F., et al, Phys. Rev. Lett. 55 (1985) 75.
/4/ Gormezano, C., these proceedings.
/5/ Tonon, G., Wegrowe, J.G., in Non Inductive Current Drive in tokamaks (IAEA tech. meeting, Culham 1983).
/6/ Fisch, N.I., Phys. Fluids 28 (1985) 245.
/7/ Girard, A., et al, these proceedings.

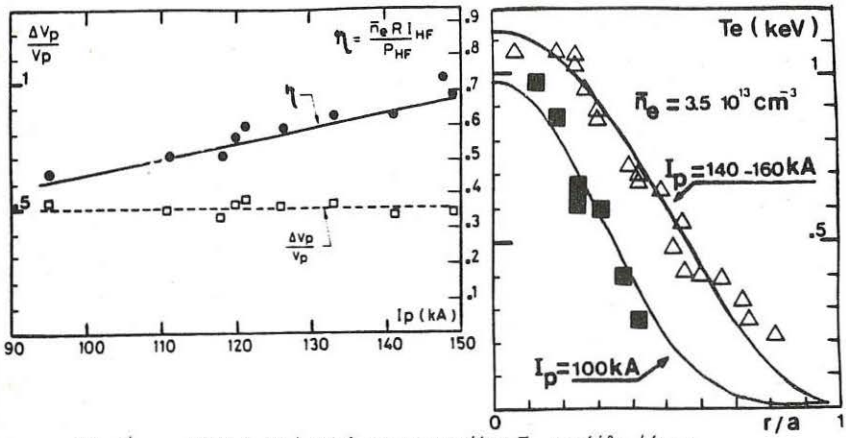

Fig.4 : ΔV/V & (Ip) with corresponding T_e profile (from Thomson diffusion)

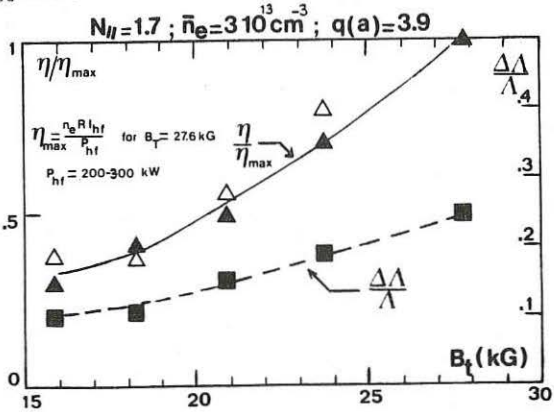

Fig.5 : Figures of merit versus magnetic field.

CURRENT DRIVE BY FAST MAGNETOSONIC WAVES NEAR THE LOWER HYBRID FREQUENCY IN THE JIPP T-IIU TOKAMAK

K. Ohkubo, Y. Hamada, Y. Ogawa, A. Mohri, R. Akiyama, R. Ando, S. Hirokura, E. Kako, K. Kawahata, Y. Kawasumi, K. Masai, K. Matsuoka, M. Mugishima, N. Noda, M. Sasao, K.N. Sato, S. Tanahashi, Y. Taniguchi, K. Toi

Institute of Plasma Physics, Nagoya University, Nagoya 464, Japan.

Introduction

This paper deals with the experimental study of current generation by interaction of fast magnetosonic (FMS) waves with slide-away electrons in an ohmic discharge. The current drive experiments have been studied for hydrogen plasmas in the JIPP T-IIU tokamak (R=93 cm, a=25 cm and B_t=26 kG) by using a four-element dipole antenna with a double Faraday shield fed by RF at f_0=800 MHz. It is found that the plasma current of $\sim$ 50 kA is maintained by RF power of $\sim$ 80 kW in the low density region of $\simeq 3\times 10^{12}$ cm^{-3} and that a density limit for FMS current drive is observed contrary to theoretical expectations based on linear wave propagation.

Launcher and Power Spectrum

As shown in Fig. 1, the four-element dipole antenna system consists of four sets of dipole antennas with 2.0 cm in width and 19.6 cm in length and separated by a distance of 3.6 cm. The electrostatic field along the toroidal direction which is produced by the phase difference $\Delta\varphi$ between adjacent antennas is eliminated by the double Faraday shield. This shield also prevents electrons from directly approaching each dipole antenna. Before the fast wave launcher was installed in the tokamak, E_x, E_y and E_z components were measured. These measurements show that the E_z component is negligible, while the E_y component along the y-drection has a sinusoidal amplitude distribution. Thus, the radiating field pattern shows that the antenna system can only excite the fast wave.

The power spectrum calculated by using the surface admittance of fast waves[1] shows that the ranges of $N_\parallel$ launched for $\Delta\varphi$= 0° and 180° are $|N_\parallel|$ = 1-2 and 3-6, respectively. The minimum $N_\parallel$ of FMS-waves which can propagate to the plasma center with $n_{e0} = 4\times 10^{12}$ cm^{-3} determines the lower bound of accessible $N_\parallel$ ($N_{\parallel acc} = 1.2$). Ignoring toroidal effects, we can obtain the maximum $N_\parallel$ given by the attenuation in the evanescent region extending from the launcher ($x = 0$) to the cutoff ($x = x_c$). By using $|k_\perp(0)|\, x_c = 1$ and $\omega_{pe}^2(x_c) = \omega_0\omega_{ce}(N_\parallel^2-1)$ and assuming the edge density profile as a step plus a ramp model, $n_e(x)=n_e(0)+x(\nabla n_e)_0$, where $|k_\perp(0)| = (N_\parallel^2-1)^{1/2}\omega_0/c$, we obtain the upper bound of accessible $N_\parallel$: $N_{\parallel cut}^2 \simeq 1+(c(\nabla n_e)_0/(\omega_{ce}n_{co}))^{2/3}+(2/3)(\omega_0 n_e(0))/(\omega_{ce}n_{co})$, where n_{co} is the cutoff density defined by $\omega_{pe} = \omega_0$. In our experiments the third term including the effect of the density step can be neglected. The value of $N_{\parallel cut}$ is about 1.4 by substituting $(\nabla n_e)_0 \simeq 1.1\times 10^{11}$ cm^{-4} which is measured by three sets of double probes. Thus, the accessible $N_\parallel$ window to the plasma ($N_{\parallel acc} < N_\parallel < N_{\parallel cut}$) is rather narrow. Although toroidal effects cause an $N_\parallel$-upshift of the waves penetrating into the plasma, fast waves with $N_\parallel$ larger than 2.6 are cut off even at the plasma center.

Experimental Results

The power reflection characteristics of individual dipoles and global reflection from the launcher are investigated. Reflections in vacuum and for plasma loaded dipoles ($\bar{n}_e = 3\times 10^{12}$ cm^{-3}) show almost the same behaviour as a function of $\Delta\varphi$. The typical global reflections $|R|^2$ at $\Delta\varphi=0°$ are measured as functions of $\bar{n}_e$ and launcher position r_l. The density gradient $(\nabla n_e)_0$ increases for high $\bar{n}_e$ and for small r_l. Therefore, it is inferred that $|R|^2$ decreases with increasing $\bar{n}_e$ and by reducing r_l because the accessible $N_\parallel$ window expands due to the decrease in evanescent length.

The time evolution of plasma parameters for a typical discharge is plotted in Fig. 2 (a)-(h). When 80 kW of net RF power P_{RF} is applied with $\Delta\varphi = 0°$, a plasma current I_p of about 50 kA is sustained with a negative loop voltage V_L at constant line-averaged density $\bar{n}_e = 3\times 10^{12}$ cm^{-3}. Microwave emission near the second electron cyclotron harmonic I_{ece} at the frequency of ~ 150 GHz and X-ray counts N_x integrated over the energy range of 10 - 300 keV with a Ge detector are strongly enhanced. The measured X-ray spectrum shows an exponentially decreasing tail with $T_{etail} \simeq$ 90 keV and extends out to around 300 keV which corresponds roughly to $N_{\parallel acc}$ =1.2. It should be noted that even in the absence of RF, a small amount of slide-away tail with $T_{etail} \simeq$ 30 keV is observed in the plasma. Because both the central electron temperature T_{e0} measured by the Thomson scattering, and the peripheral electron temperature T_{ep} deduced from the intensity ratio of OV(2s-3p) line to OV(2s-2p) line decrease during the RF pulse, the RF-induced changes in I_p and V_L do not result from bulk electron heating. The negative V_L ($\simeq$ -0.2 V) with $dI_p/dt \simeq 0$ eliminates the possibility that the sustainment of plasma current can be attributed to an enhanced conductivity owing to a modification of the electron tail distribution. Therefore, it is concluded that the plasma current carried by tail electrons is caused by FMS current drive. The efficiency of current drive by FMS-waves η ($=I_p \bar{n}_e R/P_{RF}$) is 1.7×10^{-2} (10^{20} kAm^{-2} kW^{-1}) which is as high as that of slow waves in our tokamak.

The electron density was varied in order to examine whether current drive by FMS-waves can be realized in the high density region as expected from linear theory. As shown in Fig. 3, the result fails to meet expectations. The changes in V_L and I_{ece} due to current drive disappear around $\bar{n}_e \simeq 8\times 10^{12}$ cm^{-3} which is almost the same value as the density limit $\bar{n}_{elim}$ in slow wave current drive[2,3]. With a perpendicular charge exchange analyser fast ions are observed during RF as shown in Figs. 3(c), 3(d) and 4. The energy spectra of charge exchange neutrals show the existence of a tail component and an increase in $T_{i\perp}$ when $\bar{n}_e > 6\times 10^{12}$ cm^{-3}. From the time evolution of $T_{i\perp}$ which increases quickly after RF switch-on, the fast ions are not created at the plasma center but near the periphery through the after-mentioned parametric decay processes. From the view point of linear theory FMS-waves with small $N_\perp$ can not interact directly with ions. To confirm the correlation of parametric decays into ion cyclotron and ion quasi-modes[4] with the ion tail formation, RF spectra including intensities I_{pump} and I_{lsb} of the pump and lower sideband near the frequency ($f_0 - f_{ci}$), respectively, are monitored with an electrostatic RF probe at the scrape-off region. With increasing $\bar{n}_e$ the spectrum of received high frequency signals changes from a monochromatic pump to a spectrum with pump broadening accompanied by a weak lower sideband at 770 MHz (Fig.2 (e) and (f)). If the frequency separation between the pump and the lower sideband is attributed to the local ion cyclotron frequency, the position where ion cyclotron parametric decay processes occur would be the outer periphery of the plasma column.

It is concluded that the occurrence of parametric decay correlates with ion tail formation and results in depositing a part of the RF power at the peripheral region.

Recently, the threshold of the ion cyclotron parametric decay instability directly-excited by a fast wave was studied theoretically[5], and it was shown that for the fast wave pump larger RF powers or higher electron densities are necessary than that for the slow wave pump. The slow surface wave ($N_{\parallel} < N_{\parallel acc}$) created by confluence with the fast wave, or the slow wave ($N_{\parallel} > N_{\parallel acc}$) converted by density fluctuations[6] propagate towards the wall. Because the bouncing back and forth of waves in the peripheral region increases the wave energy density, we can expect the excitation of parametric decay and an increase in the half maximum $\Delta f_{1/2}$ of the pump. It is inferred that the observed ion cyclotron parametric decay results from these surface waves or from the slow waves which are mode-converted by density fluctuations. The fact that $\Delta f_{1/2}$ in the density range above $\bar{n}_{elim}$ is 1-1.5 MHz which is much wider than the drift wave frequency spread, implies that the injected wave suffers from repeated scattering or that parametric decay into ion-sound quasi-mode occurs[4]. A high resolution measurement of the spectrum shows that the peak frequency with symmetric spectrum is not downshifted with respect to the pump frequency. Therefore, it becomes evident that the pump broadening is caused by scattering at low frequency density fluctuations. Thus it can be concluded that the disappearance of the preformed slide-away tail and the power flow to the ion tail must be responsible for the density limit.

Relative changes in V_L, I_{ece}, N_x, electron temperature, and I_{pump} during RF were measured as functions of $\Delta\varphi$. It is noted that no distinct effect of the directivity of wave propagation on the plasma parameters is observed. At present, we cannot understand the reason why the wave directivity does not clearly affect the current drive efficiency.

If, in view of the present result, we wish to extend the region of current drive to higher densities, the problems of the spectral gap, the density limit, and the frequency scaling of FMS current drive should be studied further. But the prospects for fast wave current drive in high temperature plasma have been greatly enhanced by the success of FMS current drive by interaction with the slide-away electrons.

The authors would like to express their thanks to Drs. S. Kitagawa, T. Watari, K. Yamazaki and D. Eckhartt for their discussions.

References

[1] K. Theilhaber, A. Bers, Nucl. Fusion 20, 547 (1980).
[2] K. Ohkubo *et al.*, Nucl. Fusion 22, 1085 (1982).
[3] J-G. Wegrowe, F. Engelmann, Comments Plasma Phys. Controlled Fusion 8, 211 (1984).
[4] Y. Takase *et al.*, Phys. Fluids 28, 983 (1985).
[5] V.K. Tripathi, Phys. Fluids 27, 2869 (1984).
[6] P.L. Andrews *et al.*, Phys. Fluids 28, 1154 (1985).

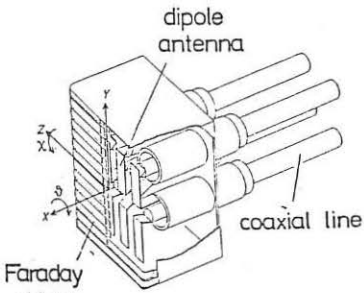

Fig. 1 : Four-element dipole antenna array

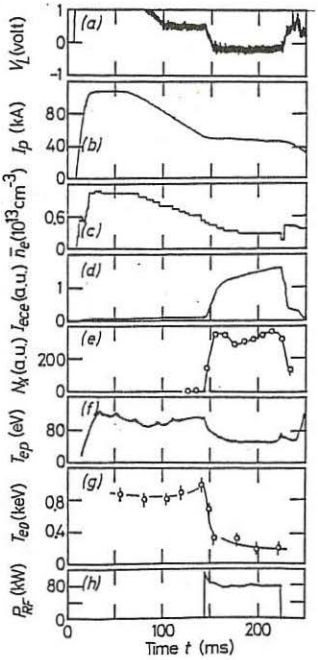

Fig. 2 : Time evolution of (a) loop voltage; (b) plasma current; (c) line-averaged electron density; (d) microwave emission near the second electron cyclotron harmonic; (e) integrated counts of X-rays (10 - 300 keV); (f) peripheral electron temperature deduced from the ratio of the *OV* lines; (g) central electron temperature; (h) RF net power.

Fig. 3 : Density dependence of (a) relative change of loop voltage ; (b) microwave emission near second electron cyclotron harmonic; (c)total energy and (d) temperature of tail ions measured by the perpendicular charge exchange analyzer; (e) amplitudes of the pump and its lower sideband near the frequency ($f_0 - f_{ci}$); (f) full width at the half maximum of the pump. Here, $I_p \simeq$ 60 kA, $P_{RF} \simeq$ 95 kW, $\Delta\varphi = 0°$ and B_t =26.4 KG.

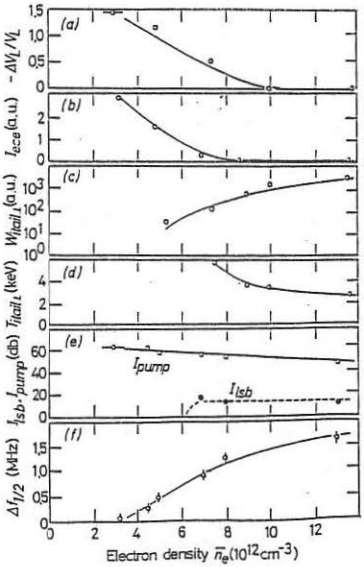

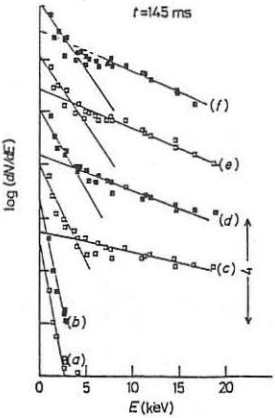

Fig. 4 : Perpendicular charge exchange spectra for various $\bar{n}_e$ of (a) 3×10^{12} cm^{-3}, (b) 5×10^{12} cm^{-3}, (c) 7×10^{12} cm^{-3}, (d) 8×10^{12} cm^{-3}, (e) 1.1×10^{13} cm^{-3} and (f) 1.4×10^{13} cm^{-3}. The curves for different $\bar{n}_e$'s are displaced for display purposes.

STABILISATION OF SAWTOOTH OSCILLATIONS BY LOWER HYBRID WAVES IN ASDEX

F. X. Söldner, D. Eckhartt, F. Leuterer, K. McCormick, G. Becker,
H. S. Bosch, H. Brocken, H. Derfler, A. Eberhagen, G. Fussmann,
O. Gehre, J. Gernhardt, G.v.Gierke, E. Glock, O. Gruber, G. Haas,
J. Hofmann, A. Izvozchikov[1], G. Janeschitz, F. Karger, M. Keilhacker[2],
O. Klüber, M. Kornherr, K. Lackner, M. Lenoci, G. Lisitano, F. Mast,
H. M. Mayer, D. Meisel, V. Mertens, E. R. Müller[2], M. Münich, H. Murmann,
H. Niedermeyer, A. Pietrzyk[3], W. Poschenrieder, H. Rapp, H. Riedler,
H. Röhr, J. Roth, F. Ryter[4], F. Schneider, C. Setzensack, G. Siller,
P. Smeulders[2], E. Speth, K.-H. Steuer, T. Vien, O. Vollmer, F. Wagner,
D. Zasche, M. Zouhar

Max-Planck-Institut für Plasmaphysik
EURATOM Association, D-8046 Garching

Introduction:

Stabilisation of sawteeth has become a clue problem for high power additional heating in large tokamaks where the oscillations in the central electron temperature may be as high as 50 % /1/. In Lower Hybrid experiments the sawteeth of Ohmic discharges have been observed to disappear /2/, /3/. In this paper we study the parameter range for stabilisation of sawteeth accessible with the LH-system on ASDEX /4/, /5/. The role of the LH wave spectrum is discussed. For application to NBI heating the LH-power requirements and the benefits for the energy confinement in sawtooth-free discharges are investigated.

Stabilisation of sawteeth in OH-discharges

The sawtooth period τ_{st} rises upon injection of LH waves in a density range where the waves couple to suprathermal electrons ($\bar{n}_e \lesssim 3 \times 10^{13} cm^{-3}$). In the case of LH-current drive τ_{st} continues to change during the rf pulse. The values for the first sawtooth after start of the LH and for the saturated state are shown in Fig. 1 for a power scan at $\bar{n}_e = 1.6 \times 10^{13}$ cm^{-3}. At low power the sawtooth period rises continuously until the end of the rf. For $P_{LH} > 400$ kW τ_{st} first increases and then decreases, at high rf power even below the Ohmic value. Above a threshold P_{LH}^* the sawteeth finally disappear. The time delay τ_d between start of the LH and the last sawtooth collapse depends strongly on the density and it decreases with increasing rf power as shown in Fig. 2. The threshold P_{LH}^* there is marked by dashed lines. Stabilisation of sawteeth is possible only by applying LH-current drive spectra. With symmetric spectra in the LH-heating mode the sawtooth period may be changed but sawteeth remain present during the whole LH pulse ($\tau \leq 1.5$ s) even at rf powers more than a factor of 2 above the threshold P_{LH}^* with LH-current drive.

The mechanism for sawtooth stabilisation might therefore be seeked in the change of the current profile j(r) connected with LH current drive. The internal inductance l_i may be derived from magnetic measurements with some precautions. From the quantities $\beta_p^{equ} + l_i/2$ (derived from the equilibrium fields) and β_p^i (from diamagnetic measurements) l_i can only be determined if

---

[1]Academy of Sciences, Leningrad, USSR; [2]Present address: JET Joint Undertaking, England; [3]Univ. of Washington, Seattle USA; [5]CEN Grenoble, France

the pressure is isotropic. During heating and current drive with LH waves of high phase velocity ($\bar{v}_{ph,\parallel} = c/2$), however, the pressure may become highly anisotropic due to the generation of fast electrons parallel to the magnetic field /7/. Therefore direct measurements of j(r) were made for various modes of LH operation in ASDEX /8/, /9/. In the case of the LH power scan at $\bar{n}_e = 1.6 \times 10^{13}$ cm^{-3} (Figs. 1,2) the pressure anisotropy remains small and the stationary value of $(\beta_p^{equ} + l_i/2) - \beta_p^{\prime}$ then gives l_i. At low rf power l_i increases while it drops during LH current drive with $P_{LH} > 400$ kW as seen from Fig. 3. Consequently, the current profile is peaking during low power LH-current drive and the higher increase of the sawtooth period τ_{st} in Fig. 1 might then be explained by an expansion of the sawtooth-unstable region within r(q=1). The drop in l_i at higher power indicates a flattening of j(r) and the reduction in τ_{st} could be explained in like manner by a shrinking of the q=1-surface. With $P_{LH} > P_{LH}^*$ j(r) flattens to such an extent that the q=1 surface disappears and $q > 1$ in the entire plasma region /9/. Stabilisation of the sawteeth is therefore achieved if j(r) is modified such that the instability condition (q=1 at some radius) is removed. On ASDEX, so far, this is the only method how sawteeth could be suppressed by means of LH waves.

In the parameter range where sawteeth were stabilized about half of the rf power necessary for complete LH-current drive was required. For discharges with q(a) = 3.5 this can be seen from Fig. 4 where the relative reduction in Ohmic input $-\Delta P_{OH}^*/P_{OH}$ due to LH current drive at the stability margin with $P_{LH} = P_{LH}^*$ is plotted versus $\bar{n}_e$ together with the absorbable fraction $P_{LH,acc}^*$ of the rf power launched in these cases. Because of the uncertainty in the deposition profile two cases have been considered for accessibility to a/3 and 2a/3 /7/.

Stabilisation of sawteeth during NBI:

The sawtooth period τ_{st} during NBI increases with increasing beam power P_{NI} (Fig. 5) and above a certain threshold in P_{NI} which augments with $\bar{n}_e$ no sawteeth are observed during NBI. In sawtoothing discharges with NBI τ_{st} rises upon injection of LH power both in heating and current drive mode. Suppression of sawteeth is possible with LH current drive only. The mechanism of stabilisation is again related to a flattening of the current profile j(r) as indicated by a decrease of l_i. The drop in l_i does not depend on P_{NI} but only on P_{LH} and on the wave spectrum. The minimum rf power required for stabilisation P_{LH}^* is reduced for higher P_{NI} as seen from Fig. 5.

This suggests that the current profile is flattened in the central plasma region already by NBI alone and less LH-power is therefore required for higher P_{NI} to remove the q=1 surface from the plasma.

With counter-NBI the threshold power P_{LH}^* is even further reduced as seen in Fig. 5. Also with NBI alone sawteeth disappear already at lower power in this case. This seems to be mainly due to the broad $T_e(r)$ profiles which are observed with counter-NBI. The shorter sawtooth period (Fig. 5) might be also explained by this fact. A contribution from a counter-driven beam current reducing the net plasma current in the center and thereby flattening j(r) as proposed in a scenario for sawtooth suppression /10/ cannot be ruled out.

In sawtooth-free discharges with NBI higher central electron temperatures can be obtained. The $T_e(r)$ profiles are plotted in Fig. 6 for the Ohmic phase, NBI alone and for NBI combined with LH current drive. With $P_{LH} = 540$

kW which is below P_{LH}^* the $T_e(r)$ profiles still resemble the profiles with NBI alone. The additional LH power replaces mainly the drop in P_{OH} in this case. With $P_{LH} > P_{LH}^*$ (P_{LH} = 720 kW) sawteeth are suppressed and the central temperatures increase. The resulting increase in total energy content is small because of the small volume where sawteeth dominate the power loss. With lower q(a) the sawtooth-unstable region is larger and a larger gain for global plasma heating can be obtained. At q(a) = 2.75 (I_p = 380 kA, B_t = 2.2 T) sawtooth suppression with P_{LH} = 550 kW resulted in a 30 % increase of the total plasma energy content from NBI with P_{NI} = 1.8 MW. Improvement of the central confinement by stabilisation of the sawteeth therefore contributes also to an appreciable improvement of the global confinement.

References

/1/ J. Jacquinot, et al., Plasma Physics and Controlled Fus. 28, 1 (1986).
/2/ J.E. Stevens, R. Bell, S. Bernabei, et al., 12th Europ. Conf. on Contr. Fusion and Plasma Physics, Budapest, 1985, Vol. II, p. 192.
/3/ F. Parlange, et al., in Ref. /2/, Vol. II, p. 172.
/4/ D. Eckhartt, et al., 4th Int. Symposium on Heating in Toroidal Plasmas, Rome, 1984, Vol. I, p. 501.
/5/ F. Leuterer, F. Söldner, D. Eckhartt, et al., Plasma Physics and Controlled Fusion 27, 1399 (1985).
/6/ F. Leuterer, D. Eckhartt, F. Söldner, et al., in Ref. /2/, Vol. II, p. 240.
/7/ F. Söldner, D. Eckhartt, F. Leuterer, et al., in Ref. /2/, Vol. II, p. 244.
/8/ K. McCormick, et al., in Ref. /2/, Vol. I, p. 199.
/9/ K. McCormick, et al., this conference.
/10/ J. Jacquinot, private communication.

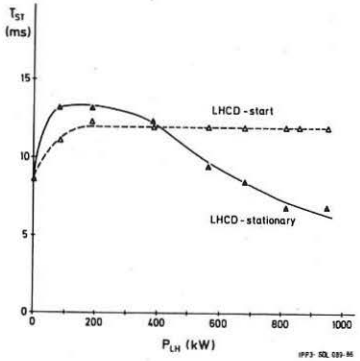

Fig. 1: Sawtooth period τ_{st} during LH-current drive versus LH-power.

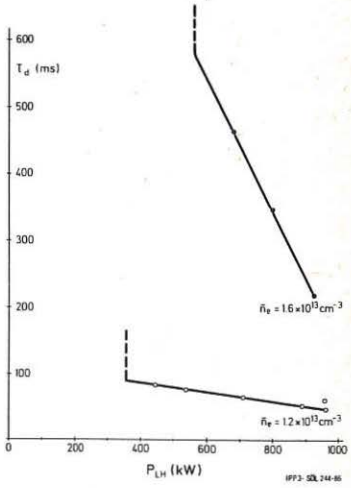

Fig. 2: Time delay τ_d for sawtooth suppression after start of LH versus LH-power.

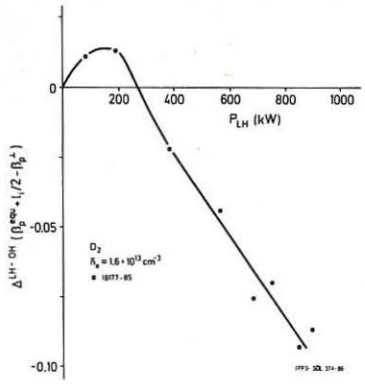

Fig. 3: Variation of the quantity $(\beta_p^{equ} + l_i/2) - \beta_p^r$ with P_{LH} during LH-current drive.

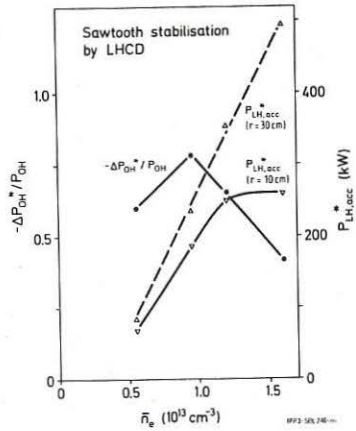

Fig. 4: Drop in ohmic power $-\Delta P_{OH}^*/P_{OH}$ and accessible fraction of LH-power $P_{LH,acc}^*$ at the margin for sawtooth stabilization $P_{LH} = P_{LH}^*$ as function of $\bar{n}_e$.

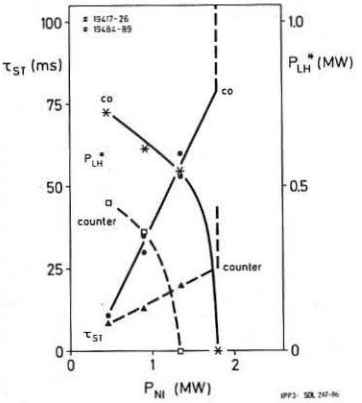

Fig. 5: Sawtooth period τ_{st} for NBI and threshold power P_{LH}^* for sawtooth stabilization by LH during NBI for co- and counter-injection as function of P_{NI}.

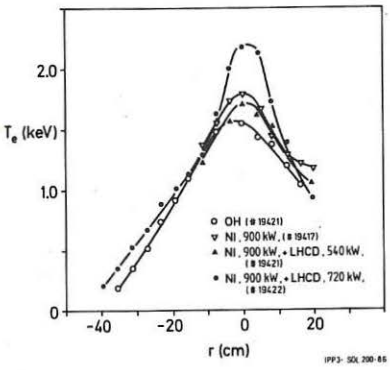

Fig. 6: $T_e(r)$ profiles during OH- and NBI-heating and for the sawtooth-free phase of NBI + LHCD (P_{LH} = 720 kW).

INFLUENCE OF THE LOWER HYBRID WAVE SPECTRUM ON THE CURRENT DISTRIBUTION IN ASDEX

K. McCormick, F.X. Söldner, F. Leuterer, H. Murmann, D. Eckhartt, G. Becker, H. S. Bosch, H. Brocken, A. Eberhagen, G. Fussmann, O. Gehre, J. Gernhardt, G.v.Gierke, E. Glock, O. Gruber, G. Haas, J. Hofmann, A. Izvozchikov[1], G. Janeschitz, F. Karger, M. Keilhacker[2], O. Klüber, M. Kornherr, K. Lackner, M. Lenoci, G. Lisitano, F. Mast, H. M. Mayer, D. Meisel, V. Mertens, E. R. Müller[2], H. Niedermeyer, A. Pietrzyk[3], W. Poschenrieder, H. Rapp, H. Röhr, J. Roth, F. Ryter[4], F. Schneider, C. Setzensack, G. Siller, P. Smeulders[2], K.-H. Steuer, F. Wagner, D. Zasche

Max-Planck-Institut für Plasmaphysik
EURATOM Association, D-8046 Garching

Abstract: Measurements of the plasma current density distribution j(r) during injection of stationary or propagating lower hybrid wave spectra have been performed on ASDEX. Positive current drive leads to broader j(r) profiles - while $T_e(r)$ is peaking - coupled with an increase in q from $q \lesssim 1$ to $q > 1$. The other spectra influence j(r) only to the extent predicted from classical conductivity based on changes in $T_e(r)$ under the condition $q(0) \sim 1$.

Introduction: It has been demonstrated on various experiments that lower hybrid current drive (LHCD) can be used to suppress sawtooth oscillations /1-4/ or influence m/n = 2/1 tearing modes /2-4/. Based on magnetic signals and the monitoring of MHD activity it has been conjectured that these effects have their origin in an LHCD-induced broadening of the j(r) profile /2-4/. In the same way, magnetic signals have been interpreted as inferring a strong peaking of j(r), attained by appropriately adjusting the LH wave spectrum /4/. These points have been investigated on ASDEX by direct measurements of j(r) for a variety of LH spectra.

Experiment: ASDEX was operated in the divertor configuration with parameters: $\bar{n}_e = 1.2 \times 10^{13}$ cm^{-3} ($0\,\pi\,0\pi$: 8×10^{12} cm^{-3}), $I_p = 292 - 301$ kA, $B_T = 21.5$ kG, a ~ 39.4 cm and R ~ 167 cm. Approximately 560 kW ($0\,\pi\,0\,\pi$: 340 kW) of rf power was launched into the plasma via an 8-waveguide grill with a phase difference $\Delta\phi$ between the waveguides such that a spectrum with $\bar{N}_{\parallel} \sim 2$ ($0\,\pi\,0\,\pi$: $\bar{N}_{\parallel} \sim 4$) was generated symmetrically ($0\,0\,\pi\,\pi..$, $0\,\pi\,0\,\pi...$; LHH), parallel ($\Delta\phi = +\pi/2$, LHCD) or antiparallel ($\Delta\phi = -\pi/2$) to the plasma current /5/. Z_{eff} in the ohmic heating (OH) phase - deduced assuming neoclassical conductivity - and the OH/LH loop voltages V_L are given in Table I.

The resulting incremental changes in the diamagnetic beta signal $\Delta\beta_{p\perp}$ and $\Delta(\beta_p^{equ} + l_i/2)$ (measured by poloidal flux loops) are depicted in Fig. 2. It is seen that $\Delta\beta_{p\perp}$ increases to a plateau in ~100 - 150 ms. The behavior in $\Delta(\beta_p^{eq} + l_i/2)$ is different; the initial increase in this quantity, common to all cases, is followed by a slow decrease over ~300 ms to a plateau below the OH value for $+\pi/2$ and $0\,\pi\,0\pi$. We note that $\beta_{p\perp}$ is sensitive only to the perpendicular energy $W_\perp$ and β_p^{eq} to the entire energy $W=(W_\perp+W_\parallel)/2$, so that $D = \Delta(\beta_p^{eq} + l_i/2) - \Delta\beta_{p\perp} = \Delta(W_\parallel - W_\perp)/2 + \Delta l_i/2$. Hence, the discrepancies D

[1]Academy of Sciences, Leningrad, USSR; [2]Present address: JET Joint Undertaking, England; [3]Univ. of Washington, Seattle, USA; [4]CEN Grenoble, France

seen between $\Delta\beta_{p_\perp}$ and $\Delta(\beta_p^{eq} + l_i/2)$ in Fig. 2 can be ascribed to the production of a pressure anisotropy between the directions perpendicular and parallel to the magnetic field, and/or to a change in Δl_i, i.e. to a redistribution in j(r).

The effect on j(r) was determined directly by means of a neutral lithium beam probe which measures the magnetic field pitch angle $\theta_p = \tan^{-1}(B_p/B_T)$ at the intersection between the beam and optical axis of the detecting system (Fig. 1) /6-7/; j(r) can be calculated using $\theta_p(r)$ in conjunction with Maxwell's equations. $T_e(z)$ is registered along a vertical chord (not passing through the magnetic axis) by a 60 Hz pulsed Thomson scattering system (Fig. 1) /8/.

Results: The measured pitch angle profiles θ_p^c, adjusted to cylindrical geometry, for $+\pi/2$ are plotted vs. the flux-surface radius r_f in Fig. 2 (top, right) for the OH and steady-state LHCD phases along with the corresponding q(r) and j(r) profiles (top, left). It should be noted that the OH points are well documented with two points each at r_f = -1.7, +10.3, 14.3 and 29.2 cm. The indicated error bars on θ_p^c reflect the noise level associated with the base line of θ_p^c and of θ_p^c itself. For OH, the q=1 radius is in rough agreement with the ECE sawtooth inversion radius (hatched region) r_{st}. The application of LHCD leads to a broadening of the j(r) profile (from which $\Delta l_i \sim -0.12$ is computed) and an associated increase in q(0) from 0.98 + 0.03/-0.01 to ~ 1.14, in concord with previous results /7/. While T_e profiles are not available for this series, the experience is always that T_e peaks with LHCD in the fashion seen with 0 0 π π, thereby demonstrating that the LH-driven current is decoupled from the classical conductivity profile.

The (Fig. 3) θ_p^c and T_e profiles for $-\pi/2$ exhibit no significant change between the OH and LH phases, i.e. D is due solely to a large anisotropy in the non-thermal electron population in favor of the component parallel to the magnetic field. A comparison between the experimental θ_p^c points and the curves predicted from Spitzer or neoclassical (neo) conductivity (assuming Z_{eff} and the electric field E are constant) shows no consistent agreement with either case. (Fig. 3 - the curve spread reflects the T_e error bars.) However, neither model correctly predicts r_{st}: neo gives q(0) values far below the q(0) ~ 0.96 determined from the lithium beam, whereas Spitzer generally yields q ~ 1 only very near the axis. If a central zone of anomalous resistivity or a smaller E is postulated such that q ~ 1 is fulfilled, then neoclassical conductivity would describe the experimental points reasonably well in the q > 1 region. However, for fiducial purposes the Spitzer curves are used in comparison hereafter.

The failure of the experimental θ_p^c curves to cross the axis at r_f = 0 for both $-\pi/2$ and 0 0 π π (consecutive series) is probably due to a slight (~0.3°) beam misalignment. The systematic trend of the $r_f < 0$ θ_p^c points to increase for $-\pi/2$ is not understood, as a symmetric behavior for $r_f \sim 10$ cm is not observed.

The heating spectrum 0 0 π π produces a pronounced peaking in $T_e(r)$, but no distinct change in θ_p^c. In contrast to the OH phase, the Spitzer θ_p^{LH} profiles lie above the experimental θ_p^c points, demonstrating that j(r) has not tracked the $T_e(r)$ change - suggestive that a mechanism which always maintains q(0) ~ 1 is operative.

The 0 π 0 π T_e^{OH} profile is broader in the central region compared to 0 0 π π, leading to a narrower j(r) distribution (synonymous with higher θ_p^c values) as corroborated by the Li-beam measurements. LHH produces a decrease in T_e ($r \leq a/2$), which j(r) follows up to $\Delta t_{LH} \sim 300 - 400$ ms as confirmed by θ_p^c from experiment (Fig. 3). Hence j(r) has been altered by affecting the bulk thermal electron population, changing $q^{OH}(0)$ from ~0.97 to $q^{LH}(0) \sim 1.06$ and l_i^{OH} from 1.35 to $l_i^{LH} \sim 1.15$. The behavior after $\Delta t_{LH} \sim 400$ ms cannot be considered here.

Discussion: Table I summarizes the experimentally determined changes in q(0) and l_i, from which we see that $q^{OH}(0) = 0.96 - 0.98$. This implies that only a few per cent of the current inside the q = 1 surface needs be displaced outwards in order to achieve q > 1 and an associated suppression of sawteeth. Such a small change can take place inside one sawtooth period, which is congruous with the observed invariance of r_{st} up to the moment of sawtooth disappearance described elsewhere /1/.

Taking the experimental Δl_i it is possible to compute $\Delta\beta_p^{eq}$ for all cases, the values of which are indicated on Fig. 2 by arrows. Accordingly, +π/2 produces a nearly isotropic pressure (i.e. $\Delta\beta_p^{eq} \gtrsim \Delta\beta_{p_\perp}$), whereas -π/2 exhibits an extreme anisotropy and 0 0 π π lies in between. These deduced trends are consistent with direct measurements of the non-thermal electron population on ASDEX /9/.

In passing it should be mentioned that the profiles discussed here are interesting candidates for a "profile consistency" analysis /10/ inasmuch as $T_e(r)$ and j(r) are loosely coupled for 0 0 π π and decoupled for π/2, but both yield approximately the same T_e profile. Further, for 0 π 0 π, LHH produces a large, coupled change in $T_e(r)$ and j(r).

Finally, the Li-beam measurements reported here support the thesis /11/ that sawtooth stabilization on ASDEX occurs only when the condition q > 1 prevails in the central region.

References:

/1/ J.E. Stevens, et al., 12th Eur. Conf. on Contr. Fusion and Plasma Physics 2, 192 (Budapest, 1985).
/2/ F. Parlange, et al., Ref. /1/, 2, 172.
/3/ D. van Houtte, et al., Nucl. Fusion Lett. 24, 1485 (1984).
/4/ D. van Houtte, et al., Course/Workshop on "Tokamak Startup-Problems and Scenarios related to the transient phases of ignited tokamak operations" (Erice, 1985).
/5/ F. Leuterer, F. X. Söldner, et al., Plas. Phys. 27, 1399 (1985).
/6/ K. McCormick, M. Kick, et al., 8th Eur. Conf. on Contr. Fusion and Plasma Physics, 140 (Prague, 1977).
/7/ K. McCormick, et al., Ref. /1/, 1, 199.
/8/ D. Meisel, H. Murmann, H. Röhr, K.-H. Steuer, this conference.
/9/ R. Bartiromo, M. Hesse, et al., this conference.
/10/ B. Coppi, Comments Plas. Phys. Contr. Fusion 5, 201 (1980).
/11/ F. X. Söldner, et al., this conference.

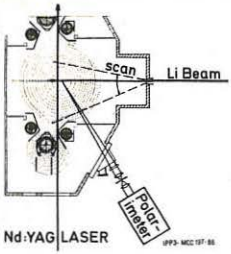

Fig.1 Diagnostic Layout

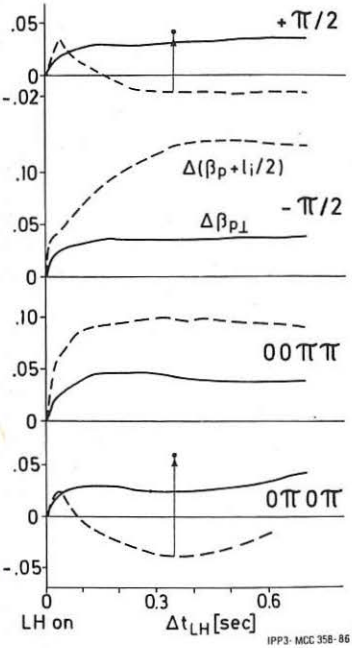

Fig.2: The incremental change in $\beta_{p\perp}$(-) and $\beta_p + l_i/2$(--) arising from LH. The arrows and points indicate the Li-beam derived values for $-\Delta l_i/2$ and $\Delta\beta_p^{eq}$, respectively. OH values: $\beta_{p\perp} \sim 0.2$, $(\beta_p + l_i/2) \sim 0.9$.

Table I: Experimental Results

	Z_{eff}^{neo}	$V_L^{OH}:V_L^{LH}$	$q^{OH}(0)$	$q^{LH}(0)$	Δl_i
π/2	?	0.9:0.3	0.98	1.14	-0.12
-π/2	2.4	0.9:0.62	0.96	0.99	0
00ππ	"	0.9:0.57	"	0.96	0
0π0π	4.0	1.0:0.54	0.97	1.06(?)	-0.2

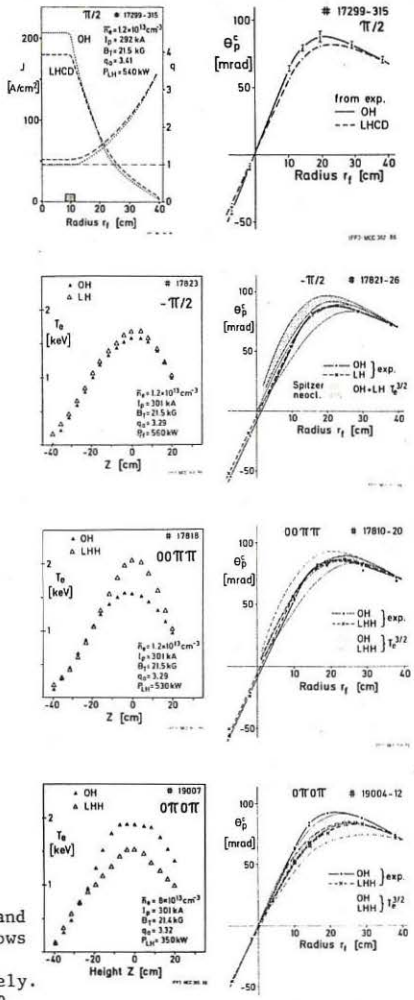

Fig.3: j(r) and q(r) profiles (top, left) derived from the experimental pitch angle curves (top, right) for OH and LHCD. Successively, the T_e and experimental θ_p^c profiles (on the left and right, respectively) for the OH and LH discharge phases are shown for opposite current drive -π/2, and the heating spectra, 00ππ, 0π0π.

SAWTOOTH BEHAVIOUR IN LOWER HYBRID HEATED FT DISCHARGES

F. Alladio, R. Bartiromo, F. De Marco, G. Mazzitelli, A.A Tuccillo, G. Vlad

Associazione EURATOM-ENEA sulla Fusione, Centro Ricerche Energia Frascati,
C.P. 65 - 00044 Frascati, Rome (Italy)

INTRODUCTION

Sawtooth oscillations in Tokamak plasmas are considered responsible for lowering the maximum attainable central electron temperature. In the last year all the major LH experiments have succeeded in stabilizing sawteeth [1] even in presence of additional heating [2]. In the FT case, the available power was not sufficient to fully stabilize sawteeth for lack of access. In the range of power used ($P_{RF} \leq 3/4\ P_{OH}$) an increase of sawtooth period, reaching about a factor 4 at maximum coupled power, is observed on soft x ray signals. In this paper we report about the dependence of this increase on the launched spectra and on the related changes in plasma properties, namely: electrical resistivity and electron thermal conductivity. The experimental sawtooth behaviour is then interpreted with a code solving the coupled non-linear diffusion equations for the perturbed electron temperature and magnetic field.

EXPERIMENTAL RESULTS

Two launchers are installed on FT at 90° and 180° away from the poloidal limiter in the current direction having a 2×2 and 4×2 wave-guide array respectively. All the results presented here are obtained at B_T = 60 kG, $I_p \sim 300$ kA, $\bar{n}_e = 3 \div 4 \times 10^{13}$ cm^{-3}. This corresponds to the electron interaction regime, the density limit being about $\bar{n}_e = 5 \times 10^{13}$ cm^{-3} for the used frequency of 2.45 GHz. The launched spectra are shown in Fig. 1. Generally the 2×2 grill is phased at π launching a symmetric spectrum with most of the power below $n_{//}=3$ (Fig. 1a). This spectrum is practically identical to the spectrum of the 4×2 grill phased $0,0,\pi,\pi$. Figure 1b shows the 4×2 grill spectrum when phased $0,\pi/3,2\pi/3,\pi$. This asymmetric spectrum travels in the electron drift direction. Both spectra are able to increase the sawtooth period as shown in Fig. 2, but the asymmetric one is the most effective. The sawtooth period reaches roughly the same value but with lower coupled power for the asymmetric spectrum. A different behaviour is also observed at the RF switch-on. Also in this case there is a greater increase for the asymmetric spectrum. Figure 2 shows both the sawtooth repetion time and the time delay between the sawtooth crash and the detection of the heat pulse at half radius. This quantity too shows a step at the RF switch-on and then a slower increase (this time more pronounced with the symmetric spectrum). Figure 3 summarizes the power dependence of sawtooth repetition time after 100 ms of RF power (data from symmetric spectra are plotted with half the coupled power). From this figure it is confirmed that asymmetric spectra are by far the most effective. This effect can be ascribed to the greater effectiveness of the asymmetric spectrum in driving current via fast electron generation thus

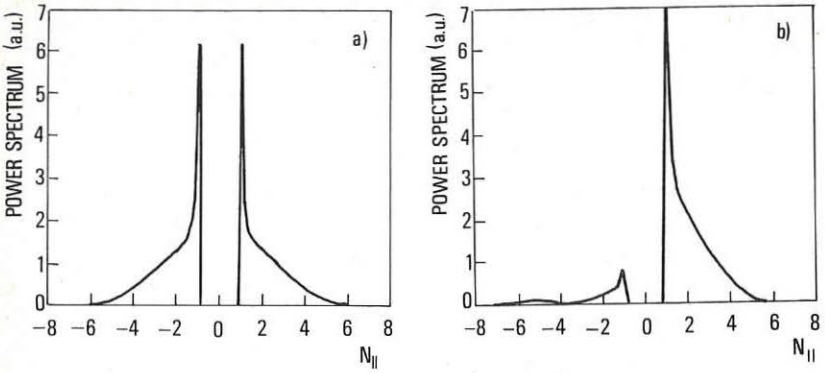

Fig. 1 - Power spectrum a) $\phi = 0, 0, \pi, \pi$ (as grill 2 × 2 with $\phi = 0, \pi$); b) $\phi = 0, \pi/3, 2\pi/3, \pi$

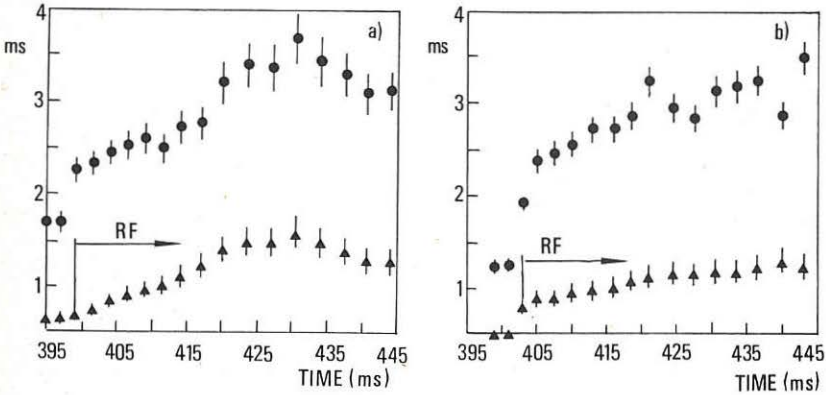

Fig. 2 - Time behaviour of sawtooth repetition time (dots) and time delay (triangles) of sawtooth heat pulse at half radius: a) $\phi = 0, 0, \pi, \pi$; b) $\phi = 0, \pi/3, 2\pi/3, \pi$

lowering central electrical resistivity. Up to the maximum power launched the position of the surface q=1, as detected by space resolved soft x-ray, is not observed to change. Figure 4 shows the time delay at half radius of the sawtooth crash propagation normalized with density vs the corresponding sawtooth period for two series of reproducible shots. It can be seen that the delay with the asymmetric spectrum saturates at a lower level despite the increase in the period. The two discharges are very similar in the ohmic phase and the major difference during RF is due to the larger increase of the electron temperature with the symmetric spectrum [3] ($\Delta T_{eo} \sim 700$ eV, $P_{RF} \sim 280$ kW). In the other case only $\Delta T_{eo} \sim 200$ eV is measured with $P_{RF} \sim$ ~ 180 kW, thus suggesting a favourable dependence of electron thermal con-

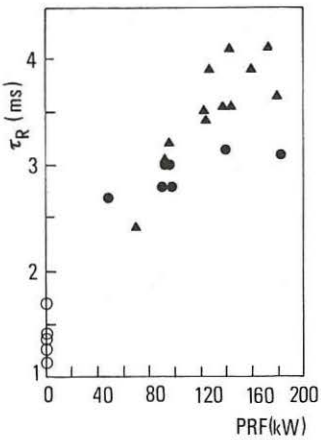

Fig. 3 - Sawtooth repetition time vs coupled RF power (dots $\phi = 0,0,\pi,\pi$, at half the coupled power; triangles $\phi = 0,\pi/3,2\pi/3,\pi$)

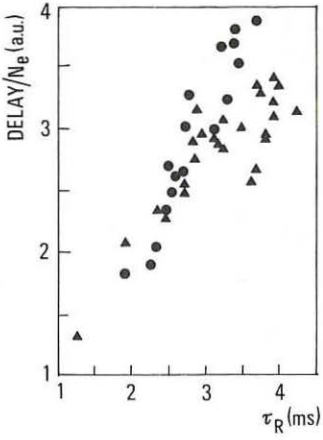

Fig. 4 - Time delay at half radius of sawtooth heat pulse normalized with density vs sawtooth repetition time (dots $\phi = 0,0,\pi,\pi$; triangles $\phi = 0,\pi/3,2\pi/3,\pi$)

ductivity on T_e at least in this power range. For the discharges with symmetric spectra where a complete power balance has been performed, data on the confinement obtained from the heat pulse propagation are roughly in agreement with the power balance results [4].

In order to model the experimental behaviour of sawteeth we have developed a code solving the system of coupled non-linear diffusion equations for the perturbed quantities $\tilde{T}_e$ and $\tilde{B}_\theta$, enabling us to obtain sawtooth characteristics for a given discharge. Details of this calculation are reported in Ref. [5]. Using the electron thermal conductivity obtained from the power balance and the measured value of the electrical conductivity, we obtain the experimental repetition time and the time delay of the sawtooth heat pulse in the ohmic phase. To model the RF phase we simply multiply the two quantities by a factor constant over the radius. Figure 5 shows such a simulation compared with the experimental values about 10 ms after the start of the RF pulse ($P_{RF} \sim 280$ kW) with symmetric spectrum. As it can be seen the repetition time can be modeled by reducing the electrical resitivity by about 70%, well in agreement with the total plasma conductance measurement, while the time delay requires a reduction of the electron thermal conductivity similar to the one necessary in the energy balance analysis.

CONCLUSION

The increase of sawtooth repetition time is in agreement with an increase of electrical conductivity. This effect is more important when waves traveling in the electron drift direction are injected into the plasma with respect to the case when a symmetric spectrum is utilized. The increase of the time delay for the propagation of the heat pulse has to be ascribed to a

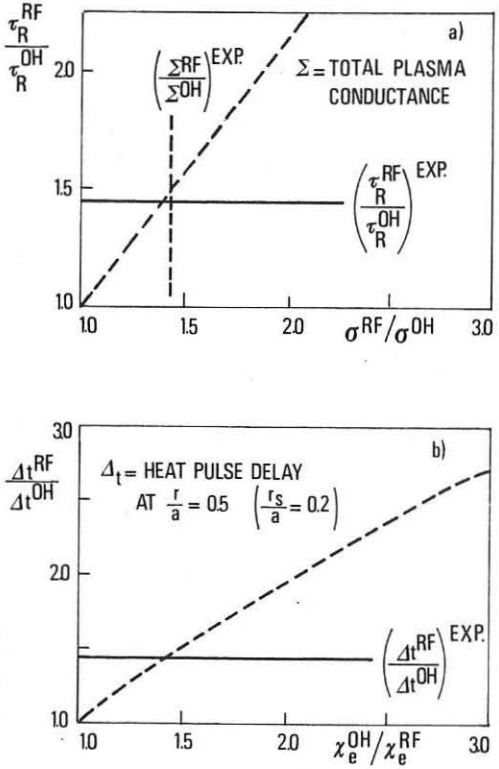

Fig. 5 - Simulation of sawtooth repetition time vs electrical conductivity a) and of heat pulse time delay at half radius vs electron thermal conductivity b)

reduction of the electron thermal conductivity. These results are in good agreement with a model of the sawtooth dynamics and with the energy balance results.

REFERENCES

[1] J.E. Stevens, R. Bell, S. Bernabei et al., 12th Eur. Conf. on Contr. Fusion and Plasma Phys., Budapest 1985, II, 192 (1985)
[2] F. Söldner and ASDEX Group, this Conference
[3] F. Alladio, E. Barbato, G. Bardotti et al., Plasma Phys. and Controlled Fusion, 28, 1A, 179 (1986)
[4] L. Pieroni and FT Group, Invited Paper this Conference
[5] F. Alladio, G. Mazzitelli, A.A. Tuccillo, G. Vlad, 12th Eur. Conf. on Contr. Fusion and Plasma Phys., Budapest 1985, I, 138 (1985)

SUPPRESSION OF SAWTOOTH OSCILLATIONS BY LOWER HYBRID CURRENT DRIVE IN THE PETULA-B TOKAMAK

D. van Houtte, C. Agarici, H. Bottollier-Curtet, P. Briand, G. Briffod, P. Chabert, M. Clément, C. David, A. Girard, C. Gormezano, P. Grelot, W. Hess, M. Hesse, G.T. Hoang, G. Ichtchenko, A. Panzarella, F. Parlange, F. Ryter, G. Tonon, J.C. Vallet

Association EURATOM-CEA DRFC/SIG
CENG - 85 X - 38041 Grenoble (France)

INTRODUCTION

Powerful additional heating experiments on large tokamaks have shown limitations of performances due to the presence of internal disruptions. Thus, since the early work of the Petula Group on the low-m tearing mode stabilization (van Houtte et al, 1984), the Lower Hybrid Current Drive (LHCD) experiments are mainly aiming at the suppression of sawtooth instabilities which exist in inductively driven discharges.

A new 3.7 GHz RF system (Rey et al, 1986) ($P_{RF} \leqslant 400$ kW - $\Delta t < 100$ ms) in operation on Petula-B allows an RF current to be driven at densities up to $\bar{n}_e = 8.x10^{13}$ cm^{-3} although with a residual amount of Ohmic Heating (OH) power. Then extensive studies of sawteeth suppression in large range of plasma parameters could be done.

PLASMA AND RF PARAMETERS

The LHCD experiments were carried out on Petula-B (R = .72 m and a = .165 m) in the density range $1.x10^{13} \leqslant \bar{n}_e\ (cm^{-3}) \leqslant 8.x10^{13}$ for a magnetic field of $B_T = 2.8$ T.
The plasma current (I_p (kA) $\leqslant 230$) is initially driven by the ohmic heating circuit and kept constant during the RF pulse. The 3.7 GHz RF System consists of a multijunction type grill with 9 waveguides on a row. Different phasings give a parallel index in the range $1.7 \leqslant \langle N_{//} \rangle \leqslant 2.7$.
The sawtooth behaviour has been studied by using collimated surface barrier diodes to measure the soft X-ray emission along different chords and one movable channel heterodyne IR interferometer to measure density fluctuations. Tearing mode with m > 1 (n=1) has been observed by a set of Mirnov coils located around the plasma.

EXPERIMENTAL RESULTS

Evidence that LHCD modifies the current density profile and affects the plasma MHD behaviour has been obtained firstly in low density ($\bar{n}_e \leqslant 1.5x10^{13}\ cm^{-3}$) discharges with the 1.3 GHz RF system (large $N_{//}$ spectrum centered around 2.5). Sawteeth oscillations, initially present in the Ohmic Heating (OH) current drive discharges, were suppressed within a few msec for very low power levels and simultaneously a m=2 tearing mode was triggered. It was concluded that LHCD creates a flattening of the central q-profile rising q(o) above 1 and

increases the gradient near the q=2 surface (D. van Houtte et al, 1984). With the new 3.7 GHz RF system, the study of sawtooth stabilization has been extended to higher densities.

- In low density discharges ($\bar{n}_e \leq 1.5 \times 10^{13}\ cm^{-3}$) with $< N_{//} > = 2.7$, the plasma MHD behaviour is similar to those obtained with the 1.3 GHz RF system. The same conclusions are done.

- When the RF current is driven in medium density range ($1.5 \times 10^{13} < \bar{n}_e (cm^{-3}) \leq 4.5 \times 10^{13}$), the m=2 mode is triggered later and later in the RF pulse as density is increased. When low RF power is applied, the sawteeth which are present in OH phase, increase in relative amplitude (Fig. 1) and in periodicity (Fig. 2) for the first sawtooth occuring during the RF pulse. As the RF power is further raised, the characteristics of the sawteeth change markedly. The sawteeth look like the so-called "coumpound" sawteeth (Fig. 1) observed in large tokamaks (Campbell et al, 1985). For high enough RF power, sawtooth stabilization is achieved at the beginning of RF application and lasts for time depending on RF power level.

- For densities $4.5 \times 10^{13} < \bar{n}_e\ (cm^{-3}) \leq 8. \times 10^{13}$, a low RF power level increases only the total soft X-ray emission without marked change in relative amplitude and frequency of the sawteeth. When the RF power is high enough, depending on plasma current and density, the sawtooth oscillations are suppressed. In Fig. 3, a typical shot at a density of $\bar{n}_e = 6. \times 10^{13}\ cm^{-3}$ with 240 kW of RF power for a 125 kA discharge, is shown. It is to be noted that in this case, only 35 % of the total plasma current (as inferred from the relative loop voltage drop) is RF driven.

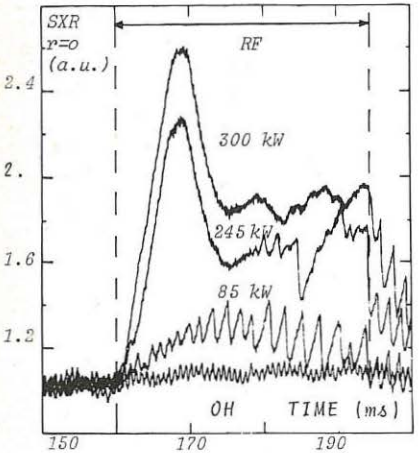

Fig.1-Central soft X-ray emission in OH sawtoothing regime and for various RF power levels. $I_p = 120$ kA, $\bar{n}_e = 3. \times 10^{13}\ cm^{-3}$ and $< N_{//} > = 1.7$

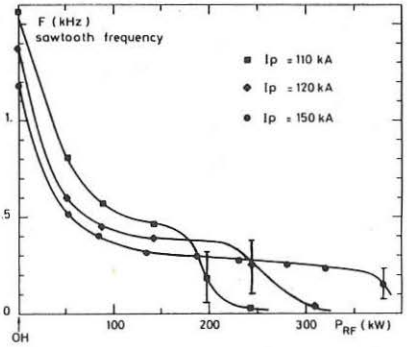

Fig. 2 - Sawtooth frequency as a function of RF power for different plasma currents at $\bar{n}_e = 3. \times 10^{13}\ cm^{-3}$ with $< N_{//} > = 1.7$

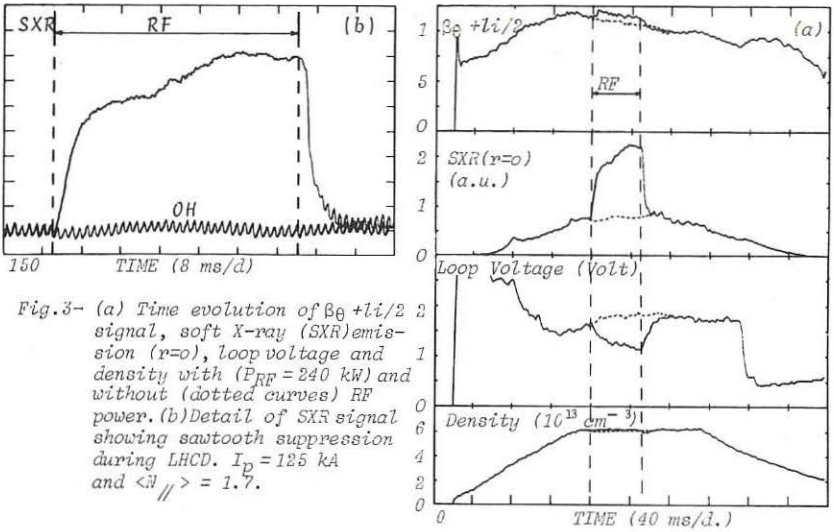

Fig.3- (a) Time evolution of $\beta_\theta + li/2$ signal, soft X-ray (SXR) emission (r=o), loop voltage and density with (P_{RF} = 240 kW) and without (dotted curves) RF power. (b) Detail of SXR signal showing sawtooth suppression during LHCD. I_p = 125 kA and $\langle N_{//} \rangle$ = 1.7.

The radius of the sawtooth inversion surface as inferred from soft X-ray emission and IR density fluctuations is a function of the plasma current and, in OH regime, the usual a/q(a) dependence is obtained for the q(r) = 1 layer radius (Fig. 4). When RF power is applied to drive part of the plasma current, the sawtooth inversion surface remains approximately at the same radial location, as a function of RF power, until the sawteeth are no longer observable. As compared to the OH case, the q(r) = 1 surface does not change or increases slightly depending on q(a) value and density (Fig. 4).

The RF power level required to suppress the sawteeth increases with the current and, is a function of q=1 surface radius as shown on Fig. 5. As a function of the density no clear dependence with the RF power necessary for sawtooth suppression, appears.

Electron temperature as inferred from Thomson scattering does not change significantly and the impurity level is about the same during the RF pulse. Thus the increase in soft X-ray emission must be mainly attributed to RF produced suprathermal electrons carrying part of the current. In the sawtooth-free discharges, the electron energy confinement time deduced from the temperature of the bulk, remains roughly constant as compared to those obtained in OH sawtoothing discharges. It is to be noted that the energy content within the q=1 surface is small as compared to the total energy content.

These sawtooth stabilization results have been obtained with a $N_{//}$ spectrum centered at $N_{//}$ = 1.7 corresponding to RF resonant energy, E_b, of 120 keV. At high density, only part of waves should be able to reach the plasma center because of wave accessibility conditions. A parallel index of $N_{//}$ = 2.7 (E_b = 40 keV) have also been used but total stabilization was not obtained in the medium and high density range with the available RF power.

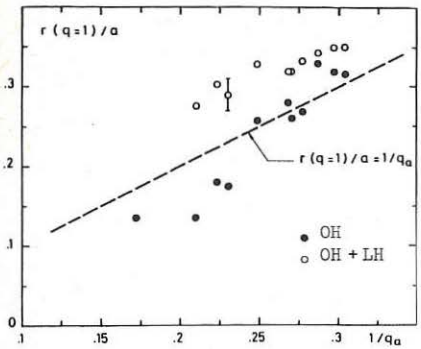

Fig.4 - Radius of the q(r)=1 surface as a function of $1/q_a$ in OH case and in (OH+LH) current drive regime. $3. \leqslant \bar{n}_e\ (10^{13} cm^{-3}) \leqslant 7.5$ and $\langle N_{//} \rangle = 1.7$.

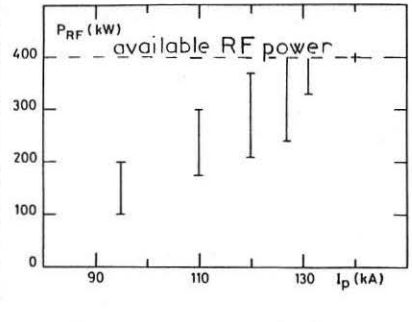

Fig.5 - RF power required to suppress the sawteeth as a function of plasma current. $2.5 \leqslant \bar{n}_e (10^{13} cm^{-3}) \leqslant 6.$ and $\langle N_{//} \rangle = 1.7$.

SUMMARY AND DISCUSSION

- The diameter of the sawtooth inversion surface does not change or increases slightly in the presence of LHCD ($\bar{n}_e > 1.5 \times 10^{13}\ cm^{-3}$) and remains approximately constant as a function of RF power. This result puts in evidence that, the mechanism responsible for internal disruptions, is inhibited with a central q-value equal of lower than those in OH sawtoothing discharge. This conclusion is confirmed by the presence of a m=1, n=1 mode into the sawtooth-free plasma discharge and by the estimation of q(o) made on Petula-B by Lister et al, (1986) using the propagation of a shear Alfven wave.

- Only about 25 % to 50 % of the total plasma current is driven by RF_3 when sawtooth-free discharges are obtained at high density ($\bar{n}_e \geq 4.10^{13}\ cm^{-3}$). However this fraction is not a sufficient condition to suppress the sawtooth activity. The necessary RF power to suppress the sawteeth depends on the radial location of the q=1 surface through the plasma current value but no clear dependence with the density appears.

- A possible mechanism of sawtooth suppression can be a replacement of the OH driven current by an RF current, carried by large enough energy suprathermal electrons, inside the q(r)=1 surface or within the m=1 magnetic island. This is in agreement with the small amount of power which can reach the plasma center due to high value of accessibility at the center ($N_{//\,acc} \sim 2$), with a launched spectrum centered at $N_{//} = 1.7$.

REFERENCES

/1/ VAN HOUTTE D. et al. (1984), Nucl. Fusion, 24, p.1485.
/2/ REY G. et al. (1986), these proceedings, paper 220.
/3/ CAMPBELL D.J. et al. (1985), In proc. of 12th Eur. Conf. on Plasma Phys. on Cont. Nucl. Fus. Res., Budapest, Vol.1, p.130.
/4/ LISTER J. et al. (1986), private communication.

MEASUREMENTS OF NON-THERMAL ELECTRON POPULATION DURING LOWER-HYBRID HEATING IN ASDEX

R. Bartiromo[1], M. Hesse[2], F. Söldner, R. Burhenn[3], G. Fussmann, F. Leuterer, H. Murmann, D. Eckhartt, A. Eberhagen, A. Giuliana[1], G. Becker, H. S. Bosch, M. Brambilla, H. Brocken, H. Derfler, O. Gehre, J. Gernhardt, G. v. Gierke, E. Glock, O. Gruber, G. Haas, J. Hofmann, A. Izvozchikov[4], G. Janeschitz, F. Karger, M. Keilhacker[5], O. Klüber, M. Kornherr, M. Lenoci, G. Lisitano, F. Mast, H. M. Mayer, K. McCormick, D. Meisel, V. Mertens, E. R. Müller[5], M. Münich, H. Niedermeyer, A. Pietrzyk[6], W. Poschenrieder, H. Rapp, H. Röhr, N. Ruhs, F. Ryter[2], F. Schneider, C. Setzensack, G. Siller, P. Smeulders[5], K.-H. Steuer, T. Vien, F. Wagner, F. v. Woyna, D. Zasche, M. Zouhar

Max-Planck-Institut für Plasmaphysik
EURATOM Association, D-8046 Garching

It has been recognized in recent years that e.m. waves in the lower hybrid (LH) frequency range can produce important effects when absorbed by plasma electrons like, for example, current generation, plasma heating and current profile modification. In these conditions the electron distribution function is not maxwellian but becomes enhanced at high energy depending on the power and phase velocity spectrum of the launched waves /1/.

The aim of the present paper is to study the plasma-wave interaction by experimentally determining the fractional population of non-thermal electrons under different plasma conditions. The experiments were carried out on the ASDEX divertor tokamak, where current drive and plasma heating can be studied up to an injected power of 1 MW at a frequency of 1.3 GHz. By changing the relative phase between successive elements in an eight-waveguide grill, the shape of the $N_{\parallel}$ index spectrum as well as its directionality can be controlled.

Data on the fractional population n_T of tail electrons were obtained from measurements of the intensity ratio of a dielectronically excited satellite line to the main resonance line of He-like titanium ions by means of high resolution X-ray spectroscopy /2/. A detailed description of the experimental apparatus and of the data analysis procedure can be found elsewhere /3/.

The results obtained in a current drive shot are compared in Fig. 1 with those obtained during electron heating. The two discharges have the same toroidal magnetic field and plasma current and nearly equal injected RF power ($P_{RF} \simeq 800$ kW) and electron density ($\bar{n}_e \simeq 1.2 \times 10^{13}$ cm^{-3}). The shape of the launched spectrum is nearly identical in the two cases and is characterized by $\langle N_{\parallel} \rangle = 2$.

In the first case the plasma current is almost completely driven by the RF waves and the feedback system regulates the ohmic power transformer to keep the plasma current to the pre-injection value; consequently the toroidal electric field is strongly reduced and comes near to zero. In these

---

[1]ENEA Frascati, Italy; [2]CEN Grenoble, France; [3]University of Bochum, W.-Germany; [4]Academy of Sciences, Leningrad, USSR, [5]Present address: JET Joint Undertaking, England; [6]University of Washington, Seattle, USA

conditions a rough estimate of the fractional population of tail electrons can be obtained by assuming from quasi-linear theory that a unidirectional plateau is formed in the toroidal direction in the velocity space from a low value V_1, a few times the thermal speed, up to a value $V_2 \gg V_1$, determined by the accessibility condition ($V_2 \simeq c/1.55$ for the present case). In this hypothesis the central current density is given by:

$$j_{RF}(0) = e \frac{V_2 + V_1}{2} n_{RF}(0)$$

where $n_{RF}(0)$ is the total density of RF-generated suprathermal electrons in the plasma center. This expression can be compared with the value obtained by assuming the q value in the plasma center close to unit, as, deduced from Li-beam measurements /4/:

$$j_{RF}(0) = \frac{2}{\mu_o} \frac{B_T}{R}$$

when R, the plasma major radius, is equal to 166 cm in ASDEX. When the value of the central electron density ($n_e(0) = 1.5 \times 10^{13}$ cm^{-3}) is taken into account we obtain for the current drive discharge $n_T(0) = 1$ % in good agreement with data in Fig. 1.

When we compare complete current drive with electron heating discharges we find a considerable enhancement of the non-thermal population in the latter case (Fig. 1). This could be explained by a better power absorption in the plasma, possibly due to small differences in the spectrum at high $N_{\parallel}$. However this should lead to an increase in the thermal energy content in heating discharges which is not observed.

Thus the higher content of non-thermal electrons in heating discharges seems to indicate that the tail extends to energies higher than in current drive discharges. However the minimum $N_{\parallel}$ accessible to the plasma center is nearly the same in the two cases and so the only possible explanation for the results is that the toroidal electric field, which is nearly vanishing only in the current drive case, is effective in accelerating the electron tail to higher energies. It is worth to note that in the heating discharges discussed here the value of the electric field is about 1.4 % of the critical runaway field. This results in a critical velocity of 0.56 c, which is lower than the upper limit of the quasilinear plateau, $V_2 = 0.62$ c, as deduced from accessibility condition.

Magnetic measurements also show that in the discharges considered here the plasma pressure becomes strongly anisotropic in the heating case while LH current drive leads to nearly isotropic heating (Fig. 2). The parallel and perpendicular components of the plasma pressure were derived from three independent measurements of β_p (diamagnetic beta), $\beta_p^{equ} + l_i/2$ (β_p^{equ} = equilibrium beta) and l_i /4/.

The influence of the shape of the $N_{\parallel}$ spectrum on the non-thermal population was also studied. A power scan with $\langle N_{\parallel} \rangle = 2$ and $\langle N_{\parallel} \rangle = 4$, (Fig. 3) shows for both cases a nearly linear dependence upon the injected power but faster waves are more effective in generating fast electrons. This is in agreement with observed heating efficiency as well as with current drive experiment results /5/.
Also shown in Fig. 3 are two measurements taken during opposite current drive experiments. In this case the waves have to push the electrons against

the applied toroidal field and consistently a lower number of tail electrons is observed.

A density scan was also performed at a medium power level ($P_{RF} \simeq 430$ kW). This is not enough to obtain complete current drive except at very low density. The results of the measurements are shown in Fig. 4. For $\bar{n}_e \geq 1 \times 10^{13}$ cm^{-3} the loop voltage is nearly equal for current drive and heating discharges with $\langle N_{\parallel} \rangle = 2$. The different behaviour in the partial current drive and heating cannot be due to electric field effects and is not fully understood. We note, however, that in this experiment heating discharges have a higher electron temperature.

At the highest density all the three spectra give nearly the same result. This corresponds to the point where the heating efficiency for the electrons is just starting to deteriorate because of the increasing ion absorption /5/. In these conditions we performed spatially resolved measurements for two values of the injected power at $\langle N_{\parallel} \rangle = 2$ (Fig. 5): we obtained hollow profile, showing a lack of wave penetration to the plasma center.

To check problem of wave accessibility to the plasma center, $\langle N_{\parallel} \rangle = 4$ spectrum was studied in the same plasma conditions, although at a reduced power level ($P_{RF} = 300$ kW), and the n_T profile was still found to be hollow. It can then be concluded that in the ion interaction regime the penetration of the waves to the plasma center is inhibited possibly due to the absorption by the plasma edge.

References

/1/ N.J. Fisch, Phys. Rev. Lett. 41, 873 (1978)
/2/ R. Bartiromo, et al., Phys. Rev. A32, 531 (1985)
/3/ R. Bartiromo, et al., to be published
/4/ K. McCormick, et al., Procs. 12th Europ. Conf. on Controlled Fusion and Plasma Physics, Budapest (1985), Vol. I, p. 189
/5/ F. Leuterer, et al., Plasma Phys. Controlled Fusion 27, 1399 (1985)

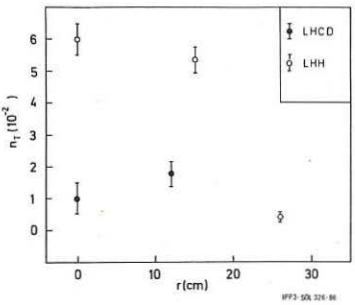

Fig. 1: The fractional population of non-thermal electrons is plotted versus the plasma radius for current drive and electron heating discharges. The plasma parameters are: $I_p = 300$ kA, $B_T = 2.4$ T. $\bar{n}_e = 1.2 \times 10^{13}$ cm^{-3} and $P_{RF} = 800$ kW. The launched spectrum has $\langle N_{\parallel} \rangle = 2$.

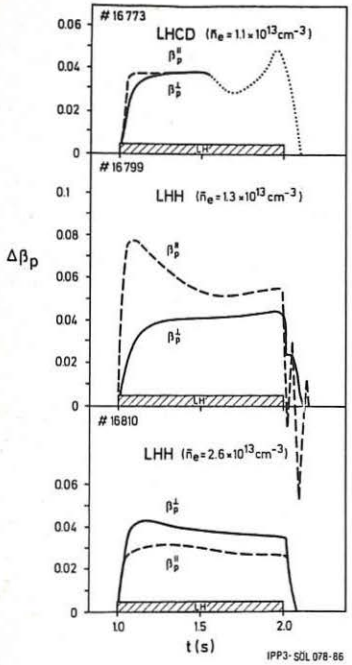

Fig. 2: Increment of β_p'' and β_p for LHCD and LHH at low and high electron density.

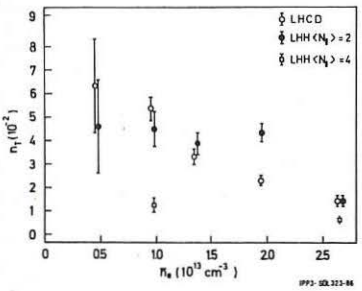

Fig. 4: Density scan for current drive with $\langle N_{\parallel}\rangle = 2$ and heating discharges with $\langle N_{\parallel}\rangle = 2$ and $\langle N_{\parallel}\rangle = 4$. Other plasma parameters are: I_p = 300 kA, B_T = 2.2 T, P_{RF} = 430 kW. Data refer to r = 11 cm.

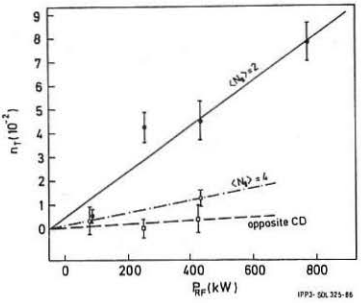

Fig. 3: Power scan for heating discharges with $\langle N_{\parallel}\rangle = 2$ and $\langle N_{\parallel}\rangle = 4$ and for opposite current drive. Plasma parameters are: I_p = 300 kA, B_T = 2.2 T, $\bar{n}_e = 1.0 \times 10^{13}$ cm^{-3}. Data refer to r = 11 cm.

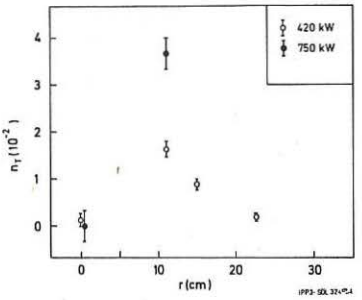

Fig. 5: Profiles of the fractional population of nonthermal electron for discharges near to the regime of prevailing ion absorption. Plasma parameters are: I_p = 300 kA, B_T = 2.2 T, $\bar{n}_e = 2.6 \times 10^{13}$ cm^{-3}. The launched spectrum has $\langle N_{\parallel}\rangle = 2$.

A MODULAR MULTIJUNCTION GRILL FOR CURRENT DRIVE STUDIES AT 3.7 GHz FOR PETULA-B AND TORE SUPRA

G. Rey - G. Berger-By - Ph. Bibet - C. David - M. Goniche - G. Tonon - G. Agarici - P. Briand - C. Gormezano - A. Panzarella - RF & PETULA Groups

ASSOCIATION EURATOM-C.E.A. - Département de Recherches sur la Fusion Contrôlée - C.E.N.G. - 85X - 38041 GRENOBLE Cedex (France)

1 INTRODUCTION

A 8 MW - quasi continuous - 3.7 GHz Lower Hybrid Heating system is being designed for mainly current-drive studies on the TORE SUPRA Tokamak. A large simplification of the L.H. antenna and of the RF transmission line is obtained by applying two main ideas : (i) modular design, (ii) internal RF power division - 3 dB hybrid junction and E-plane multijunction (M.J.). The E-plane M.J. system /1/ brings not only simplification in the building of the antenna, but also, when used in travelling wave, lowers strongly the power reflection coefficient towards the generator. This is a very important point, because such a system allows to avoid the use of circulators - expensive elements for large machine.

In order to test the physical and these technical options chosen for the TORE SUPRA experiment, a 500 kW-30 ms-3.7GHz experiment has been successfully operated on PETULA-B (see other papers in this conference /2/ to /4/).

2 GENERAL DESCRIPTION

2.1 The RF power, provided by a 500 kW-30 ms-3.7 GHz ThCSF klystron is injected to the coupler by means of an Aluminium, 6m long, SF6 pressurized, standard WR 284 transmisssion line. The RF losses including the insertion losses of the circulator and flexible waveguides are measured equal to 0.14. 3 dB hybrid junctions allow the RF power to be divided in the ratio 1/4:1/2:1/4 between the 3 modulus (1/2 in the central one).

Fig. 1 shows the general view of the low hybrid coupler on Petula. A vacuum tank composed by a large movement bellow and a rigid sector for the vacuum pumping is connected by means of Ø 400 vacuum valve to a Petula port.

2.2 Fig. 2 shows the front view of the 18 waveguide-9 column-2 line-network made from 3 juxtaposed identical modulus. Each modulus is composed of : (i) a RF alumina vacuum window with its associated arc detector, (ii) a 3 dB hybrid junction, (iii) a 90° phase shifter in order to balance the 90° phasing of the hybrid junction, (iiii) the 0-120°-240°-3 wg E-plane M.J. system (cf. fig. 3a, 3b). The phase shifters are obtained by changing the waveguide length in the wg by reducing its height. The RF matching of such sections is obtained by step transformers.

By changing the phase of the injected wave between the 3 modulus, the $N_{//}$ spectrum excited by the launcher can vary from 1.6 to 3. From code calculations /5/, the $N_{//}$ spectra obtained with a $\pm$ 90° phasing between modulus is plotted in fig. 4.

3 LOW LEVEL TEST

As expected by theorical predictions, self matching property of the 3 wg -O-120°-240°-E-plane M.J. is obtained when the 3 loads are in the same plane (fig. 5a) and the power reflection coefficient (P.R.C.) is the square of the P.R.C. of the loads. For a $\lambda_g/6$ spacing of the loads, which leads to the same phasing (180°) in each secondary wg, no self matching property is observed (fig. 5b). Self matching property is confirmed on plasma /2/.

The SWRV of each element of the modulus is lower than 1.06.

4 CONDITIONING TECHNIQUES

4.1 On a separated test line, argon glow discharges have been tested /6/ Such a technique, currently used for the 1.3 GHz experiments has been simplified by using a common longitudinal electrode. High pressure (~1 torr) argon glow discharge is needed in order to obtain a quasi homogeneous discharge in the 3 reduced waveguides (fig. 6). Due to the lower ion numbers striking the surface with a sufficient energy (~300 eV) /6/, the time duration of such a discharge has to be of the order of 10 hours. This procedure has to be verified at high RF power on the launcher itself.

4.2 Up to now, on Petula, the conditioning technique, derived from previous high RF power tests in a test bed, is the following : (i) during the cleaning session of the machine with a 10^{-4} H_2 pressure, the RF power is gradually increased with a duty cycle of 1 RF-5ms long-shot every 10 seconds. 300 to 400 pulses are so performed during such a session, (ii) between two plasma shots, about 10 short RF pulses are powered at a level slightly greater than that required for the following plasma shot.

4.3 Performances : As expected, the power density limitation due to the multifactor effect ($\mathcal{P} \sim f^2$), is greatly decreased by working at 3.7 GHz and the cleaning of the surface has been achieved by using RF shots conditioning technique.

With such a technique, after a overall one thousand RF conditioning shots, the full power - 500kW-30ms - of the klystron has been injected to the coupler. When the central modulus is fed alone with the RF power, the corresponding power density - assuming no reflected power - is ~ 20kW/cm^2 at the RF window and ~ 10kW/cm^2 at the reduced section of the grill. Such values - however with short time pulses - are twice the ones planned on TS Low Hybrid experiments.

5 REFERENCES

/1/ T.K. NGUYEN and D. MOREAU - Proc. 12th Symp. on Fusion Tech. (Jülich) Vol. 2 1381 (1982)
/2/ M. GONICHE et al. - This conf. paper n° 213
/3/ C. GORMEZANO et al. - " " " n° 217
/4/ D. VAN HOUTTE et al. -" " " n° 218
/5/ D. MOREAU, T.K. NGUYEN - Report EUR-CEA F 1199 (9-83)
/6/ D. BOILOT, M. GONICHE - Internal report 1239 (1985)

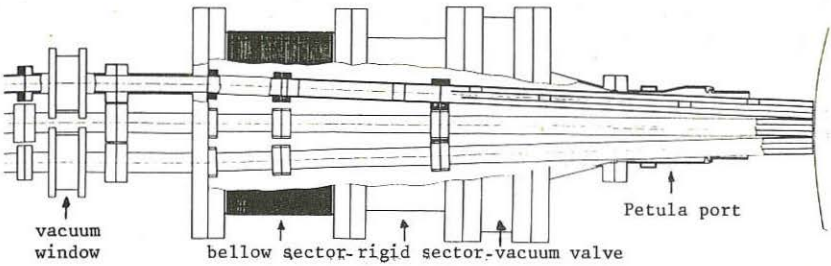

Fig. 1 - Implementation of L.H. coupler on Petula

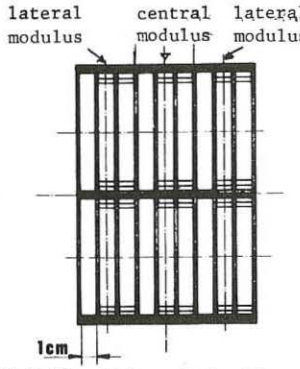

Fig. 2-Front view of the 18wg grill

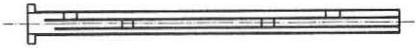

Fig. 3a - Top view of the 3wg E-plane multijunction

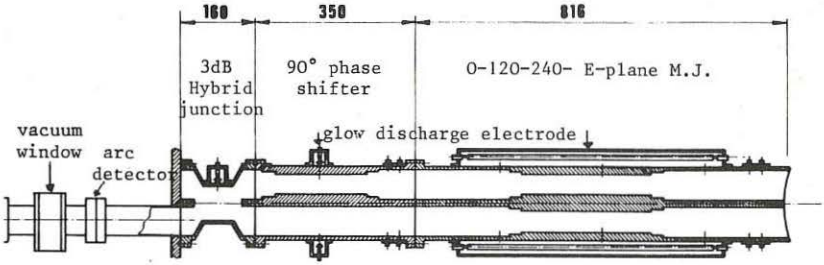

Fig. 3b - Cross section of one modulus

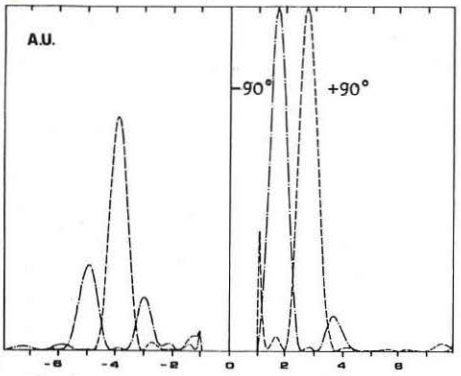

Fig.4 - $N_{//}$ spectra excited by the antenna for -90° and +90° phasing between modulus

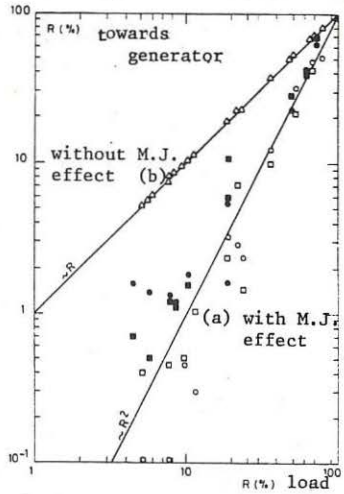

Fig.5 - Power reflection coefficient with and without M.J. effect

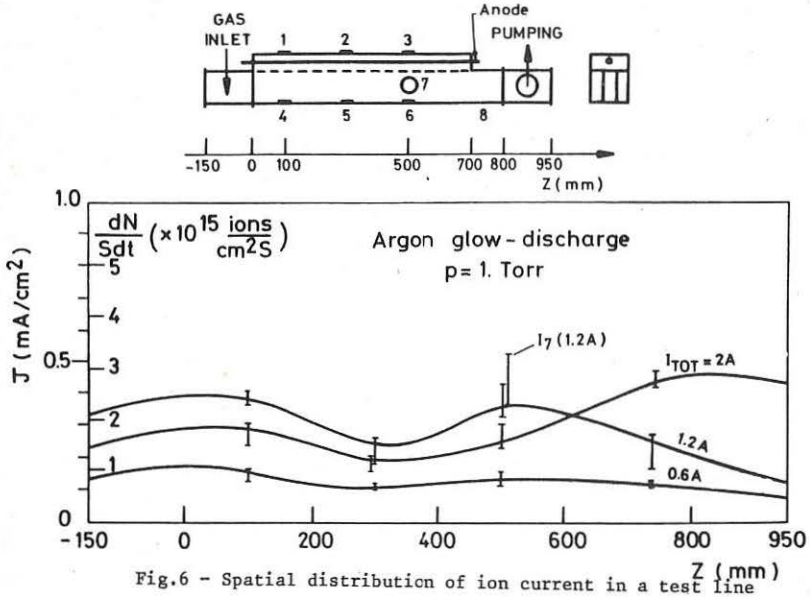

Fig.6 - Spatial distribution of ion current in a test line

NEW DEVELOPMENTS IN HIGH-POWER KLYSTRONS FOR LOWER HYBRID RESONANCE HEATING APPLICATIONS

Earl W. McCune
Varian Associates, Inc.
611 Hansen Way
Palo Alto, CA 94303 U.S.A.

INTRODUCTION

Plasma heating using the lower hybrid wave method (LHRH) requires very high power at frequencies in the range of 1 to 18 GHz. The necessary power levels are in excess of what is achievable in a single power source. Consequently, multiple power units are needed. Of particular concern is the desire to obtain the required power at a minimum cost. Total system cost projections typically reach the conclusion that for minimum cost it is necessary to use a minimum number of power units of maximum power capability. Therefore, it is important to understand the power capabilities and limitations of prospective power sources.

The klystron amplifier is the device of preference for generation of high-power levels at these frquencies. Klystrons have demonstrated good reliability while providing high power at good efficiency. Two klystrons presently in service for LHRH plasma heating are the VKS-8269A which provides 500 kW at 2.45 GHz and the VKC-7849 which provides 250 kW at 4.6 GHz. Typical performance values for these klystrons are listed in Table 1. These klystron designs provide excellent performance but do not represent the maximum power capability at these frequencies and consequently do not necessarily provide a minimum cost design for a system requiring multiple power sources.

Table 1
Typical Performance Characteristics

	VKS-8269A Klystron	VKC-7849 Klystron
Frequency	2.45 GHz	4.6 GHz
Power	510 kW	260 kW
Gain	58 dB	56 dB
Bandwidth (1 dB)	22 MHz	24 MHz
Efficiency	52 %	45 %
Beam Voltage	63 kV	46.5 kV
Beam Current	15.7 A	12.4 A
Body Current, No Drive	5 mA	5 mA
Body Current, Saturation Drive	8 mA	33 mA

KLYSTRON POWER CAPABILITY

It was recognized early in the history of klystron development that the power generating capability would ultimately be limited by the dissipation capability of the output resonator. Designs were considered, even at that time, which would distribute the rf output power over several resonators in order to increase overall capability. This technology was called "extended interaction" and was described in detail in publications

during the 1960's[1] [2] [3]. The extended interaction klystron (EIK) technology provides improved performance in two areas: increased power generation capability and increased bandwidth performance. Over the past two decades little has been done to implement this technology to provide klystrons of exceptional power capability. Only one experimental device was reported and no products resulted[4]. This situation arose because other practical problems limited power generation and EIK technology was not necessary. Devices have been developed, however, using EIK principles for designing klystrons with exceptional bandwidth capability[5].

The practical problems which traditionally limited power capability are: difficulties in forming and focusing an electron beam of high power density, difficulties in dissipating the spent beam energy, difficulties in providing a window through which the rf power could be extracted from the klystron, and of course, the difficulties associated with power dissipation of the cavity resonators. Over the years klystron technology has steadily improved, overcoming most of the above limitations. Electron gun design has benefited greatly from computer aided design technology which makes possible electron beams of high current density with excellent collimation. Beam transmission of 99.9% is commonly achieved so that beam power is separated essentially completely from the interaction cavities. Collector configurations have been developed allowing collectors of arbitrary size; therefore, the collector can be constructed as large as necessary to dissipate the residual beam power. Window designs have been developed with power transmission capability approaching the fundamental waveguide ratings. Consequently, present technology allows klystron designs for power levels limited only by the dissipation capability of the output circuit. This situation was reported in a previous paper where the power capability for klystrons using single cavity output resonators was described[6]. Since that time we have re-evaluated the impact of using extended interaction technology and have determined that it can allow designs of at least doubled power capability. Design analysis indicates that klystrons using this technology are not significantly more complex nor is the cost impact large.

THE EXTENDED INTERACTION OUTPUT CIRCUIT

The two-gap extended interaction output circuit consists basically of two simple klystron cavities coupled to each other by a slot in the common wall. The cavities are also coupled by the electron beam which passes through both cavity gaps. The power is coupled from the second cavity to the output waveguide via an inductive iris.

The circuit has two modes of resonance: at one resonance the gap voltages are in phase - this is the zero or 2 pi mode, and the other resonance is where the gap voltages are in antiphase - the pi mode. This circuit can be designed to be operated at frequencies between the two resonances and can provide wide bandwidth performance. The PT 6006 klystron, for instance, manufactured by EMI-Varian uses this technology and provides 100 kw peak output power over an 8% bandwidth around 1.3 GHz.

We have recently analyzed this design from a different viewpoint. Rather than optimize performance over a wide bandwidth, we optimized the design to evenly distribute the dissipated power to maximize the power capability. When operating at the 2 pi mode we determined that the gap-to-gap spacing allowed adequate cooling space so that each cavity can be

cooled as well as previous single cavity designs. Detailed analysis of the gap fields using our large signal klystron simulation program resulted in a design with equal gap voltages, each 0.7 times that for a single gap circuit. Consequently, this design would have twice the power capability of a single-gap design.

KLYSTRONS FOR FUTURE HEATING REQUIREMENTS

New klystron designs were investigated which take advantage of the increased power capability of the two-gap output circuit design. It had been previously reported[6] that the power generating capability of klystrons using a single output resonator is limited to a value which can be described with the "figure of merit" relationship, $PF^2=16$; where P is in megawatts and F in GHz. By using a two-gap output circuit, the power capability can be doubled, resulting in $PF^2=32$. We would still recommend a conservative design for future rf heating systems where reliability is of major importance. Consequently we have generated new designs based on $PF^2=16$ representing the appropriate power levels for frequencies from 2 to 16 GHz. The general characteristics of the new designs A through D are listed in Table 2. An important determination of this design exercise was the finding that the output circuit is still the power limiting element. There is still more than adequate power capability in all other areas of the klystron design. With this thought in mind, we are investigating extended output circuit designs using more than two cavities to determine possible designs or even high power. More cavities in the output circuit causes concerns about positive feedback with possible oscillations for operating modes away from the design value.

Table 2
Klystron Designs for Plasma Heating Applications
Using a Two-Gap Output Circuit

Typical Performance Characteristics

Design	Frequency GHz	Output Power kW	Efficiency %	Beam Voltage kV	Beam Current A
A	2	4000	60	125	53
B	4	1000	55	75	24
C	8	250	50	45	11
D	16	62	45	27	5

While the analysis of the 2-gap case indicated complete unconditional stability, that has not been determined for more complex circuits. Consequently, more analysis is necessary to determine the ultimate power capability of klystrons with multiple gap extended interaction output circuits.

CONCLUSION

New klystron designs have been presented which have power generating capability beyond what was possible with previous designs. These designs are particularly appropriate for the generation of large amounts of high

frequency power where multiple power units are necessary. Consequently, they would make possible more cost effective power generation for future LHRH systems.

REFERENCES

1. Chodorow, M. and Wessel-Berg. T., (1961), "A High-Efficiency Klystron with Distributed Interaction", IRE Trans., ED8, 44.

2. Preist, D.H. and Leidigh, W.J., (1963), "Experiments with High-Power CW Klystrons Using Extended Interaction Catchers", IEEE Trans. ED10. 201.

3. Preist, D.H. and Leidigh, W.J., (1964), "A Two-Cavity Extended Interaction Klystron Yielding 65 Percent Efficiency, IEEE Trans., ED11, 369.

4. Luebke, W. and Caryotakis, G.: "Development of a One-Megawatt CW Klystron", Microwave Journal, Vol. 9, August 1966.

5. Perring, D., Phillips, G. and Smith, M.J. "Broadband Megawatt Klystron Amplifier", AGARD Con Proc., CP197, 5.1 to 5.8, 1976.

6. McCune, E.W.: "Klystrons for Present and Future Lower Hybrid Resonance Applications", Presented at 4th Int'l Symposium on Heating in Toroidal Plasmas, Rome, March 1984.

NONLINEAR EFFECTS IN LOWER HYBRID HEATING OF TOKAMAK PLASMAS

J. A. Heikkinen and S. J. Karttunen

Nuclear Engineering Laboratory
Technical Research Centre of Finland
P.O. Box 169, SF-00181 Helsinki, Finland

ABSTRACT: Nonlinear evolution of the parametric scattering of lower hybrid heating waves off ion modes in tokamak plasmas is investigated. Harmonic generation of the low-frequency ion wave and its effect on the parametric decay of a lower hybrid pump to another lower hybrid wave is analyzed, and numerical calculations of the relevant wave-system are carried out.

INTRODUCTION: Most lower hybrid heating and current drive experiments [1] show a degradation of efficiency at high plasma densities such that $\omega_0/\omega_{LH}(0)<2$, where $\omega_0/2\pi$ is the frequency of the injected pump wave and $\omega_{LH}(0)$ is the lower hybrid frequency evaluated at the plasma centre. Parametric decay processes are often observed [2] above this same density limit, and they may be one explanation for the decreased transmission of LH-power into the plasma interior. According to the theoretical predictions [3] the most probable decay process would be the decay into a cold lower hybrid wave and a quasimode at or near the plasma edge. The linear theory of this decay is well explored, but the nonlinear evolution is less understood. By considering the harmonic generation of the low-frequency mode we shall determine the saturation effects on the level of the sideband power and thus on pump depletion.

SATURATION MODEL: The wave equations describing the low-frequency modes may be formulated in the steady-state approximation as [4]

$$[\partial\varepsilon(\omega,k)/\partial(k)]\partial n_e/\partial x - i\varepsilon(\omega,k)n_e = -\alpha_2 n_e^* n_{eH} + \alpha E_0 E_1^* \quad (1)$$

$$[\partial\varepsilon(2\omega,2k)/\partial(2k)]\partial n_{eH}/\partial x - i\varepsilon(2\omega,2k)n_{eH} = \alpha_{2H} n_e^2 \quad (2)$$

where n_e and n_{eH} are the electron density fluctuations (normalized to the background density) relating to the low-frequency mode with the frequency ω and the wavenumber k and its harmonic $(2\omega,2k)$, respectively. $E_{0(1)}$ is the lower-hybrid pump (sideband) field amplitude normalized to the pump field amplitude E_{00}, and $\alpha E_0 E_1^*$ describes the drive field for n_e in the primary decay process. We have $\alpha = -1/4\ \chi_e(1+\chi_i)(\Omega_e/\omega_0)k^2\lambda_{De}^2 u^2/v_e^2$, where $u=eE_{00}/m_e\Omega_e$ is the $(\bar{E}_0 x \bar{B})$ drift velocity. The linear dielectric function describing the low-frequency modes is

$$\varepsilon(\omega,k) = 1 + \chi_e(\omega,k) + \chi_i(\omega,k) = 1 + W(\omega/k_z v_e)/k^2\lambda_{De}^2 + \{1 + \sum_{\ell}\omega(\omega-\ell\Omega_i)^{-1}[W(\omega-\ell\Omega_i/k_z v_i)-1]\Lambda_\ell(\beta)\}/k^2\lambda_{Di}^2, \quad (3)$$

where standard notations are used (the function W is related to the plasma dispersion function Z by $Z'(s)=-2W(\sqrt{2}s)$). $\Lambda_\ell(\beta)$ is defined by the modified

Bessel function $I_\ell(\beta)$ by $\Lambda_\ell(\beta)=I_\ell(\beta)\exp(-\beta)$, and $\beta=k^2v_i^2/\Omega_i^2$. The coupling coefficients may be written as

$$\alpha_2 = -V^*/W^*(\omega/k_zv_e) \quad , \quad \alpha_{2H} = \alpha_2^*/4, \tag{4}$$

where V is the interaction coefficient

$$V = 3i(\omega_{pi}^2/\Omega_i^2)[\Lambda_\ell(\beta)^2\Lambda_{2\ell}(4\beta)\Omega_i^3/(\omega-\ell\Omega_i)^3]$$
$$\times\{\frac{\ell^2(1-W_\ell)^2(1-W_\ell)^*}{\beta} + \frac{(\omega-\ell\Omega_i)^2}{3k_z^2v_i^2}[2W_\ell W_\ell^*(1-W_\ell) + W_\ell^2(1-W_\ell)^*]\}/\beta, \tag{5}$$

which is due to the coupling between ions. The argument of W_ℓ is $(\omega-\ell\Omega_i)/k_zv_i$. It can be seen that V has sharp maxima near the ion cyclotron harmonics $\omega=\ell\Omega_i$. This is because $\Lambda_\ell(\beta)$ is small (<0,1). Note that there is no singularity at $\omega=\ell\Omega_i$ for V due to the expansion of W_ℓ at small arguments; $W_\ell\sim1+i(\pi/2)^{1/2}(\omega-\ell\Omega_i)/k_zv_i$. According to (5) V gets larger values for small β, i.e., at low ion temperatures. Thus it is expected that harmonic generation of the low-frequency mode is stronger at the plasma edge.

NUMERICAL RESULTS: The nonlinear correction (harmonic generation) in Eqs. (1) and (2) is of the same order as the linear terms, when the absolute value of $[\alpha/\varepsilon(\omega,k)]^2[\alpha_2/\varepsilon(\omega,k)]\,[\alpha_{2H}/\varepsilon(2\omega,2k)]$ exceeds 1, as may be easily checked by solving the equations for n_e (without spatial derivatives). We denote this value with C. Note that C is proportional to the squared pump intensity. We have calculated C as a function of ω for several tokamak parameters relevant inside and at the edge of the plasma. Our results indicate that at sufficently high pump intensity (>1kW/cm^2) C may be large (>1) at the temperature ($T_e\sim T_i$) less than 100eV and with the density more than 10^{18} m^{-3}. According to the linear calculations [5] the primary process, too, is strongest at these parameters, i.e., typical edge conditions. C as a function of ω_1/ω_0 ($\omega=\omega_0-\omega_1$) for $N=4\cdot10^{18}$ m^{-3} and $T_e=T_i=15$eV is seen in Fig. 1(a), where other parameters are B=4.28T, $\omega_0/2\pi=2$GHz, mass ratio 3600, RF-power 300 kW, and the width L_z of the pump resonance cone 10 cm. The parallel refractive indeces of the pump and sideband are chosen as $N_{0z}=3$ and $N_{1z}=5$, respectively. Spatial growth factor A of the sideband amplitude from the quasimode approximation (low-frequency wave strongly damped) ($E_1\sim\rho\exp(A)$, where ρ is the noise level) for the primary process is also shown. It is found that A and C both are strong near $\omega\sim\Omega_i$ (other peaks near $\omega\sim\ell\Omega_i$ were insignificant for A), and their resonance peaks coincide well. In Fig. 1(b) we have the same case, but here we represent the spatial growth factor $A'=\ell n(E_1(L_z)/\rho)$, calculated from the four-wave system including the primary and secondary process, as a function of the coordinate (η) along the pump wave propagation direction for various noise levels. ω_1/ω_0 is chosen at the maximum of A in Fig. 1(a). In this case, due to high intensity and low temperature, the primary instability (the evolution of which is also shown) is absolute in the sense that there is no convective saturation in the η direction. We may see that harmonic generation restores the convective saturation and strongly suppresses the level of amplified field amplitudes. The corresponding field amplitude profiles accross the resonance cone for E_1, n_e, and n_{eH} are shown in Fig. 2 for $\rho=0.02$ and $\eta=32$. It can be seen that the product of the amplitudes of E_1 and n_e (determines the strength of pump depletion) is more than 50 times smaller when harmonic generation is considered compared to the case when it is ignored. At smaller pump intensities

or at higher temperatures the primary instability can become convectively saturated, and the saturation effect of harmonic generation is milder depending, however, crucially on the noise level ρ. At large N_{1z} (>12) the strength of the harmonic generation strongly diminishes.

CONCLUSIONS: The effect of harmonic generation of the low-frequency mode on the lower hybrid parametric decay is investigated. With a high pump intensity and with typical plasma edge parameters the growth of the sideband is effectively restrained, and sideband power levels much less than the pump power are observed.

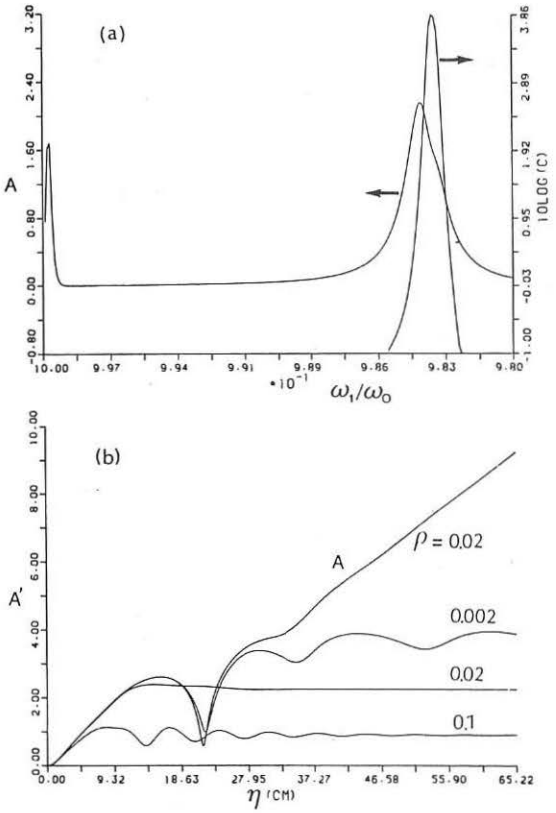

Fig. 1 (a) Spatial growth factor $A=(\alpha/\varepsilon)_R\alpha_1 L_z$ of the primary instability and the harmonic generation strength C versus sideband frequency. B=4.28T, $\omega_0/2\pi$=2GHz, mass ratio 3600, RF-power 300kW, L_z=10 cm, $N=4\cdot10^{18}m^{-3}$, $T_e=T_i$=15eV, N_{0z}=3, and N_{1z}=5. (b) Effective growth factor A' versus η for various noise levels ρ. The curve marked by A corresponds to the case without harmonic generation. Parameters are the same as in (a).

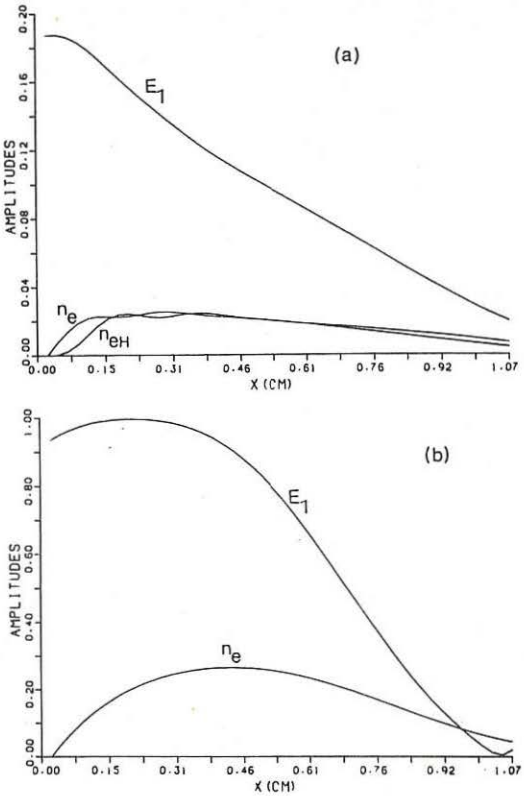

Fig. 2 Wave amplitude profiles for E_1, n_e and n_{eH} across the resonance cone at $\eta=32$ with $\rho=0.02$. Parameters are the same as in Fig. 1. (a) harmonic generation included, (b) harmonic generation ignored.

REFERENCES:

[1] W. Hooke, Plasma Phys. Controlled Fusion 26 (1984) 133, and references therein.

[2] Y. Takase et.al., Phys. Rev. Lett. 53 (1984) 274; R. Cesario and V. Pericoli-Ridolfini, Proc. 12th Europ. Conf. on Contr. Fusion and Plasma Phys. (Budapest 1985) Vol. 8B, part II (1985) 220; T. Imai et.al., Phys. Rev. Lett. 43 (1979) 586.

[3] M. Porkolab, Phys. Fluids 20 (1977) 2058; V. K. Tripathi et. al., Phys. Fluids 22 (1979) 301.

[4] J. A. Heikkinen and S. J. Karttunen, to be published.

[5] E. Villalon and A. Bers, Nucl. Fusion 20 (1980) 243.

A GENERALISED DESCRIPTION OF THE ANOMALOUS DOPPLER RESONANCE AND THE STABILISING ROLE OF ION DYNAMICS

R.O. Dendy, C.N. Lashmore-Davies, and A. Montes[a)]
Culham Laboratory, Abingdon, Oxfordshire OX14 3DB, UK
(Euratom/UKAEA Fusion Association)

a) Permanent address: Instituto de Pesquisas Espaciais, C.P. 515, 12 200 S.Jose dos Campos, S.P., Brazil.

The anomalous Doppler effect[1,2] is of interest as a fundamental limit on superthermal tail formations in tokamak plasmas, and as a probable explanation[3] of the relaxation oscillations seen in the soft X-ray signal from Ohmic plasmas[4] and in association with lower hybrid current drive.[5,6] In this application, the divergence of fast-electron motion from the parallel direction as the anomalous Doppler instability proceeds is responsible for the shift in the predominant direction of electron bremsstrahlung, which follows the fast-electron motion. A number of studies have considered such quasilinear development of the instability. The linear instability remains of interest,[7] however, and we shall examine this aspect of the phenomenon.

A collective description of the anomalous Doppler effect arising from the interaction of resonant electrons with electrostatic waves in a magnetised plasma follows from the dielectric response function. We shall show below that ion dynamics play a significant role in wave damping under conditions where the wavenumber is sufficiently large that the ions can be regarded as unmagnetised. For this reason, we include the corresponding ion contribution in the expression for the full dielectric response function:

$$\varepsilon = 1 - \frac{\omega_p^2}{k^2} \sum_{n=-\infty}^{\infty} \int_{v_\parallel=-\infty}^{\infty} \int_{v_\perp=0}^{\infty} \frac{2\pi v_\perp dv_\perp dv_\parallel}{n\Omega + k_\parallel v_\parallel - \omega} \left(\frac{n\Omega}{v_\perp} \frac{\partial f}{\partial v_\perp} + k_\parallel \frac{\partial f}{\partial v_\parallel} \right) J_n^2\left(\frac{k_\perp v_\perp}{\Omega}\right) - \frac{\omega_{pi}^2}{k} \int_{-\infty}^{\infty} \frac{dv_i}{kv_i - \omega} \frac{df_i}{dv_i} \qquad (1)$$

The real part ε_{real} of ε is in general dominated by cold electron plasma terms which are insensitive to the exact form of $f(v_\perp, v_\parallel)$. For $(\omega_p/\Omega)^2 \lesssim 0.2$, the electrostatic waves which are roots of $\varepsilon_{real} = 0$ are well described by $\omega = \omega_p k_\parallel/k$ in the frequency range of interest. The imaginary part ε_{im} of ε describes wave-particle resonance, which leads to electrostatic wave growth or damping at a rate given by $\gamma = -(\omega_p k_\parallel/k)(\varepsilon_{im}/2)$. By Eq.(2), a negative contribution from the electrons to ε_{im} arises from the $n = -1$ term at the parallel resonant velocity $v_{AD} \equiv (\omega + \Omega)/k_\parallel$. This is the anomalous Doppler resonance.

For a wave of given $(\omega, k_\perp, k_\parallel)$, growth occurs if the Landau damping terms associated with $\partial f/\partial v_\parallel$ at $v_\parallel = \omega/k_\parallel$ and df_i/dv_i at $v_i = \omega/k$ in Eq.(1) are so weak that they can be overcome by the anomalous Doppler resonant term involving $\partial f/\partial v_\perp$ at $v_\parallel = v_{AD}$. The latter is proportional to the magnitude, rather than the parallel gradient, of the parallel component of the electron distribution function at the superthermal parallel velocity $v_\parallel = v_{AD}$. Let us consider an isotropic bulk Maxwellian electron distribution, together with a small tail whose distribution in $v_\parallel$ is not yet specified, but which has a fixed perpendicular thermal velocity. We also specify a thermal ion distribution. In this case, we obtain

$$\gamma = \gamma_{AD} - (\gamma_{LB} + \gamma_{LT} + \gamma_{LI}) \tag{2}$$

Here γ_{AD} is the anomalous Doppler driving term, γ_{LB} and γ_{LT} describe electron Landau damping in the bulk and tail distributions respectively, and γ_{LI} describes Landau damping on the ions. The dielectric response function ε in Eq.(1) is given in terms of the dielectric tensor ε_{ij} by $\varepsilon = k_i k_j \varepsilon_{ij}/k^2$. In the region of instability it will be shown that the ion contribution to ε_{ij} can be neglected. For the electrostatic waves excited by the anomalous Doppler instability, we have $E_i = |\underline{E}| k_i/k$. Let us take $\underline{k} = (k_\perp, 0, k_\parallel)$. In this case, the rates of energy dissipation by the electrostatic field on the electron motion perpendicular and parallel to the magnetic field are given by

$$P_x = \mathrm{Re}(j_x E_x^*) = \omega \frac{|\underline{E}|^2}{4\pi} \left[\frac{k_\perp^2}{k^2} \varepsilon_{xx}^{im} + \frac{k_\perp k_\parallel}{k^2} \varepsilon_{xz}^{im}\right] = \frac{|\underline{E}|^2}{4\pi} 2\gamma_{AD} \frac{\Omega}{\omega} \tag{3}$$

$$P_z = \mathrm{Re}(j_z E_z^*) = \omega \frac{|\underline{E}|^2}{4\pi} \left[\frac{k_\perp k_\parallel}{k^2} \varepsilon_{xz}^{im} + \frac{k_\parallel^2}{k^2} \varepsilon_{zz}^{im}\right] = \frac{|\underline{E}|^2}{4\pi} \left[2\gamma_{LB} + 2\gamma_{LT} - (1+\Omega/\omega) 2\gamma_{AD}\right] \tag{4}$$

Here $|\underline{E}|^2/4\pi$ is the electrostatic field energy density of the wave, and the factors of 2 arise from the quadratic dependence of power on field amplitude. Eq.(3) describes the field energy dissipated by the wave in increasing the perpendicular kinetic energy of the electrons undergoing the anomalous Doppler resonance. The first two terms of Eq.(4) describe the field energy dissipated by Landau damping on the electrons, which increases their parallel kinetic energy. The final term in Eq.(4) describes the parallel kinetic energy given up by the anomalous Doppler resonant electrons. The net flow of parallel kinetic energy from these electrons to the field and to perpendicular kinetic energy occurs in the ratio 1 : Ω/ω. This reflects the original concept of Kadomtsev and Pogutse,[8] who treated $(h/2\pi)\Omega$ as the energy quantum of perpendicular gyromotion, and $(h/2\pi)\omega$ as the quantum of wave energy, both of which are drawn from the electron parallel kinetic energy. If the energy transfer to the field is sufficient to overcome the Landau damping losses, γ is positive and wave growth occurs: thus, $-(P_x + P_z) = 2\gamma|\underline{E}|^2/4\pi$ as expected. A larger energy transfer occurs from the parallel to the perpendicular component of electron motion. In both these respects, Eqs.(3,4) demonstrate explicitly how closely the collective anomalous Doppler effect follows the single-particle effect. The essential difference lies in the existence of a threshold, since Landau damping of the wave by the bulk distribution and by the ions, where appropriate, must be overcome in the collective case. This also differentiates the instability of an extended tail from that of a beam in a cold plasma. We note also that the contribution to P_z from the anomalous Doppler term in Eq.(4) is negative, independently of whether the relative magnitudes of γ_{LB}, γ_{LT}, and γ_{AD} are such as to give overall wave growth or damping. It follows that anomalous Doppler resonant electrons may reduce the absorption of driven waves that are undergoing damping, while they increase their perpendicular energy at the expense of their parallel energy.

Consideration of γ_{LB} shows that there are two candidate regimes for instability. Let v_B denote the thermal velocity associated with the isotropic bulk Maxwellian distribution. Electron Landau damping is weak firstly for $v_\parallel \gtrsim 2.5\, v_B$, beyond the main body of the bulk, and also for $v \ll v_B$, deep in the bulk distribution. In the latter case, however, a

quantitative treatment shows that the phase velocity of the waves of interest is so low that ion Landau damping prevents instability. Concentrating on the first regime, consider by way of illustration a flat tail which contains a small fraction μ of the total number of electrons and extends as far as a maximum velocity v_M:

$$F(v_\parallel) = 1/\pi^{1/2} v_M, \quad 0 < v_\parallel < v_M$$
$$= 0 \text{ otherwise} \qquad (5)$$

In the Figure, the growth rate γ/ω_p is plotted as a function of the dimensionless wavenumber coordinates ($k_\perp v_B/\Omega$, $k_\parallel v_B/\Omega$) for a distribution function as in Eq.(5) with $\mu = 0.001$, $v_M = 30 v_B$, characteristic perpendicular tail velocity $v_{T\perp} = v_B$, and $\omega_p/\Omega = 0.4$.

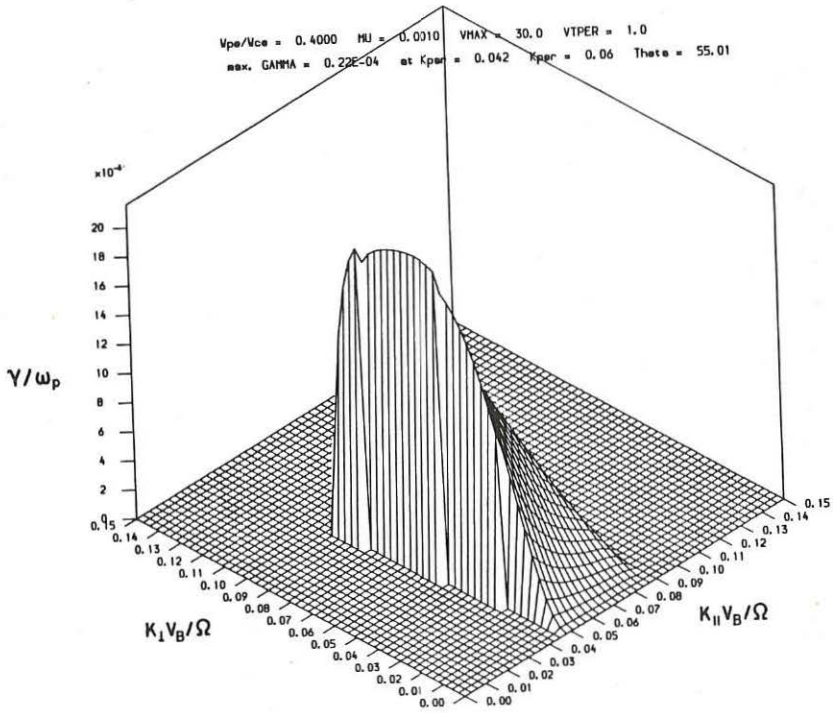

The dependence of growth rate on tail and plasma parameters has been examined numerically. For a tail fraction $\mu = 0.001$ (0.1% of electrons in the extended tail) we find that: (i) For $\omega_p/\Omega = 0.4$, instability occurs only when $v_M > 15\, v_B$. The growth rate rises to $\gamma = 2 \times 10^{-5} \omega_p$ when

$v_M = 30\ v_B$, and thereafter is insensitive to v_M. (ii) For $v_M = 20\ v_B$, $\gamma = 1.6 \times 10^{-5}\omega_p$ when $\omega_p/\Omega = 0.4$, but γ falls to zero when $\omega_p/\Omega < 0.29$. (iii) The growth rate is independent of $v_{T\perp}$. We note from Eq.(2) that the ratio of the anomalous Doppler parallel resonant velocity v_{AD} to the parallel velocity v_L at which electron Landau damping occurs is given by $v_{AD}/v_L = 1 + \Omega/\omega$. Thus, point (i) illustrates the fact that for instability to occur, the tail must extend sufficiently far for electrons to exist at v_{AD} when v_L is a few times v_B, so that Landau damping is weak. Point (ii) shows that it is possible to suppress the instability by a relatively small increase in magnetic field strength at constant density. Result (iii) holds only for a Maxwellian distribution of perpendicular velocities in the tail. If there were a plateau in the $v_\perp$-distribution in the anomalous Doppler resonant region, it is clear from Eq.(2) that the instability would be significantly affected.

Now consider the sensitivity to the choice of tail representation. A wide range of monotonically decreasing superthermal tails in the electron velocity distribution can be represented by adding $\mu F(v_\parallel)$ to the bulk thermal distribution, where

$$F(v_\parallel) = \frac{1}{\pi^{1/2} v_{T\parallel}} e^{-(v_\parallel - v_D)^2/v_{T\parallel}^2} \qquad (6)$$

The parameters (μ, v_D, $v_{T\parallel}$) can be chosen so that the tail structure has a slow, plateau-like decline , or a much steeper fall-off . In the parameter range of interest, the value of v_D is kept below $4v_B$ in order to avoid describing tails which have a bump rather than a monotonic decrease. For these distributions, it is clear that the anomalous Doppler effect can play a significant role only for those electrons for which v_{AD} is close to the characteristic drift velocity of the tail. This has two consequences. Firstly, the anomalous Doppler resonance condition can be written $k_\parallel v_D \simeq \omega_p k_\parallel/k + \Omega$ so that $k_\parallel^2 \simeq k_\parallel^2[\omega_p^2/(k_\parallel v_D - \Omega)^2 - 1]$. The requirement that $k_\parallel^2 \geq 0$ therefore gives $|k_\parallel - \Omega/v_D| \lesssim \omega_p/(\Omega/v_D)\Omega$ and under the conditions of interest, $\omega_p/\Omega \lesssim 0.5$. We conclude that for a wide range of monotonically decreasing tail formations, any unstable region in $\underline{k}$ - space must be localised around $k_\parallel = \Omega/v_D$. This conclusion applies independently of the particular region of velocity space in which Landau damping occurs. Secondly, since $v_{AD} \simeq v_D$, it follows that in general the corresponding value of v_L will be so small that it lies within the region of strong Landau damping by the bulk electron plasma. These considerations suggest that monotonically decreasing tails described by Eq.(6) are stable against the anomalous Doppler effect. This result is consistent with our numerical calculations.

1 V.L. Ginzburg, Sov. Phys. Usp. 2, 874 (1960).
2 M.V. Nezlin, Sov. Phys. Usp. 19, 946 (1976).
3 V.V. Parail and O.P. Pogutse, Sov. J. Plasma Phys. 2, 126 (1976).
4 H. Knoepfel and D.A. Spong, Nucl. Fusion 19, 785 (1979).
5 S.C. Luckhardt et al., Proc. Third Varenna-Grenoble Int. Symp. on Heating in Toroidal Plasmas, (CEC, Brussels, 1982) p.529.
6 S. von Goeler et al., Proc. Fifth APS Topical Conf. on RF Plasma Heating (University of Wisconsin, Madison, Wis., 1983) p.96.
7 S.C.Luckhardt, MIT Preprint PFC/CP-85-3 (1985).
8 B.B. Kadomtsev and O.P. Pogutse, Sov. Phys. JETP 26, 1146 (1968).

A REALISTIC MODEL FOR SUPRATHERMAL ELECTRON CYCLOTRON EMISSION AND ITS APPLICATION TO LH HEATED PLASMAS

P. Buratti, R. Lelli*, O. Tudisco

Associazione EURATOM-ENEA sulla Fusione, Centro Ricerche Energia Frascati, C.P. 65 - 00044 Frascati, Rome, Italy

INTRODUCTION

Electron cyclotron emission (ECE) measured on FT tokamak during LH heating remains at blackbody level at those frequencies for which plasma is optically thick, while optically thin frequencies are strongly enhanced if plasma density is below the density limit [1].

Enhanced ECE at $\omega = 4\,\omega_{ce}$ has been used on FT to determine the density limit and is used as well to monitor instabilities in momentum space.

Several attempts have been made to go beyond the use of suprathermal ECE as a mere monitor [2]; in this paper we describe a method developed in order to obtain quantitative information about non-maxwellian features in the electron distribution, and discuss the reliability of the obtained results.

METHOD

At least at frequencies greater than the right hand cutoff we can numerically calculate, for any given electron distribution function $f(p_{\parallel}, p_{\perp})$, absorption and emission coefficients keeping into account relativistic, finite Larmor radius and finite density effects [3], and solve the radiative transport equation. In actual experimental situations, i.e. line of sight perpendicular to magnetic field, and multiple reflections on the vacuum vessel allowed by the low optical thickness, it is not useful to try to invert the relation between $f(p_{\parallel}, p_{\perp})$ and the intensity $I(\omega, \theta)$; it is rather preferable to assume a simple model for $f(p_{\parallel}, p_{\perp})$ depending on some parameters (4 in our case), and adjust them until the computed $I(\omega, \pi/2)$ is consistent with the data.

Following current ideas on LH heating, we assumed a plateau tail distribution, i.e. a constant for $P1 < p_{\parallel}/mc < P2$, zero outside that range, and a gaussian in $p_{\perp}$, with temperature TS. P1 and P2 were assumed positive, but a counterstreaming tail would give identical results. The fourth parameter, NS, was the density, integrated on a poloidal cross-section to avoid assumptions on spatial profiles, which on the other hand are not important, since for suprathermals the inhomogeneity of magnetic field is no longer the dominant line-broadening mechanism.

In order to keep into account wall reflections, we firstly assumed partial reflection and polarization scrambling on parallel walls, adjusting the relevant coefficients on thermal spectra. In this "slab" model, the rays

that reach the detector remain perpendicular to the magnetic field, and line broadening is dominated by downshift due to relativistic electron mass increase.

The slab model is not realistic for a tokamak with corrugated walls like FT, and we developed a more realistic model, in which a total scrambling of propagation directions, as well as polarizations, was assumed. This changes the dominant line broadening mechanism from relativistic downshift to Doppler shift, which is mainly an upshift since emission is stronger in the forward direction.

This "isotropic" model requires much heavier computations, because emission has to be computed in all directions, but the agreement with experimental data is better; results from the slab model can be used to estimate the error introduced by assumptions on reflections.

RESULTS

The ECE spectrum was measured on a shot in which 150 kW of RF power at 2.45 GHz where injected with 0, π phasing on a plasma with B = 5.9 T; $\bar{n}$ = $= 4\times10^{19}$ m^{-3}, and ohmic power input 423 kW. The best values of the parameters where:

P1 = 0 ± 0.2; P2 = 2.7 ± 0.2;

TS = 22 keV; NS = 8×10^{14} m^{-1}.

The uncertainties on P1 and P2 were determined by varying the best fit value until important discrepancies appeared, whilst those on TS and NS are not indipendent: TS can be varied between 15 and 35 keV, and a good agreement with data is still obtained provided that NS·TS is kept constant.

The results of the slab model are: P1 = 0; P2 = 2; TS = 50 keV; NS = $= 1.5\times10^{14}$ m^{-1}.

The momenta of the tail distribution have been calculated and compared to the bulk ones.

Zero order momentum: the fractional number of suprathermals is 1.8×10^{-4}.

First order: assuming that no suprathermals are counterstreaming, the upper limit to suprathermal current is found to be 9%.

Second order: perpendicular β of suprathermals is 2% of the bulk one; parallel pressure is 28 times greater than perpendicular one.

We note in passing that perpendicular pressure is proportional to NS·TS, while the other quantities are affected by the uncertainty in NS.

The anisotropy of the tail can be described by the average pitch angle, which is 0.12 rad, and is likely to be consistent with collisional pitch angle scattering.

The $N_{\parallel}$ for Laundau damping at P2 is 1.07, while the accessibility con-

dition is $N_{\parallel} > 1.4$; this is probably because most of the tail ($p_{\parallel} > 0.5$ mc) is beyond the Dreicer critical speed.

Power lost by cyclotron radiation from the tail is < 200 W; the fraction reabsorbed by the bulk is about 25%.

Power P_c transferred to the bulk by Coulomb collisions is difficult to estimate because critically depends on P1 and diverges for P1 = 0; if we take $P1 = N \cdot v_{th}/c$, we find P_c = 66 kW for N = 1, and P_c = 57 kW for N = 2. For the results of the slab model P_c = 12 kW for N = 1.

CONCLUSIONS

The limits of the outlined method are essentially two: 1) no information is obtained about the spatial distribution of suprathermals; 2) the number of suprathermals is uncertain within a given model for wall reflections and is model dependent (while perpendicular pressure is fairly constant).

Significant progress in the understanding of LH waves-electrons interaction could be made in our opinion by comparing the results of our approach with data from two relatively new diagnostics: high resolution x-rays spectroscopy [4], which gives the density of suprathermals at some location, and vertical ECE measurements [5], that should give detailed information on $f(p_{\parallel}, p_{\perp})$ in a restricted energy range, and, by a scan, spatial profiles.

FOOTNOTE AND REFERENCES

* ENEA Guest

[1] F. Alladio, E. Barbato, G. Bardotti et al., Nucl. Fusion 24, 725 (1984)
[2] D.A. Boyd, , Proc. of 4th Int. Workshop on Electron Cyclotron Emission and Electron Cyclotron Resonance Heating, Rome 1984, p. 145
[3] P. Buratti, R. Lelli, O. Tudisco, M. Bornatici, Proc. of 4th Symposium on Heating in Toroidal Plasmas, Rome 1984, 1, 915
[4] R. Bartiromo, F. Bombarda, R. Giannella, Phys. Rev. 32, 531 (1985)
[5] K. Kato, I.H. Hutchinson, Phys. Rev. Lett. 56, 340 (1986).

RADIAL DIFFUSION OF PLASMA CURRENT DUE TO SECONDARY EMISSION OF ELECTROSTATIC WAVES BY TAIL ELECTRONS

Viktor K. Decyk, G.J. Morales, J.M. Dawson, and H. Abe*

University of California, Department of Physics, Los Angeles, CA 90024, USA;
*Kyoto University, Kyoto, Japan

As part of an overall program to study RF current drive, a collaborative series of simulations with Kyoto University has been undertaken to examine wave-enhanced spatial diffusion of RF generated current profiles.

In prior simulations[1,2] of relaxation of non-Maxwellian current-carrying plasmas in strong magnetic fields ($\Omega_e > \omega_{pe}$), it was observed that enhanced electric field fluctuations were associated with the evolution of the velocity distribution function.

The physical picture which developed was that "collisions" between superthermal particles involved the emission and absorption of plasma waves. Superthermal electrons emitted plasma waves and were slowed down, while slower electrons absorbed those waves and were accelerated.

Since plasma waves were not confined, it seemed reasonable that this should give rise to spatial diffusion of current in addition to the previously observed velocity diffusion.

To test this picture, an electrostatic particle simulation was set up as an initial value problem to measure current diffusion associated with plasma waves. In 2D slab geometry, an initial current channel in space was set up with electrons flowing in the direction along the magnetic field B_o, which is a periodic coordinate in the simulation (Fig. 1). The profile of the current channel was a step function in the direction perpendicular to B_o, which is a bounded coordinate in the simulation. The initial current channel is 21 electron Larmor radii ρ_e in width, compared to a width of $84\rho_e$ for the simulation region.

The initial velocity distribution inside the current channel (Fig.2a) consisted of a background Maxwellian plus a distribution of test particles with a uniform distribution along B_o, with $0 < V_\parallel < V_m$, where $V_m = 6.4\ V_{th}$. About 36% of the electrons inside the current channel were test particles. The sum of these two distributions models a "slideaway" type of distribution common in current drive plasmas. The initial perpendicular velocity distribution was Maxwellian with the same temperature as the background parallel distribution. Outside the current channel, the initial velocity distribution consisted only of the isotropic background Maxwellian. There was no external RF present in this simulation--this was a relaxation problem only.

In this 2D geometry, with $\vec{B}_o$ in the plane of simulation (defined by $\vec{E}$) one expects very little particle diffusion across B_o because all the particle drifts, e.g., $E \times B$, are in the ignorable direction. Particles can diffuse across the field only by collisions.

The simulation was carried out for $\omega_{pe}T = 2000$. At the end of this time, the current profile was indeed observed to broaden in space (Fig. 3a). The total current (volume integrated) decreased by 16%. This was due to electron-ion collisions which transferred momentum to the ions. (Total momentum was conserved to 1 part in 10^7.) As expected, the test particles do not move across the field lines, and spatial diffusion of the test particle density was completely negligible (Fig. 3b). Nonetheless, 22% of the total current was outside the initial current channel by the end of the simulation. The "3/4-width" of the current profile (defined by the interior volume, which contains 3/4 of the current), increased from 16 ρ_e to 27ρ_e. Initially, all of the current was carried by the test particles. By the end of the simulation, they carried only 31% of the total current. The rest of the current was being carried by bulk electrons.

The initial "slideaway" parallel velocity distribution inside the original current channel (for $V_\parallel > 0$) is found to relax to a half-Maxwellian (Fig. 2b). The velocity distribution with $V_\parallel < 0$ remains Maxwellian with the original temperature. The final result then is a two-temperature distribution in the parallel direction. These two half-Maxwellians come to equilibrium on a much longer time scale.

The perpendicular velocity distribution heats up, but remains Maxwellian. In the interior region, $\langle v_\perp \rangle$ increases from $\sqrt{2}\ V_{the}$ to 1.6 V_{the}. Energy conservation requires that perpendicular heating accompany parallel velocity redistribution since the final half-Maxwellian distribution has less parallel energy than the original "slideaway" distribution, even for the same momentum. (Total energy was conserved to 0.06%.)

The physical process behind this diffusion and relaxation is the excitation of non-thermal fluctuations driven by the non-thermal velocity distribution. A survey of the frequency spectrum of the electric field fluctuations for fixed $k_\parallel$ was performed. In this survey, $k_\parallel > 0$, and therefore the spectrum for $\omega > 0$ correspondes to waves traveling in the direction of electron flow and $\omega < 0$ corresponds to waves traveling in the counter direction.

The volume integrated frequency spectrum showed that waves with $\omega_{LH} < \omega < \omega_{pe}$ had about 4 times more energy than waves in the range $-\omega_{pe} < \omega < -\omega_{LH}$. These correspond to the oblique plasma waves whose dispersion is given by $\omega = \omega_{pe}k_\parallel/k$. The time evolution of these waves show no evidence of instability.

A more careful look at the spectrum revealed that for fixed $k_\parallel$, the non-thermal spectrum was confined to the range $2.5\ k_\parallel V_{th} < \omega < k_\parallel V_m$. Displaying the electric field spectrum as a function of phase velocity (Fig. 4), obtained by summing the frequency contributions of each $k_\parallel$, revealed that the enhanced waves all had parallel phase velocities corresponding to particle velocities in the non-Maxwellian part of the velocity distribution, $2.5\ V_{the} < \omega/k_\parallel < V_m$.

The energy as a function of $k_\parallel$ showed a broad range of $k_\parallel$ excited, with a gentle peak at $k_\parallel\rho_e \sim .1$, and $k_\perp \sim k_\parallel$.

The conclusion is that secondary emission of energetic non-Maxwellian plasmas can cause substantial current diffusion across the magnetic field.

Work is being done to determine if this process can be described by the Balescu-Lenard equation.

References:

1. V.K. Decyk, G.J. Morales and J.M. Dawson, Proc. IAEA Technical Committee Meeting on Non-Inductive Current Drive in Tokamaks, Culham Laboratory, Abingdon, United Kingdon, 1983, Vol. I, p. 190.

2. V.K. Decyk and J.M. Dawson, Proc. 4th International Symposium on Heating in Toroidal Plasmas, Rome, Italy, 1984, International School of Plasma Physics (Varenna), Vol. II, p. 1327.

Acknowledgments:

This work is supported by USDOE and JIFT. The simulations were carried out on the UCLA CHI computer.

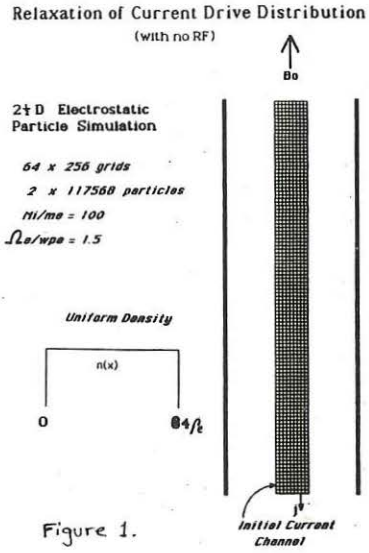

Figure 1.

Fig. 1 Geometry of 2D particle simulation of relaxation of initial current channel imbedded in uniform density, magnetized plasma.

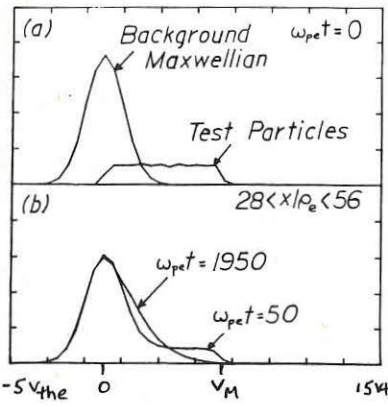

Fig. 2(a) Initial parallel velocity distribution of electrons inside the current channel consists of a background Maxwellian plus a uniformly distributed ($0 < V_\parallel < V_m$) set of test particles; (b) Evolution of parallel electron velocity distribution inside current channel shows relaxation of initial "slideaway" distribution into a half-Maxwellian for $V_\parallel > 0$, and no change from the initial Maxwellian for $V_\parallel < 0$.

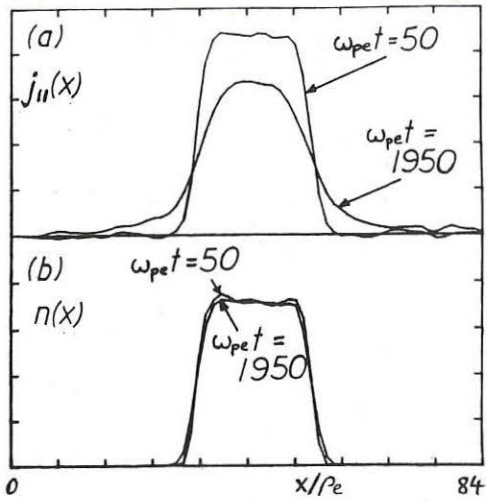

Fig. 3 (a) Initial and final parallel current profile shows substantial widening of current channel across the magnetic field; (b) Initial and final test particle density shows virtually no diffusion of test particles across the magnetic field.

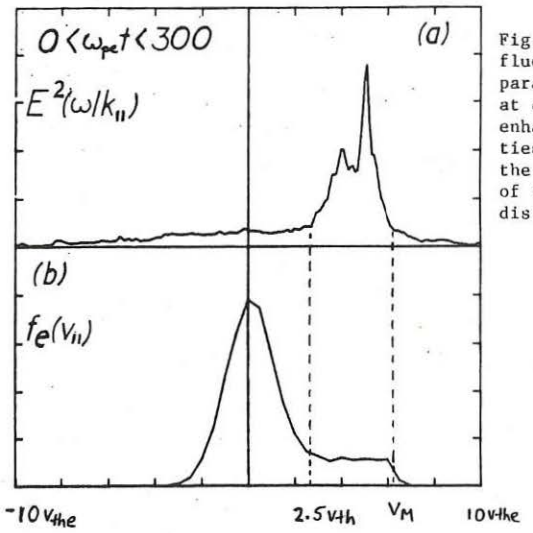

Fig. 4 Electric field fluctuation energy versus parallel phase velocity at eary times (a) shows enhancement for velocities corresponding to the non-Maxwellian part of the velocity distribution.

POWER AMPLIFICATION FACTOR ON LOWER-HYBRID WAVES DRIVEN TOKAMAKS

G. TONON

ASSOCIATION EURATOM-C.E.A. - Département de Recherches sur la Fusion Contrôlée - C.E.N.G. - 85X - 38041 GRENOBLE Cedex (France)

As shown by many studies /1/, a continuous operation is an attractive alternative for Tokamaks. Up to now, only RF waves, for which frequency is close to the lower hybrid frequency have led to a significative efficiency up to electron densities around 10^{20} e.m^{-3}. For a continuous operation of a Tokamak, the circulating power must be not too large and consequently the plasma power amplification factor Q_p has to be high enough. According to a model which determines the current drive efficiency when we consider the injection of slow-waves on the torus, in good agreement with the results of recent current drive experiments /2/ /3/, we have determined the Q_p values achievable with this type of waves.

1 POWER BALANCE MODEL

We assume an idealized Tokamak reactor driven by low hybrid waves, the power flow diagram of which is shown on fig. 1. The plasma amplification factor Q_p is given by :

$$(1) \qquad Q_p = (P_{FN} + P_{F\alpha}) / P_{HFT}$$

where P_{FN} is the neutron power, $P_{F\alpha}$ the power released by α-particle and P_{HFT} represents the HF injected power on the torus. If P_{HFK} is the power delivered by the generator (klystrons), we have :

$$(2) \qquad P_{HFT} = (1 - \bar{R}) \cdot \tau \cdot P_{HFK}$$

where τ and $\bar{R}$ are the transmission efficiency of the HF line and the coupling structure and the mean reflection coefficient of the plasma load respectively. The neutron power P_{FN} goes into the blanket and is assumed to be multiplied by additional nuclear reactions : M_B represents the blanket multiplication factor. Both the output power from the blanket, the charged particles power and the HF power are converted into electricity by a thermal converter of an efficiency η_T. When P_{EG} is the gross electrical power and P_{EC} the circulating power, we can define a device amplification factor $\mathcal{A}$ given by :

$$(3) \qquad \mathcal{A} = P_{EG} / P_{EC}$$

The minimum value of the amplification factor $\mathcal{A}$ is only limited by capital costs /4/. Typically, it seems necessary that $\mathcal{A} > 4$ to 5. From (1), (2) and (3), we obtain, using the power flow diagram shown on fig. 1 :

$$(4) \quad \mathcal{A} = \eta_T \eta_K \left[1+(1-\bar{R})\tau Q_p \frac{(h+M_B)}{h+1}\right] / \left[1+\eta_A \eta_T \eta_K \left\{(1+(1-\bar{R})\tau Q_p \frac{(h+M_B)}{h+1}\right\}\right]$$

where η_K is the efficiency of the klystron, $h=P_{F\alpha}/P_{FN} = 1/4$ for DT plasmas and η_A represents the fraction of the gross electrical power used for auxiliary needs. We have plotted on fig. 2 the variation of device amplification factor $\mathcal{A}$ as a function of Q_p for different values of the klystron efficiency η_K. Fig. 2 refers to STARFIRE values (η_T=0.36 M_B=1.23 η_A=0.073) and we consider that $(1-\bar{R})\tau = 0.8$. Typically, conventional klystrons achieve $\eta_K \sim$ 0.6 /5/ and it is possible to reach $\eta_K \sim$0.7 to 0.75 using depressed collectors /6/. From fig. 2, we see that it seems possible to reach $\mathcal{A} \simeq 4$ if the plasma power amplification factor lies between 20 and 25.

It is possible to decrease these Q_p values using advanced concepts in order to : (i) maximase the blanket multipliaction factor M_B /7/; (ii) increase the thermal efficiency η_T using high temperature cycles : $\eta_T \sim$0.55 to 0.6 are possible in this case /8/. We have plotted on fig. 3 the variation

of Q_p as a function of the thermal cycle efficiency η_T for $\mathcal{M}$ = 4 and 5. In this case, η_K = 0.7 and M_B = 1.5. We see that, using advanced high temperature cycles, useful device amplificator factors can be achieved with $Q_p \sim 10$ to 20.

2 CURRENT GENERATION WITH LOW-HYBRID WAVES

The current drive generation model is described on ref. /2/ and /3/. We use the KARNEY and FISCH calculations /9/ on the current drive efficiency $\eta_{CD} = \langle n_e \rangle . I_p . R / P_{HFT}$ with the following plasma profiles (x=r/a) :

$$(5) \quad n_e = \hat{n}_e (1-x^2)^{\gamma_n} \quad \text{and} \quad T = \hat{T} (1-x^2)^{\gamma_t} = T_e = T_i$$

In order to avoid interaction with the ionic population of the plasma /10/, the wave frequency has to be chosen in the range of 3 to 4 GHz. We have plotted on the fig. 4 the variation of η_{CD} as a function of the mean plasma density $\langle n_e \rangle$, calculated with f = 3,3 GHz, Z_{eff} = 1.3 and B_T = 6 T (toroïdal magnetic field value on plasma axis). At this frequency, the optimized value of the geometrical periodicity Δ of the coupling structure /2/ is Δ = 1.3 cm and we use 32 waveguides along the toroïdal magnetic field. We see on the fig. 4 that η_{CD} decreases with $\langle n_e \rangle$ due to the wave accessibility condition /2/ /3/. From our numerical simulations, we obtain the following analytical relation between the HF injected power P_{HFT} and the driven current I_p :

$$(6) \quad P^p_{HFT} = 3.33\,(5+Z_{eff})\,(1+\gamma_n)^{4/3} \cdot R\, I_p \langle n_e \rangle^{3/2} B_T^{-1} F(T)^{-1} \qquad (MW, MA, m, 10^{20} m^{-3}, Tesla)$$

The factor F(T) takes into account advantageous relativistic effects at high plasma temperature /11/ and we use the approximate form /12/ :

$$(7) \quad F(T) = 1 + 0{,}46 \langle T \rangle \qquad (10 \text{ KeV})$$

3 PLASMA POWER AMPLIFICATION FACTOR

By using the D.T. cross-section given by :

$$(8) \quad \langle \sigma v \rangle_{DT} = 1.15.10^{-22} . T^2 \qquad (m^3/s,\ 10 \text{ KeV})$$

we obtain :

$$(9) \quad P_{FN}+P_{F\alpha} = 0.71 \langle n_e \rangle^2 \langle T \rangle^2 \cdot V_p Z_p^{-2} \cdot \Gamma_F$$

where : plasma volume $V_p = 2\pi^2 R.a^2.K$(K = b/a = ellipticity); mean plasma charge $Z_p = \langle n_e \rangle / \langle n_i \rangle^p$; profile factor $\Gamma_F = (1+\gamma_n+\gamma_t)^2 / (1+2(\gamma_n+\gamma_t))$.

From (1), (6) and (9), we have (Z_p = 1.25, Z_{eff} = 1.3, γ_n = 0.25, γ_t=2) :

$$(10) \quad Q_p = 0.68 \langle n_e \rangle^{1/2} . a^2.K\, B_T \langle T \rangle^2 (1+0{,}46\langle T \rangle)\, I_p^{-1}$$

Using the Trayon-Wesson beta limit :

$$(11) \quad \beta_t = 0.035 . I_p / a\, B_T$$

with $\langle T \rangle$ = 20 KeV and :

$$(12) \quad q_I = 5a^2 B_T (1+K^2) / 2 R I_p$$

which leads to :

$$(13) \quad Q_p = 0.52\,(A\, q_I)^{1/2} \cdot K\,(1+K^2)^{-1/2} \cdot a.B_T \qquad (A=R/a)$$

We have plotted on fig. 5 the evolution of Q_p as a function of $(a.B_T)$ for various values of K and Aq_I. We see that in order to reach $Q_p \sim 20$, it is necessary to keep $(a.B_T) > 10$ m.Tesla.

In order to achieve a stationnary state, it is important that the burn margin defined as :

$$(14) \quad \mathcal{M}_B = (P_{F\alpha} + \mu_{ABS} \cdot P_{HFT}) / P_{loss}$$

is greater than one. On the relation (14), μ_{ABS} represents the fraction of the injected HF power which is absorbed by the plasma and :

$$(15) \qquad P_{loss} = 3/2 \langle n_e \rangle \langle T \rangle \ (1+1/Z_p) \ . \ V_p \ . \ \tau_E^{-1}$$

where τ_E is the global energy confinement time. We have plotted on the fig. 6 the evolution of the burn margin as a function of $(a.B_T)$ using the ASDEX-H mode scaling for τ_E /13/. We see that M_B is always higher than one.

4 CONCLUSION

In order to obtain high values of Q_p, we have to optimize different parameters of the plasma and machine such as :

(i) to operate the machine at high plasma temperature (~20 KeV) and moderate density ($<10^{20}$ e.m^{-3})

(ii) to keep $(a.B_T) >$ 10m Tesla.

If these conditions can be satisfied, then it is possible to obtain values of Q_p higher than 20 which are likely acceptable for a continuous Tokamak operation.

/1/ D.A. EHST et al. - Fusion Technology Vol. 8 July 1985 p. 727

/2/ G. TONON - Plasma Physics and Controlled Fusion Vol. 26 N°1A January 1984 p. 145

/3/ G. TONON - International School of Fusion Technology - Erice - Sicily- July 1985 - Proceedings to be published by Plenum Press

/4/ P.A. DAVENPORT - Nuclear Fusion 18,3 (1978) p. 420

/5/ C. BASTIEN, G. FAILLON and M. SIMON - Int. Electron Devices Meeting - Dec. 1982 - p. 190 - IEEE

/6/ W. NEUGEBAUER and T.G. MIHRAN - IEEE Trans. on Electron Devices - Vol. ED. 19 N°1 Jan. 1972 p. 111

/7/ E. GREENSPAN, A. KINROT and P. LEVIN - Fusion Technology Vol. 8 July 1985 p. 619

/8/ J.L. USHER et al. - Proceedings of the eleventh Symp. on Fusion Tech. Oxford, UK - 1980 Vol. I p. 217

/9/ C.F.F. KARNEY and N.J. FISCH - Phys. of Fluids - 22 (1979) p. 1817

/10/ J.G. WEGROVE, G. TONON - 5th Top. Conf. on RF Heating - Madison, USA (1983)

/11/ C.F.F. KARNEY and N.J. FISCH - Phys. Fluids 28-1 - January 1985 p. 116

/12/ C.D. HENNING et al. - Fusion Tech. - Vol. 8 July 1985 p. 1351

/13/ O. GRUBER - Int. Conf. on Plasma Physics - Lausanne 1984 Vol. I p. 67

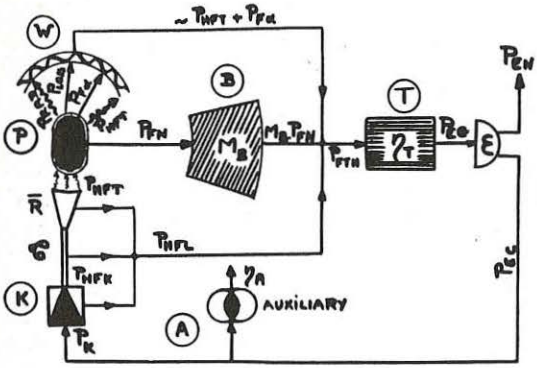

Fig. 1 - Power flow diagram :

P) - Plasma
W) - Wall and shield
B) - Blanket
T) - Thermal converter
A) - Auxiliary : magnets, cryogenics pumping...
K) - HF generator : Klystrons, transmission line, antenna.

Fig. 2 - Device amplification factor as a function of Q_p

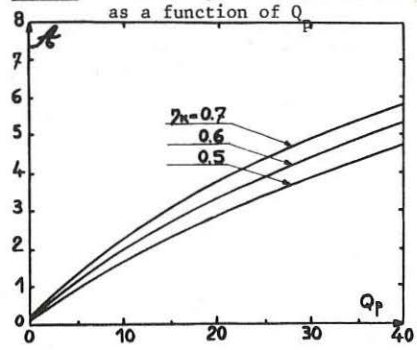

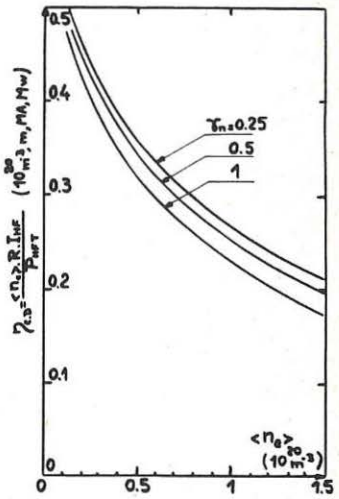

Fig. 4 - Calculated current drive efficiency η_{CD} as a function of the mean electron density

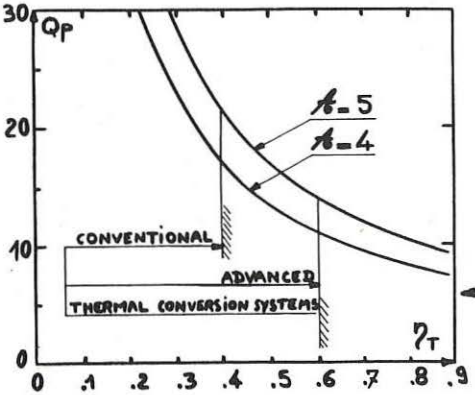

Fig. 3 - Plasma amplification factor Q_p as a function of the thermal efficiency η_T

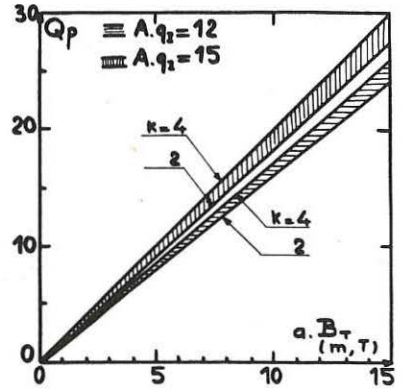

Fig. 5 - Plasma amplification factor Q_p achieved as a function of $(a.B_T)$

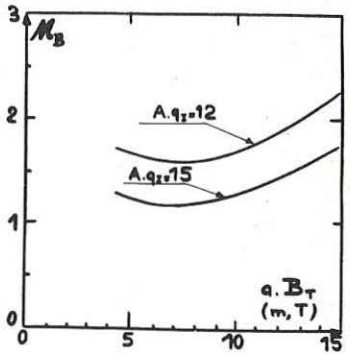

Fig. 6 - Burn margin M_B as a function of $(a.B_T)$

STUDY OF PARAMETRIC INSTABILITIES IN THE FT LOWER HYBRID EXPERIMENT

R. Cesario, V. Pericoli Ridolfini

Associazione EURATOM-ENEA sulla Fusione, Centro Ricerche Energia Frascati, C.P. 65 - 00044 Frascati, Rome (Italy)

INTRODUCTION

The interaction of 2.45 GHz radiofrequency power with the FT plasma at different line averaged densities $\bar{n}$ can be well summarized distinguishing three main density ranges as reported in Fig. 4 of Ref. [1].

The low density regime ($\bar{n} \lesssim 5\cdot10^{13}$ cm^{-3}) shows strong RF-electron interaction. In the intermediate regime ($5\cdot10^{13} \lesssim \bar{n} \lesssim 1.1\cdot10^{14}$) the interaction of RF switches to ions in the plasma periphery, while in the third regime $\bar{n} > 1.1\cdot10^{14}$ cm^{-3} strong parametric decay instabilities (PDI) develop and a large broadening of the pump is observed [2,6].

Many authors have emphasized the importance of parametric instabilities in reducing the efficiency both in lower hybrid heating and current drive experiments in the high densities regimes [3,4,5]

2. MODEL ANALYSIS

In the study of the parametric instabilities occurring in the FT high density regime we have utilized the model described in Ref.[7] for the evaluation of the threshold power for the decay of a LH pump into a LH sideband plus an ion cyclotron quasi mode strongly damped on ions. We limited our study to this channel since the threshold power of a decay involving a quasi mode shows a strong dependence on the pump amplitude [7,8]. The following relationships hold: $\omega_{ci} \ll \omega_o$, $\omega_1 \ll \omega_{ce}$; $\omega_o \gg k_{oz}\cdot v_{th,e}$, $k_{o\perp} v_{th,i}$, and the same for ω_1; $\omega_2 = \omega_o - \omega_1$; $k_2 = k_o - k_1$; $\omega_2 \sim \omega_{ci}$; $\omega_2 - \omega_{ci} \sim k_{2z} v_{th,i}$; $k_{o,1\perp}\rho_{L\,i} > 1$; $k_{o,1\perp}\rho_{L\,e} \ll 1$ where the subscripts 0,1,2 refer to the pump, sideband and low frequency wave respectively and the other symbols have their usual meaning. If we assume for the pump wavevector: $|\vec{k}_o| \ll |\vec{k}_{1,2}|$ and for the plasma density: $\omega_{LH} \lesssim \omega_o/2$ it follows: $\omega_2/k_{2z} \lesssim v_{the}$; $k_{2\perp}\rho_{Li} \gtrsim 1$, that is the electron response to the low frequency field is adiabatic. This condition makes negligible the ion nonlinearities with respect to the electron ones in driving the decay processes, even if the low frequency quasi mode is strongly damped on ions, the effects of ion absorption being contained in the linear ion susceptibility [9].

The assumption $|\vec{k}_o| \ll |\vec{k}_{1,2}|$ is not an important constraint to the model validity, but it allows us to use simpler mathematical formulas. On the other hand many interesting cases verify the above inequality, as we checked with an a posteriori control.

The amplification factor for the instability is given by [7]

$$A = \frac{0.54\ k_{1_z}\ L_{0_z}}{12(\omega_o^2/\omega_{LH}^2 - 1)}\ \frac{u^2}{c_s^2}\ \frac{\omega_2}{\omega_2-\omega_{ci}} \cdot I_1(b_i)e^{-bi} \cdot$$

$$\cdot\ [(1 + \frac{T_i}{T_e} - I_o(b_i)\ e^{-bi} - 0.35\ \frac{\omega_2}{\omega_2-\omega_{ci}}\ I_1(b_i)\ e^{-bi})^2 +$$

$$+\ 0.29\ (\frac{\omega_2 I_1(bi)}{\omega_2-\omega_{ci}}\ e^{-bi})^2]^{-1}$$

where the convective losses, due to finite pump extent, are considered as the principal loss mechanism. L_{oz} is the width of the RF grill mouth; u is the drift velocity cE/B; c_s the sound velocity = $\sqrt{(T_e+T_i)/m_i}$; $b_i = k_1^2\ \rho_{Li}^2/2$ and I_o, I_1 are the modified Bessel functions.

The threshold power is assumed as soon as A > 1.

3. RESULTS OF THE CALCULATIONS AND COMPARISON WITH EXPERIMENT

For the calculations the following profiles for the FT plasma temperature and density are assumed:

$$n_e(r) = n_{eo}(1-\alpha_n r^2/a_L^2)$$

$$T_e(r) = T_{eo}(1 - \alpha_T\ r^2/a_L^2)^{2.5}$$

where n_{eo}, T_{eo} are the peak density and temperature, a_L is the limiter radius = 20 cm and α_n, α_T are adjusted to match the values imposed at the limiter radius, n_L and T_L, which are estimated on the basis of Langumir probes measurements reported in [10]. In particular we want to emphasize that the density at the limiter radius is determined by both the plasma current I_p and the line averaged density $\bar{n}$. In Fig. 1 the graph of the estimated threshold powers as a function of the normalized plasma radius for various fixed line density values and I_p = 400 kA is reported. The minimum of the curves occurs always near the limiter radius and rapidly falls down for $\bar{n} > 10^{14}$ cm^{-3}. In Fig. 2 the calculated and measured pump power thresholds versus $\bar{n}$ at fixed I_p = 400 kA are shown. The agreement is quite good.

The variation of the threshold line density n_{th} with the plasma current, for an injected RF power ~ 100 kW, is presented in Fig. 3. Both experimental data and calculated points are shown. Again the model agrees rather well with the experiment.

CONCLUSIONS AND COMMENTS

The decay channel taken into account can satisfactorly explain many experimental findings concerning the development of the parametric instabilities, despite the many hypotesis involved. Thus it can be regarded as the main responsible of the observed decay process.

In particular it characterizes the decay as an edge plasma phenomenon, as experimentally found [2], emphasizing the importance of understanding the behaviour of the plasma border, especially when the plasma current is changed.

It remains however to explain the characteristic shape of the higher harmonics peaks envelope (see Fig. 2a of [2]) not possible in the present simple framework.

In the near future an attempt in this direction will be made, together with calculations on the possible mechanisms responsible of the pump spectral broadening, namely on multiple scattering processes and parametric decays involving ion acoustic waves.

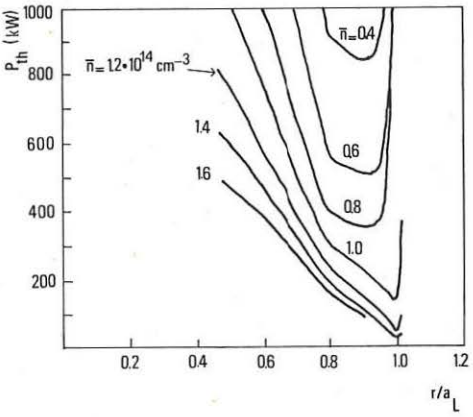

Fig. 1 Calculated threshold powers versus the ratio of minor to limiter radius, for selected line averaged densities.

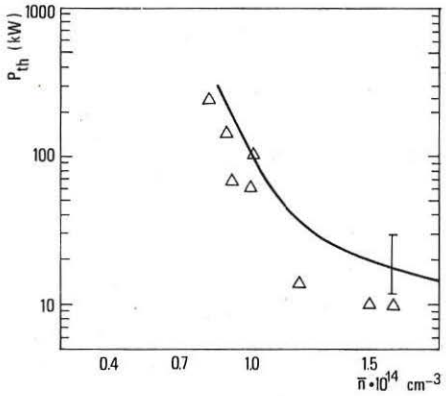

Fig. 2 Calculated (continous curve) and measured (triangles) threshold powers versus the line density.

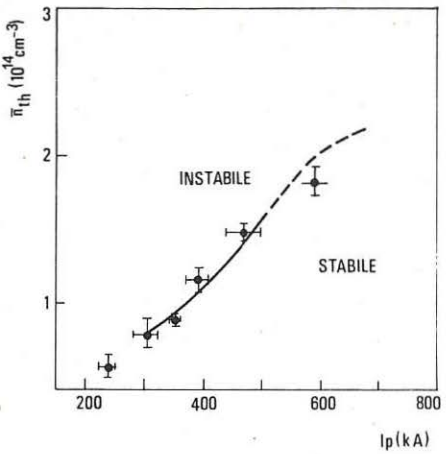

Fig. 3 Comparison of the calculated (continous curve) and experimental (dots) scaling law of the threshold density with the plasma current.

REFERENCES

[1] F. Alladio and the FT Group, Nucl. Fusion 25, 9, 1069 (1985)
[2] R. Cesario and V.Pericoli-Ridolfini, Proc. 12th European Conference on Controlled Fusion and Plasma Physics, Budapest, II, 220 (1985)
[3] M. Porkolab, Nucl. Fusion 18, 367 (1978)
[4] W. Hooke, Plasma Phys. Controlled Fusion 26, 133 (1984)
[5] F. Alladio et al., Proc. 11th European Conference, Aachen, 7D, 1, 281 (1983)
[6] R. Cesario and V. Pericoli Ridolfini, Proc. 4th International Symposium on Heating in Toroidal Plasmas, Rome, I, 704 (1984)
[7] C.S. Liu, V.K. Tripathi and V.S. Chan, Phys. Fluids 27, 7, 1709 (1984)
[8] Y. Takase, M. Porkolab, Phys. Fluids 26 2992 (1983)
[9] V.K. Tripathi, C.S. Liu and C. Grebogi, Phys. Fluids 22, 2, 301 (1979)
[10] V. Pericoli-Ridolfini, Plasma Physics and Controlled Fusion, 27, 4, 493 (1985)

SCRAPE - OFF LAYER AND COUPLING STUDIES WITH THE 3.7 GHz 18-WAVEGUIDE MULTIJUNCTION GRILL ON PETULA

M. Goniche - C. David - G. Tonon - G. Rey - P. Briand -
RF and PETULA Groups

ASSOCIATION EURATOM-C.E.A. - Département de Recherches sur la Fusion Contrôlée - C.E.N.G. - 85X - 38041 GRENOBLE Cedex (France)

A 500 kW-30 ms-3.7 GHz L.H. experiment has been operated on Petula in order to test the physical and technical options taken for the Lower Hybrid system of TORE SUPRA. The antenna used to launch the wave to the plasma is a modular 18-waveguide grill using mainly the multijunction effect /1/ (description in friend paper n° 220). This provides a great simplification of the antenna, but the 6 waveguides of a module are tightly RF coupled.

This paper presents the RF behaviour of such an antenna : self-matching properties of the multijunction, plasma R.F. wave coupling. These studies have been supported by scrape-off layer density measurements before and during the RF pulses.

1 SCRAPE-OFF LAYER DENSITY MEASUREMENTS BEFORE AND DURING THE RF PULSES

The scrape-off layer density was measured by 3 movable 4 mm microwave interferometers scanning radially from r = 145 mm to r = 210 mm (the rail limiter is at r = 165 mm). These interferometers are toroïdally set up at 120° away from the grill.

1.1 Modification of the scrape-off layer density by the RF :

The averaged edge density $\bar{n}_{eg}$ was plotted versus the averaged central line density $\bar{n}_o$ with a 200 KW RF power (fig. 1). Depending upon the core

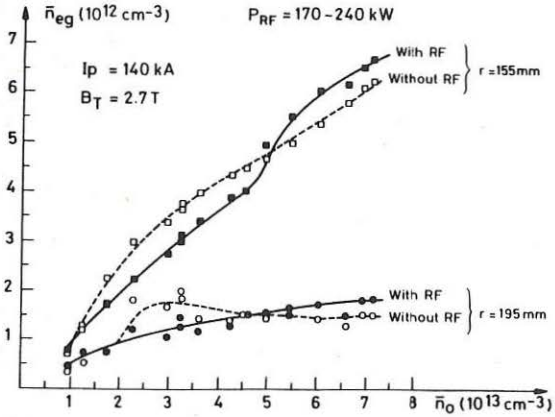

Figure 1
Edge density $\bar{n}_{eg}$ versus central density $\bar{n}_o$

plasma density $\bar{n}_o$, $\bar{n}_{eg}$ is decreased or increased by the RF wave. The threshold density is found to be $n_{th} \simeq 5 \times 10^{13}$ cm^{-3}. At 400 KW, similar results are found with a threshold density of 3×10^{13} cm^{-3}. When the RF is on, the variation in the edge density is quite rapid, of the order of 10 ms. No significant change due to the average value of $N_{//}$ was observed. For $n < n_{th}$, these results are consistant with a peaked density profile as measured by reflectometry indicating an increase of the particle confinement time /2/. The decrease of H_β signal and gas injection during RF confirm this result. At very high density ($n_o > 8 \times 10^{13}$ cm^{-3} at 400 KW), when approaching the density limit /3/, a third regime is established where the edge density is again decreased by the RF.

1.2 Scrape-off density profile for 2 central plasma densities :

In order to obtain the density in the grill region ($190 \leqslant r \leqslant 225$), scrape-off density profiles were measured at 2 densities n_o under and above the threshold, respectively 3.8 (fig. 2) and 5.7×10^{13} cm^{-3} (fig. 3) with $P_{RF} \simeq 160$ KW. These results confirm the existence of 2 regimes through the whole scrape-off layer. We found an exponential decay of the density

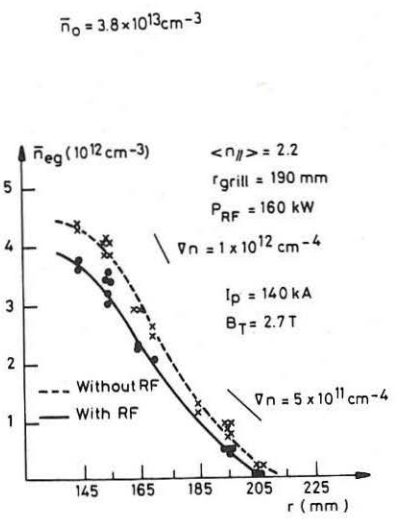

Figure 2

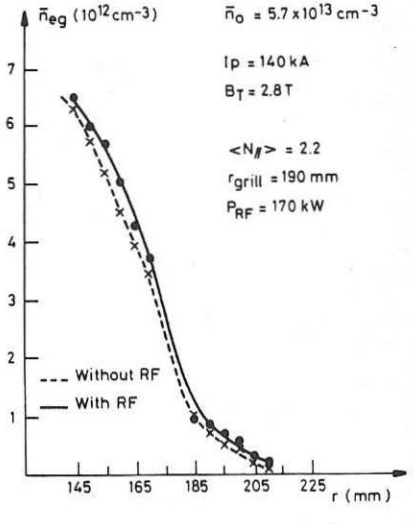

Figure 3

Scrape-off density profiles

to the wall as expected from a model assuming a perpendicular diffusion of particles to the wall. The e-fold decrease length $L_\perp$ is around 20 mm at 3.8×10^{13} cm^{-3} and 15 mm at 5.7×10^{13} cm^{-3}. This length of decay $L_\perp$ is not significantly affected by the RF. By computing $\int n_e \, dl$ with $n_e = n_o \exp(-r/L_\perp)$, local density n(r) was obtained for the 2 densities (fig. 4) in the grill region. We found a very weak influence of the grill mouth position ($190 \leqslant r \leqslant 220$) on the scrape-off layer density.

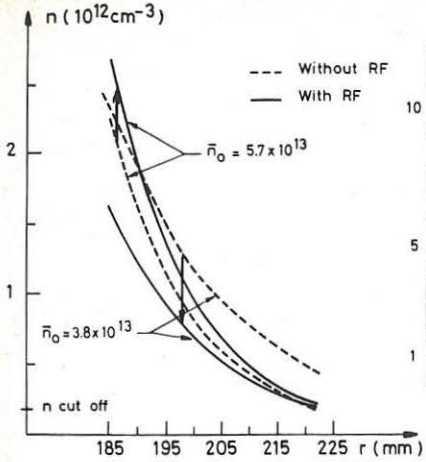

Figure 4 - Local density profiles

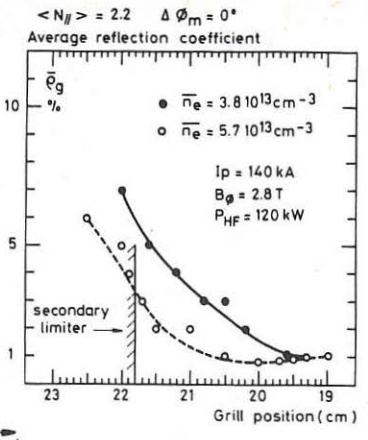

Figure 5 - Effect of n_e on the coupling

2 COUPLING STUDIES

The coupling has been studied as a function of the core plasma density, the grill position and the RF power. The average reflection coefficient, $\bar{\rho}_g$, is the mean of the 3 module reflection coefficients /4/. There is no effect of the RF power on the coupling of this multijunction grill up to 500 KW.

2.1 Effect of the core plasma density-Comparison with coupling theory :

The figure 5 shows the coupling curves obtained when the grill is moved toward the plasma for the 2 densities : 3.8 and 5.7×10^{13} cm^{-3}. As predicted by coupling theory /5/, the multijunction grill has a very low power reflection coefficient : 1%. Moreover, there is a very good agreement with the scrape-off density profiles presented in fig. 4 :

- the predicted optimum coupling density is :
$$n_{opt} = n_{cut\text{-}off} \times \langle N_{//} \rangle^2 = 8.2\ 10^{11}\ cm^{-3}.$$
This grill mouth density is effectively reached for a grill radius r=203 mm at $\bar{n}_o$=5.7 and for r=197 mm at $3.8\ 10^{13}$ (fig. 4). These radii are in good quantitative agreement with the optimum matching grill positions (fig. 5)
- At $N_{//}$=2.2, this agreement between the coupling numerical code /5/ and the experimental points is still good in a large range of grill mouth density (fig. 6).

In the high density regime ($\bar{n}_o = 9\ 10^{13}\ cm^{-3}$), it has been necessary to move the grill back in order to obtain the best matching. This has been correlated to a higher scrape-off density.

2.2 Effect of the phasing, ΔØm, between modules :

The refractive index, $N_{//}$, of the launched wave can be changed by adjusting $\Delta Øm$ /4/. The fig. 6 shows the computed degradation of the coupling for $\Delta Øm = \pm 90°$. The experiments (fig. 6 and 7) have qualitatively verified this

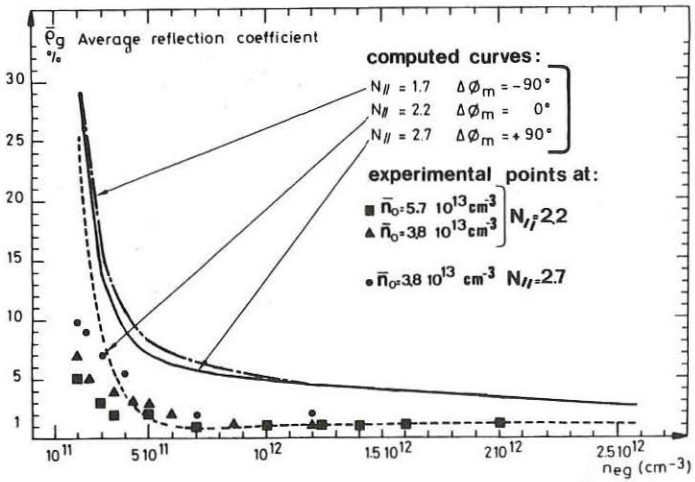

Figure 6 - Effect of the grill mouth density on $\bar{\rho}_g$ point.

Without circulators, klystrons can give their full performance only if the reflection coefficient is lower than 3%. In such conditions, the achievable range of $N_{//}$ is limited by this coupling degradation with increasing $\Delta\phi$m.

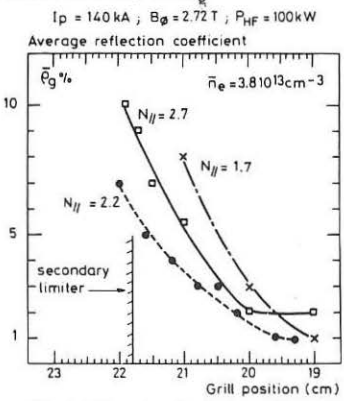

Effect of the refractive index on the grill coupling. Figure 7

3 CONCLUSION

Both the values of the reflection coefficients and of the optimum coupling density at the grill mouth have been found to be in good agreement with the data obtained from coupling theories. The multijunction effect does indeed provide a very low global reflection coefficient : 1% for the optimum grill position. This very important point gives a 10% increase of the injected RF power and can avoid the use of power circulators generally required to protect the klystrons against reflected power.

4 REFERENCES

/1/ D. MOREAU, T.K. NGUYEN - Proc. Int. Conf. on Plasma Phys. (Lausanne) : Contr. paper P17-1, Vol. 1, 216 (1984)
/2/ G. ICHTCHENKO - This Conf. paper n° 215
/3/ C. GORMEZANO et al. - This Conf. paper n° 217
/4/ G. REY et al. - This Conf. paper n° 220
/5/ D. MOREAU et al. - Report EUR-CEA-FC-1199 (9-83)

SATURATION AND CONDUCTION STUDIES IN NON-INDUCTIVE TOKAMAK DISCHARGES VIA E.C.E RADIATION MEASUREMENTS

A.Girard , J.M Rax & Petula group

ASSOCIATION EURATOM-C.E.A D.R.F.C/S.I.G

C.E.N.G - 85 X _ 38041 GRENOBLE Cedex (FRANCE)

Introduction and summary

L.H.C.D experiments on the Petula B tokamak have already shown strong modifications of the plasma behaviour when a fast electron population is sustained by L.H waves .The main response of the plasma to the absorbed power is the current but various other responses can be analyzed .This paper reports an experimental and theoretical study on the use of the Electron.Cyclotron.Emission as a diagnostic for the absorbed H.F power .The current , the conduction and the saturation of the absorption are observed and interpreted.

Link between the E.C.E and the L.H power

Recent experimental /1/ and theoretical /2/3/ studies have shown that the E.C.E is a highly sensitive diagnostic of the fast electron population .The modification of the electron distribution is a linear functionnal K of the absorbed power W(**p**) :

$$\delta F(\mathbf{p}) = \int d\mathbf{p}' \; K(\mathbf{p},\mathbf{p}') \; W(\mathbf{p}')$$

Therefore R.F induced optical properties like the cyclotron emissivity $j_{e.c.e}$ and electrical properties like the D.C conductivity σ are also linear functionnals of this power :

$$j_{e.c.e} = \int dp'\ j(p')\ W(p') \qquad , \qquad \sigma = \int dp'\ \Sigma(p')\ W(p')$$

The response functions $j(p')$ and $\Sigma(p')$ can be derived in the whole momentum space /3/ ; this involves different approximation in the three zones defined in Fig -1-

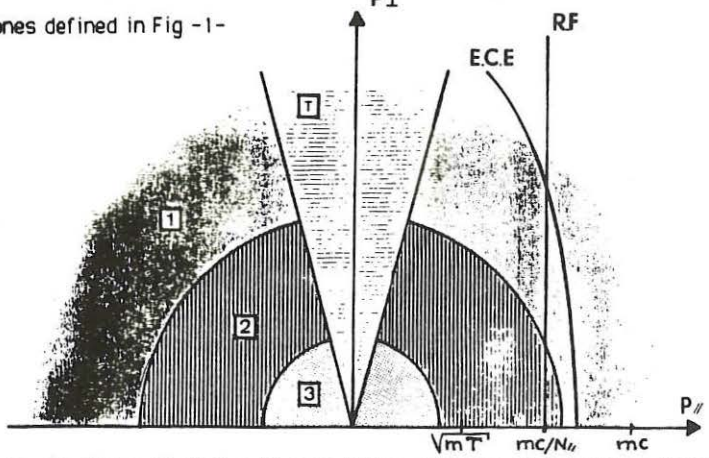

Following the method of reference /4/ an estimate of the conversion factor between the E.C.E power and the L.H absorbed power is given by :

$$W_{e.c.e}/W_{l.h} = e^2\omega_c{}^2(3mc^3\omega_s)^{-1}\partial_{\gamma}\left[(\gamma^2-1)^{5/2}(1-\mu^2)\gamma^{-1}(Z+1+\gamma)^{-1}\right]\left[\partial_{\gamma}\gamma\right]^{-1}_{p_{//}=N_{//}}$$

ω_c is the cyclotron frequency, ω_s is the (light velocity) collision frequency

A more rigorous analysis can be found in ref 2&3.

Experimental set-up

The far infrared radiation(50-800 GHz) is measured by a liquid helium cooled InSb detector (QMC) via a 70 mm diameter wedg ed quartz window and an oversized (50 mm diameter) waveguide. The emission spectrum is investigated with a Martin-Puplett type interferometer already described in

ref 5. This system gives a maximum resolution of 3 GHz and provides a spectrum every ten milliseconds.The whole diagnostic has been absolutely calibrated using a lock-in amplifier and two sources at room temperature and liquid nitrogen temperature.

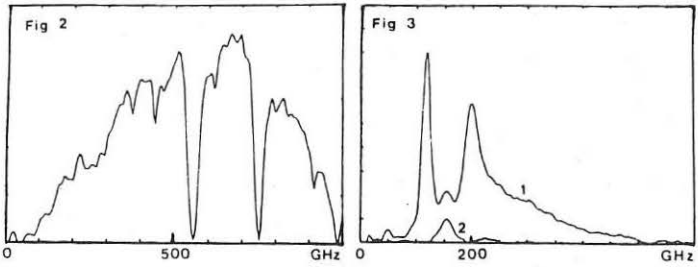

Figure 2 shows the obtained calibration spectrum ,and Fig 3 a typical current-drive discharge spectrum(1) ; a thermal spectrum is also plotted (2). In order to have an estimate of the total cyclotron radiated power,we integrate this spectrum over frequency and over the plasma surface , assuming isotropic radiation (because of the reflections on the vacuum vessel). We found nearly 50 W radiated over optically thin harmonics for P_{rf}=100kW and $\bar{n}_e$= 3 10^{13} cm-3 .

Saturation and conduction studies

It has been able to investigate many density regimes because of the high frequency (3,7 GHz) of the R.F wave .Figure 4 shows the E.C.E signals versus increasing incident H.F power at three densities $3<\bar{n}_e<6\ 10^{13}$ cm $^{-3}$. Below this density range the discharge is runaway dominated ; above this range H.F has little effect due to the lack of H.F power .The saturation of

the absorbed power is a clear experimental evidence and is in agreement with the theoretical estimations /2/3/6/ .The absorbed power thus derived allows us to verify the proposed equation for the current /3/4/6/7/8/. For example at $3.\ 10^{13}\ cm^{-3}$,the set of experimental data can be fitted by the following equation of state :

$$I_{p[kA]} = 1.7\ P_{a[KW]} + 1.7^2\ V_{p[V]}\ P_{a[KW]} \qquad (\text{if } P_{h.f} > 100\ kw)$$

in agreement with theory /3/4/6/7/8/

Fig 4

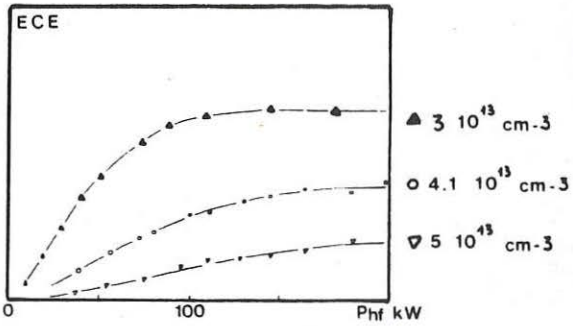

References

/1/ A. Girard et al ,Proc 12th Eur. Conf. on Controlled Fusion & Plasma Physics, Vol2,168 (1985)

/2/J-M Rax , Rep. EUR-CEA-FC-1267 may 1985 .

/3/J-M Rax , Rep. EUR-CEA-FC-XXXX april 1986(to appear) .

/4/N.J Fisch and C.F.F Karney ,Phys. Fluids **28** (10) , 3107 (1985) .

/5/ J.A How ,G.Melin , A.Girard,Proc 4th Int. Work. on ECE & ECRH ,173 (1984)

/6/ J-M Rax , Rep. EUR-CEA-FC-1270 june 1985 .

/7/C.F.F Karney and N.J Fisch ,Phys. Fluids **29** (1) , 180 (1986) .

/8/N.J Fisch ,Phys. Fluids **29** (1) , 172 (1986) .

COUPLING OF LOWER HYBRID WAVES TO THE ASDEX PLASMA

M. Zouhar, T. Vien, F. Leuterer, M. Muenich, M. Brambilla, H. Derfler, D. Eckhartt, F. v.Woyna and ASDEX-Team

Max-Planck-Institut für Plasmaphysik, EURATOM Association, D-8046 Garching,FRG

1. Introduction

The ASDEX Lower-Hybrid experiment uses an eight waveguide grill antenna to launch the waves. A mean power reflection coefficient as low as $\langle R \rangle = 0.1$ is attainable in all modes of operation. However the reflection coefficients R_k in the individual waveguides may vary over a great range (up to 0.9). This paper aims at depicting the reflection patterns $R_k = f(k)$ and comparing measurement with theory.

At high power levels (above 140 kW/waveguide) a breakdown occurs. The sequence of phenomena relating to this breakdown is documented and commented on .

2. Calculated reflection patterns

Each of the reflection patterns depicted in the diagrams below consists of eight values R_k (power reflection coefficients) in the individual waveguides. Lines are drawn between adjacent points to render the shapes of the patterns prominent; they have no physical meaning otherwise. The patterns dealt with here all result from equal incident amplitudes in the individual waveguides. In each of the diagrams representing computed data, the plasma density gradient in front of the grill is kept constant and the plasma edge density is considered as a parameter.

The following characteristics are predicted by the theory:

- in general the R_k-patterns are expected to vary fairly sensitively with the plasma edge density. This is true for all waveguide phasings.
- a characteristic transition in the R_k-pattern occurs: at low edge density the edge waveguides exhibit low reflection while in centre waveguides reflection is relatively high ("ridge-pattern"). The opposite is true for high density ("valley-pattern"). In between an intermediate density exists with low reflection in all waveguides (overall $\langle R \rangle = 0.1$).
- symmetric reflection patterns R_k (k=1...8, axis of symmetry between waveguides 4 and 5) are expected for waveguide phasings $0\pi0\pi0\pi0\pi$, $00\pi\pi00\pi\pi$, $00\pi\pi\pi\pi00$, $0000\pi\pi\pi\pi$. Characteristic "double-ridged" patterns are expected for $00\pi\pi00\pi\pi$ and $0\pi0\pi0\pi0\pi$ phasings, the "ridges" being in waveguides 3 & 6 and 2 & 7 respectively.
- asymmetric reflection patterns are expected for 90 degrees difference between adjacent waveguides (+90 deg denoted "current drive" phasing, -90 deg "opposite current drive", i.e. opposite to the sense of the OH-current) and for similar phasings (120 deg, 60 deg, etc.).
- the phasings $00\pi\pi\pi\pi00$ and $0000\pi\pi\pi\pi$ have little importance for plasma heating. However, the accompanying R_k-patterns are very particular and fairly pronounced in magnitude. They offer an additional convenient opportunity to verify the theory.
- the computed R_k-patterns are depicted in Figs. 3a through 7a.

3. Experimental reflection patterns

Good qualitative agreement between experimental and theoretical data was observed:

- the measured R_k-patterns are shown in Figs. 3b through 7b. In most cases data of shots with varying edge density are presented.
- the characteristic shapes of the R_k-patterns are clearly distinguished. Relative plasma density changes in front of the grill were measured by means of a microwave interferometer (at 136 GHz). The R_k-patterns vary with density as anticipated.
- the agreement in magnitude is rather coarse. It should be noted however that no absolute values n_{edge} and ∇n were taken. In addition, the theoretical boundary conditions are not really those of the experiment (infinite plane conducting wall surrounding the grill, parallel plate geometry).
- all theoretically symmetric R_k-patterns experienced some experimental asymmetry. Possibly the alignment of the grill relative to the plasma torus was not perfect.

4. Breakdown in front of the grill

At high power levels (above 140 kW/waveguide at low densities) a breakdown in front of the grill was detected. This breakdown was studied in more detail by testing a single waveguide (Figs. 1 and 2).

- at first (time t = 0), light is detected by the photo-diode PD1 viewing all along the waveguide into the plasma (Fig. 2, first trace, positive signal).
- coincidentally several phenomena occur:
  a. A pronounced reflection of RF-power is indicated by directional coupler DC3 (outside the grill vacuum section, trace 3, negative).
  b. At the grill mouth coupler DC1 and the grill coupler DC2 (both being sidewall couplers within the grill vacuum section, both indicating incident waves, both signals negative) amplitude modulation due to the poor directivity of these couplers is clearly visible. The fact that the DC1-signal exhibits just one trough and one crest implies that the locus of the reflection originates in some distance from DC1 and propagates backward. In passing DC1 it causes the DC1-signal to vanish (trace 5). The same happens later at DC2 (trace 6).
- 250 microseconds after t = 0: light appears at photo-diode PD2 viewing perpendicularly into the waveguide (trace 2, positive, plateau resulting from saturation).
- 750 microseconds after t = 0: the incident wave is switched off (visible at DC3, trace 3, negative) as soon as light appears at PD3 (arc detector).

A possible explanation of this sequence of phenomena is:

- breakdown at the edge of the grill.
- reflection layer (plasma) moving back to the transmitter at a speed of about 3000 m/s, driven by the combined action of ponderomotive force and the force caused by the local magnetic field gradient.

The physics of the breakdown, however, has not yet been identified.

REFERENCES

/1/ Brambilla M., Nucl. Fusion 16 (1976) 47

/2/ Stevens J. et al., Nucl. Fusion 21 (1981) 1259

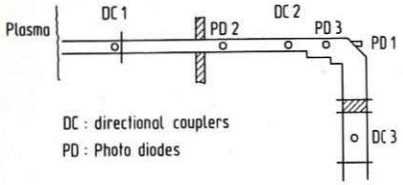

Fig. 1

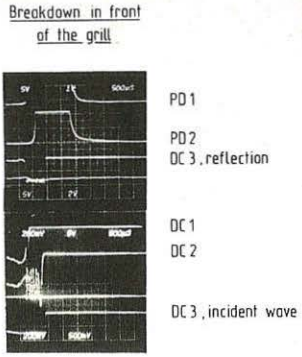

Fig. 2

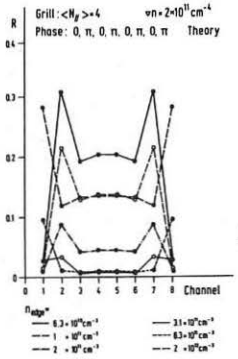

Fig. 3a

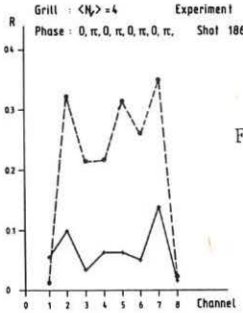

Fig. 3b

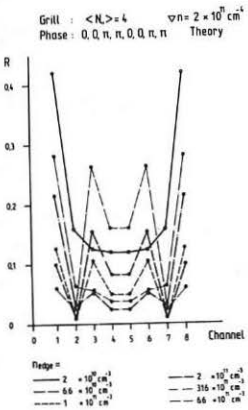

Fig. 4a

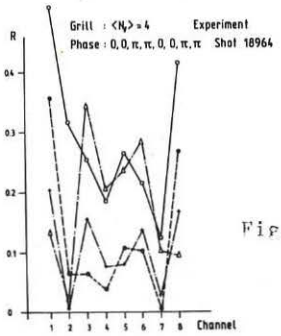

Fig. 4b

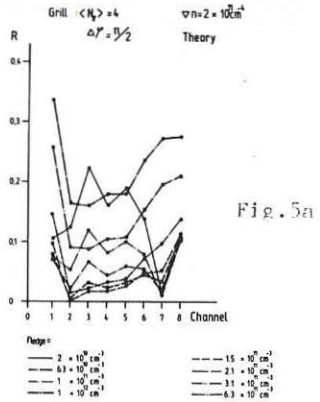

Fig. 5a

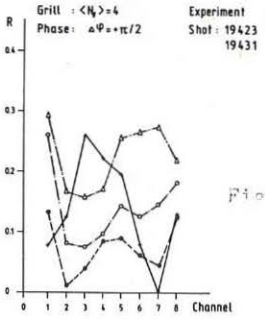

Fig. 5b

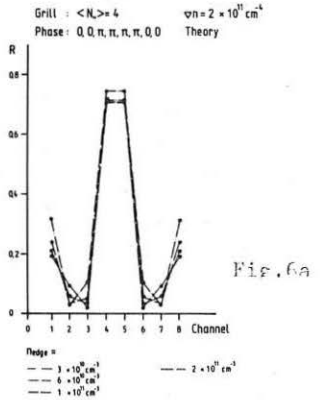

Fig. 6a

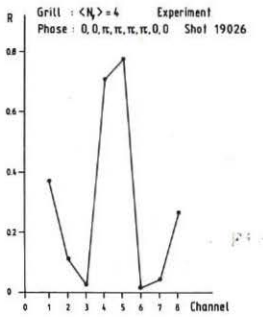

Fig. 6b

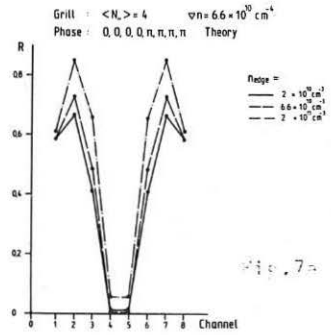

Fig. 7a

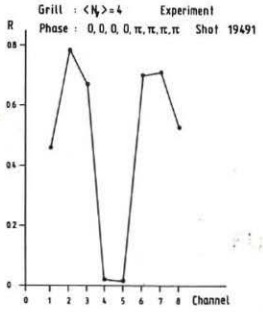

Fig. 7b

RUNAWAY EFFECTS ON LOWER HYBRID CURRENT RAMP-UP

V.S. Chan, C.S. Liu,† and Y.C. Lee‡

GA Technologies, San Diego, California, U.S.A.

Runaway effects on lower hybrid current ramp-up are studied numerically using a two-dimensional Fokker-Planck analysis and a nonlinear circuit equation. The runaways are produced by a back electric field initially created to offset the rf driven current. At high powers, the runaway production rate is large and an additional inductive effect acts to saturate the back electric field. The current ramp-up efficiency, which is proportional to this electric field, is in turn reduced. This may explain an apparent limit in efficiency observed in experiments.

However, the anomalous Doppler instability may be excited within a range of ω_p/Ω_e when the inductive field exceeds a few percent of the Dreicer field. This is shown to drastically reduce the nonlinear inductance allowing the recovery of the linear current ramp-up efficiency.

Lower hybrid (LH) current ramping has received particular attention recently because of its potential for conserving expensive volt-seconds in large tokamaks and fusion reactors where long pulse operation is essential. Experiments performed on the Princeton Large Torus (PLT) tokamak have successfully converted radiofrequency wave energy to poloidal magnetic field energy with efficiency of up to 30% [1].

A concern with respect to the efficiency of the process is that when the strength of the inductive field E exceeds a few percent of the Dreicer field $E_0 \equiv m\nu v_e/e$ where m and e are the electron mass and charge, ν is the Coulomb collision frequency, and $v_e = \sqrt{T_e/m}$ is the electron thermal velocity, a significant number of runaway electrons can be generated. Even in present experiments, when the power level exceeds a few hundred kW, an electric field of a few percent of E_0 can be expected. It is conceivable that runaway electrons can play an important role here as well as at higher power levels.

The runaways affect LH current ramping in two significant ways. First, if most of the back current is carried by runaway electrons, the resistivity of these electrons is much smaller so the decay time of the inductive field (given by the plasma inductance divided by the resistance) can be much longer. Secondly, even at the early time when the number of runaways is small, the rate of production of runaways can be significant. This results in a large rate of change of back current which in turn can inductively alter

†Present address: University of Maryland, College Park, Maryland, U.S.A.

‡Permanent address: University of Maryland, College Park, Maryland, U.S.A.

the back emf, in particular lowering its magnitude provided the runaway confinement time is long compared with the time for setting up a steady-state runaway flux. Since the efficiency of current ramping is essentially the product of the back emf and the rf current divided by the rf power, this effect will reduce the efficiency of rf current ramping. The PLT experiment reported that at the highest power of 260 kW, the current ramp up rate is 120 kA/sec which gives a net inductive ramp up power of 63 kW. Above this power, a subsidiary effect set in and limited the current ramp up process. One may speculate that this is caused by the runaway inductance effect. This inductance is contained in a nonlinear circuit equation [2]

$$(1+\mathcal{L})\,\frac{dJ}{dt} = V_{\rm rf} - \nu J - \dot{n}_R ec\,, \tag{1}$$

where J is the plasma current, $V_{\rm rf}$ is the effective rf voltage which depends on the LH power spectrum, $(1+\mathcal{L})$ $\{= 1 + (a^2\omega_p^2/4\,c^2)[\ell n[(8\,R_0/a) - 7/4]\}$ is the linear plasma inductance and $(\dot{n}_R ec)$ is the nonlinear inductance term with $\dot{n}_R$ being the runaway production rate. Physically, this term accounts for the build-up of well-confined runaway electrons. Using an expression from a two-dimensional (velocity space) analysis, $\dot{n}_R = (\sqrt{2}/\pi) n\nu (E_0/E)^{3/2}\,\exp[-E_0/E - \sqrt{2\,E_0/E}\,]$ in which the pre-exponential factor of $(E_0/E)^{3/2}$ was determined form a numerical fit using a Fokker-Planck code. J and E, the back emf are related by $E \simeq -(8\pi/\omega_p^2)\;\mathcal{L}\;(dJ/dt)$. $\dot{n}_R ec$ is a sensitive function of E/E_0 and when this term becomes comparable to the LHS, typically when $E/E_0 \gtrsim 5\%$, the nonlinear inductance term will saturate the back emf. Figure 1 shows a solution of Eq. (1) with $V_{\rm rf}$ treated as a given parameter. It demonstrates that the back emf decays in time much more rapidly when the nonlinear inductance is in effect. Since the current ramp-up efficiency is proportional to the back emf multiplied by the rf current, this will reduce and then saturate the efficiency of LH current ramp-up. For a quantitative estimate [3] we use a realistic LH spectrum in the Fokker-Planck calculation to obtain a constitutive relation between E and J for different values of applied power (Fig. 2). The rf current $J_{\rm rf} \equiv e\int_{v_{\rm min}}^{v_{\rm max}} dv_\parallel v_\parallel f$ is also obtained for various E and power. For any initial current and applied power, Fig. 2 gives $V_{\rm rf}$ and Eq. (1) describes the rate of change of J; specifically whether the decay is classical (without the $\dot{n}_R ec$ term) or nonlinear. The onset of nonlinear behavior starts at $E/E_0 \simeq 4\%$. Ramping at higher power will result in a rapid decay of E (within a few tens of ν^{-1}) back to a small enough E/E_0 after which it will decay with the classical resistive time. Knowing $J_{\rm rf}$, the ramping efficiency $\eta = E \cdot J_{\rm rf}/P_{\rm rf} \simeq 36\%$ at the onset for PLT type parameters.

However, another nonlinear process becomes important in a range of ω_p/Ω when the inductive field exceeds several percent of the Dreicer field. This is the anomalous Doppler instability driven by anisotropy of an electron distribution with a runaway tail. A consequence of the instability is wave enhanced pitch-angle scattering of the tail particles. This wave pitch-angle scattering frequency is estimated as

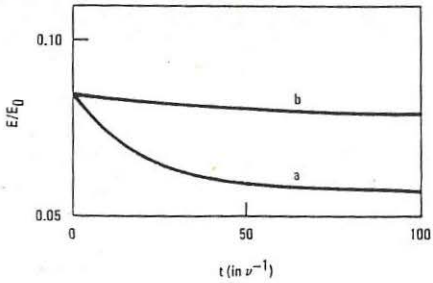

FIG. 1. Temporal evolution of inductive electric field (a) with runaway correction, and (b) without runaway correction for $T_e = 500$ eV, $n_0 = 2 \times 10^{12}$ cm^{-3}, $R = 100$ cm, $a = 20$ cm, $v_{ph} = C/8.5$ $v_m = C/2$, and runaway set-up time of 100 ν^{-1}.

$$\nu_w \simeq \left(\frac{\omega_p^3}{\Omega^2}\right)\left(\frac{E}{E_0}\right) e^{-E_0/4E}\, \ell n \left[\frac{V_D\left(1-\frac{\omega_p^2}{\Omega^2}\right)}{\sqrt{v_e^2+v_\parallel^2}-V_R}\right], \qquad (2)$$

where ω_p is the plasma frequency, Ω the electron gyrofrequency, $V_R = \sqrt{E_0/E}\, v_e$ and $V_D \simeq (\Omega/\omega_p)v_e$ for $\Omega > \omega_p$. ν_w decays only logarithmically in $v_\parallel$ and is sensitive to E/E_0. For E/E_0 greater than 5%, it becomes very effective in pitch-angle scattering the tail particles, thus stopping the runaway production. This is illustrated in Fig. 3 which is obtained by incorporating Eq. (2) in a Fokker-Planck equation. The tail distribution is isotropized by the wave pitch-angle scattering ($v_\parallel \gg 0$). The nonlinear inductance effect is reduced and one may expect the LH current ramp-up efficiency to improve over the saturated value.

This is a report of work sponsored by the U.S. Department of Energy under Contracts No. DE-AC03-84ER53158 and No. W-7405-ENG-48.

References

[1] F.C. Jobes, S. Bernabei, T.K. Chu, W.M. Hooke, E.B. Meservey *et al.*, Phys. Rev. Lett. **55** (1985) 1295.
[2] C.S. Liu, V.S. Chan, and Y.C. Lee, Phys. Rev. Lett. **55** (1985) 2583.
[3] V.S. Chan, C.S. Liu, and Y.C. Lee, to be published in Phys. Fluids (1986).

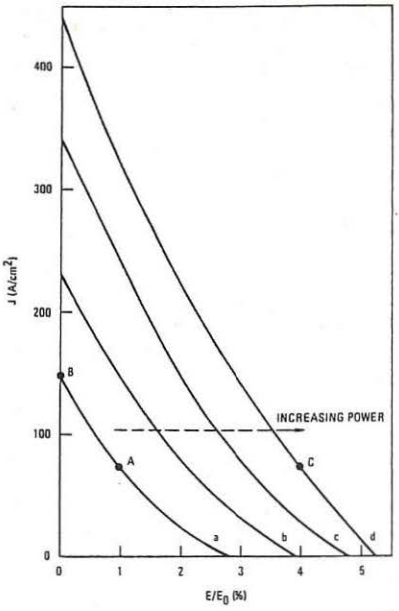

FIG. 2. Constitutive relation between J and E for rf driven plasma. Curves a to d correspond to increasing applied power of 50, 100, 200, and 400 kW. $c/v_e = 30$ and $n_0 = 2 \times 10^{12}$ cm^{-3}.

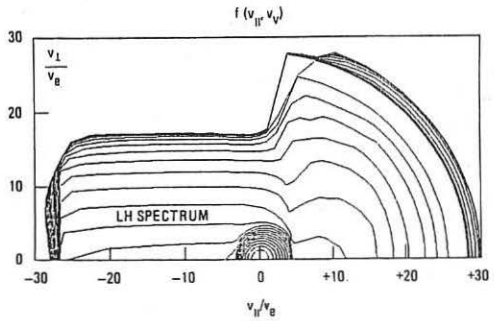

FIG. 3. Two-dimensional contour of current ramp-up electron distribution with wave instability, and reduced distribution.

TOROIDAL EFFECTS ON CURRENT DRIVE WITH LOWER HYBRID WAVES

Wang Zhongtian, Qiu Xiaoming, Cheng Xiaoping, Jian Kuangde
Southwestern Institute of Physics, Leshan, Sichuan, China
T.M. Shih
Mathematical Department, Hong Kong Polytechnic, Hong Kong

It is important to drive steady-state plasma current in tokamak by using radio-frequency waves. Various experiments conceived to test the efficiency of a current drive based on quasilinear Landau decay proposed by Fisch /1/ indicate that such a driving mechanism may be operating. The essence is the function through the quasilinear Landau damping process. However, there is a puzzle in the current drive. Outside the range of the phase velocity of rf-waves there are a number of supra-thermal electrons with lower parallel velocity. What fills the gap? Toroidal effects may be responsible for this.

In present paper quasilinear Fokker-Planck equation is developed by using gyrokinetic equation. Bounce frequency is introduced into resonant denominator due to transit motion of electrons along the magnetic lines. The resonant region is considerably broadened by the additional period. More electrons are involved in the resonances. Full collision term is employed in the numerical computation. Differential equations are solved by the shooting method as a two-point boundary value problem. The energy gap is partially interpreted.

QUASILINEAR THEORY FOR AXISYMMETRIC TOROIDAL SYSTEM

A characteristic time of the quasilinear process, τ_{QL}, as usual, considerably exceeds both the period of particle motion along the small torus azimuth, τ_b and the particle cyclotron period, τ_β. This enables us to obtain simplified quasilinear equations for the averaged particle distribution function.

For low frequency, we proceed from the guiding center Vlasov's equation /2/ in the limit of electrostatic approximation

$$\frac{\partial f}{\partial t} + (v_\parallel \underset{\sim}{b} + \underset{\sim}{v}_d)\cdot\nabla f + \frac{c}{B}\underset{\sim}{b}\times\nabla\Phi\cdot\nabla f - e(v_\parallel \underset{\sim}{b} + \underset{\sim}{v}_d)\cdot\nabla\Phi\frac{\partial f}{\partial \mathcal{E}} = 0 \qquad (1)$$

where $f(\mathcal{E}, \mu, \underset{\sim}{x}, t)$ is the guiding center distribution function $\mathcal{E} = Mv^2/2$ is the particle energy, $\mu = Mv_\perp^2/2B$ is the conserved magnetic moment, $v_\perp$ is the component of velocity of the charged particle perpendicular to the ambient magnetic field, Φ is the perturbed electric potential, x is the guiding center position, $\underset{\sim}{b} = \underset{\sim}{B}/B$ is unit vecter tangential to the magnetic field line, e is the charge, M is the mass, c is the speed of light,

$$V_{\parallel} = \pm [2(\mathcal{E} - \mu B)/M]^{1/2} \tag{2}$$

is the parallel velocity and

$$\underset{\sim}{V_d} = \frac{c}{eB} \underset{\sim}{b} \times [M V_{\parallel}^2 \underset{\sim}{b} \cdot \nabla \underset{\sim}{b} + \mu \nabla B] \tag{3}$$

is the unperturbed guiding center drift velocity across the magnetic field.

Considering the collision of the charged particle, we get the quasilinear equation

$$\frac{\partial f}{\partial t} + \frac{1}{\Omega \tau_b} \nabla J \times \nabla f_0 \cdot \underset{\sim}{b} = -\sum_k \hat{\Pi}_0 I_m I_k \hat{\Pi}_0 f_0 + C(f, f) \tag{4}$$

where $\hat{\Pi}_0 = \frac{1}{\tau_b} \int_0^{\tau_b} dt \, \hat{\Phi}_k \exp\left\{ i \int_0^t d\tau \, \Omega_k \right\} \cdot \left[\frac{c}{B} \underset{\sim}{k} \times \underset{\sim}{b} \cdot \nabla + e \underset{\sim}{V} \cdot \underset{\sim}{k} \frac{\partial}{\partial \mathcal{E}} \right]$,

$\Omega = \frac{eB}{cm}$, $J = \oint V_{\parallel} \, dl$, $\Omega_k = \omega_k - \underset{\sim}{k} \cdot \underset{\sim}{V}$, $\bar{\Omega}_k = \frac{1}{\tau_b} \int_0^{\tau_b} \Omega_k \, dt$,

$I_k = \Sigma \frac{1}{\bar{\Omega}_k - s\omega_b}$, $\omega_b = 2\pi / \tau_b$

C(f,f) is the collision term, f_0 is the regular part of the electron distribution function.

NUMERICAL RESULTS AND DISCUSSION

The magnetic configuration proposed by Kadomtsev and Pogutse /3/ is used in the numerical calculation. Considering the resonant condition

$$\omega_k - (m + nq)\omega_b = s\omega_b \tag{5}$$

where m and n are the poloidal mode number and the toroidal mode number, respectively, q is the safety factor, $\omega_b = V_{\parallel}'/R_0 q$, R_0 the magnetic axis, for the passing particle we obtain

$$R(x) = \frac{6 \nu_L}{\gamma_c V_e^3 \Lambda} \left\{ J_s^2(y_s) \frac{k_0}{k_0 + s} \left[x^3 \Gamma(x - u_s) - (u_s + 2u_s^3) x \right] \right\} \tag{6}$$

where R(x) is the similar driving term to that in Ref. (4), J_s the Bessel function of order s, $k_0 = m + nq$, $u_s = \frac{k_0 u_0}{k_0 + s}$, $u_0 = \frac{\underset{\sim}{k} \cdot \underset{\sim}{V_0}}{k_0 V_e}$, $V_e = \sqrt{2 T_e / M_e}$ is the thermal velocity of the electron, $x = v/v_e$, $y_s = (k_0 + s) \cdot r/R_0$, s is an integer.

With the velocity v increasing, the electron experiences many resonances. In other words, the resonance region is broadened about the launched phase velocity. The integer, s, could be any value in principle. Actually J_s^2 drops gradually with absolute s increase. Finite term is enough for the calculation. For example, when $u_0 = 2.0$, $J_s^2/J_0^2 < 2.1 \times 10^{-3}$ for $s = 120$. For $R_0 = 100$ cm,

$q = 1.5$, $V_e = 1.88 \times 10^9$ we have $u_{120} = 1.16$. Setting $\beta = u_o/u_{120}$, the factor by which the index of refraction, n , is upshifted. It seems in agreement with Karney /5/.

Numerical results are presented in Fig. 1 for the inverse aspect ratio $r/R_o = 0.1$, using the technigul proposed by Cordev /4/, in which full collision term is taken into account.

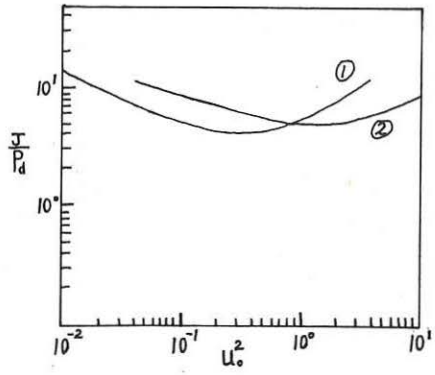

Fig. 1: Current density per power density, J/P_d, as a function of u_o^2 for the Landau camping scheme
Curve 1 is the result presented by Cordey;
Curve 2 is our result including toroidal effects.

When toroidal effects are taken into account, higher efficiency can be achieved at both high and low phase velocity. It is similar to the result presented by Cordey /4/. Yet, our result is in favour of the waves with low phase velocity.

The waves with low phase velocity may be excited by the runaway electron /6/. C.S. Liu /7/ has given detail study on the problem.

We greatly appreciate useful discussions with Professor Ding Hou-chang and Yin Yong-xiang.

REFERENCES

/1/ N.J.Fisch, Phys. Rev. Lett., 41, 837, (1978).
/2/ T.M.Antonsen, Jr. and Y.C.Lee, Phys. Fluids, 25, 132 (1982).
/3/ B.B.Kadomtsev and P.Pogutse, Rev. Plasma Phys, Vol. 5 (1967).
/4/ J.G.Gordey, T.Edlington and D.F.Start, Plasma Phys. 24, 73 (1982).
/5/ C.F.F.Karney, N.J.Fisch and F.C.Jobes, PPPL-2152 (1982).
/6/ V.V.Parail, O.P.Pogutse, Nucl. Fusion, 18, 303 (1978).
/7/ C.S.Liu, Phys. Rev. Lett., 48, 1479 (1982).

ELECTROMAGNETIC WAVE PROPAGATION AND ABSORPTION IN TOKAMAK PLASMA AT TWO-ION HYBRID RESONANCE

D.L. Grekov, V.E. D'yakov and A.V. Longinov

Kharkov Institute of Physics and Technology, Ukrainian SSR Academy of Sciences, 310108 Kharkov, USSR

RF plasma heating using the fast-to-slow mode conversion of fast magnetosonic waves (FMSW) in the vicinity of the two-ion hybrid resonance [1] has been widely applied since the early experiments on TFR [2]. However, the possibilities contained in this method have not been exhausted as yet, encouraging particularly the investigations of the conditions providing a peaked energy deposition profile in the plasma center as well as the efficient power coupling to the majority ions.

This report deals with the propagation and absorption of FMSW excited with a high-field side antenna. The calculations are performed with the ray-tracing technique for standard T-10 conditions: B_0=3 T, $n_e(0)$=7 10^{13}cm^{-3}, T_e=T_i=1 keV, D+4%H plasma, I_p=400 kA, a=35 cm, R_0=150 cm, and the density, temperature and current profiles are parabolic. For these parameters one can neglect the FMSW penetration through the evanescent zone near the two-ion hybrid resonance. It is taken into account that near the conversion point the ray width of the FMSW fast mode (FM) $\sim 5\kappa_A^{-1} = 5B_0(\sum_i 4\pi n_i m_i)^{-1/2}\omega^{-1}$ is considerably narrower than the wave packet width. The calculations include the following mechanisms of the RF energy absorption: electron Landau damping, TTMP, and absorption at the first and second harmonics of the ion cyclotron frequency for different ion species. The energy deposition profile $P_\alpha = 2\pi r\langle Q_\alpha\rangle$ (α=i,e) is calculated by integrating along each ray and subsequently summing up over all the rays. The deposition profiles obtained are used to construct the temperature increase (ΔT_α) profiles.

It is assumed for simplicity that the temperature conductivity $\chi_\alpha(r)$ is constant.

From the calculations performed it can be inferred that

(1) to obtain a peaked deposition profile (the main mechanism is the electron Landau damping of the FMSW slow mode (SM)) and to increase ΔT_e it is worth-while to use antennae covering a poloidal angle $\vartheta_A \lesssim 2\pi/3$ and to shift the two-ion resonance towards the weak magnetic field relative to the plasma center (Fig.1). The energy radiated by the antenna elements located

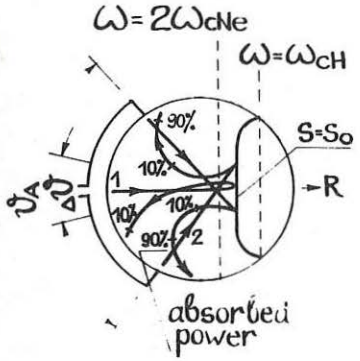

Fig.1 Ray projections on the minor cross section for $n_e(0)=7\times10^{13}cm^{-3}$ and $T_d(0)=1keV$.

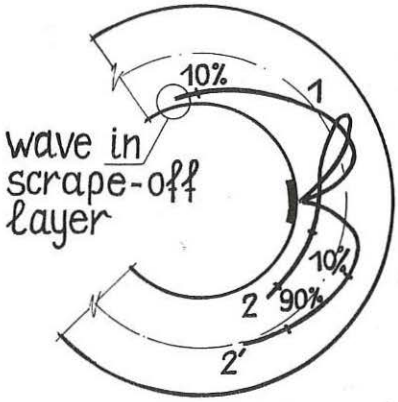

Fig.2 Ray projections on the equatorial plane: (1) $\vartheta_o=0$, (2,2') $\vartheta_o=0.86$, $N_{IIO}=\pm 6$.

in the equatorial plane is absorbed rather poorly, with the deposition profile being peripheral. A considerable portion of the energy can be carried by the SM into the scrape-off layer (Fig.2), not only decreasing the heating efficiency, but also contributing to the impurity influx from the walls due to increased T_e of the scrape-off layer and the Debye layer potential rising as the SM is reflected from the wall [3]. These effects may be responsible for the radiation increasing greatly at low ratios n_H/n_d in T-10 and TFR experiments. Therefore in the case of Landau damping it is advantageous to use antennae with the radiating surface in the vicinity of the equatorial plane ($\Delta\vartheta \lesssim 0.5$) removed;

(2) under the above conditions the poloidal field is the major

influence on the SM propagation and absorption. As the electron damping length $\ell_e = 1/\mathrm{Im}\,K \sim T_i^{5/2} n_e^2$, under low density and low T_i conditions the energy deposition profile becomes more peaked and the heating efficiency increases. This is confirmed by the calculations carried out with $n_e(0)=3.5\times10^{13}\,cm^{-3}$ and $T_i=0.5$ keV (Fig.3);

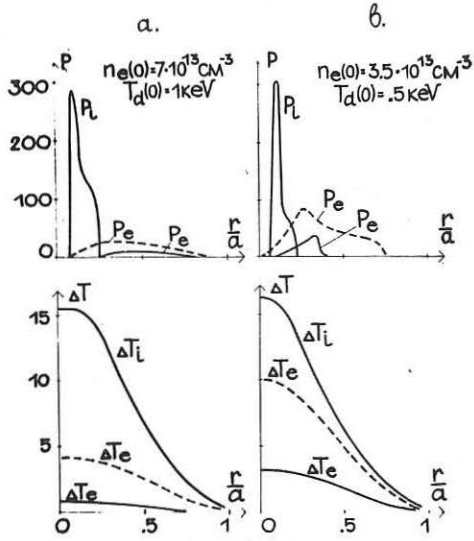

Fig.3 Energy deposition profiles P_α and temperature increases ΔT_α in D+H plasma (- -) and D+H+Ne plasma (—) in arbitrary units.

(3) the value of N_{II} ($N_{II}=\vec{N}\cdot\vec{B}/|B|$) on a ray in the region of strong SM absorption depends slightly on the initial value of N_{II0} (Fig.4). The sign of N_{II} is determined by the position of the ray origin relative to the equatorial plane of the torus and not by the sign of N_{II0}. Thus the antenna asymmetric about the equatorial plane and located on that side whereto the toroidal ion drift is directed, can be used for current drive in the direction of the plasma current (the antenna shifted to the opposite side would generate the countercurrent). Without going into details of this phenomenon, we only note here an apparent advantage of the current-drive method proposed which permits one to use even antennae with spectra symmetric in N_{II};

(4) the FMSW propagation and absorption are investigated in the plasma with the heavy ion minority [3,4] (Ne^{22}, $n_{Ne}/n_d = 5\times10^{-3}$, $T_{Ne}=5T_d$). Under these heating conditions most of

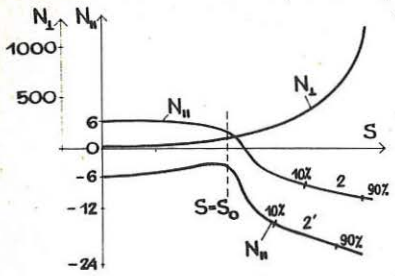

Fig.4 N_{II} and $N_{\perp}$ vs the ray projection length on the minor cross section for $n_e(0)=7\times 10^{13}cm^{-3}$, $T_d(0)=1$ keV and $\vartheta_0 = 0.86$ ($N_{II0}=\pm 6$).

the energy is absorbed by the heavy ion minority, providing a highly peaked energy absorption profile (Fig.3). A proper choice of the plasma parameters would permit the energy transfer due to Coulomb collisions from the heavy admixture either mainly to deutons or to electrons [4]. Therefore the ΔT_{Ne} profile can be regarded as either a ΔT_d or a ΔT_e profile. In the latter case the peaked shape of the energy deposition profile is comparable with that in ECRH and at higher densities is even more pronounced. As can be seen in Fig.3, the heavy ion minority heating (HIMH) permits highly efficient heating of the ion majority with the maximum value of $\Delta T_i(0)$. HIMH is especially advantageous for low Z_{eff} tokamaks in which there is no ion heating due to cyclotron absorption by natural impurities (TEXTOR, etc). The electron damping of the SM in the region between the two-ion resonance and ICR for the heavy ion minority is only significant at low n_e and T_i and can be avoided through a proper choice of the hydrogen minority concentration and the location of the two-ion hybrid resonance relative to the plasma center. The discrepancies between the results presented and those of the TFR group [5] who found Landau damping to be significant even in the vicinity of the conversion point are probably due to the model used in this work being more realistic and the parameters properly chosen.

In the case of high RF power coupled to the plasma the above phenomena can be modified by the two-ion parametric or two-stream turbulences.

1. R.Klima et al., Nucl.Fusion, 1975, 15, p.1157.
2. TFR Group, in: 1st Varenna-Grenoble Symp.,1978, 2, p.207.
3. A.V.Longinov, K.N.Stepanov,in:RF Plasma Heating, Gorky,1983.
4. A.V.Longinov et al.,in:12th Eur.Conf.,Budapest,1985,2,p.132.
5. TFR Group, Preprint EUR-CEA-FC-1283 (1985).

AN ATTEMPT AT MHD MODE CONTROL BY FEEDBACK MODULATION OF L.H. DRIVEN CURRENT

F. PARLANGE, J.C. VALLET and PETULA GROUP

ASSOCIATION EURATOM-C.E.A. - Département de Recherches sur la Fusion Contrôlée - C.E.N.G. - 85X - 38041 GRENOBLE Cedex (France)

MHD activity in Tokamak discharges with lower hybrid current drive has distinct features which can be used to stabilize tearing modes /1/. The m=2 mode in particular is easely triggered by the RF pulse. It is present in Petula, in all discharges with RF current at densities $n_e < 2\ 10^{13}$ cm^{-3}. This occurs for any q_a value, even when the RF current is only a small fraction of the total current. However, the mode has generally a low amplitude except when it is already present in the discharge before the RF pulse ($q_a \simeq 3$). In this case, driving even partially the current by waves has the effect of slowing down the island structure rotation and of damping the magnetic field perturbation by a factor of 2 /2/ /3/.

This stabilizing effect is probably due to a change in the current profile giving a lower value for Δ', the key parameter in tearing mode stability. Peaking of thecurrent profile is likely, although it is not consistent with the lowering of internal inductance which is sometimes observed in that density range, at high RF power for example.

A different way of reducing the m=2 tearing mode was recently proposed, consisting in driving more current at the O point of the islands than at the X point, by means of amplitude modulated lower hybrid waves /4/ /5/. This was tested in Petula in the following way. A L.H. wave pulse at 1.3 GHz with $N_{//} = 2.4$, asymetric spectrum is used to drive a current in a discharge showing a large amplitude m=2 mode. The main characteristics of this discharge are (fig. 1) : $R = 0.72$m $\quad a = 0.165$m $\quad B_T = 2.8$ T $\quad I_p = 174$kA $\quad \bar{n}_e = 1.5\ 10^{13}$ cm^{-3} $\quad q_a = 3.0$ $\quad P_{HF} = 170$kW

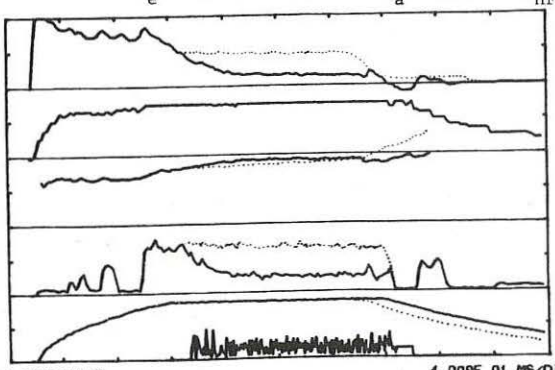

Fig. 1 - Plasma parameters for shot with modulated RF pulse (solid line) and without RF (broken line)

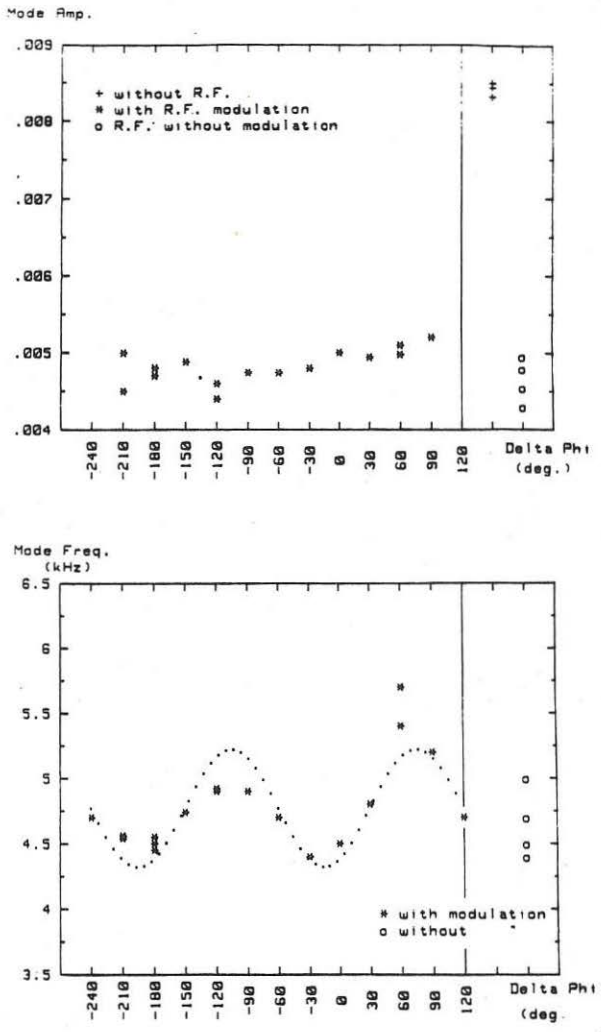

Fig. 2 - $\delta\tilde{B}_\theta$ / B_θ and mode frequency as a function of the phase of the RF modulation. On the right are the corresponding values for the unmodulated case.

The signal of a Mirnov coil is used to modulate the amplitude of the low power oscillator which drives the klystron amplfier. The phasing of the modulation, respect to the island structure is changed from shot to shot, by using successively 12 Mirnov coils located 30° apart in the poloïdal direction. The gain of the feedback loop was set in such a way that 100% modulation of the klystron output was maintained throughout the pulse.

A reference coil signal and the klystron power are recorded and analyzed by FFT technique. As usual, in lower hybrid current drive experiment in Petula, the magnetic field fluctuation was reduced by a factor of two, not more than in the unmodulated case, and independently of the relative phasing of the lower hybrid wave modulation and the island structure within experimental errors (fig. 2a).

The q = 2 radius was estimated to be 13 cm and the width of the island was reduced from 4 to 3 cm typically.

The island rotation was slowed down as in the unmodulated case, from 6.6 kHz without RF to about 5 kHz. However, its frequency was a function of the Mirnov coil number. Fig. 2b shows the relationship between the Mirnov oscillation frequency and the phase difference between the RF power modulation and the island rotation. 0° means that there is an island in front of the grill when RF is at maximum. The experimental points clearly show the m=2 structure. For these shots, the frequency is minimum when RF is switched on shortly before an island is passing in front of the grill. In other circumstances, the minimum may be obtained when the RF lags on the island rotation by 45°.

These results are different from what is predicted by feedback stabilization theory. Two points should be noted when discussing the absence of island width reduction with a modulated RF pulse.

First of all, the decrease in the tearing mode amplitude in the unmodulated case did not receive yet any clear explanation. It is observed whether the ratio of the current in the plasma central zone to the total current increases or decreases with respect to the ohmic case /6/. So that, current peaking cannot be systematically associated to this mode stabilization.

Preferential heating inside the islands due to their already higher temperature as proposed by Reiman /7/ should be ruled out, since modulating the wave would have reinforced the effect.

On the other hand, the experimental situation is far from being optimum for a comparison with the theory of feedback stabilization by Rutherford /5/. The mechanism relies on the generation of current inside the island and implicitly assumes that the rest of the current distribution is left unchanged. This would be the case if power absorption in the island was so strong that there be no power left for inside the q = 2 surface, or alternatively if accessibility prevented the wave to go further than this surface. For the case considered here, ray tracing fig. 3 shows that the wave penetrates in the island zone at 40 cm from the grill and travels inside for about 1m (1/5 of the torus). In the poloïdal direction, the wave has to turn by 10° before getting in the island. Wave absorption on the other hand is still a matter of discussion since interaction of the grill spectrum to a maxwellian distribution leads to current much smaller than observed (the so called gap problem). However, even if some link is missing in the theory, the absorption, in any case, should have a strong temperature dependance.

As a consequence of the weak temperature at the edge and of the rather

fast propagation of the wave out of the island, the amount of current generated inside the island, compared to the total current is probably quite small.

The dependance of the island rotation on the phase of the modulation however shows that Lower Hybrid current drive is sensitive to the presence of magnetic islands, whether this is a propagation effect due to changes in magnetic field direction or a damping effect due to different electron population inside and outside the islands. The island behaviour, in turn, is modified by this slight modification of the electron distribution.

/1/ D. VAN HOUTTE and al. - Nuclear Fusion 24 (1984) 1485
/2/ F. PARLANGE and al. - Proceedings of the 12th European Conf. on Cont. Fusion and Plasma Physics Vol. II p. 172
/3/ J.C. VALLET - Thesis (to be published)
/4/ Y. YOSHIOKA, S. KINOSHITA, T. KOBAYASHI - Nuclear Fusion 24 (1984) 565
/5/ R.B. WHITE, P.H. RUTHERFORD, H.P. FURTH, W. PARK, L. CHEN - Proc. of the Cargèse Workshop on Mag. Reconnection and Turbulence 1985 Les Editions de Physique
/6/ G. COLLINS, J. LISTER, P. MARMILLOD - This Conf. paper n°
/7/ A.H. REIMAN - Physics of Fluids 26 (1983) 1338

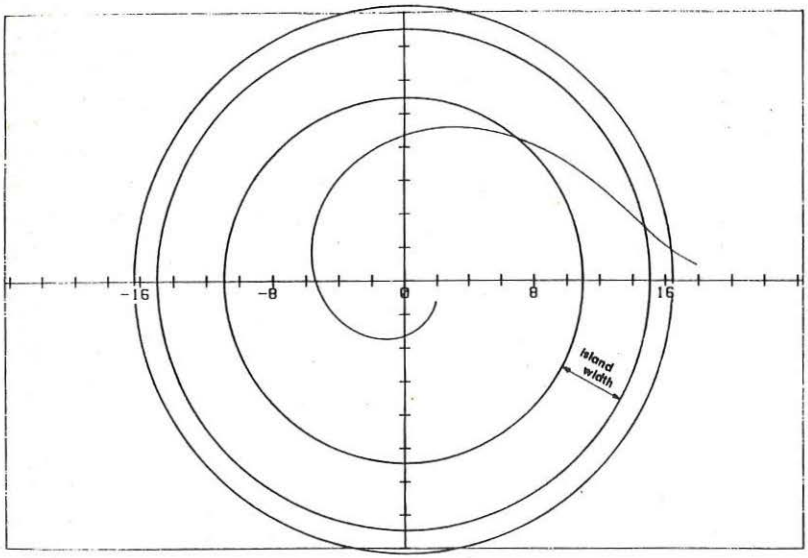

Fig. 3 - Ray path in the poloïdal section

PROBE MEASUREMENTS OF PLASMA INHOMOGENEITIES IN THE SCRAPE-OFF LAYER OF ASDEX DURING LH

M. Lenoci, G. Haas, G. Becker, H. S. Bosch, H. Brocken, A. Eberhagen, D. Eckhartt, G. Fussmann, O. Gehre, J. Gernhardt, G.v.Gierke, E. Glock, O. Gruber, J. Hofmann, A. Izvozchikov[1], G. Janeschitz, F. Karger, M. Keilhacker[2], O. Klüber, M. Kornherr, K. Lackner, F. Leuterer, G. Lisitano, F. Mast, H. M. Mayer, K. McCormick, D. Meisel, V. Mertens, E. R. Müller[2], H. Murmann, H. Niedermeyer, A. Pietrzyk[3], W. Poschenrieder, H. Rapp, H. Röhr, J. Roth, F. Ryter[4], F. Schneider, C. Setzensack, G. Siller, P. Smeulders[2], F.X. Söldner, K.-H. Steuer, N. N. Tsois[5], F. Wagner, D. Zasche

Max-Planck-Institut für Plasmaphysik
EURATOM Association, D-8046 Garching

Electron temperature and density have been measured routinely at the edge of the ASDEX main plasma by means of a Langmuir triple probe /1/ which gives the saturation current and T_e on-line. Therefore one can get with a fast radially moved triple probe a complete $n_e(r)$ and $T_e(r)$ profile in one shot. The probe installed in ASDEX can be moved from a preset position 100 mm radially inward and backward within 200 msec. It is placed 22.50° toroidally away from the LH launching grill and 5° poloidally above the equatorial plane; the tips are arranged in the form of a triangle with distances of 7 mm. For a proper function of triple probes it is necessary that the deviations between the floating potentials of the 3 tips are small compared to T_e/e. In ohmic discharges this is fulfilled while during LH application we observed differences of the order of T_e/e. We have investigated this under different plasma and LH parameters as shown in Table 1.

Table 1

Series	LH		Plasma				Measurements
	Power (kW)	$n_{\parallel}$	B_T(T)	I_p(kA)	$\bar{n}_e$(cm^{-3})	Species	
I	770	2	2.37	300	1.4×10^{13}	D_2	profiles of float.pot. diff.
II	750	2	"	"	2.7×10^{13}	"	" "
III	370	4	2.18	"	2.1×10^{13}	"	" "
IV	275	4	"	380	2.7×10^{13}	"	" "
V	500	2	"	300	1.4×10^{13}	"	" , I-V-charact., combined double probes
VI	"	2	"	"	2.9×10^{13}	"	" "
VII	"	2	"	"	1.4×10^{13}	D_2+He	I-V-charact., independent double probes
VIII	"	2	"	"	2.9×10^{13}	"	explorative, independent double probes

[1]Academy of Sciences, Leningrad, USSR; [2]Present address: JET Joint Undertaking, England; [3]Univ. of Washington, Seattle, USA; [4]CEN Grenoble, France; [5]NRC Democritos, Athens, Greece

From the floating potential differences we have constructed the electric field vector. The direction and absolute value of this show a strong radial dependence (Fig. 1, 2). In the series I, II, V, VI we found a large component parallel to the magnetic field at the innermost radial position. At the radial position of the grill the absolute value of the vector is much smaller. Despite of the different main plasma density in the series V and VI we found a very similar radial dependence of the direction. The same we got for the two series III and IV with lower RF power, for which the absolute value of the vector was always rather small. The reason for the deviations in floating potentials may be local inhomogeneities in electron temperature or in plasma potential or in flux of suprathermal eletrons. These can arise from effects connected to decay processes inbetween the grill and the separatrix described e.g. by Derfler /2/ or by Motley and Glanz /3/.

In order to distinguish between these possible explanations we operated for the series V, VI, VII and VIII couples of tips of the triple probe as double probes. The fast movement was modified in such a way that the probe stays for about 100 msec at the innermost position where the I-V characteristics were taken. In series V and VI we measured with two combined double probes with tip 3 as common reference tip. Under these conditions tip 3 has to carry the sum of the currents of tip 1 and 2 and from the characteristics one cannot find floating potential differences. They have to be measured independently. The characteristics (Fig. 3, 4) show only small differences between high and low main plasma density (corresponding to the ion-RF and the electron-RF interaction regime resp.) and indicate for couple 1-3 a lower temperature than for couple 2-3. This is in agreement with the direct floating potential measurements (Fig. 1,2), but not with the relative shift of the two characteristics.

For series VII with parameters like series V but with a changed plasma composition we have increased the voltage range to 0 - 600 V in order to reach well the saturation. We have used the two couples 1-3 and 2-3 alternatively and not connected. In this case we find again a lower temperature for the couple 1-3 than for couple 2-3 (Fig. 5) (67 and 80 eV resp.). Now the floating potential difference derived from the shift of the characteristics (30 V) is within 30 % in agreement with the temperature difference.

In addition to this series in the electron regime we have done also some explorative measurements in the ion regime but otherwise under the same conditions (series VIII). We have found again no significant difference between high and low density. This may indicate that a plasma exists inbetween the LH-grill and the separatrix dominated by the LH-wave or by any decay waves and decoupled from the main plasma.

In other exlorative measurements we have investigated for comparison purpose ohmically heated discharges with plasma parameters like series VI and VIII. We have found much lower electron temperature (15 eV instead of 65-80 eV) and higher electron densities ($2.5 - 3 \times 10^{12}$ cm^{-3}) (Fig. 6). This is at least for the electron regime in agreement with mesurements done by Pericoli on FT /4/ and El Shaer on ASDEX /5/ who found a strong redution of the density in front of the LH grill during RF application.

Conclusion

We have observed during LH application on ASDEX with a Langmuir probe having 3 tips strong poloidal and toroidal deviations in the floating potential. The probe was positioned roughly 1 m away from the LH-grill in a magnetic

flux bundle directly connected to the space in front of the RF-coupler. These deviations exist at all plasma and LH conditions investigated until now and can inhibit the operation of a triple probe at all. But other fast moved elctrostatic probes may also be disturbed too, since the radial dependence of the floating potential differences acts like a temporal change of the probe potential which cannot be controlled. The most important reasons for these deviations are changes in the electron temperature of typically 10 - 20 eV over a distance of 7 mm. But some findings like an additional shift in the I-V characteristic or large components of the floating potential differences parallel to the magnetic field lines cannot be explained by temperature differences. One has to assume also locally inhomogeneous fluxes of suprathermal electrons and differences in the plasma potential.

References:

/1/ S. L. Chen, T. Sekiguchi, J. Appl. Phys. 36, 2363 (1965).
M. Kamitsuma, S.L. Chen, J.S. Chang, J. Phys. D 10, 1065 (1977).
/2/ H. Derfler, private communication.
/3/ R. W. Motley, J. Glanz, Phys. Fluids 25, 2107 (1982).
/4/ V. Pericoli-Ridolfini, Plasma Phys. and Contr. Fus. 27, 709 (1985).
/5/ M. El Shaer, IPP Garching Report IPP III/96 (1984).

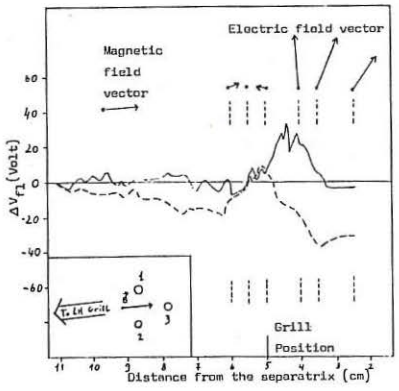

Fig. 1: Radial profiles of floating potential differences. SERIES VI
——— tips 1-3
------- tips 2-3

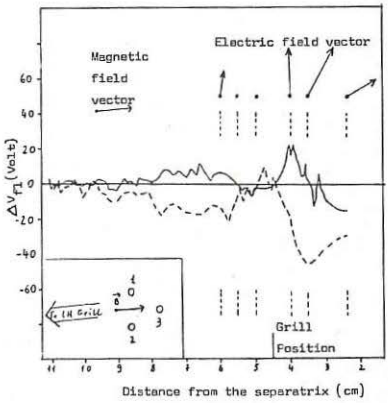

Fig. 2: Radial profiles of floating potential differences. SERIES V
——— tips 1-3
------- tips 2-3

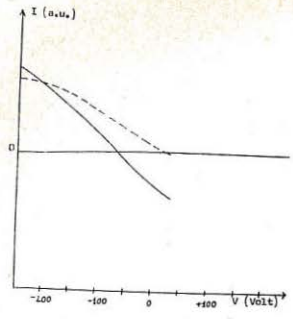

Fig. 3: I-V characteristics SERIES VI
——— Tips 1-3
------- Tips 2-3

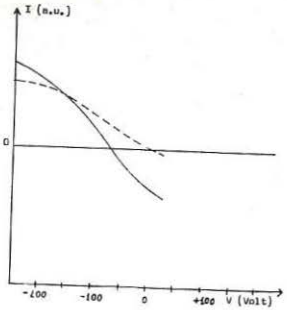

Fig. 4: I-V characteristics SERIES V
——— Tips 1-3
------ Tips 2-3

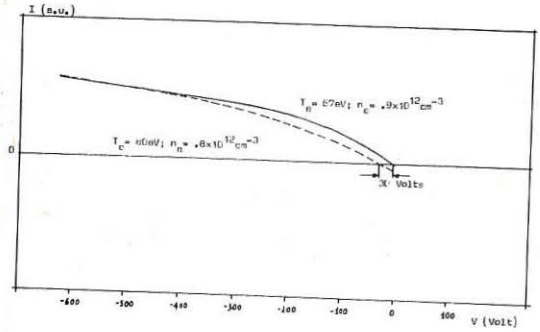

Fig. 5: I-V characteristics SERIES VII
——— Tips 1-3
------- Tips 2-3

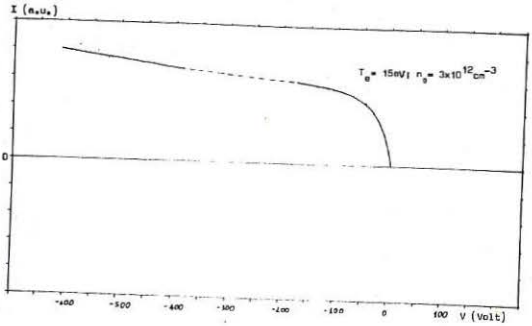

Fig. 6: I-V characteristics OH-discharge
$\bar{n}_e = 2.9 \times 10^{13}$ cm^{-3}

LOWER HYBRID CURRENT DRIVE IN THE PRESENCE OF A CONSTANT DC ELECTRIC FIELD ON PETULA-B

D. Van Houtte, G. Briffod, C. Gormezano, A. Panzarella, F. Parlange

Association EURATOM-CEA DRFC/SIG
CENG-85X - 38041 Grenoble (France)

In present LHCD experiments, the research is directed towards a combined RF current drive and inductive current drive. This hybrid current drive appears to be the most promising method both to help the OH transformer to save volt-second during higher plasma current ramp-up or longer plasma current flat top of the large tokamaks (Van Houtte et al, 1985) and to improve their plasma performances (Gormezano et al, 1984). For such hybrid discharges, an optimum operating mode is obtained on Petula-B at low RF power level in the presence of a DC electric field.

LHCD experiments were carried out on the Petula-B tokamak (R = 72 cm, a = 16,5 cm) at a density of $\bar{n}_e = 8 - 9 \times 10^{12}$ cm^{-3} for a magnetic field of $B_T = 2.8$ T. The ohmic current is driven by an iron core transformer. The 1.3 GHz RF system consists of an 8 waveguide grill fed by a klystron with $P_{RF} < 1$ MW such that the parallel index of the wave is $< N_{//} > = 2 (\Delta N_{//} = 1.5)$.

In LHCD plasma discharges, the Spitzer conductivity, obtained in OH regime, no longer holds because the plasma resistance R_p is lowered significantly by a suprathermal electron tail generated by the LH waves (Van Houtte and Parlange, 1983). Consequently the total plasma current I_p in LHCD regime may be written as :

$$(1) \qquad I_p = I_{RF} + (1/R_p^{RF}) \left[V_{RF} - (d(LI_p^2/2)/dt)/I_p \right]$$

$$\text{with } R_p^{RF} = R_p^{OH} + \Delta R_p$$

V is the loop voltage and L is the sum of the plasma internal inductance L_i and the external inductance L_b which represents the energy stored between the plasma and the vacuum chamber where the loop voltage is measured.

In the mode of operation where the plasma current I_p is maintained constant and L_i is assumed constant, we have :

$$(2) \qquad I_{RF} - (\Delta R_p / R_p^{OH} \, R_p^{RF}) V_{RF} = - I_p (\Delta V / V_{OH})$$

$$\text{with } \Delta V = V_{RF} - V_{OH}$$

In this operating mode, the DC electric field is absent only in the "steady state" phase where the plasma current is entirely driven by the RF waves ($I_{RF} = I_p$ with $V = 0$). When the RF power is used to drive a part of the plasma current ($V > 0$) or to overdrive it {ramp-up or recharging of the OH transformer ($V < 0$)}, the LH waves interact with parallel or opposing induced electric field. I_{RF} is the RF current drive that results without DC E-field and $\Delta\sigma . V (\Delta\sigma = \sigma_{RF} - \sigma_{OH} = - \Delta R_p / R_p^{OH} \, R_p^{RF})$ is the additional current

that results from the simultaneous presence of RF power and DC electric field as defined by Fisch (1984) in a steady regime $\{d(LI_p^2/2)/dt = 0\}$.

The global RF current drive efficiency η may be written as :

$$(3) \qquad \eta = \eta_o(1 + \Delta\sigma.V_{RF}/I_{RF}) = - I_p(\Delta V/V_{OH})/P_{RF}$$

where $\eta_o = I_{RF}/P_{RF}$ is the current drive efficiency obtained in a regime where no DC electric field is present into the plasma (Fisch, 1978).

The current drive efficiency is a function of the RF power through the additional current $\Delta\sigma.V_{RF}$. However, in this mode of operation, as V_{RF} is not an independant variable, it is not possible from the relative loop voltage drop to evaluate the improvement in efficiency due to the electric field.

In contrast, the mode of operation where the loop voltage V is kept constant, permits to obtain an hybrid (OH + RF) current regime maintaining constant the total DC electric field whatever the level of RF driven current. We have :

$$(4) \qquad I_{RF} + \Delta\sigma(V - L\dot{I}_p^{RF}) = I_p \left[1 - (V - L\dot{I}_p^{RF})/(V - L\dot{I}_p^{OH}) \right]$$

where $\dot{I}_p = (dI_p/dt)$, L being assumed constant. The rate of change in the plasma current as a function of the loop voltage and plasma current ramp for various loop voltages, in the constant loop voltage operating mode, are displayed in Fig. 1. In the (OH + RF) case, an RF power of 36 kW is applied. The rate of change in the plasma current is a linear function of the residual OH power in both pure OH and hybrid (OH + RF) regimes, indicating no beneficial effect for a particular DC electric field value. The straight lines may be represented by the equation :

$$(5) \qquad dI_p/dt = V/L - R_p\,(I_p - I_{RF})/L$$

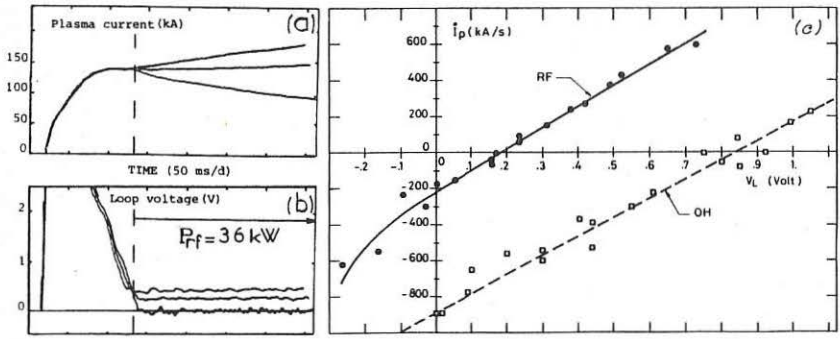

Fig. 1 -(a) Plasma current for (b) various loop voltages and (c) rate of change in the current as a function of the loop voltage with and without RF power. $\bar{n}_e = 9.\times 10^{12}\,cm^{-3}$, $I_p = 140$ *kA and* $P_{RF} = 36$ *kW* ($< N_{//} > = 2$)

and justifie the assumption where the inductance L is kept constant for obtaining eq. (4).

In this V = C^{st} operating mode, where V is the sum of a resistive component $R_p^{RF}(I_p^{RF} - I_{RF})$ and an inductive component $L\dot{I}_p^{RF}$, LHCD efficiency may be written as :

$$(6) \quad \eta = \eta_o\left[1 + \Delta\sigma(V - L\dot{I}_p^{RF})/I_{RF}\right] = I_p\left[1 - (V - L\dot{I}_p^{RF})/(V - L\dot{I}_p^{OH})\right]/P_{RF}$$

Then it is possible to calculate the current drive efficiency as a function of loop voltage for various RF power levels. Such an efficiency is shown in Fig. 2. For a given RF power the current drive efficiency is constant as a function of the total DC electric field present in the discharge. In contrast, as in the $I_p = C^{st}$ operating mode, the efficiency is inversely proportional to the injected RF power through the additional current $\Delta\sigma . L\dot{I}_p^{RF}$ (Fig. 3).

The rate of change in the current as a function of the total power for various residual OH powers are plotted in Fig. 4. The dashed curve corresponds to the pure OH case (P_{RF} = 0) and the P_{OH} = 0 curve corresponds to the pure RF case. Between these two pure cases we show various hybrid (OH + RF) cases. A particular regime with a negative loop voltage (V = - .2 Volt) regulation is plotted. In this latter case a constant electric field is directed opposite to the RF phase velocity . Correspondingly to the RF power dependence of the current drive efficiency, it can be noted on Fig. 4, an improved efficiency at low RF power level whatever the amount of residual OH power. The latter is due to the additional current $\Delta\sigma(V - L\dot{I}_p^{RF})$ which makes the RF power more efficient that OH power to ramp-up the plasma current in this RF power range.

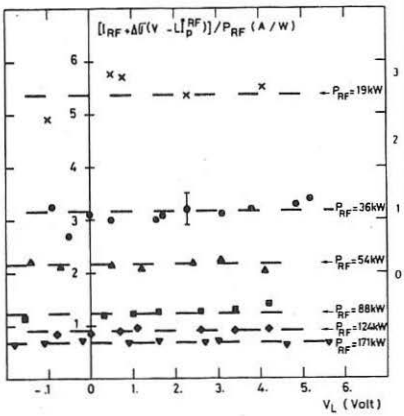

Fig. 2 - Current drive efficiency as a function of the loop voltage for various RF power levels. I_p = 140 kA and $\bar{n}_e = 9.\times10^{12}$ cm^{-3}

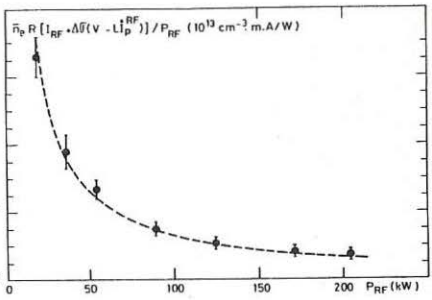

Fig. 3 - Current drive efficiency as a function of RF power. I_p = 140 kA and $\bar{n}_e = 9.\times10^{12}$cm^{-3} (V= C^{st})

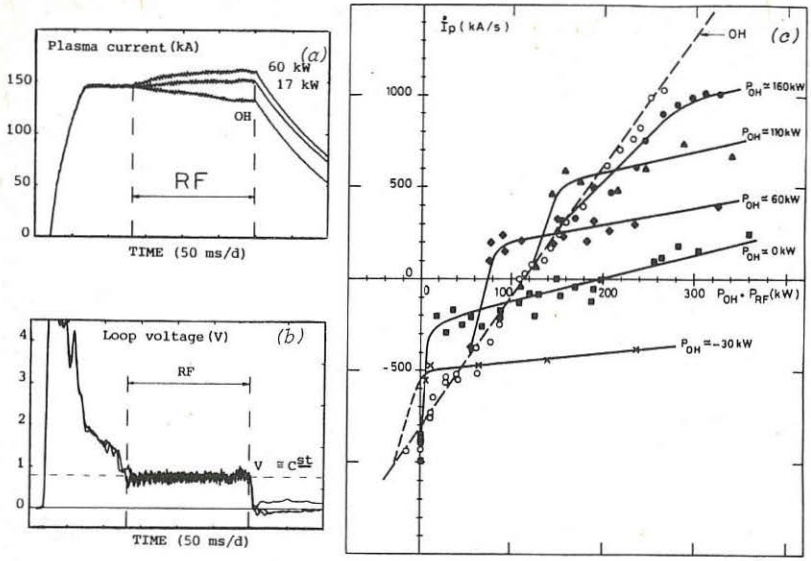

Fig. 4 -(a) Plasma current for various RF power levels in the $V = C^{st}$ (b) operating mode and (c) rate of change in the current as a function of the total power for various residual OH powers. I_p = 140 kA, $\bar{n}_e = 9.10^{12}$ cm^{-3}.

SUMMARY

A new mode of operation where the loop voltage is maintained constant has been studied experimentally on Petula-B. In this operating mode, it is possible to maintain a constant DC electric field parallel or opposite to the RF phase velocity and less than or greater than the Dreicer field. The current drive efficiency written as $\eta = \eta_o[1 + \Delta\sigma(V - L\dot{I}_p^{RF})/I_{RF}]$ does not depend on the value of the total DC electric field $\{E \sim (1/2\pi R)V\}$ present in the discharge but it is a function of the RF power through the additional current $\Delta\sigma . L\dot{I}_p^{RF}$ due to the electric field $\{E_{L^\sim} (1/2\pi R)L\dot{I}_p\}$ caused by the increasing plasma current.

REFERENCES

/1/ VAN HOUTTE D. et al. (1985). In Proc. of Tokamak Startup, Erice.

/2/ GORMEZANO C. et al. (1984). In Proc. of 10 th Int. Conf. on Plasma Physics on Cont. Nucl. Fusion Res., London, Vol. 1, p. 473.

/3/ VAN HOUTTE and F. PARLANGE (1983). IAEA Technical Committee Meeting. on Non Inductive Current Drive in Tokamaks, Culham, Vol. 2, p. 356.

/4/ FISCH N.J., (1984). rep. PPPL 2108, Princeton University.

/5/ FISCH N.J., (1978). Phys. Rev. Lett. 41 , p. 873.

NUMERICAL STUDIES OF LH CURRENT DRIVE IN THE PRESENCE OF AN ELECTRIC FIELD

S. Succi, K. Appert and J. Vaclavik

Centre de Recherches en Physique des Plasmas
Association Euratom - Confédération Suisse
Ecole Polytechnique Fédérale de Lausanne
21, Av. des Bains, CH-1007 Lausanne / Switzerland

Abstract : The dynamical response of a homogeneous plasma to the simultaneous application of an RF power source and an opposing d.c. electric field is investigated by means of a 2-D + 2-D quasilinear code. The code evolves in time the electron distribution function, $f(v_\parallel, v_\perp, t)$ and the corresponding self-consistently generated wave spectral distribution $W(k_\parallel, k_\perp, t)$, both in two dimensions. The time evolution of the most relevant physical quantities, in particular the plasma current can therefore be straightforwardly evaluated.

Introduction : Recent current-drive experiments in PLT and ASDEX [1,2] have clearly demonstrated the ability of lower-hybrid waves not only to maintain a steady plasma current, but also to increase it ("ramp-up") during the discharge. Since the time variation of the current induces a d.c. electric field opposite to the direction of RF waves, any appropriate theoretical description of current ramp-up requires the knowledge of the plasma dynamical response to the simultaneous application of the RF power and opposing electric field.

A few theoretical models for such a problem have already been developed. The earliest one, due to Borrass and Nocentini [3], is based on a one-dimensional time-independent Fokker-Planck analysis and it has therefore a rather limited range of validity. Later on, Fisch and Karney prompted out a series of papers in which a linearized Boltzmann equation was solved, either by integrating the corresponding Langevin equations [4], or, more recently, with a more sophisticated approach based on the adjoint formulation [5].

In this paper we present the first results obtained with an entirely different, purely numerical approach, based on a finite-element expansion of the two-dimensional electron distribution function, $f(v_\parallel, v_\perp, t)$, and the corresponding wave spectral distribution $W(k_\parallel, k_\perp, t)$. Our code solves the 2-D + 2-D quasilinear equations self-consistently in time without any simplifying assumption and provides therefore a very detailed information on the plasma dynamical behaviour .

In this paper no attempt is made to simulate any particular Tokamak discharge. We rather investigate the initial value problem represented by the quasilinear equations with the electric field, as such. We take therefore a licence to treat the electric field strength as a free parameter and study its influence on the electron distribution function in the presence of an RF power source. Particular attention is paid to the dynamics of the mechanism by which the electric field opposes and finally overcomes the RF driven current.

Basic Equations : The basic equations of our model are the following:

$$\frac{\partial f}{\partial t} = \left(\frac{\delta f}{\delta t}\right)_{COLL} + \left(\frac{\delta f}{\delta f}\right)_{QL} + \frac{\nu ei}{\omega pe} E\frac{\partial f}{\partial v_{\parallel}}$$

$$\frac{\partial W}{\partial t} = (2\gamma - \nu_{ei} Z)\, W + S_0 s(k)$$

where cylindrical coordinates $v_{\parallel}$, $v_{\perp}$ and $k_{\parallel}$, $k_{\perp}$ are adopted for both f and W.

The term $\left(\frac{\delta f}{\delta t}\right)_{COLL}$ represents a linearized 2-D collision operator, $\left(\frac{\delta f}{\delta t}\right)_{QL}$ the quasilinear diffusion operator , and 2γ the corresponding wave damping rate (only the Cerenkov resonance is included in the present work). The explicit expressions are given in [6]. Z represents the ion-charge number and ν_{ei} the electron-ion collision frequency. The term $S_0 s(k)$ models the RF-power source, s(k) being a shape function normalized as $\int s(k) k^2 dk = 1$ and S_0 a scale parameter which fixes the total RF power input. The normalizations adopted are:

$k \to k\lambda_D^{-1}$; $v \to v v_{te}$; $t \to t\omega_{pe}^{-1}$; $W \to W 4\pi n T \lambda_D^3$; $E \to E E_D$

where λ_D is the Debye length, $E_D = m_e v_{te} \nu_{ei}/e$, ω_{pe} the plasma electron frequency and v_{te} the electron thermal speed $\sqrt{(T/m_e)}$.

Apart from the numerical aspects, which will be presented elsewhere [7], there are two basic novel features with respect to our previous model [8] that are worth mentioning. First of all no assumption is made on the perpendicular shape of the distribution function, so that non-maxwellian dependencies on $v_{\perp}$ are free to develop. Second, and more important for the present work, a d.c. electric field is included in the kinetic equation.

The results : Before presenting our numerical results let us briefly recall the basic mechanism which governs the competition between the RF waves and the electric field.

In the absence of the electric field the current is ultimately provided by the number of non resonant ($v_{\parallel} < v_1$) electrons which can flow to the resonant region ($v_1 < v_{\parallel} < v_2$). When the electric field is present, we have basically two scenarios how this flow is opposed.

The first possibility (for a relatively small field) is that the non resonant electrons are allowed to access the resonant region, but subsequently leave it under the combined action of the electric field and pitch-angle scattering. These electrons will contribute to the bulk or runaway ($v_{\parallel} < -v_D \equiv -\sqrt{1/E}$) anticurrent depending on whether they quit the resonant region with a velocity smaller or larger than v_D. Note that the number of antirunaways can be enhanced by the presence of the RF waves because the particles in the resonant strip can be pitch-angle scattered in the opposite direction with a velocity larger than v_D.

As the field becomes larger it is more and more difficult for the electrons to access the resonant region and the conditions of a pure antirunaway situation are approached. The fate of the electrons depends essentially on the location of the resonant strip with respect to v_D. In this paper we kept v_1, v_2 fixed and just varied v_D.

We have performed a series of computations assuming the following set of parameters:

$S_0 = 10^{-7}$, $\nu_{ei} = 0.75 \times 10^{-7}$, $v_1 \sim 3.5$, $v_2 \sim 10$,

which correspond roughly to the PLT ramp-up conditions [1] with a total power of about 130 kW.

In Fig. 1 the time evolution of the plasma current density, $j(t)$, is shown for several values of the d.c. field amplitude, E. From this figure we see that an electric field of about 0.06 is sufficient to impede any current ramp-up ($j(0) \sim j(t \to \infty) \simeq 0.20$). The plateau level on the distribution function is reduced about a factor 2 with respect to the case without d.c. field and most of the anti current (75%) is carried by the slow electrons with $|v_\parallel| < v_1$. For E = 0.04 one has a ramp-up rate of about 1000 kA/sec, almost an order of magnitude higher than typical experimental values.

A realistic value of E lies therefore somewhere between 0.04 and 0.06. For E = 0.04 the anticurrent is completely dominated by slow electrons, so that one expects the theory proposed in Ref.[3] to be appropriate for the prediction of the correct steady state value $j_E^\infty \equiv j(E; t \to \infty)$. This is rapidly checked by evaluating the parameter γ_0, defined as $\gamma_{0_{num}} = 2(j_0^\infty - j_E^\infty)/E j_E^\infty$ and comparing it with the theoretical value $\gamma_0^{TH} = (v_2^2 - v_1^2)/2 \ln v_2/v_1$. By taking $v_1 \sim 3$ and $v_2 \sim 10$ one has $\gamma_0^{TH} \sim 40$, not far from the numerical value of about 60. As the parameter E is increased this good agreement disappears (we have $\gamma_0 \sim 90$ for E=0.06 and $\gamma_0 \sim 190$ for E=0.08), showing that the range of validity of this theory has been overcome. In this parameter regime one expects the rôle of high-$v_\parallel$ anticarriers to become more and more important.

This is, in fact, the case as shown in Fig. 2, where the distribution function integrated over $v_\perp$, $F(v_\parallel)$, is represented for E=0.04 and E=0.08. In particular, the RF-produced antirunaway tail is clearly displayed in Fig. 3, where the negative high-$v_\parallel$ portion of $F(v_\parallel)$ is shown for E=0.08, with and without RF power. In the present context the value E=0.08 is purely academical since we have seen that a realistic value has to be anyway smaller than 0.06. However, it is also true that for higher RF power, larger values of E will be involved in realistic situations so that the rôle of RF produced antirunaways is likely to be important. This, and other questions concerning the influence of the relevant parameters, like density, location of the RF spectra and so on, will be subject of future investigations.

References:

[1] F.C. Jobes et al., Phys. Rev. Lett. 55 (1985) 1295.

[2] F. Leuterer et al., Phys. Rev. Lett. 55 (1985) 75.

[3] K. Borras and A. Nocentini, Plasma Physics and Controlled Fusion, 26 (1984) 1299.

[4] N.J. Fisch and C.F.F. Karney, Phys. Rev. Lett. 54 (1985) 897.

[5] C.F.F. Karney and N.J. Fisch, Phys. Fluids 29 (1986) 180.

[6] S. Succi et al., 3rd Europ. Workshop on Problems in the Numerical Modelling of Plasmas, Varenna, 1985. To appear in Comput. Phys. Communication.

[7] S. Succi, K. Appert and J. Vaclavik, 8th Europhysics Conf. on Comp. Phys., Eibsee, 1986.

[8] S. Succi et al., in Plasma Phys. and Contr. Nuc. Fusion Research (Proc. 10th Int. Conf., London, 1984), Vol. 1, IAEA, Vienna (1985), 549.

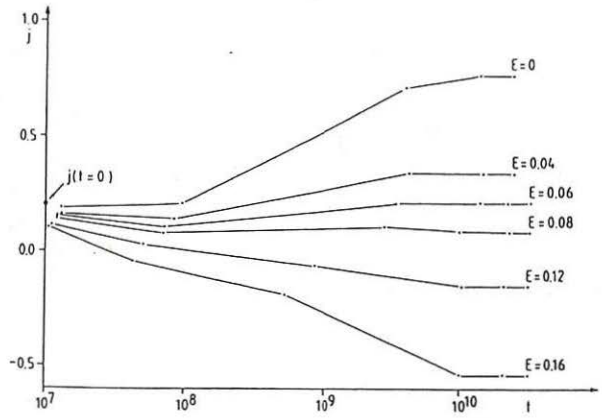

Fig. 1

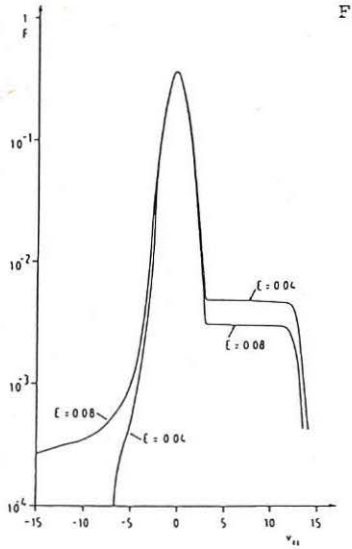

Fig. 2

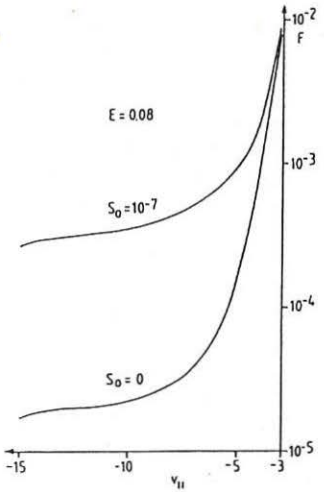

Fig. 3

INFLUENCE OF THE $N_{\parallel}$-SPECTRUM ON LOWER HYBRID CURRENT DRIVE IN ASDEX

F. Leuterer, M. Brambilla, D. Eckhartt, K. McCormick, M. Münich,
F. Söldner, M. Zouhar, G. Becker, H.S. Bosch, H. Brocken, A. Eberhagen,
G. Fussmann, O. Gehre, J. Gernhardt, G. v.Gierke, E. Glock, O. Gruber,
G. Haas, J. Hofmann, A. Izvozchikov[1], G. Janeschitz, F. Karger,
M. Keilhacker[2], O. Klüber, M. Kornherr, K. Lackner, M. Lenoci[3],
G. Lisitano, F. Mast, H.M. Mayer, D. Meisel, V. Mertens, E.R. Müller [2],
H. Murmann, H. Niedermeyer, A. Pietrzyk[4], W. Poschenrieder, H. Rapp,
H. Röhr, J. Roth, F. Ryter[5], F. Schneider, C. Setzensack, G. Siller,
P. Smeulders[2], K.-H. Steuer, F. Wagner, D. Zasche
Max-Planck-Institut für Plasmaphysik
EURATOM Association, D-8046 Garching

The lower hybrid current drive experiments in ASDEX so far have been performed mainly by operating successive waveguides of the grill at a relative phase of $\Delta\varphi = \pi/2$ and with equal amplitudes. The spectrum thus excited is considered in this paper as a reference spectrum and is shown as spectrum C 1 in Fig. 1. With such a spectrum it has been observed, like in many other related experiments, that the primary current rate of change, $-\dot{I}_{OH}$, necessary to maintain a constant plasma current I_p, decreased with increasing rf-power, P_{RF}. At a specific value of P_{RF}, depending on density and plasma current, $\dot{I}_{OH}$ becomes zero and the plasma current is driven by rf alone, while at higher powers the transformer gets recharged /1/. The scaling of these effects was found to depend on the accessibility of the lower hybrid waves and to agree with theoretical predictions /2, 3/. It was also shown that the current density profile j(r) for rf-current drive is different from that obtained for inductive current drive and is no longer directly determined by the electron temperature profile /4, 5/. In this paper we describe experiments with "tailored" spectra where phase and amplitude in each waveguide are specifically set to produce a $N_{\parallel}$-spectrum with a definite wing at the high $N_{\parallel}$-side. Such a wing is considered essential in explaining the magnitude of the driven currents as observed in the experiments /6/. These spectra are obtained by appropriately superimposing in the grill waveguides fields producing each by itself different $N_{\parallel}$-spectra, resulting in

$$U_n = e^{i(n-1)\Delta\varphi_1} + a \cdot e^{i\alpha}\, e^{i(n-1)\Delta\varphi_2} \qquad (1)$$

Here U_n is the wave amplitude in the n-th waveguide of the grill. One set of such spectra where we used $\Delta\varphi_1 = \pi/2$, $\Delta\varphi_2 = 5\pi/6$, and α and a were varied, is shown in Fig. 1. Other combinations of $\Delta\varphi_1$, $\Delta\varphi_2$, a, and α were used in order to tailor the wing of the spectrum in different ways (for example Fig. 6). In the experiment we have excited each one of these spectra with the same total input power of 400 kW. This was about a power limit for those experiments because of the very different powers (up to 130 kW) to be applied to the individual waveguides. A density of $\bar{n}_e = 6 \times 10^{12}$ cm^{-3} was then chosen in order to obtain a stationary current drive ($\dot{I}_{OH,RF} = 0$) in the case of the reference spectrum C 1.

---

[1]Academy of Sciences, Leningrad, USSR; [2]Assigned to JET Joint Undertaking, England; [3]ENEA Frascati, Italy; [4]University of Washington, Seattle, USA; [5]CEN Grenoble, France

Figure 2 shows the primary current $I_{OH}(t)$ which is necessary to maintain a constant plasma current Ip before and during the application of LH-power with the spectra shown in Fig. 1. The curves are displaced for clarity. We recognise that for spectra with an increasing fraction of power at high $N_{\parallel}$ the current drive becomes less efficient, i.e. $-\dot{I}_{OH,RF}$ increases. The same $\dot{I}_{OH,RF}$ would be obtained with a smaller amount of power, $P^{o}_{RF,Cn}$, if the applied spectrum were the reference spectrum C 1. In Fig. 3 we plot the ratio $P^{o}_{RF,Cn}/P_{RF,C1}$ where $P_{RF,C1}$ is the power resulting in $\dot{I}_{OH,RF} = 0$ for the spectrum C 1. The LH-driven current scales, as:

$$I_{RF} \sim \mu \cdot g \cdot P_{RF}/\bar{n}_e ,$$

where

$$\mu = \int_{N_{\parallel 2}}^{N_{\parallel 1}} P(N_\parallel)\,dN_\parallel \Big/ \int_{-\infty}^{+\infty} P(N_\parallel)\,dN_\parallel \quad , \quad g = \left(N_{\parallel 1}^2/N_{\parallel 2}^2 - 1\right)\Big/\left(N_{\parallel 1}^2 \ln N_{\parallel 1}/N_{\parallel 2}\right)$$

and $N_{\parallel 2}$ is determined by accessibility or the lower $N_\parallel$-boundary of the spectrum /7,8/. We therefore may write:

$$P^{o}_{RF,Cn}/P_{RF,C1} = (\mu \cdot g)_{Cn}/(\mu \cdot g)_{C1} \ .$$

The factor $(\mu \cdot g)$ depends of course on the choice of the spectrum boundaries $N_{\parallel 2}$ and $N_{\parallel 1}$. The two lines in Fig. 3 show the calculated ratio $(\mu g)_{Cn}/(\mu g)_{C1}$. For line a we chose $N_{\parallel 2} = N_{\parallel acc} = 1.5$ and the upper boundary $N_{\parallel 1}$ was determined by $r = \int_0^{N_{\parallel 1}} P(N_\parallel)dN_\parallel / \int_0^{\infty} P(N_\parallel)dN_\parallel = 0.97$. For line b $N_{\parallel 2}$ was either $N_{\parallel 2} = N_{\parallel acc} = 1.5$ or determined by $r = 0.1$ and $N_{\parallel 1}$ was determined by $r = 0.9$, thus shifting $N_{\parallel 2}$ to values greater than 1.5 for the spectra C 7 to C 13. We see that in the experiment the current drive efficiency is always greater than in the calculation b, while for calculation a this is true only for spectra C 3 and C 5, but less than calculated for C 9 to C 13. From this we conclude that in using the above equation for g, which is derived for a rectangular power spectrum /8/, we overemphasise the high $N_\parallel$-part of the spectrum while the low $N_\parallel$-part is more efficient with respect to current drive. To describe our experimental results in more detail we would thus need instead of the function g a function which does not only depend on the boundaries $N_{\parallel 2}$ and $N_{\parallel 1}$ of the spectrum but also upon its shape.

We further observed that the signal $\Lambda + 1$ as deduced from the equilibrium field depends remarkably upon the applied spectrum. As an example we show in Fig. 4 the difference between $\Lambda + 1 = \beta_p^{equ.} + li/2$ and $\beta_p^{\perp}$ (from the diamagnetic loop). This difference changes when LH-power is applied due to the wave generated anisotropy in the electron velocity distribution, $\beta_p^{equ.} - \beta_p^{\perp}$ which occurs on a fast time scale and is positive, and also because of a slowly decreasing l_i. The dependence of l_i as a function of the applied spectrum is shown in Fig. 5 for the set of spectra shown in Fig. 6. We see that $-\Delta l_i$ increases with increasing power in the high $N_\parallel$-part of the spectrum. This has also been observed in a phase scan where the shape of the spectrum remains roughly constant but the mean value $\langle N_\parallel \rangle$ is shifted from 2 to 4 with a directivity dropping to zero. The change in l_i is thus not only related to the amount of rf-driven current, but also to the shape of the spectrum, and the maximum Δl_i does not coincide with a maximum current drive efficiency. This suggests that the higher $N_\parallel$-part of

the spectrum is absorbed further radially outward than the low $N_{\parallel}$-part. The generated current density profile depends on the choice of the spectrum, and is not only determined by the direct rf-driven current, but also by an rf-modified conductivity profile due to bulk heating or suprathermal electrons.

We should also note that while l_i is decreasing additional power from the decreasing poloidal field energy is available in the plasma, leading to a further reduction in the loop voltage.

REFERENCES

/1/ F. Leuterer et al., Phys.Rev.Lett. 55 (1985) 75
/2/ F. Leuterer et al., Plasma Phys. and Contr. Fus. 27 (1985) 1399
/3/ F. Leuterer et al., Proc. 12th Europ. Conf. on Contr. Fusion an Plasma Physics, Budapest 1985, Vol. II, p. 240
/4/ K. McCormick, ibid., Vol. I, p. 199; also this conference
/5/ F. Söldner et al., this conference
/6/ S. Succi et al., Proc. 10th IAEA-Conf. Plasma Physics and Contr. Nucl. Fusion, London 1984, Vol. I, p. 549
/7/ G. Tonon, D. Moulin, 4th Int.Symp. Heating in Toroidal Plasma, Rome 1984, Vol. II, (1984) 1343
/8/ C.F. Karney, N. Fisch, Phys.Fluids 22 (1979) 1817

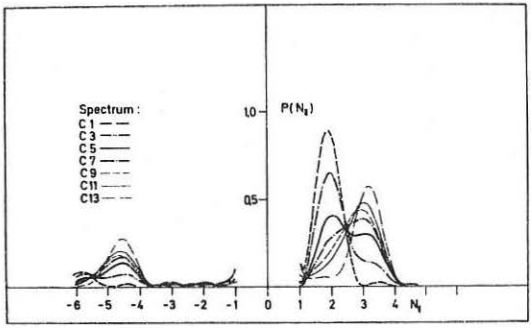

Fig. 1

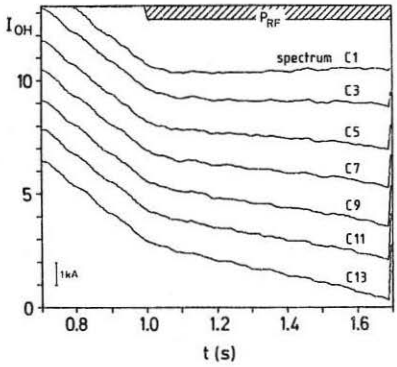

Fig. 2

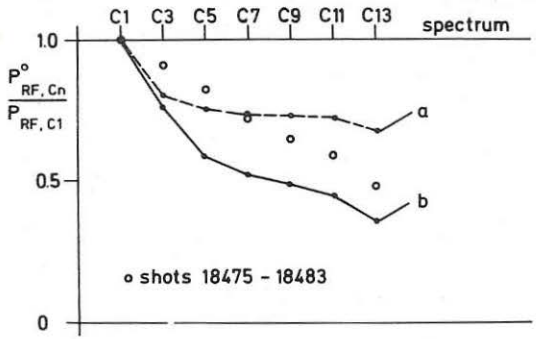

Fig. 3

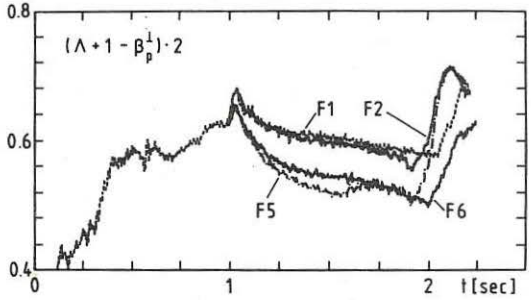

Fig. 4

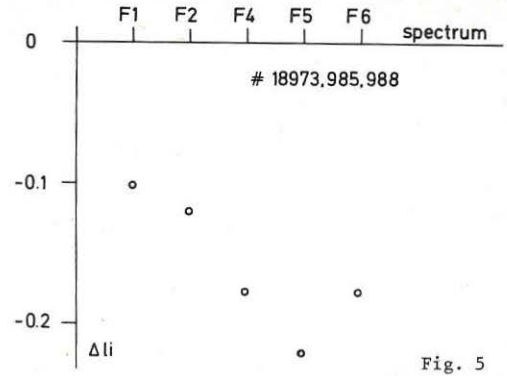

Fig. 5

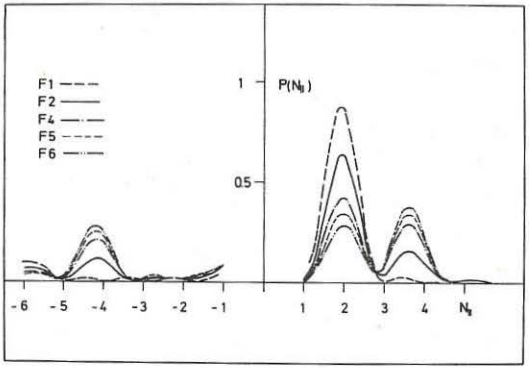

Fig. 6

BEAT-WAVE CURRENT DRIVE

J.T. MENDONÇA

Centro de Electrodinâmica, Instituto Superior Técnico
1096 Lisboa Codex, Portugal

1. Introduction

In recent years, a number of theoretical papers and experimental results have shown that it was possible to generate steady-state currents in toroidal discharges, by electron Landau damping of lower hybrid waves. Various other schemes have also been proposed, including electron-beam injection and the use of other kinds of waves in the radio-frequency ranges.

A different approach to this problem is considered in the present work. Here we study the nonlinear excitation of an electrostatic mode of the plasma, by the beating of the high-frequency electromagnetic waves. The subsequent interaction of the electrostatic oscillations with nearly resonant particles can lead to a current. The frequencies of the two beating waves can be chosen heigher than any resonant frequency of the plasma, in order to avoid the accessibility problems which appear in the lower hybrid scheme.

We present the results of both fluid and kinetic calculations. The plasma fluid model can be used to estimate the saturation amplitude of the excited waves. With the kinetic description we can derive a closed set of equations, describing the evolution of the electrostatic wave amplitude and the slow modification of the particle distribution functions.

2. Fluid model

We assume an infinite and homogeneous plasma, in the presence of a static magnetic field $\vec{B}_o = B_o \hat{z}$, subjected to the

action of two high-frequency electromagnetic waves, described by the fields:

$$\vec{E}_j(\vec{r},t) = \frac{E_j}{2}\,\hat{a}_j \exp(i\vec{k}_j.\vec{r}-i\omega_j t) + c.c. \qquad (1)$$

where $j=1,2$ and $\hat{a}_j$ are the unit polarization vectors. We assume that the linear dispersion relations $D(\omega_j,\vec{k}_j)=0$ are satisfied and that the two waves are beating ressonantly at a frequência $\omega=\omega_1-\omega_2$, which is nearly equal to the frequency of some eigen--oscillation of the plasma. In this case, we expect that the ponderomotive force induced by the two waves (1) will drive plasma oscillations with growing amplitude. If collisions are taken into account, this amplitude will saturate at given level.

The simplest way to describe the beat-wave excitation and saturation is using the hydrodynamic equations for the electron and ion fluids, together with the Poisson equation for the electrostatic field $\vec{E}$. If we look for a forced solution of these equations of the form

$$n_\alpha = N_\alpha (1-e^{-\nu t}) \exp(i\vec{k}.\vec{r}-i\omega t) + c.c. \qquad (2)$$

where $\vec{k}=\vec{k}_1-\vec{k}_2$, ν is the inverse of the saturation time and n_α the electron ($\alpha=e$) and ion ($\alpha=i$) density fluctuations, we can easily obtain:

$$N_\alpha = -\frac{n_o}{2\nu}\left(r_\alpha + \frac{\vec{k}.\vec{p}_\alpha}{\omega-i\nu}\right) \qquad (3)$$

where r_α and $\vec{p}_\alpha$ are the ponderomotive terms appearing in the equations of mass and momentum conservation, respectively.

Let us consider, as an exemple, the beat-wave excitation of electron-plasma oscillations by two electromagnetic waves, propagating along the magnetic field lines. Eq. (3) then leads to the following saturation amplitude for the plasma oscilla tions:

$$N_e = \frac{n_o}{2\nu_e}\left(\frac{e}{m}\right)^2 \frac{E_1 E_2^* k}{\omega_1\omega_2\omega}\left(\frac{\omega_2 k_1}{\omega_{ce}-\omega_2} - \frac{\omega_1 k_2}{\omega_{ce}-\omega_1}\right) \qquad (4)$$

A detailed exploration of eq. (3) can give us some information about the most convenient configurations for beat-wave current-drive /1/. Further developments of the fluid model can include nonlinear saturation effects and oscillation breakdown /2/.

3. Kinetic model

A further step in the theory is to consider a self-consistent description of wave-particle interactions, in the frame of the usual weak-turbulence theory. The saturation levels of the excited oscillations are determined by quasi-linear processes which lead to current drive.

It can be shown /3/ that the evolution equation for the zero-order distribution functions $f_{o\alpha}$, takes the form:

$$\left[\frac{\partial}{\partial t} + \frac{q_\alpha}{m_\alpha}(\vec{v}\wedge\vec{B}_o)\frac{\partial}{\partial \vec{v}}\right] f_{o\alpha} = -\nu_\alpha f_{o\alpha} - \frac{q_\alpha}{m_\alpha}\int \vec{E}_E(\vec{k})\frac{f_B(-\vec{k})}{\partial \vec{v}}\frac{d\vec{k}}{(2\pi)^3} \qquad (5)$$

where $\vec{E}_B(\vec{k})$ and $f_{o\alpha}(\vec{k})$ are the Fourier components of the electric field and the corresponding distribution function for the electrostatic beat wave. They are determined by the quasi-linear equations, which can be solved by using a multiple time scale technique. We can also replace the phenomenological collision frequency ν_α by the rate of collision drag due to binary collisions between resonant and non-resonant particles. A steady-state solution is then derived, which is equivalent to that obtained by Fisch for the lower-hybrid current-drive. The main diference is that, in the beat-wave case, the diffusion in phase space is determined directly by the intensity of the incident electromagnetic waves, and not by the intensity of the electrostatic oscillations. If we now apply these results to the case of two beating CO_2 laser beams, with a typical intensity of 10^{11} W/cm^2 and assume typical Tokomak parameters ($n_o = 10^{14}$ cm^{-3}, T_e = 10 KeV) we see that a current of .1 ($e\, n_o\, V_{th}$) can be driven, in agreement with previous simulations.

With respect to the other current-drive schemes, the method described here has the advantage of being insensitive

to acessibility limitations and to allow for very localized effects, which can be useful for current profile control. But it also has the desadvantage of being a nonlinear or second--order effect and to require two different sources of radiation.

Rerefences

1 - J.T. Mendonça, F. Serra and C. Varandas, Fusion Theory Meeting, Wébion (1986).

2 - J.T. Mendonça, J. of Plasma Phys. 34, 115 (1985)

3 - J.T. Mendonça and R.M.O. Galvão, J. of Plasma Phys. (1986).

AN ICRF CURRENT DRIVE EXPERIMENT ON JIPP T-IIU

R. Ando, E. Kako, Y. Ogawa, T. Watari,

Institute of Plasma Physics, Nagoya University,
Nagoya 464, Japan

ABSTRACT

In JIPP T-IIU tokamak the fast wave current drive with five loop antennas has been successfully carried out at a relatively high density plasma ($\omega_{pe}^2/\omega_{ce}^2 \sim 5$). The RF frequency is 40 MHz and the toroidal field is 2 kG, which corresponds to $\omega = 13\omega_{cH}$. To exclude the effect of the inductive field, the plasma production and the start-up of the plasma current have been done with ICRF wave only. The density and temperature of a plasma produced by the RF wave are that $\bar{n}_e \sim 2 \times 10^{18} m^{-3}$ and $T_e \sim 10$ eV, where only the fast wave can propagate excluding out the possibility of a slow wave current drive. This density is two orders of magnitude higher than the density limit predicted for the slow wave current drive.

The maximum plasma current of 3.5 kA is driven with the rf power of about 400 kW. The efficiency $\eta = I_p \bar{n}_e / P_{rf}$ is around 2×10^{16} $A \cdot m^{-3}$ /W, which is two orders of magnitude lower than that of recent lower hybrid current drive. We have observed the clear dependence of the current drive efficiency as a function of the phase difference $\Delta\varphi$. When antennas are phased with $\Delta\varphi = \pi/4$, the maximum efficiency is obtained. A calculation shows that the wave spectrum is then peaked around $N_\parallel \sim 4$. However, a large MHD oscillation is observed, although the safety factor q_a is about 10 or more. The relatively low current drive efficiency observed will be attributed to the low electron temperature.

1. Introduction: The development of non-inductive current drive is one of the key issues in the investigation of tokamaks and the lower hybrid slow wave current drive is the only successful means discovered so far [1,2]. Its density limit, however, makes its prospectives very bleak, and various alternative candidates have been proposed and discussed in the design work of DEMO reactor [3]. The current drive experiment presented here belongs to high speed magnetosonic current drive. Here, rf frequency is chosen much higher than the ion cyclotron frequency with a plasma density high enough not only for a fast wave to propagate, but also for a slow wave to be pushed away behind the limiter. Any mode conversion processes from fast to slow wave could not, therefore, occur either because of the natural density fluctuation of the plasma or the reflection at the vaccum vessel wall. With such conversion mechanism of any small rate, a sizable effect will be brought about because the wave absorption mechanism for a slow wave is much stronger than that of a fast wave. To avoid the possibility of the slow wave current drive, the following inequality is, therefore, requried,

$$\omega^2 < \omega_{LH}^2(edge) \equiv \frac{\omega_{pi}^2}{1+\omega_{pe}^2/\omega_{ce}^2}\Big|_{edge} , \qquad (1)$$

where all quantities are refered to at the edge of the plasma.

2. Experimental Results: The experiment was conducted on JIPP T-IIU tokamak (R/a = 0.91m/0.23m) with the rf frequency of 40 MHz. The toroidal field is as low as 0.2 T so that the rf frequency is high enough to avoid the wave to couple with ions. This frequency corresponds to the 13 ω_{cH}. Inside the vacuum chamber were installed five loop antennas side by side for the fast wave current drive. The phase differece $\Delta\varphi$ between each antenna element is continuously variable. Figure 1 shows the wave $N_{\parallel}$- spectrum calculated using an three dimentional wave excitation code, which is an improved version of that written by Messiaen et al. [4] , allowing arbitral plasma density profiles and multi-antenna array. We can see from Fig. 1 that the wave energy is neatly shaped around $N_{\parallel}$ =7 when the relative phase difference at each antenna is $\Delta\varphi=\pi/2$.

The plasma is lit by rf itself with a filling pressure of $(2\sim4)\times10^{-4}$ torr. Figure 2 shows signals of a typical discharge, where the plasma current of 3.5 kA is ramped up with the rf power only. The rf pulse shown in the bottom picture indicates a power level around 300 kW with a pulse length of about 30 ms. It takes about 7 ms after the turn on of the rf to break the gas into a discharge. When the plasma is fired, there occurs a sudden increase in the antenna loading followed by a gradual increase of plasma current I_P. The one turn voltage V_L is negative when the current rises and positive when it falls. The plasma density sustained by the rf is about 2×10^{18} m^{-3}, which is high enough to make fast wave propagate, and to satisfy the inequality given by eq. (1). Here, the primary winding of the Ohmic transformer is short-circuited in order to minimize the energy stored in the iron core. The signals of the magnetic proble show that the plasma is kept in the center of the vaccum chamber during the discharge.

The relative phase angle between five antenna array was changed in order to observe whether the current driven in these experiments is due to wave/plasma interaction or not. It is important to exclude out possible equilibrium current. Theories demand that the current should be driven in the direction to which the wave is emitted, either because of the momentum input or caused resistivity anisotropy. The direction of the current is found to be primarily determined by that of the vertical field. The plasma current driven by the rf is plotted in Fig. 3 as a function of the phase difference $\Delta\varphi$ for different direction of the vertical field. When the vertical field is pointing upwards (downwards), the current flows clock-wise (counter-clock-wise) and best efficiency is obtained around $\Delta\varphi=\pi/4$ ($\Delta\varphi=-\pi/4$). The results of these two cases are consistent to the theoretical expectation, where the wave gets its best clock-wise directionality with $\Delta\varphi=\pi/2$ and counter-clock wise directionality with $\Delta\varphi=-\pi/2$. Quantitatively, however, the best current drive efficiencies in the experiment are obtained with a little shallower phasing angles than $\Delta\varphi=\pm\pi/2$. This may be explained in terms of the $N_{\parallel}$- spectrum of the launched wave. In Fig.1 wave $N_{\parallel}$- spectrum is compared for the two cases $\Delta\varphi=\pi/2$ and $\Delta\varphi=\pi/4$, where experimental parameters are used in the computation. Obviously the wave has the peak at a lower $N_{\parallel}$ for $\Delta\varphi=\pi/4$ case than that of $\Delta\varphi=\pi/2$ case. Since the wave couples to faster electron with a lower $N_{\parallel}$, the current drive efficiency could be better with a shallower phasing than $\Delta\varphi=\pi/2$.

The dependences on the rf power and the plasma density have been examined. Figure 4 shows the power dependence of the driven current, where plasma density is fixed to 2×10^{18} m^{-3}. The current drive efficiency $\eta=I_P\bar{n}_e/P_{rf}$ is read out to be around 2×10^{16} $A\cdot m^{-3}$ /W which is two orders of magnitude lower than that of conventional LH current drive. It may be attributed to the low electron temperature; because this experiment is a start-up experiment, electron temperature is low if radiation barrier is not broken through. It was estimated to be around 10 eV from the time evolution

of several visible impurity lines.

With I_P=3 kA which yields safety factor q_a around 10 or more, the plasma should have enough rotational transform for good particle confinement. Thus the plasma is expected to exceed the radiation barrier with the power level as high as 200 kW. The reason for this low electron temperature (Te $\sim$ 10 eV) is in the MHD instability. There is no adequest theory for explaining this instability with a safety factor q_a as high as 10 and a Reynolds number as low as S = 2.1×10^4 . A possible conjecture is that the instability is due to the evolution of the plasma parameters $\bar{n}_e$ and q_a violating the range allowed by the Murakami's empirical law ($1/q_a \cdot B_T/n_eR \sim 0.7\ T/m^{-3}\cdot m$).

3. Discussion and Summary: The merit of an ICRF current drive is in its nature of density limit free. Experiments in LHCD quotes an empirical law $\omega_{pe}^2/\omega_{ce}^2 \sim 1$ as density limit. This value is as high as 5 in our experimental conditions, demonstrating that this new regime has nothing to do with the density limit as observed in the LHSWCD. According to the model proposed by Wegrowe et al. [5] , the density begins to be limited when the coupling of the wave with ions sets in. This gives the formula for the critical density

$$\frac{1}{(\bar{n}_e/10^{20})} = \frac{4.39}{f^2(GHz)}\left(\alpha + 1.6\frac{T_i}{A_iT_e}\right) - \frac{10.3}{B_T^2}, \qquad (2)$$

where α is a value around unity. This equation yields the density limit about $3\times10^{16}\ m^{-3}$ with relevant plasma parameters on the right hand side. The plasma density in our experiments is $2\times10^{18}\ m^{-3}$ far exceeding the value predicted for LHSW current drive.

In conclusion, we have demonstrated the fast wave current drive at $\omega \sim 13\ \omega_{ci}$ with a relatively high density plasma $\omega_{pe}^2/\omega_{ce}^2 \sim 5$, which is two orders of magnitudes as large as that predicted by the LHCD theory. The maximum plasma current is 3.5 kA with the rf power of 400 kW, and the efficiency is much lower than that of the present LHCD. This low efficiency seems to be attributed to the low electron temperature ($T_e \sim$ 10 eV), because of the onset of MHD instability. The amplitude of the induced current depends strongly on the phase difference, and the maximum efficiency is achieved at $\Delta\varphi \sim \pi/4$ ($N_\parallel \sim 4$).

Acknowledgements: The authors would like to thank members of CS group in IPP, Nagoya Univ., for fruitful discussion and supports of operations and diagnostics.

References

[1] Jobes, F., Stevens, J., Bell, R., Bernabei, S., Cavallo, A. et al., Phys. Rev. Lett. 52 (1984) 1005.
[2] Toi, K., Ohkubo, K., Kawahata, K., Kawasumi, Y., Matsuoka, K., et al., Phys. Rev. Lett. 52 (1984) 2144.
[3] Ehst, D., in Non-Inductive Current Drive in Tokamaks (Proc. of IAEA Technical Comittee Meeting, Culham, 1983) Vol. 1 (1983) 442.
[4] Messiaen, A. M., Koch, R., Bhatnagar, V. P., Evrard, M. P., Luwel, M., Vandenplas, P.E., and Weynants, R.R., in "Heating in toroidal plasma", commision of the Euratom communities, Vol. I (1982) 243.
[5] Wegrowe, J-G., and Engelmann, F., Comments on Plasma Physics and Controlled Fusion, 8 (1984) 211.

Figure Captions

Fig. 1 The wave spectra of the five antenna array for (a) $\Delta\varphi=\pi/4$ and (b) $\Delta\varphi=\pi/2$, taking the plasma/antenna coupling of the fast wave into account. The wave spectrum peaks at a lower $N_{\parallel}$ for a shallower phasing angle.

Fig. 2 The time evolution of the plasma current, one turn voltage and the programmed vertical field, with P_{rf} = 300 kW.

Fig. 3 The plasma current I_p versus $\Delta\varphi$, where $\Delta\varphi$ is the relative phase difference of two antennas next to each other. The plasma current flows clock-wise (counter-clock-wise) for the solid (broken) line, when the direction of the vertical field is upwards (downwards).

Fig. 4 The power dependence of the driven current I_P as a function of the injected rf power P_{rf} .

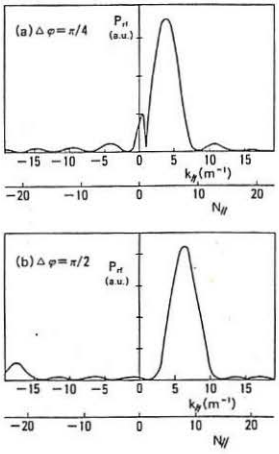

Fig. 1

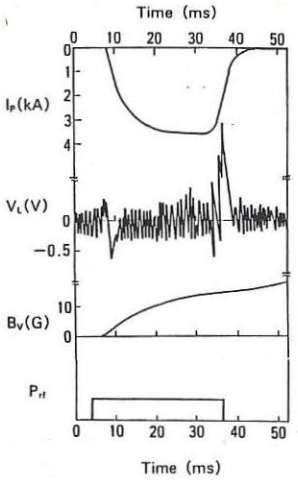

Fig. 2

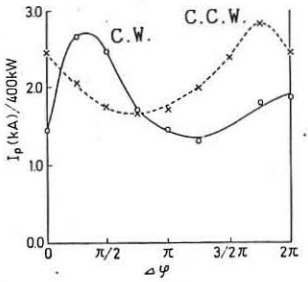

Fig. 3

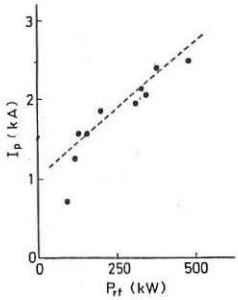

Fig. 4

FAST WAVE ELECTRON CURRENT DRIVE

D. Moreau*, J. Jacquinot, P.P. Lallia

JET Joint Undertaking.
Abingdon, Oxon, OX14 3EA, UK

* From EUR-CEA Grenoble, France

Abstract

As a basis for investigating the possibility of controlling current profiles in JET we present a short analysis of transit time magnetic pumping of electrons by fast magnetosonic waves above the ion cyclotron frequency.

1. Introduction

The "profile consistency" observed to limit the performances of additionally heated tokamak discharges stressed the interest of decoupling their temperature and current density profiles.

The fast magnetosonic wave has been considered as an attractive candidate for non-inductive current drive /1-2/. Unlike the slow wave in the lower hybrid frequency range, it has indeed the potentiality of being efficient at high density and high temperature. Interaction with the bulk of the electron distribution in the centre of the discharge, although not the most efficient, would provide the required absorption of the RF power. In particular the fast wave could be very well suited for driving a reverse current in the central hot and dense plasma of large tokamaks, with the hope of suppressing "sawteeth relaxations" /3/.

A mode conversion current drive scheme near a two-ion hybrid resonance (Bernstein wave current drive) has been proposed /4/. As an alternative, we shall concentrate in this paper on direct electron current drive from the high frequency Alfvén wave itself. We shall draw some preliminary conclusions with respect to wave absorption by the electrons, bearing in mind that other loss channels such as absorption from ions at harmonics of Ω_{ci} or from high energy fusion products will have to be avoided or overcome.

2. Electrodynamics of the fast wave above the ion cyclotron frequency

We consider frequencies such that $\Omega^2_{ci} < \omega^2 < \Omega_{ci}\,\Omega_{ce}$ and densities higher than the lower hybrid resonance density ($\omega^2_{pi} \gg \omega^2$). The wave has both electrostatic and electromagnetic components, ie. $\vec{E} = -\frac{1}{c}\frac{\partial \vec{A}}{\partial t} - \nabla\phi$, its electric field is mostly perpendicular to the equilibrium magnetic field $\vec{B}_o$ and its magnetic field $\vec{B}$ parallel to $\vec{B}_o$. Parallel currents exist due to a small parallel electric field but also to the bulk $\mu\nabla B$ force exerted on the electron fluid. This force is the only thermal effect taken into account. Solving Maxwell's equations within these assumptions, one obtains the following results:

- at densities such that $\omega_{pi} >> \omega$ only the fast branch propagates and there is no problem of accessibility up to a few harmonics of Ω_{ci};
- near cutoff the wave has all the characteristics of the right handed circularly polarized whistler mode and then transforms itself into the high frequency Alfvén wave (HFAW), $n = n_A = \omega_{pi}/\Omega_{ci}$, at almost perpendicular propagation.
- if $\vec{B}_o$ is along $\vec{O}z$, $\vec{k}$ in the Oxz plane and if α is the angle between $\vec{k}$ and $\vec{O}x$ we find the following polarization for the HFAW:

$A_y = -jn_A \phi \cos\alpha \, \Omega_{ci}/\omega$, $A_x << A_y$, $E_y = j k_o A_y$, $B_z = j k_o n_A A_y \cos\alpha$ and $E_x = -j k_o n_A \phi \cos\alpha$;

- the energy density carried by the wave is mostly in magnetic and ion kinetic energy and can be expressed as

$W = W_m + W_i = 2W_m = B_z^2/\mu_o = 0.5 \, n_e T_e \beta_e \left| e\phi/T_e \right|^2$ where β_e is the usual ratio of electron pressure to magnetic pressure.

3. Interaction of the fast wave with electrons : TTMP vs. LANDAU DAMPING

Both parallel (-eE// force) and perpendicular ($-\mu\nabla//B$ force) electric fields act upon the parallel velocity of the guiding centre of the electrons. However, unlike ions in TTMP heating, electrons see opposite forces and the interaction vanishes at some critical perpendicular energy $W_{\perp crit}$. Because the parallel electric field adjusts itself so as to give a zero net force on the bulk electron fluid (in the limit of zero electron inertia and $\omega_{pi} >> \omega$) we expect this critical energy to be near the thermal energy of the bulk electrons. TTMP diffusion will therefore be most efficient on electron tails having perpendicular energies a few times above thermal.

Our detailed calculations show that the total force applied on the guiding centre is

$$F// = j k_o e \phi \, n// \frac{\omega^2}{\Omega_{ce} \Omega_{ci}} \left[1 - \frac{W_\perp - \langle W_\perp \rangle}{mc^2} \frac{\omega^2_{pi}}{\omega} \cos^2\alpha \right]$$

so that the critical energy defined above is indeed

$$W_{\perp crit} = \langle W_\perp \rangle + mc^2 \, \omega^2/\omega^2_{pi}$$

where $\langle W_\perp \rangle$ is the average perpendicular energy of the electron fluid ($\langle W_\perp \rangle \simeq T_e$). It is to be noted that at high density and low frequency (50 MHz) $W_{\perp crit}$ is indeed near T_e whereas at higher frequencies (800 MHz) it is much larger so that Landau damping is the dominant absorption process (cf. Fig. 1).

From the expression of the total force given above, it is straightforward to obtain the quasilinear diffusion coefficient and the corresponding damping rate. We assume a Gaussian distribution in k// space for the wave energy density and, after some algebra, we find that we can approximate the diffusion coefficient by the following expression:

$$D_{ql} = 0.5 \langle \Delta v//^2 \rangle / \Delta t = \frac{\sqrt{\pi}}{2m^2 k_o} \frac{|F//|^2}{\nabla//} \frac{1}{\Delta n//} \exp \left[- \left(\frac{n// - n//_o}{\Delta n//} \right)^2 \right]$$

where $n//_o$ is the peak parallel wavenumber and $\Delta n//$ the half width of the spectrum. The thermal velocity v_{te} is defined by $T_e = \frac{1}{2} m v^2_{te}$ and $\left| e\phi/T_e \right|^2$ is related to the average wave energy density $\bar{W}$ by the expression given at the end of the precedent section.

In high temperature plasmas and at moderate resonant velocities the

Maxwellian distribution will not be much distorted and we find the following damping rate for the wave energy:

$$2\gamma = dW/Wdt = (\sqrt{\pi}/4)\ \omega\ \beta_e\ x_e\ \exp(-x_e^2)\left[1 + \left(\frac{\omega^2}{\omega_{pi}^2}\cdot\frac{mc^2}{T_e}\right)^2\right]$$

where $x_e = \omega/k//v_{te}$.

4. Absorption of the fast wave and steady state current drive

The results sketched above have been inserted into a Fokker-Planck code developed at Culham /5/. For a given energy density, ie. a given maximum diffusion coefficient, we obtain the steady state current density and absorbed power density and we compute the corresponding absorption length $L_{abs} = v_A/2\gamma = v_A W.(dW/dt)^{-1}$, where v_A is the Alfvén velocity. Future calculations will include trapping and relativistic effects which may reduce the current drive efficiency.

An example of electron distribution that we obtained is displayed on Fig. 2 and it is clearly seen that substantial distortions from Maxwellian distributions take place at high perpendicular energy.

Fig. 3 shows the absorption lengths resulting from high power (~ 0.1 MW/m^3) quasilinear interaction, as a function of β_e and T_e. It is clear that high β_e values ($\geq 5\%$) and bulk interaction will be required if the wave is to be absorbed in a few passes. In this respect, the advantage that the centre of the plasma is accessible to waves with relativistic phase velocities along the magnetic field may turn out to be of little practical interest.

Nevertheless, as shown on Fig. 4, current drive based on bulk electron interaction seems feasible in JET with efficiencies ($\eta = j/2\pi R\ P_{abs}$) of the order of 0.1 A/W. This is of the same order of magnitude as lower hybrid current drive efficiencies; however, we must emphasize that fast wave current drive should occur basically at the centre of the hot and dense JET discharges whereas lower hybrid current drive should be more peripheral at high temperatures. Both schemes (LHCD and FWCD) seem therefore rather complementary as far as profile control is concerned and could provide the additional "knobs" that one seeks for improving tokamak performances.

Finally, a suggestion for enhancement of the T.T.M.P. absorption could be to start from a pre-formed non-Maxwellian distribution having high perpendicular energy ($\gamma \alpha W_\perp^2$). Slide-away discharges or synergic effects from combined lower hybrid and fast wave current drive could for instance be beneficial.

Acknowledgments

We are deeply indepted to M. O'Brien, M. Cox and D.F.H. Start for use of their "BANDIT" Fokker-Planck code and for fruitful discussions.

References

/1/ F.W. Perkins, in ORNL/FEDC-83/1, Oak Ridge, 1983
/2/ D. Moreau and C.M. Singh, in "IAEA Technical Committee Meeting on Non-Inductive Current Drive in Tokamaks", Culham, 1983
/3/ H. Hamnén and J.A. Wesson, private communication
/4/ J. Jacquinot, Erice Course on Tokamak Startup, Erice, 1985
/5/ M. O'Brien, M. Cox and D.F.H. Start, paper submitted to Nuclear Fusion, 1986

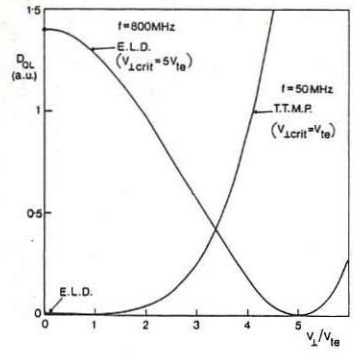

Fig. 1 Quasilinear diffusion coefficient versus perpendicular velocity at high (Landau damping) and low frequency (T.T.M.P.)

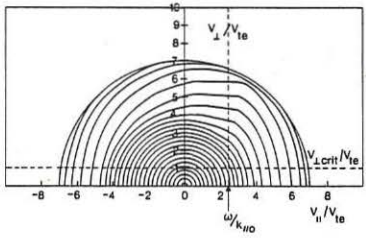

Fig. 2 Electron distribution contours for B_o = 2.2 T., f = 50 MHz, T_e = 5 keV, n_e = 1.8 x 10^{20} m^{-3} (β_e = 7.5%) in a H_2 plasma. The wave spectrum is Gaussian with $n//_o$ = 2.9 and $\Delta n//$ = 0.5

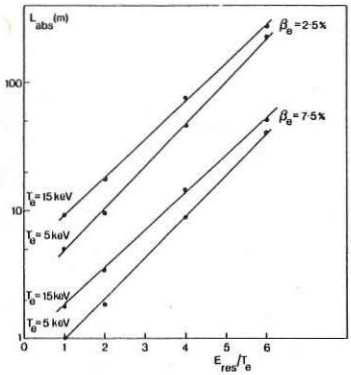

Fig. 3 Absorption length versus ratio of peak resonant energy to electron temperature (E_{res}/T_e) for β_e = 2.5% and 7.5%, and for T_e = 5 keV and 15 keV. Other parameters are B_o = 2.2 T., f = 50 MHz, $\Delta n//$ = 0.5 and H_2 plasma

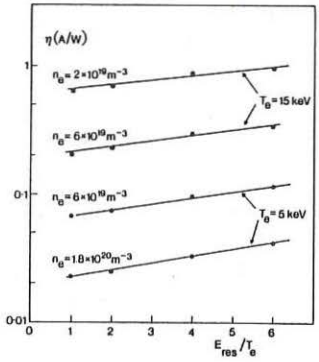

Fig. 4 Current drive efficiency versus E_{res}/T_e. Same cases as for Fig. 3 i.e. β_e = 2.5% and 7.5% and T_e = 5 keV and 15 keV

ION CURRENT DRIVE USING ICRF AND COMBINED ICRF/NBI

H. Hamnén*
JET Joint Undertaking, Abingdon, Oxon., OX14 3EA, UK.
*On attachment from Chalmers University of Technology, Göteborg, Sweden.

Introduction

Among the various proposals to drive non-inductive currents in tokamaks are suggestions to use radio frequency current drive in the ion cyclotron range of frequencies. In the so-called minority regime, this could be done by heating a thermal minority ion species [1], or by heating a neutral beam injected minority species [2].

In the original proposal by Fisch [1], of current drive using minority ions, only a qualitative estimate of the current drive efficiency was done. In the subsequent papers [3,4], analytical studies based on the Fokker-Planck equation were carried out, for thermal and injected minority ions respectively.

In this paper, we will report on a numerical study of the current drive efficiency for these two schemes. Only the current carried by the minority ions will be included, leaving aside possible currents in the electron species. Electron currents could be created either by direct interaction with the wave through Landau- and transit-time damping, or as a "return current", resulting from momentum transfer from the minority ions.

For the calculations presented here, the effects of toroidicity on the particle motion along the field lines will be neglected. The Fokker-Planck equation for the minority ions then reads:

$$\frac{\partial f}{\partial t} = C(f) + Q(f) + S \qquad (1)$$

Here C(f) is the collision operator which has been derived assuming Maxwellian distributions of equal temperature for the background species, and using a linearised operator for the self-collisions [5]. Further Q(f) is the RF- operator, using the quasi-linear approximation [5], and S is a narrow Gaussian source function representing neutral beam injection. Also included in S is a low-temperature Maxwellian sink, with loss rate equalling the injection rate.

For the wave-particle interaction we will use the equation:

$$Q(f) = \frac{1}{v_\perp} \frac{\partial}{\partial v_\perp} \left(v_\perp D_o F(v_\parallel) \frac{\partial f}{\partial v_\perp} \right) \qquad (2)$$

Here D_o is a constant, dependent on the electrical field strength. For $F(v_\parallel)$ we will use the simple model:

$$F(v_\parallel) = \exp - \left(\frac{v_\parallel - v_o}{w} \right)^2 \qquad (3)$$

Numerical Results and Discussion

The scaling given by Fisch [1], for the minority ion current drive is

$$\frac{j}{P} \sim \frac{T}{n_e} \qquad (4)$$

where j is the current density and P is the power density.

The results presented here have been calculated using the 2-D finite-element code BAFIC, [6]. We have used one single set of plasma parameters. For the ion species we have chosen hydrogen minority ions and deuterium background ions, with $Z_{eff} = 1$, $T_e = T_i = 8$keV and $n_e = 5 \times 10^{19}$ m^{-3}. Throughout, the minority ion species concentration has been set at 5%. For the NBI cases, the injected power density has been set at 0.1MW/m^3 and the injection point corresponds to a pitch angle of 15°.

Shown in Fig. 1 is the efficiency of the pure ICRF scheme for three different interaction velocities v_o vs absorbed power density, using a velocity space interaction width $w = 0.5v_{th}$. For interaction velocities $v_o \geq 3v_{th}$ it is difficult to achieve good numerical convergence. In spite of low power absorption (< 5kW/m^3), very long high-energy tails are produced. Since the current drive is critically dependent upon the variation of the collision frequency, the best efficiency is found if the particles stay in a region of velocity space where this variation is strong. Being pushed too far out in the tail, electron collisions start to dominate and the collision frequency becomes almost constant. Thus, it seems to be difficult to achieve the optimum efficiencies predicted by Fisch [1], which occur for $v_o \sim 5v_{th}$, with the high power levels expected in forthcoming experiments.

By tuning the wave to a neutral beam injected species, one may hope to overcome this draw-back, simply because there are now more particles in the optimum interaction zone, implying less power per particle. That indeed this scheme has a much more favourable scaling with power is illustrated in Fig.2, which has been calculated setting the velocity space interaction velocity v_o (Eq.(3)), equal to the NBI injection velocity.

Both schemes are compared in Fig. 3, again using a very low RF power absorption (~ 1kW/m^3). Also shown is Fisch's qualitative estimate [1]. Surprisingly good agreement is found. However, as noted above, raising the RF-absorption for the pure ICRF scheme, the peak efficiency drops drastically.

The efficiency for combined ICRF/NBI is shown in Fig. 4, for different values of the velocity space interaction width w (Eq.(3)), again setting the velocity space interaction velocity v_o equal to the NBI injection velocity. It is interesting to note that also with homogenous RF-interaction in velocity space ($w = \infty$ in Fig. 4), there will be considerable currents resulting from this scheme.

Conclusions

The current drive efficiency

$$\eta = \frac{1}{2\pi R} \cdot \frac{j}{P} \quad (A/W)$$

has been evaluated for pure ICRF minority heating and for combined ICRF/NBI (where for the latter scheme j/P denotes the incremental efficiency associated with the RF-interaction). For low RF-power, the efficiencies for both schemes agree well with Fisch's qualitative estimate [1]. The pure ICRF scheme, however, has a very strong power dependence, the efficiencies dropping dramatically for realistic power densities. This power dependence is much less pronounced for the combined scheme.

Using typical JET discharge parameters, it is found that currents of the order of 2-4MA could be driven with the planned ICRF- and NBI-capacity.

Acknowledgements

It is a pleasure to acknowledge a number of helpful discussions with Drs. T. Hellsten and W. Core.

References

[1] Fisch, N.J., Nucl. Fus. 21 (1981) 15.
[2] Okano, K., Inoue, N., Uchida, T., Nucl. Fus. 23 (1983) 235.
[3] Chiu, S.C., Chan, V.S., Hsu, J.Y., Guest, G.E., Prater, R., Rawls, J.M., Nucl. Fus. 23 (1983) 499.
[4] Cox, M., Start, D.F.H., Nucl. Fus. 24 (1984) 399.
[5] Stix, T.H., Nucl. Fus. 15 (1975) 737.
[6] Succi, S., Appert, K., Core, W., Hamnén, H., Hellsten, T., Vaclavik, J. (to be published in Comp. Phys. Comm.)

Figure Captions

Fig.1 Current drive efficiency vs. absorbed RF-power density for the pure ICRF case: a) $v_o=v_{th}$, b) $v_o=2v_{th}$ and c) $v_o=3v_{th}$. The velocity space interaction width $w=0.5v_{th}$.

Fig.2 Current drive efficiency vs. absorbed RF power density for the combined ICRF/NBI case: a) $v_o=5v_{th}$, b) $v_o=2v_{th}$ and c) $v_o=3v_{th}$. The NBI injection energy is 80keV and $w=0.5v_{th}$.

Fig.3 Current drive efficiency vs. velocity space interaction velocity for the two cases. The dashed curve shows Fisch's estimate, [1]. The absorbed RF power density was kept very low ($< 5kW/m^3$).

Fig.4 Current drive efficiency for NBI only and the incremental efficiency for the combined case (for three different choices of interaction width), vs. NBI injection velocity ($v_o=v_{inj}$).

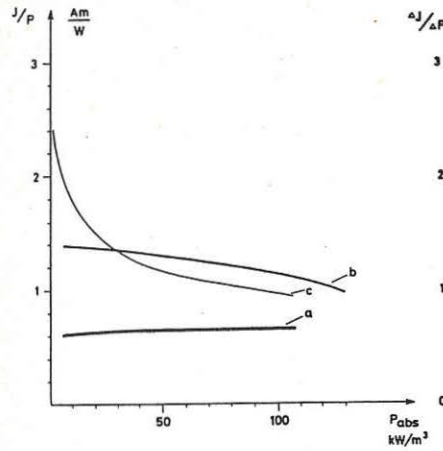

Fig.1

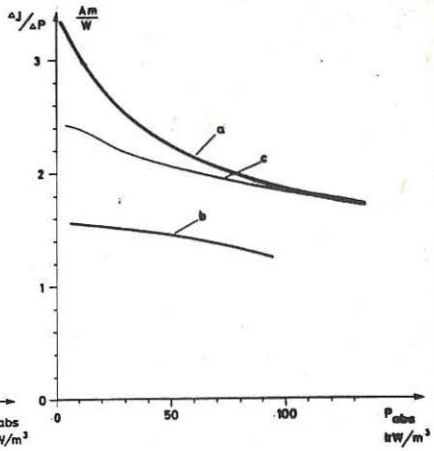

Fig.2

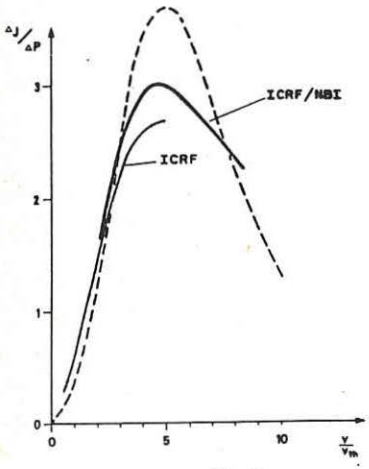

Fig.3

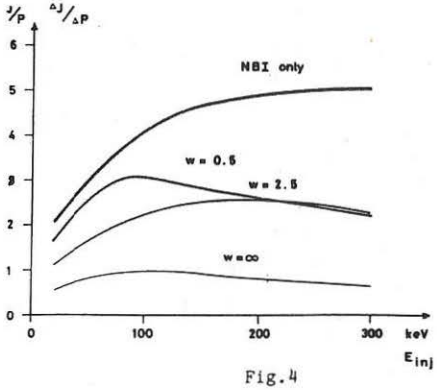

Fig.4

EFFECTS OF EDGE DENSITY MODIFICATION ON WAVEGUIDE COUPLING DURING LOWER HYBRID CURRENT DRIVE IN A TOKAMAK

K. Matsumoto*) and K. Ohkubo

Institute of Plasma Physics, Nagoya University, Nagoya 464, Japan
*Department of Electrical Engineering, Yamagata University, Yonezawa 992, Japan

<abstract> During lower hybrid current drive, changes in amplitude and phase of reflected signals at the waveguide grill, and also decreases in the edge plasma density measured by double probes are monitored. The influence of plasma density and its gradient at the grill mouth on the coupling between waveguides and plasma are investigated by a simplified linear grill theory based on a step plus a ramp density model. It is confirmed from the comparison with the theoretical analysis that change in waveguide coupling during current drive is mainly caused by reduction of density in the scrape-off plasma.

I. INTRODUCTION

It has been recently observed that the lower hybrid current drive (LHCD) by the slow wave of which the refractive index N_z along the magnetic field is relatively small ($\simeq$ 1 - 2) led to a considerable decrease[1,2] in the density of the scrape-off layer, but the influence of the density drop to RF coupling was not studied. In this paper, we describe the effect of the LHCD on the coupling properties which is observed in the JIPP T-IIU tokamak. We show the detailed comparison with the numerical analysis based on the simplified formulation of the grill theory in which the step plus ramp density model[3,4] is adopted for edge density profile at the waveguide mouth.

The simplified theory is derived by extending the method discussed by Pacher[5] to the case of arbitrary density n_{wgd} at the waveguide mouth. Here the higher order evanescent modes and an intermediate medium as the vacuum between the mouth and plasmas are neglected. According to the theory[3], good coupling is achieved by satisfying the equation $n_{wgd} \simeq n_{co} \left| N_z^2 - 1 \right|$, where n_{co} is the density corresponding to the slow wave cutoff. The relation indicates that the waveguide array should be movable in order to minimize the reflected RF power for the waves with N_z determined from a given phasing.

II. EXPERIMENTS AND DISCUSSIONS

(a) RF Measurements

Each high power RF amplified by two klystrons is divided by the magic-T and fed to the four-waveguide grill. The RF frequency is 800 MHz (n_{co} = 7.9×10^9 cm^{-3}). Each waveguide mouth with the cross section of 3.5 cm in width and 247.6 cm in height is separated by a 0.5 cm septum. In order to control phasing between the waveguides three phase shifters are installed and in order to maximize the grill coupling the waveguides in bellows is movable. The conventional directional couplers on the WR 975 waveguides are mounted to measure the forward and reflected power.

Forward and reflected phases of RF with 800 MHz are monitored as the following: each picked-up signal at the four special directional couplers developed by one of the authors[6] is mixed with the RF from the local oscillator with $\simeq$ 799 MHz. The beat signals with $\simeq$ 1 MHz from the IF output in the mixers are applied to synchroscopes, where the beat signal related

to forward RF in the first waveguide is connected as a reference to the external trigger input of synchroscopes. Here, in order to make monitoring clear, a ramp signal triggered at RF switched-on time is superposed on the each beat signal, and beam intensity of synchroscopes is modulated with the gated 200 Hz rectangular wave triggered at the same time. We can measure the phases of forward and reflected RF in the each waveguide at interval of 5 msec.

(b) Results and Discussions

Time evolutions of plasma parameters during LHCD are plotted in Figs. 1(a) and (b) for relatively low RF power P_{rf} ($\simeq$ 78 - 40 kW) and for phasing between the waveguides $\Delta\phi = \pi/2$, where RF power is injected into hydrogen plasma at B_t = 26 kG. After RF is applied at t = 112 msec, loop voltage V_L drops to -0.2 volts, and decreasing rate of the plasma current I_p reduces, where small inductive field resulted from $L_p dI_p/dt$ remains. The position of plasma column is well-controlled within 0.5 cm during RF in the horizontal and the vertical direction (Fig. 1(c)).

The density n_e in scrape-off layer is measured by the fixed three sets of double probe located at different radial positions, where probes are set 90 degrees toroidally away from the grill. The time evolution of n_e at r = 26.8 cm is plotted in Fig. 1(f) with and without LHCD. The density decreases by a factor of 2 and its time dependence is similar to the waveform of V_L. As discussed in the reference of (2), the density drop may results from the decrease in the Bohm diffusion coefficient $D_\perp$ in the scrape-off layer due to the vanishing DC field. It is noted that scale length of density in the scrape-off layer and line averaged density $\overline{n_e}$ are almost unchanged by LHCD. Therefore, the density gradient near the limiter (r = 24.5 cm) must increase. The change in density profile in the plasma edge region may be related to the increase in global confinement time[7] with LHCD ($\simeq$ 3 msec to $\simeq$ 6 msec).

The power reflection coefficients $|R_k|^2$ and phases $arg\ R_k$ for four waveguides are shown in Fig. 1(g) and (h), where k is a waveguide number and the waveguide mouth is positioned at r = 27.0 cm. It is found that the density drop in scrape-off layer influences $|R_k|^2$ and $arg\ R_k$ (k = 1,—,4). Here we transform the observed phase difference between forward and reflected signals at the special directional coupler to that at the waveguide mouth by using the phase difference between the coupler and the mouth.

By moving the grill as shown in Fig. 2, we examine the power reflection coefficients and phases in two inside waveguides at the RF switched-on time for $\Delta\phi = \pi/2$. We compare the results with the simplified grill theory by substituting the experimental values of forward electric field (in individual waveguide) Q_k (k = 1,—,4) normalized by that in the first waveguide, the density and its gradient on the waveguide mouth which are estimated from the measured density profile:

$$n(r)\ [cm^{-3}] = 1.8 \times 10^{10} exp\{ - (r\ [cm] - 27)/0.69 \}. \qquad (1)$$

In the theoretical model, the mouths of two outside waveguides are connected to the wall in the same plane. However, the grill is protruded into the scrape-off layer from the wall. Thus, the reflection properties of only two inside waveguides which are not strongly influenced by the vacuum wall are discussed. As shown in Fig. 2, the experimental results of $|R_k|^2$ and $arg\ R_k$ in the second and third waveguides during LHCD agree roughly the theoretical ones.

By changing $\Delta\phi$, as shown in Table I, we examine the power reflection coefficients and phases at the RF turn-on time as functions of N_z. The power reflection coefficients agree approximately with the theoretical values. Except for the case of $\Delta\phi = 0°$, deviation of observed phases from the

theoretical values are within $\pm 30°$. The reason why both calculated $|R_2|^2$ and $arg\ R_2$ are not the same as both $|R_3|^2$ and $arg\ R_3$ for $\Delta\phi = 0$ and π originates in different Q_k ($k = 1,--,4$) in each waveguide, where the largest deviation of Q_k from the average value is about 10%.

Now we analyse time evolution of power reflection coefficients and phases of second and third waveguides. As already shown in Fig. 1(g) and (h), $|R_k|^2$ and $arg\ R_k$ ($k = 2,3$) evolve in time due to scrape-off density drop during LHCD. The calculated results accompanying with experimental ones are shown in Fig. 3. The RF coupling in LHCD is explained by the density change in front of the grill. If we wish to obtain good coupling during LHCD, it should be necessary to control dynamically N_z by decreasing $\Delta\phi$ so as to satisfy $n_{wgd} \simeq n_{co} |N_z^2 - 1|$.

When the grill was more deeply inserted by 1 cm ($r = 26$ cm) and RF power of LHCD increases up to 120-80 kW in $\Delta\phi = \pi/2$, large changes were observed in reflection coefficients and phases of the reflected signals in all the waveguides. Especially, the phases during the early time after RF switched-on remarkably led as compared with ones calculated with density and its gradient (estimated from Eq. (1)) at the waveguide mouth. Possible explanation for the above phenomenon is that if the tenuous plasma would be produced in the waveguides near the grill mouth, large changes both in amplitude and phase of reflected signals occur as a result of the movement of tenuous plasma towards the transmitter[8].

〈Acknowledgments〉 The authors would like to express their thanks to all the members of the JIPP T-IIU group for their support. One (K.M.) of the authors wish to thank Prof. M. Sato for their continuous support.

REFERENCES

(1) Pericoli-Ridolfini,V., Plasma Physics and Controlled Nuclear Fusion, 27, 709(1985).
(2) Ichtchenko,G., and the Petula group, *in Proceedings of International Conference on Plasma Physics, Lausanne, 1984, (Commission of the European Communities, Brussels)* p.217.
(3) Stevens,J., Ono,M., Horton,R., Wilson,J.R., Nuclear Fusion 21, 1259(1985).
(4) Gormezano,C., Moreau,D., Plasma Physics and Controlled Fusion, 26, 553(1984).
(5) Pacher,H.D., *Optimization of Power Spectrum of Multiwaveguide Grills*, Max-Plank-Institut für Plasma Physik, IPP2/247 (1979).
(6) Ohkubo,K., J. Phys. E; Sci. Instrum., 16, 715 (1983).
(7) Kawahata,K., private communication.
(8) Eckhartt,D., private communication.

Table I: $|R_k|^2$ and $arg\ R_k$ ($k = 2,3$) versus grill phasing

$|R_k|^2$

	experiment		calculation	
$\Delta\phi$	2nd waveguide	3rd waveguide	2nd waveguide	3rd waveguide
$-\pi/2$	0.13	0.11	0.14	0.12
0	0.73	0.52	1.76	1.26
$\pi/2$	0.18	0	0.15	0.13
π	0	0	0.23	0.13

$arg\ R_k$ *(degree)*

	experiment		calculation	
$\Delta\phi$	2nd waveguide	3rd waveguide	2nd waveguide	3rd waveguide
$-\pi/2$	-165	-190	-197	-177
0	-90	-65	-180	-179
$\pi/2$	-192	-180	-156	-179
π	-20	-45	-11	-14

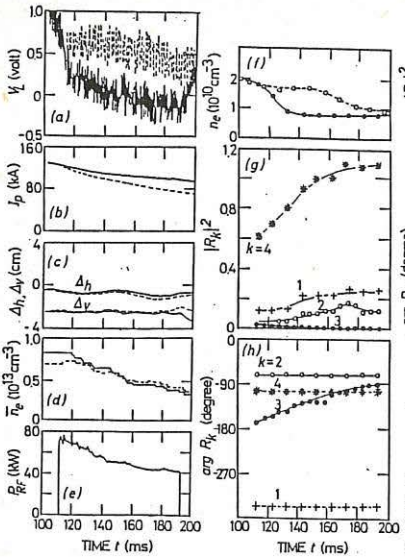

Fig. 1: Typical plasma parameters during low power LHCD, where waveguide mouth is at r = 27 cm. Time evolutions of (a) plasma current; (b) loop voltage; (c) the horizontal and the vertical displacements of plasma position, Δ_h and Δ_v, respectively; (d) line-averaged density; (e) total RF power; (f) density in the scrape-off layer (r = 26.8 cm); (g) power reflection coefficients and (h) phases in individual waveguides for $\Delta\phi = \pi/2$. Here the dashed curves represent results without RF.

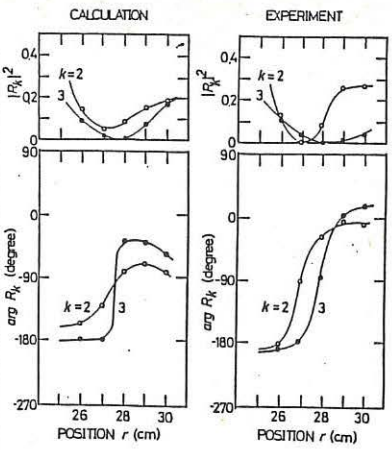

Fig. 2: Variation of power reflection coefficients and phases of the internal waveguides with the grill position during low power LHCD for $\Delta\phi = \pi/2$. Experimental data are plotted at the time just after RF is switched on. For theoretical calculation of $|R_k|^2$ and $arg\ R_k$ (k = 2,3), the density and its gradient at the waveguide mouth are estimated from Eq. (1).

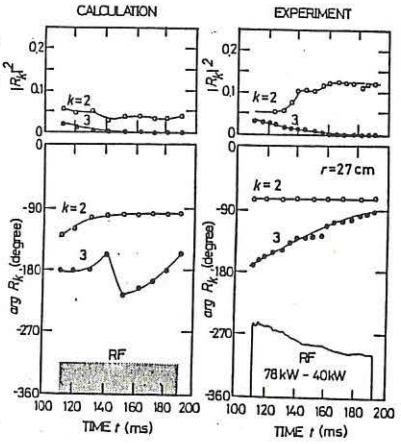

Fig. 3: Time evolution of power reflection coefficients and phases in the internal waveguides with the density variation in the scrape-off layer during low power LHCD for grill position at r = 27 cm in the same condition as Fig. 1. For the theoretical estimation, the scrape-off density evolution at r = 27 cm is used.

ICRF CURRENT-DRIVE BY USE OF PHASE-CONTROL OF ANTENNAS

Y.Kishimoto[a)], K.Hamamatsu[a)], A.Fukuyama[b)], S.I.Itoh[c)] and K.Itoh[d)]

a). Japan Atomic Energy Research Institute, Tokai, Ibaraki 319-11, JAPAN
b). School of Engineering, Okayama University, Okayama 700, JAPAN
c). Institute for Fusion Theory, Hiroshima University, Hiroshima 730, JAPAN
d). Plasma Physics Labolatory, Kyoto University, Uji, Kyoto 611, JAPAN

Introduction

ICRF wave has been adopted as a major heating method in toroidal plasma and has obtained considerable success. ICRF wave can also drive the current by introducing the toroidal momentum using an array of phase-shifted antenna. In this paper, we present the global analysis of the ICRF current-drive considering a whole antenna-plasma system. We restrict our analysis to the current-drive that electrons directly absorb the wave momentum through Landau damping. Within the framework of quasi-linear theory, the Fokker-Planck calculation is combined to the ICRF wave propagation-absorption analysis.

Wave Equation

We employ a one-dimensional model of ICRF wave propagation which includes the kinetic effects and the plasma inhomogeneity in the x-direction as $B(x)=B_0/(1+x/R)$, $n_s(x)=(n_{s0}-\hat{n}_s)(1-x^2/a^2)+\hat{n}_s$, $T_s(x)=(T_{s0}-\hat{T}_s)(1-x^2/a^2)+\hat{T}_s$. The plasma is surrounded by the vacuum region $a<|x|<b$ and the resistive wall is located at $x=\pm b$. The multiple antennas with different phases$(\delta_1,\delta_2,\ldots,\delta_N)$ are placed in the z-direction at $x=-d$ in this case$(a<d<b)$. We assum that the plasma is homogeneous in the y- and z-directions. The wave equation is

$$\nabla\times\nabla\times\vec{E} - \frac{\omega^2}{c^2}\vec{E} = i\omega\mu_0\{\sum_s \vec{J}_s + \vec{J}^A\} , \qquad (1)$$

where $\vec{J}^A(z;\delta_1,\delta_2,\ldots,\delta_N)$ is the total antenna current. The explicit form of the induced current $\vec{J}_s$ is given in Ref.[1]. We retain terms up to the 2nd order of $k_x\rho_i$(ρ_i: ion gyroradius) and the kinetic effect parallel to the magnetic field is described by the plasma dispersion function.

Velocity Space Equation

The evolution of the space-averaged electron distribution function is governed by the equation,

$$\frac{\partial f_e}{\partial t} = \frac{\partial}{\partial v_z} D_w \frac{\partial f_e}{\partial v_z} + \left(\frac{\delta f_e}{\delta t}\right)_{coll.} , \qquad (2)$$

where D_w is the quasi-linear diffusion coefficient and $(\delta f_e/\delta t)_{coll.}$ is the Fokker-Planck collision term. Introducing the parallel wave number $k_n=n/R$, the quasi-linear diffusion coefficient is given by

$$D_w(v_z,x) = \frac{e^2}{2m^2} \sum_n \frac{\Delta_n |E_n(x)|^2}{(\omega - k_n v_z)^2 + \Delta_n^2} \quad , \tag{3}$$

where $E_n(x)$ is the k_n-th Fourier component of the electric field which is obtained by solving Eq.(1) and Δ_n represents the width of each resonance zone. All available wave numbers are summed up in Eq.(3). The width of each resonance is essential for determining the steady state DC current. We assume that the width is the maximum value between the collision frequency and the trapping frequency, $\Delta_n \equiv \mathrm{Max}\{\nu_e(v_e), \sqrt{ek_n|E_n|/m}\}$. As for the collision operator, a Maxwellian distribution in the perpendicular direction is assumed and Eq.(2) is integrated over that direction. We employ the model collision operator in a multiply ionized plasma as

$$\left(\frac{\delta F}{\delta t}\right)_{coll.} = \nu_0 \frac{\partial}{\partial u}\left[g(u)\left(\frac{\partial F}{\partial u} + uF\right)\right] , \tag{4}$$

$$g(u) = \frac{Z_{eff}}{4\sqrt{2}} G\left(\frac{u}{2}^2\right) + \frac{1}{3\sqrt{2\pi}+|u|^3} ,$$

where $G(x)=\sqrt{\pi}\exp(x)[1-\phi(\sqrt{x})](1+2x)-2\sqrt{x}$ (ϕ: error function), $Z_{eff}=\sum_{s(ion)} Z_s^2 n_s/n_e$; effective ion charge state and $u \equiv v_z/v_e$. The collision operator, Eq.(4), is obtained by interpolating the solution between higher velocity region $v_z >> v_e >> v_i$ and lower velocity region, $v_e >> v_z >> v_i$ with respect to the electron-electron collision. The steady state solution is obtained from Eqs.(2) and (4) as

$$F(u) = C\exp\{-\int_0^u \frac{u\,du}{1+\hat{D}_w/g(u)}\} , \tag{5}$$

where $\hat{D}_w(u)=D_w/\nu_0 v_e^2$ and the constant C is determined from conservation of particles. The DC current is determined from Eq.(5).

Numerical Results[2]

Plasma parameters are taken as follows, R=1.31m, a=0.35m, d=0.395m, b=0.415 m, $f(=\omega/2\pi)$=18MHz, B_0=1.3T, $n_{e0}=1\times10^{20}m^{-3}$, $T_{e0}(=T_{D0}=T_{H0})$=4keV, n_{H0}/n_{D0}=10%, $\hat{n}_s/n_{s0}$(s=e,D and H)=0.05, simulating the JFT-2Mparameters.

Figure 1 illustrates the two-dimensional structure of the RF waves. Five antennas(A_1 to A_5) are set in the high-field-side as shown in Fig.1 and their phases are given by ($0,\pi/4,\pi/2,3\pi/4,\pi$). The fast wave excited by 5-antennas propagates into the plasma center and the major part of the incident wave is mode-converted to the ion Bernstein wave(E_x- and E_z-components).

Figure 2 shows the diffusion coefficient, $\hat{D}_w(u)$ (a) and the deviation from the Maxwellian distribution, $\delta F=F(u)-F_M(u)$ (b) at the radial point x/a=-0.96 (arrow in Fig.1(c)). The sharp two peaks of the diffusion coefficient due to

the plasma cavity effect are observed at $k_n R=4$ and 5 modes and these waves mainly contribute to the power absorption and the current-drive.

Figure 3-(a) illustrates the absorption profiles of electrons and ions averaged over the z-direction and the energy flux. Profiles of the induced current and the normalized efficiency are shown in Figs.3-(b) and (c). The major part of the incident wave is absorbed by electrons. About 87% of the emitted power is absorbed by electrons and 10% is the wall loss. The ion absorptions are very weak in this case. The strong absorption in the central region and near the plasma surface is due to the Landau damping of the fast wave and the ion Bernstein wave. The ion Bernstein wave damps off near plasma surface. Sharp peaks of $P_e(x)$ and $J(x)$ are originated from the peaks of the wave amplitude. It is found that the current profile follows the absorption profile $P_e(x)$. The total induced current, $\overline{J}(\equiv\int_{-a}^{a} J(x)dx)=26.0$kA/m and the global current-drive efficiency, $\overline{J}/\overline{P}_e=0.03\overline{A/m}$ are obtained.

Figure 4 shows the density dependence of the global current-drive efficiency in the case of $T_{e0}=4$keV. Inverse dependence of the efficiency with respect to the density is observed.

Summary

We have studied the ICRF current-drive by combining the 1-D wave code and the Fokker-Planck calculation. We have examined the radial profile of the induced current and the global current-drive efficiency. In the medium size tokamak, the electron power absorption and the associated driven current

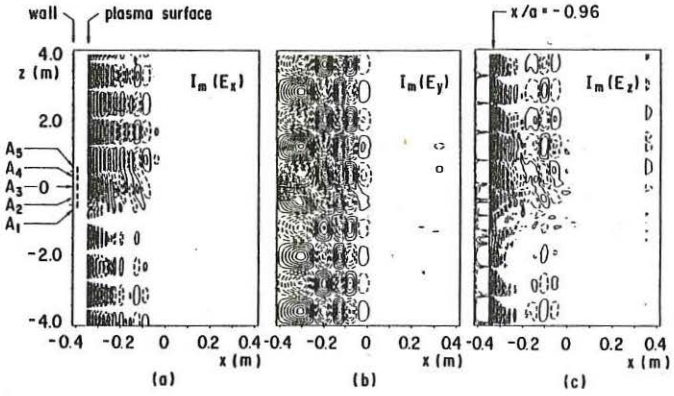

Fig.1 Two-dimensional structure of the RF waves in x-z plane.

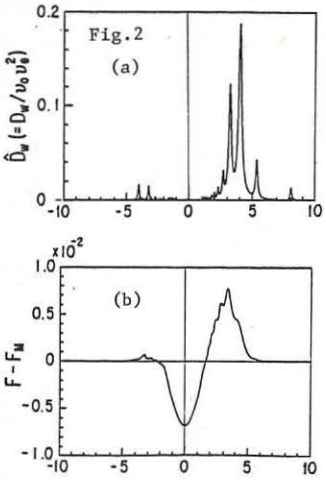

Fig.2 Diffusion coefficient $\hat{D}_w$(a) and a plot of $F(u)-F_M(u)$(b) as a function of $u(=v_z/v_e)$.

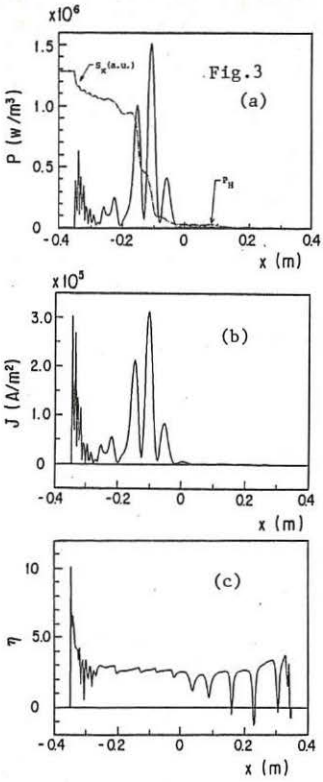

Fig.3 Spatial structure of the power absorption P_s and energy flux S_x(a), induced currect density J (b) and the normalized efficiency of the current drive η (c).

are found to be affected by the plasma cavity resonance.

References

[1] A.Fukuyama, S.Nishiyama, K.Itoh and S.I.Itoh, Nucl. Fusion 23(1983)1005.

[2] Y.Kishimoto, K.Hamamatsu, A.Fukuyama, S.I.Itoh and K.Itoh, "ICRF Current-Drive by Use of Phase-Control of Antennas" Research Report HIFT-120 (Hiroshima Uni.,1986).

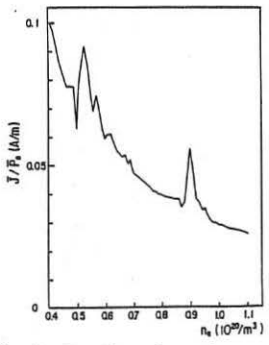

Fig.4 Density dependence of global efficiency.

RF HEATING AND CURRENT DRIVE EXPERIMENTS ON THE JFT-2M TOKAMAK

T.Yamamoto,K.Hoshino, Y.Uesugi,H.Kawashima,M.Mori,Y.Miura,N.Suzuki,
T.Matoba,A.Funahashi,S.Kasai,T.Kawakami,T.Matsuda,H.Matsumoto,
K.Odajima,H.Ogawa,T.Ogawa,H.Ohtsuka,S.Sengoku,T.Shoji,H.Tamai,T.Yamauchi,
M.Hasegawa*,S.Takada**

Department of Thermonuclear Fusion Research, Naka Fusion
Research Establishment, Japan Atomic Energy Research Institute
Tokai-Mura, Naka-Gun, Ibaraki-Ken, Japan

ABSTRACT

The second harmonic electron cyclotron heating (ECH) of Ohmic-heated (OH) plasma or lower-hybrid (LH) current driven plasma is investigated in the JFT-2M tokamak. For the OH plasma, it is shown that the ECH makes an appreciable change in the plasma current profile followed by excitation or suppression of MHD fluctuations through adjustment of the toroidal magnetic field. It is also shown that for the LH current driven plasma, the ECH results in a selective heating of fast electrons at a large down-shifted electron cyclotron frequency, which suggests to produce high efficient current drive.

INTRODUCTION

The electron cyclotron heating offers a promising approach to modifying the radial profiles of electron temperature and plasma current for OH plasma because the ECH can be highly localized. The optimum profile control could lead to improvement of the energy confinement, achievement of the high beta plasma, and prevention of major disruption [1]. On the other hand, an effect of selective ECH of an LH sustained electron tail is of interest for improvements of the LH current drive (LHCD). The electron heating for mildly relativistic energy is the most appreciable method for optimizing the ratio J/P_d where P_d is the power per unit volume dissipated to sustain the current J [2].

EXPERIMENTAL SETUP

The experiments have been carried out in the JFT-2M (JAERI Fusion Torus) tokamak, which has a D shaped vacuum vessel with major radius R_0 = 1.31 m and an iron core transformer. The target plasma has the circular or D-shaped cross section with minor radius defined by inner or outer graphite limiter in the mid-plane, a. The ECH system consists of two gyrotrons and two oversized waveguide transmission lines. The rf power is generated by Varian gyrotron capable of producing 200 kW at frequency f_0 = 60 GHz for up to 0.1 sec. The rf transmission system consists of single mode sections, two kinds of mode converters, and a conical horn antenna propagating TE_{11} mode. The horn antenna, placed outside of torus in the mid-plane, radiates the electron cyclotron waves with vertical polarization at the injection angle of $\theta = 10°$ to the perpendicular of the toroidal magnetic field at the plasma center. The LH waves are launched by four waveguides array which is fed by four 0.75 GHz klystrons. The phase difference between adjacent waveguides is set at 90°. The Brambilla rf spectrum is concentrated between $N_{/\!/}$ = 1 and 4 in the parallel electron drift direction.

On leave from * Mitsubishi Electric Co., ** Mitsubishi Electric Computer System Tokyo Co..

PROFILE CONTROL BY ECH

Figures 1(a)-(c) show the time evolution of the plasma parameters with and without the ECH pulse for three different toroidal magnetic fields, $B_t = 1.08$ T, 1.19 T, and 1.24 T corresponding to the radial positions of the second harmonic electron cyclotron resonance (ECR) layer of $r_c = 0.01$ m, 0.15 m, and 0.21 m, respectively. For these discharges, 240 kW of the ECH power was radiated into the circular plasma with $a = 0.27$ m and the flux safety factor at the plasma boundary $q_s \simeq 3$. The top traces in Figs. 1(a)-(c) show the envelopment of the MHD fluctuations picked up by the magnetic probe which have the poloidal mode number of $m = 3$ and the dominant frequency of $f_{MHD} \simeq 4$ kHz. It is observed that the MHD fluctuations are suppressed for $B_t = 1.08$ T and 1.24 T and those for $B_t = 1.19$ T are excited by application of the ECH pulse. The dominant frequency increased by ~2 kHz when the suppression of the MHD fluctuations occurred, while the frequency decreased in the case of the excitation. The ECH is found to make remarkable increases in $\Lambda + 1/2 = \beta_p + l_i/2 - 1/2$ and stored plasma energy W^{DIA} and drop of the loop voltage for $B_t = 1.08$ T as shown in Fig. 1(a), where β_p is the poloidal beta and l_i is the internal inductance per unit length. The value of $\Lambda + 1/2$ was evaluated from the poloidal magnetic field fitting method, and W^{DIA} was determined by the diamagnetic measurement, for which the base line was in uncertainty. For off-center resonance ECH, it is observed that the signal of $\Lambda + 1/2$ decreases even for no decreasing the incremental increase of the stored plasma energy ΔW^{DIA} during the ECH pulse (see Figs. 1(b) and (c)). For these discharges, the broadening of the current profile compared with that of the OH plasma is indicated through the relation of $\Delta l_i = 2(\Delta\Lambda - \Delta\beta_p^{DIA})$ where $\Delta\beta_p^{DIA}$ is estimated from ΔW^{DIA}. Furthermore, it should be noted that ΔW^{DIA} declines ~20 msec after the initiation of the ECH pulse and falls to zero level at the end of the ECH pulse (see Fig. 1(b)). This result seems to indicate a considerable degradation in energy confinement related to the broadening of the current profile. The similar results have been observed in the ECH experiments on T-10[3]. Figure 2 shows $\Delta\Lambda$ and $\Delta\beta_p^{DIA}$ as a function of the toroidal magnetic field as well as the position of ECR layer. The data points were obtained at the end of ECH pulse. It is found out in Fig. 2 that no increase of W^{DIA} correlates well with the broadening of the current profile. Note that the calculated absorbed ECH powers in single path at the end of the ECH pulse are 230 kW, 120 kW, and 0.1 kW for $B_t = 1.08$ T, 1.19 T and 1.24 T respectively.

ECH OF LH CURRENT DRIVEN PLASMA

The initial combined experiment of the ECH and LHCD was conducted with the net radiated ECH power of $P_{ECH} = 80$ kW and the pulse width of $t_d = 100$ msec. It was observed that the radiated cyclotron waves couple effectively with fast electrons created by the LH waves at a large down-shifted electron cyclotron frequency. The measured soft X-ray spectrum and electron cyclotron emission indicated a selective ECH of the fast electrons with the parallel velocities satisfying the relativistic cyclotron resonance condition [4].

The experiments with $P_{ECH} = 240$ kW and $t_d = 50$ msec have been carried out to improve the LHCD and to investigate the energy confinement of the LH current driven plasma. Figure 3 shows the time behavior of the plasma parameters for $B_t = 1.4$ T at which no ECR layer lies in the plasma column. For this discharge, the target plasma has the D-shaped cross section with minor radii $a \times b = 0.34$ m $\times$ 0.46 m and the plasma current is feedback-controlled to keep constant during a flat-top current. The ECH is applied during the LH pulse which produces the noticeable drop of the loop voltage resulting from the generation of the LHCD. The ECH makes the marked increases in W^{DIA}, $\Lambda + 1/2$, and electron cyclotron emission and no increase in the averaged

electron density. It should be noted that the ECH yields the more negative drop of the loop voltage which suggests an additional current drive by the ECH. On the other hand, efficient heatings were obtained for $B_t = 1.07$ T corresponding to the center resonance heating of the thermal electrons. In addition, the appreciable interactions of the electron cyclotron waves with the fast electrons at the peripheral plasma were observed that resulted in the increases in the loop voltage and the electron density and the decrease in the electron cyclotron emission. Figure 4 shows ΔW^{DIA} due to the ECH and the absorbed ECH power P_{ab} as a function of the toroidal magnetic field. The value of P_{ab} was estimated from dW^{DIA}/dt just after the initiation of the ECH pulse. The experimental conditions are the same as in Fig. 3 except the toroidal magnetic field.

Calculated absorbed ECH power in single path and resultant additional driven current I_{ECH} under the presence of the fast electrons created by the LH waves are shown in Fig. 5. In the calculation, it was assumed tha the lower and upper limits of the parallel momentum of the fast electron tail are $P_1 = 0.2$ mc and $P_2 = 0.7$ mc which correspond to the velocities of the electrons coupled to the LH waves with $N_{/\!/}$ of 5.0 and 1.5, respectively, where m is the electron rest mass and c the light velocity. Radial profiles of the perpendicular temperature $T_\perp(r)$ and the density $n_b(r)$ of the fast electron tail are assumed to be $T_\perp(r)/T_{\perp 0} = \{1 - (r/a)^2\}^{\alpha_T}$ and $n_b(r)/n_{b0} = \{1 - (r/a)^2\}^{\alpha_n}$ with $n_{b0} = (2/ce)(\alpha_n + 1)I_{rf}/\{\pi a^2(p_1 + p_2)\}$, respectively, where I_{rf} is the driven current by the LH waves. The result shown in Fig. 5 was calculated with $\alpha_T = 3$ and $\alpha_n = 8$, on which the total ECH power absorbed by the fast electrons depends weakly. It is shown that a peak of P_{ab} around $B = 1.07$ T comes from the bulk electron heating at the plasma center and the increase in P_{ab} for $B_t \gtrsim 1.2$ T with increasing B_t results from the down-shifted ECH. The calculation also indicates that the more efficient current drive of the ECH is made for the higher B_t. The dependence of the calculated P_{ab} on B_t with $T_{\perp 0} = 13 - 15$ keV seems to be consistent with the observed one. This suggests that at least ~90 kA of the additional current with a figure of merit of $I_{ECH}/P_{ab} = 3.2$ A/W for $B_t = 1.4$ T is driven by the ECH.

ACKNOWLEDGEMENTS

The authors are grateful to the members of the operation groups. They gratefully acknowledge the continued encouragements of Mr. K. Suzuki, Drs. Y. Tanaka, M. Tanaka, K. Tomabechi and S. Mori.

REFERENCES

[1] Yoshioka, Y., et al., Nucl. Fusion 24 (1984) 565.
[2] Fidone, I., et al., in Heating in Toroidal Plasma (Pro. 4th Int. Symp., Rome, 1984) Vol. 2 (1984) 872.
[3] T-10 Group, in Proceeding of the 12th European Conference on Control Furion and Plasma Physics, Budapest, Hungary, Vol. 9F part I (1985) 42.
[4] Hoshino, K., et al., ibid. Vol. 9F part II (1985) 184.

FIGURE CAPTIONS

FIG. 1 Time evolution of the plasma parameters with and without (solid and dotted lines) the ECH pulse for three different toroidal magnetic fields.

FIG. 2 Dependence of the incremental increases of Λ and poloidal beta on the toroidal magnetic field as well as the position of ECR layer. P_{ECH} = 240 kW.

FIG. 3 Time behavior of the plasma parameters at B_t = 1.4 T for the combination of the ECH and the LHCD. P_{ECH} = 240 kW and P_{LH} = 140 kW.

FIG. 4 Absorbed ECH power and incremental increase of the stored plasma energy versus the toroidal magnetic field.

FIG. 5 Calculated absorbed ECH power and additional current drive by ECH versus the toroidal magnetic field as a parameter of the perpendicular temperature of the fast electrons.

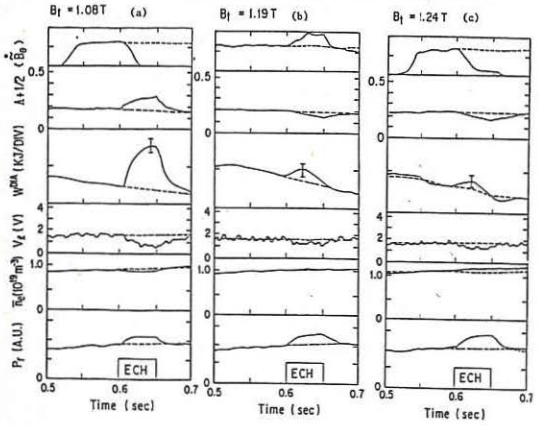

FIG.1

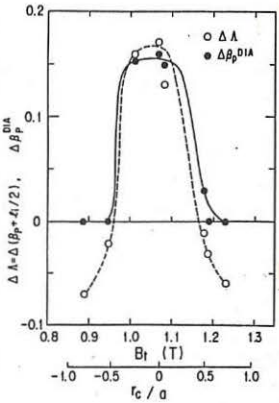

FIG.2

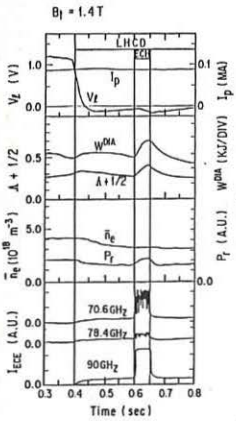

FIG.3

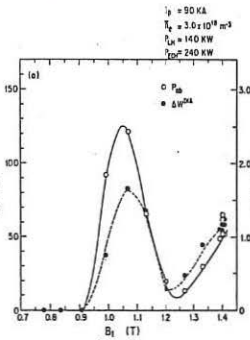

FIG.4

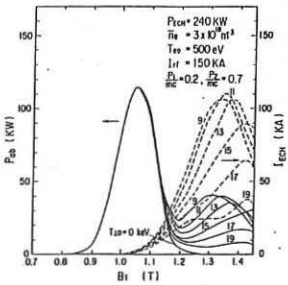

FIG.5

INTRINSIC ELECTRON RADIAL TRANSPORT ASSOCIATED WITH A LARGE AMPLITUDE FAST WAVE USED FOR CURRENT DRIVE

D. Jovanovich and G.J. Morales

Physics Department, University of California at Los Angeles, Los Angeles, CA 90024, USA

Abstract: An analytical study is made of the cross-field transport caused by the combined action of the perpendicular electric and magnetic fields of a fast wave used to generate a current by Landau damping on resonant electrons.

Introduction: At the present time there exists considerable interest in the possibility of using fast waves of frequency larger than the ion gyrofrequency ($\omega_0 > \Omega_i$) to generate steady-state currents in tokamak devices. The underlying idea is to accelerate resonant electrons ($v = \omega_0/k_z$) with the component of the wave electric field E_z along the confining magnetic field $\underline{B}_0$. Most theoretical studies of this topic have concentrated on effects pertaining to pure velocity-space modifications caused by E_z. However, fast waves are known to carry their energy primarily through the oscillating magnetic field and perpendicular electric field $\underline{E}_\perp$; the part associated with E_z being relatively small. Consequently, in the process of accelerating electrons for current drive purposes the wave causes an intrinsic radial displacement through the combined action of the $\underline{E}_\perp \times \underline{B}_0$ drift and the perpendicular wave magnetic field, which for the electrons behaves as a low frequency magnetic fluctuation akin to those frequently invoked to explain anomalous electron heat transport.

The present study aims to illustrate the principal features of the intrinsic radial transport by considering the prototype problem in a simplified geometry, namely the modification of the average electron distribution function, in velocity as well as in configuration space, produced by a Landau damped (temporally) fast wave in a slab plasma. To further ellucidate the process, some examples of particle trajectories are investigated numerically.

Analysis: We envision a slab plasma confined by a uniform magnetic field $B_0\hat{z}$ in which the zero order density $n_0(x)$ varies in the $\hat{x}$ direction perpendicular to $\hat{z}$) and the invariant direction is $\hat{y}$. A temporally damped fast wave is assumed to propagate unidirectionally along $\hat{z}$, but to exhibit a standing wave pattern in the x direction. For the sake of brevity, we do not discuss the general case including y propagation; here we consider $k_y = 0$ only. Since the real part of the wave frequency ω_0 is much smaller than the electron gyrofrequency Ω_e, but much larger than the electron collision frequency, the electron behavior is described by a collisionless drift-kinetic equation

$$\left(\frac{\partial}{\partial t} + v\,\frac{\partial}{\partial z}\right) f(\underline{r},v,t) + \nabla\cdot\left[\underline{v}_D f(\underline{r},v,t)\right] + A_z\,\frac{\partial}{\partial v}\,f(\underline{r},v,t) = 0 \qquad (1)$$

where $\underline{v}_D = (\tilde{\underline{E}} \times \hat{z})(c/B_o) + v\tilde{\underline{B}}_\perp/B_o$ is the perpendicular drift caused by the wave fields $\tilde{\underline{E}}$ and $\tilde{\underline{B}}_\perp$, and $A_z = (-e\tilde{E}_z + \tilde{F})/m$ is the parallel acceleration in which the mirror force $\tilde{F}$, produced by the wave, appears. For sufficiently large ω_o, F is small compared to the electrical force, so we neglect it in the present discussion. The quantity v is the velocity component along z, and the gyro-averaged distribution $f(\underline{r},v,t)$ has been integrated over perpendicular velocities. The first order perturbed distribution function $f_1 = (1/2)\{\tilde{f}_1(x,v)\exp[i(kz - \omega t)]+c.c.\}$, with $\omega = \omega_o + i\gamma$, $\gamma < 0$, $|\gamma| << \omega_o$, is obtained by linearizing Eq. (1) around the initial time independent distribution $f_o(x,v)$.

The slow time (compared to $2\pi/\omega_o$) evolution of the spatially averaged (along z) modified distribution $f_2(x,v,t) = \langle f(\underline{r},v,t)\rangle - f_o(x,v)$ is calculated to order $|\tilde{\underline{E}}|^2$ from

$$\frac{\partial}{\partial t} f_2 = - \nabla\cdot(\langle \underline{v}_D^{(1)} f_1 \rangle) + \frac{e}{m}\frac{\partial}{\partial v}(\langle \tilde{E}_z f_1 \rangle) , \tag{2}$$

where the first order drift $\underline{v}_D^{(1)}$ is obtained from a knowledge of the first order wave fields. Upon evaluation of the right-hand side of Eq. (2) and integration over v, we obtain the slow time evolution of the averaged plasma density n(x,t)

$$\frac{\partial}{\partial t} n(x,t) = \frac{d}{dt}\left(e^{2\gamma t}\right) \mathrm{Re}\left\{ \frac{\partial}{\partial x}\left[\left(\frac{c}{B_o\omega_o}\right)^2 \hat{E}_y(x)\frac{\partial}{\partial x}\left(\hat{E}_y^*(x) n_o(x)\right)\right] + \right. \tag{3}$$

$$\left. 2\frac{\partial}{\partial x}\left[k\left(\frac{\Omega_e}{\omega_o}\right)\left(\frac{c}{B_o\omega_o}\right)^2 \left(\hat{E}_y(x)\hat{E}_z^*(x)\right) n_B(x)\right] - 2\pi a \frac{\partial}{\partial x}\left[\left(\frac{\Omega_e\omega_o}{k\bar{v}^2}\right)\left(\frac{c}{B_o\omega_o}\right)^2 \hat{E}_y(x)\hat{E}_z^*(x) n_R(x)\right]\right\},$$

where $a \approx 1 + (\omega_o/\gamma)\arg E_z$, $n_R = (\gamma/k)(\partial f_o/\partial v)(v = \omega_o/k)$ is the density of resonant particles that contribute to current drive, and $n_B = n_o - n_R$ is the bulk density. Two physically different radial transport mechanisms are present in Eq. (3): 1) diffusion, represented by a second spatial derivative; 2) flow, described by a first spatial derivative. The diffusion term does not exhibit a wave-particle resonance, and can be understood physically as arising from a diffusion coefficient $D \sim (\Delta x)^2/\Delta t$, where the displacement, Δx, is due to the $\tilde{E} \times \tilde{B}_o$ drift in one wave cycle, i.e., $\Delta x \sim (cE_y/B_o\omega_o)$, and the characteristic decorrelation time is the damping time, i.e., $D \sim (c/B_o\omega_o)^2|E_y|^2\gamma$. The flow terms contain a nonresonant (bulk plasma) contribution that is physically related to a bulk radial velocity $v_B \sim (\Delta x/\Delta t)$, where $\Delta x \sim (\Delta z)(\tilde{B}_x/B_o)$, with the parallel displacement Δz caused by the nonresonant acceleration due to E_z, $\Delta z \sim (eE_z/m\omega_o^2)$, and the effective interaction time being, again, $\Delta t \sim 1/\gamma$, to yield $v_B \sim \gamma k(\Omega_e/\omega_o)(c/B_o\omega_o)^2 E_y E_z$. The physical picture behind the resonant flow is similar, but the parallel displacement is modified kinetically because the resonant particles see a constant field, i.e., now $\Delta z \sim (eE_z/m)/(k\bar{v})^2$.

The consequence of the cross-field bulk diffusion and flow is an enhancement in the zero order heat confinement. If the current drive scenario is tried on a target plasma carrying a bulk current, then these terms also cause a rearrangement of the current profile. The resonant particle radial flow may decrease the tail confinement, but a beneficial

by-product is that it helps to broaden the RF driven current profile. It should be mentioned that in the presence of a $k_\parallel$ spectrum of waves. Equation (3) generalizes (to order $|\tilde{E}|^2$) to a sum over $k_\parallel$.

The previous discussion pertains to small wave amplitudes such that particle trapping does not occur. We have considered the single wave trapping case and find that the familiar phase-mixing in (v,z) phase space results in a flattening of the resonant particle density profile about a shifted radial equilibrium. Figure 1 illustrates some features associated with the radial transport of resonant electrons in the trapping regime. The bottom half displays the (Δv,z) phase-space (elliptical trajectory) in the wave frame and just below it the corresponding radial displacement (Δx,z) inthe presence of a single wave having scaled strength p = 0.1, where p $\equiv cE_y k_x/\omega_0 B_0$. The non-zero radial displacement associated with the bouncing particle is evident. The top-half of the figure displays the corresponding behavior found in the presence of 3 neighboring waves, each of amplitude p = 0.1. The (Δv,z) phase-space (top panel) shows a complicated sequence of partial trapping and free streaming that results in the net radial displacement (Δx,z) pattern shown in the lower panel.

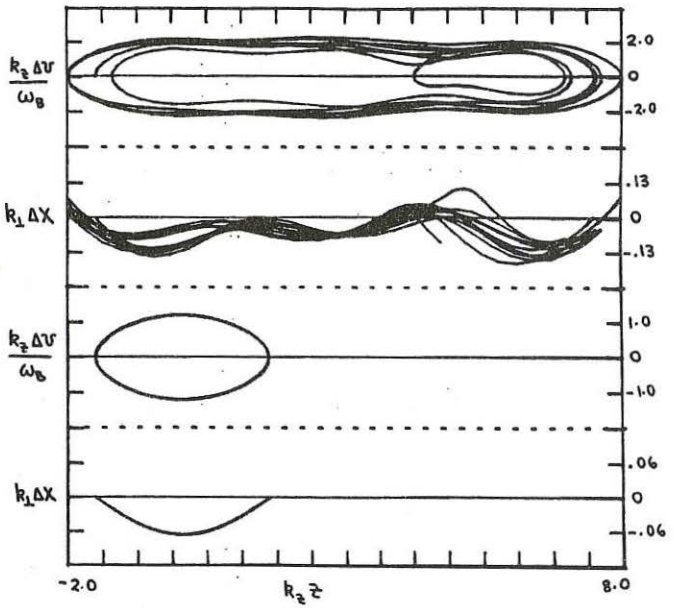

Fig. 1 Simultaneous phase-space (Δv,z) and radial displacement (Δx,z) pattern for a trapped particle. Bottom half is a single wave case. Top half shows the effect of 3 neighboring waves of equal amplitude and frequency but different $k_\parallel$.

The behavior of a passing particle under the combined action of a single wave of amplitude p = 0.1 and a random (noise) uniform electric field in the y direction is illustrated in Fig. 2. The top half shows the phase-space ($\Delta v,z$) and radial displacement ($\Delta x,z$) when the wave effect in the x direction is turned off, but with E_z and random E_y present. The bottom half shows the behavior when the radial effect of the wave is turned on. It is found that the particle executes radial oscillations about a randomly diffusing center. Strong Δx nonlinearities are found (not shown) at levels of $p \gtrsim 2$.

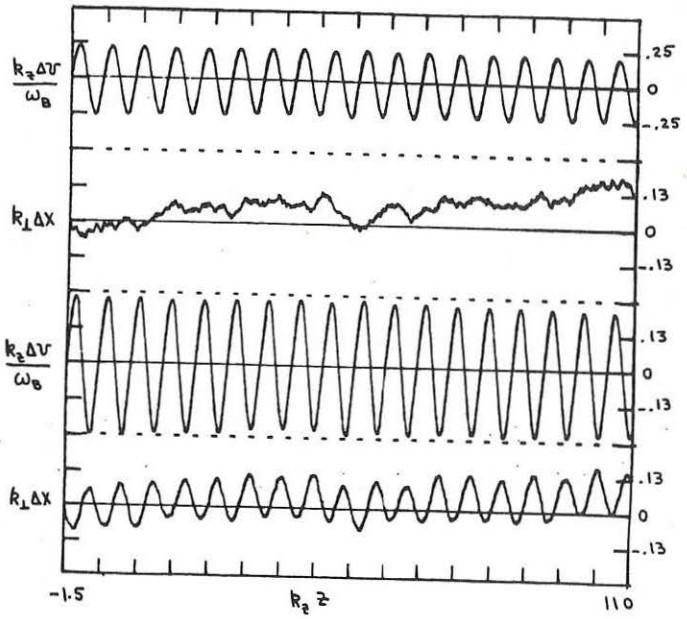

Fig. 2 Combined effect of single wave and random electric field in y direction on phase space ($\Delta v,z$) and radial displacement ($\Delta x,z$). In top half, radial wave effect is off; in bottom half is on.

This work is supported by USDOE.

SAWTOOTH STABILIZATION AND ELECTRON HEATING BY HIGH POWER LOWER HYBRID WAVES IN ALCATOR C

M. Porkolab, S. Knowlton, Y. Takase, S. Texter, P. Bonoli, C. Fiore, C. Gomez, R. Granetz, D. Gwinn, S. McDermott, J. Terry -- Plasma Fusion Center, MIT, Cambridge, Massachusetts 02139 USA

Lower hybrid current drive and electron heating experiments were carried out in sawtoothing discharges in Alcator C (R_o = 64 cm, a = 16.5 cm) at "moderate" magnetic fields. Sawtooth stabilization experiments were performed at B = 6.2 T, $\bar{n}_e \simeq 1.1 \times 10^{14}$ m^{-3}, with adjacent waveguides phased at $\Delta\phi = 90°$, while electron heating experiments were carried out at B = 5.5 T, $\bar{n}_e \simeq 1.5 \times 10^{14}$ cm^{-3}, with $\Delta\phi = 180°$. Up to three sets of 4 x 4 waveguide arrays, operating at f = 4.6 GHz, were employed for injecting up to 1.5 MW of rf power in the lower hybrid frequency regime./1,2/ In contrast to previous experiments on Alcator C /3/ in which SiC-coated carbon limiters were used, molybdenum limiters were employed in the present experiments. The advantage of using molybdenum limiters is that Z_{eff} did not increase nearly as much as in previous experiments, and the grill mouths were not contaminated by carbon deposits; hence the rf power handling of each grill was outstanding. The disadvantage of operating with molybdenum limiters is that the high-Z impurity radiation from the center of the plasma rose significantly during rf injection. The radiation was monitored by spectroscopic means, and in these experiments was found to be a small fraction of the total injected power.

ELECTRON HEATING EXPERIMENTS

In Fig. 1 we display the time history of a typical heating shot with $P_{rf} \simeq 1.0$ MW for $\Delta\phi = 180°$ phasing of the waveguide arrays. For the deuterium plasma parameters $\bar{n}_e \simeq 1.4 \times 10^{14}$ cm^{-3}, I $\simeq$ 260 kA, and B = 5.5 T, the value of Z_{eff} rose from 1.5 prior to rf injection to 2.1 during the rf pulse. The ion temperature increase measured by neutron yield was $\Delta T_i \simeq 250$--300 eV, which was consistent with charge exchange neutral diagnostic measurements of T_i. The electron temperature rise, as measured by Thomson scattering, was approximately $\Delta T_{eo} \simeq 600$ eV from an initial value of $T_{eo} \simeq 1200$ eV with no apparent change in the electron temperature profile. The resistive loop voltage decreased from 1.8 volt to 1.3 volt during the rf injection, in agreement with the observed electron heating and rise in Z_{eff}. The total energy content of the plasma was calculated from the kinetic temperature profile measurements of a number of similar shots. The results are plotted in Fig. 2 as a function of total injected power ($P_{tot} = P_{oh} + P_{rf}$). We notice that the slope of the curve is reduced from that of a straight line which would connect the origin to the initial ohmic heating points, indicating a deterioration of the global energy confinement time, τ_E. In the same plot we also indicate with the solid line the predictions of the Kaye-Goldston scaling for NBI-heated plasmas./4/ We see that the present results do not deviate greatly from such a scaling. This is further demonstrated in Fig. 3 where we display a plot of τ_E versus P_{tot}, as deduced from the data in Fig. 2. We have also added a second set of data points which are obtained by subtracting the total power radiated by molybdenum, as deduced by spectroscopic measurements of the molybdenum line emission (the radiated power due to iron was found to be negligible). The maximum radiated power remained within 10-20% of the total injected power up to the $P_{rf} \simeq 1.0$ MW ($P_{tot} \simeq 1.3$ MW) level (at

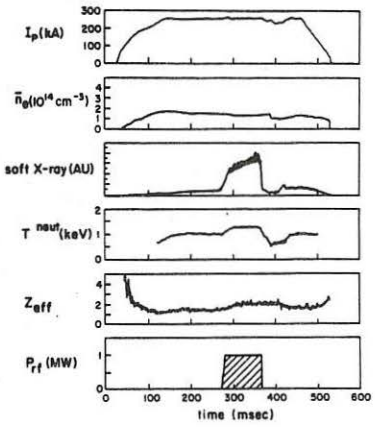

Fig. 1. Time evolution of a typical shot in Alcator C during heating experiments. B = 5.5 T, P_{rf} = 1.0 MW, $\Delta\phi$ = 180°.

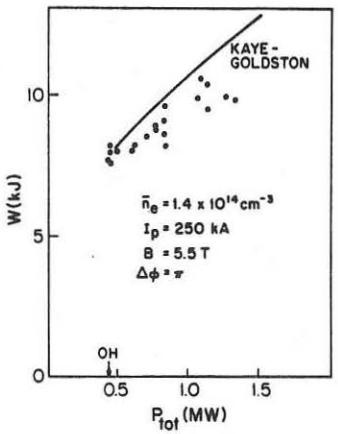

Fig. 2. Energy content, W, versus $P_{tot} = P_{oh} + P_{rf}$. Same conditions as in Fig. 1.

higher powers the radiated power began to increase significantly, and the data were not used). Bolometric measurements of the inner half of the plasma column supported these conclusions. Thus, within experimental error the results are similar to Kaye-Goldston scaling for input power. However, detailed experimental studies of confinement scaling with plasma current were not carried out, and hence a full comparison with such a scaling law is not established here. Furthermore, the injected rf power in these experiments did not exceed the ohmic power by more than a factor of ~ 3, while the empirical Kaye-Goldston scaling was obtained for values near and above this level.

Numerical studies of these results were carried out using the Bonoli-Englade LH ray tracing and transport code./5/ It was found that approximately 25% of the injected rf power is absorbed by electron-ion collisions in the plasma periphery. The remaining 75% of the power was absorbed via electron Landau damping. The experimentally measured temperature increases were found to be consistent with not more than a 30% increase in χ_e^{rf} relative to χ_e^{oh} (where χ_e is the electron thermal diffusivity). This apparent degradation in confinement is also consistent with the earlier SiC limiter results in which a 40% larger increase in T_e ($\Delta T_e \simeq 1.0$ keV) and a 100% larger increase in T_i ($\Delta T_i \simeq 600$ eV) were observed./3/ Code modeling, which included a simulation of the large increase of Z_{eff} associated with the carbon and silicon injection, indicated that the larger temperature rises were a consequence of the significant reduction of deuterons due to the injection of low Z impurity ions and of an increase in input ohmic power. The agreement with Kaye-Goldston scaling may be coincidental, and further experiments at even higher rf power will be needed to clarify confinement scalings of lower hybrid heated plasmas.

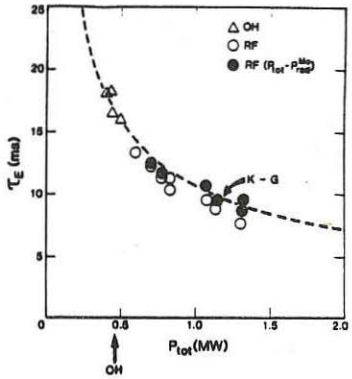

Fig. 3. Energy confinement time, τ_E versus P_{tot}. Same parameters as in Figs. 1 and 2.

SAWTOOTH STABILIZATION EXPERIMENTS

Sawtooth stabilization experiments were carried out in the current drive mode of operation ($\Delta\phi$ = 90°) at $I_p \simeq 250$ kA, $\bar{n}_e \simeq 1.1 \times 10^{14}$ cm^{-3}, B_T = 6 T, q(a) = 5. As shown in Fig. 4, the sawteeth in the central soft x-ray signal were suppressed during the rf pulse. Sawtooth suppression was also evident on the electron cyclotron emission. The large increase in the x-ray emission resulted from an increase in metallic impurities (molybdenum). However, when the relative waveguide phasing was changed to $\Delta\phi$ = 180° in discharges with similar parameters, similar impurity injection was observed, yet the sawteeth were not suppressed, but became even larger (see Fig. 1). Furthermore, in both current drive and heating modes of operation the central electron temperature increased by comparable values ($\Delta T_e \sim 500$ eV) above the initial ohmic values. These results suggest that the stabilization is associated with rf current drive, rather than by central cooling due to enhanced impurity radiation. The central temperature increased with rf power even in the current drive mode and the temperature profile remained nearly constant. The sawtooth inversion radius also remained nearly constant at r ≃ 3 cm, at least up to the threshold power level above which sawteeth were stabilized, and hence were no longer observable. The sawteeth were eliminated once the rf power exceeded the initial OH power level, $P_{oh} \simeq 450$ kW. This is shown in Fig. 5, where we see that $P_{rf} \gtrsim 500$ kW is necessary to eliminate the sawteeth. At signficantly higher powers ($P_{rf} \gtrsim 850$ kW) the sawteeth were stabilized only for time durations of $\Delta t \sim 50$ msec into the rf pulse, but then returned for the remainder of the pulse. (We note that 50 msec is approximately the L/R time constant). Based on these results, it is not clear whether the q(0) > 1 condition is attained during the rf pulse (which would stabilize sawteeth), or a more subtle effect is operative, such as stabilization by replacement of a fraction of the resistive ohmic current with nearly collisionless current carried by the rf-driven tail electrons. Our estimates from the loop voltage drop and heating indicate that under these conditions only 15-20% of the total current is replaced by rf-driven currents. Code modeling indicates similar values, and also predicts that the local rf current generation is not sufficiently large to raise q(0) above unity. At present it has not been established if either an

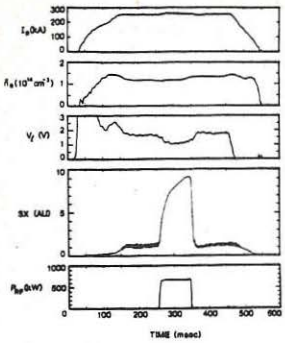

Fig. 4. Typical sawtooth stabilization shot in Alcator C; B = 6.2 T, $\Delta\phi$ = 90°, SX denotes the central soft x-ray signal.

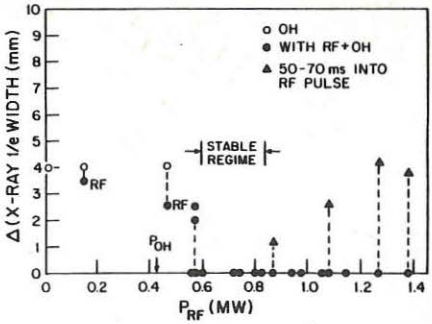

Fig. 5. Change in width of the soft x-ray brightness profile (indicative of sawtooth intensity) versus P_{rf}. The sawtooth activity disappears for $0.55 \lesssim P_{rf}(MW) \lesssim 0.85$. The triangles indicate recurrence of sawteeth 50-70 ms into the pulse, after initial quenching.

improved energy confinement time, or increased impurity concentration near the plasma center accompanies the sawtooth elimination. Further studies will be carried out to answer some of these questions.

ACKNOWLEDGMENTS

We thank the Alcator technical staff and Mr. D. Griffin for invaluable assistance in carrying out these experiments.

REFERENCES

/1/ M. Porkolab, et al., Proc. 11th Eur. Conf. on Contr. Fusion and Plasma Phys., Aachen, 1983 (EPS, 1983) Vol. I, 269.
/2/ M. Porkolab, et al., in Plasma Phys. and Contr. Nucl. Fus. Res., (Proc. 10th Int. Conf., London, 1984) Vol. I, IAEA, Vienna (1985) 463.
/3/ M. Porkolab, et al., Phys. Rev. Lett. 53, 1229 (1984).
/4/ S. M. Kaye and R. J. Goldston, Nucl. Fusion 25, 65 (1985).
/5/ P. Bonoli, R. Englade, and M. Porkolab, in Heating in Toroidal Plasmas (Proc. 4th Int. Symp., Rome, 1984, ed. by H. Knoepfel and E. Sindoni) publ. by Int. School of Plasma Phys., Varenna 1984, Vol. II, 1311.

Work supported by U.S. Department of Energy contract #DE-AC02-78ET51013.

ENERGY DEPOSITION PROFILE CALCULATION FOR LH WAVES AND COMPARISON WITH FT EXPERIMENT

E. Barbato and V. Zanza

Associazione EURATOM-ENEA sulla Fusione, Centro Ricerche Energia Frascati, C.P. 65 - 00044 Frascati, Rome (Italy)

INTRODUCTION

A realistic description of the physics of heating and current drive by LH waves in tokamaks would involve wave propagation in toroidal plasmas, absorption by strongly distorted electron and ion distribution functions, and transport processes [1,2]. If we want to do something simpler, retaining the physics, we may adopt a simplified model for the propagation, keeping the calculation of the absorption by the strongly distorted distribution functions [3]. Transport processes take place on a longer time scale with respect to the quasi-linear generation of the tail distribution function (d.f.) and can be neglected at least in a first approach. In this paper we present a calculation of the power deposition profile in LH heated plasmas, using such a model. In Sec. 2 the model is briefly described; in Sec. 3 the results obtained in applying it to FT experiments [4] are discussed; conclusions follow.

THE MODEL

A WKB approximation in cylindrical geometry is used in the treatment of the wave propagation, as well as a cold plasma dispersion relation in the electrostatic limit. As a consequence of the cylindrical geometry and of the fact that the poloidal wave momentum launched by the grill is vanishing, $n_\perp$ has only the radial component, while $n_\parallel$ has only the z component and it is a constant of motion. Furthermore, we restrict our attention only to those solutions providing all the absorption during the first inward pass. Within this scheme the equation determining the $n_\parallel$-spectrum of the wave energy density $W(n_\parallel)$ at each radial position, in the steady state, is

$$\frac{d}{dr}(v_{gr} W r) = -2\Gamma r W \qquad (1)$$

with the boundary condition at r=a

$$W(a,n_\parallel) v_{gr}(a,n_\parallel) = P_{RF}(n_\parallel)/2\Pi R\ 2\Pi a \qquad (2)$$

here v_{gr} is the radial component of the group velocity, $P_{RF}(n_\parallel)$ is the power spectrum at the plasma edge and $\Gamma=\gamma e+\gamma H+\gamma D+\nu c$ is the absorption rate due to resonant wave particle interaction (γe refers to the electron, γH to a minority of hydrogen and γD to deuterons) and to nonresonant collisional absorption on thermal electrons (νc) [5].

Equation (1) is coupled through the γ's to the equations for the electron and ion d.f., which in turn depend on W through the RF quasi-linear diffusion term. At each radial position the electron tail d.f. is described by the steady state 1-D equation [6]:

$$\frac{\partial}{\partial v_{\parallel}} [D_{QL}^{(e)} \frac{\partial}{\partial v_{\parallel}} fe(v_{\parallel}) + C^{(e)}(\frac{\partial}{\partial v_{\parallel}} + \frac{v_{\parallel}}{v_{The}^2})fe(v)] = 0 \qquad (3)$$

(The notations are the same as in Ref.[6].)

Similar equations [1] are assumed to hold for the two ion species present in the plasma (a minority of hydrogen in a deuterium plasma). In this case the perpendicular dynamic has to be retained:

$$\frac{1}{v_{\perp}} \frac{\partial}{\partial v_{\perp}} v_{\perp} [D_{QL}^{(i)} \frac{\partial fi(v_{\perp})}{\partial v_{\perp}} + C^{(i)}(\frac{\partial}{\partial v_{\perp}} + \frac{v_{\perp}}{v_{Thi}^2}) fi(v_{\perp})] = 0 \qquad (4)$$

where C^i is given in Ref.[7].

Following Valeo [1], to prevent the solution from extending to unphysically high energies, we truncate the ion d.f. at some velocity v_{LOSS} which is connected with some physical process (for example banana-losses). Solving the coupled Eqs (1-4) means finding the particle distribution functions with the self-consistent power spectrum. This can be easily done, since in order to find the distribution functions relevant to a certain radial shell we only need the power leaving the previous radial shell.

THE RESULTS

The model has been applied to a typical FT discharge in the electron heating regime [4]. Two different peak temperatures are considered: the one ($\hat{Te}$=1.7 keV) relative to the ohmic phase at the beginning of the RF pulse and the other relative to the steady state heated phase ($\hat{Te}$=3 keV). The other plasma parameters were $\hat{ne}=6.10^{13}cm^{-3}$, B=8 T. The Brambilla spectrum of the 2x2 waveguides grill was used.

Figure 1 shows the absorbed power density vs radius for $\hat{Te}$=1.7 keV (full line) and for $\hat{Te}$=3 keV (dotted line), while Fig.2 shows the residual power and the integrated absorbed power vs radius in the two cases.

It is worth mentioning that, although most power is launched within $n_{\parallel} \lesssim 3$, the power spectrum is actually extending up to $n_{\parallel}$=6 (see Fig.3). The power at high $n_{\parallel}$ plays an important role, as in the 0-D case [8]; when the conditions for the absorption of this part of the power spectrum occur, also a fraction of the power at low $n_{\parallel}$ is absorbed. This is shown by Fig.3 where the power spectrum at the plasma edge and at r=5 cm and at r=1 are shown. Coming back to Fig.2, we can comment on it in this way: at the beginning of the RF pulse only 50% of the power is absorbed at the first inward pass, while in the heated phase, almost all the power is absorbed. This is consistent with preliminary β poloidal measurements performed on FT in spite of the copper shell [9]. We get similar results when the 2x4

(ОПОП) power spectrum is used, but the deposition profile is more peripherical and a larger fraction of the power is absorbed both in the low and the high temperature cases.

When the density is increased, absorption by a 2% hydrogen minority begins to play a role; an average density $\bar{n}e=1.1\ 10^{14}cm^{-3}$ has to be reached in order to have more power absorbed by the hydrogen ions than by the electrons. The deposition profile for this case is shown in Figs 4 and 5, where standard FT density and temperature profiles were used. Although the model can reproduce the sharp switching off of the wave electron interaction experimentally observed [10], it gives a density limit a factor 2 higher than the experimental one ($\bar{n}e=5\ 10^{13}cm^{-3}$).

To conclude, we summarize the main results:

a) In the low density regime, where electron heating works, most power, in the heated phase, is absorbed within half radius by the electrons, without invoking any ad hoc broadening of the $n_{\parallel}$ spectrum.
b) The deposition profile depends on the launched spectrum.
c) At higher density absorption by a minority of hydrogen ions begins to play a role, giving rise to a density limit in the electron wave interaction which is a factor 2 higher than the experimental one.

REFERENCES

[1] E.J. Valeo, D.C. Eder, Course and Workshop on Applications of RF Waves to Tokamak Plasmas, Varenna, Vol.II, 493 (1985).
[2] P. Bonoli, R. Englade, M. Porkolab, Mass. Inst. of Technology, Plasma Fusion Center, rep. PFC/CP 84-6 March 1984.
[3] M. Brambilla, Y. Chen, Nucl. Fusion 23, 541 (1983).
[4] F. Alladio et al., Budapest 1985, Plasma Physics and Controlled Fusion, 28 N1A 179 (1976).
[5] P.M. Bellan, M. Porkolab, Phys. Fluids 19, 995 (1976).
[6] C.F.F. Karney, N.J. Fisch, Phys. Fluids 22, 1817 (1979).
[7] C.F.F. Karney, Phys. Fluids 22, 2188 (1978).
[8] S. Succi et al., Plasma Phys. 27, 863 (1985).
[9] F. Alladio, F. Crisanti, P. Micozzi, to be published.
[10] F. Alladio et al., Nucl. Fusion 24, 725 (1984).

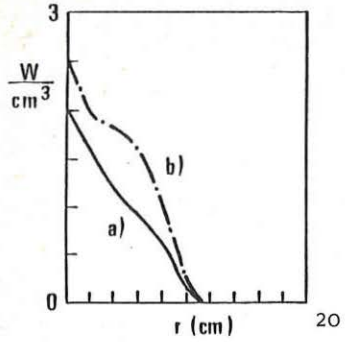

Fig. 1 Power density profile absorbed by the electrons at $\hat{n}e=6\times10^{13}$ cm^{-3} a) $\hat{T}e=1.7$ keV; b) $\hat{T}e=3$ keV

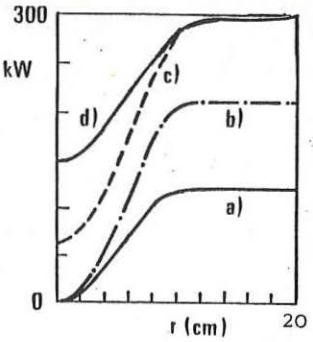

Fig. 2 Residual power vs r (d),c)) and integrated absorbed power vs r (a), b)) at $\hat{n}e = 6\times10^{13}$ cm^{-3}. Full lines $\hat{T}e=1.7$ keV; dotted lines $\hat{T}e=3$ keV

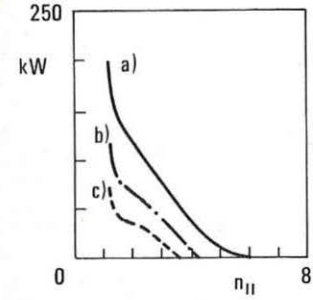

Fig. 3 Power Spectrum vs $n_{\parallel}$ for $\hat{T}e=3$ keV. a) at the edge; b) at r=5 cm; c) at r=1cm.

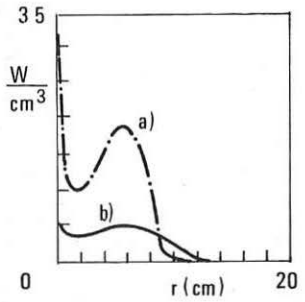

Fig. 4 Power density profile at $\hat{n}e=1.6\times10^{13}$, $\hat{T}e=1.2$ keV, $\hat{T}i=1$ keV. a) absorption by hydrogen minority; b) absorption by electrons

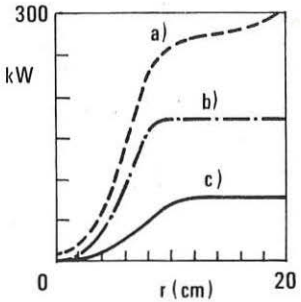

Fig. 5 The same plasma as Fig. 4. a) residual power vs r; b) integrated power absorbed by hydrogen minority; c) integrated power absorbed by electrons

LOWER HYBRID WAVE ACCESSIBILITY AS A MEANS FOR CURRENT PROFILE CONTROL

G. BRIFFOD - C. GORMEZANO - F. PARLANGE - D. VAN HOUTTE

Association EURATOM-CEA - Département de Recherches sur la Fusion Contrôlée
CENG-85X - 38041 Grenoble Cédex (France)

Powerful ICRH experiments on JET /1/ and Neutral Beam Injection of various species on TFTR /2/ have recently confirmed the insensitivity of the temperature and safety factor profile shapes to the heating profile and the important role played by the sawtooth activity on the overall performances. In order to overcome these limitations, we propose in this paper, in a Tokomak operating at constant plasma current :

. to control the resistive part of the current by driving and H.F. current by Lower Hybrid Wave.
. To act on the current profile, with the constraint that $q(o) > 1$ by controlling the wave penetration.

Constant plasma current Tokomak discharges in which a part of the current is driven by L.H.W. have been extensively studied on PETULA /3/ and this mode of operation has proven to be very efficient in stabilizing the sawtooth and M.H.D. activity /4/.

CONTROL OF THE OHMIC PART OF THE PLASMA CURRENT

In a purely ohmic Tokamak discharge, $j(r)$ and $T(r)$ are connected through the conductivity. The current profile can usually be expressed as :

$$J_p = J_{(o)} \left(1 - \frac{r^2}{a^2} \right)^{\nu} \text{ with } J_{(o)} = \frac{I_p}{\pi a^2} (\nu + 1) \text{ and } q_{(o)} = \frac{q(a)}{\nu+1}$$

a being the plasma radius. If in this discharge, operating at constant plasma current, a part of the current is driven by L.H.W. the loop voltage and the ohmic current drop in order to satisfy : $I_p = I_\Omega + I_{HF} = C^{st}$ (1)
where I_{HF} is the total H.F. current which includes the additional term computed by N. Fisch /5/ in presence of a D.C. electric field. Then, by the control of the H.F. power, I_{HF} can be adjusted in order that the safety factor on the axis due to the ohmic part of the plasma current is such that $q(o) = 1$. This condition and the fact that I_Ω, remains connected to the temperature permit to write :

$$J_\Omega = J_{\Omega(o)} \left(1 - \frac{r^2}{a^2}\right)^{\nu} \text{ with } J_{\Omega(o)} = J_{(o)} \frac{q(a)}{\nu + 1} \text{ and } I_\Omega = I_p \frac{q(a)}{\nu + 1} \quad (2)$$

with the condition $I_{HF} = I_p - I_\Omega = I_p \left(1 - \frac{q(a)}{\nu + 1}\right)$ (3)

The current profile $J_p = J_\Omega + J_{HF}$ is then fixed by the radial localization of J_{HF}. If there is no H.F. current on axis, $q(o)$ is fixed by the ohmic part of the plasma current.

CONTROL OF THE CURRENT PROFILE

In the current drive regime, $\omega > \omega_{LH}$, the wave is mainly electrostatic and

its penetration inside the plasma is fixed by the accessibility condition :

$$N_{//} \geq N_{acc(o)} = (1 + 1{,}02\,\frac{n}{B\phi^2} - \alpha\,\frac{n}{f^2})^{1/2} + (1{,}02\,\frac{n}{B\phi^2})^{1/2}$$

. If the wave index $N_{//}$ is greater than $N_{acc(o)}$ on axis, the wave reaches the plasma center and J_{HF} is peaked on the axis. The safety factor is then fixed by the sum of the two currents. The stabilization of the sawtooth which is observed in these conditions /7/ is due to the generation inside the q = 1 surface of an H.F. current carried by energetic electrons ($V_{//} = C/N_{//}$).

. If $N_{//}$ is lower than $N_{acc(o)}$, the wave penetration is limited to a radius $r = r_s$ fixed by accessibility condition $N_{//} = N_{acc}$. Moreover, if the width of the spectrum, $\Delta N_{//}$, is such that $N_{//} + 1/2\Delta N_{//} < N_{acc(o)}$, J_{HF} is localised in a ring around the axis. In this case, the safety factor on axis is fixed by $I\Omega$ alone, and the constraint $q_o > 1$ is satisfied by the condition (3). In absence of an analytical expression of J_{HF}, due to the gap problem, the current profile has been modelized /8/ by $J_{HF} = J^* \{1 - (\frac{r - r_s}{a - r_s})^2\}$

Two examples of the variation of the current profile which can be obtained by the localization of J_{HF} are shown in the Fig. 1 for :

$q_{(a)} = 2$, $\nu = 3$ and $r_s = 0{,}5\ a$ and $r_s = 0{,}75\ a$

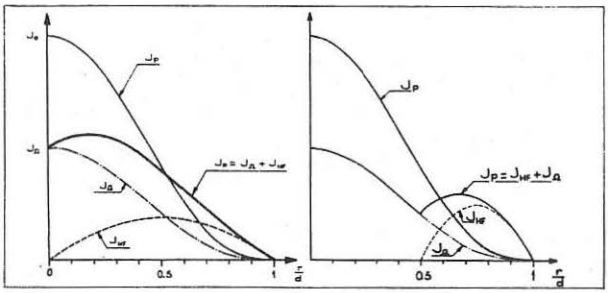

APPLICATION TO JET

Fig. 3 reproduces two JET temperature profiles /9/. One of these profiles is measured at t = 6 sec. when some skin effect is still present and the plasma free of sawtooth relaxation. The other one is measured at t=8.5 sec. when sawtooth activity has developped. To maintain $q_{(o)} = 1$ with the parameters of this discharge ; $\bar{n}_e = 2.6\ 10^{13}$, $B_\phi = 3.45$ T, $I_p = 2.86$ MA the required H.F. current is : $I_{HF} = I_p\,(1 - \frac{q(a)}{\nu + 1}) = 0.7$ MA

assuming $\nu = 4.5$ and $q(a) = 4.1$. From the curve $N_{acc} = f(\frac{r}{a})$ displayed on Fig. 2 for f $\simeq$ 4 GHz it can be seen that localization of I_{HF} on a ring of radius $r = r_s = 0.4$ a is obtained with a wave spectrum such that :

$$N_{//max} = 1.91 \qquad < N_{//} > = 1.61 \qquad \Delta N_{//} / <N_{//}> = 0.37$$

The number N_g and the width b of the waveguides needed to produce this spectrum are $N_g = \frac{4\pi}{\Delta\phi}\,\frac{<N_{//}>}{\Delta N_{//}} > 22$ $\quad b = \frac{\Delta\phi}{2\pi}\,\frac{\lambda}{<N_{//}>} = 1.26$ cm for $\Delta\phi = \frac{\pi}{2}$

This grill can be easily made with 6 multijunctions /10/ of 4 waveguides each. The control of the phase between the multijunctions allowing the localization of J_{HF} to be changed at a given density or the localization to be

kept constant when the density change. The power required to drive this H.F. current is : $P_{HF} = \frac{n(10^{13})\ R(m)\ \bar{I}_{HF}(MA)}{\eta} \simeq 3$ MW

In this estimation, $\bar{n} = 2.6\ 10^{13}$, $I_{HF} = 0.7$ MA, R = 3 m and $\nu = 1.8$. The value of the efficiency η is taken from PETULA-B data /11/ obtained for similar conditions ; f = 3.7 GHz, $\bar{n} = 3.1\ 10^{13}$, $B_\phi = 2.8$ T, $I_{HF}/I_p = \Delta V/V = 0.3$ (cf. Fig. 4). It should be noted that the improvement in the efficiency due to the D.C. electric field is greater on PETULA-B than on JET. However, this effect must be compensated by the higher magnetic field in JET (3.4 T) and the better directivity of the grill envisaged for JET as compared to the present PETULA-B grill. More detailed informations on this extrapolation may be found in ref. /12/.

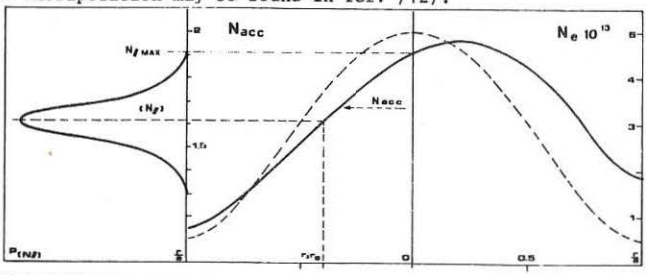

SCALING EXPERIMENTS ON PETULA

In view of an application on JET, experiments have been performed at high density, $\bar{n} = 6.10^{13}$, $B_\phi = 2.8$ T, with 400 kW, 3.7 GHz generator and a grill allowing a wave spectrum with an $\langle N_{//} \rangle$ ranging from 1.7 to 2.7 to be launched /6/.

For $\langle N_{//} \rangle = 1.7$ and $\bar{n} = 6.10^{13}$, the wave index is lower than $N_{acc(o)}$ on the axis. However, the wave penetrates inside the plasma as it can be seen from the fact that :

. The reflection coefficient remains unchanged and is very low indicating that the wave is not reflected back into the grill /13/.
. Significant loop voltage drop is observed and sawtooth activity disappears.

Sawtooth stabilization is obtained for $I_{HF}/I_p \simeq \Delta V/V = 0.3$ and for H.F. power of the order of the ohmic power /7/. For $N_{//} = 2.7$ and the same density, sawtooth relaxation cannot be suppressed with the available power.

In the whole range of density where sawtooth stabilization is observed $\bar{n} = 1$ to $6\ 10^{13}$, the accessibility condition, for $\langle N_{//} \rangle = 1.7$, changes from $N_{//} > N_{acc(o)}$ to $N_{//} < N_{acc(o)}$. However, no evidence of a modification of the radial profile of J_{HF} with density can be concluded from our present measurements. This may be due to the fact that in small size Tokamak like PETULA, significant H.F. current can only be driven in the central part of the plasma where the higher temperature (1 KeV) provide the fast electrons required to carry the current. On JET where the same temperature is observed at r = 0.75 a, and reaches more than 2 KeV at r = 0.5 a, the localisation of H.F. current should be easier.

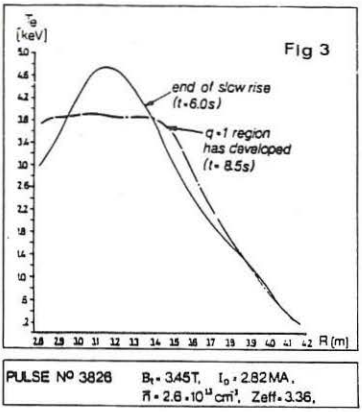

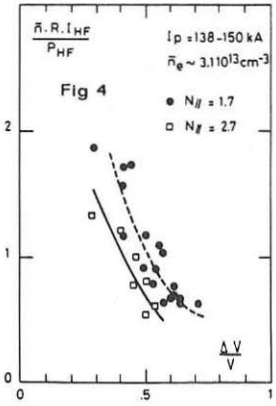

CONCLUSION

Lower Hybrid waves at 3.7 GHz and $\langle N_{//} \rangle = 1.7$ have been launched in Tokamak discharges where $\langle N_{//} \rangle < N_{acc(o)}$. The H.F. current generated in these conditions allow the sawtooth activity to be stabilized up to a density of $6\ 10^{13}$ p/cm^3.

On the basis of these results and on the fact that in hot plasma, the radial localisation of the wave should be easier it appears that in Tokamak operating at constant plasma current the replacement of a part of the ohmic current by an equivalent H.F. current carried by fast electrons along the lines of force and radially localized can be a new and efficient way to control the equilibrium and the stability of hot and dense plasma.

REFERENCES

/1/ J. JACQUINOT, 12th Eur. Conf., Budapest Sept. 1985
/2/ M. MURAKAMI and al, 12th Eur. Conf., Budapest Sept. 1985
/3/ C. GORMEZANO and al, I.A.E.A. Conf., London Sept. 1984
/4/ D. VAN HOUTTE and al, Nucl. Fusion, Vol. 24 N° 11 1984, Workshop on Tokamak Start up ERICE, July 1985
/5/ N.J. FISCH, Phys. of Fluids, 28, 1985 p. 245
/6/ G. REY and al, these proceedings
/7/ D. VAN HOUTTE and al, these proceedings
/8/ G. BRIFFOD, Rep. EUR-CEA FC, 1286, Sept. 1985
/9/ P.H. REBUT, 12th Eur. Conf., Budapest Sept. 1985
/10/ D. MOREAU, T.K. NGUYEN, Rep. EUR-CEA FC, 1246, 1983
/11/ C. GORMEZANO and al, these proceedings
/12/ C. GORMEZANO and al, JET report to be published
/13/ M. GONICHE and al, these proceedings.

Suppression of Magnetic Islands by Injection of Fast Waves in the JIPP T-IIU Tokamak

K. Toi, K. Ohkubo, R. Ando, R. Akiyama, Y. Hamada, S. Hirokura, E. Kako, K. Kawahata, Y. Kawasumi, K. Masai, K. Matsuoka, M. Mugishima, I. Ogawa, S. Tanahashi, Y. Taniguchi
Institute of Plasma Physics, Nagoya University, Nagoya 464, JAPAN

Abstract

In the high density regime of $f_o/f_{LH} \cong 1$ (pump frequency: f_o=800 MHz ; f_{LH} is lower hybrid frequency), m=2 tearing modes and major disruptions at $q(a) \sim 3$ are suppressed through rf current drive and/or production of high energy tail electrons by injection of fast waves near the lower hybrid frequency. Stabilization of m=2 tearing modes is observed in following three cases: in case I $\bar{n}_e \sim 5\times10^{12}$ cm^{-3}, $B_t \cong 1.2$ T, in case II $\sim 9\times10^{12}$ cm^{-3}, $\cong 1.7$ T, and in case III $\sim 1.5\times10^{13}$ cm^{-3}, $\cong 2.4$ T. The frequency of the poloidal field fluctuations decreases by about 70 % in case I and by about 30 % in case II during the rf pulse. On the other hand, the frequency increases by about 30 % in case III. The stabilization in cases I and II is considered to be achieved by slow wave current drive localized in the outer plasma region ($r/a \gtrsim 0.5$), since most of the fast waves launched can be mode-converted to slow waves in this region. The stabilization in case III, where most of the rf power in fast waves can be transmitted to the central high density plasma, is inferred to be due to fast wave current drive and/or production of high energy tail electrons assisted by an ohmic heating field.

1. Introduction

In many tokamaks, major disruptions were studied for low β_t or high β_t plasmas sustained by an ohmic heating current alone. These experiments showed that a large magnetic island caused by the m/n=2/1 tearing mode had a dominant role to trigger the major disruption. According to resistive mhd theory, tailoring of a current density profile is quite effective for suppression of m=2 tearing mode and disruptions [1,2] . As methods for tailoring the profile the following two options are possible: (i) local electron heating just outside the q=2 surface, and (ii) current profile control by rf current drive. The former option was successfully tested in the JIPP T-II tokamak using an additional current rise by the ohmic heating field [3,4] , and in T-10 using off-axis electron cyclotron heating [5] . The latter option is more advantageous than the former one because the current density profile is determined by the power spectrum of launched waves almost independent of electron energy transport. It has been pointed out by recent theoretical work that the local current drive in phase with island rotation is most efficient [6-8] . Several experimental supports on the latter option are obtained from lower hybrid current drive experiments: in PETULA-B large island of m=2 tearing modes are suppressed [9] , and in PLT sawteeth oscillations are suppressed exhibiting an enhanced bulk electron heating near the plasma center [10] . In this paper, we present the suppression of m=2 modes and disruptions through current drive and/or production of high energy tail electrons by injection of fast waves.

2. Experimental Setup

The experiments are carried out in the JIPP T-IIU tokamak (R_o = 91 cm, a_L = 23 cm) at B_t=1.2-2.4 T and $\bar{n}_e$=0.3-1.6×10^{13} cm^{-3} . The fast magnetosonic waves at f_o=800 MHz are launched with powers up to 150 kW into hydrogen plasmas from a four-element dipole antenna array [11] , where f_o roughly corresponds to the 20-th to 40-th ion cyclotron harmonic. In the experiments, the phase difference between adjacent antennas has been set at $\Delta\varphi$=0° to minimize the rf power reflected. The ohmically heated target plasmas are produced in the following operation regime of safety factor at plasma surface $q(a)\cong$2.5-3.5 and $\bar{n}_e/(B_t/R)\cong$0.5 , where m=2 tearing modes are strongly excited and major disruptions frequently occur.

3. Stabilization in Low and Medium Density Regimes (cases I and II)

When more than 60 kW rf power is injected into low density plasmas ($\bar{n}_e\lesssim$7×10^{12} cm^{-3}) with large m=2 fluctuations ($\tilde{B}_\theta/B_\theta\cong$1.5-2 %) which bring about major disruptions, the plasma current is almost replaced by rf-driven current ($I_{rf}/I_p\cong$1). Then, the amplitude of the fluctuations is clearly reduced to the noise level ($\lesssim$0.1 %) as shown in Fig.1. The rf power injected is roughly a third of the ohmic input in the case without rf. A dramatic reduction in frequency of the fluctuations is observed during the rf pulse. Note that the direction of the mode rotation is that of electron diamagnetic drift. The reduction in the frequency is consistent with the decrease in bulk electron temperature due to rf current drive. This result suggests that a tokamak plasma sustained by rf-driven current alone is quite stable against low-m tearing modes. In the medium density regime of $\bar{n}_e$=7-9×10^{12} cm^{-3} (case II), the plasma current is partially replaced by rf-driven current ($\eta=I_{rf}/I_p\lesssim$0.3). Then, both amplitude and frequency of the modes are reduced roughly by the factor $(1-\eta)$.

4. Stabilization in High Density Regime (case III)

In the fast wave current drive, we encountered the so-called density limit [11] which is similar to that in lower hybrid current drive, i.e., $n_{li_m}\cong$8×10^{12} cm^{-3} . The stabilization of tearing modes has been tried in the higher density $\bar{n}_e$=1.4-1.6×10^{13} cm^{-3} at B_t=2.4 T. The relative amplitude of fluctuations in the case without rf is about 0.3 % and grows to more than 2 %, then the discharge is disrupted. The fluctuation amplitude is clearly reduced to less than 0.1 % by injection of fast waves (Fig.2). By the application of rf, the plasma current rises accompanying the slight decrease in a loop voltage. The second harmonic electron cyclotron emission near the plasma center increases by about 50 %. Note that the tail electron temperature derived from X-ray spectra increases from ~4 keV to ~9 keV. The energy spectra of charge exchanged neutrals exhibit only a slight tail component ($n_{it}/n_{ib}\lesssim$5-10 % on assumption of bi-Maxwellian; n_{it}/n_{ib} is a ratio of tail ion component to the bulk one). In contrast to cases I and II, the frequency of the poloidal field fluctuations gradually increases during the rf pulse. The increase in the frequency may be due to the increase in bulk electron temperature by collisional power flow from tail electrons.

In Fig.3, we summarize the stabilization effects by fast wave current drive and/or production of high energy tail electrons for the above three cases. This figure shows the relative amplitude of m=2 mode

fluctuations as a function of rf power injected into the torus. This figure also shows the results in lower hybrid current drive using a 4-waveguide grill [12] , where the phase difference between adjacent waveguide is set at $\Delta\varphi=90°$. They are essentially similar to those in case II.

5. Discussion

From a linear theory of propagation of fast waves near the lower hybrid frequency, we calculate the range of $n_{\parallel}$ for propagation without mode conversion to slow waves, i.e., $1.6 \lesssim n_{\parallel} \lesssim 2.1$ for case I, $1.4 \lesssim n_{\parallel} \lesssim 2.3$ for case II and $1.2 \lesssim n_{\parallel} \lesssim 2.4$ for case III. The power spectrum of launched waves spreads in the range of $1 \lesssim n_{\parallel} \lesssim 2.2$ at $\Delta\varphi=0°$. For case I, most of rf power may be deposited in the outer plasma region of $r/a \gtrsim 0.5$. The stabilization is considered to be due to current drive by slow waves mode-converted in the outer region. In case II, fast waves with about 30 % of launched power can propagate into the plasma center. The fast waves with the remaining power will be mode-converted in the outer plasma region and absorbed there. In this case, also mode-converted slow waves will play an essential role in current drive and stabilization of tearing modes. The case III is in a typical regime where fast waves launched with most of the rf power can penetrate in the plasma center. The fast waves will produce high energy tail electrons around that region. A peaked current density profile which is stable against the m=2 tearing mode [1] is expected through current drive and/or high energy tail production assisted by an ohmic heating field. The above discussion seems to be consistent with the experimental observations.

The rf power required to stabilize the m=2 mode seems to be appreciably larger than the theoretical prediction, although the prediction depends on the detailed shape of the current density profile. It is inferred that in this experiment rf-driven current and/or high energy tail electrons are not always generated preferentially in the O-point of a magnetic island against the X-point.

Acnowledgements

The authors would like to thank all the members of JIPP T-IIU group and Dr. D Eckhartt for their discussions.

References

[1] FURTH, H.P., et al., Phys. Fluids 16 (1973) 1054.
[2] GLASSER, A.H., et al., Phys. Rev. Lett. 38 (1977) 234.
[3] TOI, K., et al., Nucl. Fusion 19 (1979) 1643.
[4] TOI, K., et al., Nucl. Fusion 22 (1982) 465.
[5] ALIKAEV, V.V., et al., Proc. 10th Intern. Conf. on Plasma Phys. and Controlled Nucl. Fusion Res., London(1984), IAEA Vienna (1985) vol.1, p. 419.
[6] YOSHIOKA, K. et al., Nucl. Fusion 24 (1984) 565.
[7] RUTHERFORD, P.H., PPPL report PPPL-2277(1985).
[8] IGNAT, D.W., et al., PPPL report PPPL-2278(1985).
[9] VAN HOUTTE, D., et al., Nucl. Fusion 24 (1984) 1485.
[10] CHU, T.K., US JAPAN Workshop on RF Heating and Current Drive, Kyoto(1985).
[11] OHKUBO, K., et al., this conference.
[12] MATSUMOTO, K., et al., this conference.

Fig.1 Discharge characteristics in the low density regime (case I); I_p: plasma current, $\bar{n}_e$: line-averaged electron density, P_{OH}: ohmic input, P_{rf}: net rf power, $\tilde{B}_\theta/B_\theta$: relative amplitude of poloidal fluctuations, and $P(f)$: power spectrum of the fluctuations.

Fig.2 Discharge behavior in the high density regime (case III); I_μ: second harmonic electron cyclotron emission.

Fig.3 Relative amplitude of m=2 modes as a function of net rf power for cases I, II, III and that for lower hybrid current drive.

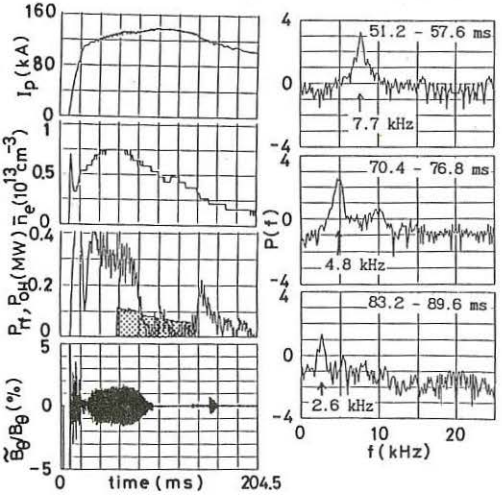

Fig.1

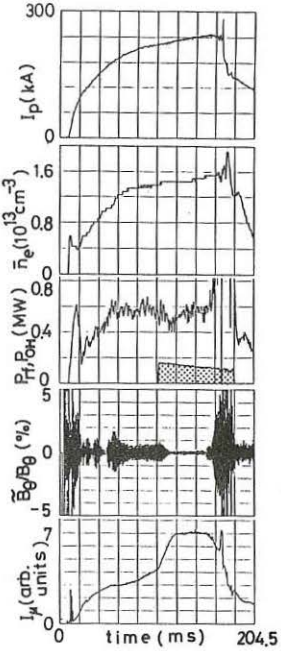

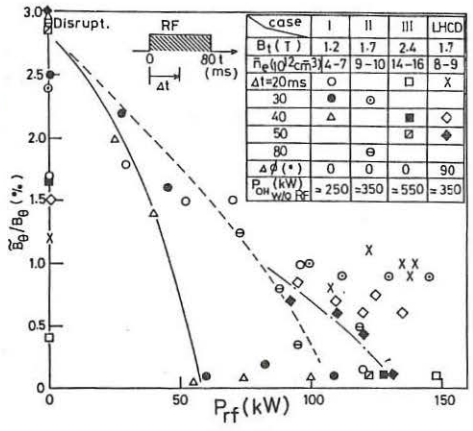

Fig.3

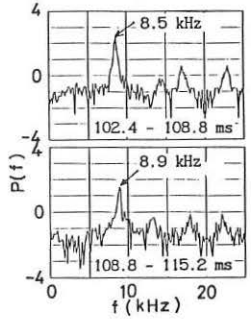

Fig.2

Index